

ADA112069

AFWAL-TR-81-3049



COMPUTERIZED BUCKLING ANALYSIS OF SHELLS

DAVID BUSHNELL

APPLIED MECHANICS LABORATORY
LOCKHEED PALO ALTO RESEARCH LABORATORY
3251 HANOVER STREET
PALO ALTO, CA 94304

December 1981

Final Report for period October 1977 - December 1980

Approved for public release; distribution unlimited.

FLIGHT DYNAMICS LABORATORY
AIR FORCE WRIGHT AERONAUTICAL LABORATORIES
AIR FORCE SYSTEMS COMMAND
WRIGHT-PATTERSON AIR FORCE BASE, OHIO 45433

DTIC FILE COPY

DTIC
ELECTED
MAR 16 1982
H

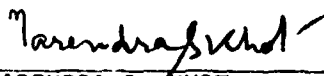
82 03 16 003

NOTICE

When Government drawings, specifications, or other data are used for any purpose other than in connection with a definitely related Government procurement operation, the United States Government thereby incurs no responsibility nor any obligation whatsoever; and the fact that the government may have formulated, furnished, or in any way supplied the said drawings, specifications, or other data, is not to be regarded by implication or otherwise as in any manner licensing the holder or any other person or corporation, or conveying any rights or permission to manufacture use, or sell any patented invention that may in any way be related thereto.

This report has been reviewed by the Office of Public Affairs (ASD/PA) and is releasable to the National Technical Information Service (NTIS). At NTIS, it will be available to the general public, including foreign nations.

This technical report has been reviewed and is approved for publication.



NARENDRA S. KHOT
Project Engineer



FREDERICK A. PICCHIONI, Lt Col, USAF
Chief, Analysis & Optimization Branch

FOR THE COMMANDER



RALPH L. KUSTER, JR., Col, USAF
Chief, Structures & Dynamics Div.

"If your address has changed, if you wish to be removed from our mailing list, or if the addressee is no longer employed by your organization please notify AFWAL/FIBR _____, W-PAFB, OH 45433 to help us maintain a current mailing list".

Copies of this report should not be returned unless return is required by security considerations, contractual obligations, or notice on a specific document.

REPORT DOCUMENTATION PAGE		READ INSTRUCTIONS BEFORE COMPLETING FORM
1 REPORT NUMBER AFWAL-TR-81-3049	2 GOVT ACCESSION NO AD-A112 069	3 REPORT CATALOG NUMBER
4 TITLE (and Subtitle) Computerized Buckling Analysis of Shells	5 TYPE OF REPORT & PERIOD COVERED FINAL REPORT Oct 1977 - Dec 1980	6 PERFORMING ORG REPORT NUMBER
7 AUTHOR(s) David Bushnell	8 CONTRACT OR GRANT NUMBER(s) AFOSR GRANT F49620-77-C-0122 and USAF CONTR: F33615-76-C-3105	
9 PERFORMING ORGANIZATION NAME AND ADDRESS Applied Mechanics Laboratory Lockheed Palo Alto Research Laboratory 3251 Hanover Street Palo Alto, California 94304	10 PROGRAM ELEMENT PROJECT, TASK AREA & WORK UNIT NUMBERS 2307-N1-02	
11 CONTROLLING OFFICE NAME AND ADDRESS Flight Dynamics Laboratory (AFWAL/FIBRA) AF Wright Aeronautical Laboratories (AFSC) Wright-Patterson Air Force Base OH 45433	12 REPORT DATE June 1981	13 NUMBER OF PAGES 418
14 MONITORING AGENCY NAME & ADDRESS (if different from Controlling Office)	15 SECURITY CLASS (of this report) UNCLASSIFIED	15a DECLASSIFICATION DOWNGRADING SCHEDULE
16 DISTRIBUTION STATEMENT (of this Report) Approved for public release; distribution unlimited.		
17 DISTRIBUTION STATEMENT (of the abstract entered in Block 20, if different from Report)		
18 SUPPLEMENTARY NOTES		
19 KEY WORDS (Continue on reverse side if necessary and identify by block number) Shells Composites Buckling Stiffened Numerical Methods Elastic-Plastic Nonlinear Survey		
20 ABSTRACT (Continue on reverse side if necessary and identify by block number) The purpose of the many examples of buckling presented here is to give the reader a physical "feel" for shell buckling. With such knowledge the engineer will have an enhanced ability to foresee situations in which buckling might occur and to modify a design to avoid it. He will be able to set up more appropriate models for tests and analytical predictions with the use of sophisticated computer programs.		

A brief description of the two kinds of buckling, collapse and bifurcation, is first given. This followed by a simple mathematical example involving a shallow truss, which displays most of the phenomena to be illustrated later with thin shells. Many examples of classical buckling of uniformly loaded cylindrical and spherical shells are then shown, with comparisons between test and theory to emphasize the sensitivity of these buckling loads to initial imperfections. Illustrations are presented in which the cause of failure is nonlinear collapse due either to large deflections or to both large deflections and nonlinear material behavior. A major section follows in which are given examples of axisymmetric shells that fail by bifurcation buckling. In these examples nonuniformity or nonlinearity of the prebuckling behavior is significant. The effects of boundary conditions and eccentric loading on bifurcation buckling of shells of revolution are demonstrated, with emphasis on buckling of monocoque or stiffened shells under uniform external pressure and axial compression. In the following section interaction curves are given for monocoque cylinders under combined axial compression and internal or external pressure corresponding to various boundary conditions. Interaction curves are also presented for ring-stiffened cylinders and angle-ply laminated cylinders. Examples of buckling of nonuniformly loaded shells, with thermal as well as mechanical loading, are then presented, including cylindrical and conical shells heated along narrow axial strips. Buckling of ring-stiffened cylinders is illustrated by a variety of examples that demonstrate discrete vs. smeared ring models, the effects of residual stresses and deformations due to welding and cold bending, and the influence of ring web flexibility on buckling load predictions. Buckling of prismatic structures such as oval cylinders and panels is treated next. Included are descriptions of modal interaction in panels built up of thin sections and demonstrations of local cross section deformation in the bifurcation buckling modes corresponding to general instability. The following section focuses on the sensitivity of predicted buckling loads to initial geometrical imperfections. Koiter's asymptotic theory of initial post-bifurcation behavior is summarized and several examples are given in which use of this and other nonlinear models of post-bifurcation behavior lead to predictions of failure loads of imperfect shell structures. The volume closes with a chapter on axisymmetric collapse and bifurcation buckling of bodies of revolution that consist of combinations of thin shell segments and solid segments to which shell theory cannot be applied with sufficient accuracy.

Accession For	
NTIS	<input checked="" type="checkbox"/>
DTIC	<input type="checkbox"/>
U.S. Govt.	<input type="checkbox"/>
Justice	<input type="checkbox"/>
By	
Distrib	<input type="checkbox"/>
Avail	
Dist	<input type="checkbox"/>

FOREWORD

This report describes the work performed by Lockheed Palo Alto Research Laboratory, Palo Alto, California 94304. The work was sponsored by Air Force Office of Scientific Research, Bolling AFB, Washington, D.C. under Grant F49620-77-C-0122 and by the Flight Dynamics Laboratory, Air Force Wright Aeronautical Laboratories, Wright-Patterson AFB, Ohio under Contract F33615-76-C-3105.

The work was completed under Task 2307N1, "Basic Research in Behavior of Metallic and Composite Components of Airframe Structures." The work was administered by Lt Col J. D. Morgan (AFOSR) and Dr N. S. Khot (AFWAL/FIBRA)

The contract work was performed between October 1977 and December 1980. The technical report was released by the Author in December 1981.

TABLE OF CONTENTS

SECTION	Page
1. DESCRIPTIONS OF TYPES OF INSTABILITY AND CLASSICAL BUCKLING PROBLEMS	1
Introduction	1
Summary of this Chapter	2
Purpose	6
Why Do Shells Buckle?	7
What is Buckling?	8
Various Types of Bifurcation Buckling	10
Capsule of Recent Progress in Buckling Analysis	12
Asymptotic Analysis	13
General Nonlinear Analysis	13
Axisymmetric Structures	15
Simple Examples to Illustrate Various Types of Buckling	16
Column Buckling	16
Prebuckling Solution of Fundamental Equilibrium Path	17
Bifurcation Buckling	17
Post-Bifurcation Stability	19
Loss of Stability and Imperfections	20
Buckling of Plates	21
"Classical" Buckling of Cylindrical and Spherical Shells	23
Cylindrical Shells Under Axial Compression	23
A Caution for Novice Users of Computer Programs for Buckling	27
Stiffened Cylinders Under Axial Compression	27
Cylinders Under Uniform External Pressure or Torsion	28
Spherical Shells Under Uniform External Pressure	28
Spherical Caps	29
2. NONLINEAR COLLAPSE	31
Summary	31
Elastic-Plastic-Creep Collapse of Axially Compressed Monocoque Cylinders	31
No-Creep	31
Creep Included	33
Creep Collapse of Ring-Stiffened Cylinder Under External Hydrostatic Pressure	34
Snap-Through of Very Shallow Spherical Caps	35
Straight and Curved Tubes Under Bending and External Pressure	36
Introduction	36
Long Tubes and Elbows: A Survey of Work Done	38
Elastic Models	38
Bending Tests on Long Elastic-Plastic Straight Pipes and Elbows	40
Elastic-Plastic Piping Analysis	40
Axisymmetric Model of Long Pipe or Elbow Bending Problem	41
Simulation of the Pipe Bending Problem by Thermal Loading of a Torus	43
Collapse and Bifurcation Buckling Moment of a Long Straight Pipe	43

TABLE OF CONTENTS (continued)

	<u>Page</u>
Collapse of a 90° Elastic Plastic Elbow	45
Collapse and Bifurcation Buckling Due to Bending of Straight Elastic Pipes of Finite Length	45
Collapse of Cylindrical Panels and Shells with Concentrated Loads and Cutouts	49
Introduction	49
Cylindrical Panels and Shells with Concentrated Normal Loads . .	51
Panels	51
Complete Cylindrical Shells	52
Collapse of Axially Compressed Cylindrical Shells with Cutouts .	53
Rectangular Cutouts	53
Circular Cutouts	56
Collapse of Axially Compressed Noncircular Cylinders	57
Axially Compressed Elliptical Cylinder	57
Axially Compressed "Pear-Shaped" Cylinder	58
Axially Compressed Cylindrical Shell with Local Load Path Eccentricity	60
3. BIFURCATION BUCKLING IN WHICH NONUNIFORMITY OR NONLINEARITY OF THE PREBUCKLING STATE IS IMPORTANT	61
Introduction	61
Summary	62
Bifurcation Buckling Due to Edge Effects and Localized Circumferential Compression	63
Bifurcation Buckling Due to Edge Effects	63
Cylindrical Shell Under Axial Compression	63
Externally Pressurized Spherical Caps with Edge Rings . . .	64
Buckling of Shallow and Deep Spherical Caps	67
Buckling Due to Localized Hoop Compression	70
Thermal Buckling of Cylindrical Shells	70
Introduction	70
Buckling of Cylinder Heated Halfway along Length	72
Buckling of Axisymmetrically Heated Clamped Cylinder . . .	75
Buckling of an Internally Pressurized Rocket Ruel Tank	77
Local Buckling at a Field Joint in a Large Rocket Payload Shroud	78
Bifurcation Buckling of Spherical Shells Under Meridional Tension Combined with Hoop Compression	80
Axial Load Applied Uniformly Over Latitude with Finite Radius r_1	80
Axial Load Applied at a Point	83
Buckling of Internally Pressurized Vessel Heads	84
Introduction	84
Cause and Characteristics of Nonsymmetric Bifurcation Buckling .	86
Difference in Elastic Behavior of Ellipsoidal and Torispherical Heads	88
Elastic Bifurcation Buckling	88
Elastic-Plastic Bifurcation Buckling	91
Conclusions about Bifurcation Buckling of Internally Pressurized Heads	95

TABLE OF CONTENTS (continued)

	<u>Page</u>
Bifurcation Buckling Near the Axisymmetric Collapse Load	99
A Summary of Examples Already Described	99
Failure of a Water Tank	101
An Attempt to Predict Elastic-Plastic Buckling of the Large Steel Water Tower Including Fabrication Effects	104
Tank Configuration and Discretized Model	104
Welding	105
Mismatch	106
Cold Bending	106
Conclusions	109
 4. EFFECT OF BOUNDARY CONDITIONS AND ECCENTRIC LOADING	110
Introduction	110
Summary	114
Effect of Boundary Conditions on Buckling of Monocoque Shells	115
Cylinders Subjected to Uniform External Hydrostatic Pressure .	116
Cylinders Subjected to Uniform Axial Compression	117
Inextensional Buckling	118
Simulation of Effects of Local Plastic Flow by Appropriate Con- straint Conditions	120
Effect of Boundary Conditions and Loading Eccentricity on Buckling of Axially Compressed Stiffened Cylindrical Shells	122
Boundary Conditions	122
Load Eccentricity	127
 5. INSTABILITY OF SHELLS OF REVOLUTION SUBJECTED TO COMBINED LOADS AND NONSYMMETRIC LOADS	130
Summary	130
Combined Loading	130
Nonsymmetric Loading	131
Monocoque Cylindrical Shells Under Combined Loading	132
Axial Compression or Bending and Internal Pressure	132
Torsion and Internal Pressure	134
Stiffened Cylindrical Shells Under Combined Loading	136
Buckling of Composite Cylindrical Shells Under Combined Loading . .	138
Definitions	138
Previous Work Done	138
Buckling Under Combined Loads	139
Buckling of Nonaxisymmetrically Loaded Shells of Revolution	141
Modeling Considerations	141
Examples of Buckling of Nonsymmetrically Loaded Shells of Revo- lution	143
Thermal Buckling of Nonsymmetrically Heated Shells	145
Introduction	145
Anderson and Card Tests	149

TABLE OF CONTENTS (continued)

	<u>Page</u>
Simply-Supported Cylinder Heated on an Axial Strip	150
Parameter Study - Cylinders Heated on Axial Strips	152
Buckling of Conical Shells Heated on Axial Strips	153
Conclusions	154
Buckling of Nuclear Reactor Containment Vessel due to Ground Motion during an Earthquake	155
 6. BUCKLING OF RING-STIFFENED SHELLS OF REVOLUTION	 157
Introduction	157
Summary	159
Elastic Buckling of Ring-Stiffened Cylinders under External Hydrostatic Pressure	160
Elastic-Plastic Buckling of Ring-Stiffened Cylinders under External Hydrostatic Pressure	162
Effects of Residual Stresses and Deformations on Plastic Buckling of Ring-Stiffened Shells of Revolution	165
Review of Previous Work	165
Cold Bending	166
Welding	167
Bending and Welding	168
Residual Deformations from Welding Internal v. External Rings	171
Effect of Cold Bending and Welding on Buckling of Ring-Stiffened Cylinders	172
Cold Bending of a Flat Sheet into a Cylindrical Shell of Infinite Length	173
Initial Elastic Loading	174
Elastic-Plastic Loading	175
Relaxation	176
Obtaining a Value of R_0	177
Simulation of Cold Bending in BOSOR5	178
Procedure for Using BOSOR5 to Calculate Buckling Loads Including Residual Effects due to Cold Bending and Welding	179
Comparison with Tests on Cold-Bent Sheet	180
Buckling of Cold Bent and Welded Ring-Stiffened Cylinder: comparison of Test and Theory	180
Possible Causes of the Remaining Discrepancy between Test and Theory	183
Effect on Buckling of Deformations of the Ring Cross Sections	184
General and Local Instability	184
Modal Interaction	185
Comparison with Tests in which Local Ring Deformations are Important	190
Crippling of Ring Web	190
Wide Column Ring Web "Buckling"	191
General Instability of Ring-Stiffened Shallow Conical Shell	193

TABLE OF CONTENTS (continued)

	<u>Page</u>
7. BUCKLING OF PRISMATIC SHELLS AND PANELS	194
Summary	194
Use of a Computer Code for Shells of Revolution to Predict Buckling	
Loads of Prismatic Structures	195
Introduction	195
Analysis Technique	198
Convergence Studies	200
Numerical Results	201
Nonuniformly Loaded Circular Cylindrical Shells	202
Stress and Buckling of Elliptic Cylinders	203
Cylinders of Noncircular Cross Section under Axial Compression	206
Bifurcation Buckling of Axially Compressed Panels	207
Introduction	207
Numerical Results	211
Buckling of Axially Compressed Corrugated and Beaded Panels	211
Effect of Manufacturing Method on General and Local Buckling of a Semi-Sandwich Corrugated Panel	214
Modal Interaction and Imperfection Sensitivity of Axially Compressed Prismatic Structures	218
Introduction	218
Two Types of Modal Interaction	218
Previous Work Done	220
Summary of This Section	221
Modal Interaction in an Axially Compressed Two-Flange Column	225
The Perfect Column	226
Buckling with Imperfect Flanges but Straight Column Axis	227
Stability of Equilibrium at the Bifurcation Load, K_b	229
Buckling of Columns with Imperfect Flanges and Imperfect Axes	230
Modal Interaction in Axially Compressed, Eccentrically Stiffened Panels	231
Optimization of Imperfect Columns and Panels in which Modal Interaction Occurs	233
Columns	233
Panels	234
Axially Stiffened Cylindrical Shells	238
Transverse Shear Deformation Effects	241
Laminated Composite Materials	242
8. IMPERFECTION SENSITIVITY	245
Introduction	245
Summary	245
Asymptotic Post Buckling Theory - A Summary	247
Elastic Post-Bifurcation Analysis	249
Elastic-Plastic Post-Bifurcation Analysis	252
Perfect Elastic-Plastic Structures	253
Imperfect Elastic-Plastic Structures	254

TABLE OF CONTENTS (continued)

	<u>Page</u>
Qualitative Guidelines for Imperfection Sensitivity	256
Axially Compressed Cylindrical Shells and Panels	258
Brief Survey of Work Done	258
Nonlinear Post-Buckling Behavior of Perfect Shells	258
Various Boundary Conditions and Nonuniform or Nonlinear Pre-buckling Effects	259
Empirically Derived Design Formulas for Monocoque Cylinders	261
Design Rules for Stiffened Cylinders	261
Effect of Geometric Imperfections	263
Governing Equations for Asymptotic Post-Buckling Approach	266
Kármán-Donnell Equations	266
Prebuckling Analysis	268
Asymptotic Analysis	269
Initial Post-Bifurcation Load-Deflection Curve	273
Imperfection Sensitivity	274
Numerical Methods Used to Solve the Various Boundary-Value Problems and Evaluate b , \bar{b} , and α	274
Governing Equations for the Nonlinear Approach	276
Hutchinson's Formulation [4.340]	277
Árbocz and Babcock's Formulation [4.341]	280
Behavior of Perfect Cylinders	282
Behavior of Imperfect Cylinders	282
Axially Compressed Monocoque Cylindrical Shells: Numerical Results	284
Cylinders with Sinusoidal Axisymmetric Imperfections	284
Cylinders with Localized Imperfections	287
Cylinders with Random Imperfections (Axial Compression or External Pressure)	288
Cylinders with Internal Pressure	291
Axially Compressed Cylindrical Panels	293
Axially Compressed Oval Cylinders	295
Axially Compressed Stiffened and Composite Cylindrical Shells: Numerical Results	296
Asymptotic Post-Buckling Analysis of Axially Stiffened Cylinders	296
Laminated Cylindrical Shells Made of Composite Material	302
Calculation of Load-Carrying Capability Based on Measurements of Imperfections	306
Design Method for Axially Compressed Cylinders	308
Critical Load from Wide-Column Theory	309
Critical Load from Extended Version of Koiter's Special Theory	310
Design Philosophy	312
Numerical Results	312
Conclusions	313
Imperfection Sensitivity of Cylinders Under Uniform Hydrostatic Pressure and Torsion	315
Uniform Hydrostatic Pressure	315
Monocoque Cylinders	315
Axially-Stiffened Cylinders	316
Ring-Stiffened Cylinders	317
General Conclusions	318

TABLE OF CONTENTS (continued)

	<u>Page</u>
Cylinders Under Torsion	319
Imperfection Sensitivity of Spherical Shells	319
Introduction	319
Governing Equations for the Asymptotic Post-Buckling Analysis	323
Application to a Shallow Spherical Segment	330
Classical Buckling Analysis	330
Post-Buckling Equilibrium Paths	331
Special Theory vs. General Theory	335
Difficulties Encountered in the Asymptotic Analysis of Complete Spherical Shells	335
Other Asymptotic Imperfection Sensitivity Analyses for Doubly-Curved Shells of Revolution	337
Spherical Caps with Axisymmetric Loading Over Part of the Surface	337
Results of Fitch and Budiansky [4.391].	337
Questions Raised by the Results Shown in Figure 4.304	339
Nonsymmetrically Loaded Spherical Shell	342
Initial Post-Buckling Behavior of Toroidal Segments	343
Limitations of Asymptotic Imperfection Sensitivity Theory	343
Bifurcation Buckling with Stable Post-Buckling Behavior	345
Spherical Shell with an Inward-Directed Point Load	345
Stable Post-Buckling Shearing Deformations	347
Wagner Beam	347
Computerized Analysis of a Complex Stiffened Curved Panel Under Shear	348
Wrinkling of an Antenna Membrane	348
The Southwell Method for Determination of Buckling Loads from Non-Destructive Tests	351
Definition of the Method	351
Examples of Application of the Southwell Method	354
Limitations of the Southwell Method	355
9. BUCKLING OF HYBRID BODIES OF REVOLUTION	360
Introduction	350
Summary	361
Ring-Stiffened Cylindrical Shells Under Uniform Hydrostatic Pressure	363
Spherical Shells Embedded in Structural Foam	365
Elastic-Plastic Instability of Axially Compressed Shells of Revolution with Axisymmetric Frangible Joints	366
Comparison of Test and Theory for a Frangible Joint Embedded in a Simple Cylindrical Shell	367
Test Configuration and BOSOR6 Model	367
Discretization	369
Pads	369
Material Properties	370
Junction and Contact Conditions Between the Primacord Tube and the Cavity Provided for It	371
Numerical Results	373

TABLE OF CONTENTS (continued)

	<u>Page</u>
Frangible Joint Embedded in a Complex Shell Structure	375
Structural Configuration and Segmented Model	376
Substitution of Uniform Axial Compression for the Actual	
Loads	377
Axisymmetric Collapse of the Rocket Interstage	378
Effect of a Minor Design Change	378
Effect of a Steel Primacord Tube	379
REFERENCES	380
TABLES	419
FIGURES	446

SECTION 1
DESCRIPTIONS OF TYPES OF INSTABILITY
AND CLASSICAL BUCKLING PROBLEMS

Introduction

To the layman, buckling is a mysterious, perhaps even awe-inspiring phenomenon that transforms objects originally imbued with symmetrical beauty into junk (Fig. 1). Occasionally unaware of the possibility of buckling, engineers have designed structures (Fig. 2(a)) with inadequate safety margins (Fig.

2(b)). The large cylindrical tower on the left in Fig. 3(a) failed in 1956 [4.1] because of buckling of a torispherical end closure at its lower end. The 38-meter-tall water tower sketched in Fig. 4(c) collapsed in 1972 [2] when it was being filled for the first time. The collapse of the entire tower (Fig. 4.4(a)) was triggered by local instability in the conical section at the deepest water level (Fig. 4(b)). A large expensive shroud for a payload to be orbited around the earth (Fig. 5(a)) failed during proof testing because of local buckling near a field joint (Fig. 5(b, c)) [3].

The purpose of this volume is to remove some of the mystery associated with buckling of thin shells by showing many examples of its occurrence and explaining its cause. Perhaps the material presented here will help to prevent future disasters of the type just illustrated.

Summary of the Volume

Section 1 contains a brief description of two kinds of buckling, collapse and bifurcation, followed by a simple mathematical example involving a shallow truss, which displays most of the phenomena to be illustrated later with thin shells. Many examples of classical buckling of uniformly loaded cylindrical and spherical shells are then shown, with comparisons between test and theory to emphasize imperfections.

Section 2 concerns shell structures in which the cause of failure is nonlinear collapse due to either large deflections or to both large deflections and nonlinear material behavior. In certain of the cases the predicted nonlinear load is compared to a critical load calculated from a linearized bifurcation buckling model. Included in Section 2 are descriptions of elastic-plastic collapse of cylindrical shells subjected to uniform axial compression or external pressure, elastic-plastic collapse of straight and curved pipes subjected to external pressure and bending, elastic collapse of shallow spherical caps under external pressure and elastic collapse of cylindrical panels and shells under combined axial compression and concentrated loads. Section 2 closes with descriptions of collapse failure of axially compressed cylinders with cutouts, noncircular cylinders, and cylinders with local axisymmetric load path eccentricity.

Section 3 gives examples of axisymmetric shells in which failure is due to bifurcation buckling. In all of the examples nonuniformity or nonlinearity of the prebuckling behavior is important. Several illustrations are provided of bifurcation buckling due to local edge effects and local hoop compression. These are followed by numerous examples in which the prebuckled state is characterized by meridional tension combined with hoop compression. Bifurcation buckling of internally pressurized torispherical shells, both in the elastic and in the plastic range of material behavior, is described in detail. The section closes with an example in which bifurcation buckling and axisymmetric collapse occur almost simultaneously.

Section 4 provides examples that illustrate the effects of boundary conditions and eccentric loading on bifurcation buckling of shells of revolution. The emphasis is on buckling of monocoque and stiffened cylindrical shells under uniform external pressure and axial compression. Examples are also given of inextensional buckling modes, which are associated with very low critical loads; of change in effective "boundary" condition due to development of a plastic region in the prebuckling phase; and dependence of the buckling load on small inward and outward axisymmetric imperfections of an axially compressed stringer-stiffened short cylindrical shell.

Section 5 is devoted to combined loading of cylindrical shells and nonsymmetric loading of shells of revolution. Interaction curves are given for monocoque cylinders under combined axial compression and internal or external pressure corresponding to various boundary conditions. Post-buckling configurations are shown for either axial compression or torsion combined with internal pressure. Interaction curves are also presented for ring or stringer-stiffened cylinders and angle-ply laminated cylinders. Examples of

nonsymmetrically loaded shells of revolution include buckling of a payload shroud such as that shown in Fig. 5(a) due to nonsymmetric pressure, buckling of a ring-stiffened cylinder under combined bending and nonuniform heating, buckling of cylindrical and conical shells heated along narrow axial strips, and buckling of a steel containment vessel due to compressive stresses generated by vertical and horizontal components of ground acceleration during an earthquake.

Section 6 is on bifurcation buckling and collapse of ring-stiffened shells with emphasis given to cylindrical shells. The section begins with an illustration of the effect of discrete rings on the prebuckling state and general instability bifurcation buckling mode. Comparisons between test and theory are given for elastic buckling of machined specimens in a study in which the effect of axial restraint at the boundaries is investigated. Elastic-plastic buckling of a series of steel specimens is then described, followed by an example of a titanium shell which is predicted to fail by nonsymmetric bifurcation buckling when creep is neglected and by axisymmetric collapse when creep is included in the analysis. The effect on predicted buckling loads of initial imperfections and residual stresses due to weld shrinkage at stations where discrete rings are attached to a shell is illustrated for an ellipsoidal shell subjected to hydrostatic compression. The combined effects on failure of cold bending an initially flat sheet into a cylindrical shell and subsequently welding ring stiffeners to it are described. The section closes with a number of examples showing the importance in certain cases of treating discrete ring webs as flexible shell branches in analytical models for prediction of axisymmetric collapse and nonsymmetric bifurcation buckling.

Section 7 contains several illustrations of buckling of prismatic shells and panels, that is, structures that have a cross section that is constant in one of the coordinate directions. Included are descriptions of modal interaction in panels built up of thin sections and demonstrations of local cross section deformation in the bifurcation buckling modes of initially perfect panels. Predicted bifurcation buckling modes are shown for noncircular cylinders under axial compression and comparisons between test and theory are given for oval cylinders under external pressure. The section closes with brief discussions of the effect of transverse shear deformation on the buckling of composite plates and on the usefulness of the Southwell plot for prediction of instability failure.

Section 8 focuses on the sensitivity of predicted buckling loads to initial geometrical imperfections. The section opens with a chart of empirical knockdown factors for monocoque cylinders subjected to axial compression and a review of various types of pre- and post-buckling load deflection curves. The Koiter theory is briefly summarized and imperfection sensitivity factors for various systems are plotted. A design method for other than monocoque shells is outlined and illustrated for cylinders with combined axial compression and internal pressure. Charts are given that show typical measured imperfections in small laboratory models and a large industrial ring and stringer stiffened shell. Buckling interaction curves for a laminated cylindrical shell are plotted and compared to test results on an imperfect specimen. The section closes with several examples in which bifurcation buckling is stable and the structures carry increasing loads far into the post-buckling regime.

Section 9 demonstrates axisymmetric collapse and bifurcation buckling of bodies of revolution that consist of combinations of thin shell segments and solid segments to which shell theory cannot be applied with sufficient accuracy. An example is given of buckling of a hydrostatically compressed ring-stiffened cylinder in which the rings and portions of shell to which the rings are attached are modeled as solid regions with use of isoparametric quadrilaterals of revolution and the rest of the cylinder is modeled as a series of thin shell segments. Other examples include buckling of a spherical shell embedded in a softer elastic material and collapse of a complex cylinder-cone combination containing a frangible joint. The region in the immediate neighborhoods of notches in the frangible joint are modeled with use of solid elements.

Purpose

The purpose of the many examples presented here is to give the reader a physical "feel" for shell buckling. With such knowledge the engineer will have an enhanced ability to foresee situations in which buckling might occur and to modify a design to avoid it. He will be able to set up more appropriate models for tests and analytical predictions, including failure due to buckling. The emphasis in this chapter is not on the development of equations for prediction of instability. For such material the reader is referred to the book by Brush and Almroth [4] and the material in Ref.[430].

Throughout the text numbers in square brackets [] refer to references listed at the end of the text.

Why Do Shells Buckle?

The property of thinness of a shell wall has a consequence that has been pointed out in Ref. [430]: The membrane stiffness is in general several orders of magnitude greater than the bending stiffness. A thin shell can absorb a great deal of membrane strain energy without deforming too much. It must deform much more in order to absorb an equivalent amount of bending strain energy. If the shell is loaded in such a way that most of its strain energy is in the form of membrane compression, and if there is a way that this stored-up membrane energy can be converted into bending energy, the shell may fail rather dramatically in a process called "buckling," as it exchanges its membrane energy for bending energy. Very large deflections are generally required to convert a given amount of membrane energy into bending energy.

The way in which buckling occurs depends on how the shell is loaded and on its geometrical and material properties. The prebuckling process is often nonlinear if there is a reasonably large percentage of bending energy being stored in the shell throughout the loading history. Two types of buckling exist: nonlinear collapse and bifurcation buckling. Nonlinear collapse is predicted by means of a nonlinear stress analysis. The stiffness of the structure, or the slope of the load-deflection curve, decreases with increasing load. At the collapse load the load-deflection curve has zero slope and, if the load is maintained as the structure deforms, failure of the structure is usually dramatic and almost instantaneous. This type of instability failure is often called "snap-through," a nomenclature derived from the many early tests and theoretical models of shallow arches and spherical caps under

uniformly distributed loads. These very nonlinear systems initially deform slowly with increasing load. As the load approaches the maximum value, the rate of deformation increases until, reaching a status of neutral equilibrium in which the average curvature is almost zero, the shallow arches and caps subsequently "snap through" to a post-buckled state which resembles the original structure in an inverted form.

The term "bifurcation buckling" refers to a different kind of failure, the onset of which is predicted by means of an eigenvalue analysis. At the buckling load, or bifurcation point on the load-deflection path, the deformations begin to grow in a new pattern which is quite different from the prebuckling pattern. Failure, or unbounded growth of this new deflection mode, occurs if the postbifurcation load-deflection curve has a negative slope and the applied load is independent of the deformation amplitude.

What is Buckling?

To most laymen the word "buckling" evokes an image of failure of a structure which has been compressed in some way. Pictures and perhaps sounds come to mind of sudden, catastrophic collapse involving very large deformations. From a scientific and engineering point of view, however, the interesting phases of buckling phenomena generally occur before the deformations are very large when, to the unaided eye, the structure appears to be undeformed or only slightly deformed.

To reiterate and enlarge upon what was written above, in the static analysis of perfect structures, the two phenomena loosely termed "buckling" are collapse at the maximum point in a load vs. deflection curve and bifurcation buckling. These two types of instability failure are illustrated in Figs.

6 and 7. The axially compressed cylinder shown in Fig. 6 deforms approximately axisymmetrically along the equilibrium path OA until a maximum or limit load λ_L is reached at point A. If the axial load λ is not sufficiently relieved by the reduction in axial stiffness, the perfect cylinder will fail at this limit load, following either the path ABC along which it continues to deform axisymmetrically, or some other path ABD along which it first deforms axisymmetrically from A to B and then nonaxisymmetrically from B to D. Limit point buckling, or "snap-through" occurs at point A and bifurcation buckling at point B. The equilibrium path OABC, corresponding to the axisymmetrical mode of deformation, is called the fundamental or primary or prebuckling path and the postbifurcation equilibrium path BD, corresponding to the nonaxisymmetrical mode of deformation is called the secondary or post-buckling path. Buckling of either collapse or bifurcation type may occur at loads for which some or all of the structural material has been stressed beyond its proportional limit. The example in Fig. 6 is somewhat unusual in that the bifurcation point B is shown to occur after the collapse point has been reached. In this particular case, therefore, bifurcation buckling is of less engineering significance than axisymmetric collapse.

A commonly occurring situation is illustrated in Fig. 7(a). The bifurcation point B is between O and A. If the fundamental path OAC corresponds to axisymmetrical deformation and BD to nonaxisymmetrical deformation, then initial failure of the structure would generally be charac-

terized by rapidly growing nonaxisymmetrical deformations. In this case the collapse load of the perfect structure λ_L is of less engineering significance than the bifurcation point, λ_C .

In the case of real structures which contain unavoidable imperfections there is no such thing as true bifurcation buckling. The actual structure will follow a fundamental path OEF, with the failure corresponding to "snap-through" at point E at the collapse load λ_S . If point B in Fig. 7(a) corresponds to bifurcation into a nonsymmetric buckling mode, the collapse at E will involve significant nonsymmetric displacement components. Although true bifurcation buckling is fictitious, the bifurcation buckling analytical model is valid in that it is convenient and often leads to a good approximation of the actual failure load and mode.

Various Types of Bifurcation Buckling

In Fig. 7(b) the load is plotted as a function of amplitude of the bifurcation buckling mode. Since the bifurcation buckling mode is orthogonal to the prebuckling displacement pattern of the perfect shell, its amplitude remains zero until the bifurcation point B is reached. The curve BD in Fig. 7(b) implies that the post-buckling state is unstable: the load carrying capability λ decreases with increasing amplitude of the bifurcation buckling mode.

All real structures are imperfect. The imperfection shape is, in general, not orthogonal to the bifurcation buckling mode. If one expressed the deformation of the imperfect structure as a sum of two components, the fundamental prebuckling equilibrium state of the perfect structure plus the bifurcation buckling mode of the perfect structure (presumed here to be unique),

then one would obtain the curve OEF in Fig.7(b) if one plotted the amplitude of the bifurcation modal component vs. load for the imperfect structure. The amplitude of the bifurcation modal component would increase at an increasing rate until instability via nonlinear "snap-through" or collapse would occur at the reduced load λ_S . The difference between the critical bifurcation load λ_C of the perfect structure and the collapse load λ_S of the imperfect structure depends on the amplitude of the initial imperfection w_{bo} . A chart of λ_S/λ_C vs w_{bo} would characterize the sensitivity of the maximum load λ_S to initial geometrical imperfections. According to the jargon that has become accepted over the years, the structure to which the curves in Fig. 7(b) correspond is called "imperfection sensitive" because imperfections reduce its maximum load carrying capability. (Of course, it is not the structure that is sensitive to imperfections, but the maximum load it can safely support!)

Neither all structures nor mathematical models of them behave as shown in Fig. 7(b). Figure 8 shows various types of post-buckling behavior. A linearized model of elastic stability, that is an eigenvalue formulation of the buckling problem, implies load-deflection behavior shown in Fig. 8(a): The amplitude of the eigenvector, the bifurcation buckling mode, is indeterminate, which implies that the load λ remains constant $\lambda = \lambda_C$ with increasing deflections w_b . The equilibrium path for the slightly imperfect structure follows the rectangular hyperbolic path,

$$w_b = w_{bo}/(\lambda_C/\lambda - 1) \quad (1)$$

shown dotted in Fig. 8(a).

If nonlinear post-buckling effects are accounted for, equilibrium paths for most structures have the forms shown in Fig. 8(b, c, d). The asymmetric nature of the curves in Fig. 8(b) indicates that the structure continues to carry loads above the bifurcation load λ_c if it is forced to buckle one way, but collapses if allowed to buckle the other. An example of this type of behavior is a structure with parts that move relative to each other as buckling proceeds in such a way that these parts come in contact and support each other for positive deflections but move away from each other forming gaps for similar negative deflections. Specifically, a built-up panel consisting of a flat sheet riveted to a corrugated sheet is such a structure. Roorda [5] has demonstrated this asymmetric post-buckling behavior for perfect and imperfect frames with eccentric loads. His results are presented in [4]. The symmetric stable post-buckling behavior displayed in Fig.8 (c) is typical of axially compressed isotropic flat plates. The perfect plate loaded precisely in its neutral surface buckles either way with equal ease and the post-buckled equilibrium state is stable. The symmetric unstable post-buckling behavior shown in Fig. 8(d) is typical of the early post-bifurcation regimes of axially compressed thin cylindrical shells and externally pressurized thin spherical shells.

Capsule of Recent Progress in Buckling Analysis

Recent progress in our capability to predict buckling failure can be categorized into three main areas:

(1) development of asymptotic post-buckling theories and applications of these theories to specific classes of structures, such as simple plates, shells, and panels [6 - 8];

(2) development of general-purpose computer programs for calculation of static and dynamic behavior of structures including large deflections, large strains, and nonlinear material effects [8 - 10];

(3) development of special purpose computer programs for limit point axisymmetrical buckling and nonaxisymmetrical bifurcation buckling of axisymmetric structures [11 - 14] .

Asymptotic Analysis: The asymptotic post-buckling analyses surveyed in [6 - 8] rest on theoretical foundations established by Koiter [15], whose general elastic post-bifurcation theory leads to an expansion for the load parameter λ in terms of the buckling modal amplitude w_b which is valid in the neighborhood of the critical bifurcation point in (λ, w_b) space. The primary aims of the asymptotic analyses are to calculate limit loads for perfect and imperfect structures. These analyses have contributed vital physical insights into the buckling process and the effect of structural or loading imperfections on this process.

General Nonlinear Analysis: The general-purpose computer programs in widespread use since the early 1970's and presently being written are based on principles of continuum mechanics established for the most part by the late 1950's and set forth in several texts [16 - 21]. The structural continuum is discretized into finite elements as described in the texts [22 - 25] and various strategies are employed to solve the resulting nonlinear problem [8]. The nonlinearity is due to moderately large or very large deflec-

tions and nonlinear material behavior. Various plasticity models are described in texts, conference proceedings, and survey articles identified in Ref. [8]. Additional papers on the formulation, discretization, and solution of nonlinear structural problems appear in many symposia proceedings, also identified in Ref. [8]. The primary aim of this vast body of work, most of which was done in the 1970's, has been to produce reliable analysis methods and computer programs for use by engineers and designers. Thus, the emphasis in the literature just cited is not primarily on the acquisition of new physical insight into buckling and post-bifurcation phenomena, but on the creation of tools that can be used to determine the equilibrium path OEF in Fig. 7 (a) for an arbitrary structure and on proof that these tools work by use of demonstration problems, the solution of which is known. In most cases, no formal distinction is made between prebifurcation and post-bifurcation regimes; in fact, simple structures are modeled with imperfections so that potential bifurcation points (such as B in Fig. 7 (a)) are converted into limit points such as E. The buckling problem loses its special qualities as illuminated so skillfully in the asymptotic treatments and becomes just another nonlinear analysis, requiring perhaps special physical insight on the part of the computer program user because of potential numerical traps such as bifurcation points and limit points.

Figures 7 (a) and (b) illustrate the two very different approaches to the buckling problem described in the last two paragraphs. In the general nonlinear approach the computations involve essentially a "prebuckling" analysis, or a determination of the unique equilibrium states along the fundamental path OEF in Fig. 7 (a). In the asymptotic approach, Fig. 7(b), the

prebuckling state is often known a priori. The secondary path BD of the perfect structure and (in the elastic case) the limit point E on the fundamental path of the imperfect structure are determined by expansion of the solution in a power series of the bifurcation modal amplitude which is asymptotically exact at the bifurcation point B.

Axisymmetric Structures: The third approach to the buckling problem, development of special-purpose programs for the analysis of axisymmetric structures, forms a sort of middle ground between the asymptotic analysis and the general-purpose nonlinear analysis. The approach is similar to the asymptotic treatment because in applications it is restricted to a special class of structures and the distinction between prebuckling equilibrium and bifurcation buckling is retained. It is similar to the general nonlinear approach in that the continuum is discretized and the nonlinear prebuckling equilibrium problem is solved by "brute force." The emphasis is on the calculation of the prebuckling fundamental path, OB or OA in Fig. 7(a), and determination of the bifurcation point B and its associated buckling mode, not on calculation of post-bifurcation behavior BD or of the load-deflection path OEF of the imperfect structure. The goals of this third approach are to create an analysis tool for use by engineers and designers and to use this tool in extensive comparisons with tests both to verify it and to obtain physical insight into the buckling process.

Simple Examples to Illustrate Various Types of Buckling

Column Buckling

In order to make the discussion of the basic concepts introduced in connection with Figs. 7 and 8 less abstract, we will relate it to a simple two-column structure that exhibits the types of behavior displayed in Fig. 8. This example is from Ref. [4].

The behavior of a column under an axial load is governed by the equation (see, for instance Ref.[26]) :

$$EI \frac{\partial^2 \theta}{\partial s^2} = - P \sin \theta \quad (2)$$

where s and θ are defined in Fig. 9. For all values of P this equation has the solution $\theta = 0$, corresponding to unbuckled equilibrium. However, for values of $P > P_{CR} = EI(\pi/L)^2$ a solution with $\theta \neq 0$ also exists. This solution corresponds to equilibrium forms with a bent column and is illustrated in Fig. 9. In the plot, η represents the part of the column shortening that is caused by the bending of the column. Hence, the equilibrium path corresponding to the first solution (straight column) is represented by the vertical axis. The Euler load P_{CR} is the value of the axial load at which the vertical axis is intersected by the post-buckling curve corresponding to the bent equilibrium form.

Figure 10 shows a structure consisting of two flexible bars or columns subjected to a load P . Denoting the length of the deformed column by L' we have

$$\frac{N}{EA} = \frac{1}{L} (L-L') = 1 - \cos B / \cos \beta \quad (3)$$

where $B = \arcsin (b/L)$ and N is the axial load in the columns, i.e.,
 $N = P/(2 \sin \beta)$. With

$$\lambda = EI(\pi/L)^2, \quad \rho = I/A(\pi/L)^2 \quad (4)$$

we introduce

$$P^* = P/\lambda \quad \text{and} \quad N^* = N/\lambda \quad (5)$$

The relation between deformation δ/L and load P^* is readily obtained in the parametric representation

$$\begin{aligned} \delta/L &= \sin B - \sin \beta \\ P^* &= \frac{2}{\rho} \sin \beta (1 - \cos B / \cos \beta) \end{aligned} \quad (6)$$

Prebuckling Solution or Fundamental Equilibrium Path: Numerical solutions of Eq. (6) are shown in Fig. 11 for two different structures, both with $h/L = 0.1$, one with $\rho = 2 \times 10^{-4}$ and one with $\rho = 4 \times 10^{-4}$. With increasing load the stiffness $\partial P^* / \partial \delta$ decreases and at a deformation corresponding to $\delta/L = 0.04$ ($\delta/h = 0.4$) a maximum occurs in each of the two load displacement curves. We consider the case in which P is a dead weight load. Then as the maximum is reached and the structure cannot carry additional load, it snaps into an inverted position such that the two columns are subjected to tension. The curves in Fig. 11 labeled $\rho = 2 \times 10^{-4}$ and $\rho = 4 \times 10^{-4}$ are analogous to the curve OAC in Fig. 7 (a).

Bifurcation Buckling: We notice, however, that if $N^* > 1$, i.e., $N > EI(\pi/L)^2$ then the columns will buckle. From the post-buckled load-deflection curve

for the column (Fig. 9) we see that for reasonably small buckling deflection the column deforms under constant load $N^* = 1$. For all practical purposes, then, we can assume that the axial load for the buckled column is independent of the shortening and given by $N^* = 1$. A secondary or post-buckled equilibrium form with slightly bent bars is represented by

$$P^* = \frac{\tan B - \delta/b}{[1 - (\tan B - \delta/b)^2]^{1/2}} \quad (7)$$

This equilibrium form corresponds to $N^* = 1$ and exists only for values of δ larger than that for which buckling occurs

At the point of intersection between the fundamental equilibrium path Eq. (6) and the secondary solution represented by Eq. (7), the columns will begin to buckle. This occurs for the more slender columns, $\rho = 2 \times 10^{-4}$, at $P^* = 0.155$. The load cannot be increased beyond this value: The structure fails by bifurcation buckling with the columns temporarily bending during the process. For the structure with $\rho = 4 \times 10^{-4}$, the point of intersection (bifurcation) occurs beyond the maximum in the primary load displacement curve, indicating that the columns are straight at the inception of snap through. The behavior represented by the curve OA'B'D in Fig. 11 is analogous to that represented by the curve OABD in Fig. 6; the behavior represented by the curve OBD in Fig. 11 is analogous to that represented by the curve OBD in Fig. 7(a).

In bifurcation buckling analysis it is often assumed that nonlinearities and geometrical changes in the prebuckling range can be omitted. As the columns buckle at $N^* = 1$, the critical load of the structure in such a model is

$$P^* = 2 \sin B = 2h/L \quad (4.8)$$

Figure 12 shows how the critical load of the two-column structure varies with the parameter h/L . With h/L less than about 0.075 the structure will collapse at the maximum in the load displacement curve - the columns are straight as snap-through begins. With higher values of h/L the critical load is represented by the curve marked "Bifurcation with Nonlinear Prebuckling." For comparison, the critical load is also shown corresponding to the simplified analysis in which precritical deformations are omitted (Eq. (8)). For larger values of h/L this represents a good approximation. At $h/L = 1$ it is a rigorous solution.

Post-Bifurcation Stability: We consider now a structure that has been slightly modified as shown in Fig. 13 by addition of a linear spring which carries a part of the load.

Figure 14 shows load displacement curves for two structures with $b/L = 0.1$ and $\rho = 2 \times 10^{-4}$. One is without a spring ($c = 0$) and the other includes a spring with spring constant $c = 2.5$. The load displacement diagrams with spring, primary and secondary, are obtained by addition of $P_{\text{SPRING}}^* = c(\delta/L)$ to the value of P^* corresponding to $c = 0$.

With a spring, buckling occurs, of course, at the same value of δ/L . However, if the spring constant is sufficiently large the slope of the line for the secondary solution becomes positive. The increase of the load in the spring is more than sufficient to compensate for the decrease in the load carried by the columns.

The two-column structure discussed here illustrates the behavior of structures of a more general nature. For example, the curve in Fig. 11 labeled OA'B'D is typical of failure of axially compressed cylindrical shells which buckle plastically and develop nonsymmetric folds after the load has reached its maximum value, as shown in Fig. 6. The curve in Fig. 11 labeled OBD is typical of shallow spherical caps under uniform external pressure in which nonlinear prebuckling effects are important but failure is by nonsymmetric bifurcation buckling. A rather thick cylindrical shell under axial compression deforms axisymmetrically throughout the collapse process. This would be indicated in Fig. 11 by a primary equilibrium path similar in shape to the curve OA'B'C but lying under it and not intersecting the column bifurcation line at all. A very thin complete spherical shell under uniform external pressure would have a primary equilibrium path that is linear in the prebifurcation range OB. Similarly, very thin cylindrical shells supported in such a way as to prevent early buckling at the ends would display essentially linear prebifurcation behavior. Heavily stiffened shells display behavior similar to that represented by the curve OBD in Fig. 14. After the skin buckles at B, much of the load that was originally carried by it is gradually transferred to the stiffeners as the depths of the buckles grow in the post-bifurcation regime BD.

Loss of Stability and Imperfections: It is important to notice that in the passing of a maximum in the primary path the structure loses stability. Under a load exceeding this maximum there exists no equilibrium configuration in the immediate neighborhood. The structure is set in motion and the process of buckling is violent.

On the other hand, the existence of a bifurcation point indicates only that the equilibrium on the primary path loses its stability. The consequences of this loss of stability on the primary path are not immediately clear. As the equilibrium on the primary path loses its stability at the bifurcation point, the structural behavior is governed by the conditions on the secondary path. Thus a bifurcation point signifies only a load level at which a new deformation pattern begins to develop. It does not necessarily indicate loss of structural stability. The equilibrium on the secondary path may be unstable. This is the case in our example of a two-column structure without the spring. In this case the loss of stability on the primary path results in the loss of stability of the structure. Buckling is violent and in addition the critical load is more or less sensitive to imperfections. With some initial crookedness the columns begin to bend in the prebuckling regime. There is no real bifurcation but the primary path approaches gradually the secondary path for a perfect structure. The behavior of imperfect structures is indicated by the broken lines in Fig. 14.

On the other hand, if equilibrium on the secondary path is stable, as in the case with $c = 2.5$ in Fig. 14, the structure can take additional load beyond the bifurcation point. However, a new deformation pattern, in some sense orthogonal to the prebuckling configuration, begins to develop and the stiffness of the structure may be considerably reduced.

Buckling of Plates

In Figure 15 (a) is shown a plate simply supported on all four edges and subjected to axial compression. It is assumed that the axial load P_x is

applied by means of a rigid block that enforces uniformity in the y -direction of axial edge displacement u_0 . Figures 15 (b) and (c) show load-deflection curves for perfect and imperfect plates. In tests of actual plates, which of course contain unavoidable imperfections, it is difficult to detect the onset of buckling because it happens gradually, as one might expect from Fig. 15 (b). The bifurcation point on the load-deflection curve for the perfect plate does not correspond to failure of the structure, but indicates a load at which the perfect plate starts to bow laterally. With further increase in uniform end shortening above the bifurcation value, the axial compressive stress resultant N_x begins to redistribute, becoming more and more concentrated near the edge supports, as depicted in Fig. 16 (b).

The stress resultant distributions across the width of the plate at a certain axial station x are shown for four values of axial compression by the curves 1-1, 2-2, 3-3, and 4-4 in Fig. 16 (b). At bifurcation the stress resultant is uniform and equal to N_{cr} . Near the edges the axial fibers are straighter than they are near the middle. Therefore, the end shortening is accomplished primarily by membrane compression, resulting in a large N_x . Near the midwidth the same end shortening is accomplished primarily by bending, resulting in a small N_x . The behavior would be qualitatively similar if the plate were compressed by uniform axial load rather than uniform end shortening: The regions in the neighborhood of the ends $x = 0$ and $x = a$ remain fairly straight because of the restraint against lateral displacement w there. As the post-bifurcation lateral displacement in the central region increases the edge regions at $x = 0, a$ act as webs which, through shear, transfer the load away from the central region of the plate to similar effective axially oriented beams near the edges at $y = \pm b/2$. These effective axial beams carry most of the compressive load.

Approximate maximum loads for axially compressed stiffened plates are derived for design purposes from the so-called von Karman effective width formula [27]:

$$b_{\text{eff}} = b (N_{\text{cr}}/N_{\text{max}})^{1/2} \quad (9)$$

in which b_{eff} is an effective width shown in Fig. 16(c) over which one can assume that the load in the plate is carried, and N_{max} is the maximum stress resultant that can be carried because of yielding or some other stress failure criterion. In the past the effective width formula (4.9) was used to calculate maximum bending moments carried by airplane fuselages and wings.

Similar design procedures have been developed for plates subjected to in-plane bending or shear loading. A comprehensive discussion of the ultimate strength of plates in bending, shear, and combined bending and shear is given in Chapter 5 of Ref. [28].

"Classical" Buckling of Cylindrical and Spherical Shells

Cylindrical Shells Under Axial Compression

The problem of buckling of thin cylindrical shells under axial compression has received far more attention than most problems in structural mechanics because of the extraordinary discrepancy between test and theory which remained unexplained for so many years. Hoff [29] gives a meticulous and very readable survey of work done up to 1966. Brush and Almroth devote a major portion of a chapter of their book [4] to the subject.

The post-buckled state of an axially compressed cylinder is illustrated in Fig. 17. During a test of even a very carefully made cylinder an isolated buckle initially appears at an average stress considerably below the predicted bifurcation value of

$$\sigma_{cl} = [3(1-\nu^2)]^{-1/2} Eh/a \approx .6Eh/a \quad (10)$$

This buckle is generally followed by a cluster of buckles in the same neighborhood which very rapidly deepen, change shape, and spread over a considerable portion of the surface. The post-buckled pattern shown in Fig. 17 was obtained by axial compression of the cylinder with a close fitting mandrel inside to prevent excessive growth of the buckles and consequent formation of plastic hinges at their boundaries. Thus the buckle pattern spread over the entire surface. Figures 18 and 19 demonstrate the dramatic discrepancy between test and theory over a wide range of radius-to-thickness and length.

The most significant trend of these data is the increasing discrepancy between test and theory with increasing radius-to-thickness ratio a/h . It is this trend that provides the clue that the discrepancy arises from the extreme sensitivity of the critical load to initial imperfections: A reasonable measure of geometrical quality is the ratio of initial deviation $w_0(x,\theta)$ from the perfect cylindrical shape to thickness h . It is clear that for a given fabrication method, this ratio will increase with increasing radius-to-thickness ratio.

One of the first studies of the sensitivity of the critical load to initial geometric imperfections was carried out by Donnell and Wan [30]. Figure 20(a) shows load-deflection curves obtained from their analysis. The Koiter theory [6], to be described later, provides rigorous proof of the extreme sensitivity of the critical load to initial geometric imperfections.

For many years several researchers attempted to obtain safe design loads for thin axially compressed cylinders by using numerical methods to calculate the post-buckling load deflection curve from nonlinear theory. It was thought that the minimum post-buckling load would provide a lower bound to the load-carrying capability of the shell. These attempts are very carefully documented by Hoff [29], from which Fig. 20(b) is taken. The post-buckled curves labeled "CASE(1)",..."CASE(7)" indicate results of calculations on the digital computer with use of various trigonometric series expansions to express the post-buckling deflection pattern. A converged solution for the problem was never found. This approach was dropped because the extensive experimental evidence in Fig. 18 shows that the predicted post-buckling minimum load (CASE (7)) is unrealistically low to be useful as a guide to designers for all but the very thinnest shells. Hence, the current approach is to use Koiter theory combined with empirical results to provide a confidence index, as will be described more fully later.

There was also an attempt to explain the discrepancy between test and theory by consideration of various boundary conditions. These studies are surveyed by Hoff [29]. The lowest critical load obtained for any set of edge conditions reported in Ref. [29] is $\sigma_{cr}/\sigma_{cl} = .38$. This load requires the tangen-

tial displacement v to be free at the boundaries. Several sets of edge conditions yield $\sigma_{cr}/\sigma_{cl} = 0.5$. However, they all require that either the normal deflection w or tangential displacement v be free at the edge. In view of measurements of deflections actually occurring during tests, it appears that sufficient friction is present to prevent significant displacements v and w at the edges. The critical mode for the cases in which v is free corresponds to 2 circumferential waves, which does not resemble observed buckling modes.

The cylinder under axial compression is very sensitive to small initial imperfections because the critical buckling load corresponds to a mode the axial and circumferential wavelengths of which are quite small compared to the radius. Also the critical load is insensitive to wavelength. Note that the classical formula, originally derived for axisymmetric buckling by Lorenz in 1908 [31] and for nonsymmetric buckling by Timoshenko in 1914 [32], does not contain any reference to n or m , the number of waves in the buckling pattern in the circumferential or axial directions, respectively. Thus, a great variety of small initial imperfections occurring anywhere on the entire shell surface would contain significant components of critical or almost critical bifurcation buckling mode shapes, modes of deformation that would grow as the load is increased, eventually causing snap-through at a load far below that predicted for bifurcation buckling of the perfect shell, as shown in Fig. 20(a).

A Caution for Novice Users of Computer Programs for Buckling: It is worth emphasizing that the problem of the axially compressed cylinder, which appears superficially to be an excellent, simple test case for a person learning to use a computer program that he has acquired elsewhere, is really quite demanding. The simplicity of the geometry tempts one to use a discretization with fewer degrees of freedom than are needed to obtain a converged solution corresponding to a buckling pattern with short axial waves. The result obtained from the computer program will probably be compared with the Timoshenko formula, Eq. (10), which is based on the assumption of a uniform membrane prebuckling state. Depending on the edge conditions, the nonuniformity and nonlinearity of the prebuckling state near the edges lowers the predicted critical load from 8% to 20%, as seen from the case described in detail in the discussion in Ref.[430] associated with Figs. 29 to 32. If nonlinear prebuckling analysis is used, the problem is further complicated by the fact that the nonsymmetric bifurcation buckling load is fairly close to the axisymmetric collapse load. A final difficulty is that several eigenvalues for the bifurcation loads are clustered near the critical load, especially in models for which edge effects in the prebuckling phase are not present or are ignored by the computer program. All of these difficulties are discussed in the example of the axially compressed monocoque cylinder presented in Ref.[430] The reader is urged to study that material before dismissing a computer program because it "can't even predict the classical buckling load for an axially compressed monocoque cylindrical shell."

Stiffened Cylinders Under Axial Compression: The post-buckling state of an axially stiffened cylinder is shown in Fig. 21. Notice that the buckling mode has much longer characteristic wavelengths than does that for the monocoque cylinder pictured in Fig. 17. This is due to the increased axial bending stiffness and results in milder sensitivity of the buckling load

to initial imperfections. Figure 22 shows ratios of experimental to theoretical buckling loads for a variety of cases, among them stringer stiffened shells. Comparison of the ratio $P_{\text{test}}/P_{\text{cl}}$ for stringer stiffened shells with that for monocoque short cylinders and that for the other monocoque cylinders illustrated in Fig. 18 reveals the milder nature of the imperfection sensitivity of the stringer stiffened shells.

Cylinders under Uniform External Pressure or Torsion : Figures 23 - 27 show post-buckling states of cylinders subjected to hydrostatic pressure or torsion and comparisons between test and theory. As with the stringer stiffened axially compressed cylinders, the buckling modes are characterized by long axial wavelengths and relatively few circumferential waves which results in a milder sensitivity of buckling loads to initial geometric imperfections. The most sensitive systems are short cylinders ($10 \leq Z \leq 100$) under hydrostatic compression, cases for which the bifurcation buckling phenomenon resembles that for cylinders under axial compression. (See Fig. 25.)

Spherical Shells Under Uniform External Pressure: Kaplan [37] gives a thorough survey of buckling of spherical shells subjected to uniform external pressure. Early tests revealed that buckling initiates at some spot at which a small dimple forms. To the writer's knowledge the formation of multiple buckles in a complete spherical shell, as observed in axially compressed cylindrical shells, has not been observed for shells without an interior mandrel. Figure 28 shows a post-buckled state in a shell with a closely fitting interior mandrel. Each buckle subtends a small solid angle, just as in the case of an axially compressed monocoque cylinder in which

each buckle covers a very small fraction of the surface. As might be expected from this behavior, the critical load of a spherical shell subjected to uniform external hydrostatic pressure is highly sensitive to initial geometric imperfections.

Spherical Caps: The fact that an initial buckle subtends a small solid angle stimulated those initially interested in complete spherical shells to model the problem of buckling of a complete spherical shell with use of a shallow spherical cap clamped at its edge. Over the years the shallow cap configuration evolved into a "classical" problem in its own right, studied with almost the same intensity and frequency as the axially compressed cylinder. However, as demonstrated in Fig. 29, the shallow cap problem has certain characteristics not present in the case of a complete spherical shell. These arise from the presence of the edge.

In Fig. 29 load-deflection curves are shown corresponding to linear and nonlinear theories for prebuckling axisymmetric deformations of caps clamped at the boundary. The open circles on the linear load-deflection lines indicate bifurcation buckling at the "classical" pressure for the complete spherical shell with the same radius-to-thickness ratio as the spherical cap. The classical buckling stress is given by the same formula as that for the cylindrical shell subjected to axial compression, Eq. (10). λ is a cap shallowness parameter given by

$$\lambda = 2 [3(1-\nu^2)]^{1/4} (H/h)^{1/2} \quad (11)$$

where H is the rise of the cap above the plane in which the edge lies and h is the thickness.

For λ less than about 7 or 8 the behavior of the shallow cap little resembles that of the complete spherical shell. With $\lambda = 0$ (flat circular plate) there is no similarity at all: The load-deflection curve exhibits a stiffening characteristic which results from the build-up of in-plane tension as the plate deforms (Fig. 29(a)). With λ less than about 3.5 the load-deflection curve has no horizontal tangent and no bifurcation point so that there is no loss of stability on the primary equilibrium path(b). For λ less than about 6 there is axisymmetric snap-through, but no bifurcation buckling(c). For $\lambda > 6$ bifurcation buckling into a nonsymmetric mode occurs at a lower load than either axisymmetric snap-through of the cap or classical buckling of a complete spherical shell(d,e,f). Notice that as λ increases above 7 the prebuckling behavior becomes more and more linear. Figure 29(f) corresponds to a configuration in which the cap is no longer "shallow" if that word may be used as a means of classifying structural behavior: The nonuniformity of prebuckling behavior occurs in a relatively narrow band or "boundary layer" near the edge. Any further increase in λ results in no further alteration in the curves or locations of the bifurcation points presented in Fig. 29(f). No matter how high λ is, the behavior of the incomplete spherical shell clamped at its boundary will never be the same as that of the complete spherical shell because the presence of the boundary gives rise to edge buckling at a pressure from 80% to 90% of the classical value p_{cl} .

For actual spherical shells and shallow caps random imperfections play a major role in the loss of stability under uniform external pressure. Figure 30 demonstrates that the effect of initial imperfections is just as severe as in the case of cylindrical shells subjected to axial compression.

SECTION 2

NONLINEAR COLLAPSE

Summary

As has been emphasized already in the discussion of the two-column shallow truss (Figs. 10 - 14), loss of stability of a shell structure may be due to nonlinear collapse ("snap-through") or to bifurcation buckling. The purpose of this section is to present many examples in which the failure mode is nonlinear collapse. Examples are given of axisymmetric collapse of elastic-plastic-creeping monocoque cylinders under axial compression and ring-stiffened cylinders under external hydrostatic pressure, of general collapse of curved and straight pipes under uniform bending, of cylindrical shells and panels with concentrated loads and cutouts, and of noncircular cylinders under axial compression. The section closes with an example of axisymmetric collapse of an axially compressed complex rocket interstage. The collapse is caused by a local load path eccentricity that gives rise to concentrated bending and local plastic flow.

Elastic-Plastic-Creep Collapse of Axially Compressed Monocoque Cylinders

No Creep: Tests have been conducted on cylinders by Lee [40], Batterman [41], Sobel and Newman [42], and others referenced in Sewell's survey [43] . Tests on truncated cylinder-like (steep) conical shells have recently been conducted by Ramsey [44]. In all the tests, end displacement was controlled. Local end effects such as bulging due to Poisson's effect, so obvious in Fig. 6, are ignored in early analyses of plastic buckling of axially compressed cylinders. Batterman [41] used flow theory and Gerard [45] used deforma-

tion theory. Murphy and Lee [46] were the first to include the effect of radial and restraint on plastic buckling load predictions. Their predictions are shown in Figs. 31 and 32 with the results of Batterman [41], Gerard [45], and Bushnell [47] superposed in Fig 32. End effects are accounted for in the analyses of Bushnell [47], who used the BOSOR5 computer program, and Sobel and Newman [42], who used STAGSC [48]. All of the studies in which end effects are included are based on incremental flow theory and all predict that the collapse load corresponding to axisymmetrical deformation occurs before bifurcation, as shown in Fig. 6. The comparisons between BOSOR5 predictions and Lee's tests [47] are listed in Table 1 and between BOSOR5 predictions and Batterman's tests [47] are listed in Table 2. The far post-buckled collapse mode for cylinders with R/t less than about 30 is shown Fig. 33.

Two important conclusions can be drawn from the results presented in Figs. 31 and 32 and Tables 1 and 2:

(1) The inclusion of end radial restraint in theoretical models essentially eliminates the discrepancy between test and theory, and reveals that in the case of plastic buckling of axially compressed cylinders tested in the usual way it is not necessary to resort to the use of bifurcation buckling analysis with deformation theory or flow theory with a singularity in the loading surface in order to bring test and theory into agreement.

(2) Fairly thick metallic cylinders ($R/t < 90$) are not very sensitive to initial random imperfections if they buckle at stresses above the material proportional limit. The axisymmetric bulge which develops near an end, so evident in Fig. 6 and in Murphy and Lee's prediction shown in Fig. 31, represents a predictable "imperfection" that grows with load and is much more significant than any unknown imperfections due to fabrication or handling errors, providing the cylinder is machined.

Gellin [49] shows that collapse loads of axially compressed cylinders buckling in the plastic range are not as sensitive to initial axisymmetric imperfections as are collapse loads of elastic cylinders. Hutchinson [50] demonstrates the same result for externally pressurized elastic-plastic spherical shells. This fact, the fact that the tangent modulus of most metals decreases by more than an order of magnitude within a stress range of 20% of the .2% yield stress, the fact that high quality cylinders with the relatively low radius-to-thickness ratios required for plastic buckling are easier to fabricate than those with high R/t, and the fact that significant predictable axisymmetric bulges due to radial end restraints grow as the load is increased, combine to reduce dramatically the deleterious effect of random unknown imperfections. We can therefore make fairly accurate predictions of collapse loads of axially compressed cylinders tested in the usual way. Note that this conclusion may not apply to cylinders in which the ends are locally tapered and other devices are introduced into a test to prevent failure due to bulging as shown in Figs. 6 and 31. It also may not apply to cylinders which have been fabricated by cold bending and welding rather than by machining.

Creep Included: Figure 34 shows the normal deflection (axisymmetric) near the clamped end of an axially compressed cylindrical shell which creeps according to the power law

$$\bar{\epsilon}_c = A \sigma^m t \quad (12)$$

in which $\bar{\epsilon}_c$ is the effective creep strain. The material is stressed locally beyond the proportional limit. The BOSOR5 computer program [47] was used to obtain the results, which agree well with those from a test conducted by Samuelson [51]. The small plots inserted within the frame of the large

plot show peak normal displacement near the edge and applied loading as functions of time.

Axisymmetric creep collapse is caused by the increasingly rapid growth of the edge bulge caused by the Poisson effect coupled with radial restraint at the end of the cylindrical shell. In addition to creep, local plastic flow occurs due to bending in the waves near the clamped end.

Creep Collapse of Ring-Stiffened Cylinder Under External Hydrostatic Pressure

Figures 35(a) and 36(a) show a titanium ring-stiffened cylinder and axisymmetric collapse mode due to uniform external hydrostatic pressure applied in steps as shown in Fig. 35(b). The creep law for the titanium is

$$\bar{\epsilon}_c = A \sigma^m t^n \quad (13)$$

in which $m = 13.89$ and $n = 0.189$ and $\bar{\epsilon}_c$ is the effective creep strain. The dots along the middle surface of the cylindrical shell shown in Fig. 35(a) indicate nodal points in the axisymmetric discretized model [47]. Symmetry conditions were applied at the symmetry plane, as is evident in the deflected shapes plotted in Fig. 36(a). Solutions were obtained for each time indicated by a dot in the loading schedule plotted in Fig. 35(b).

Fig. 36(b) gives load-deflection curves for computer runs in which the creep is neglected and included. If creep is neglected the predicted failure mode is nonaxisymmetric bifurcation buckling with 12 circumferential waves at a pressure of about 1810 psi. The prebuckling deflected shape

(exaggerated) and the bifurcation buckling mode are shown in Fig. 36(c). With creep included, the predicted failure mode is axisymmetric collapse at a pressure of about 1700 psi. The presence of creep causes the axisymmetric inward deflection between the second and third ring (Fig. 36(a)) to be bigger than it would be with creep neglected in the analysis, leading to a lower axisymmetric collapse load.

Snap-Through of Very Shallow Spherical Caps

From Figure 29 we saw that for small "shallowness" parameter λ spherical caps clamped at the edge collapse axisymmetrically rather than exhibit non-symmetric bifurcation buckling. Figure 29(c) shows a load-deflection curve for such a case. In a test in which the pressure is held constant rather than the displacement, the cap would snap through to its inverted state at the pressure for which the load-deflection curve has a horizontal tangent. Figure 37 shows instability pressure vs. shallowness parameter and comparisons between test and theory for very carefully fabricated specimens. This figure should be compared to Fig. 30, on which many early test points corresponding to less well made specimens are included. The predicted transition at about $\lambda = 6$ from axisymmetric collapse to nonsymmetric bifurcation buckling is qualitatively supported by the newer test results displayed in Fig. 37.

Introduction

One of the earliest efforts in nonlinear structural analysis was presented in 1926 by Brazier [52]. His paper is concerned with the problem of the stability of cylindrical shells under bending. If a long tube is subjected to bending, its cross section flattens. Consequently, its bending stiffness deteriorates with increasing load. The primary path, a graph showing the bending moment as a function of applied curvature, exhibits a maximum. Brazier performed a somewhat approximate analysis and found that the limit of stability is given by

$$M = \frac{2\sqrt{2}}{9} \frac{E\pi a h^2}{\sqrt{1-\nu^2}} \quad (14)$$

If the maximum stress caused by this moment is computed with use of the undistorted cross section properties we find (with $\nu = 0.3$)

$$\sigma_{CR} = 0.33 E(h/a) \quad (15)$$

The problem of stability of circular cylindrical shells under bending was solved as a bifurcation buckling problem by Seide and Weingarten in 1961[53]. Assuming that the prebuckling behavior can be defined with sufficient accuracy by a linear membrane solution, they found that the critical buckling stress is only 1.5 percent higher than the critical uniform compression stress for a shell with $a/h = 100$. For thinner shells the difference is even smaller. Thus for all practical purposes, the critical stress corresponding to the Seide-Weingarten model with $\nu = 0.3$ is

$$\sigma_{CR} = 0.605 E(h/a)$$

(16)

This value is well above the critical stress found by Brazier for infinitely long cylinders. Boundary conditions usually restrict deformations so that at the shell edges the cross section remains circular. This restrains the cross section flattening at all axial stations. Finite length shells therefore collapse at load levels that are higher than is predicted by Brazier's analysis. For sufficiently short shells the prebuckling behavior is well approximated by the linear membrane solution. With neglect of the effect of initial imperfections Eq. (16) represents a satisfactory solution.

For longer shells there is a coupling between the flattening of the cross section and the formation of a short axial wavelength or wrinkling buckle pattern. The flattening of the cross section increases the local radius as well as the actual bending stress. Consequently, it reduces the load level at which the wrinkling pattern appears. For the infinitely long shell we must consider the possibility that the critical load corresponds to bifurcation from a nonlinear prebuckling state. For a cylinder of finite length, the wrinkling pattern is not orthogonal to the smooth prebuckling flattening mode and therefore we do not have a situation of pure bifurcation. However, the wrinkling mode as a component of the prebuckling displacement is extremely small until a load level is reached at which it begins to grow rapidly. The structural behavior is therefore approximately the same as if a bifurcation point did exist.

The elastic-plastic collapse and bifurcation buckling analysis of straight and curved tubes subjected to bending is needed for design and evaluation of nuclear power plant piping components, offshore pipelines, and other structures involving tubular members. Most of the recent work on piping has been motivated by a desire to be able to predict stress, stiffness, and limit moments of piping systems in nuclear reactors. Since the most flexible and highly stressed piping components are elbows, a significant portion of the total effort has been focused on test and analysis of various elbows under in-plane and out-of-plane moments. In the offshore oil industry the laying of underwater oil pipelines involves bending of rather large diameter straight pipes in the presence of external hydrostatic pressure. The degree of ovalization of the pipe cross section under bending is very much affected by the external pressure, as will be seen later.

Elastic Models: The bending of elastic piping components is explored in Refs. [52] - [62]. Brazier [52] was the first to calculate collapse moments, including in his theory the important effect of increasing ovalization (flattening) of the pipe cross section as the bending moment is increased. Clark and Reissner [54] used an asymptotic formulation in which ovalization of initially curved tubes under bending is assumed to be symmetric about a tube diameter normal to its plane of curvature. Wood [55] expanded Brazier's treatment to include pressure, and Reissner [56] further improved the theory by including higher order nonlinear terms and introducing the effect of pressure on the bending of slightly curved tubes. Aksel'rad [57] was the first to predict bifurcation buckling of straight pipes under bending, including the effect of flattening of the cross section in the

prebuckling analysis. In all of the analyses just cited, end effects are ignored; the pipes are assumed to be infinitely long. Stephens, et al [58] used the STAGS computer program [48] to calculate collapse and bifurcation buckling of initially straight tubes of finite length. For tubes with radius-to-thickness $R/t = 100$ they carried out a parameter study, predicting limit and bifurcation bending moments for length-to-radius ratios $3.4 \leq L/R \leq 20$. They included internal and external pressure in their analysis.

Elastic analyses of piping elbows have been performed by Dodge and Moore [59] who wrote a computer program, ELBOW, based on a model similar to Clark and Reissner's [54] and Hibbitt, et al [60], who introduced a curved piping finite element into the MARC computer program [63]. This element, called #17 in the MARC element library, is based on neglect of elbow end effects. Discretization is in the circumferential coordinate only. Sobel [61] used the MARC #17 element in a convergence study with mesh size. He referred to Clark and Reissner's asymptotic formulas to establish optimal finite element nodal point density in the hoop direction as a function of elbow geometry. Rodabaugh, et al [62], performed a study of 45° , 90° , and 180° elbows, determining the stiffening effects of straight pipes attached to the ends of the elbows. They used the EPACA computer program [64] for their analysis in which end effects are included. Although EPACA includes the capability to treat structures made of elastic-plastic material, the work described in Ref. [62] is restricted to elastic behavior.

Bending Tests on Long Elastic-Plastic Straight Pipes and Elbows: Several test programs on bending of elastic-plastic straight pipes and elbows have been carried out in the past decade. Bolt and Greenstreet [65] give load-deflection curves for 14 commercial 6-in. diameter carbon steel elbows and one 6-in. diameter stainless steel elbow with and without internal pressure. Vrillon et al [66] compare test and theory for the in-plane bending of a 180° elbow subjected to both opening and closing moments. They used the TRICO program [67] for their analysis. Sherman [68] tested several straight pipes, noting formation of relatively short axial wavelength buckles just before collapse. A comparison between one of Sherman's experiments and theoretical results obtained with a modified version of the BOSOR5 computer program [47], [69] is given later. Sobel and Newman [70] describe a test on a 90° elbow carried out on the multiload test facility (MLTF) at the Westinghouse Advanced Reactors Division. Bung, et al [71], ran tests at elevated and room temperature on 304 stainless steel elbows.

Elastic-Plastic Piping Analysis: There are basically three types of elastic-plastic piping analysis for the prediction of stress, stiffness, and buckling failure of straight and curved tubes and combinations thereof:

- 1) A "brute force" method in which the tubes are divided into a two-dimensional field of finite elements;
- 2) A simplified model in which tube end effects are ignored and discretization is in the circumferential coordinate only;
- 3) A further simplified model in which resultant forces and moments integrated over the tube cross section are related to strains and changes in curvature of the tube axis (beam model).

The STAGSC computer program [48], the EPACA code [64], and the TRICO code [67] have been used for the "brute force" analysis of elastic-plastic elbows attached to straight pipes. Vrillon, et al [66], Roche and Hoffman [72] and Skogh and Brogan [73], used these general purpose shell analysis computer programs to calculate moment-deflection curves for combinations of straight pipes and elbows, including elastic-plastic material behavior and moderately large deflections. Remseth et al [74], calculated elastic-plastic collapse of straight tubes subjected to combined bending and external pressure in a two-dimensionally discretized model in which arbitrarily large rotations are permitted. These nonlinear analyses require large amounts of computer time. The more economical but less rigorous one-dimensionally discretized model has been employed by Mello and Griffin [75] and Sobel and Newman [76] who used the MARC computer program [63] element #17 [60], and by Bushnell [69], who modified BOSOR5 [47] to obtain predictions for the bending and buckling of straight pipes and elbows. The most economical and more approximate beam-type models have been used by Roche, et al [77], Spence and Findlay [78, 79] and Calladine [80]. Popov, et al [81], used a beam bending model combined with a rigorous axisymmetric large deflection elastic-plastic analysis to predict axial wrinkling of pipes under combined internal pressure, axial loading and flexure. However, they neglect the important effect of ovalization of the pipe cross section during bending.

Axisymmetric Model of Long Pipe or Elbow Bending Problem:

In the following section results from an approximate analysis of the second type (one-dimensional discretization) are given for a straight pipe and an elbow. The theoretical results were obtained with a modified version of BOSOR5 [47, 69]. In [69] a uniformly curved pipe is treated as if it were part of a toroidal shell. The model is similar to that described in

Ref. [82]. Bending in the plane of the curvature of the pipe centerline is applied by means of an appropriate temperature distribution over the pipe cross section, as is described in [69] and summarized here. Every cross section of the uniformly curved pipe is assumed to deform identically. Therefore, the structure can be treated as a shell of revolution, a torus. Figure 38(a) shows the undeformed curved pipe reference surface with centerline radius of curvature, b , and meridional radius of curvature, a . The centerline radius of curvature of the deformed pipe reference surface (Fig. 38(b)), is R and the cross section has ovalized such that a generator that was originally at a radius $r=b + a \cos \phi$ is now at a radius $R + z$, where z is given by

$$z = (a+w)\cos\phi - u \sin\phi \quad (17)$$

If we assume that the centerline remains inextensional, the reference surface axial strain is

$$e = \frac{(R+z)\frac{b}{R} - (b + a \cos\phi)}{b + a \cos\phi} \quad (18)$$

Rearrangement of Eq. (18) and use of the relationships

$$\cos\phi = r/R_2; \sin\phi = -r' \equiv -dr/ds \quad (19)$$

leads to the expression

$$e = \frac{b}{R} (w/R_2 + ur'/r) + \frac{a(\frac{1}{R} - \frac{1}{b}) \cos\phi}{1 + \frac{a}{b} \cos\phi} \quad (20)$$

in which R_2 is the normal circumferential radius of curvature of the reference surface of the undeformed torus, r is the radius to a point on the torus reference surface, and r' is the derivative of r with respect to meridional arc length s . These quantities are indicated in Fig. 38(c).

Simulation of the Pipe Bending Problem by Thermal Loading of a Torus: In order to use BOSOR5 to create the problem of elastic-plastic bending and bifurcation buckling of a curved pipe, it is necessary to write the axial strain given by Eq. (20) as a stress-producing prebuckling hoop strain for the shell-of-revolution (torus) analysis. This is easily done by definition of the prebuckling stress-producing hoop strain as

$$e = e_2 - \alpha_2 \Delta T \quad (21)$$

in which, from Eq. (20) it is seen that

$$e_2 = \frac{b}{R} (w/R_2 + ur'/r) \quad (22)$$

$$\alpha_2 \Delta T = -a \left(\frac{1}{R} - \frac{1}{b} \right) \left| \frac{\cos \phi}{1 + \frac{a}{b} \cos \phi} \right| \quad (23)$$

In this way, the problem of bending of a curved pipe is simulated by a problem of a nonuniformly heated torus. Further details of the analysis are given in [69].

Collapse and Bifurcation Buckling Moment of a Long Straight Pipe: Figures

39 and 40 pertain to the elastic-plastic bending, collapse, and bifurcation buckling of a straight pipe tested by Sherman [68]. (In Sherman's tests there was no pressure, however.)

Figure 39 shows test results and the results of two BOSOR5 runs, one in which the pressure is zero and the other in which the pressure is one-half the external pressure p_{cr} that would cause buckling in the absence of an applied bending moment, M . The pipe material is elastic perfectly plastic with a yield strength of 421 N/mm^2 . The quantity k is the curvature change of the pipe axis (Fig. 38(b)). With zero external pressure, bifurcation buckling is predicted to occur at an applied moment slightly below that corresponding to nonlinear collapse due to flattening of the cross section. Thus, in a test of such a pipe one would expect to see relatively short axial-wavelength wrinkles or a single wrinkle appear just before failure. Indeed Sherman observed the formation of such buckles in his tests.

With external pressure, ovalization or flattening of the pipe cross section is predicted to occur more precipitously with increasing applied curvature change $k = (1/R - 1/b)$. Note, however, that the maximum moment-carrying capability of the pipe is not much less than that of the pipe without external pressure. In the case treated here bifurcation buckling occurs with a somewhat shorter axial wavelength at a value of k slightly greater than that corresponding to collapse due to flattening of the cross section. Hence, if the moment M is applied rather than the curvature change k , axial wrinkles would not appear before failure. Figure 40 shows the predicted deformations of the pipe cross sections with and without external pressure at $k = .0432 \text{ m}^{-1}$. The deformations are exaggerated but plotted to the same scale in Figs. 40(a) and 40(b).

Collapse of a 90° Elastic Plastic Elbow: Figure 41 shows a moment-deflection curve from a test on a 304 stainless steel elbow by Sobel and Newman [70] compared with results from the BOSOR5 analysis just summarized. The BOSOR5 results underestimate the true strength because straight pipe sections to which the elbow was attached in the test as well as attachment flanges prevented the ends of the test elbow from flattening as the moment was increased. In the BOSOR5 analysis the degree of ovalization is assumed to be constant along the curved axis of the elbow. Unlike the case of the straight pipe there is no bifurcation involving short axial waves or wrinkles before the maximum moment is reached. Other results for both opening and closing moments and 180° elbows are presented in [69].

Collapse and Bifurcation Buckling Due to Bending of Straight Elastic Pipes of Finite Length: Stephens, et al [58], investigated the effect of length on instability of straight elastic tubes. Figure 42(a) and (b) demonstrate this effect. The ends of the pipes are constrained to remain circular. Figure 42(a) gives load-deflection curves (dashed) and maximum moments (solid) for pipes of various length-to-radius L/r with radius-to-thickness $r/t = 100$. The normalization factor M_{cr} is

$$M_{cr} = 0.605 \pi r t^2 E \quad (24)$$

which corresponds, for $\nu = 0.3$, closely to the critical moment originally calculated by Seide and Weingarten in 1961 for bending of simply supported cylindrical shells [53]. This formula results when one assumes that the moment M_{cr} is generated by an axial resultant N_x that varies around the circumference as

$$N_x = -N_{cr} \cos \theta \quad (25)$$

so that

$$M_{cr} = N_{cr} \pi r^2 \quad (26)$$

For short cylinders under bending, buckling is of the bifurcation type and occurs approximately for N_{cr} equal to the critical value corresponding to uniform axial compression, that is

$$N_{cr} = .605 E t^2 / r \quad (27)$$

Use of the right-hand side of Eq. (27) in Eq. (26) yields the result for M_{cr} given in Eq. (24).

As shown in Fig. 42(b), straight unpressurized cylinders of any length subjected to bending become unstable by bifurcation buckling, not by snap-through at a limit point on the load-deflection curve. However, the bifurcation point lies just below the limit point throughout the range of L/r . Furthermore, for long cylinders bifurcation occurs only after considerable flattening of the cylinder cross section, as can be seen from Fig. 42(a). The results of the analysis of Stephens, et al [58], are included in this major section on nonlinear collapse rather than in the next on bifurcation buckling because they obtained them via a collapse or limit load analysis with use of the STAGS computer program [48]. This they did by introduction of a very small initial imperfection with a short axial wavelength

$$w_1/t = (10^{-3}) \cos (\pi(L/2-x)/\lambda) \cos n\theta \quad (28)$$

in which $\lambda/L = 0.017$ and

$$n = \begin{cases} 3 & \text{for } 6 \leq L/r \leq 15 \\ 2 & \text{for } L/r = 20 \end{cases} \quad (29)$$

Thus, Stephens et al [58] converted a bifurcation point such as Point B in Fig. 7(a) into a "snap-through" point such as Point E. Because the initial imperfection given by Eq. (28) is so small, this limit point for all practical purposes, coincides with the bifurcation point.

The nonlinear collapse is defined in [58] as that load for which the curve relating the applied bending moment to the growth of an axial wrinkle of the form given in Eq. (28) has a horizontal tangent. Generally, this axial wrinkle does not begin to grow until a considerable amount of bending moment has been applied. The procedure for determining buckling loads is illustrated in Figure 43 for a cylinder with geometric properties of $L/r = 10$ and $r/t = 100$, and an external pressure equal to $-0.5p_{cr}$, where p_{cr} is defined in [58] as

$$p_{cr} = .926 Et^{5/2}/(r^{3/2}L) \quad (30)$$

Usually, the growth of the wrinkling mode is not easily detected since its amplitude is small in comparison to other shell deformations, in particular, to the Brazier type flattening of the pipe cross section. To detect the growth of the wrinkling mode it is convenient to take a displacement state at a load level near where this growth is suspected to initiate and use it as

a datum state. This datum state is subtracted from all subsequent displacement fields at higher load levels. The difference δw in the normal displacements is calculated at the meridian of maximum compression and is plotted as a function of axial distance in Figure 43(a), where an axial wave of amplitude "a" is shown to be developing near the midlength of the cylinder. The applied bending moment is then plotted as a function of the amplitude of the wave as shown in Figure 43(b). If this moment versus amplitude curve approaches a horizontal tangent, then a mode of collapse has occurred which is called the short-wave axial buckling mode in [58].

After wrinkling starts to develop, the wrinkle amplitude increases rapidly with small increases in load. The rapid growth, although not a true bifurcation, may be considered to indicate that bifurcation based on a non-linear prebuckling state would have occurred near this load if no imperfections had been present. In [58] collapse is assumed to occur when relatively large increases in wrinkle amplitude occur for increases of moment of the order of 0.01%. Buckling and, therefore, collapse for this particular example occurs at approximately a value of M equal to $0.636M_{cr}$.

Other results, including the effect of internal and external pressure, are given in [58].

Collapse of Cylindrical Panels and Shells

with Concentrated Loads and Cutouts

Introduction

Most of the examples of nonlinear collapse shown so far can be analyzed with mathematical models in which the discretization is one-dimensional. An exception is the collapse of finite length tubes in bending just described. The problems described in this section must also be treated with two-dimensional discretization. The distinction between one and two-dimensional discretization is important because of the great difference in computer cost for cases with equivalent nodal point density. With one-dimensionally discretized models, convergence with increasing nodal point density is not too important because one can generally afford to provide more than enough nodes to be on the safe side. With two-dimensionally discretized models, however, limitations of budget for computer runs and limitations of computer core and auxiliary mass storage capacity often dictate the use of models with rather sparse nodal point distributions. The quality of the solutions is questionable because the sparsely discretized models behave differently from the actual continuum and the size or even the sign of the error is rarely known.

Prediction of nonlinear collapse of structures that require two-dimensional discretization is expensive because large systems of equations must be set up and solved iteratively for many load increments. These systems of equations have fairly large bandwidths. The great expense of solving such systems has been a motivating factor in the search for efficient and accurate numerical strategies. Many of these are described in Ref. [8].

One of the strategies is to treat the two-dimensional problem as a linear bifurcation problem, a modeling technique that is usually more appropriately applied in cases involving shells of more general geometry. (In the linear bifurcation model the lowest bifurcation point on the linear prebuckling load-deflection line is calculated. The point shown in Fig.23 of [430] corresponding to the pressure P_{1b} is an example.) This shortcut is cheaper because it involves solution of only one linear equilibrium problem plus one eigenvalue problem, which is usually equivalent to solution at about two to four load steps of a nonlinear equilibrium analysis. We shall see several cases in this section, however, for which the linear bifurcation model is inadequate.

The question arises, of what use would a nonlinear bifurcation model be? There are two reasons why such a model is not usually advantageous. In the first place, bifurcation from the nonlinear fundamental state in perfect two-dimensional nonlinear shell problems is much more rare than for axisymmetric shells simply because there is less symmetry in the two-dimensional case. Therefore, bifurcation modes that are orthogonal to the prebuckled state determined from nonlinear analysis are less likely to exist. In the second place, it is generally just as expensive to calculate the nonlinear prebuckling state for the perfect system as it is to calculate the nonlinear precollapsed state for the same system in which a small general imperfection has been introduced in order to convert any bifurcation points, such as Point B in Fig. 7(a), into limit points, such as Point E.

The only way in which a nonlinear bifurcation model might be used to advantage would be to provide intermittent estimates of the collapse load such that the total number of load increments required to find this critical load is reduced. Also, it may turn out that collapse corresponds to rapid development of a short wave mode superposed on a smooth precollapsed state, as is seen in the example of the finite length tube in bending. In such cases one might set up two discretized models, a fairly crude one to capture the smooth nonlinear precritical deformation and a locally fine one in order to calculate accurately the short wave bifurcation from the smooth precritical deformed state. The generally expensive prebifurcation nonlinear iterative solution would be carried out with the sparsely discretized model and the far less frequently performed eigenvalue analysis would be carried out with the more finely discretized model.

Cylindrical Panels and Shells with Concentrated Normal Loads

Panels: Figure 44 shows a panel simply supported on all four edges. This panel collapses and snaps through to an inverted position. The strategy used to follow the load-deflection curve over the maximum is described in [84] and summarized in [8]. Bergan, et al, calculated the entire dashed curve with load incrementation and decrementation. A similar configuration is shown in Fig. 45. In this example the cylindrical panel has free longitudinal edges. The simply supported panel collapses because distortion (flattening) of the cylindrical cross section reduces the axial bending stiffness, an effect similar to the Brazier flattening of a long complete cylindrical shell due to bending. If the curved edges are restrained from axial motion (clamped), axial tension develops as the panel deflects, preventing collapse.

Note that linear bifurcation buckling predictions for this case bear little relationship to the true behavior. In the simply supported case the linear bifurcation load greatly overestimates the load at which the panel collapses because the bifurcation analysis does not account for the flattening of the cross section. In the clamped case bifurcation is predicted when no collapse occurs because the linear analysis does not account for the stabilizing axial tension that develops in the panel as it deflects vertically.

Complete Cylindrical Shells: Okubo, et al [86], investigated the instability of cylindrical shells under combined internal pressure, bending, and inward-directed concentrated normal loads. For small concentrated loads the cylinders failed in a general instability mode that resembles the buckling mode of a cylinder under uniform axial compression: A cluster of buckles, centered on the site of the concentrated load, develops on the compression side of the cylinder. In these cases the contribution of the concentrated load is to produce an effective imperfection that triggers general instability. The shell cannot sustain higher bending moments after buckling. For large concentrated loads there are two failure modes: Initially the moment-deflection curve displays a local maximum which corresponds to a local snapping phenomenon involving development of a single dimple at the site of the concentrated load. At this maximum the overall compressive stress from the bending moment is small enough so that the buckle pattern does not spread to regions remote from the location of the concentrated load. The shell sustains moments in excess of this local maximum, eventually failing as before in general instability.

Figure 46 is one of the interaction curves experimentally determined by Okubo, et al [86] for the case of no internal pressure. The solid lines

represent a curve-fitting of the experimental data. Essentially the same failure loads were found for the same specimen tested on two different dates. For concentrated loads Q less than about 0.03 lb, the critical moment is unaffected: The concentrated load simply produces an imperfection that is less than or equally severe to those already present in the unloaded shell. For large concentrated loads, local instability or snapping precedes general instability. The moment-deflection curve has a local peak analogous to that shown for the axially compressed oval cylinder in Fig. 4 of Ref. [430]. The critical moment corresponding to general instability exceeds that corresponding to local snapping and is independent of the value of the concentrated load Q . In this range of Q the imperfection created by the concentrated load acts essentially as a cutout, as shall be seen from results presented next. For the intermediate range of Q the critical moment depends on Q and the load deflection curve monotonically increases until failure of the shell occurs in a general instability mode.

Collapse of Axially Compressed Cylindrical Shells with Cutouts

Rectangular Cutouts: Figures 47 - 53 pertain to this section. Figures 47 and 48 show a buckled cylinder which has two diametrically opposed rectangular cutouts. A plot of load vs. normal deflection at a point on the edge of the cutout is given in Fig. 49, along with a prediction of failure from linear bifurcation buckling theory. In this case the bifurcation analysis underestimates collapse by more than a factor of two. The bifurcation model predicts the load at which the vertical edge of the cutout buckles. It is clear why this load does not correspond to failure of the structure: As bending occurs near the vertical edges of the cutouts the compressive stresses are redistributed away from these regions and the

load is carried by the remaining portions of the shell. Thus, the shell shown in Figs. 47 and 48 collapses after significant stress redistribution has taken place. In the post-bifurcation range the deformations in the neighborhoods of the cutouts have the effect of making these cutouts appear bigger structurally than they do visually.

Note that in this case the relationship of the bifurcation buckling load estimate to the actual collapse load is opposite to that for the case in Fig. 45. This is because the consequences of the nonlinearity are different for the two situations. The geometry change in the cylindrical panel with the concentrated load weakens the panel globally and does not result in any alternative means for the storage of strain energy. Similarly, the geometry change in the cylinder with the cutout weakens the structure. However, the weakening, local in this case, has a different result: Strain energy is transferred from the rapidly deforming regions to other regions which are capable of accepting more axial compression before becoming unstable.

In general, one can assume that if the bifurcation buckling mode is fairly local and if alternate post-bifurcation load paths are available, then a linear bifurcation buckling model will yield a conservative estimate of the collapse load. On the other hand, if the bifurcation buckling mode is global and if precollapse deformation is significant, global, and of an unfavorable nature (e.g., curvatures decreasing), and if no alternative load paths are available in the post-buckled state, then the linear bifurcation buckling model will generally yield an unconservative estimate of the collapse load.

Figures 50 - 52 show comparisons between test and theory for buckling of cylinders with two diametrically opposed rectangular cutouts [87]. The STAGS computer program [48] was used for the analysis. Figure 51 shows how the axial stress is redistributed away from the cutout edge as local bending occurs there. Figures 50 and 52 show that the agreement between test and theory is very good even though these axially compressed cylinders are very thin ($R/t = 437$). The cutout is large enough that it represents a predictable imperfection that is much more significant than the unavoidable, random, unmeasured imperfections in middle surface geometry, thickness, material properties, and boundary conditions.

Figure 53 gives load-deflection behavior and a linear bifurcation buckling load for an axially compressed cylinder of the same geometry as that shown in Fig. 50 with the rectangular cutout reinforced. Collapse initiates in the neighborhood of Point B. The effect of the axial stiffeners is to absorb the axial load that would otherwise pass through the shell near the vertical edge of the cutout, as seen in Fig. 51, and to prevent bending of this edge. Thus, the bifurcation load is increased substantially. In fact, the bifurcation load is no longer a conservative estimate of collapse because random imperfections begin to play a significant role. The stiffeners along the cutout edge drastically reduce the precollapse deformations near the cutout and thus make the cutout appear to be a smaller imperfection than formerly. Consequently, because of the relative increase in significance of random imperfections, comparisons between test and theory for shells with reinforced cutouts show less agreement than do those with unreinforced cutouts.

Circular Cutouts: The STAGS computer program [48] has also been used for collapse analysis of axially compressed cylinders with circular cutouts [88]. Figure 54 shows a discretized model. In [89] Starnes reports the results from a large number of tests on cylinders with circular cutouts. He finds from the experimental results that a parameter $\alpha = r/\sqrt{ah}$ determines the shell behavior where r is the radius of the circular cutout. For cylinders with relatively small cutouts, this conclusion is verified by the analysis reported in [88]. However, for cylinders with sufficiently large cutouts, the value of α cannot alone determine the behavior of the shell. With two cutouts, for example, the critical load must be zero when $r/a = \pi/2$. This will occur for $a/h = 100$ at $\alpha = 5\pi$, and for $a/h = 400$ at $\alpha = 10\pi$. Therefore, for cylinders with relatively large cutouts, there must be separate curve branches for different a/h values in the P_{cr} versus α diagram. This was found to be the case when the critical loads were compared for two cylinders with $a/h = 6$. The cylinder with $r/a = 0.3$ and $a/h = 400$ carries a significantly larger axial load than one with $r/a = 0.6$ and $a/h = 100$.

Results obtained from the analysis with uniform shortening are shown in Fig.

55, together with a curve fitted to these computed data and the obvious locations of the end points of the curves. Test data for a cylinder with two cutouts were provided by Starnes. These are also plotted in the figure, and it appears that experimental and theoretical results are in very close agreement.

It may be noticed also that virtually the same critical load is obtained whether the cutout is circular or square. Figure 56 shows the outward displacement at the cutout edge (midlength) as a function of the applied axial load for two cylinders with $\alpha = 1.5$, one with a circular and one with

a square cutout. Because of the difference in amplitude of the normal displacement at the edge of the cutout, the result that a cylinder with a square cutout can carry as high a load as a cylinder with a circular cutout is somewhat unexpected. The reason seems to be that larger displacements at the edge of the square cutout allow a more significant stress redistribution to occur.

Collapse of Axially Compressed Noncircular Cylinders

Axially Compressed Elliptical Cylinder

Load vs. end shortening curves for perfect and imperfect elliptical cylinders are shown in Fig. 57. The cylinder has a length of 1.0 in., a thickness of 0.0144 in., and semiaxes of lengths 1.75 in. and 1.0 in. Young's modulus is 10^7 psi and Poisson's ratio is 0.3. It is submitted to a uniform end shortening with the edges free to rotate but restrained from moving in the radial and circumferential directions. The load-end-shortening curve for the perfect shell is that indicated by OABC. The other curves correspond to imperfect shells with the imperfection shape given by

$$w_{\text{imp}}/t = -\zeta \sin(\pi x/L) \cos(6\theta) \quad (31)$$

In a test on this shell, sudden changes in the deflection pattern (buckling) would be noticed at A, B, and C. Notice that the shell may carry more load than the initial peak A indicates. While the primary buckling load A is rather sensitive to imperfections, it appears that the second maximum B is relatively insensitive to imperfections. Hence, it may be suitable as a design limit.

The curves Δw vs. S at the bottom of Fig. 57 are buckling modes calculated by subtraction of displacement vectors obtained in two sequential steps in end shortening and normalization of the result. Such a subtraction yields the shape of the fastest growing displacement component, which might be interpreted as a buckling mode. As one traces one's way along the load-deflection curve OABC, the axial stress in the shell is constantly being redistributed by the local growth of normal displacement. For example, early in the load history the most rapid growth of normal displacement occurs at the point labeled $S = 2.2$, the area of minimum curvature. This growth relieves the axial stress there and permits loading above the initial peak A. At point B the most rapid growth of normal displacement is about halfway between the ends of the minor and major axes. This growth relieves the axial stress in the corresponding area and thus permits loading to an even higher peak, C, where the rapid growth of normal displacement occurs near the end of the major axis in an area of relatively large curvature. The results shown in Fig. 57 were obtained with use of the STAGS computer program [48].

Axially Compressed "Pear-Shaped" Cylinder

A similar stress redistribution phenomenon occurs in the case of the non-circular cylinder, half of which is depicted in Fig. 58(a). The behavior of this shell subjected to uniform end shortening was also investigated with the STAGS code [48]. The theoretical results given in Figs 58(b-d) are based on a two-dimensionally discretized model with 45 circumferential nodes and 9 axial nodes covering one-half of the circumference and one-half of the length.

As seen from Fig. 58(b) the linear range in this case represents less than 1/30 of the total load history of the shell. The rapid change in slope of the load-deflection curves at about $P=100$ lb corresponds to rapid growth in normal deflection (buckling) of the flat portions of the shell. Associated with this rapid growth in w is a redistribution of the axial stress so that the curved portions begin to take up a larger percentage of the total axial load P . As more and more of the axial load is borne by the curved portions, the slope of the load-end-shortening curve increases until just before collapse, at which load the entire structure fails. Figures 58(c) and 58(d) show the circumferential distributions of normal outward displacement w and axial compression/length N_x at the shell midlength for $P=1164$ lb. At this load both w and N_x are growing very rapidly with P in the curved portions $0 \leq \theta \leq 45^\circ$ and $90^\circ \leq \theta \leq 157.5^\circ$.

The rather complex behavior in this case indicates the need for a flexible strategy for calculation of collapse loads of shells. Small load steps and frequent refactorings of the equation system matrix are required in the load region between 100 and 200 lb, even though the displacements are relatively small in this range. Farther out on the load-end-shortening curve, where the displacements are larger, rather large load steps can be used and few refactorings are necessary. Just before collapse many small load steps and frequent refactorings of the stiffness matrix are again required. Efficient use of the STAGS code, or any code for predicting nonlinear behavior of shells, requires a sophisticated iteration strategy built into it and a well-trained user to take advantage of this strategy.

Practical shell structures are often built up of several parts fabricated at different places. These parts must be assembled to create the finished product. The mating of the various parts often gives rise to instability problems which do not exist for the separate pieces, the design of which may not have included consideration of these "global" problems. Figure 59 represents such an assembled shell structure. It is a missile interstage with two sections, a forward adaptor made of composite material from missile station (M.S.) 170.0 to M.S. 175.4, and an equipment section made of aluminum from M.S. 175.4 to M.S. 182.8. There is an aluminum primacord backup ring with a cavity for primacord at a notched separation joint at M.S. 177.0. This complex cylindrical shell structure must withstand axial compression during launch. The most severe problem of instability arises from inward excursion of the axial load path in the region between M.S. 175.4 and M.S. 177.6, shown enlarged in Fig. 60. This axisymmetric inward excursion causes axisymmetric deflections shown in Fig. 61, which was obtained with use of the BOSOR5 computer program [47]. Failure of the complex structure is due to elastic-plastic collapse in the short, thin ($t=.07$ in.) aluminum section located at M.S. 175.9 and denoted Segment ④ in Fig. 60. In a test of this structure failure occurred at a load within one percent of that predicted in the analysis.

Section 3

BIFURCATION BUCKLING IN WHICH NONUNIFORMITY OR NONLINEARITY OF THE PREBUCKLING STATE IS IMPORTANT

Introduction

All of the examples in this section involve axisymmetric shells. The feature that unifies these examples, that makes it logical to include them all in this particular section, is the major influence of certain nontrivial aspects of the prebuckling solution on predictions of bifurcation buckling loads. Whereas the emphasis in the last major section was on nonlinear collapse rather than bifurcation buckling, the emphasis here is on bifurcation buckling with nontrivial prebuckling behavior. As was pointed out before, bifurcation from a nonlinear prebuckling state is of practical interest only in configurations with a great deal of symmetry. That is why the applications here all involve axisymmetrically loaded shells of revolution.

There are two principal kinds of influences that the prebuckling state has on the bifurcation buckling load: (1) The prebuckled loaded shell has a different shape from the unloaded shell; given a membrane prestress distribution this new shape may be more likely or less likely to lose its stability than the original undeformed shape; (2) The prebuckling membrane stress distribution is an important factor; given a prebuckled shape of the shell, the membrane stress distributions calculated from linear or nonlinear analysis and membrane or bending shell theory may drastically affect the predicted bifurcation buckling load and mode shape.

In this section many examples will be given in which the combination of these two influences is present.

Summary

The section opens with several examples of nonsymmetric bifurcation buckling in the neighborhood of an edge. It is shown that this edge buckling is due primarily to local circumferential (hoop) compression which is greater near the edge where local meridional bending is significant than remote from the edge where a membrane prebuckled state prevails. Many figures follow which involve a closely related situation -- nonsymmetric bifurcation buckling due to localized hoop compression sometimes near an edge and sometimes not. One of the most important effects demonstrated is the great influence of prebuckling axisymmetric shape change on predicted bifurcation buckling loads. Next, several examples are given of nonsymmetric bifurcation buckling of shells of revolution in which meridional tension is combined with circumferential compression. Particular emphasis is given to elastic-plastic bifurcation buckling of internally pressurized torispherical shells, a complex problem for which both prebuckling shape change and nonlinear material properties greatly affect the prediction of the critical load. The chapter closes with an example in which the nonsymmetric bifurcation buckling load is near the axisymmetric collapse load. The results of experimental and theoretical investigations of an elastic idealized model of a water tank are compared with a more complex elastic-plastic model in which certain fabrication processes such as cold bending and welding are included in the simulation of failure of the large steel water tower illustrated in Fig. 3.

Bifurcation Buckling due to Edge Effects and Localized Circumferential Compression

Bifurcation Buckling Due to Edge Effects

Cylindrical Shell Under Axial Compression: Figure 62(a) shows the postbuckled state of an axially compressed cylindrical shell. In Fig. 62(b) the predicted axisymmetric prebuckling state and nonsymmetric bifurcation buckling mode corresponding to 18 circumferential waves are shown on either side of a discretized generator. The generator of the lower half of the cylinder is divided into two segments. Nodal points have been concentrated in the relatively short edge segment in order to obtain converged solutions for the prebuckling state and the bifurcation buckling load and mode. The solution was obtained with the BOSOR4 program [14]. Further details on this case are given in Figs. 29 to 32 and associated discussion in Ref. [430]. In near-perfect shells edge buckling occurs before general instability remote from the edge and before axisymmetric collapse near the edge because of the narrow band of hoop compression combined with the axial compression that occurs only in the edge "boundary layer." This hoop compression as well as nonlinear behavior due to moderately large axisymmetric prebuckling meridional rotation cause an approximately 20% reduction in the bifurcation buckling load below the classical value of $N_{cr} = .605 Et^2/R$.

Such edge buckling is often not observed in axially compressed very thin elastic cylindrical shells because of the presence of initial random imperfections which act as triggers for buckling at isolated locations anywhere in the shell. The axial load corresponding to the edge buckling mode

is not especially sensitive to initial imperfections. However, the axial load corresponding to the classical buckling formula, $N_{cr} = .6 Et^2/R$, is extremely sensitive to initial imperfections. Therefore, a small imperfection located at some point remote from the edge will trigger buckling at a lower axial load than will a larger imperfection located within the bending "boundary layer" near the edge.

Thicker metallic cylindrical shells that buckle in the plastic range exhibit axisymmetric collapse which initiates at the edges as shown in two of the photographs inserted in Fig. 6. Bifurcation buckling does not occur before axisymmetric collapse in these cases because the axisymmetric prebuckling hoop forces that resist changes in diameter are diminished due to yielding, the amplitude of the edge bulge increases faster in the plastic region due to the increase in Poisson's ratio to 0.5 for incompressible flow; and the doubly curved bulge that develops near the edge resists nonsymmetric buckling.

The load at which these thicker shells collapse can be fairly accurately predicted because the shells, being thicker, are easier to make more perfectly; because the material softens so drastically within a fairly small range of stress; and because the critical mode of failure-axisymmetric collapse near the edges-resembles a built-in non-random predictable, prebuckling imperfection: local axisymmetric bulges that grow near each end of the cylinder.

Externally Pressurized Spherical Caps with Edge Rings: Figs. 63- 68 and Table 3 pertain to this section. Bifurcation buckling is due to the narrow band of circumferential compression that develops near the edge. Figure 63 gives comparisons between theoretical results obtained with use of the BOSOR4

computer program [14] and experiments performed by Wang [93]. The normalizing factor p_{cl} is the classical buckling pressure of the complete spherical shell. Figure 64 shows the prebuckling distributions of circumferential compression for two models of Wang's test specimen, and Fig.

65 gives predicted nonsymmetric bifurcation buckling modes corresponding to two values of edge moment M_o , which was applied in the tests by hanging weights from a small projection attached to the edge ring.

There are two factors other than external pressure that influence the amplitude of the local axisymmetric prebuckling circumferential compression: the eccentricity (e_1, e_2) of the edge ring and the fixed edge moment M_o . The influence of ring eccentricity is indicated in Fig. 64. The test, described in [93], most resembled case 1. In case 2, the shell is considered to penetrate the ring and terminate at the ring centroid. In the two cases shown, the external pressure is assumed to be reacted by an axial load acting through the ring centroid. Buckling occurs at the pressures p_{cr} indicated, and the predicted buckling pattern with 18 circumferential waves is concentrated in the area near the edge, where the hoop stress resultants are maximum compressive. In this case, the predicted buckling pressure is most sensitive to the axial component e_2 of the stiffener eccentricity. Because of this component, the meridional resultant N_{10} produces a clockwise moment about the ring centroid, which acts to reduce the destabilizing hoop compression near the edge of the cap. Notice that the local hoop compression distributions corresponding to the two very different values of critical pressure, $p_{cr}(\text{Case 1}) = 0.619$, $p_{cr}(\text{Case 2}) = 0.357$, are very similar, providing a clue that it is this quantity that has the greatest influence on the bifurcation buckling load and not the meridional compression or the prebuckling shape change of the spherical cap.

For cases such as this in which bifurcation buckling is due to a localized effect, the predicted buckling load is often very sensitive to seemingly insignificant changes in the structure or in the analytical model of it. The results in Fig. 64 provide an example. If the analyst perceives that such a buckling phenomenon may occur, for instance, if he performs a stress analysis and notices local regions of destabilizing compressive membrane forces, he should take great care with the modeling. Local load path eccentricities, meridional discontinuities, prebuckling shape change effects, and prebuckling geometric and material nonlinear behavior should be faithfully modeled and included in the stability analysis. If a stress analysis reveals a local band of circumferential compression, then a bifurcation buckling analysis should be performed. The minimum buckling load will generally correspond to a rather high number of circumferential waves, as shown in Fig. 65. A reasonably accurate estimate, at least to within an order of magnitude, of the critical circumferential wave number can be calculated from the assumption that the axial and circumferential wavelenghts of the buckles will be of approximately the same lengths. If the analytical model of the structure is reasonably good, the predicted buckling load should be fairly close to test loads. Sensitivity to imperfections is much less important in such cases because the structure has a built-in local imperfection that is generally large compared to any random manufacturing errors. Note that the local stress concentrations implied in this discussion may cause some plastic yielding of the material. Bifurcation buckling loads will be overestimated if this material nonlinearity is neglected.

Figures 66 - 68 and Table 3 reveal the effect of ring size on predicted bifurcation buckling pressures of spherical caps of various depths. The theoretical

results were obtained with an early version of BOSOR. The ring has a square cross section and its centroid is assumed to coincide with the edge of the spherical cap. In Fig. 66 the normalized critical pressure is plotted versus a rather complicated ring area parameter $A^* = (A/at)(a/t)^{1/2}$ through which the dependence of the normalized buckling pressure p_{cr}/p_{cl} on radius-to-thickness ratio a/t is almost eliminated for a given value of shell shallowness parameter $\lambda = [12(1-\nu^2)]^{1/4}(a/t)^{1/2}\alpha$. The dependence of p_{cr}/p_{cl} on λ is weak even though the predicted meridional bifurcation mode shape and critical circumferential wave number vary a great deal. There is a strong dependence of the p_{cr}/p_{cl} on the degree of edge fixity, A^* . The critical pressures for $A^* \rightarrow \infty$ agree with those calculated by Weinitschke [94] and Huang [95] for clamped caps. The degree of reduction exhibited by Wang's tests below the theoretical critical pressures for perfect shells is reasonable for spherical shells with similar shallowness parameter λ as seen in Figs. 30 and 37.

Figure 67, which corresponds to a cap with $a/t=100$, $\lambda=16$, shows the pre-buckling state at the critical pressure ratio $\rho = p_{cr}/p_{cl}$ for various values of edge ring parameter A^* and bifurcation buckling modes for two extremes, $A^*=0$ (free) and $A^* \rightarrow \infty$ (clamped). The mode shapes have peaks that coincide with the peaks in the circumferential compression.

Buckling of Shallow and Deep Spherical Caps: Figures 63 - 67 apply to shallow caps in which the edge angle α is less than about one radian. The most important factors influencing the bifurcation buckling pressure for such configurations are the prebuckling hoop compression just in from the edge and the stiffness of the shall wall. The buckling mode is an edge mode of the type shown in Fig. 65 for a rather high value of λ ($\lambda=25$) and in

Fig. 67(d) for a lower value of λ ($\lambda=16$). The buckling modal displacement is small at the edge. For shallow caps supported as shown in Fig. 67 there are two reasons why the buckling displacement almost vanishes at the edge for $\alpha \leq 0.88$ rad: (1) with small edge rings a band of stabilizing hoop tension develops with increasing pressure as shown in Fig. 67(b); (2) with large edge rings the area moment of inertia of the ring prevents non-symmetric buckling.

A different kind of buckling occurs if the edge ring is reasonably small and if α is greater than about 1.2 radians. With $\alpha \geq 1.2$ radians and $A^* \leq 16$, the nonsymmetric buckle pattern of a spherical shell is almost inextensional with $n = 2$ circumferential waves. The maximum buckling displacement occurs at the edge where the ring ovalizes. The buckling load can be very small compared to the classical load, a phenomenon that is pointed out by Cohen [96] in the case of axially compressed cylindrical shells with ring-supported edges. As seen from the results listed in Table 3, for $A^* = 6.4$ the inextensional mode occurs only for $1.57 \leq \alpha \leq 2.26$. With $\alpha = 2.65$ and 2.92 , "classical" type buckling occurs and the buckling load is almost independent of n . For these cases the ring is of such a size that the prebuckling equilibrium state is almost exactly a uniform membrane contraction. When $A^* \geq 25.6$ or when the very deep shell is hinged at the edge, buckling is again an edge phenomenon.

Figure 68 shows buckling modes of spherical shells with $a/t = 100$, $\alpha = 2.65$ radians, and $A^* = 0.4, 6.4$, and 25.6 . The figure illustrates the different types of buckling reviewed next in connection with Table 3.

Table 3 lists dimensionless buckling loads ρ_{cr} and corresponding circumferential wave numbers n for shells with $a/t = 100$ and $0.22 \leq \alpha \leq 2.92$ radians. The shells are supported as shown in Fig. 67 and $A^* = 0, 0.4, 1.6, 6.4, 25.6$, and ∞ . The value $A^* = \infty$ corresponds to clamping at the edge. Buckling loads are also shown for shells hinged at the edge.

Inspection of Table 3 reveals that, in the range of parameters investigated, four types of buckling occur: axisymmetric collapse, $n = 0$; edge buckling $n \geq 2$; inextensional buckling, $n = 2$; and "classical" buckling (ρ_{cr} almost independent of n). Table 3 is divided into regions according to the type of buckling behavior exhibited. When the shell is very shallow ($\alpha = 0.22$) it collapses axisymmetrically for all edge conditions. There are values of α , such as $\alpha = 0.33$, for which the type of buckling depends on the degree of edge fixity.

When $A^* \geq 1.6$ and $\alpha = 0.33$ the shell buckles into two waves. The buckle pattern, while not confined to a narrow region near the edge, does involve considerable stretching of the middle surface, and the buckling of these shallow shells might be classified as an edge phenomenon. The buckling of shells with $\alpha = 0.495$ and 0.88 ($\lambda = 9$ and 16) is an edge phenomenon for all types of edge conditions. Prebuckling and buckling displacements are shown for the $\lambda = 16$ case in Fig. 67, which was discussed previously. It is seen that the buckling loads associated with edge buckling are not strongly dependent on the edge angle α . Buckling loads calculated for $\alpha = 0.495$ and $\alpha = 0.88$ with $A^* \rightarrow \infty$ agree with the loads for clamped caps calculated by Huang in Ref. [95].

Buckling Due to Localized Hoop Compression

The examples in this section are similar to those of the last, the differences being that buckling is not necessarily at an edge and in several of the cases the prebuckling change in shape of the shell has a major influence on the bifurcation buckling load. First, thermal buckling of cylindrical shells will be described. The buckling of an internally pressurized ellipsoidal rocket motor dome will be discussed. In both of these problems prebuckling shape change has a significant influence on the predictions of bifurcation buckling.

An example will follow which is similar to that shown in Figs. 59-61; the localized hoop compression is caused by an axisymmetric inward excursion of the load path. The difference here is that failure is due to nonsymmetric bifurcation buckling rather than axisymmetric collapse.

Thermal Buckling of Cylindrical Shells

Introduction: In the problems examined in this section the most important single influence on bifurcation buckling is the axisymmetric change in shape of the cylinder in the prebuckling phase. This shape change is most pronounced just where the localized destabilizing axisymmetric hoop compression is maximum and is a stabilizing influence, since its effect is to transform a developable surface into a more stable doubly curved surface, as will be seen. The discussion here comes from Ref. [97].

Two problems are treated: an "infinite" cylinder heated uniformly over half its length and a clamped cylinder with an axial thermal gradient near the edge. In both cases the cylinders are free to expand axially. The cylinder

heated along half of its length does not buckle at any temperature because the destabilizing effect of the circumferential band of hoop compression near the thermal discontinuity is more than counteracted by the stabilizing effect of the shape change of the cylinder as it is heated. Predicted buckling temperatures of clamped cylinders are strongly dependent on details of the thermal gradient very close to the clamped edge. Agreement with test results is obtained only if prebuckling meridional rotations are included in the stability analysis.

Thermal discontinuities, or rather high thermal gradients, arise at "hard points" or heat sinks such as ring stiffeners and bulkheads. Junc- tures between dissimilar materials or boundaries of an environment, such as the surface of a cryogenic fluid, also give rise to thermal stresses which vary rapidly in the axial direction. Several authors [98 - 103] have treated problems of this sort. Hoff [98] calculated buckling loads for uniformly heated simply-supported cylinders; Johns [99] did the same for uniformly heated clamped cylinders; and Anderson [100] and Chang and Card [101] calculated buckling loads for cylinders under combined axial compression and nonuniform heating. In the work of Hoff and Johns, it is assumed that the temperature distribution is axisymmetric and that no axial restraint exists. The predicted buckling is caused by hoop compression near the simply-supported or clamped edges, which decays rapidly with increasing distance from the edge. In the work by Anderson [100] and by others at Stanford University [104 - 106] the temperature either varies around the circumference or the cylinder is assumed to be rigidly fixed at the boundaries. Buckling in these cases arises because of axial thermal stresses, not from hoop stresses. This section is not concerned with this latter class of problems, examples of which will be described later.

The purpose of this section is to describe the effect of prebuckling deformations on the predicted buckling temperature of axisymmetrically heated cylinders which are not axially restrained. Two problems are treated: buckling of a cylinder with a sudden change in temperature along its length, and buckling of a cylinder clamped at its edges and heated along its length with steep gradients near the end supports. In both cases the cylinder is free to expand in the axial direction.

Buckling of Cylinder Heated Halfway along Length: Figure 69 gives the geometry, material properties, temperature distribution, and prebuckling solution. The cylinder is shown to be 2000 in. long and 200 in. in diameter. The cylinder length is immaterial, however, provided that it is large compared to twice the axisymmetric boundary-layer length (about 60 in. in this example) and large compared to the longest buckling wavelength (about 50 in., as seen in Fig. 72(a)). In the computerized analysis "symmetry" conditions are applied at the ends of the cylinder in order to simulate infinite length. The prebuckling solution shown in Fig. 69 is given by Flugge [107]. If the cylinder is to buckle, such behavior would be caused by the narrow band of hoop compressive stresses occurring adjacent to the temperature discontinuity on the hot side. The prebuckling solution for a uniformly heated cylinder simply-supported at the location of the temperature discontinuity is similar: the amplitude of the hoop stress is doubled, no solution exists, of course, for $x < 0$, and the $1/2$ in the expression for w in Fig. 69 becomes unity.

In Ref. [102] it is mentioned that the uniformly heated simply-supported cylinder analyzed by Hoff [98] apparently does not buckle at any tempera-

ture. This rather odd prediction results only if the prebuckling deformations of the shell are accounted for in a consistent manner in the stability analysis. In Ref. [102] it is suggested that perhaps the moderately large rotation limitation used in the shell theory is responsible for the peculiar result. Because of the investigation described here, it is now felt that the prediction of no buckling is physically realistic. As the shell is heated the compressive hoop stresses grow, it is true. However, the generators become curved in the neighborhood of the compressive stresses and this curvature "stabilizes" the shell. Apparently, as the temperature increases further, the further increase in curvature more than makes up for the increase in hoop stress, so that the shell becomes more, not less, stable. Mathematically this behavior is reflected in the growth of the stability determinant with increasing temperature for any circumferential wave number, n .

The case shown in Fig. 69 behaves in a manner analogous to the simply-supported uniformly heated cylinder. Figure 70 shows the stability determinant as a function of increasing temperature rise for $n = 14$ circumferential waves. (This is the critical wave number if prebuckling rotations β_0 are neglected in the stability analysis.) These results were calculated with the BOSOR4 computer program [14]. The stability determinant is the determinant of the coefficient matrix of the equation shown in Fig. 70. This equation is discussed in Ref. [430] . (See Eq.76 in Ref. [430] .)

The stability determinant exhibits the monotonically increasing behavior only if the prebuckling deformations are accounted for. In order to check

the correctness of the theory in which the shape change of the shell is accounted for in the stability analysis, a model was constructed which treats the prebuckling shape change as independent of the temperature, a sort of given, fixed imperfection. Buckling analyses of several distorted cylinders were performed, where the prestress hoop compression is given by the distribution shown in Fig. 69 and the initial distortions or imperfections represent the prebuckling shapes corresponding to various amplitudes T_0 of temperature rise. Figure 71 shows results for three "imperfect" cylinders, the properties of which are given in Fig. 69. The imperfection shape is given by the expression for w in Fig. 69 with $T_0 = 0^\circ$, 2500° , and 5000° . The eigenvalues were determined from an analysis in which further prebuckling meridional rotations from the initial imperfect state are neglected. The critical circumferential wave number n increases as the prebuckling meridional curvature increases, and the curves never cross, indicating that at any wave number the stability determinant will never vanish as temperature is increased, provided that the shape change of the cylinder is included in the equations governing stability. Note that it has not been proven beyond any doubt whatsoever that such is the case. The results obtained herein given a strong indication that buckling will not occur. Furthermore, the physically realistic explanation given previously supports this hypothesis.

Figure 72 shows the prebuckled shapes of the shells and the buckling mode shapes. Both the axial and circumferential wavelengths of the buckle pattern become shorter as the degree of prebuckling distortion increases. These results apply to a shell with radius-to-thickness ratio of 100. Similar results (with higher wave numbers n and shorter axial wavelengths) were obtained for $a/t = 500$. It seems probable that no buckling will occur for any simply supported cylinder heated as shown in Fig. 69. It has not

been shown that buckling will not occur independent of the axial distribution of temperature. Such a proof is beyond the scope of this section.

Buckling of Axisymmetrically Heated Clamped Cylinder: Johns [99, 108] performed tests and obtained theoretical results. The effect of prebuckling deformations is not included in the analysis of Ref. [99]. Figure 73 shows a clamped cylinder with the same a/t as that tested by Johns, et al [108]. Symmetry conditions are applied at 500 in. from the clamped end, a distance approximately equal to $10(at)^{1/2}$. Nodal points are concentrated in the edge zone 100 in. in length where prebuckling and buckling displacements vary rapidly. Two buckling modes and critical temperatures are given in Fig. 73: the one with 140 circumferential waves corresponds to a case in which the prebuckling rotations β_0 are retained in the stability analysis, and the one with 100 circumferential waves corresponds to β_0 being set to zero in the stability analysis. This latter solution is about half of that computed by Johns. The solution including prebuckling rotations is only half of the experimental buckling temperature obtained by Johns.

The large discrepancy between the test and the theoretical results given in Fig. 73 for uniform heating can be explained by the presence of the axial gradients near the boundaries of the cylinder. Figure 74 shows several gradients, including the gradient measured by Johns, Houghton, and Webber [108] and another measured by Ross, Hoff, and Horton in tests reported in Ref. [104]. These gradients arise because of the relatively large heat sinks present at the clamping supports. Also shown in Fig. 74 are the test configuration, material properties, and circumferential temperature distribution for the Johns' test [108, 109].

Figure 75 shows buckling temperatures calculated for the Johns' cylinder ($a = 7.0$ in., $t = 0.00275$, $E = 27 \times 10^6$ psi, $\nu = 0.287$, $\alpha = 11.5/^\circ\text{C}$ with the various gradients and with and without the effect of prebuckling rotation β_0 . The "best" solution shown in Fig. 75, in the sense that the most accurate analytical model is used, is represented by the curve labeled "Johns' Gradient," $\beta_0 \neq 0$. The critical temperature, 280°C is still somewhat below the test result, a disturbing finding since one suspects that although this edge buckling phenomenon is not very sensitive to initial imperfections, any imperfections in the shell should cause the opposite situation to occur.

In order that this discrepancy be explained, a further inquiry into the shape of the edge gradient was made [109]. It was found that the temperature at $x = 0$ was not measured, but was extrapolated from the readings labeled (3), (4), (5) in Fig. 74. Furthermore, the two thermocouples on the bulkhead, labeled (1) and (2) in Fig. 74, measured temperature rises of 9, 16, and 8.7°C (mean values for 7 tests). Therefore, it was felt that the temperature at $x = 0$ might have been somewhat less than 47% of the maximum, as indicated in Fig. 74. A sensitivity study was performed in which the temperature at the edge was varied from 20% to 47% of the maximum value. The trial gradients and analytical results are shown in Fig. 76. Circumferential waves corresponding to the critical temperature are shown in parentheses. The effect of prebuckling rotations becomes increasingly significant as the steepness of the gradient increases. The lowest values on the curves are the same as the minima of the curves labeled Johns' Gradient in Fig. 75. Test and theory are brought into agreement by a small and physically reasonable adjustment of the edge temperature.

In Webber's letter [109] other reasons were given for possible discrepancy between text and theory: buckling was measured by dial gages located along the generator labeled "290°C" in Fig. 74, not along the generator where the gradient was obtained. The critical temperature was recorded when these gages indicated large out-of-plane deflections. This happened a short time after the onset of buckling. Also, the shell thickness varied from 0.0025 to 0.0030 in., whereas a nominal value of 0.00275 has been used in this analysis.

Results corresponding to gradient 1 and gradient 2 are included in Fig. 75 in order to provide more data on the sensitivity of thermal buckling loads to details in the shape of the edge gradient. The Ross edge gradient is given in Fig. 74 to demonstrate the possibility of rather large nonuniformities in experimental temperature distributions. In order that good correlation between tests and analytical predictions be obtained, it is clear that temperature distributions have to be carefully controlled and measured in tests and variations accounted for in analysis.

Buckling of an Internally Pressurized Rocket Fuel Tank

Figures 77 - 79 pertain to this section. The geometry of the problem is shown in Figs. 77 and 78. Under small internal pressure the portion of the rocket fuel tank depicted in Fig. 78 is drawn radially inward as shown greatly exaggerated in Fig. 79 (a), resulting in development of a narrow band of hoop compression that might lead to bifurcation buckling. Figure 79 (b) shows a bifurcation buckling mode predicted with use of BOSOR4 [14]. The modal normal displacement component $w_b(s, \theta)$ varies around the circumference as $w_b(s) \cos 90\theta$. The prediction shown in Fig.

79 (b) corresponds to bifurcation from the linear prebuckled state with prebuckling meridional rotation β_0 neglected in the stability analysis.

At the top of Fig. 78 is shown a bifurcation buckling mode predicted with use of linear theory. The modal normal displacement component $w_b(s, \theta)$ varies around the circumference as $w_b(s) \cos 90\theta$.

This is a problem for which use of linear theory in the prebuckling phase of the analysis is inadequate. As the internal pressure is increased the ellipsoidal dome changes shape. The hoop stresses are redistributed and grow more slowly than linearly with pressure, as indicated in the bottom part of Fig. 78. As the internal pressure p is increased, the hoop resultant becomes tensile in the region where linear theory predicts bifurcation buckling to occur, and the peak hoop compression initially increases more slowly than predicted by linear theory, eventually reaching a maximum value of about -800 N/mm at a pressure of 1.4 N/mm^2 , after which it decreases with further increases in internal pressure. Thus, the prediction with non-linear prebuckling effects included is that bifurcation buckling will not occur at all. More will be written in a later section on buckling of internally pressurized torispherical shells, which exhibit similar behavior.

Local Buckling at a Field Joint in a Large Rocket Payload Shroud

In Fig. 5 is illustrated a local failure of a large corrugated payload shroud which was subjected to axial compression and bending. Most of Fig.

5 is repeated in Fig. 80. The nature of the problem is similar to the complex missile interstage shown in Figs. 59 - 61: The failure is triggered by the axisymmetric inward excursion of the axial load path at Station 468. In this case, however, buckling initiated in the elastic range of material behavior and the failure was due to nonsymmetric bifurcation rather than axisymmetric collapse.

Figure 80(d) shows why buckling occurs. Under the axially compressive test load the field joint ring at Station 468 rolled over a small amount because the doubler above it was slightly thinner than the doubler below it. Figure 81 displays the model analyzed with use of the BOSOR4 program [14]. Figure 82 (a) shows the distribution of axisymmetric prebuckling radial displacement w for 60 inches on either side of the field joint at Sta. 468. Most of the cylindrical shell moves radially outward due to the Poisson effect. However, in short regions on either side of the field joint, where the external corrugations are cut away, the axial load path is deflected inward from the neutral axis of the cross section of combined corrugations and skin to the middle surface of the skin and doubler. This inward deflection of the load path creates the localized hoop compression that causes nonsymmetric bifurcation buckling in a mode shown in the photograph in Fig. 80 (c) and plotted in Fig. 82 (b). Because of the short axial length of the circumferentially compressed region, the critical mode has a rather large number of circumferential waves ($n = 35$). Further details on this problem are given in Ref. [3].

Bifurcation Buckling of Spherical Shells

Under Meridional Tension Combined with Hoop Compression

Axial Load Applied Uniformly Over Latitude with Finite Radius r_1

Figure 83 demonstrates the buckling phenomenon. Tension is applied through the vertical rods which are attached to rigid spherical mandrels inside the shell. The lower hemisphere is completely supported by an interior mandrel and a little less than 45° of the top part of the upper hemisphere is so supported. A single buckle (a) initially forms at some axial load, which can be further increased until a multi-lobed buckle pattern (b) develops around the entire circumference. Bifurcation buckling is due to the band of hoop compression that develops between the supported regions. The buckles are elongated in the axial direction because of the meridional tension. Yao [110] studied this phenomenon both experimentally and analytically and Bushnell [111] performed a computerized nonlinear analysis. One of Yao's post-buckled specimens is shown in Fig. 84.

Table 4 shows critical loads $r_1 V_{cr} (1 - \nu^2) E t^2$ for $0.05 \leq \alpha_1 \leq 1.16$ rad and $R/t = 100, 455, \text{ and } 1600$. ($r_1, \alpha_1, \alpha_2, V$ are identified in Fig. 85.) Values for α_2 are given in the footnote. Spherical segments of this geometry buckle near the edge at α_1 when α_1 is less than about 0.9 rad. The buckling loads are independent of α_2 when it is greater than the values specified in the footnote of the table. The critical loads in the column headed "linear" are calculated from stability equations in which the pre-buckling stress resultants, N_{10} and N_{20} are given by membrane theory values $N_{10} = -N_{20} = r V R / r^2$ and the prebuckling meridional rotation β_0 is set equal

to zero. The critical loads in the column headed "nonlinear" are obtained from the same stability equations, except that N_{10} , N_{20} , and β_0 are calculated from the nonlinear equations presented in Chapter 2. The values of n when $\alpha_1 \geq 0.25$ correspond to the minimum $r_1 V_{cr}(n)$. The minimum is included in the calculations for $\alpha_1 \leq 0.20$. Columns are also included in which $r_1 V_{cr}$ is calculated from a "semiempirical" equation to be given. The following facts emerge from an inspection of Table 4:

- 1) The critical load $P_{cr} = 2\pi r_1 V_{cr}$ increases as r_1 increases.
- 2) The linear theory can be applied over a larger range of α_1 for shells with greater R/t . The values of $r_1 V_{cr}$ for the nonlinear theory are always greater than those for the linear theory.
- 3) When $\alpha_1 \leq 0.2$, the nonlinear theory predicts buckling into a greater number of circumferential waves than does the linear theory. This discrepancy increases with increasing thickness.
- 4) The value of $r_1 V_{cr}$ and the corresponding value of n approach appropriate limits as $\alpha_1 \rightarrow 0$, as shall be seen.

In addition, the solutions for $R/t = 455$ and 1600 with $\alpha_1 = 1.16$ and $\alpha_2 = 1.57$ rad are quite close to the theoretical results of Ref [110]. Yao obtained buckling loads $r_1 V_{cr} (1 - \nu^2)/Et^2 = 0.591$ and 0.553 , respectively, for these cases.

Figure 85 shows the axial prebuckling displacement u_{v0}/t , the normalized stress resultant $N_{20} (1 - \nu^2)(R/t)/Et$, and the modal normal displacement w/t plotted vs $s/(Rt)^{1/2}$ for $\alpha_1 = 0.7$ and $R/t = 100$ and 1600 . The maximum displacement in the buckling mode occurs where N_{20} is maximum compressive. It is seen that this maximum compressive hoop stress is fairly close to the local value predicted by membrane theory; this is also shown in the figure.

It is possible to derive simple approximate formulas for the buckling load rV_{cr} and the corresponding wave number n . These formulas are derived with the help of physical reasoning and experimental or computer-generated data. Such a formula for the buckling load is

$$r_1 V_{cr} (1 - \nu^2) / Et^2 = 0.622 \sin^2 [\alpha_1 + 3.1 / (R/t)^{1/2}] \quad (32)$$

The number of circumferential waves in the buckle pattern can be predicted accurately by means of the equation

$$n = 1.84 (R/t)^{1/2} \sin [\alpha_1 + 4.2 / (R/t)^{1/2}] \quad (33)$$

Equation 32 is derived through the following assumptions: (1) Buckling occurs when the maximum negative value of $N_{20} (R/t) (1 - \nu^2) / Et = 0.622$, independent of shell geometry. (2) The point at which N_{20} is maximum compressive is located a distance $3.1(Rt)^{1/2}$ from the edge at α_1 , and its value at that point can be determined accurately from membrane shell theory.

Equation (33) is derived through the following assumptions: (1) The maximum normal displacement w in the buckling pattern occurs where N_{20} is maximum compressive. (2) The circumferential wavelength is proportional to $(Rt)^{1/2}$.

There is a current important engineering problem to which this type of buckling of spherical shells applies. Very large spherical tanks for transporting liquid natural gas (Figs. 86(a)) are supported on short cylindrical shells as illustrated in Fig. 86(b). When the tank is less than half filled the weight of the liquid natural gas creates axial tension that might cause buckling of the type shown in Figs. 83 or 84.

Pedersen and Jensen [112] have studied this problem. Fig. 87 shows results from their analysis.

Axial Load Applied at a Point

Figure 88 shows the post-buckled state of a very thin spherical shell with axial tension applied at a point rather than over a finite radius r_1 . Table 4 lists critical loads for small α_1 and $\alpha_1 = 0$. As might be expected, nonlinear prebuckling effects are very important in this case. From Table 4 it is seen that for $\alpha_1 \leq 0.05$ rad the critical loads in the column headed "nonlinear" are much higher than those in the column headed "Linear."

Table 5 gives dimensionless loads PR/Et^3 and wave number n as functions of R/t . For practical purposes, PR/Et^3 is independent of R/t when R/t is greater than about 500. In the entire range $R/t \geq 50$ the buckle pattern has 8 circumferential waves.

Figure 89(a) shows the dimensionless vertical prebuckling displacements u_{v0}/t and the dimensionless circumferential stress $N_{20}(1 - \nu^2)(R/t)/Et$ for the loads at which bifurcation occurs in 8 circumferential waves. The values of R/t used in the calculations are 50, 100, 455, 1600, and 3040. Displacements and stresses are plotted vs a dimensionless arc length $s/(Rt)^{1/2}$. As might be expected, the maximum displacement occurs at the point of load application. The maximum compressive hoop stress occurs at $s/(Rt)^{1/2} = 4.25$ and $N_{20}(1 - \nu^2)(R/t)/Et = 0.667$. The values of N_{20} calculated from membrane shell theory are also shown in Fig. 89(a).

Figure 89(b) shows the modal displacements w/t , $(v/t)(R/t)^{1/2}$, and $(u_H/t)(R/t)^{1/2}$ corresponding to bifurcation in an 8-wave pattern. The maximum displacements occur near the point where the maximum prebuckling compressive hoop stress N_{20} occurs. For $R/t \geq 50$, w/t , $(v/t)(R/t)^{1/2}$, and $(u_H/t)(R/t)^{1/2}$ are almost independent of R/t when these quantities are plotted vs $s/(Rt)^{1/2}$. The displacements are confined to fairly shallow portions of the spherical shells.

Buckling of Internally Pressurized Vessel Heads

Introduction

The examples presented here fall into the same class as those of the previous section: buckling under meridional tension combined with hoop compression. However, the shells described here are not spherical. The problem is of special significance to designers of pressure vessels, many of which have torispherical or ellipsoidal heads. An example of a typical post-buckled pattern for an elastic shell is shown in Fig 90.

This class of problems is particularly interesting because in the range of practical design parameters predicted behavior is found to be sensitive to prebuckling geometric nonlinearity as well as material nonlinearity, the former effect increasing the critical pressure and the latter decreasing it. Therefore, the problem serves as an excellent demonstration of the kinds of nonlinear phenomena an engineer should be aware of when he undertakes a stability analysis. The description here applies to both torispherical and ellipsoidal vessel heads, although most of the applications shown in Fig. 90 - 104 and Table 6 are to torispherical heads.

Interest in internally pressurized torispherical heads was stimulated by the failure of a large fluid coker undergoing a hydrostatic proof test at Avon,

California in 1956. The failed vessel is shown in Fig. 3. Galletly [113, 1] determined from an elastic, small-deflection analysis that the stresses exceeded the yield point of the material by considerable margins over substantial portions of the vessel. Galletly's work [113] stimulated Drucker and Shield [114, 115] to perform limit analyses of shells of revolution using simplified yield surfaces for a Tresca material. Other elastic-plastic analyses of torispherical shells were published by Gerdeen and Hutula [116], Crisp and Townley [117], and Simonen and Hunter [118]. Calladine [119] presented a novel analysis of the limit pressure of torispherical heads which gives results similar to those obtained by Shield and Drucker [115]. Savé [120] conducted a series of tests on torispherical, toriconical, and flat heads. Several papers on the elastic-plastic analysis of pressure vessel heads may be found in Ref. [121], including contributions by Gerdeen [122], Mescall [123], and Marcal [124]. Other references to work in this area are given by Esztergar [125].

The possibility of nonaxisymmetric buckling of internally pressurized torispherical heads was first predicted by Galletly [1]. Fino and Schneider [126] reported such buckling in a head designed according to the ASME code, but at a pressure slightly below the design pressure. It is likely that the unexpectedly low buckling pressure resulted from nonaxisymmetric imperfections generated when spherical and toroidal gores were welded together to form the very large head. Mescall [127] was the first to present a solution of the nonaxisymmetric stability analysis. He used elastic small deflection theory. Adachi and Benicek [128] conducted a series of buckling tests on torispherical heads made of polyvinyl chloride (PVC), chosen primarily because of the high ratio of yield stress to Young's modulus, which ensures that buckling occurs before large-scale yielding. The correlation of elastic analysis

with these tests was much improved by inclusion of nonlinear geometric effects. Thurston and Holston [129] were the first to account for moderately large axisymmetric prebuckling meridional rotations in the stability analysis of these heads. Since publication of Ref. [129] many computer programs have been written which calculate nonsymmetric buckling loads of arbitrary elastic shells of revolution including geometric nonlinearity in the prebuckling analysis and prebuckling shape changes in the stability analysis [11 - 14].

Recently, several papers have appeared on nonsymmetric buckling of elastic-plastic pressure vessel heads: Brown and Kraus [130] calculated critical pressures for internally pressurized ellipsoidal heads with use of small deflection theory. Bushnell and Galletly [131] found buckling loads for externally pressurized torispherical heads pierced by nozzles and for conical heads with use of large deflection theory in the prebuckling analysis, and Bushnell and Galletly [132], Lagae and Bushnell [133], and Galletly [134, 135] used the BOSOR5 computer program to compare theoretical predictions with tests by Kirk and Gill [136], Patel and Gill [137], and Galletly [134, 135] for buckling of internally pressurized torispherical and ellipsoidal heads.

Cause and Characteristics of Nonsymmetric Bifurcation Buckling

Figure 91(a) shows a discretized model used for the BOSOR5 analysis of a torispherical head. Finite difference nodal points are concentrated in the region where buckles are expected to appear. Figure 91(b) is a schematic of the meridian as deformed axisymmetrically by internal pressure. Circum-

ferential (hoop) compression develops wherever the radius r is diminished from the undeformed state. It is this hoop compression that causes nonsymmetric bifurcation buckling. The value of the buckling pressure p_{cr} depends most strongly on the value and meridional distribution of the hoop stress resultant N_{20} , on the curvature of the deformed meridian in the region where N_{20} is compressive, on the material properties, and of course on the thickness of the shell. The circumferential bending rigidity C_{55} (Eq. (84) of Ref. [430]) is probably the most important component of stiffness in the calculation of the stability determinant because the critical circumferential wave number n_{cr} is usually very high for such a geometry and the strain energy associated with the buckling mode thus varies approximately as $C_{55} n_{cr}^4$. Figure 94(b) shows typical buckling modes corresponding to an elastic analytical model. The buckles are shown outward although of course they vary as $\cos 50\theta$ and $\cos 90\theta$ in the circumferential direction.

The development of visible buckles such as shown in Fig. 90 is a process and not the single event predicted by a bifurcation (eigenvalue) buckling analysis. As the pressure in a test specimen is increased above some critical value a very localized isolated incipient buckle forms in the knuckle region, invisible to the naked eye but detectable by a sensitive probe or a strain gage. The buckle grows slowly at first and then more rapidly, and suddenly becomes visible. This visible buckle generally covers most of the knuckle region in the meridional direction but has a very short circumferential wavelength. After formation of the first buckle the pressure can be further increased substantially, causing the formation of other visible buckles in the knuckle region, each one isolated circumferentially from its neighbors, as shown in Fig. 90. An isolated buckle, generated by circumferential compression in the knuckle

region, apparently causes the relief of this compression within a sector surrounding the buckle, thereby preventing the formation of the uniform buckle pattern typical of buckled axially compressed cylindrical or externally pressurized spherical shells.

The theoretical results shown here are derived from an analysis which is founded on the assumption that we are especially interested in the pressure at which the first incipient buckle forms. Therefore, buckling is treated as a single event, predicted by means of the eigenvalue formulation summarized in the previous analysis section.

Difference in Elastic Behavior of Ellipsoidal and Torispherical Heads

Figure 92 shows the hoop stress resultant distribution in an elastic 2:1 ellipsoidal head compared to that in a similar torispherical head with geometry as shown in the Figure. Dimensions of the ellipsoidal shell are shown in Fig. 93(a). The buckling mode in the torispherical head has a maximum at a location nearer to the axis of revolution than does that in the ellipsoidal head, corresponding to the different locations of the peak compressive hoop resultant at the critical pressure.

Elastic Bifurcation Buckling

Accurate prediction of bifurcation buckling loads in the elastic range of material properties requires an accounting for nonlinear geometric effects in the axisymmetric prebuckling analysis and inclusion in the nonsymmetric stability (eigenvalue) analysis of the fact that the prebuckled head has a new axisymmetric shape.

Figure 93(a) shows a discretized model of an ellipsoidal head analyzed with BOSOR5 [47]. The axisymmetric prebuckling deflected shape is shown in Fig.

93(b) and a nonsymmetric bifurcation buckling mode with critical pressures from linear and nonlinear theories are given in Fig. 93(c).

What causes the difference between the buckling pressures calculated for elastic material with small deflection theory and with large deflection theory? Fig. 93(d) helps to explain. The predicted bifurcation pressure depends on the distribution of the meridional and hoop stress resultants and on the wall curvature in the area where the first buckles appear. The values of these quantities depend on whether or not moderately large deflection effects are included in the analysis.

Assuming that the wall material remains elastic, the most significant determinant of the buckling pressure for a shell of given properties is the hoop stress resultant N_{20} in the area of the knuckle where buckling occurs. Fig. 93(d) shows that in this region N_{20} does not grow linearly with pressure but quite a bit more slowly. The slower-than-linear growth of compressive N_{20} in the axisymmetric prebuckling regime is due to two factors: As the pressure is increased the ellipsoidal shape "tries" to become more spherical. For a small internal pressures, a given increment in pressure causes a relatively large shape change because the meridional curvature varies steeply in the region where N_{20} is compressive. For higher internal pressures the variation of meridional curvature has become more gradual and the given pressure increment therefore causes less of a further change in shape. The second and smaller factor causing slower-than-linear growth of N_{20} is the pressure-rotation effect. The nonlinear growth of N_{20} explains why the buckling pressures from nonlinear elastic theory are higher than those from linear theory.

There is another nonlinear phenomenon which has the opposite effect on the buckling load: As the pressure is increased, the meridional curvature diminishes in the region where buckling occurs, as can be seen from Fig. 93(b). This axisymmetric decrease in meridional curvature in the prebuckling regime has the effect of reducing the circumferential stress resultant required to cause buckling. The middle curve in Fig. 93(d) gives the critical hoop resultant distribution predicted with use of small deflection theory -- a theory which neglects the reduction in meridional curvature due to the axisymmetric prebuckling change in shape of the ellipsoidal head. Notice that this critical hoop resultant distribution is generally larger in absolute value than is the critical distribution of N_{20} predicted with use of large deflection theory.

Figure 93(e) shows the buckling modes from the large and small deflection analyses. The peaks in the buckling modes follow the same trend as the peaks in the distribution of compressive N_{20} .

Similar nonlinear geometric effects are present in the case of torispherical pressure vessel heads. Figure 94(a) shows a discretized model of a torispherical head of the type tested by Adachi and Benicek [128]. Analytical and experimental results for elastic torispherical heads of various geometries are given in Figs. 94(b) and 95. The nonlinear theory always leads to prediction of higher buckling loads and these predictions are generally in much better agreement with the test results than are the predictions obtained with use of linear theory. The nonlinear results from BOSOR5 are in reasonably good agreement with the critical pressures predicted by Thurston and Holston [129]. Typical buckling modes are shown in Fig. 94(b).

Figures 96 (a) and (b) show post-buckled states of a small machined torispherical head made of aluminum and a large torispherical head fabricated by forming. Buckling for these heads occurred in the plastic range of material behavior. The buckles are isolated from each other and have short circumferential wavelengths, as observed for the elastically buckled model shown in Fig. 90, but they protrude from rather than indent the shells. This protruding mode was observed in the post-buckled specimens tested by Galletly [134, 135], Kirk and Gill [136], and Patel and Gill [137].

The two biggest effects of plastic flow on the predicted bifurcation buckling pressure are the following:

1. The rate of change of the compressive hoop stress resultant with increasing pressure is strongly dependent on the rate at which the material strain hardens;
2. The integrated constitutive coefficients $[D_{TO}]$ (See Eq. 255 of Ref. [430]) are reduced from their elastic values.

Figures 97 (a) and (b) show the peak hoop resultant as a function of internal pressure for two values of post-yield hardening modulus E_T . A typical behavior of mild steel torispherical shells is that they buckle nonsymmetrically at pressures for which the hoop compression is diminishing in the knuckle region, as shown in Fig. 97 (c). (Yielding initiates in this shell at $10^6 p/E=1.33$) Figure 98 shows the very large difference between predictions of prebuckling stress from linear and nonlinear analyses. The nonlinear results were obtained

by application of BOSOP5 [47] to a specimen tested by Adachi [128], and they agree with the measurements.

Table 6 lists test and predicted incipient buckling pressures for many of the internally pressurized torispherical machined specimens analyzed with BOSOP5. The nominal dimensions of the specimens are given in Table

6. The quantities, t , R_c , R_t , R_s , and L_c are the nominal thickness, radius of the cylinder to which the head is attached, radius of the toroidal knuckle, radius of the spherical closure, and length of the cylindrical portion to which the head is attached, respectively.

The thicknesses of the test specimens varied in both the circumferential and meridional directions. Typical circumferential variations of thickness in the toroidal knuckle where buckling occurs are shown in Fig. 99. BOSOP5 runs were made using the minimum thicknesses measured at each meridional station. In the BOSOP5 models as well as in the actual specimens the thickness varied in the meridional direction by as much as 30%. The differences in the BOSOP5 predictions for specimens with the same nominal geometry arise from different meridionally varying thickness distributions used in the discretized models.

Plastic flow prior to bifurcation buckling occurs in a fairly broad axisymmetric band near the junction between the spherical and toroidal portions. Stress-strain curves for the specimens and maximum effective strains at buckling are shown in Fig. 100. There is reasonably good agreement between test and theory for the aluminum specimens. Discrepancies may be due to the fact that the actual specimens were nonsymmetric

because of circumferentially varying thickness and meridian profile, whereas the BOSOP5 models are axisymmetric. Also, the material flow law (associated with von Mises yield surface) and hardening law (isotropic) may not be adequate to describe the actual plastic behavior. Figure 101 shows that with a small amount of strain hardening the path followed by a material point in stress space as the pressure is increased monotonically is sharply curved. We do not yet understand metal plasticity well enough to be able to predict with certainty the state of a structure that has undergone nonproportional biaxial loading.

In general the BOSOP5 computer program [47] seems to predict bifurcation buckling at a location nearer to the sphere-torus junction than observed in the tests, and the critical circumferential wave number obtained from the theories in which plasticity is included are somewhat lower than the values observed from the post-buckled states of the specimens.

From Table 6 it is seen that the buckling pressures predicted with use of deformation theory are somewhat less than those obtained with use of flow theory. The primary reason for the lower values associated with deformation theory is that the constitutive law coefficient D_{T550} (Eq.(225) in [430]) including elastic-plastic effects, is considerably smaller in the region where buckling occurs if deformation theory is used. This coefficient relates the change in circumferential curvature during buckling to the change in circumferential buckling moment resultant, and is especially important because the circumferential wavelength of a buckle is small. Therefore the circumferential bending energy required to form a buckle is perhaps the most significant part of the total strain energy balance associated with buckling.

The test and theoretical results for the four mild steel specimens are not in close agreement, as seen in Table 6. A detailed explanation is suggested in Ref. [132]. To summarize here, it is possible that the buckling mode associated with the lowest predicted eigenvalue grows very little in the post-buckling regime and so this mode was therefore not observed in the tests. This explanation seems likely in view of the characteristic shown in Figs.

97(b) and (c) that the compressive hoop resultant in the knuckle region decreases steeply after yielding of the elastic-perfectly plastic material. Also likely is the fact that because circumferential nonuniformities in the thickness of test specimens cause relatively large circumferential pre-bifurcation bending strains to develop as the pressure is increased, the compressive destabilizing circumferential stress resultant grows more slowly with increasing pressure than predicted by the axisymmetric BOSOR5 model. A more detailed explanation is offered in Ref. [132].

From Table 6 it is seen that use of linear elastic theory always leads to a lower prediction of bifurcation buckling pressure than use of nonlinear elastic theory. The reasons for the different predictions are given in the discussion associated with Fig. 93.

Figures 102 - 104 pertain to aluminum torispherical specimens tested by Patel and Gill [137]. Figure 103 gives comparisons of predicted and measured incipient buckling pressures for the heads shown in Figs. 102(a) and (b). The ranges of pressures over which the buckling patterns were observed to develop are also indicated in Fig. 103. In Fig. 103:

P_{ACT} = pressure at which the first buckle was fully developed,

P_{CLEAR} = pressure at which the first buckle could be felt by touching the surface of the specimen,

$P_{INCIPIENT}$ = pressure at which the first buckle was detected by a sensitive probe revolved around the circumference at

a station in the toroidal knuckle.

Figure 104 shows the growth of a minute incipient buckle pattern in one of Patel and Gill's specimens over a pressure range $0.402 \leq p \leq 0.617 \text{ MN/m}^2$. Again, we see that in actual specimens what we are characterizing as a single event called "bifurcation buckling" is actually a process that occurs over a finite range of internal pressure.

Results given by Lagae and Bushnell [133] indicate that reasonably accurate predictions of incipient buckling can be obtained with models in which constant thickness is assumed, the model thickness being taken as the average measured thickness along the toroidal knuckle meridian for which this average is minimum. The quality of the theoretical predictions of incipient buckling as well as the behavior of the test specimens as the pressure is increased above the incipient buckling pressure indicate that these types of vessels are not particularly sensitive to initial imperfections.

Conclusions about Bifurcation Buckling of Internally Pressurized Heads

1. The major effect of moderately large axisymmetric prebuckling deformation is to cause the band of circumferential compression which occurs in the knuckle to increase more slowly than in proportion to the pressure, as shown in Figs. 93(d) and 97. Thus, buckling pressures predicted with use of geometrically nonlinear prebuckling theory are higher than those predicted with use of linear prebuckling theory (Table 6).
2. A smaller counteracting influence of moderately large deflections is due to the effect of the increase in meridional radius of curvature of the knuckle region during prebuckling deformations on the nonaxisymmetric stability analysis: This curvature change causes a reduction of the pre-

dicted buckling pressure from a value that would result if terms related to it were dropped from the equations governing the stability analysis, as demonstrated by the middle curve in Fig. 93(d).

3. For monotonically increasing pressure above that causing initial yielding, the circumferential and meridional stresses in the knuckle do not increase proportionally. The curvature of a path in stress space followed by a given point depends very strongly on the amount of post-yield strain hardening exhibited by the material from which the vessel head is fabricated: The less the strain hardening, the more this path is curved, as shown in Fig. 101.

4. As might be expected, the predicted buckling pressure obtained with elastic-plastic analysis is less than that obtained with elastic analysis (Table 6).

5. Use of deformation theory rather than flow theory in the stability analysis leads to lower predicted buckling pressures (Table 6).

6. The distribution and magnitude of the hoop compression in the knuckle region depends very strongly on the degree of strain hardening exhibited by the material. The peak compressive hoop resultant in a vessel head fabricated from mild steel or other material with negligible strain hardening increases initially with increasing pressure, but very soon starts to decrease as the knuckle is stressed into the plastic range, as seen in Figs. 97(b) and (c). In contrast, if the material exhibits a moderate amount of strain hardening, the peak compressive hoop resultant continues to in-

crease to higher pressures before it reaches a maximum value, as disclosed by Fig. 97(a). This difference in behavior of the destabilizing hoop resultant affects the strategy to be used for calculation of bifurcation buckling eigenvalues, as pointed out in Ref. [133].

7. Buckling occurs only for very thin specimens. For example, with 2:1 heads nonsymmetric buckling occurs only if the diameter-to-thickness ratio is greater than about 500. It is not presently within the state of the art to fabricate by machining specimens of reasonable size for testing in the laboratory with thickness variations around the circumference less than five to ten percent. These small nonaxisymmetric variations cause the growth of circumferential waves in the knuckle at pressures well below the buckling pressure. It is felt that the circumferential nonuniformity is responsible for rather large discrepancies between measured and predicted strains in the knuckle region of torispherical shells for pressures exceeding the proportional limit of the material.

8. The observed buckling pressure depends on how buckling is defined. In the tests on torispherical shells performed by Galletly [134], the first buckling pressure is defined as that pressure at which the first buckle becomes visible to the unaided eye. In the tests by Kirk and Gill [136], the buckling pressure is defined as that pressure at which a short-wavelength disturbance is first detected by a sensitive displacement transducer rotated around the circumference at the midpoint of the knuckle. In one of Kirk and Gill's specimens there was more than a 50 percent increase in the pressure from that at which the transducer detected a small wave to that at which the wave grew to such a size that it became visible.

9. Finally it is concluded that in order to obtain a fuller understanding of the elastic-plastic behavior of thin vessel heads under internal pressure, a better understanding of the biaxial flow of metals subjected to nonproportional loading is needed, as well as the capability to manufacture very thin test specimens in which the tolerance on axisymmetry of thickness is about an order of magnitude smaller than is possible with state-of-the-art fabrication techniques.

A Summary of Examples Already Described

We have already seen many examples in which nonsymmetric bifurcation buckling of shells of revolution occurs near the axisymmetric collapse load. The classical equation for buckling of a monocoque cylindrical shell under uniform axial compression contains no reference to the number of circumferential waves. Indeed, it is disclosed in Ref.[430], Fig.29 that for very thin cylinders, use of nonlinear theory leads to a prediction of axisymmetric elastic collapse due to bending near the edge at an axial load only 20% higher than that corresponding to nonsymmetric bifurcation buckling with $n_{cr} = 18$ circumferential waves. The thicker axially compressed cylinder shown in Fig. 6 fails initially in an axisymmetric collapse mode, but just after the peak in the load-deflection curve has been passed a nonsymmetric deformation pattern begins to develop, indicating the presence of a bifurcation point near the maximum load.

The two-column shallow truss shown in Fig. 10 displays simultaneous symmetric collapse and bifurcation buckling for a certain value of the shallowness parameter h/L , as demonstrated in Fig. 12. The shallow spherical cap under uniform external pressure exhibits analogous behavior. Shallow spherical caps clamped at the edge fail by axisymmetric collapse and bifurcation buckling at the same pressure for a value of the shallowness parameter λ of about 6, as seen in Fig. 37. Caps with edge rings act in a similar fashion, as revealed by the predictions listed in Table 3 for small edge angles.

The axisymmetric collapse and bifurcation buckling loads of fairly thick ring-stiffened cylinders under external hydrostatic pressure are often close. Figures 35 and 36 indicate that inclusion of room temperature creep leads to a prediction of axisymmetric collapse at a slightly lower load than that corresponding to nonsymmetric bifurcation buckling predicted for the same model with creep neglected. Similar differences in buckling behavior might be expected to result from application of hydrostatic pressure to two similar ring-stiffened cylinders, one made of a material that displays less strain hardening than the other. The specimen made of the milder material is more likely to collapse axisymmetrically whereas the other might buckle nonsymmetrically, depending on geometry.

Finally, infinite and finite length long straight pipes under bending fail by collapse due to smooth flattening of the cross section combined with a short axial wavelength wrinkle or bifurcation buckling mode that develops just before the peak moment is reached, as shown in Figs. 39 and 43. With a high enough external pressure applied in addition to the bending moment, the wrinkling mode develops just after the maximum in the moment-curvature-change path has been attained. Figure 42(b) indicates that collapse and bifurcation buckling occur at almost the same critical moment for cylinders of any length. Certainly this is true for very short cylinders because these behave, at the circumferential location where axial compression is maximum, in a way similar to cylinders under uniform axial compression. We have already seen from Fig. 29 of Ref. [430] that axisymmetric collapse and nonsymmetric bifurcation buckling for uniformly axially compressed cylindrical shells occur at loads that are fairly close.

Failure of a Water Tank

In 1972 in Belgium a steel water tower of 1500 m^3 capacity collapsed as it was being filled for the first time. This accident and analyses of the structure are described in [2] and [140]. Figure 3 shows the tower after failure and its overall dimensions. The collapse occurred when the water was almost at the maximum level for which the tank was designed. It is felt that collapse probably initiated in the conical section near the deepest water level. Figure 3(b) shows a wrinkled meridian at this location which gives credence to this hypothesis.

As might be expected the catastrophic failure of such a large, expensive, and fairly complex shell structure motivated engineers to seek an explanation. Professor Vandepitte, Dr. Laize, and their coworkers at the University of Ghent in Belgium tested models made of mylar [141]. Figure 105 shows a specimen before and after collapse which occurred when the model was filled to a level 38 cm above the clamped base. With linear prebuckling analysis the BOSOR4 computer program [14] yields a prediction of a critical load factor $p = 1.12$ corresponding to nonsymmetric bifurcation buckling with 14 circumferential waves. In other words, if a prebuckling stress state is calculated from linear theory corresponding to a water level of 38 cm, and a solution is obtained of an eigenvalue problem of the type in Eq.(123) in Ref.[430], in which K_1 is the stiffness matrix of the unloaded shell and K_2 is the load-geometric matrix corresponding to the membrane stress resultants in the wall of the tank when it is filled to a level of 38 cm, the lowest eigenvalue λ corresponds to $n = 14$ circumferential waves and its value is $\lambda = p = 1.12$. The predicted buckling mode is shown in Fig. 105(d). Buckling is caused by meridional compression which is maximum at the clamped base. This com-

pression is combined with a circumferential stress resultant distributed as shown in Fig. 106. The phenomenon is analogous to buckling of an axially compressed cylinder with internal pressure.

Figure 107 shows a plot of maximum prebuckling normal deflection w vs load factor p corresponding to the tank with internal hydrostatic pressure linearly varying over the constant axial distance of 38 cm above the clamped base. The problem is solved here in a slightly unrealistic way: The level of the fluid is held constant at 38 cm, which corresponds to the level at which failure occurred in the test. The amplitude p of the linearly varying normal pressure is increased in increments, indicated by points on the prebuckling load-deflection curve shown in Fig. 107. Thus the load paths in stress space seen by theoretical material points in the BOSOR4 model are different from those actually experienced by the corresponding points in the shell wall during the test. As long as the predicted load multiplier is fairly close to unity this path difference is immaterial, since no path-dependent plastic flow occurred in the test specimen. Even if plastic flow does occur before predicted failure, which as shall be seen is the case for the BOSOR5 model of the large steel water tower shown in Fig. 3, the path difference is very small in the critical region if buckling occurs over a relatively short meridional distance near the bottom of the tank as it does in the elastic model (Fig. 105(c,d)).

In Figure 107 bifurcation buckling points p_{lb} and p_{nb} corresponding to the critical number of circumferential waves, $n_{cr} = 14$, are shown on the linear and nonlinear prebuckling load-deflection paths. The buckling modes in both cases are almost identical (Fig. 105(d)).

Figure 108 shows the axisymmetric prebuckling displacement distributions predicted from linear bending theory at $p = 1.0$ and nonlinear theory for two load levels near axisymmetric collapse. The meridional variation of w at the load multiplier $p = 0.993$ corresponding to collapse resembles the nonsymmetric bifurcation buckling mode displayed in Fig. 105(d).

The theoretical and experimental results are very close, indicating that the test model was well made and the critical load is not as sensitive to initial imperfections as one might expect for a very thin conical shell in which the destabilizing prestress component is axial compression. There are two reasons for the apparent milder sensitivity to initial imperfections displayed by this problem than that for axially compressed thin cylindrical shells which it resembles: The highest axial compression occurs in a fairly local region near the clamped base and, more significant, a stabilizing circumferential tension exists. It has been found that critical loads for axially compressed cylindrical shells with internal pressure are less sensitive to initial imperfections than are those without internal pressure [34]. One reason for this decreased sensitivity is that the internal pressure increases the amplitude of the local axisymmetric bulges near the edges, creating a rather large predictable imperfection that grows as the axial load is applied. Without the internal pressure, a similar bulge of much smaller amplitude is created only by the Poisson effect.

The numerical solution of this problem has many pitfalls. These arise from:

- (1) The close proximity of loads corresponding to axisymmetric collapse and nonsymmetric bifurcation buckling;

- (2) The sensitivity of the results to nodal point distribution in the critical area where buckling occurs;
- (3) The numerical difficulty caused by the fact that the shell can buckle under external pressure as well as internal pressure, leading to the possibility that the smallest eigenvalue λ of the system represented by Eq.(123) of Ref.[430] might correspond to solution of the wrong physical problem.

An Attempt to Predict Elastic-Plastic Buckling of the Large Steel Water Tower Including Fabrication Effects

In this section an attempt is made to explain the unexpected collapse of the steel water tower shown in Fig. 3 by accounting separately for residual stresses and deformations caused by axisymmetric cold bending or welding or mismatch between structural segments. The analysis shows that axisymmetric models of these effects do not explain the discrepancy between the predicted collapse under hydrostatic pressure and the actual collapse in 1972 of the 1500 cubic-meter tower. However, the modeling techniques and results are included here to demonstrate how such effects might be accounted for in an approximate manner and the influence they have on predicted collapse loads. More is written on this subject in the section on ring-stiffened cylinders. The results described here were obtained with use of the BOSOR5 computer program [47].

Tank Configuration and Discretized Model: Figures 109(a) and (b) depict the water tank geometry and discretized, segmented model for use with BOSOR5. Material properties, locations of discrete rings, and locations of circumferential welds are indicated in Fig. 109(c).

Welding: Girth welds are located as indicated in Fig. 109(c). These locations correspond to the junctions between Segments (9) and (10), Segments (10) and (11), and Segments (11) and (12) (109(b)). The water tower had other girth welds, of course, but they were in locations which were less critical for stability and therefore not included in the BOSOR5 model. Longitudinal welds could not be included in the model because they produce a non-symmetric residual stress and displacement pattern.

The welding process introduces destabilizing stresses and deformations because of shrinkage of the weld material during cooling. The effects of weld shrinkage are simulated in [8] and [142] by introduction of an initial thermal loading phase in which it is assumed that a certain amount of material in the local neighborhoods of each girth weld is cooled below ambient temperature to a difference approximately equal to the annealing temperature. The amount of cooling is also determined such that weld shrinkage amplitudes typical of those observed in tests are generated. Faulkner [143] has observed radial girth weld shrinkages of approximately 10% of the shell wall thickness. The residual stress distribution thus generated is characterized by local tensile circumferential yielding in the immediate neighborhoods of the girth welds and elastic circumferential compression over broader bands of width proportional to the "boundary layer" $(Rt)^{1/2}$, in which R is the normal circumferential curvature and t is the shell wall thickness. In addition to this residual stress pattern, the girth welds introduce axisymmetric geometrical imperfections-- local shrinkages that are amplified by the meridional compression generated when the tower is filled with water.

Figure 110(a) shows the assumed temperature distribution along the conical portion of the water tower in which three girth welds are being simulated. In the BOSOR5

analysis this thermal loading is applied first and the shell thus pre-stressed is subsequently further loaded by the hydrostatic pressure. Figure

111 shows the weld shrinkages generated by welding. The deformed meridians near collapse, neglecting and including initial effects due to girth welding, are shown in Figures 112(a) and (b), respectively. The quantity λ is a load factor such that a factor $\lambda_{cr} = 1.0$ would indicate perfect agreement between the numerical prediction and the actual collapse condition.

Mismatch: When the water tower is assembled, the middle surfaces of the various sections are imperfectly aligned. In the BOSOR5 model it is necessary to restrict the mismatch to be axisymmetric. The two mismatch conditions investigated here are shown in Fig. 110(b).

Cold Bending: The tower was fabricated from steel sheet which was initially flat. The various sections were cold formed to the appropriate radii of curvature. This cold forming operation is simulated by initial thermal loading cycles in the developable Segments (1), (2), (4), and (7) through (12).

The procedure is described in detail in [142]. In each segment the amplitude of the temperature, which varies linearly through the thickness as shown in Figure 113, is initially increased in time to simulate cold bending to a die radius, R_o . Subsequently, the temperature amplitude is decreased to simulate springback to the final design radius of curvature, R . The maximum temperature amplitude T_o is assumed to be constant along the meridian in each segment and is derived for each segment from the formula

$$\alpha_2 T_o = t/(2R_o) \quad (34)$$

in which t is the shell wall thickness and R_o , the average normal circumferential radius of curvature to which the segment is bent before springback, is given by

$$1/R_o = |M| \cdot 12 (1-\nu^2)/(Et^3) + 1/R \quad (35)$$

with

$$|M| \approx \sigma_y t^2 / [4(1-\nu_e + \nu_e^2)^{1/2}] \quad (36)$$

for elastic-perfectly plastic material. In Eq. (34) α_2 is the coefficient of thermal expansion in the circumferential direction. The coefficient of thermal expansion in the meridional direction is assumed to be zero. In Eq. (35) M is the maximum cold bending moment and R is the average normal circumferential curvature in the segment after springback (given by the water tower geometry). In Eq. (36) σ_y is the material yield stress (236 N/mm²). Eq. (34) is derived from Eq.(35) of Ref.[142] and Eq. (35) is derived from Eq.(17) of Ref. [142]. Eq.(36) appears as Eq.(17a) in Ref.[142]. The quantity ν_e is the effective Poisson's ratio, taken as 0.5 here.

The time to complete relaxation of the cold bending moment is given by

$$t_{\text{relax}} = (1 + |M| \cdot 12 (1-\nu^2) R_o/Et^3) t_o; (t_o = 1.0) \quad (37)$$

which appears as Eq.(15) in [142]. Rather than using Eq. (36) for M in calculating t_{relax} , we use BOSOR5 to calculate the circumferential moment M_2 (BOSOR5) corresponding to time $t = 1.0$ in Figure 113 and then set $M = M_2$ (BOSOR5) in Eq. (37). This is done because the residual stresses are quite sensitive to t_{relax} and M , as given by Eq.(36) with $\nu_e = 0.5$, is only an approximation. The temperature amplitudes T_0 and the relaxation times for the various segments are given in Figure 113. After the thermal loading cycle is completed at time $t = 2.0$, the hydrostatic pressure loading is begun.

Figure 114 shows the deformed meridian at time $t = 1.0$ (before springback), $t = 2.0$ (after springback), and at four hydrostatic pressure amplitudes, $\lambda = 0.5, 1.0, 1.4$, and 1.7 . $\lambda = 1.0$ corresponds to the hydrostatic pressure amplitude at which the tower actually failed. The BOSOR5 computer program predicts axisymmetric collapse at lower hydrostatic pressures than non-axisymmetric bifurcation buckling in all the cases treated here.

Table 7 lists predicted failure factors for all the cases investigated. The water tower is considered to be filled to the level indicated in Figure 109(c) and the factors λ_{cr} listed in Table 7 correspond therefore to factors on the density of water, as was the case in the previous section on the tests of mylar models. It is seen from the results in Table 7 that introduction of residual stresses and deformations due to cold bending flat sheets into curved parts of the water tower has the largest effect on the predicted failure load, but that none of the axisymmetric models studied here explains the discrepancy between the predicted collapse load and the disastrous failure that occurred as the reservoir was being filled in 1972.

Conclusions: It is concluded from this study that the early failure of the water tower was not due to the axisymmetric effects included here. Figure 3(b) shows a meridional wrinkle similar to those depicted in Figures 112 and 114 occurring in the neighborhood of a meridional weld. Such a weld causes nonaxisymmetric compressive meridional prestresses that reduce the hydrostatic pressure required to cause yielding in a more direct way than does the axisymmetric membrane circumferential compression typical of a girth weld or the complex circumferential residual stress pattern through the thickness generated by cold bending. Also not included in the present analysis are the effects of nonaxisymmetric geometrical imperfections and the effect of initial residual stresses in the flat steel plates from which the tower was subsequently cold bent. These residual stresses arise from fabrication (rolling) of the sheet and cutting of it to size. Also, due to certain input limitations in BOSOR5, the simultaneous effects of welding, cold bending, and mismatch were not studied. Of all the effects not included in this investigation, the largest are probably due to nonaxisymmetric geometrical imperfections and residual stresses from meridional welds.

As a result of the study reported in Ref. [2], however, the tower was redesigned as shown in Fig. 115(a). The predicted collapse of the new design occurs at a much higher load factor, $\lambda = 2.65$, as indicated in Fig. 115(b).

Section 4
EFFECT OF BOUNDARY CONDITIONS AND
ECCENTRIC LOADING

Introduction

This section is devoted mostly to cylindrical shells. Practically all of the investigations of the effect of boundary conditions on stability have been specialized to this most important geometry. The study of the effect of eccentric loading is concentrated even more specifically on axially stiffened cylinders under axial compression.

Practical shell structures are very often built in parts with different organizations of even companies being responsible for the design of "their" part. Very often buckling loads for each part are calculated with the sometimes unjustified assumption of simple support or clamping at the boundaries of that part. The main purpose of the discussion and examples presented here is to give the reader a physical feeling for the influence of various boundary conditions and load eccentricity on buckling loads and thereby to sound a note of warning not to take these factors for granted, especially in the final analysis stage of a project.

Figures 116(a) and (b) show a photograph of a specimen tested by Singer, et al [33] and a schematic of a rather complex boundary clamp in the specimen that might simulate an edge condition between two sections of a rocket. Figure 21 shows the post-buckled state of one such stiffened cylinder subjected to uniform axial compression. One might analyze this cylinder by

including all the parts A through G plus the stiffened cylinder, H, itself and assume that the loading is applied by uniformly moving the end plates "A" toward each other. In such a model it would not be necessary to worry about boundary conditions or eccentricity of load application at the end of the stiffened cylinder H. These factors would emerge as results of the analysis; they would not play the role of the assumptions. Often this is the best approach to the buckling problem, especially if the structure is axisymmetric and a one-dimensionally discretized model is sufficient. The general rule here would be to include in the model all parts of the structure that are defined, or all parts between stations at which there is no doubt as to what boundary conditions and loading should be assumed.

However, because of limitations in computer budget or lack of definition of the adjacent structural parts, it may be necessary to establish a boundary at which there is some doubt as to what the support conditions are and where the load path is. For example, if one assumes that the end of the cylinder H coincides with the location of the lowest row of rivets shown in Fig.

116(b), one must then decide which of the displacement components u , v , w , β are to be restrained and at what radius is the axial load to be applied. The purpose of this section is to reveal the sensitivity of predicted bifurcation buckling loads to these assumptions.

It should be emphasized now that boundary conditions and eccentric loading influence the stability, in particular the bifurcation buckling load, in two ways:

- (1) The prebuckling membrane stress resultants at a given load depend on these factors; therefore the load-geometric matrix, K_2 in Eq. (123) of Ref.[430] depends on them.

- (2) The prebuckling deformations and the structural stiffness at the boundary depend on these factors; therefore the stiffness matrix, K_1 in Eq. (123) of Ref.[430] , depends on them.

We have already seen examples in which boundary conditions and edge load eccentricity affect bifurcation buckling loads. Figures 29 - 31 of Ref.[430] and 62 show how restraint of the radial displacement w at the edge gives rise to local edge buckling in a monocoque axially compressed cylindrical shell at a load approximately 20% less than the classical load, $N_{cr} \approx 0.6 Et^2/R$. Figures 64 and 65 demonstrate, for an externally pressurized spherical cap, the influence of edge support eccentricity on the destabilizing prebuckling hoop compression and therefore on the bifurcation buckling pressure. Figure 68 and Table 3 show the effect of the stiffness of the edge support on bifurcation buckling. The emphasis in those examples is on the nonuniform prebuckling behavior and how it influences the bifurcation buckling load and mode.

Although not strictly true, it might be said for the sake of simplicity that in general the boundary conditions affect the bifurcation buckling load and mode most strongly through their influence on the stability stiffness matrix K_1 , whereas the load eccentricity affects the bifurcation buckling load and mode most strongly through its influence on the prebuckling state and hence on the load-geometric matrix K_2 . This statement is probably more valid when applied to cylindrical shells than to shells of other geometries.

For example, the prebuckling state of a uniformly axially compressed fairly long monocoque cylindrical shell loaded at its middle surface depends on the

boundary conditions only within a "boundary layer" or a distance of approximately two or three times $(Rt)^{1/2}$ of the edge. The prebuckling conditions at the edge have only a mild influence on the predicted bifurcation buckling load, as seen in Figs. 29 - 31 of Ref. [43C]. However, there are several different sets of boundary conditions for which the prebuckling behavior and hence the load-geometric matrix, K_2 , is the same but the bifurcation buckling load and mode shape change radically. For instance, any change in the boundary condition having to do with the circumferential tangential displacement v , which does not appear in the prebuckling problem at all, drastically affects the bifurcation buckling load through changes in the stability stiffness matrix K_1 only. A dramatic example is an axially compressed cylindrical shell with free edges. The axisymmetric prebuckling solution is still characterized essentially by the uniform compressive axial resultant $N_{10} = -P/2\pi R$, but the bifurcation buckling load P_{cr} is several orders of magnitude smaller than the classical value because the possibility of inextensional buckling exists. A specific example of this type of buckling is shown later, both for an axially compressed cylindrical shell and an externally pressurized spherical shell.

On the other hand, the major effect of load eccentricity on cylindrical shells under axial compression is to produce bands of prebuckling hoop compression or tension as well as meridional curvature change. The load eccentricity effect is especially significant in cylinders with axial stiffening because the boundary layers near the supported edges are longer than they are in the case of monocoque cylinders. Therefore, the circumferential tension or compression generated in these boundary layers has an important effect on the load-geometric matrix K_2 and hence on the buckling load.

Summary

Buckling pressures for hydrostatically compressed monocoque cylinders will first be discussed. The results tabulated here are derived from an analysis in which the prebuckling state is given by membrane theory: axial resultant $N_{10} = pa/2$, circumferential resultant $N_{20} = pa$, no prebuckling deformation. Therefore, the differences in critical pressures p_{cr} and circumferential wave numbers n_{cr} are entirely due to the effect of the various boundary conditions on the stability stiffness matrix K_1 in Eq. (123) of Ref. [430]. (Note that when we relate boundary conditions to the stability stiffness matrix K_1 we are tacitly assuming that the Lagrange multiplier method is being used as shown in Fig. 24 of Ref. [430] or that certain rows and columns of K_1 have been modified to account for the boundary constraint conditions).

Following is a discussion of the effect of boundary conditions on the buckling of monocoque axially compressed cylinders. Most of the results correspond to a rigorous nonlinear prebuckling analysis including edge effects, although a comparison is given for one set of boundary conditions in which membrane theory and exact bending theory are used in the prebuckling analysis. Again, the differences in the critical loads corresponding to the various boundary conditions arise primarily from the changes in the stability stiffness matrix K_1 and not from changes in the prebuckling state leading to modification of a load-geometric matrix K_2 .

Examples of inextensional buckling of a stiffened cylindrical shell under axial compression and part of a monocoque spherical shell under external pressure are shown next. It is demonstrated that the critical loads can be several orders of magnitude less than the classical values because very little strain energy is required to deform these shells in their near-inextensional buckling modes.

An example of bifurcation buckling of a complex shell in the plastic range is then given. Because of the local nature of the plastic flow near a stress con-

centration at a structural junction, an elastic model can be set up in which the development of the plastic hinge is simulated in the stability analysis by modification of one of the compatibility conditions at the structural junction where plastic flow occurs.

Some examples are then given of the effect of boundary conditions on the buckling of stiffened cylindrical shells under axial compression. It is shown that the effect of the boundary conditions has a significant influence over a larger range of length-to-radius L/R than is the case for monocoque shells.

The section closes with examples of the effect of load eccentricity on bifurcation buckling of axially stiffened cylindrical shells under uniform axial compression. In particular the dependence of the critical load on eccentricity of the load, length of the shell, use of membrane v. bending prebuckling analysis, and external or internal location of the stringers are explored for a particular case.

Effect of Boundary Conditions on Buckling of Monocoque Shells

Much of the early work on the effect of boundary conditions on the buckling of cylindrical shells is reviewed by Hoff [29]. Von Mises [144], Nash [145], Galletly and Bart [146], Singer [147] and Sobel [148] studied cylindrical shells under uniform hydrostatic external pressure. Nachbar and Hoff [149], Stein [150], Fischer [151], and Almroth [152] and others identified in [29] treated cylindrical shells under uniform axial compression. The most definitive investigations were carried out by Sobel [148] and Almroth [152]. They assumed that buckling would be symmetrical about the midlength of the cylinder generator (not necessarily true in the case of axially compressed cylindri-

cal shells), and they calculated buckling loads for eight boundary conditions as listed in Table 8.

Cylinders Subjected to Uniform External Hydrostatic Pressure

Sobel [148] assumed a membrane prebuckled state. His results are listed in Table 9 for different values of length-to-radius L/a with radius-to-thickness a/h fixed at 100 and Poisson's ratio equal to 0.3. The set of boundary conditions represented by $S_1 (w = M_x = N_x = v = 0)$ is the same as that used in von Mises' solution [144] for a simply supported cylinder. The results of Sobel for the set S_1 agree with von Mises' results to four significant figures, the degree of accuracy used in Sobel's analysis. Table 9 also gives the results obtained by Nash [145] and by Galletly and Bart [146] for clamped cylinders. The combination of boundary conditions used in Refs. [145, 146] is here represented by the set $C_4 (w = w_{,x} = u = v = 0)$.

From a comparison of results for C_4 and S_4 we see that restraint of meridional rotation $w_{,x}$ does not significantly increase the critical hydrostatic pressures unless the cylinders are quite short. Moreover, this same result is always obtained whenever critical pressures for cylinders with $w_{,x} = 0$ are compared with those for cylinders with $M_x = 0$ (edge moment = 0), all other conditions being equal.

The most significant result of Sobel's analysis is the revelation of the important effect of axial restraint $u = 0$ on buckling pressures even for moderately long cylinders. Table 9 is organized to emphasize this effect, the first four columns of results corresponding to u free ($N_x = 0$) at the edge and the next four to u fixed.

Almroth [152] accounted for prebuckling bending in his analysis, which includes buckling under combined axial compression and internal or external lateral pressure. Computed critical values of the axial load for the case of zero lateral pressure are shown in Table 10. For comparison corresponding results were also obtained by Almroth with use of the membrane prebuckling solution. With boundary conditions corresponding to cases S3 and S4, ($M_x = 0$, $N_{xy} = 0$) these results differ very little from those listed in Table 10. In the other six cases the critical load with the membrane prebuckling solution, within the parameter range considered, is equal to or insignificantly higher than the classical buckling load for simply supported cylinders ($N_{cr}/N_{cl} = 1.0$).

It appears from Table 10 that, with the exception of very short shells, the critical load is practically independent of the parameters r/t and L/r in all of the cases. In contrast to expectations, lower values of the critical load are in some cases found for the very short shells. Therefore, the influence of the shell length on the critical load was studied in more detail. The critical load vs the parameter L/r , for a cylinder with $r/t = 100$ and with boundary conditions corresponding to case C2, is shown in Fig. 117(a). Here the number of circumferential waves is held constant ($n = 8$). For long shells the critical load is independent of shell length, and for very short shells the critical load is, as expected, monotonically increasing with decreasing shell length. In the intermediate range an oscillatory behavior is displayed.

A similar variation of the critical load with L/r occurs for the cases S3 and S4. In Fig. 117(b) the critical load is shown vs L/r for case S3. It is seen in this case that the general behavior does not change when the influence

of lateral restraint in the prebuckling analysis is neglected. For relatively long cylinders the curve with the membrane prebuckling solution is slightly below the rigorous solution. However, for very short cylinders this difference increases, as may be expected.

The most significant results obtained by Almroth are those corresponding to S3 and S4, for which the circumferential tangential displacement v is free ($N_{xy} = 0$). This result, first calculated by Stein [150], is similar to that obtained by Nachbar and Hoff [149] for axisymmetric buckling of an axially compressed cylinder with a completely free edge. However, neither type of free-edge buckling is likely to occur in practice because friction at the ends of the axially compressed cylindrical shell is sufficient to prevent the buckling modes from developing.

Inextensional Buckling

Even lower buckling loads for axially compressed cylindrical shells than those calculated by Almroth [152] are possible if one assumes that the edges are completely free. Cohen [96] was the first to point this out. The critical buckling mode is antisymmetric about the midlength of the cylinder and involves no change in curvature of the generators. This mode is of course prevented if the buckling modal displacement pattern is assumed to be symmetrical at the symmetry plane at the cylinder midlength. The buckling mode is inextensional; that is, the middle surface undergoes no stretching. Therefore, the membrane component of buckling modal strain energy is zero. Again, this mode is unlikely to occur in tests of axially compressed cylindrical shells because of friction.

Buckling loads associated with inextensional mode shapes can be very low indeed, as shown in Figs. 118 and 119. Figure 118 gives buckling loads of an axially compressed 5° cone (almost a cylinder), supported at its edges by rings of square cross section. The buckling mode with $n = 2$ circumferential waves is inextensional if the edges are free and very close to being inextensional for all ring sizes. Figure 119 shows buckling pressures of incomplete spherical shells with edge rings of various areas. Again, unless the ring is fairly large, buckling loads may be many orders of magnitude smaller than the buckling load for a clamped or simply supported shell of the same geometry.

A physical appreciation of inextensional behavior can be gained by cutting a ping-pong ball in half and squeezing one of the halves between your fingers. Large deflections occur with very small applied force. A coffee cup dispensed from a vending machine is made with a reinforcing ring at the top to limit the amplitude of inextensional deformations caused by the squeezing pressure of your fingers required to keep the full cup from dropping to the floor. A conical planetary reentry vehicle, such as the Viking shell (Figure 190), is designed on a similar principle: potentially large inextensional deformations caused by nonsymmetric reentry pressures are prevented by a large edge ring.

Because of the small amount of energy required to deform shells inextensionally, designers should avoid configurations in which inextensional deformations of the wall are free to occur in systems subjected to destabilizing loads. Analysts investigating buckling of shells should avoid the use of boundary conditions that might permit inextensional buckling unless these conditions represent the actual support. It is the writer's experience that users of BOSOR4 [14] have had difficulty when leaving some branch of the

structure free at the end because "it's not the part I'm really interested in." Often the lowest eigenvalue corresponds to large buckling modal displacements at the end left dangling. The user is not able to obtain buckling in the region of his concern without restraining this troublesome end.

Simulation of Effects of Local Plastic Flow by Appropriate Constraint Conditions

There are two reasons for including this discussion here. The first is stated in the subtitle: to describe a certain application of constraint conditions as a modeling technique to simulate a condition in which plastic flow has occurred without actually accounting for this flow explicitly. The other reason is to demonstrate the appropriateness of sometimes using different constraint conditions in the prebuckling and bifurcation buckling phases of an analysis. The phrase "constraint conditions" is used rather than "boundary conditions" because the phenomenon described here has to do with conditions at a junction between two structural segments rather than at an edge.

Figure 120(a) shows the geometry of three specimens tested by Galletly [154] and analyzed by Bushnell and Galletly [131]. These specimens were subjected to external pressure. One of the buckled specimens is shown in Fig. 120(b). A discretized BOSOR5 model [47] is shown with the axisymmetric prebuckling deformed shape in Fig. 120(c). Plastic flow occurs before bifurcation buckling in a very narrow circumferential band surrounding the meridional slope discontinuity between the conical and cylindrical segments. Figure 120(d) shows predicted bifurcation buckling modes and pressures for models in which the elastic-plastic flow is explicitly accounted for and compatibility of meridional rotation at the junction between segments (2) and (3) is enforced in both the prebuckling phase and bifurcation buckling phase of the analysis.

Table 11 lists the test results, the BOSOR5 results with use of elastic-plastic analysis, and predictions in which plasticity is ignored but an attempt is made to simulate its effect by modification of the compatibility conditions at the junction between segments (2) and (3). It is seen that for the configurations investigated a good elastic model is one in which meridional moment compatibility at the cone-cylinder junction is enforced in the prebuckling analysis but relaxed in the stability analysis (Case 5). That the predicted buckling loads are close to the test values for this simplified elastic model apparently is the result of two counteracting errors: The prebuckling model is too stiff and therefore at a given pressure the stress resultants, which appear in the stability equations, are too small. Counteracting this effect is the underestimation of the meridional bending rigidity at the junction in the stability analysis. Clearly both effects are important, since introduction of the hinge in the prebuckling analysis lowers the predicted buckling pressure considerably, and enforcement of elastic meridional moment compatibility in the stability analysis raises it considerably.

A similar result is obtained for the case of externally pressurized torispherical heads pierced by cylindrical nozzles as shown in Figs. 121(a-d). Plastic flow occurs in the immediate neighborhood of the nozzle-head junction. Comparisons of predicted and test buckling loads are shown in Figs.

121(c) and (d) and listed in Table 12. The same modeling "trick" yields good results for this geometry. Further details on geometry, material properties, and discretization are given in Ref. [131].

Effect of Boundary Conditions and Loading
Eccentricity on Buckling of Axially Compressed Stiffened Cylindrical
Shells

Boundary Conditions

We have seen from Table 10 and Figures 117(a) and (b) that the influence of shell length on the buckling of axially compressed monocoque cylindrical shells is very small unless the shell is extremely short. This is not true for cylinders stiffened in the axial direction, as seen from the example in Fig. 122(a). Buckling loads are given there for clamped axially compressed cylinders of various lengths with a wall construction consisting of a longitudinally corrugated sheet welded to an inside smooth sheet (Fig. 122 (b)). The internal Z-shaped ring stiffeners are heavy enough to cause local buckling as shown. The asymptote represents the predicted buckling load of a simply supported bay 15 inches long. Intuitively, it is surprising that the clamping condition at the edge significantly affects the critical load for cylinders with many bays. Since buckling occurs between rings, one might think that the critical load would approach the asymptote much more rapidly as the number of bays is increased. However, the theoretical results shown in Fig. 122(a) have been confirmed by tests, as will be described.

Figure 122(c) helps to explain the slow convergence. The nonsymmetric moment applied at the simply supported edge simulates the effect of clamping there during the transition from an axisymmetric prestressed state to a post-buckling state with 16 circumferential waves. Our intuition of what length of cylinder is required before the buckling load becomes independent of length is based on the more familiar but much shorter axisymmetric boundary layer length, $\sim 3 \sqrt{Rt_{eff}}$, also illustrated in Fig. 122(c) in the frame

labeled " $n = 0$." (t_{eff} is the effective thickness of a monocoque wall with the same axial flexural rigidity as the axially stiffened wall.)

The length effect demonstrated in Fig. 122(a) has been confirmed by tests. The panel photographed in Fig. 123(a) failed at 2550 lb/in axial compression in a mode predicted by the BOSOR4 computer program to occur at 2800 lb/in with 13 circumferential waves. The theoretical buckling mode is shown in Fig. 123(b). A much longer panel (116 in. instead of 52 in.) with $t=0.02$ in, $t_s = 0.032$ in. and with rings on 15-in centers buckled at 1580 lb/in compression, compared to a predicted buckling load of 1680 lb/in in a mode with 16 circumferential waves.

Ignorance of the length effect might result in designs which are not optimum with respect to weight. For example, the dimensions of the corrugated semi-sandwich wall construction shown in Fig. 122(b) may be arrived at by an assumption that local crippling, such as illustrated in Fig. 124, is to occur at the same axial load as inter-ring buckling, such as shown in Fig.

122(a). If the critical load level for inter-ring buckling is calculated with the assumption that the panel is of length equal to the ring spacing and is simply supported at its ends, then the local dimensions of the wall cross section will be established based on a critical load equal to that indicated by the asymptote in Fig. 122(a). However, actual panels used in a practical structure contain a finite number of bays and may be effectively clamped at certain bolted connections, as shown in Fig. 125(a). Because of the significant length effect displayed in Fig. 122(a), these structures will cripple in a mode such as that photographed in Fig. 124 before buckling in general instability modes involving both skin and corrugations such as those shown in Figs. 122(a) and 123.

The fact that the critical load plotted in Fig. 122(a) approaches the asymptote rather slowly makes it very difficult to design test specimens properly. Cost usually dictates the use of rather short specimens. Figure 125 gives an example of the problem. An actual shroud is pictured in Fig. 125(a). It was desired to determine experimentally the effect of the field joint depicted in Fig. 125(b) on the buckling load corresponding to the type of general buckling indicated in Fig. 123. Figure

125(c) shows the sad results: the test panel failed in a crippling mode at $N_{cr} = 1620$ lb/in., far below the predicted critical load of $N_{cr} = 3450$ corresponding to general instability, and well below the predicted load $N_{cr} = 2287$ lb/in for a similar specimen without a field joint. Figure 125(d) shows prebuckling behavior of the specimens with (A) and without (B) the field joint. Early crippling near the edge at $N_{cr} = 1620$ lb/in, which occurred in both tests of panels with and without the field joint, is due to the local biaxially compressive stress field there, as proven in Ref. [3], where other details are given.

In general, engineers interested in designing a particular segment of a larger structure should make every effort to determine as accurately as possible the actual boundary conditions at the ends of "their" segment. Portions of the adjoining segments should be included in the model, possibly with a cruder mesh. If little is known about the adjoining structures, sensitivity studies should be performed in which both upper and lower bounds on the degree of boundary constraint are assumed. Before expensive test specimens are fabricated analytical simulations of the test should be performed, with proper representation of the boundary conditions to be applied and account for the possibility of local buckling. The effort in building and testing

the rather expensive panel shown in Fig. 125(c) was largely wasted because the question, "What effect does the field joint have on general instability?", was not answered due to early failure in an unexpected mode.

Singer and his coworkers have been contributing for several years to our knowledge of the buckling and vibration behavior of stiffened cylinders under axial compression [156 - 158]. They have been focusing their efforts on the effects of boundary conditions and load eccentricity. Tables 13 and 14 show comparisons between test and theory for cylinders of the type shown in Fig. 21 supported at the edges as illustrated in Fig. 116. The theoretical results were obtained with the BOSOR4 computer program [14]. A typical buckling mode is shown in Fig. 21. It appears that the actual support condition pictured in Fig. 116 can most accurately be simulated by SS3 (classical simple support) rather than by the other postulated end conditions, although as Singer points out [158] the picture is complicated by the presence of load eccentricity.

Figure 126, which is analogous to Fig. 122(a), demonstrates the effect of cylinder length on the critical axial load. The figure shows results from analyses in which the prebuckled state is predicted from membrane theory (labeled linear) and from BOSOR4 [14] and a treatment by Block [159] in which the prebuckled state is derived from a rigorous analysis. As with all of the examples in this section, the axial stiffeners are "smeared out" over the circumference in the manner described in the classical paper by Baruch and Singer [160]. Two important points might be made with regard to the results shown in Fig. 126:

- (1) For long shells nonuniform prebuckling effects are unimportant;
and
- (2) The effect of constraint of axial displacement u in the bifurcation buckling analysis is rather significant even for long shells.

This behavior may be contrasted to that of monocoque axially compressed cylinders. The columns headed "S1" and "S2" in Table 10 correspond to what Singer calls "SS4" and "SS3", respectively. In the case of monocoque cylinders the normalized critical load predicted with a model in which nonuniform prebuckling effects are included is reduced from 1.0 to approximately .85 even for infinitely long shells because the buckling modal displacements occur in and near the "boundary layer" near the edge as shown in Fig. 62. Buckling with such a short axial wavelength is not possible for axially stiffened cylinders because of the bending stiffness of the stiffeners. Therefore, stiffened cylinders buckle as shown in Fig. 21 in the region where the prebuckling state is pure axial compression. Inclusion of prebuckling bending is important only if this nonuniformity occurs over most of the shell length. Comparison of the columns headed "S1" and "S2" in Table 10 reveals that the axial component of edge restraint has a much smaller influence on the critical load for the monocoque shell than for the stiffened shell to which Fig. 126(b) applies.

Figure 127 demonstrates the effect of elastic axial restraint on predicted buckling for one of Singer's specimens. Further details are given in

Ref. [33].

Load Eccentricity

One of the first studies of the effect of eccentricity of axial load on the buckling of axially compressed cylinders is reported in Ref. [161].

Singer and his colleagues have published several papers on this topic [156 - 158]. The examples exhibited here are taken from Ref. [153].

The definition of axial load eccentricity is somewhat arbitrary. Singer [156] defines any axial load that is not applied at the middle surface of the skin as eccentric. Almroth and Bushnell [153] use the neutral surface of the skin and stringer combination as a reference for load eccentricity. Figure 128 (a-c) shows how load eccentricity might be deliberately introduced and varied in test specimens and how most axially stiffened cylindrical shells are actually tested (d).

The remainder of the discussion in this section is based on axially compressed axially stiffened cylindrical shells with geometry shown in Fig.

129. (Note that the stringers may also be external.)

Results for cylindrical shells of length 95 in. are listed in Table 15. Critical axial loads were computed for the cases in which the shells were simply supported (S2) at the midsurface of the skin, at the neutral surface of the cross section, and at the midpoint of the rectangular stiffeners, respectively. Clamped shells were also considered and, for each type of loading, critical loads were obtained for shells with both external and internal stiffening.

For comparison critical loads are shown also as computed by use of the membrane prebuckling analysis. For the buckling analysis classical simple support conditions were assumed (S2 or SS3). Hence, there is no axial restraint, and with a membrane prebuckling analysis there is no loading eccentricity effect. The results from the first three loading cases are therefore identical.

It may be seen from Table 15 that changes in the loading eccentricity have drastic effects on the critical load. For the case in which the shell is loaded through its neutral surface, for example, it is interesting to compare results obtained with membrane prebuckling analysis with those obtained with nonlinear prebuckling analysis. The difference is due to the Poisson expansion in connection with radial restraint at the edges. This effect is large for shells with such a small L/R ($L/R = 0.5$) particularly for shells with outside stiffening.

For shells with end moments it is easy to see that the presence of a moment which tends to bend the cylinder into a barrel shape greatly increases the critical load. A moment in the opposite direction, developing prebuckling compressive hoop stresses, has the opposite effect. In Fig. 130 prebuckling radial displacements (u_{HO}) and buckling modes (w) are shown for cylinders with inside stiffening. Curves are shown for loading through the neutral surface as well as for loading through the center of the stiffeners.

For cylindrical shells the effects of load eccentricity were studied also for the case in which the buckling displacements in the axial direction are restrained ($u = 0$). The results are shown in Fig. 131. It can be seen that the critical load varies sharply with the position of the point of load

application. For both large positive and large negative eccentricities the critical load calculated with membrane prebuckling theory approaches the critical load with clamped edges. This is because any rotation in the buckling mode about the eccentrically located end points forces the shell wall to deform in a mode with significant membrane strain energy due to axial stretching and compression of the neutral surface.

For cylinders with external stiffening and small positive values of the eccentricity parameter, the buckling mode is antisymmetric about the midpoint of the shell. In all other cases it is symmetric.

The cylinders for which results have been given previously are quite short, the decay-length for the edge moment being about half the shell length. It appears that the influence of edge moments disappears as the shell length increases. This effect is demonstrated in Fig. 132, which shows critical loads as functions of shell length for cylinders loaded through the neutral surface and for cylinders loaded through the centroids of the stiffeners.

For very shallow toroidal segments a study was undertaken of the influence on the critical axial load of the shell rise H (difference between radius at equator and radius at edge). The analysis includes shells with positive shell rise (positive Gaussian curvature) as well as shells with negative shell rise, and the results are shown in Fig. 133. As expected, the critical load increases with the value of the Gaussian curvature. At zero shell rise, the curve for shells with outside stiffeners is much steeper than the curve corresponding to inside stiffeners. This result indicates that shells with outside stiffeners should be more sensitive to initial imperfections, which has been shown by Budiansky and Hutchinson [162] to be the case.

Section 5

INSTABILITY OF SHELLS OF REVOLUTION SUBJECTED TO COMBINED LOADS AND NONSYMMETRIC LOADS

Summary

The emphasis in this chapter is on monocoque and stiffened cylindrical shells.

Combined Loading

We have already seen examples of buckling behavior under combined internal pressure and axial compression. Figures 105 - 108 display the buckling phenomenon of a conical water tank. Bifurcation buckling behavior of the conical water tank is similar to that of a cylindrical shell with internal pressure subjected to axial compression: The buckles are elongated in the circumferential direction and the critical axial load is less sensitive to initial geometric imperfections than that for the shell with no internal pressure. The diminished sensitivity to initial imperfections is revealed by the results in Fig. 22 for pressurized cylindrical shells, as well as by the excellent agreement between test and theory for buckling of the mylar model of the water tank shown in Figs. 105 - 108.

This section first gives illustrations of post-buckled states of monocoque cylindrical shells under combined axial compression and internal pressure. Next several interaction curves are presented for monocoque cylinders subjected to axial compression combined with internal or external pressure. These curves cover a wide range of boundary conditions, radius-to-thickness ratio, r/t , and length parameter $Z = (1-\nu^2)^{1/2} (L^2/rt)$. Post-buckled states of monocoque cylinders under combined torsion and internal pressure are then depicted

with an interaction curve including test points. This is followed by a comparison of theoretical and experimental buckling loads for elastic buckling of stringer-stiffened and ring-stiffened cylindrical shells made of epoxy and subjected to axial compression and external pressure. The section closes with computed interaction curves for laminated composite cylinders under axial compression, external pressure, and torsion.

Nonsymmetric Loading

Nonsymmetric loading on axisymmetric shells may originate from many sources, commonly occurring ones being wind or water loads, thermal loads, and inertial loads arising from ground acceleration during an earthquake. The section opens with two examples of buckling of shells of revolution under nonsymmetric pressure and axial compression caused by launching a rocket and by its passage at an angle of attack through the atmosphere. A closely related problem is buckling due to nonsymmetric thermal loading from aerodynamic heating. Comparisons between test and theory are given for a nonsymmetrically heated ring-stiffened cylindrical shell with applied bending moments and for a monocoque conical shell heated along a narrow axial strip. The section closes with prediction of a buckling load factor for a typical steel containment vessel for a nuclear reactor under combined vertical and horizontal components of ground acceleration experienced during an earthquake.

Axial Compression or Bending and Internal Pressure

Interest in this problem was stimulated primarily by concern for the proper design of pressurized aircraft fuselages. Lo, et al [163] and Harris, et al [164, 36] obtained design curves by testing cylinders and by collecting experimental data from previous tests and performing statistical analyses to obtain buckling loads vs. radius-to-thickness ratio r/t for best fit, 90% probability of survival, and 99% probability of survival. Suer, et al [165] did the same for cylinders under combined bending and internal pressure.

Figures 134 (a-e) illustrate post-buckled patterns for cylinders under axial compression or bending with various amounts of internal pressure. As the internal pressure is increased the buckles become smaller and more elongated in the circumferential direction. If the pressure is high enough, buckling under uniform axial compression occurs in an axisymmetric mode, as seen in Fig. 134 (e). Recall that in the case of the water tank shown in Fig. 105 nonsymmetric bifurcation buckling occurs at a load factor only one percent below axisymmetric collapse (Fig. 107). The water tank problem shares many of the characteristics of the buckling of a uniformly axially compressed cylindrical shell with internal pressure.

Figures 135 (a-d) show coefficients C_b , C_{bp} , and ΔC_{bp} from Suer, et al [165] for buckling of cylinders under bending. Figures 135 (a,b) demonstrate the scatter of test results plotted vs. radius-to-thickness ratio

r/t for unpressurized cylinders, and Figures 135 (c,d) demonstrate the stabilizing influence of internal pressure. The straight horizontal line at $C_b = .78$ in Figs. 135 (a,b) corresponds to the theoretical result for buckling of cylinders under bending found by Flügge [166]. The straight inclined lines labeled " $\sigma_{cr} = pr/2t$ " in Figs. 135 (c,d) represent the axially compressive stress required to cancel the tensile stress $\sigma_x = pr/2t$ caused by internal pressure. The shape of the region of compression test data indicated in Fig. 135(c) by a dashed closed curve shows in a rough way that critical axial loads for cylinders with higher internal pressure are somewhat less sensitive to initial imperfections than are those with lower internal pressure.

Almroth [152] calculated interaction curves for buckling under combined axial compression and external or internal pressure. He accounted for edge effects in the prebuckled state. Predicted critical load combinations are shown in Figs. 136 - 139 for the various boundary conditions S1-S4 and C1-C4 listed in Table 8. In cases S1 and S2 (Fig. 136) the value of r/t has practically no influence on critical combinations of the axial stress and external pressure parameters, within the range of geometrical parameters under consideration.

The analysis with the membrane prebuckling solution indicates that the difference in critical loads for cases S3 and S4 is negligible for all values of the pressure parameter. However, in the presence of internal pressure the use of a rigorous prebuckling solution leads to different results. This is shown by the interaction curves in Fig. 138. With S3 or S4 boundary conditions the number of circumferential waves corresponding to the minimum critical load generally is two. For higher values of the pressure in case S3 this minimum occasionally occurs at a larger number of waves.

In case S3 the curves show that for most combinations of geometrical parameters there exists a range of the pressure parameter within which three solutions are obtained. Of course, when the axial load on the shell is increased under constant internal pressure, only the lowest of these solutions is meaningful.

For clamped cylinders, it was found again that the parameter r/t has no influence on critical combinations of the axial stress and pressure parameters. It was found also that circumferential tangential (v) restraint at the edge does not affect the critical load. Interaction curves for clamped cylinders are shown in Fig. 139.

Torsion and Internal Pressure

The effect of internal pressure on the torsional buckling stress was first considered by Crate, Batdorf, and Baab [167], who developed a semi-empirical interaction formula

$$R_s^2 + R_p = 1 \quad (38)$$

for combined pressure and torsion based on a limited series of tests. In Eq. (38) R_s denotes the ratio of critical shear stress with internal pressure to critical shear stress under torsion alone, $R_s = \tau_{cr}/\tau_{ocr}$, and R_p is the ratio of internal pressure to critical external pressure, $R_p = p/p_{ocr}$.

Hopkins and Brown [168] derived a small deflection theoretical analysis by modifying Donnell's original analysis for unpressurized cylinders. Their theoretical calculations generally agree well with the experimental results of Ref. [167] and substantiate the semi-empirical interaction curve. Harris

et al [36] performed additional tests in order to extend the data to the range of internal pressures and radius to thickness ratios of interest in missile and aircraft design. They tested a total of 5 unpressurized and 15 pressurized model circular cylinders in torsion. For the internally pressurized specimens, the longitudinal tensile stresses induced by pressure were balanced by a compressive load. A photograph of a typical buckle pattern for an unpressurized cylinder is shown in Fig. 140 (a) and for a pressurized cylinder in Fig. 140 (b). As expected, the angle which the buckles make with the axis of the cylinder increases as the ratio of the internal pressure to the torque increases.

In Fig. 141, the test data are compared to the interaction curve of Ref. [167]. In calculation of the values of R_s , the buckling stress σ_{ocr} for torsion alone was defined in [36] as the average of the experimental values. In calculation of the values of R_p , the buckling stress for external lateral pressure alone was calculated from Ref. [169]. It may be seen in Fig. 141 that the interaction curve adequately describes the behavior of circular cylinders in torsion with internal lateral pressure. Based on their data, Harris, et al [36] recommended for design the interaction curve of Fig. 141.

It should be noted that the experimental data of Fig. 141 are for cylinders under lateral pressure only and therefore the data indicate the direct benefit of internal lateral pressure on the torsional buckling stress. If, in addition, the cylinder is axially pretensioned to a stress of $pr/2t$ by the internal pressure on the cylinder heads, an additional benefit would result. It can easily be shown by a Mohr's circle construction that a torsional stress of $0.707 pr/t$ is required before compression is induced in the skin of a hydrostatically pressurized cylinder. At low values of pr/t , the benefit of the

axial tension is relatively small. At large values of $p r / t$ the effect of the axial stress induced by internal pressure can be expected to predominate.

Stiffened Cylindrical Shells Under Combined Loading

Tennyson [170] and his coworkers have performed tests on buckling of unstiffened and stiffened cylindrical shells made of epoxy plastic by a spin casting technique that produces specimens of very high quality. In Ref. [170] they give comparisons between test and theory for elastic buckling of perfect and imperfect clamped shells under combinations of internal or external hydrostatic pressure and axial compression.

Figures 142 and 143 show Tennyson's results for stiffened cylindrical shells under axial compression and external pressure. The solid lines in Figs. 142 (b,c) and 143 (b,c) represent theoretical predictions for perfect shells from Ref. [170], with labels "outside" and "inside" in Fig.

142 (b,c) referring to the rings. There is little interaction effect below $p_{cr}/p_{cro} = 0.8$ for the ring-stiffened specimens because the critical buckling mode for pure axial compression (short axial wavelength) does not at all resemble that for pure external pressure (single half wave along the cylinder generator). On the other hand, there is a strong interaction effect for the stringer-stiffened specimens because the critical buckling mode for pure axial compression has a much longer axial wavelength than that for the ring-stiffened specimen, this mode resembling that corresponding to buckling under pure external pressure.

Inspection of Figures 142 (b,c) and 143 (b,c) reveals that for many of the specimens the theory of Ref [170] underestimates the actual buckling loads. This discrepancy is probably caused by the representation of stiffeners as if they were attached along single lines; that is, in the theoretical model the stiffness is underestimated because the rings do not contribute to the axial bending stiffness of the shell wall and the stringers do not contribute to the circumferential bending stiffness. Actually, the stiffeners probably add considerably to the bending rigidity because they are integral with the skin along finite arc lengths b_{r2} (Fig. 142a) and b_s (Fig. 143a) of the shell wall. Bushnell [171] has found this effect to influence predicted plastic buckling pressures of ring-stiffened cylinders under external hydrostatic pressure by as much as 13%. A larger effect would be expected for elastic buckling than for buckling beyond the proportional limit of the material because the softening nature of a yielding material generally renders predictions insensitive to minor changes in the model.

Also worthy of note in Figs. 142 and 143 is the differing influence of initial imperfections in the ring-stiffened as opposed to stringer-stiffened specimens. In the range $p_{cr}/p_{cr_0} < 0.8$, where short-axial-wavelength buckling occurs in the case of ring-stiffened cylinders, axisymmetric short-wavelength imperfections clearly weaken the shells. Similar axisymmetric imperfections actually strengthen the stringer-stiffened specimens, however. Presumably this is because the imperfections induce a prebuckling axial waviness, a sort of circumferential corrugation that stabilizes the shells, much as the axisymmetric prebuckling shape change in the heated cylinder shown in Fig. 69 postpones nonsymmetric buckling as demonstrated in Figs. 70 - 75.

Buckling of Composite Cylindrical Shells Under Combined Loading

Definitions

By "composite" is meant a shell with a wall construction for which the most general integrated constitutive law is given by Eq. (205) of Ref [430]. Typically, the shell wall is made up of layers or laminae of orthotropic material. Each lamina has principal material axes oriented at some angle θ with respect to the coordinate axes for the shell. An important subclass of such composite shell walls is that for which the constitutive law is given by Eq. (84) of Ref. [430]. This class contains shells of revolution with isotropic skin and rings and stringers that follow principal lines of curvature that are "smeared out" in the mathematical model as described by Baruch and Singer in [160]. Laminated shells of revolution, the plies of which are all oriented parallel to meridians ($\theta = 0^\circ$) and normal to meridians ($\theta = 90^\circ$) also belong to this class. If the wall construction is symmetric with respect to a middle surface the "B" terms in Eq. (205) of Ref. [430] vanish. Such laminates are termed "balanced" and the wall is called "orthotropic." The more general constitutive matrices given Eqs. (205) and (84) of Ref. [430] are associated with wall constructions that are called "anisotropic."

Previous Work Done

Tennyson [172] gives a survey of work done up to 1975 on the buckling of composite cylinders. The earliest analyses were based on orthotropic theory (B-terms in Eq. (205) of [430] are zero) with membrane prebuckling theory. The motivation of much of this early work was to calculate buckling loads of ring and stringer stiffened aircraft fuselages and rocket boosters. One of the first studies was performed by March, et al in 1945 [173], who calculated

torsional buckling loads of plywood cylinders. Frequently referenced works, primarily from the 1960's, on buckling of orthotropic and anisotropic cylindrical shells include Refs. [174 - 190] and [101]. During the late 1960's and early 1970's several computer programs were developed [11 - 14] that can be used to calculate buckling of composite shells of revolution, including nonuniform prebuckling states predicted with use of nonlinear theory. Jones and Hennemann [191] performed parameter studies to determine the influence of nonuniform prebuckling edge effects on bifurcation loads of composite axially compressed cylinders. They found an effect similar to that observed for isotropic cylindrical shells [152]. (See Fig. 117(b)).

Buckling Under Combined Loads

Recently Booton and Tennyson[192] calculated interaction curves for buckling of anisotropic cylindrical shells under axial compression, external pressure, and torsion. Their results are summarized in Figs. 144 - 147. Prebuckling edge effects are accounted for in the analysis. All results correspond to a laminated shell with three layers $(\theta, 0, -\theta)$, which is a very unbalanced laminate and ordinarily does not represent a realistic design. The axisymmetric imperfection assumed for generation of Figs. 144 (b) and 145 (b) has an amplitude of a tenth the wall thickness ($\mu = 0.1$) and an axial wavelength corresponding to that of the axisymmetric buckling mode calculated from classical theory (membrane prebuckling state). Note from Fig. 144(b) that, as in the case of the ring stiffened cylindrical shell under combined axial compression and pressure (Fig. 142(c)), the axisymmetric imperfection causes a reduction in the capability of the shell to carry the axial component of the load but little or no reduction in its capability to carry the circumferential (pressure) component. A similar result is evident in Fig. 145(b) for the case of torsion combined with axial compression.

The curves in Figs. 144(c), 145(c), and 146(c) in which theory and test and compared are plotted in coordinate frames with \bar{R}_p , \bar{R}_x , and \bar{R}_s . These quantities are respectively the ratios $p_{cr}/p_{cr_o}^*$, $P_{cr}/P_{cr_o}^*$, and $\tau_{cr}/\tau_{cr_o}^*$ in which all quantities refer to the imperfect shell and the starred quantities are predicted buckling loads for an axisymmetrically imperfect shell with no other load components acting on it. The amplitude of the imperfection μ is given by $\mu = \sqrt{2} \delta_{rms}/t$, where δ_{rms} is the largest root-mean-squared value of the imperfection determined from profile measurements along several generators. The axial wavelength of the imperfection is equal to that of the classical axisymmetric buckling mode. The correlation with test results is reasonably good, although the actual measured imperfection was not axisymmetric. Had the nonsymmetric nature of the imperfection been accounted for in the analysis, test and theory would doubtless have been brought into closer agreement, especially in cases for which the combined loading involves relatively large components of external pressure.

Figure 147 shows the buckling interaction curve for axial compression and external pressure in the range of small $\bar{Z} = L^2/rt$. Tennyson, et al [193] earlier demonstrated for isotropic shells the transition from concave to convex interaction curves (as viewed from the origin) as \bar{Z} decreases. The convex curves for $\bar{Z} \leq 20$ cannot be predicted without use of a rigorous prebuckling analysis.

Modeling Considerations

In many practical applications, shells of revolution are submitted to non-axisymmetric dynamic loads. Computer programs for the nonlinear dynamic analysis of nonsymmetrically loaded shells of revolution and parts of shells of revolution subtending less than 360° of circumference have been written by Stricklin et al [194], Klein [195], Ball [196], Underwood [197], Huffington [198], and Hubka [199]. Stricklin's, Klein's, and Ball's programs perform both static and dynamic analyses with expansion of the circumferential variations in trigonometric series. Underwood's, Huffington's, and Hubka's perform dynamic analyses with division of the shell into two-dimensional finite difference grids. All of these programs require the same order of magnitude of computer time as any two-dimensional numerical analysis of a shell of general shape, such as that performed by STAGSC [48].

The analyst may wish to embark on a parameter study of buckling of non-symmetrically loaded shells of revolution but may have a limited budget for computer costs. The following questions arise: When can the problem be treated as static? When can the nonlinearities be neglected? When can the nonsymmetries be neglected? As with the axisymmetrically loaded shells discussed previously, static stability phenomena fall into two classes, nonlinear collapse and bifurcation (eigenvalue) buckling. If the structure or loading is such that the shell collapses in a manner similar to that shown in Fig. 45, for example, then one of the computer programs described in [194 - 199] or a general shell analyzer such as

STAGSC [48] must be used for the analysis. If the shell fails by bifurcation buckling, more questions must be asked: Is the behavior r to bifurcation linear? Does buckling occur locally in some area where the stress field is maximum compressive in some biaxial sense? If the behavior prior to bifurcation is nonlinear, as is true for bending of long cylinders discussed in connection with Figs. 39 and 42, can the non-axisymmetric nature of the problem be neglected? If the answer to the first two or the last question is affirmative, then a one-dimensional numerical analysis such as performed by any of the computer programs described in [47] or [11 - 14] can be used. If the prebuckling behavior is linear the nonaxisymmetrical prestress can be determined by superposition of stresses caused by a Fourier harmonic of the nonaxisymmetric load. The program user can then select the meridian where he thinks buckling will start and, assuming that the stress field along that meridian is axisymmetric, calculate bifurcation loads from the same stability equations used for the treatment of axisymmetrically loaded shells. The prebuckling behavior may be nonlinear but rotation of the shell wall about a meridian (ψ in Fig. 17 of Ref. [430]) may be small. If the analyst feels that this nonlinearity cannot be neglected but that the nonsymmetry can, then the bifurcation buckling analysis can be performed with a one-dimensional numerical analysis as described in Ref. [430] . This type of modeling simplification was used to generate the predictions of local failure of the rocket payload shroud shown in Fig. 5. The results are discussed in connection with Figs. 81 and 82.

Whether or not the prebifurcation behavior is linear depends, of course, on the case. As for bifurcation buckling, it is generally true that if the maximum compressive stresses do not vary much in the circumferential direc-

tion within one-half of a buckling wave, then the eigenvalue will not be sensitive to the nonsymmetry of the prebuckling stresses. Bushnell and Smith [200] present a limited study on the sensitivity of predicted thermal buckling loads to the circumferential variation of prebuckling compression. The critical loads are surprisingly insensitive to this variation in the cases studied, as will be seen.

Examples of Buckling of Nonsymmetrically Loaded Shells of Revolution

Figures 148 and 149 show two examples in which buckling under nonsymmetric loading can be estimated by a one-dimensional numerical analysis. The short cylinder depicted in Fig. 148 represents a portion of a rocket subjected during launch to a nonsymmetric combination of axial compression V and external pressure p . The buckling load factor of 1.8 and the buckling mode were predicted from a model in which the one-dimensional discretization is around the circumference of the cylinder rather than along its generator. The short, simply-supported (S2 in Table 8) cylinder is modeled as a toroidal segment with a very large radius b from its axis of revolution to its center of meridional curvature. The prebuckled state is calculated from membrane theory. This modeling technique, conversion of a simply-supported prismatic shell or panel into a toroidal segment, is described in detail in [82] and in a later section here.

Figure 149 shows nonsymmetric pressure loading on the rocket payload shroud depicted in Fig. 5(a). The pressure distribution, measured in a wind tunnel, corresponds to a small angle of attack. The payload shroud, attached to a heavy motor stage at its aft end, bends as a beam and the side under maximum axial compression, the leeward side, buckles between discrete rings. (Buckling does not occur at the root of the beam because

the shell wall is made of thicker gage material there, as indicated in Fig. 5(a).) Here the one-dimensionality of the model is preserved as follows: The nonsymmetric prebuckling state, including bending, is calculated from linear theory; the buckling load and mode are then obtained from an analysis in which it is assumed that the prebuckling stress distribution along the meridian on the leeward side of the shroud is axisymmetric.

The two very different models described in connection with Figs. 148 and 149 lead to preservation in the stability analysis of different aspects of the nonuniform, nonsymmetric loading: the torus model (Fig. 148) leads to preservation of the effect of the circumferential nonuniformity of the prebuckling membrane stress in the stability analysis but neglect of its variation along the meridian; the shroud model (Fig. 149) leads to preservation of the meridional variation of the prebuckling membrane stress but neglect of its circumferential nonuniformity in the stability analysis. The torus model is inadequate for the analysis of the payload shroud because of the axial variation of wall properties, the discrete rings, and the fact that the critical buckling mode corresponds to buckling between the rings, rendering invalid the option of smearing them out. A measure of the error induced by treatment in the stability phase of the problem of the prebuckling stress state along the leeward meridian as if it were axisymmetric can be obtained by setting up a torus model of a short segment between two adjacent rings and comparing critical loads corresponding to two prebuckling stress states, one in which the prestress varies around the shroud circumference as $\cos\theta$ and the other in which it is axisymmetric. Because of boundary effects which propagate along the

shroud meridian as emphasized in the discussion associated with Fig. 122, the absolute values of the two buckling load factors may be inaccurate. However, their relative difference should yield a good qualitative estimate of the error induced by neglect in the stability phase of the problem of the circumferential variation of prestress.

Thermal Buckling of Nonsymmetrically Heated Shells

Introduction: Interest in thermal buckling of thin shells was originally motivated by design requirements for high-speed aerospace vehicles. More recently important applications include thermal buckling of nuclear reactor components and storage tanks for liquid natural gas. Several investigations in this field were made in the late 1950's and early 1960's. Hoff [201] very clearly discussed various aspects of thermal buckling from the points of view of the effect of temperature on material properties, creep, and the effect of nonuniformity of temperature distribution in a structure. We have already seen several examples of buckling due to axisymmetric heating (Figs. 69 - 76). This section is concerned with buckling under nonaxisymmetric temperature distributions.

The early work on thermal buckling of shells deals with monocoque and ring-stiffened cylinders. Anderson [100] gives a brief survey of the work done prior to 1962. He established two classes of problems: buckling of cylinders due to circumferential stresses that vary in the axial direction and buckling due to axial stresses that vary in the circumferential direction. Solution of the first class of problems is motivated by supersonic and hypersonic airframe design involving frame-reinforced fuselages in which the

thin skin heats up rapidly while the more massive frames remain relatively cold. Radial expansion of the skin is thus prevented in the neighborhood of the frames, giving rise to hoop compressive stresses that vary rapidly in the axial direction. These local compressive stresses can cause buckling, as we have already seen in the case of the uniformly heated clamped cylinder (Figs. 73 - 75). Solution of the second class of problems is also motivated by highspeed airframe design, with the emphasis in this case on the fact that because the aircraft is at some angle of attack, the skin heats up nonuniformly around the circumference. The circumferential gradient gives rise to axial stresses which if compressive can cause buckling.

A number of papers has been written on the thermal buckling of axisymmetrically heated ring-stiffened cylinders. Hoff [98] calculated buckling loads for cylinders with hoop stresses which vary in the axial direction. Johns [99] obtained buckling loads for cylinders with compressive line loads, simulating the effect of a cold ring attached to a hot shell. The analyses of Hoff and Johns include the effect of rings as either clamping or simple support or as compressive line loads. Anderson [202] included the flexibility of the rings in an analysis of buckling of ring-stiffened cylinders under combined axial compression and heating. Buckling charts are given in Ref. [202] which cover a wide range of cylinder proportions with boundaries either clamped or simply-supported. Chang and Card [101] calculated buckling loads of ring and stringer-stiffened cylinders under combined axisymmetric axial compression and heating. The rings are treated as discrete elastic structures. Bushnell [102] used a finite-difference energy method to calculate stress and buckling of ring-stiffened shells of revolution subjected to combined axisymmetric pressure, axial load, and non-uniform heating.

There also exists a rather large body of work on buckling of cylinders heated nonuniformly around the circumference. Abir and Nardo [203] concluded that the axial buckling stress under circumferentially variable thermal stress conditions is close to the critical stress of the uniformly compressed cylinder if the variation of the intensity of the thermal stress is not large within a half-wavelength of the buckling pattern.

Hill [105] performed tests and analyzed aluminum and steel cylinders heated on very narrow axial strips of a given width. The prebuckling stress in the shell is calculated assuming that the cylinder is infinite. Hill tested his shells with boundary conditions intending to simulate simple support and clamping. However, only the simple support case represents a valid test, since his "clamping" support rig was far too flexible to prevent end motions of his 48-in. long specimens. Ross, Mayers, and Jaworski [106] extended the experimental work of Hill, studying buckling of clamped cylinders heated uniformly along axial strips of various widths. As might be expected, the analytical and experimental results of Hill and Ross et al. indicate that uniform circumferential heating (with restraint against axial expansion) leads to lower buckling temperatures than does heating along a rather narrow axial strip.

Some work has been done on the more complex problem of determination of thermal stress and buckling of ring-stiffened cylinders in which the temperature varies in both the axial and circumferential directions and in which the shell and rings are at different temperatures. Anderson and Card [204] studied thermal stress and buckling of stainless steel ring-stiffened cylinders subjected to a combination of bending and nonuniform

heating. They obtained the thermal hoop prestress in the cylinder from the analysis of Ref. [202]. The thermal axial prestress was calculated from an analysis in which the cylinder is divided into a number of bays, the axial stress being assumed independent of the axial distance within each bay and variable from bay to bay. Reasonably good correlation was obtained between test and theory. Holmes performed tests for thermal stress [205] and buckling [206] of ring-stiffened cylinders subjected to nonuniform heating and axial compression.

Less work has been done on the problem of predicting thermal stress and buckling of conical shells. Lu and Chang [207] calculated thermal prestress distributions and bifurcation buckling loads of axisymmetrically heated clamped cones and nonsymmetrically heated simply-supported cones. They performed several parameter studies in a range of geometry for which the conical shell behaves essentially as would an equivalent cylindrical shell. In further work Chang and Lu [208] analyzed thermal buckling using nonlinear equations to determine early postbuckling behavior of axisymmetrically heated shells. Bendavid and Singer [209] performed an analysis of conical shells heated non-uniformly along an axial strip. They applied the Ritz method with Hill's technique [105] of using a shape factor to increase rate of convergence of the series expansion of the buckling modal displacements in the circumferential direction.

Most of the work just cited predates the development of rather general computer codes for the analysis of shells of revolution. Thermal expansion effects are included in computer programs written by Cohen [11], Kalnins [12], Svalbonas [13] and Bushnell [14, 17]. The analytical results of this section were obtained with BOSOR [14]. In the following text the phrases "critical temperature" and "buckling temperature" mean the same

thing: the smallest eigenvalue or bifurcation point. "Temperature" denotes the temperature rise above the ambient or zero-stress value.

Convergence checks were made in all cases by calculation with increasing numbers of nodal points and Fourier harmonics. The solutions given in the following sections would change by no more than one or two percent if the given numbers of harmonics and mesh points were doubled.

Anderson and Card Tests [204]: One of the tests in the Anderson and Card series was simulated with the BOSOR code. Cylinder 9 in the test series was chosen for comparison, since Ref. [204] contains all the input data required for this particular specimen. The cylinder which was rigidly clamped at one end and supported by a very heavy ring at the other, was subjected to pure bending and then heated rapidly over a portion of its surface until buckling occurred. Figure 150 shows the input data for the determination of thermal stress. The outer (faying) flanges of the z rings were considered to be at the same temperature as the shell skin at the ring attachment points, and the ring webs and inner flanges were assumed to be at room temperature. The very large ring at the end of the shell was assumed to be rigid but free to translate and rotate as a rigid body. Temperature distributions along the shell length and around the circumference were supplied to the BOSOR program directly from Ref [204]. The circumferential Fourier series expansion of the temperature is calculated in BOSOR, and the result of a 20-term expansion is shown as a dotted line passing through the data input points in Fig. 150(b). Thermal stresses were obtained for this distribution. The rings were treated as discrete elastic structures with all components of moment and product of inertia accounted for. The shell was analyzed in two segments, with 91 nodal

prints in the segment between rings 3 and 5 and 43 nodal points in the segment between rings 0 and 3.

Figure 151 shows circumferential distributions of axial thermal stress at the middle of the bay between rings 1 and 2 ($x = 16.5$) and at the middle of the bay between rings 4 and 5 ($x = 2.224$). Unfortunately, no test results are presented in Ref. [204] corresponding to the heated part of the cylinder.

To compute the buckling load factor the following procedure was used: the axial stress given in Table I of Ref. [204] ($-19.1 \cos \theta$) was added to the thermal stress distribution derived by BOSOR. The generators with the highest compressive axial stress resultant correspond to $\theta = \pm 40^\circ$. The distribution of axial and hoop stress resultants along these generators is therefore used in the stability equations. Buckling loads for various circumferential wave numbers are calculated with the assumption that the axial load and temperature vary proportionally. Because of the rather stiff ring there, stability boundary conditions are introduced to permit antisymmetric buckling at the symmetry plane shown in Fig. 150(a). The minimum theoretical buckling load corresponds to $n = 16$ circumferential waves and an axial load-temperature combination factor λ equal to 1.41 times that obtained experimentally. Buckling is predicted to begin in the bay between rings 4 and 5 at the generators located $\pm 40^\circ$ from the generator at $\theta = 0$ corresponding to maximum heating. Maximum compressive stress resultants occur at $\theta = 40^\circ$ because of the large thermal gradient between 50° and 70° apparent in Fig. 150(b). Figure

152 shows the predicted buckling mode. Agreement between test and theory would doubtless be improved by treatment of the ring webs as flexible shell branches, a technique which will be discussed later (Figs. 182 - 185).
Simply-Supported Cylinder Heated on an Axial Strip: Hill's test [105]

on simply-supported steel cylinders heated uniformly on a very narrow axial strip afford a good check case for the BOSOR computer program, since the bound-

ary conditions are easily modeled and the problem of finite flexibility of supposedly clamped boundaries does not arise. Hill tested 48-in.-long cylinders with diaphragms in the ends. Some cylinders were tested with one diaphragm at each end and some with two diaphragms at each end located 4 in. apart as shown in Fig. 153. The cylinders were otherwise unsupported during the tests. Hill records that the specimens with one diaphragm at each end did not buckle as expected. Instead a ridge formed directly under the heat lamps with subsequent plastic flow. To prevent this nonlinear behavior Hill introduced an additional diaphragm four inches from each end of the cylinder. Figure 153 gives the shell geometry and heating distribution with plots of normal displacement w and axial stress resultant N_x corresponding to $T_0 = 1.0^\circ\text{F}$. These results were obtained with the BOSOR code with 40 Fourier harmonics being used for the expansion in the circumferential direction and 134 nodal points in the axial direction. The diaphragms were modeled as discrete rings rigid in their planes and of zero stiffness for bending normal to their planes. The results are in agreement with those obtained by Hill [105]. It is seen that Hill's assumption of an infinite cylinder is valid for the specimens with two diaphragms at each end of the 48-in. specimen. The formation in the one-diaphragm case of an axial ridge directly under the heating lamps is also predicted by the BOSOR theory. As seen in Fig. 153, this ridge occurs over a range of θ of $-40^\circ < \theta < 40^\circ$ and is about 10^{-3} in from trough to peak for each degree F temperature rise. No such ridge is predicted to occur for the two-diaphragm model.

The straightforward way to use BOSOR to calculate buckling loads for the cylinder heated on a strip would be to assume the axial stress $N_x(x, \theta)$ at $\theta = 0$ is axisymmetric and to use this distribution in the stability equations for the cylinder. However, the compressed region is very narrow and the pre-

stress varies a great deal within a half wavelength of the buckle pattern for the axisymmetrically loaded cylinder. The assumption of axisymmetry of prestress would therefore lead to a somewhat conservative estimate of the buckling load.

The circumferential nonuniformity of axial prestress can be accounted for through the technique described in connection with Fig. 148: the cylinder is treated as a portion of a very slender torus. Figure 154(a) shows the geometry and temperature distribution. A cylinder with an axially uniform prestress is transformed into a torus with a circumferentially uniform prestress. The buckling load is minimized with respect to the toroidal circumferential wave number n , which is inversely proportional to the wavelength of the buckle pattern along the axis of the cylinder. Figure 154(a) shows the buckling mode shape corresponding to the minimum predicted critical temperature rise, $\Delta T_{cr} = 194^{\circ}\text{F}$. In the analysis the region $0 \leq \phi \leq 180^{\circ}$ is divided into three segments, with 81 nodal points in the range $0 \leq \phi \leq 12^{\circ}$, 56 nodal points in the range $12^{\circ} \leq \phi \leq 45^{\circ}$, and 35 nodal points in the range $45^{\circ} \leq \phi \leq 180^{\circ}$. The toroidal circumferential wave number n associated with $\Delta T_{cr} = 194^{\circ}\text{F}$ is 160,000, which corresponds to an axial half-wavelength of 0.34 in., a result in agreement with Hill's analysis [105]. Hill tested two steel cylinders with two diaphragms in both ends of each. One buckled at $\Delta T = 143^{\circ}\text{F}$ and the other at 169°F .

Parameter Study - Cylinders Heated on Axial Strips: Ross, Mayers, and Jaworski [106] tested several steel cylinders heated on axial strips of various widths. The cylinder geometry and approximate temperature distribution are shown in Fig. 154(b). Buckling temperatures were calculated with BOSOR for strips of various widths. The analyses were made as just described, by

treatment of the cylinders as toroidal shells heated on circumferential strips. The point $k = 0$ corresponds to the classical solution $\Delta T_{cr} = 0.6t/(r\alpha) = 188^\circ\text{F}$. The analytical results indicate that buckling temperatures are not very sensitive to width of the heated portion, even if very narrow regions are heated.

Buckling of Conical Shells Heated on Axial Strips: Smith [210] tested a series of conical shells heated on axial strips of various widths such that k in Fig. 154(b) lay in the range $5 \leq k \leq 35$.

Because his colleagues at Stanford had encountered difficulties with support systems of unknown stiffness [104 - 106], Smith took particular care to provide maximum rigidity of his test rig, a schematic of which is shown in Fig. 155(a). The support system consisted of two thick steel end plates connected by a thick central steel tube. This assembly was made more rigid by the introduction of 8 half-inch thick steel webs welded at equal circumferential intervals to the larger diameter plate and central tube. Further details on the test method and specimens are given in Ref. [200].

Figure 155(b) shows the temperature distribution at buckling in a typical case. In the BOSOR analysis the conical shell was divided into three segments, as shown in Fig. 155(a). Nodal points were concentrated near the ends, 29 points being taken in the segment labeled (2) in Fig. 155(a), 39 in (3) and 31 in (4).

In the stability analysis of the cone, the "worst" meridional prebuckling membrane stress distribution is identified ($\theta = 0$) and assumed to be axisymmetric. Figure 155(c) shows the prebuckling membrane stress state at $\theta = 0$, the circumferential variation of prebuckling quantities, and

buckling modal displacements w for the three lowest eigenvalues and eigenvectors corresponding to $n_{cr} = 20$ circumferential waves. The difference between the lowest eigenvalue λ and unity represents the discrepancy between test and theory, since the prebuckling stress distribution corresponds to that at the experimental ΔT_{cr} . Critical temperature factors do not vary much with circumferential wave number n . The values of λ listed in Fig. 155(c) would be about 5% higher if the test rig were considered to be flexible in the stability analysis.

The effect of circumferential nonuniformity of axial compression is very small in these cases, since k (Fig. 154(b)) is 12.8. Inclusion of this effect would lead to an additional 5% increase in the predicted value of λ .

Conclusions: The BOSOR computer program was used to calculate thermal stress and buckling of nonuniformly heated monocoque cones and ring-stiffened cylinders. Several comparisons between test and theory have been given which demonstrate the applicability of the code to bifurcation buckling of a rather wide variety of nonsymmetrically loaded shells. Linear theory is used to calculate thermal stress and buckling under heating that varies in both the axial and the circumferential directions. Perfect cylinders or cones heated on narrow axial strips buckle theoretically at approximately the same temperature as do uniformly heated shells, even if the half-wavelength of the buckle pattern is approximately the same as the circumferential extent of the heated region.

The maximum prebuckling stress in an imperfect cylinder or cone heated on a narrow axial strip is likely to exceed that of the uniformly heated shell simply because the worst imperfections are not likely to occur in the heated region. The effect of circumferential nonuniformity of temperature

can often be accounted for by treatment of the cylinder or cone as a very slender torus in which circumferential variations are transformed into axial variations admissible within the shell-of-revolution stability analysis.

It is of interest to compare "knockdown factors" $\phi = \Delta T_{cr}(\text{test})/\Delta T_{cr}(\text{theory})$ obtained from the above analyses of the Anderson and Card [204] tests ($\phi = 1/\lambda = 0.71$), the Hill [105] tests ($\phi_1 = 143^\circ/194^\circ = 0.74$, $\phi_2 = 169^\circ/194^\circ = 0.87$), and the Smith [210] tests [$(1/1.52) \leq \phi_2 \leq (1/1.11)$ or $0.66 \leq \phi \leq 0.89$]. These values of ϕ should be compared with the values determined empirically for uniformly axially compressed cylinders with appropriate radius-to-thickness ratios. Table 16 summarizes the results. The "typical knockdown factors for uniform axial compression" are taken from Figs. 1 and 2 of Ref. [34]. Notice that the thinner the heated strip, the higher the knockdown factor above the corresponding range for uniform compression.

Buckling of Nuclear Reactor Containment Vessel due to Ground Motion During an Earthquake

A rough idea of the buckling margin may be obtained from a quasi-static analysis in which the loading on the shell consists of body forces due to the inertia of the shell as it is accelerated as a rigid body during an earthquake. Figures 156(a) - (c) show the geometry and inertial reactions due to vertical and horizontal components of ground acceleration g_v and g_h , respectively. The quantities p_v and p_h are vertical and horizontal components of "pressure" proportional to the (mass/area), ρt , of the shell reference surface and to the acceleration components g_v and g_h ; and V and H are "line loads" proportional to the discrete ring (mass/length), ρA , and the acceleration components. Under this system of inertial reactions the containment

vessel deforms as shown in Fig. 157. The membrane components of stress are plotted in Fig. 158. Buckling is possible due to shear N_{12} , which is maximum at $\theta = \pm 90^\circ$ or due to axial compression, which is maximum along the meridian at $\theta = 0$. The critical buckling load factor and mode are shown in Fig. 159.

Dynamic effects may be accounted for approximately by performance of a linear transient analysis of the containment vessel followed by a series of static bifurcation buckling analyses in which the prebuckling states are "snap shots" of the shell at instants in time chosen by the analyst because they correspond to peak compressive membrane stress fields. This method is conservative if the bifurcation buckling load factors are modified by appropriate knock-down factors to account for initial geometric imperfections.

Section 6

BUCKLING OF RING-STIFFENED SHELLS OF REVOLUTION

Introduction

In previous sections many examples have been given of buckling of shells of revolution, especially cylinders, reinforced by equally spaced rings or by rings at the edges. Figure 22, which reveals the sensitivity of critical axial load to initial imperfections in cylindrical shells of various wall constructions, seems to indicate that ring-stiffened cylinders are less sensitive than the other types for which test results are shown. In Figs.

35 and 36 buckling characteristics are illustrated for a ring-stiffened titanium cylindrical shell which collapses at stresses exceeding the proportional limit of the material. With creep neglected in the analysis the shell is predicted to buckle nonaxisymmetrically in a bifurcation mode with 12 circumferential waves. With creep included the predicted mode of failure is axisymmetric collapse.

Figures 64 - 68 reveal the complex behavior of buckling of externally pressurized shallow and deep spherical caps with a ring reinforcement at the boundary. Table 3 shows that depending on the depth of the cap and the size of the edge ring, buckling may be of the snap-through axisymmetric type ($n_{cr} = 0$ circumferential waves), may be inextensional nonsymmetric ($n_{cr} = 2$ circ. waves), may be an edge phenomenon (n_{cr} is rather large), or may resemble classical buckling of a complete spherical shell (p_{cr} is independent of n). Figure 64 demonstrates the sensitivity of buckling pressure of a spherical cap to axisymmetric eccentricity of the edge ring. It is explained that this sensitivity is caused by the strong influence of ring eccentricity on the axisymmetric prebuckling hoop compression near the edge of the cap.

Figures 81, 82, 122, and 123 illustrate various buckling phenomena for axially stiffened (corrugated) cylindrical shells with equally spaced internal rings. In Figs. 81 and 82 the emphasis is on a local load path eccentricity which causes local buckling and the effect of the rings is of secondary importance. In Figs. 122 and 123 nonaxisymmetric buckling is shown to be local between rings, that is the rings are large enough to prevent buckling displacement of the shell at the circumferential lines of attachment to the rings, with local maxima of the normal buckling modal displacement field occurring midway between adjacent rings. The fact that the axial bending stiffness is very large compared to the circumferential bending stiffeners in these corrugated configurations causes the influence of the boundary conditions on the buckling load to decay surprisingly slowly with increase in the length of the cylinder and increase in the number of equally spaced rings. Figure 149 displays the buckling mode for a corrugated, ring-stiffened rocket payload shroud under nonaxisymmetric aerodynamic pressure.

Other examples already shown of buckling of ring-stiffened shells of revolution include theoretical and experimental results of Tennyson [170] for perfect and axisymmetrically imperfect integrally ring-stiffened cylindrical shells under combined axial compression and external pressure (Fig. 142), buckling under combined bending and nonaxisymmetric heating of a ring-stiffened cylinder tested by Anderson and Card [204] (Figs. 150 - 152), and buckling of a typical ring-stiffened steel containment vessel due to vertical and horizontal acceleration of its base during an earthquake (Fig. 159)

Summary

The purpose of this section is to reveal additional physical phenomena of buckling of ring-stiffened shells in order to acquaint the analyst with various effects and failure modes, thereby providing guidance for the construction of appropriate experimental and analytical models.

The section opens with comparisons of test and theory for elastic ring-stiffened cylindrical shells under external hydrostatic pressure. Emphasis is given to the effect of boundary conditions on bifurcation buckling pressures. Local and general instability are demonstrated. Results from a rather extensive study of elastic-plastic buckling of hydrostatically compressed internally ring-stiffened cylindrical shells are presented next. The comparisons between test and theory include an investigation of the effect of finite ring thickness on the shell wall axial bending rigidity and hence on the buckling pressures of some of the specimens.

Following is a discussion of the influence on stability of residual stresses and deformations due to welding and cold bending. After a brief review of the literature, examples are provided of the effect on buckling pressure of the welding of rings to an ellipsoidal shell. Residual deformation patterns are displayed for two cylindrical shells: one with rings welded to the inside surface and the other with rings welded to the outside surface. Comparisons between buckling pressures from test and theory are then presented for two ring-stiffened cylinders of identical dimensions, one of which was machined from a single billet and the other of which was fabricated by first cold bending a flat sheet about a cylindrical die and then welding rings to it.

The closes with several examples in which instability failure of a ring-stiffened shell occurs in modes that involve local deformations of the ring cross sections. These modes include circumferential crippling of the ring, axisymmetric sideways of the ring, local buckling of the shell between adjacent rings in which the ring cross sections not only rotate but also deform, and general instability of shell and rings together in a mode in which the ring cross sections deform.

Elastic Buckling of Ring-Stiffened Cylinders under External Hydrostatic Pressure

Table 17 gives a comparison between test and theory for the buckling ring-stiffened aluminum cylinders under hydrostatic pressure. Shell and ring geometries are shown in Figs. 160(a) and 160 (b). Cylinders of this geometry with various sizes of T rings (called "Frames" in Fig. 160) were tested by Blumenberg at the Naval Ship Research and Development Center in 1965 [211]. The shells were analyzed with BOSOR [14]. The heavy frames were treated as discrete elastic structures but the small rings were "smeared out" according to the equations of Baruch and Singer [160]. Eccentricity effects are retained for both small and large rings. The cylinders are "cut" at their planes of symmetry and buckling loads are calculated for both modal symmetry and antisymmetry at these planes. Fig.

161 shows one of the cylinders, prebuckling normal displacement w_0 and meridional moment M_{10} , and buckling modal displacement components u , v , w corresponding to general instability with $n_{cr} = 2$ circumferential waves. The nodal points are concentrated around the attachment points of the large frames in the BOSOR model.

Two theoretical values are given in Table 17 for each cylinder. These values correspond to clamped edges and to free edges with large end rings such as shown in Fig. 160(a). Buckling with two or three circumferential waves always corresponds to general instability (buckling of shell and heavy frames together) as shown in Fig. 161, and buckling with 4 or 5 waves always corresponds to local instability (buckling between heavy rings).

Mode shapes corresponding to general ($n = 2$ circumferential waves) and local ($n = 4$) instability are plotted in Fig. 162. "General instability" denotes buckling in a mode in which both rings and shell deflect. The term "local instability" denotes buckling in a mode in which the rings are at nodes, as shown in Fig. 162 for $n = 4$. If one plotted a curve of critical load vs. circumferential wave number n for a single specimen there might be several minima: The general instability load may correspond to a minimum $p_{cr}(n)$ at a low value of n , and minima at higher values of n may occur corresponding to buckling of each bay between adjacent rings. An example of nonsymmetric buckling of an optimally designed conical shell in which there are multiple minima in the curve $p_{cr}(n)$ v. n is given in Fig. 33 of Ref. [430]. In calculating critical buckling loads of shells of revolution, especially those which have been optimally designed with respect to local and general instability, users of computer programs such as those described in Refs. [11 - 14] and [47] should be certain that they have covered all ranges of circumferential wave number n in which minima of $p_{cr}(n)$ v. n may lie.

In many cases the theoretical critical pressures are rather strongly dependent on the boundary conditions. This is especially true for the specimens in which the mode of failure is general instability. In Blumenberg's tests [211] the cylinders were supported at the edges by the heavy rings shown

in Fig. 160(a). Additional support was provided by end plugs, which were furnished with O-rings for sealing. As is the case in most experiments of this type, it is difficult to determine just how much additional support was provided by the end plugs. Therefore, two sets of calculations were made, one for clamped edges and one for free edges with large edge rings. It is seen from Table 17 that the assumption of no additional support by the end plugs is too conservative in Cases 1-1 through 7-7 and in all of the cases in Group 2.

It is likely that in the tests the end plugs provided some restraint for all of the displacement components and that this restraint is dependent on the circumferential wave number of the buckling mode. Table 18 supports this hypothesis. Notice that in Group 2 the difference between the loads for shells with clamped and free edges with large end rings is small for $n = 3$ but that restraint in the axial direction alone has a large effect on the critical pressures for $n = 2$. It is clear from the experimental results for Group 2 that enough axial restraint was present to cause these cylinders to buckle into more than two circumferential waves. This discussion is included to emphasize the need to control carefully the boundary conditions in experiments and to specify them correctly in analyses.

Elastic-Plastic Buckling of Ring-Stiffened Cylinders under External Hydrostatic Pressure

In 1965 Boichot and Reynolds [212] tested 69 integrally ring-stiffened aluminum 7075 T6 cylinders under external hydrostatic pressure. The cylinders failed in the plastic range. In 1976 the BOSOR5 computer program [47] was used to obtain theoretical buckling pressures [171]. Photographs of some of the failed specimens are shown in Fig. 163. A schematic

of the geometry of all the Boichot and Reynolds specimens is shown in Fig. 164, with the actual dimensions given in Table 1 of Ref. [171]. The stress-strain data used in the analysis are listed in Table 2 of Ref [4.171].

Previous analyses applicable to some or all of these specimens have been performed by Lunchick [213], Krenzke and Kiernan [214], Reynolds [215], Lee [216], and Gerard [217]. All of the analyses agree reasonably well with the test results, owing largely to the fact that the tangent modulus of the material decreases by more than an order of magnitude within a 20% stress range of the 0.2% yield stress.

Comparison of test and theory for bifurcation buckling and axisymmetric collapse of the 69 specimens is given in Fig. 165. Of the 69 test specimens, 24 (designated "F", in Fig. 164, had fillets near the boundaries and where the rings join the shell wall. From the photographs in Ref. [212], from which Fig. 163 is reproduced, it appears that practically all of the specimens without fillets fractured during failure. However, it is not possible to determine from the test data alone whether fracture caused the failure or whether fracture occurred later as the shell was deforming in its buckling mode. On the other hand, there is almost no evidence of fracture occurring in the case of the 24 specimens with fillets. Therefore, it is reasonable to predict that better agreement between test and theory will be obtained for the specimens with fillets than for those without. Furthermore, analytical predictions that are too high for the specimens without fillets would lead one to favor the hypothesis that failure was caused by fracture rather than buckling in these tests, since the analytical model (BOSOR5) is incapable of predicting fracture. This would be particularly true if the too high predictions correspond to the thicker specimens for which imperfections are less significant.

There are three different nominal radius/thickness ratios involved in the test series: $R/t \approx 12$, 20, and 50. Buckling pressures for the $R/t \approx 50$ specimens are somewhat sensitive to imperfections because buckling, especially of the models in this class with small ring stiffeners, occurs at average stresses that are barely in the plastic range. Indeed, the test results for the thinnest specimens exhibit the most scatter, as indicated in Fig. 165.

The generally upward sloping trend with increasing b/\sqrt{Rt} in Fig. 165 results primarily from the fact that the analytical model becomes increasingly conservative with increasing b/\sqrt{Rt} : The discrete rings are assumed to be attached to the shell at a single point with the shell free to bend in the axial direction in the immediate neighborhood of this point. The neglected effect on the shell meridional bending stiffness of the finite thicknesses of the rings leads sometimes to predictions of axisymmetric collapse with relatively short axial wavelengths when the test specimens actually failed nonsymmetrically. The short-wavelength axisymmetric mode of failure is hindered by the increased local meridional bending stiffness afforded by the finite axial intersection lengths of shell and rings more than is the relatively long wavelength general instability mode of failure.

With use of BOSOR5 it is possible to investigate analytically the effect on predicted critical pressures of including some additional axial bending stiffness due to the finite axial length of the shell-ring intersection areas. This increase in axial bending rigidity is modeled as shown in Fig. 166. Additional nodal points are provided in the neighborhoods of the discrete rings with meridional rotation β constrained to be equal at nodal points corresponding to the bottom and top surfaces of each discrete ring. The solid line, labeled Model 1, corresponds to the original analytical models

of the test series 15-5XF in which the discrete ring is considered to be attached at one point and the shell is free to bend under the ring. That is, the prebuckling meridional rotation β_0 and bifurcation buckling modal rotation β_b are free to change along the shell wall within the shell-ring intersection area. With the extra constraint conditions (Model 2) the analytical predictions are closer to the test results. The critical failure mode for the specimen with the thickest rings, Specimen 15-58F for which $b/\sqrt{Rt} \approx 0.3$, is predicted to be axisymmetric inter-ring collapse with use of Model 1 and non-axisymmetric general instability with use of Model 2. In the cases for which general nonaxisymmetric instability is predicted with use of Model 1, introduction of extra constraint conditions as depicted in Fig. 4.166 does not change the prediction very much. Analytical results for all of the cases investigated with use of Model 2 are given in Table 7 of [171]. Unfortunately, the budget for computer time did not permit analysis of the entire series of tests with use of Model 2.

Figure 167 shows the predicted axisymmetric failure modes for Specimen 25-88 ($b/\sqrt{Rt} = 0.431$) with use of Model 1 and Model 2 analysis. It is clear from these plots why introduction of the extra constraint conditions raises the predicted axisymmetric collapse load.

Effect of Residual Stresses and Deformations on Plastic Buckling of Ring-Stiffened Shells of Revolution

Review of Previous Work

In 1958 Ketter [218] identified four sources of residual stresses and deformations of fabricated metal structures: differential cooling during

and after rolling sheet metal, cold bending, various erection procedures, and welding. He considered the effect of differential cooling in the fabrication process on buckling loads of axially compressed I-beams.

Cold Bending: Several authors have investigated residual stresses due to cold bending. Almen and Black [219] give the residual stress pattern through the thickness of a bar which has been bent about a circular die. Queener and De Angelis [220] derive approximate formulas for residual stresses and the ratio of die radius R_0 to final radius after springback R_f for materials with stress strain curves of the form $\sigma = K\epsilon^n$. They performed tests for various materials and a wide range of R_0/R_f , obtaining good agreement between test and theory. Their treatment is based on deformation theory. Lunchick [221] determined the effect of cold bending on buckling loads of cylindrical pressure vessels. He calculated effective stress-strain curves for the prestressed material by averaging effective stresses and strains at twelve stations through the thickness of the shell wall. Such curves depend on the service loads. Lunchick's model is based on elastic-perfectly plastic material and deformation theory. It is determined in [221] that bending residual stresses have the greatest weakening effect for cylindrical shells in which the effective stress in the wall is near the material proportional limit at the buckling pressure calculated with neglect of these residual stresses. For such structures, the reduction in buckling pressure due to cold bending can be as much as 30%.

Shama [222] derived a simple method for calculating the magnitude and distribution of cold bending residual stresses for any beam cross section. The effects of the shape of the stress-strain curve, section characteristics, and the degree of bend are investigated. Tacy [223] has written a computer

program for the calculation of the residual stress distribution and the effective stress-strain curve of cold bent beams for a wide range of practical cross section geometries. The Bauschinger effect and possible inelastic behavior on springback are accounted for. The hardening rule used in Tacey's program is a combination of isotropic and kinematic rules.

Welding: During the 1970's much work has been done on the numerical modeling of multipass welding. The ASME volume, Numerical Modeling of Manufacturing Processes [224], contains several papers on this subject [225 - 230]. Masubuchi [231] wrote a survey of the field in 1975. Three frequently referenced papers are by Hibbitt and Marcal [232], Nickel and Hibbitt [233], and Friedman [234]. The results presented in these papers are generally obtained from sophisticated computer programs for multidimensional analysis. Although the heat conduction and the thermal stress problems are uncoupled, the models include nonlinear boundary conditions for solid and liquid regions, temperature-dependent material effects, latent heat effects, and convective and radiative heat transfer boundary conditions.

It is impractical to incorporate such elaborate models of the welding process into an analysis of buckling of a ring-stiffened shell with many welds. A simple, computationally efficient model is introduced in [47], in which buckling pressures are calculated for a welded ring-stiffened ellipsoidal shell. The shell and rings are assumed to be machined and stress relieved separately and then welded together. The effects of weld shrinkage are simulated in [47] by means of the assumption that a certain amount of material in the local neighborhoods of each weld is cooled below ambient temperature to a reference approximately equal to the annealing temperature. The residual stress distribution thus generated is characterized by local

tensile circumferential yielding near the welds and elastic circumferential compression over the rest of the cross sections of the shell wall and ring stiffeners. The structure prestressed in this way remains axisymmetric, of course, but the radial shrinkage varies in the meridional direction, introducing an axisymmetric imperfection with a characteristic wavelength equal to the ring spacing. The weld effect thus modeled reduces the predicted buckling pressure by about 10%. Similar calculations are described in [235] for axisymmetric creep buckling of girth-welded titanium spherical vessels subjected to external pressure.

Bending and Welding: Few papers exist in which residual stresses are calculated for more than one fabrication process. Chen and Ross [236] calculate residual stresses from cold bending a flat sheet into a cylindrical shape and then welding the longitudinal seam. They suggest that these residual stresses will cause early column buckling of long cylinders under axial compression. In his computer program, Tacey [223] permits introduction of arbitrary initial stresses and then calculates residual stresses for a series of up to ten sequential bending processes. Faulkner [237] gives a survey of work done on calculation of residual stresses due to welding ring stiffeners to cylindrical shells and cold bending sheets into cylindrical shells and beams into rings. He states that when ring stiffeners are welded to a cylindrical shell of thickness t there is tensile yielding over a length of shell equal to $2\eta t$ and over a length of the ring web equal to ηt . These tensile regions are balanced by compressive residual stresses distributed over the remainder of the shell and ring cross sections. Typical values of η obtained from measurements are in the range $1.5 \leq \eta \leq 4.5$. The measured radial shrinkage at the welds is approximately 10% of the shell thickness t .

Figures 109 - 115, Table 7, and the accompanying discussion describe an unsuccessful attempt to explain the unexpected failure of a large steel water tank by accounting for residual stresses and deformations due to cold bending flat sheets into a conical form and then welding them circumferentially.

Effect of Welding on the Plastic Buckling Pressure of an Ellipsoidal Ring-Stiffened Shell

The geometry of an ellipsoidal shell with internal ring stiffeners is shown in Fig. 168. The purpose of the analysis of this structure is to determine the effect on predicted buckling pressure of axisymmetric distortions and residual stresses due to welding the rings to the shell.

Figure 169 shows the BOSOR5 model which consists of 313 degrees of freedom in the axisymmetric prebuckling analysis and 466 degrees of freedom in the nonaxisymmetric stability analysis. Symmetry conditions are imposed at the equator in both the prebuckling and bifurcation buckling analyses. (It was determined in preliminary runs on the computer that the lowest bifurcation buckling pressure corresponds to a mode symmetric rather than antisymmetric about the symmetry plane. The locations of the discrete ring attachment points and centroids are indicated in Fig. 169 (b).

The effect of the welds shown in Fig. 170 (a) is introduced into the analytical model by means of the temperature distribution shown in Fig. 170 (b): A certain amount of the material of ring web and shell wall in the neighborhood of the welds is considered to be cooled down below room temperature.

The value 1000°F corresponds approximately to the anneal temperature of the steel from which the structure is presumed to be fabricated. The anneal temperature is used as a reference value because residual stresses are relieved for higher temperatures than this. The zero-stress temperature distribution corresponds to the weld region being hot (above 1000°F) and the rest of the material being at room temperature. As the weld material cools down from 1000°F to room temperature, stresses build up in the shell and ring, tensile in the region that was originally heated above 1000°F and compressive elsewhere. Thus, the non-zero stress state corresponds to a uniform ambient temperature distribution. In BOSOR5 it is not possible to generate a non-zero initial thermal stress state with a uniform temperature distribution. Therefore, one must simulate the growth of residual stresses and deformations by treating the weld region as if it were cooled down below ambient temperature.

Figure 171 shows the prebuckling axisymmetrically deformed shape with increasing external pressure and a comparison with and without welding effects. The relatively advanced scalloping of the meridian corresponding to $p = 4100$ psi with the weld effect arises because of increased local plastic flow near the ring attachment points. The ring at the plane of symmetry moves inward rapidly with pressure increasing above 3500 psi because the flange yields and flows plastically, having zero tangent modulus for $p > 3500$ psi. (There is more welding required in the neighborhood of this ring than the others because the ring must first be welded to one of the halves of the shell and then the two halves of the shell must be welded together. Hence, in this area more of the material is cooled down by an amount approximately equal to the anneal temperature.)

Figure 172 shows predicted incipient buckling modes with and without the weld thermal effect. The lowest predicted critical pressure corresponds in both cases to nonaxisymmetric buckling with 5 circumferential waves. The buckle modes are quite different in the two cases because of the increased amount of prebuckling plastic flow in the ring at the plane of symmetry predicted with the model which includes the weld effect.

Residual Deformations from Welding Internal v. External Rings

In 1957 Krenzke [238] investigated experimentally the effect of welding residual stresses and deformations on plastic buckling of ring-stiffened cylinders under external hydrostatic pressure. Two of his specimens, designated "M1" and "M2" were nominally identical except that the rings of Specimen M1 were internal and those of Specimen M2 were external. Krenzke measured average welding distortions for Specimen M1 approximately equal to those exhibited in Fig. 173 (b), which are predicted by BOSOR5 [47] to result from the imposed nonuniform temperature distribution shown in DETAIL AA. An analogous temperature distribution corresponding to externally welded rings yields a predicted residual deformation shown in Fig.

173 (c). These displacements have the distribution measured by Krenzke for Specimen M2 but the amplitude of the predicted waves is about twice that measured. It seems that, in this case at least, about half as much "cool-down" is required to simulate the welding process with external rings as is required for the simulation of welding internal rings.

In the tests the externally stiffened specimen M2 collapsed at a pressure about 5% higher when corrected for different material yield strengths than that for the internally stiffened specimen. The same difference is predicted by BOSOR5. The collapse mode is characterized by formation of an axisymmetric

inward dimple, as shown in Fig. 36(e). The "hungry horse" residual welding deformation pattern displayed in Fig. 173 (b) represents an initial imperfection that is more harmful than the "caterpillar" mode exhibited in Fig. 173(c) because the former resembles the collapse mode illustrated in Fig. 36 (e) whereas the latter has a shape opposite to that of the collapse mode.

Effect of Cold Bending and Welding on Buckling of Ring-Stiffened Cylinders

The BOSOR5 computer program can be used for calculation of bifurcation buckling of cold bent and welded ring-stiffened cylinders under external pressure. Residual stresses and deformations from cold bending and welding can be included in the model for buckling under service loads by introduction of these manufacturing processes as functions of a time-like parameter, "time", which ensures that the material in the analytical model experiences the proper sequence of loading prior to and during application of the service loads. The cold bending process is first simulated by a thermal loading cycle in which the temperature varies linearly through the shell wall thickness, initially increasing in "time" to simulate cold bending around a die of radius R_0 and then decreasing in "time" to simulate springback to a final somewhat larger design radius R . The welding process is subsequently simulated by the assumption that the material in the immediate neighborhoods of the welds is cooled below the ambient temperature by an amount that leads to weld shrinkage amplitudes typical of those observed in tests. Buckling loads are calculated for a configuration including and neglecting the cold bending and welding processes. These predictions are compared to values obtained from tests by Kirstein and Slankard [239] and Slankard [240] on two nominally

identical specimens, shown in Figs. 174 (a-c). The specimen designated BR-4 was fabricated by cold bending the shell and then welding machined ring stiffeners to it, and the specimen designated BR-4A was carefully machined.

Cold Bending of a Flat Sheet into a Cylindrical Shell of Infinite

Length: During the cold bending process the axial and circumferential strain components in a bent sheet of thickness h are approximately

$$\begin{aligned}\epsilon_1 &= 0 \\ \epsilon_2 &= (z/R_0) f(t/t_0) \quad -h/2 \leq z \leq +h/2\end{aligned}\quad (39)$$

in which z is the coordinate normal to the middle surface and $R_0 - h/2$ is the radius of the die about which the sheet must be rolled so that when it springs back the final radius of the bent sheet is the design radius of the cylindrical shell R . The quantity t is a parameter (such as time) which determines how much of the bending process has been completed; t_0 is the value of t when the initially flat sheet has been bent into a cylinder of radius R_0 (before relaxation of the applied circumferential moment), and

$$\begin{aligned}f(t/t_0) &= t/t_0 \quad \text{for } 0 \leq t/t_0 \leq 1.0 \\ f(t/t_0) &= 2 - t/t_0 \quad \text{for } 1.0 < t/t_0 \leq (t_r/t_0) \\ f(t/t_0) &= 2 - t_r/t_0 \quad \text{for } (t_r/t_0) < t/t_0\end{aligned}\quad (40)$$

Equation (40a) gives the function of normalized "time" $f(t/t_0)$ during which the radius into which the initially flat sheet is being bent decreases until it reaches the minimum value R_0 . Equation (40b) gives the function $f(t/t_0)$ during the interval when the moment causing the bending is relaxed, so that

at $t = t_r$ there are no resultant forces or moments in the circumferential direction. Equation (40c) indicates that the state of the bent sheet does not change for $t > t_r$.

The following approximations form the basis for Equations (39):

1. Strains are small compared to unity.
2. The sheet is long enough so that end effects can be ignored.
3. The ratio t/R is negligible compared to unity.
4. Effects of strains normal to the sheet surface are negligible.
5. There is no average tension or compression during bending; the neutral axis remains at the middle surface.

During the bending and relaxation process, each material point in the sheet passes through three distinct regimes: an initial elastic loading regime, an intermediate elastic-plastic regime, and a final elastic unloading regime.

Initial Elastic Loading: In the initial elastic regime, the axial and circumferential stresses are given, respectively, by

$$\begin{aligned}\sigma_1 &= \frac{E}{(1-\nu^2)} (\epsilon_1 + \nu\epsilon_2) = \frac{E}{(1-\nu^2)} (z/R_o) (t/t_o) \quad (41) \\ \sigma_2 &= \frac{E}{(1-\nu^2)} (\epsilon_2 + \nu\epsilon_1) = \sigma_1/\nu\end{aligned}$$

The von Mises yield criterion is

$$\bar{\sigma} = (\sigma_1^2 + \sigma_2^2 - \sigma_1\sigma_2)^{1/2} = \sigma_y \quad (42)$$

From Eqs (41) and (42), the normalized time to yield can be computed as

$$t_{\text{yield}}/t_o = [\sigma_y (R_o/|z|)/E] [(1-\nu^2)/(1+\nu^2-\nu)]^{1/2} \quad (43)$$

Elastic-Plastic Loading: In the elastic-plastic regime,

$(t_{\text{yield}}/t_0) \leq t/t_0 \leq 1.0$, the calculation of the stress and plastic strain components must be performed incrementally because the plastic flow "direction", according to the normality rule, depends on the stress state. As set forth in [24], the total meridional and circumferential strain increments, $\Delta\epsilon_1$ and $\Delta\epsilon_2$, consist of the sums of elastic and plastic strain increments:

$$\Delta\epsilon_1 = (\Delta\sigma_1 - \nu\Delta\sigma_2)/E + \Delta\bar{\epsilon}^p (\partial\bar{\sigma}/\partial\sigma_1) \quad (44)$$

$$\Delta\epsilon_2 = (\Delta\sigma_2 - \nu\Delta\sigma_1)/E + \Delta\bar{\epsilon}^p (\partial\bar{\sigma}/\partial\sigma_2)$$

in which $\Delta\bar{\epsilon}^p$ is the effective plastic strain increment. It is known from Eqs (39) that

$$\Delta\epsilon_1 = 0 ; \quad \Delta\epsilon_2 = (z/R_0) (\Delta t/t_0) \quad (45)$$

and from Eq (42) that

$$(\bar{\sigma} + \Delta\bar{\sigma}) = \sigma_y = [(\sigma_1 + \Delta\sigma_1)^2 + (\sigma_2 + \Delta\sigma_2)^2 - (\sigma_1 + \Delta\sigma_1)(\sigma_2 + \Delta\sigma_2)]^{1/2} \quad (46)$$

and

$$\frac{\partial\bar{\sigma}}{\partial\sigma_1} = (2\sigma_1 - \sigma_2)/(2\bar{\sigma}) ; \quad \frac{\partial\bar{\sigma}}{\partial\sigma_2} = (2\sigma_2 - \sigma_1)/(2\bar{\sigma}) \quad (47)$$

If we assume (in this section only!) that the material is elastic-perfectly plastic ($\sigma_y = \text{constant}$) and that the stress increments are small compared to the stresses, $\Delta\bar{\sigma}$ is zero and Eq.(46) leads to

$$\Delta\sigma_1 = -[(2\sigma_2 - \sigma_1)/(2\sigma_1 - \sigma_2)] \Delta\sigma_2 \quad (48)$$

The three equations (44a), (44b), and (48) can now be solved for the three unknowns $\Delta\sigma_1$, $\Delta\sigma_2$, and $\Delta\bar{\epsilon}^p$ for each time increment Δt between

$t=t_{\text{yield}}$ and $t=t_0$. At the end of each time increment, the new stress state is

$$\sigma_1^{(n+1)} = \sigma_1^{(n)} + \Delta\sigma_1 ; \sigma_2^{(n+1)} = \sigma_2^{(n)} + \Delta\sigma_2 \quad (49)$$

and the plastic strain components are

$$\begin{aligned} \varepsilon_1^{p(n+1)} &= \varepsilon_1^{p(n)} + \Delta\varepsilon^{p(n)} (2\sigma_1^{(n)} - \sigma_2^{(n)}) / (2\sigma_y) \\ \varepsilon_2^{p(n+1)} &= \varepsilon_2^{p(n)} + \Delta\varepsilon^{p(n)} (2\sigma_2^{(n)} - \sigma_1^{(n)}) / (2\sigma_y) \end{aligned} \quad (50)$$

The state of the material at various points in space, $z = \pm m\Delta z$, $m=1,2,\dots,M$, and in time, $t_{\text{yield}} + n\Delta t$, $n=1,2,\dots,N$, can thus be calculated recursively for an arbitrary number of time increments N in the interval $t_{\text{yield}} \leq t \leq t_0$.

Relaxation: if the relaxation process in the third regime $t_0 < t \leq t_r$ is assumed to be elastic, the stress components at the end of the interval, $t=t_r$, are:

$$\begin{aligned} \sigma_1^{(t_r)} &= \sigma_1^{(t_0)} + \frac{\nu E}{(1-\nu^2)} (z/R_0) (1 - t_r/t_0) \\ \sigma_2^{(t_r)} &= \sigma_2^{(t_0)} + \frac{E}{(1-\nu^2)} (z/R_0) (1 - t_r/t_0) \end{aligned} \quad (51)$$

in which $\sigma_1^{(t_r)}$ and $\sigma_2^{(t_r)}$ denote, respectively, the axial and circumferential stresses after the applied bending moment has been completely relaxed. The normalized time to complete relaxation, t_r/t_0 , can be calculated from the requirement that after relaxation the circumferential moment resultant is

$$M_2^{(t_r)} \equiv \int_{-h/2}^{h/2} \sigma_2^{(t_r)} z \, dz = 0 \quad (52)$$

With use of Eq (51b), Eq (52) yields

$$t_r/t_o = 1 + \left| M_2^{(t_o)} \right| \frac{12 (1-\nu^2) R_o}{Eh^3} \quad (53)$$

in which $M_2^{(t_o)}$, the bending moment just before relaxation begins, is given by

$$M_2^{(t_o)} \equiv \int_{-h/2}^{h/2} \sigma_2^{(t_o)} z \, dz \quad (54)$$

The circumferential moment result $M_2^{(t_o)}$ can be calculated by Simpson's rule integration of the stress through the wall thickness.

Obtaining a Value of R_o : The given quantity in this problem is the final cylinder design radius R after elastic springback. It is necessary to bend the initially flat sheet to a somewhat smaller radius R_o such that after relaxation it springs back to the design value R_c .

The change in curvature due to elastic springback is

$$\frac{1}{R_o} - \frac{1}{R} = \frac{M_2^{(t_o)} (1-\nu^2)}{EI} = \frac{M_2^{(t_o)} 12(1-\nu^2)}{Eh^3} \quad (55)$$

In general, $M_2^{(t_o)}$ depends in a complex way on the unknown R_o , through Eq (54) and the recursive relations (49) and (50). One might solve for R_o iteratively by trying a value, computing $M_2^{(t_o)}$ from Eqs (4.49)

and (54), and using Eq (55) to derive an updated value. For perfectly plastic materials, the moment $M_2^{(t_o)}$ is given approximately by

$$M_2^{(t_o)} = \sigma_y h^2 / [4(1-\nu_e + \nu_e^2)^{1/2}] \quad (56)$$

in which ν_e is an effective Poisson's ratio in the range $\nu < \nu_e < 0.5$. Equation (56) can be used to obtain a starting value for R_o in the iterative process. Alternatively, one could use the formula derived by Queener and De Angelis[4.220] for strain hardening materials with stress-strain curves given by $\sigma = K\epsilon^n$:

$$R_o/R = 1 - \frac{3K(1-\nu^2)}{E(2+n)(3/4)^{(1+n)/2}} \left(\frac{2R_o}{h} \right)^{1-n} + \left[\left(\frac{2R_o}{h} \right) \left(\frac{\nu}{E} \right)^{1/(1-n)} \right]^3 C \quad (57)$$

in which

$$C \equiv \frac{3(1-\nu^2)^{3+n}}{(2+n)(3/4)^{(1+n)/2}(1-\nu+\nu^2)^{(2+n)/2}} - \frac{(1-\nu^2)^3}{(1-\nu+\nu^2)^{3/2}} \quad (58)$$

Equation (57) reduces to Eq (55) with Eq (56) if the last term on the right-hand side of Eq (57) is neglected, K is set equal to $\sigma_y, n=0$, and $\nu_e = 0.5$.

Simulation of Cold Bending in BOSOR5: The cold bending process is simulated in a BOSOR5 model by use of a thermal loading cycle. In the BOSOR5 analysis the elastic stresses in the cylindrical shell are given by

$$\sigma_1 = \frac{E}{1-\nu^2} [(\epsilon_1 - \alpha_1 \Delta T) + \nu (\epsilon_2 - \alpha_2 \Delta T)] \quad (59)$$

$$\sigma_2 = -\frac{E}{(1-\nu^2)} [\nu (\epsilon_1 - \alpha_1 \Delta T) + (\epsilon_2 - \alpha_2 \Delta T)]$$

in which α_1 and α_2 are the meridional and circumferential coefficients of thermal expansion. ΔT , a function of z , is the difference between the applied temperature and the zero-stress or ambient temperature. Since the sheet in the BOSOR5 model is already in its bent form, the temperature distribution $T(z,t)$ should be such as to cause the total strains $\epsilon_1(z,t)$ and $\epsilon_2(z,t)$ to be zero. In addition, in the initial elastic regime, we know that σ_1 and σ_2 are given by Eqs. (41). These facts and Eqs (59) lead to the equations

$$\nu (z/R_0) (t/t_0) = - (\alpha_1 + \nu \alpha_2) \Delta T \quad (60)$$

$$(z/R_0) (t/t_0) = - (\nu \alpha_1 + \alpha_2) \Delta T$$

for which the solution is

$$\alpha_2 \Delta T = -(z/R_0) (t/t_0); \quad (61)$$

$$\alpha_1 = 0$$

The minimum bend radius is calculated from Eq (55) or Eq (57).

Procedure for Using BOSOR5 to Calculate Buckling Loads Including Residual Effects Due to Cold Bending and Welding: Residual stresses and deformations due to cold bending are first calculated with BOSOR5 in two computer runs. The first run gives the peak bending stresses at $t=t_0=1.0$ and yields the circumferential bending moment $M_2^{(t_0)}$, which is needed in order to determine the relaxation time, t_r , from Eq (53). The second run yields the residual state after complete relaxation of the bending moments. Subsequent computer runs include application of welding, as described in the discussion associated with Figs. 168- 173, followed by application of the service loads. The thermal loading and service loading are applied in the proper sequence by means of specification of them as functions of pseudo-time such as shown in Figure 175, which applies to buckling predictions of Slankard's test specimen [240]. (See Figs. 174 a,c.)

Comparisons with Tests on Cold-Bent Sheet: Figure 176 shows residual stresses through the thickness of a specimen tested by Queener and DeAngelis [220]. The BOSOR5 results are practically indistinguishable from the theoretical results of [220]. Queener and De Angelis describe how they obtained the test points. The parameters of the problem are given in the figure. The stress-strain curve used in the BOSOR5 analysis is linear up to the proportional limit σ_{pl} and follows the curve $\sigma = K\epsilon^n$ in a piecewise linear fashion for $\sigma > \sigma_{pl}$. In the BOSOR5 simulation, the configuration is a cylinder which is long compared to $(Rt)^{1/2}$ with symmetry conditions applied at both ends. The temperature varies linearly through the wall thickness h as shown in Fig. 176, and varies with time as given by Eqs 40 $t_0=1.0$ and $t_r=-1.25$.

Buckling of Cold Bent and Welded Ring-Stiffened Cylinder: Comparison of Test and Theory: Figure 174 shows two ring-stiffened cylinders buckled by external hydrostatic pressure [239], [240]. Both test specimens are made of the same material and have the same dimensions. The one on the left, designated "BR-4" in [240], was fabricated by cold forming the cylindrical shell from a flat sheet and then welding on rings which had been machined. The one on the right, designated "BR-4A" in [239], was machined from a single thick tube.

Dimensions of the specimens are given in Fig. 174(c). The material is called "Alan Wood Steel" in [239] and [240], with a yield stress of 50,600 psi. An elastic perfectly plastic property was assumed for the BOSOR5 models. The test specimens were sealed at the ends in such a way as to suggest the use of simple support boundary conditions in the analysis.

In the tests the cold formed, welded specimen BR-4 buckled at 390 psi and the machined specimen BR-4A buckled at 540 psi. The BOSOR5 analysis of

BR-4 yields a predicted buckling pressure of 460 psi and the analysis of BR-4A yields a predicted buckling pressure of 540 psi. Since the BOSOR5 models are identical except for the simulation of cold bending and welding, it is the residual stresses and deformations arising from these fabrication processes that cause the decrease in predicted buckling pressure from 540 psi to 460 psi.

Two BOSOR5 models of the cold formed, welded specimen BR-4 were analyzed. These are shown on the left-hand side of Figure 177 (Figures 177a and f). In the first model, Fig. 177a, the cylindrical shell was treated as a single segment and the welding process was ignored. The cold bending process was simulated with a temperature gradient with a maximum temperature rise $\Delta T_c = 1243^\circ$ corresponding to a coefficient of thermal expansion $\alpha = 6 \times 10^{-6}/^\circ$. Figures 177 b-d show the axisymmetrically deformed generator at certain stages of the analysis. The predicted buckling mode depicted in Figure 4.177e corresponds to twelve circumferential waves. The predicted buckling pressure ignoring welding is 460 psi, the same as that in which simulation of the welding is included, as described next.

Figure 177f shows the BOSOR5 model for the case in which both cold bending and welding are simulated by thermal loading. This is a much more elaborate model than that shown in Figure 177a: the cylinder generator is divided into fifteen segments in order to be able to specify different spatial distributions of temperature for the cold bending and the welding phases of the fabrication process. The welding process is simulated in the short segments near the ring stiffeners and the cold bending process is simulated in the rest of the cylindrical shell. (This segmentation with different ΔT distributions in the long and short segments leads to the slightly wavy result in Fig. 177g.)

Figure 178 shows the two spatial temperature distributions used in the simulations. A reasonable maximum welding shrinkage of approximately 8% of the shell thickness is produced by the assumption that the material near and in part of each ring stiffener is cooled to 700° below ambient temperature. The extent of the weld affected zone shown in Figure 178 corresponds to a value of Faulkner's η between 2 and 3, well within the range observed in tests [237].

Figure 175 shows the BOSORS time functions associated with the two fabrication processes and the pressure loading. The predicted shapes of the axisymmetrically deformed cylinder generator at various times are shown in Figures

177g through 177j, and the predicted buckling mode with welding simulation included is shown in Figure 177k. While inclusion of welding shrinkage does not change the predicted buckling pressure or mode in this case, it does considerably change the prebuckling displacement distribution, as seen from a comparison of Figures 177d and 177j. The radial shrinkage due to welding is maximum at the ring stiffeners (equal to about 8% of the shell thickness) and minimum midway between rings, a mode similar to that shown in Fig. 173c. The welding process apparently has little influence on the buckling pressure because of two counteracting effects: the residual welding stresses weaken the shell but the "caterpillar" type residual deformations strengthen it.

Figure 179 shows the predicted stresses through the wall thickness midway between rings at various times of particular interest. The bands of plastic flow indicated in Fig. 179(d) result from the residual compressive stresses due to cold bending located in the corresponding regions of the wall thickness, as seen in Figs. 179(b,c). More details are given in Ref. [142].

Possible Causes of the Remaining Discrepancy between Test and Theory: The BOSOR5 simulation of the fabrication process explains a little more than half of the experimental difference between the buckling pressures of the machined model BR-4A and the cold bent, welded model BR-4. The remaining discrepancy is probably caused by some combination of the following effects not included in the BOSOR5 model:

1. There exist nonaxisymmetric initial imperfections which are greater for fabricated models than for machined models. These include nonuniformity in shell thickness. Measurements of the steel plate from which Specimen BR-4 was fabricated indicate that the thickness varied by as much as 10% [240].

2. The stress-strain curve of the "Alan Wood Steel" from which Specimen BR-4 was made is unknown. The material proportional limit may have been less than the yield stress quoted in [240]. If so, inclusion of the Bauschinger effect in the BOSOR5 model would have generated yielding in compression at lower pressures than those calculated with the present model, which is based on an isotropic hardening law. Presumably, the critical pressure would then also have been lower.

3. The welding simulation is a heuristic model which is in qualitative agreement with measurements on other specimens made of other material [47, 237, 238]. A rigorous treatment including welding sequence and nonaxisymmetric effects might lead to a lower critical pressure.

4. The sheet from which Specimen BR-4 was fabricated may have contained initial residual stresses due to differential cooling during and after it was rolled into its flat form of thickness .132 in.

Effect on Buckling of Deformations of the Ring Cross Sections

General and Local Instability

Most of the examples in this section involve cylindrical shells subjected to external hydrostatic pressure. Such structures are often designed through use of an optimality criterion: Dimensions of the shell wall and ring spacing are determined such that buckling in a general instability mode, such as shown in Fig. 180(a), occurs at the same value of p_{cr} as buckling of the skin between adjacent rings, such as shown in Fig. 180(b). The heights and thicknesses of the ring segments are established such that local crippling of each of these parts as shown in Figs. 180(c,d), occurs at the same critical compressive circumferential strain as that in the shell wall corresponding to general and local instability (a,b). The design is arrived at by calculation of buckling strains with the assumption that each part can be analyzed separately and can buckle independently of the rest of the structure. Simple support edge conditions are imposed at the boundaries of each part in order to permit use of simple expressions for the assumed buckling mode, such as $\sin(\pi x/L)\sin n\theta$.

Local ring stiffener buckling modes are characterized by buckling of individual stiffener segments with no translation of the junctures between these segments. Simple support conditions are imposed at segment junctures, as illustrated in Figs. 180(c,d). Each of the internal segments, that is a segment with both edges connected to another segment, may buckle with a different number of circumferential waves n . Each end segment has one free edge and does not deform but rotates about the juncture with the neighboring internal segment. The number of circumferential waves in the critical buckling pattern of each

end segment is equal to the number of circumferential waves in the critical buckling pattern of its neighboring internal segment. Behavior of a typical end segment is shown in Fig. 180(d).

Figures 180 (e-g) show another type of stiffener buckling, called "rolling". Three kinds of stiffener rolling are depicted, one (e) in which the panel skin participates and two (f,g) in which it does not. In the first (e) the stiffener cross section does not deform but simply rotates about its line of attachment to the skin. In the other two rolling modes (f,g) the stiffener web deforms and the portion of the ring cross section attached to this web translates and rotates. Buckling of type (f) occurs because of compression perpendicular to the plane of the paper. The buckling mode usually has several circumferential waves. Buckling of type (g) occurs in the cases of internal rings on externally pressurized cylindrical shells or external rings on internally pressurized cylindrical shells. It is due to compression in the web in the plane of the paper, a compression generated because the portion of the ring attached to the end of the web resists radial displacement. The resulting radial compression in the web can lead to axisymmetric "wide-column" buckling of the web.

Modal Interaction

One might think at first that the design method just summarized should be conservative if the effect of geometrical imperfections is ignored. It is clear that local buckling of the skin between two adjacent rings cannot occur as drawn in Fig. 180(b) without forcing the rings to rotate. Similarly, local buckling of each ring cross section segment cannot occur as exhibited in Figs. 180 (c,d) independently of the other segments, because these seg-

are not hinged at their junctions. The model with many hinges between its parts should yield lower bound estimates of buckling loads and therefore thicker parts than required for the actual (perfect) structure, a designer might well reason.

However, because of the interaction of local and general instability modes and the interaction of various local instability modes, critical buckling loads calculated for an assembled perfect structure are usually lower than are those calculated separately for parts of this structure treated as if they were hinged at their boundaries. Figure 181 illustrates the effect of interaction between general and local buckling modes on predicted buckling pressures of a cylindrical shell with external T-shaped rings. This shell was optimized with respect to weight through use of two interactive computer programs described in [242] and [243], which perform the optimization with use of simple membrane theory prebuckling analysis and assumed one-term buckling mode shapes such as expressed in Fig. 180. The results shown in Fig. 181 were obtained with BOSOR4 [14], in which axially nonuniform prebuckling behavior is accounted for and no assumptions are made about the shape of the buckling mode in the axial coordinate direction.

Buckling pressure factors λ and mode shapes corresponding to two BOSOR4 models are displayed in Fig. 181, one in which the rings are smeared out (a,b) and the other in which they are discrete (c-f). A value of $\lambda = 1.0$ would indicate perfect agreement with the results of the optimization programs [242, 243]. It is seen that the general instability mode and pressure from the model with smeared rings (b) and the local instability mode and pressure from the model with discrete rings (f) agree well with the corresponding

modes and pressures from the simplified optimization analysis, but that the general instability pressure from the model with discrete rings (e) is more than 10% below that for the models with smeared rings (b). The general instability mode corresponding to this model has a slight waviness which represents a mild interaction with the local instability mode (f). This interaction effect becomes stronger as the critical circumferential wave numbers n_{cr} for general and local instability approach each other.

Figure 182 reveals a similar reduction in predicted buckling pressure due to interaction of the ring rolling mode #2 [Fig. 180(f)] with the local skin buckling mode [Fig. 180(b)]. The dashed line in Fig. 182 corresponds to a buckling analysis in which the ring is treated as a discrete line structure with certain cross section area, A , moments of inertia I_y , I_x , for in-plane bending stiffness and out-of-plane bending stiffness, and torsional rigidity GJ . This line structure is located eccentrically with respect to the shell reference surface: at the shear center of the ring, which is where the flange and web intersect. In this discrete ring model the ring cross section is free to translate and rotate but cannot deform. The buckling mode resembles that drawn in Fig. 182 except the web cross section of the ring remains straight and the flange is therefore forced to bend more in its own plane (axial direction). The solid line in Fig. 182 corresponds to a discretized model in which the web and flange of the ring are treated as shell branches. During buckling in the mode indicated, the web cross section of the ring bends as shown, allowing the shell wall to buckle locally between rings without forcing the flange to bend in its plane as much as it has to in the discrete ring model.

Figures 183 - 185 demonstrate a more complex example of buckling of an internally ring-stiffened cylindrical shell subjected to uniform external hydrostatic pressure. Half of the cylinder length is shown in Fig. 183 with symmetry conditions imposed at the plane of symmetry and simple support conditions (S2 in Table 8) imposed at the edge. The insert in Fig. 183 depicts the discretized branched shell model provided as input to BOSOR4 [14].

The configuration with dimensions identified in Fig. 183 was arrived at in the following way: Given that the structure must be an internally ring-stiffened cylinder with Young's modulus $E = 17 \times 10^6$ psi, radius $r = 50$ in., and length $L = 100$ in., we are asked to find the configuration corresponding to minimum weight subject to the constraint condition that the perfect shell will not buckle under a uniform external hydrostatic pressure of 1820 psi. Application of the optimization programs described in Refs. [242] and [243] leads to a minimum weight configuration with very closely spaced rings, as with the cylindrical shell generator depicted in Fig. 181(d). If one is willing to accept a rather small penalty in weight (about 3%) one can impose a lower bound on the ring spacing so that the final design is more amenable to analytical treatment as a branched shell. (Actually, the ring stiffeners in submarine pressure hulls, for example, are farther apart than a simple optimization scheme would dictate because of the expense and practical spatial problems encountered in welding the rings to the shell.) The dimensions called out in Fig. 183 correspond closely to the optimum design with the lower bound on ring spacing set equal to 7.692 in. This optimum design is generated from the simplified buckling models described in connection with Fig. 180.

The dashed line near the bottom of Fig. 183 shows buckling pressures predicted from simplified theory corresponding to ring web wide column buckling ($n = 0$;

Fig. 180(g)), general instability ($n = 3$; Fig. 180(a)), ring rolling mode #1 ($n = 6$; Fig. 180(e)), and local skin buckling ($n = 12$; Fig.

180(b)), all of which are active buckling constraint conditions at the optimum design point.

The other curves in Fig. 183 were all obtained with the BOSOR4 computer program [14]. If the shell were perfect and if the material remained elastic, buckling would occur with five circumferential waves at a pressure of 1646 psi, as indicated by the minimum load on the curve labeled "Branched shell (nonlinear)." This curve represents results of the most accurate analysis of the shell. Unlike the example shown in Fig. 181, for which there is significant modal interaction between general and local skin instability, the modal interaction here resembles that demonstrated in Fig. 182: the discrete ring mode yields erroneous results for high n because the ring web is not permitted to deform in that model, with the result that far too much strain energy is predicted to be stored in the flange during buckling. Replacement of the ring by a simple support restraint ($v_b = w_b = 0$; u_b, β_b free), as is done in the crude optimization analysis, leads to a far better estimate of the actual buckling pressure corresponding to $n = 12$ circumferential waves, as seen from the location of the open circle on the dashed line at $n = 12$.

Predicted buckling modes corresponding to bifurcation with linear prebuckling analysis are exhibited in Fig. 184. Local instability, identified by circles or squares in Fig. 183, corresponds to modes in which the attachment lines of the ring webs to the cylindrical shell do not move radially or circumferentially, as illustrated in Fig. 184 (a, d, e, f, and i). General instability, identified by triangles in Fig. 183, corresponds to modes in which at least one of these attachment lines moves radially, as illustrated in Fig. 184

(b, c, g, and h). Note that for $n \geq 6$ the two curves in Fig. 183 labeled "Discrete Rings" correspond to modes of the types (d) and (e) in Fig. 184. From the branched shell model it is clear from Fig. 184 that the degree of bending in the ring webs increases with increasing n . This is because the strain energy stored in the flange increases with n^4 for a given amplitude of flange neutral axis modal displacement in the axial direction. For $n = 12$ circumferential waves there is a great deal less modal axial flange displacement in the branched shell model than exists for $n = 5$, and for $n = 5$ there is less than for $n = 0$.

Figure 185 shows the prebuckled state and buckling modes corresponding to the lowest curve in Fig. 183. The critical buckling mode for $n = 5$ circumferential waves is very different from that corresponding to the linear treatment.

Comparisons with Tests in which Local Ring Deformations are Important

Crippling of Ring Web: Figure 186 shows the discretized model of a ring and buckling loads predicted for a range of circumferential waves n . BOSOR4 gives two minima in the range $2 \leq n \leq 16$. The minimum at $n = 2$ corresponds to a mode in which the cross section does not deform — i.e., the ring ovalization mode. Buckling pressures calculated for this mode are very close to those computed from the well-known formula $q_{cr} = EI(n^2 - 1)/r_c^3$, in which q_{cr} is the critical line load in lb/in. (pressure integrated along segment ①), EI is the bending rigidity of the ring, and r_c is the radius to the ring centroidal axis. The minimum at about $n = 11$ corresponds to buckling of the web in a mode similar to that shown in Fig. 180(f). In a test [244] the web crippld at about 1500 psi. The $n = 2$ mode was not observed because the ring was held in a mandrel that prevented the unlimited growth of this mode.

Wide Column Ring Web "Buckling": This type of local instability of ring stiffeners is described in the discussion associated with Fig. 180(g). An example of an externally pressurized ring-stiffened cylindrical shell that failed in this axisymmetric mode [245] is shown in Fig. 187(a). In the BOSOR4 model of the shell the slender webs are treated as flexible annuli and the flanges as discrete rings. The problem is a good illustration of a typical sequence of computer runs that might be required for analysis of a complex shell of revolution where several failure modes are possible.

As with the case shown in Fig. 183, the choice of a linear bifurcation buckling treatment for a preliminary analysis is logical because one suspects that bifurcation buckling may be the primary mode of failure, and approximate buckling pressures for a wide range of circumferential wave numbers can be obtained without too large an expenditure for computer time. It is likely that more than one minimum buckling pressure exists in a plot of $p_{cr}(n)$ vs n . The shell may buckle axisymmetrically through 'sideways' of the deep ring stiffeners; it may buckle nonsymmetrically in a low- n general instability mode in which cylinder and rings move together; it may buckle nonsymmetrically in a low- n general instability mode in which cylinder and rings move together; it may buckle nonsymmetrically in a higher- n 'panel' or 'bay' mode in which the rings are located at displacement nodes in the buckle pattern; or the webs of the rings may buckle nonsymmetrically in a still-higher n mode similar to that shown in Fig. 186. The choice of a linear bifurcation buckling analysis with a wide range of n will reveal all of these modes and cause to be calculated approximate critical pressures corresponding to them. Figure 187(b) shows the results of such an analysis. The lowest minimum corresponds to axisymmetric bifurcation buckling ('sideways' of the webs). This is the wide column buckling mode described previously.

Nonlinear axisymmetric analysis of this structure is analogous to a post-buckling analysis of a wide column or rather a group of wide columns, one corresponding to each ring web. Figure 188 gives the stability determinant $|K_1(p, n=0)|$ as a function of external pressure. At a pressure close to the bifurcation pressure obtained with use of linear theory, the stability determinant changes direction rather abruptly, indicating fairly large changes in prebuckling deformations for small changes in pressure. Since the stability determinant does not change sign there is no axisymmetric bifurcation. Performance of the nonlinear prebuckling analysis in this case is analogous to conversion of the bifurcation buckling analysis of a perfect structure to a nonlinear collapse or nonlinear post-buckling analysis of an imperfect structure, in which the imperfection is the nonuniformity of the prebuckling state.

Figure 189 contains plots of web tip deflections and effective stresses as functions of external pressure in the pressure range corresponding to the rather abrupt change in behavior of the stability determinant. Frames #2 and #3 display sudden changes in the rate of sideways because they are far enough from the clamped boundary so that their webs behave like almost perfect wide columns in axial compression. Being almost perfect, their load-deflection curves develop high curvatures in the neighborhood of the bifurcation point predicted from linear analysis. Frame #1 is in the edge bending "boundary layer" so that the junction of its web and the shell wall undergoes considerable meridional rotation. Thus, the axial deflection w of the flange of Frame #1 increases at a fairly uniform rate compared to those of Frames #2 and #3. The web of Frame #1 behaves in a manner similar to a very imperfect wide column or to a column with considerable load eccentricity. The sideways or wide column post-buckling deflections of Frames #2 and #3 cause the radial compressive membrane stresses, built up because of hoop compression in the

flanges, to be relieved, thus producing the abrupt change in behavior of the stability determinant.

In a test of this shell [245] the rings simply fell off at a pressure slightly above 3200 psi. The failure was due to high stresses at the junctions of webs and shell.

General Instability of Ring-Stiffened Shallow Conical Shell: Figure 190 shows a very light-weight, shallow conical shell with internal Z-shaped ring stiffeners. This shell was used as an aerodynamic foil to decelerate the landing module for the NASA Viking mission to Mars [246]. Because of the stringent mass limitations and the very small loadings which the shell was designed to support, the wall and rings were fabricated with very thin gage material. Figure 190(c) shows a specimen buckled under uniform external pressure. This pressure is reacted axisymmetrically at the large payload support ring located midway along the cone generator. Comparisons between test and theory [11] in Fig. 190(d) reveal that the local deformations of the rings must be accounted for in order to obtain an accurate prediction of the critical pressure corresponding to general instability. The buckling mode shape depicted in Fig. 190(e) clearly demonstrates the significant deformation of the rings during buckling.

BUCKLING OF PRISMATIC SHELLS AND PANELS

Summary

Figure 191 gives several examples of prismatic shells and panels. These are structures the cross sections of which are thin and do not vary in one of the coordinate directions, generally called the axial direction. In this chapter a method will be described in which a computer program for the analysis of shells of revolution can be used to predict buckling of prismatic shells and panels. Results will be given of convergence studies applied to cylindrical shells subjected to external lateral pressure. These studies demonstrate the validity of the technique. The method will then be applied to yield predictions of bifurcation buckling loads of noncircular cylindrical shells under axial compression or external pressure and failure of corrugated and beaded panels under axial compression. The effect of manufacturing processes on buckling and crippling of corrugated semi-sandwich panels of the type from which the rocket payload shroud shown in Fig. 5 is made will be shown.

A discussion of modal interaction in axially compressed columns and panels will follow. One form of this phenomenon has already been illustrated in the case of bifurcation buckling of ring-stiffened cylindrical shells subjected to uniform external hydrostatic pressure (Figs. 181 - 185). It will be shown that buckling loads for optimally designed structures, that is structures configured such that local and general instability occur at the same or almost the same load, are sensitive to initial geometrical imperfections.

The section closes with brief discussions of the effect of transverse shear deformations on buckling of panels made of laminated composite material.

Use of a Computer Code for Shells of Revolution to Predict Buckling Loads of Prismatic Structures

Introduction

The motivation behind much of the research activity in shell analysis is to reduce computer time and core storage required to solve complex problems. It is advantageous whenever possible to reduce the number of degrees of freedom required by separation of variables and to optimize computer efficiency by setting up stiffness matrices with as narrow band widths as possible. Currently, problems in complex shell analysis can be classified into two groups: that which involves two-dimensional discretization and that which involves one-dimensional discretization. The two-dimensional numerical analysis generally requires one to several orders of magnitude more computer time to solve than does the one-dimensional problem. The computer time increases quadratically with the bandwidth of the stiffness matrix and linearly with the number of degrees of freedom. Matrix bandwidths for two-dimensional problems are much wider than those for one-dimensional problems and the number of degrees of freedom required for convergence to a given accuracy is greater.

The establishment of the technique described here [82] was motivated by the need for economical computer solutions to problems traditionally

associated with two-dimensional numerical analyses but amenable by means of an exchange of independent variables to solution by separation of variables with consequent reduction to one-dimensional numerical treatment. In this class are included linear stress, buckling and vibration problems for simply-supported prismatic shells. Stress analysis can be performed for prismatic shells with loads that vary in the two coordinate directions. Buckling and vibration analyses are restricted to systems in which both the loads and the geometry are prismatic, that is, constant in the axial direction.

Figure 191 gives examples of prismatic shells: Fig. 191(a) shows an oval cylinder which may be subjected to combinations of pressure and axial loading; (b) shows a cylinder with a pressure or thermal load that varies only in the circumferential direction; (c) and (d) represent typical advanced structural panels considered for hypersonic vehicles, lightweight rocket payload shrouds, and space shuttles; and (e) shows a general prismatic shell with stringers which can be treated as discrete elastic structures. The oval cylinder under axial compression has been investigated by Kempner and Chen, [248] Hutchinson, [249] and Almroth, Brogan, and Marlowe [250]. Elliptic cylinders under external pressure have been treated by Yao and Jenkins [251]. Liaw [252] gives a survey of papers published before April 1969 on the stability of cylindrical and conical shells of noncircular cross section. Buckling allowables for nonuniformly loaded cylinders have been calculated by Almroth [253] who investigated band-loaded cylinders in which the external pressure varies as $p_0 + p_1 \cos\theta$ in the circumferential direction. Ross, et al. [106] determined experimentally critical temperatures of cylinders heated along an axial strip. Examples of

buckling under nonsymmetric loading in which the nonsymmetrical nature of the loading is retained in the stability equations are given in Figs. 148 and 154.

Local buckling and crippling loads for axially compressed corrugated and beaded sheets have been determined theoretically and experimentally by Plank, Sakata, Davis, and Richie [254]. Buckling loads were determined experimentally by Shang, Marulic, and Sturm [255] for axially compressed longitudinally stiffened cylinders. The geometry of the specimens of Ref. [255] was such that the circumferential buckling half wave-length and stringer spacing were approximately equal, indicating the need for analytical treatment of the stringers as discrete. Egle and Sewall [256] and McDonald [257] have calculated vibration frequencies for cylinders with stringers included as discrete structures.

The structures shown in Fig. 191 and analyzed in Refs. [248- 257] are all prismatic. If they are simply supported at the generator ends they can be analyzed as portions of shells of revolution in which the length of the prismatic shell is given by

$$L = \pi b/n \quad (62)$$

where b is the radius from an axis of revolution to some reference surface and n is the number of complete circumferential waves. The results presented here were thus obtained by means of the analysis and computer program described in [14].

Buckling of oval cylinders or nonsymmetrically loaded cylinders can be treated by a modeling of the cylinder as a portion of a torus with a very large radius b . Figure 192 illustrates the model. A cylinder of length L , small diameter d and thickness t is modeled as a small portion of a torus with radius b . As $b \rightarrow \infty$ and $L = \text{constant}$ the short curved cylinder approaches a straight cylinder. The cross section need not be circular, nor the thickness constant. The pressure can vary along the length as well as over the circumference. A limitation of the model is that the cylinder must be simply-supported at the ends $\theta \cdot b = 0$ and $\theta \cdot b = L$.

Since the torus is a shell of revolution, the BOSOR4 code [14] can be used to analyze it without any special alteration. What has been done here in effect is to exchange the independent variables in the analysis of a cylinder: the axial variable s for the cylinder becomes the circumferential variable $\theta \cdot b$ for the torus and vice versa. The circumferential displacement distribution of the cylinder, conventionally expressed in terms of $\sin n\theta$ or $\cos n\theta$ with n the input circumferential wave number, becomes the meridional displacement distribution of the torus, now expressed in terms of the displacement values at discrete nodal points in the finite difference or finite element analysis. Similarly, the meridional displacement distributions of the cylinder, conventionally expressed as discrete mesh point variables, are now expressed in terms of $\sin n\theta$ or $\cos n\theta$ with n being the number of waves around the large-diameter torus. Given the radius b , the length of the cylinder is determined by the wave number n , which in the limit of very large b is a very large number (such as 10,000, for example). The boundary conditions at $\theta \cdot b = 0$ and $\theta \cdot b = L$ are simple support: $N_\theta = M_\theta = u = w = 0$.

The user has no choice of boundary conditions at $\theta \cdot b = 0$ and $\theta \cdot b = L$, since the simple-support condition arises from the underlying assumption that the dependent variables and their derivatives vary in this direction as $\sin n\theta$ and $\cos n\theta$.

The loading on the cylinder in Fig. 192 is expressed as a Fourier expansion over the interval $-L \leq \theta \cdot b \leq L$. For example, the pressure loading in Fig. 192 (uniform for $0 \leq \theta \cdot b \leq L$ and variable around the circumference, s) is expressed as a Fourier sine series, thus:

$$p(s, \theta) = f(s) \cdot g(\theta) \quad (63)$$

in which

$$g(\theta) = \frac{4}{\pi} \sum_{m=1,3,5\dots}^{NMAX} \sin(m\pi\theta \cdot b)/L \quad (64)$$

The integer m is the number of half-waves in the interval $0 \leq \theta \cdot b \leq L$.

Therefore, the corresponding wave number n for the complete torus is $n = m\pi b/L$. The question arises, why not expand the load in a cosine series in the interval $-L \leq \theta \cdot b \leq L$? This is not possible because the $m = 0$ term corresponds to an infinite cylinder ($L = 2\pi b$). The longest half wavelength in the Fourier expansion of the load must be equal to L or an integer fraction of L .

Thus, the finite-length, simply-supported, oval cylinder under external pressure is analyzed as a toroidal shell with very large radius b and subjected to loads which vary rapidly around the circumference. In the section "Numerical Results" the behavior of a simply-supported externally pressurized elliptical cylinder is discussed.

There are additional advantages of being able to analyze cylinders in this manner. Note in Fig. 191(e) that the wall properties (thickness, modulus) in the s-direction need not be constant. Also, note that longitudinal stringers can be included in the analysis as discrete elastic structures. With the cylinder analyzed as a portion of the torus, the cylinder stringers are rings in this application of the BOSOR4 code. Also, cylindrical or flat panels with stringers, corrugations, beads, or other geometrical peculiarities and with arbitrary boundary conditions along generators can be treated, since the generators are now meridional stations. Some of these cases are discussed in the following sections.

Convergence Studies: The application of BOSOR4 to the stability analysis of cylinders of noncircular cross section and nonsymmetrical loads was validated by convergence studies for uniformly loaded circular cylinders analyzed as portions of toroidal shells with various radii b and various numbers of meridional nodal points. Membrane prebuckling analysis was used in the convergence studies. For given values of b , the cylinder lengths were established as described above by selection of appropriate circumferential wave numbers, n . This procedure is valid for simply-supported cylinders the buckling modes of which have an integral number of half-sine waves along the length.

Tables 19- 21 and Figs. 193 and 194 give the results for hydrostatically compressed circular cylinders. In Table 19 convergence with increasing toroidal radius b is given for cylinders with $L/a = 0.6$ and $L/a = 6.0$, in which " a " is the radius of the cylinder. The values of

p_a/Et for $b = \text{infinity}$ are calculated from Eqs. (11) and (12), pp. 424-425 of Flügge [258]. The lowest two eigenvalues are obtained in each case. In the limit of very large b these eigenvalues correspond to two wave numbers, $n = 10$ and $n = 12$. Figure 193 shows the normalized buckling displacement w for the second eigenvalue for increasing values of toroidal radius b . With large b the distribution over $1/4$ of the circumference of the cylinder approaches a cosine wave with three full waves. This mode corresponds to $n = 12$ for the complete cylinder. Symmetry conditions are imposed at the ends of the toroidal meridian. All calculations were performed in double precision on the Univac 1108. The data points in Fig. 193 indicate nodal points. The discretization method is described in detail in the discussion and equations associated with Fig.20 of REF. [430].

Table 20 and Fig. 194 represent the results of a convergence study in which the number of mesh points is varied for a given (very large) value of b . The buckling modes plotted in Fig. 194 correspond to $n = 10$ waves around the circumference of the cylinder with $L/a = 0.6$. Table 21 gives the convergence of buckling loads with increasing number of nodal points for the cylinder with $L/a = 0.6$ analyzed as a cylinder, not as a portion of a large-radius torus. These convergence studies indicate the degree of accuracy obtained with the BOSOR4 code and provide a guide to the user of STAGS [48] or other large-scale two-dimensional computer codes as to the number of mesh points required for adequate accuracy.

Numerical Results

In this section numerical results are presented for nonuniformly loaded circular cylinders, externally pressurized and axially compressed noncircular cylinders and axially compressed corrugated and beaded panels.

Nonuniformly Loaded Circular Cylindrical Shells: An analysis was made of a simply-supported cylinder subjected to a band pressure load which varies around the circumference as shown in Fig. 195. The cylinder was modeled as a portion of a torus with $b = 20,000$ in. and $n = 10,000$. Comparisons were made with the theory of Almroth [4.253] for a cylinder with $a = 1.0$ in., $t = 0.0025$ in., $L = 2\pi$ in. and $\Delta L/L = 1.0$ and 0.4 . For the case $\Delta L/L = 1.0$, Almroth obtains $p_{CR} a / (Et) \times 10^5 = 2.253$. The BOSOR4 program yields a value 2.292 for this parameter. The buckling modal displacement w is displayed at the bottom of Fig. 195.

Figure 196 shows the normal pressure loading at $s = 0$ on the cylinder with $L = 2\pi$, $a/t = 400$ and $\Delta L/L = 0.4$. The load is expanded in a 10-term Fourier sine series in the interval $-L \leq \theta \cdot b \leq +L$ (see Fig. 192). Figure 197 gives the axial distributions of stress resultants corresponding to the 10-term Fourier sine series expansion of the banded pressure load shown in Fig. 196. Figure 198 shows the circumferential distribution of stress resultants at the cylinder midlength $\theta \cdot b = L/2 = \pi$ inches. These values are used in the stability analysis, in which the assumption is made that they are constant around the circumference of the equivalent torus (along the axis of the cylinder) in a manner analogous to the treatment in the problems illustrated in Figs. 149, 150, and 155- 159. Therefore, the buckling loads calculated in BOSOR4 are independent of the bandwidth of the pressure for bandwidths that are long compared to a boundary layer length $(at)^{1/2}$. Thus, $p_{CR} a / (Et) \times 10^5$ equals 2.292 compared to the value of 3.0913 obtained with Almroth's more exact analysis [253].

Stress and Buckling of Elliptic Cylinders: Figure 199 shows an elliptic cylinder and gives various dimensions and material properties. The cylinders are subjected to uniform external pressure on the curved surface only. Yao and Jenkins [251] obtained buckling pressures from tests on simply-supported polyvinyl chloride shells. They compared the test results with a theory in which the prebuckled state is calculated from linear membrane theory and buckling pressures are obtained from an eigenvalue problem based on the Galerkin method.

The BOSOR4 computer program was used to calculate stresses and buckling pressures for elliptic cylinders of the geometries shown in Fig. 199. The oval cylinders were analyzed as toroidal shells with very large b and n as described above. The uniform external pressure was expanded in a 20-term Fourier sine series according to Eqs. (63) and (64). Figure

200 displays the axial distributions of normal displacement and in-plane stress resultants at $s = 0$ (end of minor axis B) for an external pressure of 1 psi on an elliptic cylinder with $A/B = 2$, $t = 0.019$, and various values of L . The quantity $\theta \cdot b/L$ is the normalized distance along the circumference of the torus of radius b (see Fig. 192). Figure 201 gives the circumferential distributions of rotation about a generator and in-plane stress resultants at the midlength $b/L = 0.5$ of the oval cylinder. Plots cover $1/4$ of the circumference. The stress distributions are very similar to those predicted by membrane theory.

Three hundred degrees of freedom were used, and 1 min, 56 sec of UNIVAC 1108 time were required for the double-precision calculations. The prestress state was checked by a run with the linear version of the two-dimensional finite-difference program, STAGS [48]. Excellent agreement was obtained.

Note that as the length L of the shell increases the hoop stress resultant at $L/2$ approaches the values predicted from membrane theory, $p_a = -8.0$ lb/in. at the end of the minor axis ($s = 0$) and $p_a = -1.0$ lb/in. at the end of the major axis. However from simple static equilibrium conditions for an elliptical ring it is known that as $L \rightarrow \infty$ the hoop stress resultant must approach -2 lb/in. at $s = 0$ and -4 lb/in. at $s = s_{\text{end}}$ for uniform external pressure of 1 psi. Clearly, the elliptical cylinders of length 4 to 10 in. with cross sections as shown in Fig. 199, while long compared to bending boundary-layer lengths, are short compared to lengths required for the effect of end cross section fixity to die out.

Buckling pressures were calculated for several cases with $A/B = 2.0$ and $A/B = 1.5$. The results, compared with Yao and Jenkins' tests and theory, are presented in Figs. 202- 206 and Tables 22- 24. Predicted buckling pressures are always higher than the test values and are rather inaccurate for the thicker shells. The thicker shells apparently buckle by collapsing gradually rather than failing by a sudden change (bifurcation) in the mode of deformation (Fig. 4 of Ref. [251]). It is probable, therefore, that the present theory is not valid for the shells with nominal thickness 0.050 and 0.090 in. A nonlinear, two-dimensional collapse analysis such as that of Ref. [250] is required for these cases. This analysis has been performed by Marlowe and is reported in Ref. [259].

Figures 204- 206 show the buckling modes for externally pressurized elliptical cylinders with $A/B = 2$, lengths $L = 2, 4, 6, 10$ in. and thickness $t = 0.019, 0.029$ and 0.091 in. Note that the plot corresponding to $L = 10$ in Fig. 204 covers $0 \leq \psi \leq 180^\circ$ of arc length, whereas all other plots

in Figs. 204- 206 cover $0 \leq \psi \leq 90^\circ$. With the exception of the case $A/B = 2$, $L = 10$, $t = 0.019$, the buckling loads given in Figs. 202- 203 correspond to modes symmetrical about the ends of both the minor and major axes. The lowest buckling pressure for the exceptional case corresponds to displacements symmetrical about $\psi = 0^\circ$ and antisymmetrical about $\psi = 90^\circ$. For all cases modes antisymmetrical and symmetrical about $\psi = 90^\circ$ correspond to pressures within a few percent of each other.

Tables 22 and 23 give buckling pressures in psi for the simply supported elliptical cylinders with $A/B = 2$ and 1.5, respectively. Theoretical values are compared with Yao and Jenkins' test results [251]. Three theoretical values, p_{CR}^1 , p_{CR}^2 , and p_{CR}^3 , are listed for each geometry. The p_{CR}^1 corresponds to BOSOR results with both prebuckling in-plane stress resultants and prebuckling rotations χ_0 about the generators included in the stability analysis. The p_{CR}^2 are calculated neglecting the cross section shape change (effect of χ_0) in the stability analysis. Note that the χ_0 effect becomes larger as L and t increase. The p_{CR}^3 are the analytical results from Ref. [251].

Table 24 gives convergence properties of buckling pressures for the elliptical cylinders $A/B = 2$, $L = 10$ in., and various values of t . The number of terms in the Fourier sine series representation of the axial load distribution is varied. In this study the value of the pressure at the midlength of the cylinder is maintained at unity, independent of the number of terms taken in the series.

Cylinders of Noncircular Cross Section under Axial Compression: Buckling loads and post-buckling behavior have been determined for axially compressed cylinders of oval cross section by Kempner and Chen [248] and Hutchinson [249]. Almroth, Brogan and Marlowe [250] have studied the nonlinear behavior of axially compressed oval conical shells through use of a two-dimensional finite difference analysis. The BOSOR4 program [14] can be used to determine bifurcation buckling loads from linear theory for axially compressed, simply supported elliptic cylinders. Membrane prebuckling theory is used in the analysis. The cylinder is treated as a portion of a large-radius torus. Figure 207 shows the buckling modal displacements in the circumferential direction for $0 \leq \psi \leq 180^\circ$. The axial distribution (normal to the plane of the paper) is a half-sine wave. The lowest two eigenvalues are very close to each other and the modes are symmetric and antisymmetric about $\psi = 90^\circ$. Note that bifurcation buckling of axially compressed oval cylindrical shells does not necessarily signify failure of the structure. Fig. 57 shows that post-buckling load-carrying capability exists in excess of the bifurcation load. However, nonlinear two-dimensionally discretized models must be used to predict this collapse load.

Figure 208 exhibits buckling modes for an axially compressed simply supported cylinder with a pear-shaped cross section. Membrane theory was used in the prebuckling analysis. The lowest two eigenvalues, $N_{cr} = 24.02$ lb/in. and 34.74 lb/in. correspond to uniform loading over the entire perimeter of the cross section, and the highest eigenvalue, $N_{cr} = 586$ lb/in., corresponds to loading over the curved portions only. Symmetry conditions were imposed at points A and B. The axial displacement variation is a half-sine

wave. The lowest two eigenvalues correspond to buckling of the flat sections. For axial loads higher than 35 lb/in. these flat sections are considered to be buckled and thus carrying no load. The third buckling mode illustrated in Fig. 208 therefore corresponds to a model in which only the curved portions of the pear-shaped cylinder are loaded. The buckling mode is similar to the displacement distribution corresponding to collapse obtained with the STAGS program [48]. However, a much lower collapse load is obtained with STAGS because the prebuckling deformations in the flat plate segments propagate into the curved segments with increasing load, thereby introducing imperfections into an imperfection-sensitive structure. The axial load at collapse integrated over half of the cross section perimeter is 1186 lbs according to the nonlinear collapse analysis with use of STAGS, results of which are displayed in Fig. 58. The axial load at bifurcation of the curved portions according to the BOSOR4 prediction is 1880 lbs over half of the pear-shaped cross section.

The reduction from 1880 to 1186 lb is due to inclusion in the STAGS analysis of the prebuckling deformation which, with increasing imposed axial end shortening, propagates from the flat portions into the curved portions, rendering imperfect these imperfection-sensitive parts of the shell. The BOSOR4 analysis is performed by treatment of the pear-shaped cylinder as a shell of four segments, as indicated in Fig. 208. Nodal points in the discretized model are indicated by small circles.

Bifurcation Buckling of Axially Compressed Panels

Introduction

As in the case of ring-stiffened cylinders, axially compressed longitudinally stiffened panels are subject to several types of failure:

long-wavelength general instability, intermediate-wavelength (panel) instability between stiffeners, and local crippling. These failure modes can often be analytically determined by separate analyses, as described for ring-stiffened cylinders in connection with Fig. 180, because the wavelengths associated with them are often quite different in magnitude. However, modern lightweight structures are frequently constructed of panels with deep, slender stiffeners, the distance between the stiffeners being of the same magnitude as their depth. For such cases the intermediate-wavelength and the crippling modes of buckling couple and a unified analysis becomes necessary. It has been shown in a previous section that this is true for ring-stiffened cylinders in which the depth of the web is the same order of magnitude as the distance between rings. Also, as will be demonstrated in this section, the general instability predictions may be rather sensitive to local deformation of the cross section of a complex panel. We have already seen an example of this sensitivity in the case of buckling of a lightly stiffened shallow conical shell used for deceleration of a payload entering the Martian atmosphere (Fig. 190)

Until about 10 years ago axially stiffened panels were analyzed as equivalent orthotropic plates. A great deal of work of this type was done by Becker, Tsai, Block, Card, Mikulas, Anderson, Jones, Peterson and others at NASA in the '50s and '60s. References to their work are given in Ref. [260]. In 1968 Wittrick [261] published an analysis of prismatic structures composed of flat plates. Since 1971 a series of papers [82, 260, 262- 269] has appeared on the treatment of buckling and vibration of prismatic shell structures. In most of the papers the buckling and vibration modes are

assumed to be sinusoidal in the axial direction, with the wavelength of deformation the same in all of the segments of the complex structure. This assumption, which limits the analysis to simply-supported panels, permits separation of variables with consequent reduction of the problem from two dimensional to one dimensional. Wittrick's analysis [261] predicts the three types of instability identified in the first paragraph - general, panel, and crippling; the treatment of Viswanathan et al. [260] extends that of Wittrick to allow orthotropic wall properties and intermittent elastic beam-type supports; Williams [263] extends Wittrick's analysis to include vibration and to incorporate substructuring techniques; Wittrick and Williams [267] formalized their treatment in a computer program called VIPASA; and Anderson and Stroud combined VIPA with an optimization routine by Vanderplaats and Moses [270] to produce a computer program called PASCO for the optimization of layered, stiffened composite panels [269].

Figures 209(a) and (b) show parts of a semisandwich corrugated panel undeformed, buckled (a) and crippled (b) under an axial load (normal to the plane of the paper). Classical analysis of buckling of such a panel treats it as an equivalent orthotropic sheet with the wall cross-section of course not permitted to deform locally. The presence of such local deformations makes it very difficult to assign a priori a torsional stiffness per length, for example. This J-factor is particularly important in this case because of the enclosed trapezoidal areas. Local distortions also affect the axial bending stiffness, another significant determinant of the predicted buckling load. The degree of local distortion is largely governed by the way in which the corrugated sheet is fastened to the flat sheet. Figures 209(a)

and (b) correspond to cases in which the centers of the troughs of the corrugations are riveted to the sheet. Bonding along the entire widths of the troughs markedly reduces the amount of distortion with corresponding increase in the stiffness and buckling load. This difference between bonding and riveting would not be reflected in a classical orthotropic plate analysis, except through the empirical introduction of appropriate knockdown factors applied to the constitutive law to bring test and theory into agreement.

Classical predictions of crippling loads of sections composed of thin flat sheets such as shown in Fig. 209(b) are based on analyses of long thin axially compressed strips simply-supported or clamped along the "corners" or at rivet or bond lines. With regard to Fig. 209(b), an assumption of clamping at the points labeled symmetry would obviously lead to overestimation of the crippling load. If simple-support were assumed at these points it is not clear whether the crippling load prediction would be too high or too low. The actual condition depicted in Fig. 209(b) appears to be clamping to an elastic foundation with some unknown stiffness.

The simplifications of the various classical analyses lead to errors of unknown magnitude. The errors frequently cancel, leading to fortuitous agreement between test and theory or between predictions with crude and refined models. An analysis is needed in which given structural configurations are modeled in various ways.

The results presented next were obtained with the BOSOR4 computer program [14], in which the models are set up as described in the discussion associated with Fig. 192. This analysis method can be used to determine general, panel, and crippling instability of complex, built-up thin sections, to evaluate various types of fastening techniques, to calculate the effect of local wall distortions on over-all stiffness and stability, and to evaluate quantitatively various simpler analytical models of a given complex shell structure.

Buckling of Axially Compressed Corrugated and Beaded Panels: Figures

191 (c) and (d) show typical advanced structural panel designs proposed for hypersonic vehicles and space vehicles. Reference 254 presents test and theoretical results for several panel configurations subjected to axial compression and shear at room temperature and elevated temperature. Panels were tested for general (panel) buckling and local crippling loads. In Ref. [254] buckling predictions are based on wide-column theory. Local crippling predictions are based on simple buckling formulas derived for constant-thickness plate and cylindrical elements representative of individual components of the complex panels.

Two configurations are analyzed here for critical axial loads: a trapezoidal corrugation and a beaded corrugation. The geometry is shown in Fig. 210. The thickness distributions and dimensions are taken from Ref. [254]. The thickness of the beaded panel (Fig. 210(a)) is assumed in the present analysis to vary linearly between stations where it is called out. That of the trapezoidal corrugations is assumed constant in each of the flat

elements. The panels are treated in BOSOR4 as segmented shells of revolution with very large radii b : for the beaded panel $b = 10^5$ in. and for the trapezoidal-corrugated panel $b = 10^4$ in. Figure 210 shows the division of the panels into segments with symmetry planes at which either anti-symmetry conditions or symmetry conditions are imposed in the stability analysis.

Figure 211 shows critical axial load/length N_{CR} for the beaded panel of Fig. 210(a) as a function of wave number n or length $L = \pi b/n$. The semi-log plot covers lengths from 50 to 0.3 in. Three types of buckling occur in this range of L , and their corresponding mode shapes are shown in Figure 211. The lowest critical load is associated with a long-axial-wave length panel buckling from bead-crest to bead-crest. The intermediate wave-length load corresponds to buckling of the beads as axially compressed perfect cylinders, and the calculated N_{CR} from $n = 150,000$ to $400,000$ is very close to the classical value $0.6Et^2/R$. The shortest length crippling load corresponds to buckling of the flat regions 0.556 in. wide between beads. The dotted curves represent critical axial loads for simply supported and clamped plates calculated from the appropriate formulas in Ref. [271]. Two cases were run on BOSOR4, one with the angle $\alpha=0$ (Fig. 210) and one with $\alpha=12^\circ$, which represents the test configuration. In the tests the long panel mode was first observed at a line load of about 412 lb/in. and a crippling mode involving both flats and beads was observed at 1250 lb/in.

The BOSOR4 code is conservative in the prediction of the long panel mode, probably because the 30-in.-long test panel was not in fact simply supported

at the ends and because it was stable in this mode in the initial post-buckling range. The BOSOR4 code is very unconservative in the prediction of crippling of the cylindrical beads because this mode of failure is sensitive to imperfections and occurred in the test at **average** stresses approaching the proportional limit of the material.

Figure 210(b) shows the trapezoidal corrugated panel, analyzed as a shell with seven segments. This many segments were taken to permit general instability across the three flat segments labeled 3, 4, and 5. Such a mode would be analogous to the long panel mode of the beaded sheet. In the BOSOR4 analysis this mode did not appear, however. Nor was this type of buckling observed in the tests reported in Ref. [254].

Symmetry conditions imposed as shown in Fig. 210(b) permit the wide-column mode for long panels (low n). In this case the wide-column mode corresponds to the lowest eigenvalue for given wave number n if $n < 4000$ or $L >$ about 7.5 in. The wide-column mode corresponds to the critical load if $L >$ about 15 in. and the panel is free at the unloaded edges.

Figure 212 shows the critical axial load versus length L or wave number n . The dotted curves represent calculations based on formulas in Ref. [271]. Test values reported in Ref. [254] correspond to a line load of about 1120 lb/in. The good agreement might be expected since the critical loads for configurations consisting of flat plates are not very sensitive to initial imperfections, and the average stress at failure in the tests was somewhat below the proportional limit of the material.

Effect of Manufacturing Method on General and Local Buckling of a Semi-

Sandwich Corrugated Panel: An example of a semi-sandwich corrugated shell wall construction is illustrated in Fig. 5(b). The rocket payload shroud shown in Fig. 5(a) has such a wall construction, which is further reinforced by Z-shaped rings spaced 16 inches apart. Under nonuniform pressure loading during ascent through the atmosphere this shroud is susceptible to buckling, as exhibited in Fig. 149(c).

Buckling pressures are calculated for the shroud in an approximate analysis in which the corrugations shown in Fig. 5(a) are smeared out according to the method of Baruch and Singer [160]. In such a model it is tacitly assumed that on a scale of order of the dimensions of a single corrugation (the lengths d , c , and b in Fig. 5(b)), the cross section of the built-up wall does not deform. However, in the actual structure there may occur in the buckling mode considerable local deformation of the individual flats of the corrugation and of the smooth sheet between adjacent troughs of the corrugation, especially if the critical mode has many rather short axial waves, as shown in Fig. 149(c). This local deformation, which is a modal interaction effect similar to those observed in Figs. 181(e), 182, 184 and 190(e), can be accounted for in an approximate way by application of appropriate reduction factors to the stiffness coefficients C_{ij} derived from the Baruch-Singer analysis. The reduction or "knockdown" factors can be derived from detailed models such as shown in Figs. 213 and 214.

Figure 213 exhibits branched shell models of semi-sandwich corrugated panels corresponding to two types of fabrication, bonded and riveted. In the model of the bonded panel the smooth skin and troughs of the corrugations

are assumed to form a single wall of thickness $t+t_s$, in which t is the thickness of the corrugated sheet and t_s is the thickness of the smooth sheet. The branched shell model consists of 13 segments, as illustrated in Figs. 212(b,c). In the model of the riveted panel the troughs of the corrugations form separate branches and are connected (clamped) to the smooth sheet along discrete axial lines (normal to the plane of the paper) labeled "RIVET" in Fig. 213(e). This branched shell model consists of 18 segments, as illustrated in Fig. 213(d). In both bonded and riveted models the pitch of the corrugations is 1.848 in. and the thickness of the flat sheet and corrugated sheet are 0.032 and 0.02 in., respectively. The material is aluminum.

Figure 214 shows discretized models, normalized buckling loads N and modes for axially compressed simply-supported panels of various lengths L . The compression is normal to the plane of the paper and is considered to be applied in such a way that the prebuckling axial strain is uniform over all segments in the branched shell models. The normalized axial loads N are calculated by division of the eigenvalues computed from the branched shell models by eigenvalues computed from a model in which the corrugations are smeared out according to the Baruch-Singer theory with no reduction factors [160]. The results displayed in Fig. 214 were obtained with the BOSOR4 computer program from models in which flat corrugated panels are treated as giant annuli with average radius from the axis of revolution equal to 2750 in.

The normalized critical loads N decrease with decreasing axial wavelength because of an increasing amount of local distortion of the wall cross-section.

Note that the distortion is greater for the riveted panels, and as one might expect, the critical general instability loads are considerably smaller for these than for the bonded panels.

Crippling of bonded and riveted panels can be calculated with BOSOR4 in the same way as general instability, the only difference being the axial wavelength of the buckles, which is fixed by the circumferential wavenumber n , as shown in Figs. 211 and 212. Figure 215 shows a crippled aluminum panel and Fig. 216 gives plots of the critical axial load vs buckle half-wavelength for models in which the extent of the bonded region is varied. In the models symmetry conditions are imposed at the midwidth of the trough and at the crown of the corrugation. The dimensions of a corrugation are given in Fig. 217. In tests conducted at Lockheed [272] riveted panels with the same cross-section properties assumed in these analytical models crippled at approximately 1100 lb/in. and bonded panels crippled at approximately 2800 to 2900 lb/in. The rivet heads were about 0.25 in. in diameter. Therefore, Model b in Fig. 216 represents a closer approximation to the riveted test specimens than does Model a.

For the analysis of large structures fabricated of semisandwich corrugated panels, or any other type of complex panel, it is clearly impractical to find buckling loads by division of the entire structure, or even a large section of it, into minute segments such as done for the models shown in Fig. 214. However, as already mentioned, these relatively small, accurate models can be used to calculate appropriate stiffness coefficients as input to a theory in which the corrugations or other stiffeners are smeared out. This has been done for the semi-sandwich corrugations and the results are shown in Fig. 217 and 218. The factors k_1 and k_3 are analytically

determined knockdown factors which depend on the axial half-wavelength of the buckling mode. Their derivation is discussed in detail in Ref. [274]. Essentially, k_1 accounts for the local distortion of the wall cross-section due to axial bending and k_3 for local distortion due to twist. A third factor k_2 is also introduced to adjust the circumferential bending stiffness. This third factor is independent of the axial wavelength of the buckle pattern.

The analytically determined knockdown factors k_1 , k_2 , and k_3 have been used to predict stresses, deformations and buckling loads of ring-stiffened non-symmetrically loaded payload shrouds with riveted and bonded wall constructions. The shroud geometry, loading, prebuckling deflection and a buckling mode are shown schematically in Fig. 149. Rings are located on 16-in. centers in the cylindrical portion of the shroud. These rings are stiff enough to cause nodes in the buckle pattern. From Figs. 217 and 218 it is seen that a 16-in buckling half-wavelength corresponds approximately to knockdown factors $k_1 = 0.94$, $k_3 = 0.3$ for the riveted construction and $k_1 = 0.98$, $k_3 = 0.6$ for the bonded construction. The circumferential bending stiffness factor k_2 is 1.17 for riveted and 1.30 for bonded construction. These analytically derived coefficients were used in BOSOR4 in a subroutine for calculation of the constitutive law relating reference surface stress and moment resultants to strains and changes in curvature (Ref. [430]) buckling stresses and deflections and bifurcation buckling loads and mode shapes were calculated for both riveted and bonded wall constructions. The lowest eigenvalues correspond to 16 circumferential waves in both cases with riveted construction yielding a load factor of 2.761 and bonded construction a load factor of 3.362 times the nonsymmetric pressure distribution displayed in Fig. 149(a) which was measured in a wind tunnel test.

For axially compressed panels, variations in fastening techniques have just been shown to have rather large effects on general instability loads and very large effects on crippling loads. Also demonstrated is the use of a small, detailed branched shell model to predict analytically stiffness properties needed for the analysis of a large structure. While this study was performed specifically for semisandwich corrugated panels, it is obvious that similar models can be set up and explored for any complex panels with curved sections and panels built up of composite materials.

Modal Interaction and Imperfection Sensitivity of Axially Compressed Prismatic Structures

Introduction

Two Types of Modal Interaction: We have already seen several examples of one type of buckling modal interaction: bifurcation buckling in which the critical mode contains characteristics of more than one kind of buckling, such as general and local instability. In Figure 181(e) is shown a general instability buckling mode of a ring-stiffened cylindrical shell subjected to uniform external hydrostatic pressure. The general instability bifurcation buckling pressure predicted with the discrete ring model is about 10% less than that predicted with the smeared ring model because this mode corresponding to the discrete ring model is not a pure sinusoid with one-half wave in the axial direction, but contains superposed on the half sine wave a small amplitude short axial wavelength waviness with period equal to the ring spacing. From Figs. 182 and 184 it is seen that buckling pressures

predicted with models in which the webs of ring stiffeners are treated as flexible shell branches are considerably lower than are those predicted with discrete ring models in which local deformation of the ring cross-section is not permitted in the bifurcation buckling mode. Similarly, in Fig. 214 the local cross-section deformations of the buckled axially compressed semi-sandwich corrugated panel are evident. They are superimposed on the half-sinusoidal spanwise "general" instability mode.

In all of these examples, the shells are assumed to be initially perfect. The modal interaction does not involve the prebuckling phase at all, but involves an apparent combination, in the bifurcation buckling mode, of more than one kind of buckling: In Fig. 181(e) modal interaction is a combination of general instability of rings and shell with local ("panel") instability of the bays between adjacent rings; in Fig. 184 it is a combination of "panel" instability of the bays between rings and local bending or crippling of the webs of the rings; and in Fig. 214 it is a combination of general instability of the corrugated panel and local crippling of the flat segments from which the complex panel is built up.

The modal interaction effect to be discussed in this section is fundamentally different from the examples just described. It is related primarily to local imperfections in the structure which have the effect of decreasing the stiffness of it in such a way as to decrease the critical axial load corresponding to general instability.

Figure 219 shows several examples of prismatic structures often used in civil engineering (a-c), aerospace (d-g), and shipbuilding (h) applications.

Under uniform axial compression buckling of these structures, which are built up of plates, may occur in column-type modes or in local modes involving crippling of the individual segments. The design of such structures is often arrived at by optimization with respect to weight. That is, the weight is minimized subject to the constraint conditions that general and local buckling shall not occur below some design load or below the design load multiplied by a factor greater than unity to allow for initial imperfections and other unknowns. This design process usually results in configurations for which local and general instability occur at the same axial load. As shall be seen, the modal interaction effect to be described here, that is the reduction in load-carrying capability due to small imperfections, is especially severe at the design point corresponding to simultaneous general and local instability.

Previous Work Done: Tvergaard [275] presents an excellent survey of the work done on modal interaction. Bijlaard and Fisher [276] established that local buckling of the plate elements in a column reduces the critical load corresponding to Euler-type buckling of the column. In 1962 Koiter and Skaloud [277] emphasized that the load-carrying capability of structures with simultaneous local plate buckling and Euler-type column buckling may be especially sensitive to initial imperfections. Van der Neut [278] proved Koiter's conjecture correct in a very thorough analysis of a two-flanged column with idealized webs. Although the axially compressed simply-supported plates from which the column shown in Fig. 220 is constructed exhibit stable post-buckling behavior, van der Neut proved that a column built up of such plates will experience sudden collapse usually associated with highly

imperfection sensitive shell structures if the local plate buckling and general column instability loads are close. Details of van der Neut's model and results will be presented later.

Thompson and Lewis [279] determined optimum designs for van der Neut's two-flange model, taking into account initial imperfections of the flanges but assuming that the column axis remains straight. They found that with growing imperfections the optimum load-carrying capacity decreases steeply from the value corresponding to simultaneous local and general instability of the perfect column, and that for very small imperfections the optimum design shifts away from that obtained from imposition of the simultaneous buckling criterion to a design in which Euler-type buckling of the column occurs at a lower load than local buckling of the flanges. Crawford and Hedgepeth [280] calculated optimum designs for lattice columns and truss-core sandwich panels with initially locally wavy members. They determined that both structures are imperfection-sensitive, the lattice column more so than the truss-core panel, and that the effect on optimum design obtained with the assumption of small imperfections is opposite to that obtained with the assumption of larger imperfections. Their major conclusion is that in neither case is the penalty great for using the conventional practice of arriving at an optimum design by equating local and general instability of a perfect structure. (However, it is obvious that a load margin has to be provided to account for initial unknown imperfections.) Maquoi and Massonnet [281] discuss the optimum design of a square box column obtained from an analysis in which the effective width concept is used and collapse is assumed to occur if the maximum stress reaches the yield stress. Graves Smith [282] calculates collapse loads of box columns including the effects of welding

residual stresses, "cylindrical" imperfections due to welding of the plates at the corners of the box column, and initial local waviness.

Plates reinforced by axial stiffeners on one side (Fig. 219 (e-h)) are common in civil, marine, and aerospace structural designs. Tvergaard [283, 284] has used Koiter's general theory of elastic stability [15] to obtain asymptotic estimates of the imperfection-sensitivity of such structures. Panels such as depicted in Fig. 219(f) are assumed to be infinitely wide with constant spacing b between the stiffeners, are simply supported at the two edges on which the compressive load acts, and are free on the unloaded edges. The eccentric stiffeners are represented as simple beams. A panel designed so that local buckling coincides with buckling as a wide Euler column displays a high sensitivity to initial imperfections due to modal interaction.

For the analysis of panels for which the local and general bifurcation buckling loads are not coincident, Tvergaard uses the Galerkin method. The strong sensitivity to small imperfections is revealed in a continuous manner for simultaneous and nearly simultaneous buckling. However, as the modal deflections increase, the post-buckling equilibrium curves tend to flatten out so that the sensitivity to larger imperfections is far less severe than that predicted by the asymptotic equations derived from Koiter's theory. The solutions are used to study the optimum design of panels with various combinations of column mode imperfections and local mode imperfections. For certain prescribed stiffener spacings the local maxima near the design point corresponding to simultaneous buckling vanishes for rather small

imperfection amplitudes. The maximum carrying capacity of the panel is attained above the critical stress for local buckling. However, from the point of view for retaining high axial stiffness at the highest possible load level, the optimum usually corresponds to a design with the Euler load lower than the critical load associated with local buckling of the skin between the stringers.

A similar panel configuration has been considered by Koiter and Pignataro [285], who found a panel with a single axial bay to be very sensitive to small initial imperfections at a design corresponding to simultaneous wide column and skin buckling but relatively less sensitive to larger imperfections, a result in agreement with those of Refs. [283] and [284]. In addition to the single-bay panel, Koiter and Pignataro treat the important case of a panel continuous over several bays in the longitudinal direction. For this multi-bay panel, the imperfection-sensitivity is found to be further decreased because half of the bays buckle in the direction in which the skin is being stretched.

Van der Neut [286] analyzed modal interaction for a hat-stiffened panel (Fig. 219(g)) with use of a two-flange model similar to that used for the box column in Ref. [278]. The sensitivity of the critical load to initial local waviness of the plate and of the top of the hat stiffeners is greatest for designs for which local and wide column bifurcation buckling loads coincide.

Thompson, Tulk, and Walker [287] performed experiments on pin-ended eccentrically stiffened panels of the type shown in Fig. 219(f) made of epoxy plastic. Local imperfections of the skin between the stringers were

"fabricated" by heating the plastic, loading it, and then cooling it, thus, "freezing" in an initial deformation pattern with relatively low residual stresses. Imperfections in the form of the Euler wide column mode were simulated by eccentric application of the end load. The sensitivity of the critical load to initial imperfections in the form of the local as well as the wide column buckling modes is observed to be maximum at designs for which local and general buckling of perfect panels coincide.

Tvergaard and Needleman [288, 289] have investigated modal interaction of elastic-plastic panels of the form shown in Fig. 219(f). They used J_2 flow theory with isotropic strain hardening. The panels are infinitely wide and the stringers are modeled as simple beams. The effect of local and global imperfections for single bay and multi-bay panels (multiple bays in the axial direction) are investigated. They found that modal interaction leads to imperfection-sensitivity in a single bay panel with column mode deflections such that the skin is being further compressed by bending. For column mode deflections in which the skin is being stretched, the considerable imperfection-sensitivity found by Tvergaard and Needleman is entirely due to the material nonlinearity. This effect of material nonlinearity explains why the multi-bay panel is not less imperfection-sensitive than the single-bay panel, as is the case in the elastic range [285].

Summary of this Section: In this section modal interaction will be illustrated by the behavior of the two flange column studied so carefully and described so clearly by van der Neut [278]. This will be followed by an account of modal interaction in eccentrically stiffened elastic plates, as studied

experimentally by Thompson, et al [287] and analytically by Tvergaard [283, 284]. The section will close with a discussion of the effect of modal interaction on optimum design in which results obtained by Thompson and Lewis [279], Crawford and Hedgepeth [280], Tvergaard [284] and Byskov and Hutchinson [290] are presented.

Modal Interaction in an Axially Compressed Two-Flange Column

Van der Neut was the first to study in detail the behavior of the axially compressed two-flange column shown in Fig. 220. The model consists of two load carrying flanges of width b and thickness h , connected at a distance $2c$ by webs which are rigid in shear and laterally but which have no longitudinal stiffness. The webs offer simple support to the flanges. In this way the flanges have boundary conditions that are easy to take into account analytically.

Figure 220 gives a preview of the buckling behavior of such a model. Long perfect columns buckle in an Euler mode ($\sigma_{cr} = \sigma_E$). The behavior of short columns is more complicated: Initially the simply supported flanges buckle locally at a stress $\sigma_{cr} = \sigma_l$. However, the post-buckling behavior of long rectangular plates is stable, so that the column with crippled flanges continues to carry additional axial load until it buckles in an Euler mode at a flange stress $\sigma_{cr} = \eta \sigma_E$, in which η is a factor (η equals approximately 0.4083 for simply supported long plates) that accounts for the reduced incremental axial stiffness of the crippled flanges. Perfect columns of such an intermediate length that $\eta \sigma_E \leq \sigma_{cr} \leq \sigma_E$ fail at $\sigma_{cr} = \sigma_l$ because of modal interaction: the crippling of the flanges causes a

"sudden" reduction in their axial stiffness with consequent reduction of the Euler stress from σ_E to $\eta\sigma_E$.

It is reasonable to suspect that the critical loads of columns in the intermediate range of lengths corresponding to the neighborhood of $\sigma_E = \sigma_\lambda$ would be sensitive to small initial imperfections, that is waviness, in the flanges. The amplitude of the waves would grow as the axial load is increased, with the result that the axial stiffness of the wavy flanges would decrease, precipitously approaching the limiting value $\eta = 0.4083$ times the stiffness of the perfectly straight flanges at a load well below σ_E or σ_λ and leading to Euler buckling of the beam in the range $\eta\sigma_E < \sigma < \sigma_E$. Curves are drawn in Fig. 220 corresponding to bifurcation buckling of columns with straight axes but initially imperfect flanges. The quantity $\bar{\xi}$ is the ratio of the amplitude of the initial flange waviness to the thickness h of the flange. It is seen that the greatest sensitivity to initial flange imperfections occurs for column designs such that $\sigma_E = \sigma_\lambda$. Please note that even for the column with initially imperfect flanges, the failure stresses plotted as solid curves in Fig. 220 correspond to bifurcation buckling in the Euler mode, not to a limit load such as point E in Fig. 7(a). The bifurcation point is converted to a limit point only if imperfections are introduced into the axis of the column.

The Perfect Column: Referring to Fig. 221, it is seen that for large slenderness of the column the Euler load K_E is less than the flange buckling load, K_λ . The stiffness of the flanges is Ebh , and the bending stiffness of the column is EI . With small slenderness, K_E exceeds K_λ . The flanges are in

their postbuckled state and their stiffness under incremental compressive axial strain $\Delta\epsilon$ is $\eta E b h$. Therefore the bending stiffness under axial load is ηEI and the column strength is $K_b = \eta K_E$.

Figure 221(b) gives two curves, K_E and K_b versus L . Fig. 221(a) shows the flange load P versus strain ϵ . The slope for $P > P_\ell$ decreases slowly with increasing P/P_ℓ but for $\epsilon/\epsilon_\ell < 3$ its variation is very slight, almost equal to 0.4083 which is the slope at $P = P_\ell$. With superimposition of prebuckling and bifurcation modal deflections at the load $K = K_\ell$, the compressive strain in one flange is increased and the incremental stiffness of this flange is $\eta E b h$. The other flange returns to the unbuckled condition, offering the stiffness $E b h$ to its strain increment. Then the bending stiffness of the column is $\frac{2\eta}{1+\eta} EI$ (the Engesser "double-modulus" formula). The column is in neutral equilibrium at K when the column length is $L_0 = \left(\frac{2\eta}{1+\eta} \pi^2 EI/K_\ell\right)^{1/2}$. For $L_2 < L < L_0$ the equilibrium at K_ℓ is stable. However for $L_1 > L > L_0$ the equilibrium is unstable; collapse occurs explosively.

The curve of Fig. 221(b) transforms into the one of Fig. 222 by replacement of the abscissa L by L^{-2} or K_E/K_ℓ . This graph is composed of three straight lines. It shows that in the range $1 < K_E/K_\ell < 1.725$, the perfect column collapses explosively at $K = K_\ell$. Within this K_E/K_ℓ -range, imperfections reduce the buckling strength K_b to values below K_ℓ .

Buckling with Imperfect Flanges but Straight Column Axis: The initial waviness z of the middle surface of a flange can be developed into a series of functions corresponding to the various buckling modes. The behavior of the flange is

mainly governed by the term which corresponds to the mode pertaining to the smallest buckling stress. Therefore the waviness is assumed in van der Neut's formulation [278] to be given by:

$$z = a \cos \pi y / b \sin \pi x / b \quad (65)$$

in which the coordinates (x,y) are shown in Fig. 223. The normalized waviness parameter α is given by $\alpha = a/h$.

The relationship between the axial flange load P and the compressive strain ϵ for this imperfect plate strip, simply supported at its edges, can be established by use of the Ritz-Galerkin approximate solution of the non-linear plate equation, taking the deflection in the shape of the buckling mode (65). Since we are interested only in the behavior at ϵ in the vicinity of the perfect plate bifurcation strain ϵ_ℓ this approximation is sufficiently accurate. Some load-strain curves are given in Fig. 223(b).

The stiffness of the flange is

$$S = dP/d\epsilon. \quad (66)$$

The reduction of stiffness with respect to the stiffness of the flat flange is given by the reduction factor

$$\eta = d(P/P_\ell)/d(\epsilon/\epsilon_\ell). \quad (67)$$

Figure 224 shows η versus P/P_ℓ (or K/K_ℓ) for various values of α . A continuous curve replaces the broken line, which corresponds to the perfect flange.

The investigation is confined to the case in which the two flanges have equal α . Then the column axis will remain straight under the load K until the buckling load K_b is reached. The bending stiffness resisting an infinitesimal deflection at the column load K is ηEI . With this bending stiffness the deflected column is in neutral equilibrium if $K = \eta K_E$. Therefore a load K is the buckling load K_b when

$$\frac{K/K_\ell}{\eta(K/K_\ell)} = \frac{P/P_\ell}{\eta(P/P_\ell)} = \frac{K_E}{K_\ell}. \quad (68)$$

K_E is a measure of the column length. Then Eq. (68) gives the relation between column length L and buckling load K_b as functions of α (η being a function of α). Evaluation of Eq. (68) by means of the data contained in Fig. 224 yields the relation between K_b/K_ℓ and K_E/K_ℓ for various values of α (Fig. 225).

The broken line for $\alpha = 0$ in Fig. 225 represents the degeneration of the smooth curves for $\alpha \neq 0$. It appears that $K_b < K_\ell$ when $K_E/K_\ell < 2$. The reduction in strength because of α is rather important in the vicinity of $K_E/K_\ell = 1$: for $\alpha = 0.0125$ it is 10%; for $\alpha = 0.05$ it is 17%; and for $\alpha = 0.2$ it is 30%. This confirms the conjecture of imperfection sensitivity on the unstable part of the perfect-column-curve (Figs. 221 and 222). The significant imperfection sensitivity is a direct result of the very large change in effective stiffness of the slightly imperfect flanges (small α) for loads below K_ℓ (Fig. 224).

Stability of Equilibrium at the Bifurcation Load, K_b : In Refs. [278] and [291] van der Neut derives the slopes of the initial post-buckling load-

deflection curves corresponding to deflections of the column axis in the form shown in Fig. 226(a). The formulation is based on Koiter's stability theory [15]. Figure 226(b) shows tangents to post-buckling load-end-shortening curves at bifurcation points K_b for columns with various K_E/K_ℓ and flange imperfections α . The dashed curves correspond to the columns with perfect flanges, and the origins for each curve with $\alpha > 0.0125$ have been shifted upward to permit display of all the data in one frame. The abrupt change in slope of each of the dashed curves at $\epsilon/\epsilon_\ell = 1.0$ corresponds to $K/K_\ell = 1.0$. Each short line segment represents the tangent to the post-bifurcation equilibrium curve corresponding to a column with a particular K_E/K_ℓ . The value of K_E/K_ℓ can be determined by reading on the K/K_ℓ axis the point of intersection of the post-bifurcation tangent with the approximately bilinear solid curve with which it is associated, identifying K with the bifurcation load K_b in Fig. 225, and reading K_E/K_ℓ from Fig. 225.

It is seen that for small flange waviness α and $0.7 < \epsilon/\epsilon_\ell < 1.0$, the post-bifurcation curves have negative slopes, indicating that the bifurcation loads K_b associated with them are sensitive to initial imperfections e_o in the axis of the column. Thus, the two flange columns with K_E/K_ℓ less than 2 will fail below the load $K_b/K_\ell = 1.0$ because of two effects: Unavoidable waviness α in the flanges of the form given by Eq. (65) will reduce the bifurcation point K_b from the dashed curve as shown in Fig. 225, and unavoidable waviness e_o/c in the column axis will further reduce the load-carrying capability by conversion of the bifurcation point K_b to a somewhat lower limit point K_f as shown in Fig. 227. Notice from Fig. 226 that the instability associated with bifurcation in the column mode almost disappears for $\alpha > 0.2$.

Buckling of Columns with Imperfect Flanges and Imperfect Axes: van der Neut used the Ritz-Galerkin method to calculate limit loads K_f of the two-flange columns with both imperfect flanges and imperfect axes. Results of the numerical evaluation are shown in Fig. 228, which gives the strength reduction $1 - \frac{K_f}{K_b}$ as a function of $\frac{e_o}{c}$ for two values of K_E/K_ℓ . Curves for equal K_E/K_ℓ and different α almost coincide, so that one single curve sufficiently represents the range $0 < \alpha < 0.1$. It should be recalled, however, that the effect of α on K_b/K_ℓ is significant (see Fig. 225). The column axis eccentricity associated with the maximum reduction in load-carrying capacity, $(e_o/c)_1$ depends very strongly on α and increases with increasing α . The approximate positions of $(e_o/c)_1$ are indicated in Figs. 227 and 228.

The validity of the results depends on the condition that the Taylor series expansion of the flange load P as a function of column end shortening ϵ used by van der Neut [278] represents sufficiently accurately the actual $P - \epsilon$ -curve. This condition appears not to be fulfilled when the flange loads P_o and P_u of the bent column (See Fig. 226(a)) differ from $\frac{1}{2}K_f$ by more than 15 to 20%. Therefore the validity of the curves is restricted to small values of e_o/c not exceeding 2%. However, the stiffness $dP/d\epsilon$, corresponding to the Taylor-expansion turns out to be smaller than the actual stiffness. Therefore e_o/c is smaller than that predicted by the computation. Below the curves a hatched region has been indicated, representing the uncertainty.

Provided the stresses remain within the elastic region, imperfection of the column axis appears to have a minor effect upon the load carrying capacity; it will maximally be of the order of 10%. The main reduction stems from initial waviness of the flanges.

This problem, studied by Tvergaard [283, 284], Koiter and Pignataro [285], van der Neut [286], and Thompson, Tulk, and Walker [287] for elastic panels and Tvergaard and Needleman [288, 289] for elastic-plastic panels, is analogous to the two-flange column problem. The interaction effect studied by these researchers involves the Euler wide column mode of the panel, the unloaded edges of which are unsupported, and the local buckling of the sheet between two adjacent stringers. Figure 229 gives the geometry and coordinate system of such a panel, which in the analysis of [283] is considered to be infinitely wide.

The curves displayed in Fig. 230 are analogous to those in Fig. 220 for the two-flange column. P_L is the load corresponding to bifurcation buckling of the skin and L_{cr} is the length for which local and Euler wide column buckling occur at the same load. (In the work of Tvergaard and others it is tacitly assumed that the Euler wide column mode is the lowest general instability type buckling mode.) It is seen from Fig. 230 that the maximum sensitivity of the failure load P_M to initial imperfections occurs for designs near the simultaneous buckling point, $P_E = P_L$. The curve labeled P_E^* is analogous to that labeled $\eta\sigma_E$ in Fig. 220 and that labeled ηK_E in Fig. 221. It corresponds to buckling of a wide eccentrically stiffened panel in which the effective stiffness of the skin has been reduced by local buckles.

Figures 231 and 232 show how the carrying capacity of a particular eccentrically stiffened panel is reduced by local and Euler-type imperfections

of various amplitudes. The results in Fig. 231, for which $P_E = P_L$, are obtained from an asymptotic expansion in the neighborhood of the bifurcation point of the perfect panel, according to Koiter's theory for simultaneous buckling modes [15]. The results shown in Fig. 231 indicate that the panel is more sensitive to imperfections in the shape of the local buckling mode than to imperfections in the shape of the Euler buckling mode.

Fig. 232 shows test results for a stiffened panel with slender stringers that also participate in the buckling mode when $W_0/h < 0$. (Initial Euler wide-column imperfection W_0 such that bending induces tension in the skin, compression in the stringers). The curves are not symmetrical about $W_0/h = 0$ because the panel configuration is not symmetrical with respect to inward or outward buckling modal displacements.

Tvergaard [284] extended the analysis of [283] to study the nonlinear post-buckling behavior of eccentrically stiffened panels corresponding to a range for which the initial post-buckling asymptotic analysis method of Koiter is not valid. He used the Galerkin method to calculate post-buckling stiffness and load-carrying capability of panels such as depicted in Fig. 229.

Some examples of the relationship between load and modal deflections found by Tvergaard are shown in Fig. 233. The solid curves give the behaviour of a perfect panel, and the dashed curves show the behaviour of a panel with small initial imperfections. λ is the axial load parameter and ξ_1 and ξ_2 are Euler mode and local mode imperfection amplitudes, respectively. The

panel corresponding to Fig. 233(a) has coincident buckling loads, while Euler-type buckling is critical in Fig. 233(b) and local buckling is critical in Fig. 233(c). In all three cases the initial post-buckling behaviour predicted by the Galerkin method agrees with that calculated by application of Koiter's general theory [15]. However, as the modal deflections increase, the equilibrium curves tend to flatten out. For example, in the simultaneous buckling case of Fig. 233(a), the sensitivity to very small imperfections predicted with the Galerkin method is as strong as that predicted by the asymptotic solution, but for imperfections so large that the limit point occurs under the flat part of the solid curve, a further increase of the imperfections results in practically no additional reduction of the limit load λ^* .

Figure 234 represents qualitative experimental confirmation of Tvergaard's results. The asymptotes correspond to the general bifurcation buckling load P_E^* for the panel with the reduced skin stiffness (See Fig. 230).

Optimization of Imperfect Columns and Panels in which Modal Interaction Occurs

The conventional criterion of optimization for thin elastic structures is that overall and local buckling loads should coincide. The validity of this so-called "naive" approach was originally questioned by Koiter and Skaloud [277] on the grounds that simultaneous buckling might give rise to severe imperfection sensitivity which could modify or destroy the apparent optimum.

Columns: Figures 235- 238 pertain to the optimum design of imperfect columns in which simultaneous local and general instability might occur.

Figures 235- 237 pertain to the two-flange column studied by van der Neut [278] and just discussed in detail. All designs corresponding to various b in Fig. 235 and various $x = K_E/K_\ell$ in Figs. 236 and 237 have the same weight. The point raised by Koiter and Skaloud [277] is illustrated by Fig. 235: An optimum design arrived at by the bifurcation buckling analysis of a perfect structure, dimensioned such that $\sigma_E = \sigma_\ell$, corresponds to some dimension $b = b_A$. However, the imperfect structure has a maximum load-carrying capability at a different design point, $b < b_A$. Thompson and Lewis [279] found that for van der Neut's two-flange column the optimum design shifts to the left (Fig. 237) for small flange imperfections and then back to the right for larger flange imperfections. The implication is that fairly well made box columns should have dimensions such that the Euler load is a bit less than the local flange buckling load.

Crawford and Hedgepeth [280] came to similar conclusions for axially compressed lattice columns and truss-core stiffened simply-supported panels (Figs. 238, 239), but in comparing the critical loads of the structures obtained from the "naive" approach with those of the same weight obtained from the "sophisticated" approach, they determined that very little strength penalty results from use of the "naive" $\sigma_E = \sigma_\ell$ criterion for the perfect structures (Fig. 240). (However, they urge the designer to be aware of the increased imperfection sensitivity resulting from optimization subject to the constraint $\sigma_E = \sigma_\ell$, and consequently to provide adequate load margins at the "naive" optimum!)

Panels: Tvergaard [284] investigated the effect of modal interaction on the optimum design of eccentrically stiffened panels of the type illustrated

in Fig. 229. Definition of an optimally designed panel involves many parameters, such as the plate thickness, eccentricity of the stiffeners, spacing between the stiffeners and the shape of the stiffeners. In Tvergaard's treatment the number of parameters is restricted because the goal of his investigation is to determine whether a design corresponding to simultaneous Euler wide column and local skin buckling has the highest carrying capacity. Thus, the distance "a" between the simple supports, the spacing b between the stiffeners, the eccentricity e of the stiffeners and the common material to be used in the whole panel are prescribed. The stiffeners, attached to one side of the plate, are assumed to have rectangular cross-sections.

For a panel built of a given amount of material per unit width, i.e. a panel with a given value of $h_0 = h + A_s/b$, where A_s is the stringer cross section area, the maximum carrying capacity or limit load λ^* can be calculated as a function of the imperfection amplitudes $\bar{\xi}_1$ and $\bar{\xi}_2$ in the Euler and local modes, respectively, and the parameter h/h_0 which specifies the ratio of the amount of material in the skin to that in the whole panel. In the following, λ_0 denotes the critical load parameter in the case where the stiffeners disappear completely ($h/h_0 = 1$).

Tvergaard considers a panel with a given weight, the geometry of which is specified by $a/b = 4$, $e/b = .05$ and $h_0/b = .0128$. In Fig. 241 the maximum carrying capacities are plotted vs. h/h_0 for different amounts of imperfections in which the wide column modal imperfection $\bar{\xi}_1$ equals $\bar{\xi}_2$. (Note that the imperfections are normalized by h_0 , so that imperfections corresponding to different points on a curve with constant $\bar{\xi}$ are equal relative to the constant measure h_0 , but not relative to the current plate thickness).

Figure 241 also shows the point N at which the initial post-buckling behaviour of the perfect structure changes from stable to unstable according to the Koiter theory. The λ^* -curve corresponding to very small imperfections intersects the $\lambda_c^{(2)}$ curve just below this point.

Figure 241 shows that if the panel is designed against the classical critical buckling stress, the optimum (minimum weight for a given axial load or maximum critical load for a given weight) is clearly the one corresponding to coincident buckling loads. However, Fig. 241 demonstrates that the carrying capacity in the vicinity of this design diminishes rapidly as small imperfections are introduced. The local maximum of the λ^* curves vanishes when the nominal imperfection amplitudes exceed a value of about 0.03. It is also obvious from Fig. 241 that the highest carrying capacities of the imperfect panels are predicted in the range where the buckling stress $\lambda_c^{(2)}$ has been exceeded. Here, the collapse load λ^* becomes even slightly larger than the critical stress of the perfect structure at the design point corresponding to simultaneous buckling. In this range, however, the limit load λ^* corresponds to quite large modal deflections (Fig. 233(c)), so that in practice plastic deformations or brittle fracture may often reduce the maximum load predicted by the elastic theory.

Tvergaard also treats an example in which the spacing b of the stiffeners is halved without changes in the length " a " between the supports, the eccentricity e of the stiffeners, or the amount of material per unit width. In this case, the panel is specified by $a/b = 8$, $e/b = .1$ and $h_0/b = .0256$. Results are displayed in Fig. 242. For this panel the design point

corresponding to simultaneous buckling of the perfect panel occurs at such a small value of h/h_0 that further enlargement of the stiffeners at the expense of plate thickness is of practically no advantage with respect to $\lambda_c^{(1)}$, as can be seen from the data at the lowest values of h/h_0 in Fig. 242. Figure 242 demonstrates that the larger the amplitude of the imperfections, the higher will be the value of h/h_0 at which the maxima of the λ^* curves occur. Tvergaard proved that local mode imperfections of a given amplitude are more serious than Euler-type imperfections of the same amplitude. The carrying capacities λ^* predicted in the range where λ^* exceeds $\lambda_c^{(2)}$ (to the left of the point N) are smaller than those in the remaining range. If imperfections can be kept small, the optimum design will correspond to values of $\lambda_c^{(2)}/\lambda_c^{(1)}$ slightly higher than unity. For larger imperfections, this value increases to about two, depending on the stiffness required.

Apart from a high limit load λ^* , the stiffness retained in the panel at a given load level λ may be of considerable interest. Tvergaard [284] defines a normalized stiffness parameter

$$S = (d\lambda/d\Delta)/(d\lambda/d\Delta)_0 \quad (69)$$

in which λ is the applied load, Δ is the end shortening, and the denominator represents the prebuckling stiffness of the perfect structure. For a perfect panel the stiffness S defined by Eq. (69) is equal to unity in the entire range below the classical buckling load. In Fig. 243 the stiffness S is plotted for two different imperfection magnitudes. It is seen that even for small imperfections the stiffness decreases significantly at relatively low loads in the range to the left of the figure where λ^* exceeds $\lambda_c^{(2)}$, so that this range is not advantageous from the point of view of stiffness.

Also, for larger imperfections a design with $\lambda_c^{(2)}/\lambda_c^{(1)}$ somewhat above unity is preferable with respect to retention of a high stiffness in the panel.

Tvergaard [284] draws the following conclusions from his study of the optimum design of axially compressed imperfect elastic, eccentrically stiffened panels: "An analysis of stiffened panels made of a given amount of material per unit width shows that in some cases the design with the highest carrying capacity is one in which the limit load is attained beyond the critical stress for local buckling. However, the stiffness properties are relatively poor for such designs. From the point of view of retaining a high stiffness at the highest possible load level, the best design is usually one in which the critical stress for Euler-type buckling is smaller than that for local buckling. In some cases, the optimum design has a local buckling stress that is more than twice the Euler buckling stress. Thus, the optimum design from the point of view of post-buckling behavior often differs significantly from the design with two simultaneous buckling stresses." [284]

Axially Stiffened Cylindrical Shells: In all of the elastic modal interaction problems involving columns and panels, each of the modes acting alone would result in behavior that is not sensitive to initial imperfections. The modal interaction problem for axially compressed, axially stiffened elastic cylindrical shells, studied by Byskov and Hutchinson [290], differs significantly in that the buckling load corresponding to the general instability mode is always sensitive to initial imperfections and that corresponding to local buckling of the skin between adjacent stringers may or may not be sensitive to local imperfections, depending on the stringer spacing. The effect of

interaction between local and general instability is to increase the sensitivity of the critical load to initial imperfections.

Byskov and Hutchinson [290] solve the problem with use of an asymptotic method similar to Koiter's [15] that provides uniformly valid results whether the modes are simultaneous, nearly simultaneous, or well separated. For the perfect shell, the optimum design has simultaneous overall and local buckling loads. Overall buckling loads and mode shapes are calculated from a theory in which the stringers are smeared out and the torsional rigidity of the stringers is neglected. Local buckling is also calculated on the basis of neglect of the torsional stiffness of the stringers. The stringers are considered to be stocky enough that they do not cripple. Initial imperfections have the form of a sum of i bifurcation buckling modes corresponding to the lowest i eigenvalues of the perfect structure.

Results from Byskov and Hutchinson's analysis are presented in Figs. 244(a-e). These figures are analogous to Figs. 241- 243 in that all points on the abscissa of each figure correspond to a given amount of material, and the ordinate represents the normalized maximum axial load $\lambda = P/P_e$. The quantity P_e is the classical buckling load of a long unstiffened cylindrical shell with the same radius R but with thickness t_e corresponding to the same total cross-sectional area of the stiffened shell:

$$t_e = t_{\text{shell}} + A_s/b; P_e = 2\pi R[0.6Et_e^2/R] \quad (70)$$

in which A_s is the cross section area of a stringer and

$$b = 2\pi R/N_s \quad (71)$$

where N_s is the number of stringers. As in Figs. 233 and 241-242, λ_1 represents the critical bifurcation load corresponding to general instability and λ_2 the critical bifurcation load corresponding to local instability of the perfect shell. The numbers in parentheses represent amplitudes of the (general, local) initial imperfections normalized by t_e . Figures 244(a-d) correspond to cylinders with rectangular stringers and Fig. 244(e) to a cylinder with T-shaped stringers.

In each example, the total amount of material, the skin thickness t , the radius-thickness ratio R/t , and the radius-length ratio R/L are held constant. The relative amount of stiffener material,

$$\alpha_s = A_s/bt \quad (72)$$

is therefore fixed, so that A_s varies inversely as the number of stringers N_s . In the case of Figs. 244(a-d) the stiffener thickness t_s is held constant, so that the stiffener height h varies inversely with N_s . In the case of Fig. 244(e) the height and thickness of the web and flange are equal and vary in proportion.

From their results Byskov and Hutchinson conclude that "the feature common to each example studied is the relatively weak dependence of λ_s (the maximum load-carrying capacity) on N_s at realistic imperfection levels. As reported in studies of other structures, design for mode coincidence ($\lambda_1 = \lambda_2$) of the perfect structure does not appear to lead to a design that would be far from optimum. In fact, the examples studied here suggest that the designer has considerable latitude in this regard, although one must not lose

sight of the fact that the imperfection sensitivity is greater for designs with coincident modes. In all cases, except that in Fig. 244(d), the optimum in the presence of imperfections tends to shift toward a design with $\lambda_2 > \lambda_1$. Furthermore, when the local mode of the perfect structure is unstable at the design of coincidence, the presence of imperfections tends to shift the optimum toward the regime in which the local mode is stable."

Transverse Shear Deformation Effects

Plate and shell theories represent means to simplify the general analysis of structures by the introduction of assumptions that make the displacements functions of two rather than three spatial coordinates, as discussed in Volume 2. Usually this reduction is achieved by use of the assumptions:

- o Normals to the reference surface remain straight during deformation
- o Normals to the reference surface remain normal after deformation
- o The transverse normal stress is negligibly small

The assumption that the normals remain normal to the deformed surface means that transverse shear deformation can be neglected. Such an assumption is certainly acceptable if the shell is sufficiently thin. In the following, such theories are referred to as first order theories. A second order theory may, for example, be obtained if the first of the three assumptions is retained but the second discarded. Such theories have been presented by Reissner [292] and Mindlin [293]. Higher order theories can be obtained if also the first assumption is discarded, but it is questionable whether use of such theories have any advantages in comparison to a complete three-dimensional analysis.

The argument for retention of the effect of transverse shear deformations in analytical models of plate and shell structures made of laminated composite materials is much stronger for geometries typical of practical designs than it is for isotropic metals because the transverse shear moduli G_{13} and G_{23} (Fig. 245) are usually one to two orders of magnitude smaller than the longitudinal modulus, E_1 . (In keeping with generally accepted nomenclature, we will refer to longitudinal and transverse elastic moduli, E_1 and E_2 , as the moduli in the plane of the lamina parallel and normal to the fiber direction. The inplane shear modulus, G_{12} , is distinguished from the two transverse shear moduli, G_{13} and G_{23} . The modulus, G_{13} , corresponding to shear along the fibers (Fig. 245) is generally somewhat larger than G_{23} .) Typical values for a lamina may be of the order $E_1/E_2 = 20$, $G_{13} = 0.6 E_2$ and $G_{23} = 0.4 E_2$. Since the transverse shear moduli for a lamina are small in comparison to the longitudinal elastic modulus, the transverse shear deformations must have a bigger effect on the buckling load of composites than it has on metallic plates or shells. That is, the composite shells must be thinner relative to inplane dimensions or wavelengths before the transverse shear effect can be omitted.

Since most generally available computer programs presently do not include the effects of transverse shear, it is important to the designer to know the limits of the first order theory. For an isotropic plate, it can be seen from Figure 246 that b/h for a simply supported plate may be close to 10 before the error exceeds 5%. In order to obtain similar accuracy for

composite material, we must restrict the first order theory to even thinner plates. Figure 247 indicates that for a material with $E_1/E_2 = 30$, the transverse shear effects should be included if the width-to-thickness ratio is less than about 20. It should be noted that the results of Refs. [294] and [295] apply to plates with simply supported edges. With respect to buckling of plates, the effect of clamping the edges is essentially equivalent to reduction of the inplane dimensions by a factor of two. It might be surmised therefore, that for clamped plates the transverse shear effect should be accounted for if $b/h < 40$. Similarly, it appears that the opposite argument applies for a flange with one free edge: the transverse shear effect can probably be omitted if $b/h > 10$. More numerical comparisons are needed for guidance in design. In particular, if composites are used at elevated hygro-thermal conditions, E_1/E_2 , E_1/G_{13} , and E_1/G_{23} may be very large, and the transverse shear deformation effect increased.

Sandwich wall construction may be thought of as a class of laminated composite shell wall which is weaker in transverse shear stiffness than ordinary isotropic or orthotropic construction. Figure 248 shows a predicted collapse mode of an actual part of a space vehicle. The cone is a ring-stiffened sandwich structure supported by a monocoque cylindrical skirt. The sandwich construction is made of aluminum honeycomb core with composite face sheets. The nonlinear collapse load of this structure was investigated with the use of two finite element models and the NEPSAP computer program [297]: In model (a) the sandwich core and facings are represented as multilayered composite elements with the effect of transverse shear deformation of the honeycomb

core neglected. To study the extent of this effect, model (b) was constructed. In this model the sandwich construction was modeled "exactly" with use of three-dimensional orthotropic solid elements for the core and composite shell elements for the facings. The cone is subjected to axial and flexural loadings which were applied as equivalent point loads around the top circumference. Because of planar symmetry, only half the structure (180°) was considered for both models.

The results of this study are shown in Figs. 248(a) and (b). Figure 248(a) shows the collapse mode, and Fig. 248(b) gives the load-deflection characteristics of the two models. Collapse occurs at a load factor of 4.0 for model (a) and 2.8 for model (b), indicating a 30% drop in the predicted value of collapse load as a result of shear deformation in the core.

Section 8

IMPERFECTION SENSITIVITY

Introduction

The emphasis in previous sections of this volume has been on buckling either as a nonlinear collapse phenomenon or as a bifurcation phenomenon, as shown in Fig. 7. It has been implied that the load at which collapse occurs, λ_s in Fig. 7(a), is obtained from a nonlinear analysis with use of a computer program for general shells such as STAGS [48] or a computer program for shells of revolution such as BOSOR [47]. The bifurcation load, λ_c in Fig. 7(a), has been identified, by implication at least, with loss of stability of the structure. Many examples have been given involving comparisons between tests and predictions of bifurcation buckling loads and mode shapes for elastic and elastic-plastic shells of revolution under uniform and nonuniform loads, including and neglecting nonlinear prebuckling effects. The effect of imperfections in the structure has been to cause discrepancies between test and bifurcation buckling theory, such as demonstrated in the extreme cases of the cylindrical shell under axial compression (Fig. 19) and the spherical shell under external pressure (Fig. 30). With the exception of the examples in the previous chapter involving modal interaction in axially compressed columns and stiffened panels, the post-bifurcation states of structures have not been considered here explicitly in determinations of their load-carrying capacities.

Summary

This section opens with a very brief account of Koiter's asymptotic theory [15] for the initial post-buckling behavior of perfect and imperfect structures.

Formulas are given for load-buckling-modal-deflection curves for the various types of post-buckling behavior exhibited in Fig. 8, and a survey of work on imperfection sensitivity of elastic-plastic shells is given. Following a short section on qualitative guidelines for the engineer with regard to imperfection sensitivity, a rather detailed treatment and survey of work done on axially compressed monocoque and stiffened cylindrical shells appears. Details of a derivation of parameters governing imperfection sensitivity are presented for a case in which stiffeners are present and nonlinear prebuckling effects are included. Asymptotic and general nonlinear approaches to the problem are discussed. This is followed by numerical results for cylindrical shells with sinusoidal axisymmetric imperfections, localized imperfections, and random imperfections. Other results from the literature are given for axially compressed cylinders with internal pressure, cylindrical panels, oval cylindrical shells, and stiffened and laminated composite cylindrical shells. The section on axially compressed cylinders closes with an outline of a design method valid for a large class of designs which is based on a less conservative approach than those commonly taken and which past experience demonstrates is reasonably safe.

The section continues with a presentation of data relative to monocoque and stiffened cylindrical shells under hydrostatic pressure and torsion and spherical shells and shallow spherical caps under external pressure and concentrated loads. A derivation of the asymptotic post-buckling theory is presented here for the case in which there exist multiple bifurcation buckling modes at the critical load, λ_c . The theory is applied to a shallow section of a complete spherical shell. The chapter closes with discussions of limitations of the asymptotic imperfection sensitivity theory, bifurcation buckling with stable post-buckling behavior, and the Southwell method.

Koiter [15, 298] was the first to develop a theory which provides the most rational explanation of the large discrepancy between test and theory for the buckling of axially compressed cylindrical shells and externally pressurized spherical shells: the early collapse is due to small, unavoidable geometrical imperfections. Excellent reviews of Koiter's theory and of the many applications of it to buckling of monocoque and stiffened elastic and elastic-plastic shells are given by Hutchinson and Koiter [6], Tvergaard [7], and Budiansky and Hutchinson [299]. The theory itself is reiterated in some detail by Budiansky [300], Seide [301], and Masur [302] and extended to dynamic buckling by Budiansky and Hutchinson [303] and Budiansky [304]. Many of the numerous applications of the theory to static buckling of shells of revolution reviewed in Refs. [6] and [305] refer to the presentation of a simplified form of the Koiter theory for static analysis given in Refs. [303] and [304]. Summaries of the main features of Koiter's theory appear in [4] and [7].

Essentially, the purposes of Koiter's theory are to:

- (1) Determine the stability of equilibrium at the lowest bifurcation point on the equilibrium path, and
- (2) To ascertain the sensitivity of the maximum load-carrying capacity of the structure to initial geometric imperfections.

In the classical stability analysis of conservative systems stable equilibrium is often illustrated by a heavy ball resting at the lowest point on a wavy surface. Any small displacement of the ball requires an input of energy to move it against the force of gravity. Removal of the small force giving rise to this small displacement causes the ball to return to its original position

at the lowest point on the surface. Unstable equilibrium is exemplified by the ball resting on a peak. The slightest disturbance will cause it to roll to a new equilibrium position with less potential energy at some point located a finite, perhaps a large distance, from this peak. Neutral equilibrium is illustrated by the ball at rest on a flat surface. The small disturbance will again cause the ball to move to some new, non-adjacent equilibrium position, but with no change in its potential energy.

A classical bifurcation buckling analysis represents a search for the load at which the equilibrium of a structure ceases to be stable and becomes neutral; it does not reveal information about the stability of the structure. Suppose that a structure is in equilibrium at some load smaller than the lowest bifurcation load, (and furthermore suppose that we are only concerned here with bifurcation buckling, not nonlinear collapse). Any small additional displacement field which satisfies the requirements of continuity (compatibility) and geometric boundary conditions (kinematically admissible displacement field), will cause the energy of the system (structure plus potential energy of loads) to increase. Thus, the structure is in a state of stable equilibrium analogous to the ball at the lowest point of the wavy surface. At a higher load corresponding to the bifurcation point, the additional energy of the system due to the small disturbance does not change: the structure is in a state of neutral equilibrium analogous to the ball on the flat surface; the equilibrium state is not unique in a small neighborhood of the prebuckling state. At loads above the lowest bifurcation point, equilibrium on the fundamental (prebifurcation) load-deflection path is unstable, analogous to the ball on the peak.

In order to learn whether or not the structure is stable at the bifurcation point, it is necessary to determine the characteristics of the post-bifurcation path in load-generalized-displacement space or in load-postbuckling-modal-deflection space in the neighborhood of the bifurcation point. Typical paths are displayed in Fig. 8. The stability of equilibrium at the bifurcation point is governed by third and fourth order terms in the energy functional expressed as a series expansion of the incremental displacement represented by the difference of the displacement field corresponding to the fundamental state at the bifurcation point and that corresponding to a state on the post-bifurcation equilibrium path close by. The first-order terms of the energy thus expressed cancel because the fundamental state at the bifurcation point is an equilibrium state; the second-order terms likewise cancel because the bifurcation point represents a state of neutral equilibrium. The shape of the post-bifurcation load-deflection curve in the neighborhood of the bifurcation point is therefore governed by the third-order terms (Fig. 8b), or if these vanish, by the fourth-order terms (Fig. 8c,d) in the expression for incremental energy.

Elastic Post-Bifurcation Analysis

At a bifurcation load λ_c where the buckling mode is unique, Koiter's general elastic post-buckling theory [15, 298] leads to an asymptotically exact expansion for the load parameter λ in terms of the normalized bifurcation buckling modal amplitude, w_b :

$$\lambda/\lambda_c = 1 + a w_b + b w_b^2 + \dots \quad (73)$$

Three types of elastic initial post-buckling behavior are shown in Fig. 249. Solid curves show the behavior of perfect structures and dotted curves the behavior of imperfect structures with imperfections in the form of the unique critical bifurcation buckling mode. The ultimate load-carrying capabilities of the structures represented by Figs. 249(a) and (b) are sensitive to initial imperfections while that represented by Fig. 249(c) is not. For the case 249(a), which is asymmetric with respect to the sign of the buckling modal amplitude w_b ($a \neq 0$), a negative normalized imperfection amplitude w_{imp} converts bifurcation buckling into limit-point or "snap" buckling at a reduced load λ_s given by Koiter's general theory as

$$\lambda_s / \lambda_c \approx 1 - 2 (-\rho a w_{imp})^{1/2} \quad (74)$$

in which ρ is a constant that depends on the imperfection shape. For the symmetric case 249(b) " a " in Eq. (73) is zero, $b < 0$, and the limit load of the imperfect structure is

$$\lambda_s / \lambda_c \approx 1 - 3 (-b/4)^{1/3} (\rho w_{imp})^{2/3} \quad (75)$$

Many applications of Eq. (74) and especially Eq. (75) appear in the literature. Several examples will be shown later in which the parameter b in Eq. (75) is plotted as a function of shell geometrical parameters or loading. Figure 250 illustrates the relationship of the coefficient b in Eqs. (73) and (75) to the imperfection sensitivity for a system such as a shell of revolution, for which the lowest bifurcation buckling mode is unique and the initial post-buckling behavior is symmetric with respect to the sign of the post-buckling displacement field and unstable. The initial post-

buckling load P of the perfect structure follows the solid curve shown in Fig. 250(a). The quantity δ is the amplitude of the postbuckling displacement field, which is assumed to be in the form of the unique buckling mode. The quantity t is the shell thickness. The dashed curve pertains to an imperfect shell. The value of b depends on details of the geometry and loading. Buckling loads are sensitive to imperfections if b is negative and insensitive to imperfections if b is positive. As shown in Fig. 250(b), more negative values of b are associated with greater sensitivity of the critical load P_s to initial geometric imperfections $\bar{\delta}$. Curves for the spherical shell under uniform external pressure and the cylindrical shell under uniform axial compression are shown in order to emphasize the extreme nature of imperfection sensitivity in these two cases. The curves are dashed because they are not derived from Eq. (75) as explained next.

There are important examples in which the lowest bifurcation point is associated with several buckling modes or in which there exists a cluster of bifurcation loads just above the critical load. The cylindrical shell under axial compression is an example of the former and the spherical shell under external pressure is an example of the latter. Structures optimized such that local and general instability occur at the same load provide another practical example. For cases in which there exist several simultaneous buckling modes Eq. (73) is replaced by N asymptotic equations for the load parameter λ in terms of the buckling modal parameters $w_{b1}, w_{b2}, \dots, w_{bN}$ of the form

$$\left[\frac{\lambda}{\lambda_c} - 1 \right] w_{bi} = A_{ijk} w_{bj} w_{bk} + B_{ijkl} w_{bj} w_{bk} w_{bl} + \dots \quad (76)$$

in which the summation convention (from one to N) is implied for repeated indices. Koiter's general theory yields asymptotic estimates of the imperfection sensitivity λ_s/λ_c in the case of elastic buckling. Due to modal interaction the effect of initial geometric imperfections is usually severe, as demonstrated in the last chapter for built-up axially compressed columns and panels and by the dashed curves in Fig. 250(b).

If the bifurcation buckling modes are nearly coincident, as they are for uniformly externally pressurized spherical shells, the imperfection sensitivity is also characterized by modal interaction, even though the initial post-buckling behavior of the perfect structure in the immediate neighborhood of the bifurcation point is governed by the expression (73) for the single mode case [306].

Elastic-Plastic Post-Bifurcation Analysis

Practically all of the development and application of asymptotic post-buckling theory including the effect of plasticity has been done in the last decade by Hutchinson, Tvergaard, Needleman and their coworkers [7, 8, 299, 307 - 317]. Hutchinson gives a summary in [307] and Tvergaard in [7]. The theory represents extensions to the general theory of uniqueness and bifurcation in elastic-plastic solids derived by Hill in 1958-1959 [308, 309] and the general post-buckling theory developed by Koiter for elastic structures in 1945 [15, 298].

Figures 251(a) and (b) are analogous to Figs. 249(a) and (b). Note that bifurcation in the plastic range occurs under increasing load, so that unlike the elastic cases, the maximum load-carrying capability of perfect structures is slightly above the bifurcation load λ_c and occurs at amplitudes w_b for which a finite amount of material has experienced strain reversal.

Perfect Elastic-Plastic Structures. For the plastic range an asymptotic theory of initial post-bifurcation behavior of perfect structures was developed by Hutchinson [310], [307]. An asymptotic expansion is obtained for the initial post-bifurcation load in terms of the bifurcation modal amplitude w_b , as in Koiter's elastic post-buckling theory. In the plastic range the treatment is complicated by the phenomenon of elastic unloading, which starts at bifurcation and spreads into the material as the buckling modal amplitude increases. When the buckling mode is unique the asymptotically exact expression for the load parameter λ in terms of the normalized buckling modal amplitude w_b is

$$\lambda/\lambda_c = 1 + \lambda_1 w_b + \lambda_2 w_b^{1+\beta} \quad (77)$$

with $0 < \beta < 1$. The value of β depends on the shape of the unloading regions [307]. The constant λ_1 is positive since bifurcation takes place under increasing load. Its value is determined by the requirement that plastic loading takes place. The coefficient λ_2 is negative, so that the truncated expansion (77) can be used to estimate the maximum support load of the perfect structure, which is slightly above the critical bifurcation load. An extension of the asymptotic expansion (77) to cases of several coincident buckling modes has not been carried out. The asymptotic theory for plastic post-bifurcation of perfect structures has been applied by Tvergaard and Needleman to study the

behavior of structures with symmetric [311] and asymmetric post-bifurcation behavior [288, 289, 312].

Imperfect Elastic-Plastic Structures. In 1972 Hutchinson [313] reported the results of a numerical axisymmetric plastic buckling analysis of perfect and imperfect spherical shells loaded by uniform external pressure. The shell material is characterized by a Ramberg-Osgood stress-strain relation

$$\epsilon/\epsilon_y = \sigma/\sigma_y + \alpha (\sigma/\sigma_y)^n \quad (78)$$

with $\alpha = 0.1$ and $n = 6$. The geometrical parameter of the sphere at bifurcation is

$$[3 (1 - \nu^2)]^{-1/2} t/(\epsilon_y R) = 3 \quad (79)$$

From Fig. 252 it is seen that corresponding to this value 3 the bifurcation stress of the perfect shell is about 1.5 times the effective yield stress σ_y and the flow theory prediction is about 7% above the prediction obtained with use of J_2 deformation theory. Figures 253 and 254 show the results of an analysis including imperfections of various amplitudes taken in the shape of the bifurcation buckling mode. Figure 253(a) reveals that even though the initial post-bifurcation slope is positive, the buckling load is sensitive to initial imperfections. The onset of elastic unloading occurs at practically the same load as the collapse load. Figure 253(b) shows that the difference in predicted failure between the J_2 flow theory and J_2 deformation theory models disappears for imperfection amplitudes greater than about one-tenth the wall thickness. Figure 254 demonstrates that for very small imperfections the plastic buckling load is not as sensitive to imperfections as is the elastic buckling load. Also, as Hutchinson [313] points out, imperfection sensitivity

is not as severe a problem for plastic as it is for elastic shells because plastic buckling requires relatively high thickness-to-radius ratios for which it is much less difficult to manufacture "reasonably perfect" shells. This conclusion is borne out by the comparisons between test and theory for a great variety of axisymmetric shells shown in previous sections. (See Tables 1, 2, 11, 12 and Figs. 120, 121, 164, 165.)

Hutchinson further discusses the effect of small imperfections on plastic buckling loads in [314]. There he provides an asymptotic estimate of the load at which elastic unloading begins. For many unstable structures this load is only slightly below the limit load. An asymptotic expression for the limit load, such as given by Koiter's general theory for elastic shells [Eqs. (74) and (75)] is not yet available. The main problem is that the limit load of the structure with an infinitesimal imperfection in the form of the critical bifurcation buckling mode is not infinitesimally close to the bifurcation point, as is true in the elastic range, but lies a finite distance away. Consequently, elastic unloading usually occurs before the limit point is reached. An asymptotic expansion of the initial part of the equilibrium solution for the imperfect structure is valid only to the point at which elastic unloading begins. Representation of the remaining part requires a second asymptotic expansion that accounts for the growing elastic unloading region.

Hutchinson and Budiansky [315], Needleman and Tvergaard [316] and Tvergaard [317] have devised asymptotic theories for the plastic limit loads λ_s of imperfect structures using hypoelastic theories (J_2 flow theory without elastic unloading). Even though these asymptotic analyses ignore elastic unloading, they yield accurate predictions of the limit loads. Figures 255 - 257

apply to elastic-plastic imperfect cylindrical panels under axial compression. A Ramberg-Osgood-type material stress-strain law was used for the analysis:

$$\epsilon = \frac{\sigma_y}{E} \left[\frac{1}{n} \left(\frac{\sigma}{\sigma_y} \right)^n - \frac{1}{n} + 1 \right] \quad (80)$$

The figures show the effects of the circumferential angle θ subtended by the panel and the material hardening parameter n on the equilibrium paths and limit loads of imperfect panels. (In each case the imperfection is in the form of the critical bifurcation mode of the perfect panel.) Figures

255 and 256 show the results of an elastic-plastic finite element analysis and Figure 257 shows a comparison between this numerical approach with the more approximate hypoelastic asymptotic approach.

Qualitative Guidelines for Imperfection Sensitivity

The question so often asked by the analyst is: given the idealized structure and loading, and given the means by which to determine the collapse of bifurcation buckling loads, what "knockdown" factor should be applied to assure a reasonable factor of safety for the actual imperfect structure?

We have seen examples (Figs. 57, 58, 84, 90, 96, 103) in which shells exhibit load-carrying capability considerably greater than that corresponding to the lowest eigenvalue. Postbuckling stability is also exhibited by simple columns and flat plates. On the other hand, it is well known that the critical loads of axially compressed cylindrical shells and externally pressurized

spherical shells are extremely sensitive to imperfections less than one wall thickness in magnitude. Figure 258 gives empirically determined knockdown factors for monocoque axially compressed cylinders as functions of the radius-to-thickness ratio. Similar curves would exist for externally pressurized monocoque spherical shells were there enough test data on which to base them. These highly symmetrical systems are very sensitive to imperfections because many different buckling modes are associated with the same eigenvalue or closely spaced eigenvalues, the structure is uniformly compressed in a membrane state, and the buckling modes have many small waves. Very small local imperfections will tend to trigger premature failure. The buckling loads of most practical shell structures are somewhat sensitive to imperfections, but not this sensitive. How much so is a very important question.

Buckling loads associated with local failure due to some known peculiarity of the structure which can be modeled a priori are generally less sensitive to unknown imperfections than are loads associated with buckle patterns covering a large percentage of the surface area. Redistribution of the stresses occurs as the load is increased; a serious unknown imperfection is less likely to appear in the local area of the failure, and considerable local prebuckling deformations occur, tending to diminish the significance of the initial unknown imperfections. Failure loads of structures that are submitted to enforced displacements are likely to be less sensitive to initial imperfections than are those for structures submitted to enforced loads. In the former case the growth of an isolated buckle near the worst imperfection tends to cause reduction of the stress in that area, shifting the load to the better parts

of the structure. Buckling of cylinders with cut outs (Figs. 47 - 56) and locally loaded shells (Figs. 150 - 155) are examples of this. Thicker shells appear to be less sensitive to imperfections than thinner shells simply because it is easier during fabrication to control the quality of the shell. Imperfection amplitude expressed in terms of wall thickness is therefore likely to be smaller the thicker the shell. Cylinders submitted to external pressure are less sensitive to imperfections than are cylinders submitted to axial compression because the axial wavelengths of the buckles are longer in the former case and eigenvalues do not cluster around the critical value. Hence, very small local imperfections do not affect the critical pressure as much as they do the critical axial load.

Axially Compressed Cylindrical Shells and Panels

Brief Survey of Work Done

The discrepancy shown in Figs. 18 and 19 between tests and classical buckling theory for axially compressed cylindrical shells has stimulated scientists and engineers to produce many papers on this subject during the past 40 years. These works focused on post-buckling load-deflection behavior of perfect shells, various boundary conditions, nonuniform and nonlinear prebuckling behavior and its effect on bifurcation buckling, empirically derived design formulas, and, most important, initial geometric imperfections.

Nonlinear Post-Buckling Behavior of Perfect Shells: It was recognized early that the discrepancy between test and theory and the scatter of critical

experimental loads shown in Figs. 18 and 19 are related to the existence of postbuckling equilibrium configurations at loads well below the critical load, and that as a consequence the shell is very sensitive to geometrical imperfections and other disturbances. The first effort to analyze the shell behavior in the postbuckling range was Donnell's in 1934 [318]. His analysis was over-simplified, and more adequate postbuckling analyses were later presented by von Karman and Tsien [319] and Tsien [320]. It was suggested at that time that the minimum post-buckling load be used as a design load. This minimum was about one third of the classical buckling load and thus reasonably close to the average of available test results. The minimum postbuckling load was termed, somewhat unfortunately - the "lower buckling load." The postbuckling analysis was successively refined in Refs. [321 - 325] as described in the very thorough and readable survey by Hoff [29] and displayed in Fig. 20(b). The results of Ref. [325] seem to indicate that with increasing shortening of the cylinder the postbuckling load asymptotically approaches zero or, if more accurate basic equations had been used, a value that is dependent on the radius-to-thickness ratio of the shell but which for practical dimensions is very small. As a result of these studies it has been determined that the minimum postbuckling load is not suitable as a design load.

Various Boundary Conditions and Nonuniform or Nonlinear Prebuckling Effects: A rather comprehensive review of the effect of edge conditions on buckling is given by Hoff [29]. Some of the papers [326, 327] retain the assumption common to most previous shell-buckling analyses that the prebuckling conditions can be sufficiently accurately described by use of a nonlinear membrane solution. In others [328, 329] an accurate nonlinear prebuckling analysis is included.

It was found in those analyses that if the shell edge were free to move in the tangential direction, the critical load would be reduced by a factor of 2. Results from Ref. [152] are listed in Table 10, and a comparison of the results of Hoff and Soong [330] and Almroth [152] for a cylinder with $r/t = 1000$ and $L/r = 1.014$ are listed in Table 25. The conditions corresponding to λ_{crit} near 0.5 (half the classical load $N_{cl} = 0.6 Et^2/r$) are not likely to be realized in practical applications. However, one could argue that it is possible that a considerable reduction in the load-carrying capacity of the cylindrical shells might result from some kind of "effective" elastic constraint at the edges. This argument has been addressed by Almroth [331] and Cohen [96] who show that a very small amount of elastic constraint is sufficient to make the critical load of the shell approximately equal to the critical load of a shell with full constraint.

Almroth [331] also investigated the effect of the prebuckling deformations caused by edge constraints by using a rigorous solution for the axisymmetric prebuckling equilibrium state. In Table 25 his results are compared with those obtained by Hoff and Soong [330], who neglected the effects of prebuckling deformations. Inclusion of the effect of the prebuckling deformations reduces the expected buckling loads by only 15 percent at most. Therefore one must conclude that neither the influence of the boundary conditions nor the effect of the prebuckling deformations caused by the edge constraint account for the large reduction in the load-carrying capacity of perfect cylindrical shells in axial compression nor do these factors explain the large amount of scatter of experimental results.

Empirically Derived Design Formulas for Monocoque Cylinders: As a consequence of the lack of an adequate theoretical analysis, the designers of axially compressed cylindrical shells have been forced to use empirical methods. In 1957, Harris et al [164] made the first attempt to devise a design limit by use of a statistical analysis of available test results. For different probability levels, a reduction factor ϕ is given as a function of the radius-to-thickness ratio. Figure 258 shows the design curves for axially compressed monocoque cylindrical shells.

The disadvantage of this statistical analysis procedure is that some test results affect the design although they are really irrelevant because of the manner of fabrication or their size. There is no bonus for the manufacturer who can produce an almost perfect shell.

For analyses such as that of Ref. [164], it appears that the number of available tests constitutes a sufficient statistical background as long as the buckling coefficient for a fixed probability is a function of only one variable, R/t . This is the case for longer shells; however, for shorter shells the shell length becomes an additional parameter and the number of available tests is not really satisfactory.

Design Rules for Stiffened Cylinders: For orthotropic shells or stiffened shells, the number of influential parameters becomes so large that a purely empirical approach is out of the question. More or less conservative design

principles have therefore been applied. For stringer-stiffened axially compressed cylinders, it has been quite generally assumed that the effect of curvature is negligible and thus that the wide column load should be applicable as a design limit. This principle has been applied also in the analysis of buckling between rings (panel buckling) for cylinders stiffened with rings as well as stringers. An approximate method for determination of the ring size such that general instability is avoided is given by Shanley [332]. The Shanley method, being purely empirical and based on a very few test results, is not reliable and in addition is restricted in application because it cannot be used for a case in which the stringers are oversized.

In Ref. [333] it is recognized that use of the wide column load as a design limit for stringer-stiffened cylinders is unduly conservative. It is suggested that a term be added to the wide column load which corresponds to the curvature effect. This term represents a reduction factor times the difference between the classical buckling load and the wide column load. After definition of an effective radius-to-thickness ratio, this factor can be obtained from test data for monocoque shells, as shown in Fig. 258. The same type of approach is used in Ref. [334], but here the wide column load is replaced by the minimum postbuckling load. It was found in the analyses of Refs. [335] and [336] that the minimum postbuckling load is relatively high for the cases in which the agreement between test and classical buckling theory is reasonably good, i.e. for short stringer-stiffened shells, ring-stiffened shells, pressurized shells, and core-filled shells. As a consequence, the method of Ref. [334] gives good results for a very general class of shells. However, it was shown later

[325] that the minimum postbuckling load, if it exists at all, may be much below the results of Refs. [335] and [336]. Hence, one is reluctant to recommend this method as a design procedure.

In Ref. [337] a set of design rules is given for stiffened cylinders. The same basic approach is used for the selection of a reduction factor as in Refs. [333] and [334], but the importance of stiffener eccentricity is recognized and, in view of the results of Ref. [325], the wide column load is relatively high (short cylinders, core-filled cylinders). More rational design criteria are needed, however, for pressurized cylinders and ring-stiffened cylinders, for which the wide column load does not take into account the stabilizing effects of internal pressure and rings. Almroth, et al [34] formulated a semi-empirical design method that will be described in more detail later.

Effect of Geometric Imperfections: Koiter [15, 298] was the first to formulate a general theory which in the special case of axially compressed cylindrical shells reveals the extreme sensitivity of buckling loads to initial geometrical imperfections. The principal elements of Koiter's theory are outlined in the previous section. In his doctoral thesis published in 1945, Koiter shows that if certain conditions prevail in the neighborhood of the bifurcation point, the buckling load of the structure is sensitive to geometrical imperfections. The axially loaded cylinder was found by Koiter to be an extreme example of such structures. In addition to the early post-buckling analyses of perfect shells, which lead to qualitative judgment

concerning the imperfection sensitivity, Koiter presents asymptotic formulas [(74) and (75)] for determination of the critical load in the presence of small-amplitude imperfections. Numerical results are given for cases in which the imperfections are axially symmetrical. Although a most important contribution in the field of thin shell stability, Koiter's work received little attention until the early 1960's because the thesis was written in the Dutch language. An English translation by Riks appears as Ref. [336]. Compact and readable presentations of Koiter's theory are given by Budiansky and Hutchinson [303] and Budiansky [304, 300].

The number of papers on the effect of imperfections on buckling of axially compressed cylinders is large. The reader is referred to the surveys by Hutchinson and Koiter [6], Tvergaard [7], Budiansky and Hutchinson [299], and Árbocz [339] for details. Only a few papers which demonstrate the scope of the field will be mentioned specifically here.

Donnell and Wan in 1950 [30] were the first in this country to recognize in a formal theory that geometrical imperfections provide the major reason for the discrepancy between test and theory. Results of their theory, which is described by Árbocz in [339], are shown in Fig. 20(a). In order to simplify their analysis, Donnell and Wan made certain assumptions which reduce the work to a qualitative rather than quantitative demonstration of the importance of imperfections.

The ultimate aim of all imperfection sensitivity analyses is to determine the maximum load-carrying capability (λ_s in Figs. 7 and 249; P_s in

in Fig. 250(a)). The search for λ_s of P_s has been accomplished in the following ways:

- (1) A general imperfection shape containing both axisymmetric and non-symmetric components has been assumed and the nonlinear compatibility and equilibrium equations of the Kármán-Donnell theory [339] have been used to trace the load-deflection curve up to and perhaps past its maximum. This is the approach taken, for example, by Donnell and Wan [30], Hutchinson [340], Árbocz and Babcock [341] and Árbocz and Sechler [342].
- (2) An axisymmetric imperfection shape has been assumed and λ_s identified as the lowest load at which either axisymmetric collapse or non-symmetric bifurcation occurs from the axisymmetrically deformed pre-buckled state. This is the approach taken by Koiter in his classic paper published in 1963 [343], by Almroth, et al [34] in their extension of Koiter's "special theory" [343] for derivation of a design method for stiffened and internally pressurized cylindrical shells, and by Tennyson and Muggeridge [344], who investigated the effect of local axisymmetric imperfections.
- (3) Koiter's "general theory" is used to obtain the factor b in Eq. (73). ("a" is zero in this case because of the periodicity of the buckling mode in the circumferential direction), and Eq. (75) or its equivalent for the multi-mode case is used to obtain the peak load λ_s . This approach is used by Hutchinson and Amazigo [345] and Hutchinson and Frauenthal [346] in their studies of eccentrically stiffened and barreled cylindrical shells, and by Amazigo and Budiansky

[347] in their asymptotic treatment of buckling of axially compressed cylinders with localized or random axisymmetric imperfections.

- (4) A "brute-force" approach is used to obtain the peak load λ_s as discussed in the chapter on nonlinear collapse. For example, the STAGS computer program [48] has been used for the analysis of axially compressed cylinders with cutouts, as illustrated in Figs. 47- 56, and the BOSOR5 program [47] has been applied to determine axisymmetric collapse loads of a complex elastic-plastic rocket interstage (Figs. 59 - 61) and elastic-plastic cylindrical shells (Tables 1 and 2).

Governing Equations for Asymptotic Post-Buckling Approach

The purpose here is to demonstrate the derivation of the imperfection sensitivity parameter b in Eqs. (73) and (75) for an important case in which stiffeners and load-eccentricity are present and for which it is necessary to account for nonlinear prebuckling behavior in the asymptotic analysis. The asymptotic formulation including nonlinear prebuckling effects was first set forth almost simultaneously by Fitch [348] and Cohen [349]. The derivation given here follows closely that provided by Hutchinson and Frauenthal [346] for slightly barreled cylindrical shells.

Kármán-Donnell Equations: These equations can be derived from the nonlinear kinematic relations of the Donnell-Mushtari-Vlasov type (see Tables 5-9 of Ref.[430]) with use of the principle of virtual work. Such a derivation is

given by Hutchinson and Amazigo in [345]. Stiffener properties are "smeared out" in the manner of Baruch and Singer [.160] to arrive at effective bending and stretching stiffnesses for the skin-stiffener combination. The governing equations can be reduced to an equation for moment equilibrium and one compatibility equation written in terms of the normal outward deflection of the shell W and a stress function F :

$$L_D[W] + L_Q[F] = F_{,xx} W_{,yy} + F_{,yy} W_{,xx} - 2F_{,xy} W_{,xy} \quad (81)$$

$$L_H[F] - L_Q[W] = W_{,xy}^2 - W_{,xx} W_{,yy} \quad (82)$$

in which x and y are the axial and circumferential coordinates in the shell middle surface. The linear differential operators are defined by

$$\begin{aligned} L_D[] &= D_{xx}[],_{xxxx} + 2D_{xy}[],_{xxyy} + D_{yy}[],_{yyyy} \\ L_H[] &= H_{xx}[],_{xxxx} + 2H_{xy}[],_{xxyy} + H_{yy}[],_{yyyy} \end{aligned} \quad (83)$$

Formulas for the effective bending and stretching stiffnesses are listed in Table 26.

Consideration is restricted here to cylinders (and slightly barreled cylinders) with an isotropic skin and axial stiffening. Three parameters are needed to

characterize the stiffening properties if the torsional rigidity of the stringers is ignored. These are the area ratio $A_s/d_s t$, the bending stiffness ratio EI_s/Dd_s and the eccentricity ratio e_s/t where A_s and I_s are the area and moment of inertia of the stringer, d_s is the distance between stringers and e_s , the distance from the skin middle surface to the stringer centroid, is taken to be positive when the stiffener is on the outer surface of the shell. The resultant membrane stresses in the skin N_x , N_y and N_{xy} and the averaged resultant membrane stress in the axial stringers N_s are related to the stress function and the normal displacement by

$$N_x + N_s = F_{,yy}; \quad N_y = F_{,xx}; \quad N_{xy} = -F_{,xy} \quad (84)$$

$$N_x = A_{xx} F_{,xx} + A_{xy} F_{,vy} + B_{xx} W_{,xx}$$

with A_{xx} , A_{xy} , and B_{xx} given in Table 26. In the brief outline of the initial postbuckling analysis which follows, the general theory will not be repeated but results from it will be translated directly into the W-F notation of Kármán-Donnell theory.

Prebuckling Analysis The axisymmetric prebuckling deformation of the perfect shell can be written as

$$W^0 = w^0(x, P) \quad (85)$$

$$F^0 = -\frac{1}{2} \gamma^2 \frac{P}{2\pi R} + f^0(x, P)$$

in which P is the total compressive load applied to the cylinder. Although the prebuckling behavior is nonlinear, the two fourth order differential equations governing w^0 and f^0 are linear in these quantities. These two equations can be reduced to a single linear fourth order equation for w^0 :

$$C_A w^{0''''} + \left(C_B + \frac{P}{2\pi R} \right) w^{0''} + C_C w^0 = \frac{\nu A_{xy} P}{2\pi E t H_{xx} R^2} + \frac{P}{2\pi R R_x} \quad (86)$$

with an auxiliary equation for f^0 :

$$H_{xx} f^{0''} = Q_{xx} w^{0''} + \frac{1}{R} w^0 - \frac{\nu A_{xy} P}{2\pi E t R} \quad (87)$$

where $()' \equiv \frac{d()}{dx}$ and

$$C_A = D_{xx} + \frac{Q_{xx}^2}{H_{xx}}; \quad C_B = \frac{2Q_{xx}}{R H_{xx}}; \quad C_C = \frac{1}{R^2 H_{xx}} \quad (88)$$

Asymptotic Analysis: The classical buckling load of the perfect structure is denoted by P_C . In all the cases examined by Hutchinson and Frauenthal [346] P_C is the load at which a nonaxisymmetric bifurcation from the prebuckling state occurs. According to the Koiter theory [15, 298, 338, 303] an asymptotic perturbation expansion of the solution, valid in the neighborhood of this bifurcation point, can be obtained in the form

$$\frac{P}{P_C} = 1 + a(\delta/t) + b(\delta/t)^2 + \dots \quad (89)$$

$$W = W^0 + \delta W^{(1)} + \delta^2 W^{(2)} + \dots; \quad (90a)$$

$$F = F^0 + \delta F^{(1)} + \delta^2 F^{(2)} + \dots \quad (90b)$$

in which δ is the amplitude of the buckling mode $W^{(1)}$. [Identify δ/t with v_D and P/P_C with λ in Eq. (73).] The prebuckling solution is also expanded about the critical load [348, 349] so that

$$W^0 = W_C^0 + (P - P_C) \dot{W}_C^0 + \frac{1}{2}(P - P_C)^2 \ddot{W}_C^0 + \dots \quad (91)$$

$$F^0 = F_C^0 + (P - P_C) \dot{F}_C^0 + \frac{1}{2}(P - P_C)^2 \ddot{F}_C^0 + \dots$$

where $W_C^0 \equiv W^0(x, P_C)$, $\dot{W}_C^0 \equiv \left. \frac{\partial W^0}{\partial P} \right|_{P=P_C}$, $\ddot{W}_C^0 \equiv \left. \frac{\partial^2 W^0}{\partial P^2} \right|_{P=P_C}$, etc.

The expansions (90a,b) with (91) generate a sequence of linear boundary value problems corresponding to like powers of δ and $P - P_C$. The problem for \dot{W}_C^0 and \dot{F}_C^0 follows directly from Eqs. (85- 87).

$$\begin{aligned} C_A \dot{W}_C^{0''''} + \left(C_B + \frac{P_C}{2\pi R} \right) \dot{W}_C^{0''} + C_C \dot{W}_C^0 \\ = \frac{\nu A_{xy}}{2\pi E t H_{xx} R^2} + \frac{1}{2\pi R R_x} - \frac{1}{2\pi R} W_C^{0''} \end{aligned} \quad (92)$$

$$H_{xx} \dot{F}_C^{0''} = Q_{xx} \dot{W}_C^{0''} + \frac{1}{R} \dot{W}_C^0 - \frac{\nu A_{xy}}{2\pi E t R} \quad (93)$$

The classical buckling problem is a linear eigenvalue problem arising from insertion of the expansions (90a,b) into Eqs. (81) and (82) and collection of all terms linear in δ . The eigenvalue problem is thus given by

$$\begin{aligned} L_D[W^{(1)}] + L_Q[F^{(1)}] + \frac{P_C}{2\pi R} W_{,xx}^{(1)} - f_C^{0''} W_{,yy}^{(1)} \\ - W_C^{0''} F_{,yy}^{(1)} = 0 \end{aligned} \quad (94)$$

Separated solutions for the buckling mode have the form

$$\begin{aligned} W^{(1)}(x,y) &= w^{(1)}(x) \cos(ny/R) \\ F^{(1)}(x,y) &= f^{(1)}(x) \cos(ny/R) \end{aligned} \quad (95)$$

in which n is the number of circumferential waves associated with the buckling mode. Ordinary differential equations follow directly from insertion of Eqs. (95) into Eqs. (94). Boundary conditions are listed in the Appendix of [346].

Anticipating that the post-buckling behavior is symmetric with respect to the sign of δ ["a" = 0 in Eq. (89)], we obtain [by insertion of the expansions (90a,b) with (91) and (89) into Eqs. (81) and (82) and collection of all terms quadratic in δ] the second-order linear boundary value problem,

$$\begin{aligned} L_D[W^{(2)}] + L_Q[F^{(2)}] + \frac{P_C}{2\pi R} W_{,xx}^{(2)} - f_C^{(0)'} W_{,yy}^{(2)} \\ - w_C^{(0)'} F_{,yy}^{(2)} \approx -\frac{1}{2} (n/R)^2 \{ (f^{(1)} w^{(1)})'' \\ + \cos(2ny/R) (f^{(1)'} w^{(1)} + f^{(1)} w^{(1)'} - 2f^{(1)'} w^{(1)'}) \} \end{aligned} \quad (96)$$

$$\begin{aligned} L_H[F^{(2)}] - L_Q[W^{(2)}] + w_C^{(0)'} W_{,yy}^{(2)} \\ = \frac{1}{2} (n/R)^2 \{ \frac{1}{2} (w^{(1)2})'' + \cos(2ny/R) (w^{(1)'} w^{(1)} - w^{(1)2}) \} \end{aligned}$$

These equations can be reduced to two systems of ordinary differential equations with separation of variables according to

$$\begin{aligned} W^{(2)} &= w_{\alpha}(x) + w_{\beta}(x) \cos (2ny/R) \\ F^{(2)} &= f_{\alpha}(x) + f_{\beta}(x) \cos (2ny/R) \end{aligned} \quad (97)$$

Solutions of the above boundary value problems are sufficient to yield the most important information about the initial post-buckling behavior and the associated imperfection sensitivity. In every case considered here the first postbuckling coefficient, a , in Eq. (89) is zero because the buckling modal displacement $W^{(1)}$ and stress function $F^{(1)}$ are harmonic with respect to the circumferential coordinate y . Therefore, the initial relationship between the load and the buckling displacement amplitude of the perfect shell hinges on the sign and magnitude of b . If b is negative the load carrying capacity diminishes following buckling and the shell is imperfection-sensitive, while if b is positive the structure retains some ability to support increased loads once bifurcation has taken place. Throughout this derivation δ is consistently identified with the amplitude of the buckling modal displacement by normalization of the maximum value of $W^{(1)}$ to be unity. Thus in Eq. (89), δ/t is the ratio of the buckling amplitude to the skin thickness and not the effective thickness of the stiffener combination. The formula for b is derived by Fitch [348] to be

$$b = \frac{F^{(2)} * (W^{(1)}, W^{(1)}) + 2F^{(1)} * (W^{(1)}, W^{(2)})}{P_C [\dot{F}_C^0 * (W^{(1)}, W^{(1)}) + 2F^{(1)} * (\dot{W}_C^0, W^{(1)})]} \quad (98)$$

in which the following shorthand notation has been used

$$A^*(B,C) = \int_S [A_{,xx} B_{,y} C_{,y} + A_{,yy} B_{,x} C_{,x} - A_{,xy} (B_{,x} C_{,y} + B_{,y} C_{,x})] dS \quad (99)$$

and the integration is over the entire middle surface of the shell.

Initial Post-Bifurcation Load-Deflection Curve: The initial slope of the generalized load-deflection curve just following bifurcation yields further information concerning the extent to which buckling can be expected to be gradual or sudden under the two limiting conditions of loading: prescribed load and prescribed generalized displacement. The generalized displacement is the average end displacement. For cylindrical shells this average end displacement can be written as

$$\Delta = \int_S (U_{,x} - qW_{,xx}) dS = \int_S (\epsilon_x - \frac{1}{2} W_{,x}^2 - qW_{,xx}) dS \quad (100)$$

where U is the axial displacement and q is the loading eccentricity, that is the distance from the radius of axial load application to the skin middle surface, positive for loads outside the middle surface. A Taylor expansion of Δ , with use of Eqs. (89 - 91) yields

$$\frac{\Delta}{\Delta_C} = 1 + \alpha \left(\frac{P}{P_C} - 1 \right) + \dots \quad (101)$$

in which α is a fairly lengthy expression in terms of $W^{(1)}$, $F^{(1)}$, etc.

which will not be given here. A similar calculation yields an expression for α for the barreled cylinders. Δ_C denotes the average end displacement at the critical bifurcation load P_C .

Imperfection Sensitivity: Finally, a measure of the imperfection-sensitivity of the structure is most easily obtained by consideration of the effect of an initial deviation of the shell middle surface from the perfect configuration in the shape of the buckling mode. Thus with an initial imperfection $\bar{w} = w^{(1)}$, the maximum support load P_S is related to the classical buckling load P_C and the imperfection amplitude $\bar{\delta}$ by the asymptotic formula [See Eq. (75)] of the form

$$P_S/P_C = 1 - 3(2)^{-2/3}(-\bar{b})^{1/3} |\bar{\delta}/t|^{2/3} + \dots \quad (102)$$

$$\cong 1 - 1.89(-\bar{b})^{1/3} |\bar{\delta}/t|^{2/3}$$

The imperfection amplitude has been normalized with respect to the skin thickness t . When the prebuckling state is a purely membrane one, $\bar{b} = b$, but in the present case in which prebuckling deformations are not ignored [348],

$$\bar{b} = \frac{b\{F_C^0 * (w^{(1)}, w^{(1)}) + F^{(1)} * (w_C^0, w^{(1)})\}^2}{\{P_C^0 [F_C^0 * (w^{(1)}, w^{(1)}) + 2F^{(1)} * (w_C^0, w^{(1)})]\}^2} \quad (103)$$

Numerical Methods Used to Solve the Various Boundary-Value Problems and Evaluate b , \bar{b} , and α : Hutchinson and Frauenthal [346] describe how they solved the boundary value problems (92, 93), (94), and (96) and evaluated ν in Eq. (98), α in Eq. (101), and \bar{b} in Eq. (103):

"In nondimensional form the several boundary value problems and associated boundary conditions are specified by the following nondimensional quantities: EI_s/Dd_s , $A_s/d_s t$, e_s/t , q/t , R/R_x , Z , nL/R and ν . The ordinary differential equations for w_C^0 , \dot{w}_C^0 , $w^{(1)}$, w_α , w_β , etc., are reduced to finite difference form and solved by use of a well-known Gaussian elimination scheme due to Potters [350]. The eigenvalue problem for the classical buckling load and mode can be solved in the usual way in which the lowest eigenvalue associated with integer values of n is found, and then the lowest of them all is identified with the classical load. Results were obtained by treating nL/R as a continuous variable and thus it was not necessary to specify the length-radius ratio of the shell. This procedure is consistent with the fact that the critical value of nL/R turns out to be a fairly large number and for an L/R of order unity or less n itself will be fairly large. Therefore, the results can be regarded as exact for any value of L/R such that the associated value of n is integer and approximate for other values of L/R with an error in the buckling load of order $1/r^2$ and an error in b , \bar{b} and α of order $1/n$. In any case, application of the Donnell-Mustari-Vlasov strain measures is restricted to shells for which $n > 5$, say. In every sample presented (by Hutchinson and Frauenthal [346]) a single buckling mode is associated with the critical eigenvalue and the expansions (89- 91) were made in anticipation of this fact."

"The expressions for b , \bar{b} and α can easily be reduced to ordinary integrations over the x coordinate and these integrations were performed with a standard numerical integration scheme. As a check on accuracy, some examples from

reference [345], in which the prebuckling deformation was identically zero and for which closed form series solutions were available, were run as special cases of the present procedure. With sixty integration stations over the half length of the shell, accuracy to within about one tenth of one percent could be obtained for the quantities b , \bar{b} and α . Slightly less accuracy should be expected for the cases in which prebuckling deformations are important. All results are for a Poisson's ratio of 0.3." [346]

Governing Equations for the Nonlinear Approach

In contrast to the method described in the previous section, this is not an asymptotic approach. The restriction imposed in Koiter's general asymptotic theory that results are valid only in the neighborhood of the bifurcation point of the perfect structure is not present. The nonlinear approach is still based on the Kármán-Donnell equations, but in this case a stress-free imperfection shape, W_0 , and series expansion are assumed for the normal displacement increment w from that corresponding to the perfect shell in the prebuckling membrane state ($W = w_{\text{membrane}} + w$). These expressions are substituted into the compatibility equation, which is solved exactly for the stress function F in terms of w_{membrane} and the assumed increment w . The equilibrium equation is then converted by means of the Galerkin procedure into a set of simultaneous nonlinear algebraic equations in terms of the load parameter λ , the imperfection amplitude $\bar{\xi}$, and the undetermined coefficients ξ_i of the series expansion assumed for the increment w .

Hutchinson's Formulation [340]: The equilibrium equation (81) and compatibility equation (82) for the initially imperfect cylindrical shell become

$$L_D[W] + L_Q[F] = F_{,xx}(W_{,yy} + W_{o,yy}) + F_{,yy}(W_{,xx} + W_{o,xx}) - 2F_{,xy}(W_{,xy} + W_{o,xy}) \quad (104)$$

$$L_H[F] - L_Q[W] = W_{,xy}(W_{,xy} + 2W_{o,xy}) - W_{,xx}W_{o,yy} - W_{,yy}(W_{,xx} + W_{o,xx}) \quad (105)$$

Any radial imperfection pattern W_o can be represented as a double Fourier series in the axial and circumferential coordinates x and y . For an isotropic shell, Hutchinson [340] considered a two-term series

$$W_o = -\bar{\xi}_1 t \cos(q_o x/R) + \bar{\xi}_2 t \cos(\frac{1}{2}q_o x/R) \cos(\frac{1}{2}q_o y/R) \quad (106)$$

in which

$$q_o^4 \equiv 12(1 - \nu^2)R^2/t^2 \quad (107)$$

The first term in Eq. (106) represents an imperfection in the form of the axisymmetric buckling mode, which Koiter [343] found to be most degrading. The second term represents a nonsymmetric buckling mode with square buckles, which Koiter [343] determined corresponds to the critical bifurcation mode of a perfect cylindrical shell or a cylindrical shell with a small

axisymmetric imperfection given by the first term in Eq. (106). The quantities $\bar{\xi}_1$ and $\bar{\xi}_2$ are the ratios of the amplitudes of the imperfection components to the shell thickness. [Identify $\bar{\xi}$ with $\bar{\delta}/t$ in Eq. (102) and ρw_{imp} in Eq. (75).]

The total radial displacement W is represented in [340] by

$$W = w_{\text{membrane}} + w \quad (108)$$

in which

$$\begin{aligned} w = & \xi_1 t \cos(q_0 x/R) + \xi_2 t \cos(\frac{1}{2}q_0 x/R) \cos(\frac{1}{2}q_0 y/R) \\ & + \xi_3 t \sin(\frac{1}{2}q_0 x/R) \cos(\frac{1}{2}q_0 y/R) \end{aligned} \quad (109)$$

with ξ_1, ξ_2, ξ_3 indicating the ratios of the amplitudes of the radial deflection increment in the axisymmetric and nonsymmetric modes to the shell thickness.

Equation (108) with Eq. (109) is inserted into the compatibility equation (105), which is then solved exactly for F in terms of $W = w_{\text{membrane}}$ plus the assumed increment w . The equilibrium equation (104) is then solved approximately by substitution therein of F thus found and the assumed W , with subsequent application of the Galerkin procedure. Hutchinson [340] thereby obtains the following nonlinear algebraic equations for the undetermined coefficients ξ_1, ξ_2 , and ξ_3 in terms of the normalized load parameter λ and

the imperfection amplitudes $\bar{\xi}_1$ and $\bar{\xi}_2$ for an axially compressed isotropic cylindrical shell with uniform internal pressure:

$$\begin{aligned} \xi_1(1 - \lambda) + \frac{3}{32} c(\xi_2^2 - \xi_3^2) + \frac{1}{8} c\xi_2\bar{\xi}_2 + \lambda\bar{\xi}_1 + \\ \frac{13}{200} c^2(\bar{\xi}_2 + \xi_2)[\bar{\xi}_2\xi_1 + (\xi_1 - \bar{\xi}_1)\xi_2] + \\ \frac{13c^2}{200} (\xi_1 - \bar{\xi}_1)\xi_3^2 = 0 \\ \xi_2(1 + \bar{p} - \lambda) + \frac{3}{2} c\xi_1\xi_2 - c\xi_2\bar{\xi}_1 + c\xi_1\bar{\xi}_2 + \\ (\bar{p} - \lambda)\bar{\xi}_2 + \frac{13}{25} c^2(\xi_1 - \bar{\xi}_1)[\xi_1\bar{\xi}_2 + \xi_2(\xi_1 - \bar{\xi}_1)] + \\ \frac{1}{8} c^2(\xi_2 + \bar{\xi}_2)(\xi_2\bar{\xi}_2 + \frac{1}{2}\xi_2^2) = 0 \end{aligned} \quad (110)$$

and

$$\begin{aligned} \xi_3(1 + \bar{p} - \lambda) - \frac{3}{2} c\xi_1\xi_3 + c\xi_3\bar{\xi}_1 + \frac{13}{25} c^2(\xi_1 - \bar{\xi}_1)^2\xi_3 + \\ \frac{1}{16} c^2\xi_3^3 = 0 \end{aligned}$$

where $c = [3(1 - \nu^2)]^{1/2}$ and $\bar{p} \equiv (pR^2/Et^2)[3(1 - \nu^2)]^{1/2}$.

The normalized axial load parameter λ is the ratio of the axial load to the classical buckling load N_{CL} of an internally pressurized cylinder

$$N_{CL} = (1 + \bar{p}/2)Et^2/[3(1 - \nu^2)]^{1/2}R \quad (111)$$

Árbocz and Babcock's Formulation [341]: This approach was used by Árbocz and Babcock [341]; Singer, Árbocz, and Babcock [351]; Árbocz [339]; and Árbocz and Sechler [342], who generalized it for application to isotropic and stiffened cylinders with measured imperfections that do not necessarily resemble buckling modes of the perfect shell. For example, for axially compressed isotropic cylindrical shells, Árbocz and Babcock [341] assume that the initial imperfection has the form

$$\begin{aligned}
 W_0 = & \bar{\xi}_1 t \cos i \frac{2\pi x}{L} + \bar{\xi}_2 t \cos k \frac{2\pi x}{L} \cos l \frac{y}{R} \\
 & + \bar{\xi}_3 t \sin k \frac{2\pi x}{L} \cos l \frac{y}{R}
 \end{aligned}
 \tag{ 112}$$

and the incremental radial deflection w is approximated as

$$\begin{aligned}
 w = & \xi_1 t \cos i \frac{2\pi x}{L} + \xi_2 t \cos k \frac{2\pi x}{L} \cos l \frac{y}{R} \\
 & + \xi_3 t \sin k \frac{2\pi x}{L} \cos l \frac{y}{R}
 \end{aligned}
 \tag{ 113}$$

They obtain much more complicated nonlinear equations than (110) for ξ_1 , ξ_2 , and ξ_3 in terms of the normalized load parameter λ , which simplify to the following if terms of order $\bar{\xi}\xi^2$, $\bar{\xi}^2\xi$, and ξ^3 are neglected

$$\begin{aligned}
& \xi_1 (C_1 - \lambda) + C_2 [\xi_2 \bar{\xi}_2 - \xi_3 \bar{\xi}_3 + \frac{1}{2} (\xi_2^2 - \xi_3^2)] \\
& \quad + C_3 [(\xi_2 + \bar{\xi}_2) \xi_2 - (\xi_3 + \bar{\xi}_3) \xi_3] = \lambda \bar{\xi}_1 \\
& \xi_2 (C_4 - \lambda) + 8C_3 [2(\xi_1 + \bar{\xi}_1) \xi_2 + \bar{\xi}_2 \xi_1] \\
& \quad + 8C_2 (\xi_2 + \bar{\xi}_2) \xi_1 = \lambda \bar{\xi}_2 \\
& \xi_3 (C_4 - \lambda) - 8C_3 [2(\xi_1 + \bar{\xi}_1) \xi_3 + \bar{\xi}_3 \xi_1] \\
& \quad - 8C_2 (\xi_3 + \bar{\xi}_3) \xi_1 = \lambda \bar{\xi}_3
\end{aligned} \tag{114}$$

with the coefficients C_1 , C_2 , C_3 , and C_4 given by

$$\begin{aligned}
C_1 &= \frac{1}{2} \left(\alpha_A^2 + \frac{1}{\alpha_A^2} \right) \\
C_2 &= \frac{c}{16} \frac{\beta^2}{\alpha^2} \\
C_3 &= \frac{c}{4} \frac{\alpha^2 \beta^2}{(\alpha^2 + \beta^2)^2} \\
C_4 &= \frac{1}{2} \left\{ \frac{(\alpha^2 + \beta^2)^2}{\alpha^2} + \frac{\alpha^2}{(\alpha^2 + \beta^2)^2} \right\}
\end{aligned} \tag{115}$$

in which

$$\alpha_A^2 = i^2 \frac{Rt}{2c} \left(\frac{2\pi}{L} \right)^2 \quad \alpha^2 = k^2 \frac{Rt}{2c} \left(\frac{2\pi}{L} \right)^2 \quad \beta^2 = \ell^2 \frac{Rt}{2c} \left(\frac{1}{R} \right)^2 \tag{116}$$

where

$$c = [3(1-\nu^2)]^{1/2} \quad (117)$$

Behavior of Perfect Cylinders: If prebuckling axisymmetric bending due to localized edge effects is ignored, the post-buckling behavior of perfect axially compressed isotropic cylindrical shells, as predicted by Eq. (114), is illustrated in Fig. 259. If $C_1 > C_4$ there is no incremental radial deformation w [Eq. (113)] until the load parameter λ equals C_4 . At C_4 bifurcation into the ξ_2 or ξ_3 mode occurs and the load λ falls along the unstable parabolic post-bifurcation branch with deformation occurring in both the ξ_1 and ξ_2 (or ξ_3) modes. Since the axisymmetric imperfection amplitude $\bar{\xi}_1 = 0$, ξ_1 can be either positive or negative. If $C_1 < C_4$, there is no deformation until $\lambda = C_1$; then deformation w in the axisymmetric mode ξ_1 occurs at a constant value of λ , since the load-deflection curve corresponding to axisymmetric post-bifurcation behavior is of the type shown in Fig. 8(a). When ξ_1 attains the value $(C_4 - C_1)/8(C_2 + 2C_3)$, bifurcation into the ξ_2 (or ξ_3) mode occurs and λ falls with deformation in the ξ_1 and ξ_2 (or ξ_3) modes as before. Since $\bar{\xi}_1 = 0$, ξ_1 can be either positive or negative.

Behavior of Imperfect Cylinders: The shell with a general imperfection shape ($\bar{\xi}_1 \neq 0$ and either $\bar{\xi}_2 \neq 0$ or both $\bar{\xi}_2$ and $\bar{\xi}_3 \neq 0$) behaves as shown in Fig. 260: the bifurcation point at either C_1 or C_4 , depending on the geometrical parameters α_A^2 , α^2 , β^2 [Eq. 116], is converted into a limit

point λ_s at which snap-through occurs to a non-adjacent equilibrium state. The behavior for a pure axisymmetric and a two-mode nonsymmetric imperfection is shown in Fig. 261 for the case $C_1 > C_4$. If the imperfection is purely axisymmetric ($\bar{\xi}_1 \neq 0, \bar{\xi}_2 = \bar{\xi}_3 = 0$), then the prebuckling deformation is purely axisymmetric until bifurcation of the solution into one of the nonsymmetric modes occurs. If $\bar{\xi}_1$ is negative, then the prebuckling deformation ξ_1 is negative and bifurcation occurs into the ξ_2 mode at $\lambda = \lambda_{bif}$. If $\bar{\xi}_1$ is positive, then the prebuckling deformation ξ_1 is positive and bifurcation occurs into the ξ_3 mode at the same load $\lambda = \lambda_{bif}$. Following bifurcation, the value of λ falls along the unstable parabolic post-bifurcation branch with deformation occurring in the ξ_2 (or ξ_3) as well as the axisymmetric mode ξ_1 . The behavior of a shell with both axisymmetric and one asymmetric imperfection ($\bar{\xi}_1 \neq 0, \bar{\xi}_2 \neq 0, \bar{\xi}_3 = 0$ or $\bar{\xi}_1 \neq 0, \bar{\xi}_2 = 0, \bar{\xi}_3 \neq 0$) is shown by the general solution curve in Fig. 261. Here the deformation occurs in both the ξ_1 and ξ_2 (or ξ_3) modes for any nonzero values of λ .

Árbocz and Babcock [341] obtained the maximum value of $\lambda(\lambda_s)$ by tracing the curve corresponding to the general solution for fixed α_A^2, α^2 , and β^2 in the (λ, ξ_2) -plane or the (λ, ξ_3) -plane. The equation of the trace was programmed on the IBM 7094 computer and used in a search for the pair of critical modal components defined as that combination of one axisymmetric and one asymmetric imperfection component that yields the lowest value for λ_s . In their analysis, Árbocz and Babcock [341] chose $k = i/2$. Then in the minimization of the buckling load $\lambda = C_4$ corresponding to nonsymmetric deformations, the circumferential wave number n is computed from

$$\alpha^2 + \beta^2 - \alpha = 0 \quad (118)$$

which is the restriction on the buckling modes imposed by the classical linearized theory (see Koiter [298]).

Axially Compressed Monocoque Cylindrical Shells: Numerical Results

Cylinders with Sinusoidal Axisymmetric Imperfections: The most significant results for this problem were obtained by Koiter in 1945 [15, 338] and 1963 [343]. They are given in Fig. 262. The curve labeled "General Theory" corresponds to the asymptotic post-buckling analysis [15] which Koiter originally claimed was valid only for imperfection amplitudes up to about 30% of the shell wall thickness. The two curves labeled "Special Theory" correspond to an analysis of the type described in the discussion associated with Eqs. (104 - 109), which is valid for larger imperfection amplitudes. In this analysis the cylindrical shell is assumed to have an axisymmetric imperfection of the form

$$w_0 = -\mu t \cos(2\pi x/R) \quad (119)$$

The "Special Theory" curves in Fig. 262 correspond to bifurcation loads, as indicated by the callout " λ_{BIF} " in Fig. 261, at which the axisymmetrically deformed prebuckled shell bifurcates into a nonsymmetric mode. Koiter selected an imperfection shape in the form of the axisymmetric buckling mode of a perfect shell, for which an axial wavelength parameter ρ is given by

$$\rho^2 = p^2 (t/R) (1/[3(1-\nu^2)]^{1/2}) = 1/2 \quad (120)$$

The two curves labeled "Special Theory" in Fig. 262 were generated with the assumption that the buckling mode has the form

$$w(x,y) = tC \cos (px/R) \cos(ny/R) \quad (121)$$

It is reasonable to assume that the buckling pattern has twice the axial wavelength of the imperfection because this choice permits nodes of the buckling modal displacement at locations along the cylinder axis where the induced prebuckling circumferential tension is maximum and maximum buckling modal radial displacements at locations where the induced circumferential compression is maximum.

In Fig. 262 τ^2 is a circumferential wave parameter given by

$$\tau^2 = n^2 (t/R) (1/[3(1-\nu^2)]^{1/2}) \quad (122)$$

For normalized imperfection amplitudes μ less than about 0.3 the lowest bifurcation load λ_1 corresponds to $\tau^2 = 1/2$ (square buckles). Larger imperfections cause buckling with smaller values of τ^2 (buckles elongated in the circumferential direction); the lowest curve in Fig. 262 is the predicted envelope of critical bifurcation buckling with various τ^2 . This curve represents an upper bound because Koiter's analysis is based on use

of a kinematically admissible approximate buckling modal displacement pattern [Eq. (121)], exact satisfaction of the compatibility equation (105), and approximate satisfaction of the equilibrium equation (104) via Galerkin's procedure.

For a constant value of $\tau^2 = 1/2$ and $u > 0.579$ there is no bifurcation buckling because the stabilizing influence of the increasing meridional curvature as the axial load is applied to the axisymmetrically wavy shell is more significant than the destabilizing influence of the compressive stress resultants. Similar curves exist for $\tau^2 < 1/2$ with the envelope of the minima of these curves plotted in Fig. 262.

Although the results of Fig. 262 qualitatively confirm Koiter's general asymptotic theory, they do not support it conclusively: The curve labeled "General Theory" in Fig. 262 corresponds to a limit load λ_s , such as shown in Figs. 249(b) and 260, whereas the Special Theory envelope corresponds to bifurcation buckling λ_{BIF} , such as indicated in Fig. 261. It remains to investigate the post-bifurcation behavior of the axisymmetrically imperfect cylindrical shell. This was done by Budiansky and Hutchinson [352] and Pedersen [353, 354]. Results are shown in Fig. 263. Budiansky and Hutchinson [352] found a transition from unstable to stable post-buckling behaviour as the bifurcation load drops below about 30 per cent of the classical value (Fig. 263 for $\beta = \beta_C$). However, for imperfection wavelengths larger than that of the classical bifurcation mode, Pedersen [353] found that this transition may take place at bifurcation loads below 15 per cent of the classical value (Fig. 263). In a subsequent paper Pedersen [354] used a Galerkin solution to demonstrate that loads can be

carried above the lowest bifurcation load, even though the initial post-bifurcation behaviour is unstable. All of these results are supported by experimental evidence, in that very few test results exist for which the critical axial load is less than about 25% of the classical load.

Cylinders with Localized Imperfections: Amazigo and Budiansky [347]

assumed an imperfection in the form

$$W_0 = -\bar{\xi} t e^{-\alpha x} \quad (123)$$

and developed an asymptotic formula for the buckling load, λ_s

$$(1 - \lambda_s/\lambda_c)^{3/2} = [3c/2]^{3/2} |\Delta| (\lambda_s/\lambda_c) \quad (124)$$

in which $c \equiv [3(1-\nu^2)]^{1/2}$ and

$$\Delta \equiv \int_{-\infty}^{\infty} \frac{W_0}{t} e^{i\bar{x}} d\bar{x} \quad (125)$$

where

$$\bar{x} \equiv \pi x/\ell_c; \ell_c = \pi[12(1-\nu^2)]^{-1/4} (Rt)^{1/2} \quad (126)$$

The length ℓ_c is the half-wavelength of the classical axisymmetric buckling mode. Hutchinson, Tennyson, and Muggeridge [355] performed a numerical analysis with use of a "cosine dimple"

$$w_0 = \frac{-\bar{\xi}t}{2} (1 + \cos \pi x / \ell_x) \quad |x| \leq \ell_x \quad (127)$$

$$= 0 \quad |x| > \ell_x$$

They obtained results for various values of ℓ_x / ℓ_c , taking into account end effects and nonlinear prebuckling deformations. They also performed tests on spin-cast epoxy-plastic cylindrical shells with axisymmetric dimples of the form (127) machined into them. Figure 264 shows the results of the test and theory of Ref. [355] compared with the asymptotic solution (124) of Amazigo and Budiansky [347] and the Special Theory of Koiter [343]. The sensitivity to a dimple of critical length ℓ_c is severe, but less so than that corresponding to imperfections extending the entire length of the cylinder in the shape of the axisymmetric bifurcation mode. Similar asymptotic results have been obtained by Amazigo and Fraser [356] for a circumferentially dimple-shaped imperfection in a pressurized cylinder. Buckling of axially compressed cylinders with another type of local imperfection - a cutout, is discussed in the chapter on nonlinear collapse, with results from various tests and analyses appearing in Figs. 47- 56.

Cylinders with Random Imperfections (Axial Compression or External Pressure):

Tvergaard [7] provides a survey:

"While most of the investigations mentioned previously consider deterministic imperfections in the shape of the critical buckling mode, some research has been directed towards the realistic situation where imperfections are known as stochastic rather than

deterministic properties. One approach is that taken by Amazigo, Budiansky and others, who consider the initial imperfection to be a sample function from an ensemble of ergodic, zero-mean, stationary Gaussian random functions with known autocorrelation. The analyses based on methods of stochastic differential equations lead to asymptotic estimates of the buckling load corresponding to a given imperfection magnitude, and due to the ergodicity hypothesis, this buckling load is given with probability one. Shell buckling results have been obtained by this method for axially compressed cylinders with random axisymmetric imperfections [347, 357] and for externally pressurized cylinders with imperfections that vary randomly in the circumferential direction [358]."

"Another approach takes an imperfection of given shape with a random amplitude, or the sum of a finite number of given imperfection shapes with random amplitudes. The applied load can also be taken as a random parameter. Then, using the deterministic relations between imperfection parameters and buckling load, the probability that failure occurs can be calculated provided the joint probability density function of these random parameters is known. Recent treatment of stochastic stability problems from this point of view, for an axially compressed cylinder and for other structures, have been given by Roorda and Hansen [359,

360], Augusti and Baratta [361] and Johns [362]. Amazigo [363] has discussed the two different approaches and used the latter on an externally pressurized cylindrical shell." [7]

Amazigo and Budiansky [347] provide a unified analysis in which they derive asymptotic formulas for the maximum load-carrying capability λ_s of axially compressed cylinders with axisymmetric imperfections of either the modal or random or local form. The formulas are written in very similar ways in terms of an appropriate measure η of the imperfection. These formulas are:

For a modal imperfection [of the type in Eq. (119)]:

$$[2(1 - \lambda_s/\lambda_c)]^2 = 2(3)^{3/2}(\lambda_s/\lambda_c)\eta \quad (128)$$

where

$$\eta = 2\Delta(1 - \nu^2)/\ell \quad (129)$$

For a random imperfection (over entire cylinder length):

$$[2(1 - \lambda_s/\lambda_c)]^{7/4} = 2(3)^{3/2}(\lambda_s/\lambda_c)\eta \quad (130)$$

where

$$\eta = \Delta(1 - \nu^2)/(2\ell)^{1/2} \quad (131)$$

For a local imperfection [of the type in Eq. (123)]:

$$[2(1 - \lambda_s/\lambda_c)]^{3/2} = 2(3)^{3/2}(\lambda_s/\lambda_c)\eta \quad (132)$$

where

$$\eta = \Delta(1 - \nu^2)^{1/2}/2 \quad (133)$$

In Eqs. (130- 133)

$$\Delta \equiv \left| \int_{-\frac{\ell}{2}}^{\frac{\ell}{2}} w_0(x) e^{ix} dx \right| \quad (134)$$

and

$$\ell \equiv q_0 L/R \quad (135)$$

with q_0 given by Eq. (107). Fig. 265 shows how the buckling load λ_s/λ_c varies with η in each of the three cases.

Cylinders with Internal Pressure: Hutchinson [340] calculated the maximum load-carrying capability of isotropic axially compressed cylindrical shells with various amounts of internal pressure. His numerical results, some of which are shown in Figs. 266 and 267, are based on Eqs. (110) with terms of order $\bar{\xi}\xi^2$, $\bar{\xi}^2\xi$, and ξ^3 neglected. The buckling load $\lambda_M = N_{CR}/N_{CL}$, with N_{CL} given by Eq. (111), corresponds either to collapse as shown in Fig. 260 or to bifurcation as shown in Fig. 261, depending on whether or not the nonsymmetric imperfection component $\bar{\xi}_2$ is present.

In Fig. 266(a) the combinations of $\bar{\xi}_1$ and $\bar{\xi}_2$ are such the unpressurized cylinder buckles at $\lambda_M = 0.7$, and in Figs. 266(b,c) the unpressurized cylinder buckles at $\lambda_M = 0.5$ and $\lambda_M = 0.3$ respectively. It is clear from the results that the asymmetric imperfections are smoothed out by the pressure, whereas the axisymmetric ones are not. If $\bar{\xi}_1/\bar{\xi}_2$ is small, λ_M

almost attains the classical value when \bar{p} is near unity. If, however, the initial imperfection is purely axisymmetric, the buckling load is much less influenced by internal pressure, as indicated by the curves for $\bar{\xi}_1/\bar{\xi}_2 = \infty$.

Figure 267 shows comparisons between the theory of Hutchinson [340] and tests on Mylar cylinders by Weingarten, Morgan, and Seide [364]. Because Mylar can undergo fairly large strains before deforming plastically, Weingarten et al. were able to perform a series of buckling tests on each specimen with increasing internal pressure. Hutchinson comments on the comparisons between test and theory [340]:

"Figure 267 presents two typical test series and two theoretical curves chosen from Fig. 266 which best fit the experimental data. Weingarten et al. did not report any information with respect to either the form or magnitude of the imperfection which would permit us to assign values to $\bar{\xi}_1$ and $\bar{\xi}_2$. Certainly the imperfection representation (106) assumed in the analysis could represent the true imperfection only in an average sense; and especially for $\bar{p} < 1$, a more exact description would require additional asymmetric terms. Nevertheless, the trends of the present theory are very much like the experimental trends, and the experimental results can be reproduced by an appropriate a posteriori choice of $\bar{\xi}_1$ and $\bar{\xi}_2$."

"The radius-thickness ratio of the previously mentioned tests ranged from 200 to 2000, with the maximum load of the unpressurized shells

ranging from about 0.6 of the classical value at $R/t = 200$ to 0.3 at $R/t = 2000$. This R/t dependence is most readily interpreted in light of the present analysis by associating larger imperfections (relative to the shell thickness) with larger values of R/t . Indeed, it seems reasonable that such would be the case."

Judging from the results presented, the relative amount of the axisymmetric imperfection is small as compared to the asymmetric imperfections in the Weingarten et al. test specimens. This is particularly the case for specimen 100.2, and the buckling load is only slightly below the classical value for $\bar{p} > 1$. Included in Fig. 267 are data from a series of tests on axially loaded, pressurized aluminum cylinders performed at the Distance Velocity Laboratory (DVL) and reported by Thielemann [365]. In this series of tests, new specimens had to be used for each test; and although the radius and thickness were unchanged, there was undoubtedly some variation in initial imperfections from specimen to specimen, as indicated by the data scatter. The important feature of these tests is that the buckling load remains well below the classical value for values of the pressure parameter well above unity. Axisymmetric initial imperfections are strongly suspected." [340]

Axially Compressed Cylindrical Panels: Koiter [366] performed an asymptotic post-buckling analysis of narrow, long cylindrical panels simply supported on the longitudinal edges. If the panel is sufficiently narrow the bifurcation stress is given by

$$\sigma_c = \frac{E\pi^2 h^2}{3(1 - \nu^2)b^2} (1 + \bar{\theta}^4) \quad (136)$$

in which the important panel "depth" parameter, $\bar{\theta}$, is

$$\bar{\theta} = [12(1 - \nu^2)]^{1/4} b / [2\pi(Rh)^{1/2}] \quad (137)$$

The geometrical parameters in Eqs. (136) and (137) are shown in Fig. 268(a), with simple support conditions presumed to exist along adjacent stringers. Figure 268(b) displays load-end-shortening curves for panels with various depths. The post-bifurcation slope for $\bar{\theta} = 0$ corresponds to that of a flat plate (see Fig. 223), and as $\bar{\theta}$ increases this slope decreases. Critical loads on panels with $\bar{\theta} > 0.64$ are sensitive to imperfections, with this sensitivity increasing toward the value for a complete cylindrical shell as $\bar{\theta}$ increases, as shown in Fig. 268(c) and (d). These plots (c,d) correspond to panels with initial imperfections in the form of the classical buckling mode with amplitude 10% of the panel thickness.

Stephens [367] extended Koiter's analysis to include internal pressure and finite torsional stiffness of the stringers at the panel longitudinal edges. Figs. 269 and 270 exhibit results from Stephens' treatment, which agrees with Koiter's [366] for internal pressure $p = 0$ and stiffener torsional rigidity parameter $\gamma = 0$. The dimensionless critical axial stress is normalized with respect to the classical buckling stress of a complete cylindrical shell with the same R/t as the panel. The maximum load-carrying capability λ_s of imperfect panels can be calculated by insertion of the

imperfection sensitivity parameter b into Eq. (75). As expected, both internal pressure and stringer torsional rigidity reduce the sensitivity of the axial buckling load to initial geometric imperfections in the form of the classical bifurcation mode.

Axially Compressed Oval Cylinders: In the chapter on nonlinear collapse is given an example of buckling of an oval cylinder subjected to uniform axial compression. Load-deflection curves for perfect and imperfect oval cylinders are exhibited in Fig. 57. These results were obtained by "brute force" from a two-dimensionally discretized model analyzed with the STAGS computer program [48]. This problem poses a special difficulty for the analyst because the maximum load-carrying capability occurs at an equilibrium state that is not in the neighborhood of the initial bifurcation point, and the deformations at this far post-buckled state do not at all resemble the classical bifurcation mode. Figure 271 shows schematically load-end-shortening behavior for three values of eccentricity B/A : Figure 271(a) corresponds to $B/A = 1.0$ or near 1.0, Fig. 271(b) corresponds to $B/A < 1.0$, and Fig. 271(c) corresponds to $B/A \ll 1.0$. Kempner and Chen [368] studied the far post-buckling range in 1964; Hutchinson [249] performed an asymptotic Koiter-type post-bifurcation analysis in 1968; and Kempner and Chen [248] used a perturbation method to obtain load-deflection curves in the near post-buckling region while retaining the capability to predict equilibrium states in the far post-buckling regime in 1968.

Figures 272 and 273 show some of Hutchinson's results from the asymptotic treatment. In Fig. 272, Mode I indicates buckling which is symmetrical

about the end of the minor axis; Mode II indicates anti-symmetry about this point. Figure 207 displays typical bifurcation modes of Types I and II predicted from an analysis with BOSOR4 [14] in which an oval cylinder is modeled as a torus. Figure 273 shows Type I modes predicted by Hutchinson [249] for various B/A . The quantity R_0 is the radius of an "equivalent cylinder", that is, a cylinder with perimeter equal to the perimeter of the oval cylinder. R_B is the radius of curvature at the end of the minor axis B . Figure 272 shows that flatter oval cross sections are less imperfection sensitive than are circular-cylinder-like geometries, a result which follows intuitively from the post-buckling behavior of axially compressed cylindrical panels exhibited in Fig. 268: the flat oval cylinder resembles two cylindrical panels placed opposite one another.

Axially Compressed Stiffened and Composite Cylindrical Shells: Numerical Results

Asymptotic Post-Buckling Analysis of Axially Stiffened Cylinders: The results shown in this section were derived by Budiansky and Hutchinson [305] and their coworkers [345, 346] from specialization of Koiter's asymptotic theory [15, 298, 303, 304]. The theory is summarized in the discussion associated with Eqs. (81) - (103). Budiansky and Hutchinson [305], in reporting on the work of Hutchinson and Amazigo [345], wrote in 1966:

"There has been much interest recently in the exciting rediscovery of van der Neut's early theoretical observation [369], now well

confirmed by tests, that outside stringers can be much more effective than inside stringers in stiffening a circular cylinder against buckling under axial compression. It has been suggested occasionally that classical theories of buckling should be reliable for the quantitative prediction of the buckling loads of stiffened cylinders, regardless of whether the stiffeners are inside or outside. Recent calculations [345], however, have shown this not to be so, and an example is given in Fig. 274 for a simply supported cylinder. If torsional stiffness of the stringers is neglected, three parameters are needed to characterize the stiffening. These are the area ratio A_s/dt ; the bending stiffness ratio EI_s/Dt ; and the eccentricity ratio $(1 - \nu^2)^{1/2}(s/t)$ where s , the distance from the skin center line to the centroid of the stringer, is considered to be positive for outside stiffening. The values chosen for these nondimensional parameters in the present example correspond to only moderately heavy stiffening and are shown in Fig. 274. The curves at the top of Fig. 274 give, as a function of Z , the buckling load per unit circumference of the stiffened cylinder divided by the corresponding quantity for the unstiffened cylinder, and were calculated on the basis of "smeared-out" stiffener properties. These results imply the superiority of outside over inside stringers. This conclusion, however, clearly must be tempered by the results for the postbuckling coefficient b which show that the cylinder with outside stiffening generally is much more imperfection-sensitive than the one with inside stiffening. It should be emphasized that the coefficient b in this figure still is defined with respect to buckling displacements normalized by the skin thickness

and not by any larger effective thickness of the shell-stringer combination. Consequently, over a substantial range of Z in the vicinity of 100, it appears that the effects of initial imperfections in reducing the strength of cylinders with outside stringers below the theoretically predicted classical buckling loads would be by no means negligible. On the other hand, it is interesting to note that in the range of high Z above 1000 both inside and outside stiffeners induce quite comparable imperfection-sensitivity, and so the benefits of outside stiffening would appear to be quite dependable in this range. In any event, the most important conclusion to be drawn is that, without supporting evidence, either experimental or theoretical, it would be incorrect to assume that classical buckling theory is adequate for the prediction of the buckling strength of stiffened cylinders under axial compression, especially if the stiffening is on the outside." [305]

The results of Hutchinson and Amazigo [345] are based on use of the membrane prebuckling state. Hutchinson and Frauenthal [346] extended the treatment of [345] to account for nonlinear prebuckling behavior and barreling of the cylinder generator [$R_x \neq 0$ in Eq. (83)]. Some of their results are given in Table 27 and Figs. 275 - 278.

Figure 275 shows the buckling load, the imperfection-sensitivity parameter \bar{b} [Eq. (103)] and the initial slope θ of the load-end shortening curve [Eq. [101)] as functions of the length parameter Z for a cylinder which

is both simply supported and loaded at the skin middle surface. The same parameters are displayed in Fig. 276 for a completely clamped cylinder. Numerical data from which these figures were plotted are given in Table 27 along with data for other quantities such as b , nL/R and θ_C^0 , the slope of the prebuckling load-end shortening curve at the critical load. The stringer parameters are $EI_s/Dd_s = 100$, $A_s/d_s t = 1$ and $e_s/t = \pm 6$. To emphasize the role of stiffening, Hutchinson and Frauenthal normalized the buckling load of the stiffened shell $(P_C)_{\text{stiff}}$ by the "classical" buckling load of a long unstiffened cylinder with the same radius R and skin thickness t .

Inclusion of nonlinear prebuckling effects does not alter the conclusions demonstrated in Fig. 274 that location of the stringers on the outer surface of the shell enhances the resistance to buckling but simultaneously increases the sensitivity to initial geometric imperfections, at least over some of the range of Z . The shell considered in Fig. 275 is identical to one of the examples analyzed in Ref. [345]. A comparison of the two sets of results demonstrates that prebuckling deformations must be correctly accounted for if accurate quantitative values are to be obtained. However, the trends indicated by the simpler analysis of Reference [345] are unchanged.

For clamped shells, Fig. 276 indicates that the imperfection sensitivity of externally stiffened shells as measured by \bar{b} diminishes steadily as Z becomes large. In contrast, however, the initial slope θ of the post-buckling load-end shortening curve is very negative, which suggests that buckling of a nearly perfect shell will not be gradual even under prescribed end displacement though the sensitivity to imperfections is very low. This example reveals that \bar{b} and θ must in general be regarded as measures of two

different characteristics of a structure. The parameters characterizing the shell in Fig. 276 correspond quite closely to some of the test specimens discussed by Card and Jones [370]. The values of Z associated with these specimens were well above 1000, and the buckling behavior of the stiffened cylinders seems to be consistent with the theoretical prediction of catastrophic buckling under prescribed end displacement coupled with relatively low imperfection sensitivity.

The simply supported cylinders discussed in connection with Fig. 275 were assumed to be supported at the skin middle surface with the axial load acting through the skin middle surface as well. Therefore, the axial load induces an end moment about the effective centroid of the skin-stiffener combination. In the case of the internally stiffened shells this moment induces a compressive hoop stress which tends to lower the buckling load. If the inside-stiffened cylinders were supported at the centroid of the stringers, then the prebuckling moment would have the opposite effect. Examples of this effect are given in Figs. 128- 132.

In Fig. 277 is presented an example which illustrates the extent to which the load eccentricity influences the initial postbuckling behavior. The internally stiffened shell marked "loaded at skin centroid" is the same as that considered in Fig. 275. The curves labeled "loaded at stringer centroid" are for the same shell but, as discussed above, simply supported at the centroid of the stringers. Loading eccentricity is clearly a very important factor in determining the buckling load particularly in the lower range of Z . At the same time, the imperfection sensitivity and the tendency for catastrophic buckling go up sharply along with the buckling load. This is

a common trend in shell buckling: design changes which raise the bifurcation buckling load of the perfect shell without increasing the amount of material tend also to increase the sensitivity of the critical load to initial geometric imperfections. We have seen this phenomenon in the case of optimization (Figs. 238- 244) and will see it again in a following section on buckling of axially compressed cylindrical shells made of laminated composite material.

Figure 278 shows the effect on bifurcation buckling and early post-buckling behavior of a small barreling of the cylinder. The usual quantities are plotted versus the shell rise parameter $8[1 - \nu^2]^{1/2}H/t$. Even slight barreling, corresponding to a rise at the equator of only several skin thicknesses, has a pronounced effect on the buckling load.

The externally stiffened shell is a good deal more imperfection-sensitive than the internally stiffened one in this example when neither is barreled. Any amount of barreling seems to diminish the sensitivity of the externally stiffened cylinder, while it increases the sensitivity of the internally stiffened one over the range in which its buckling load rises rapidly with increasing barreling. However, once the barreling is sufficiently large to cause little further increase in the classical load, then even greater barreling seems to have as its main effect a decrease in the imperfection sensitivity. This is an example which is counter to the trend just discussed, that design changes which tend to raise the bifurcation buckling load also increase the imperfection sensitivity.

As a conclusion to their study, Hutchinson and Frauenthal wrote [346]:

"In general, stiffening lowers imperfection sensitivity. Some tests on carefully prepared cylinders with moderately heavy stiffening suggest that loads close to those predicted for the perfect structures can be obtained, although it is not entirely clear what boundary conditions actually have been enforced in a number of these tests [153], [371]. More lightly stiffened cylinders show much greater discrepancies between predictions for the perfect shells and tests [153]. Recently the assertion has been made to the effect that the classical buckling analysis should adequately predict the actual buckling loads of cylindrical shell structures with practical levels of stiffening [372], [373]. The present results suggest that perhaps such a blanket assertion may be incautious until further studies and tests to determine optimal configurations of stiffening, barreling, etc., have been carried out. This note of caution seems to be further justified since catastrophic buckling has been observed in a number of the tests reported in the recent literature." [346]

Laminated Cylindrical Shells Made of Composite Material: When composite materials as opposed to metals are used in plate and shell structures, the following questions arise:

- 1) Metal plates, stiffened shells, and shallow cylindrical panels with supported edges can sometimes carry loads considerably in excess of the lowest bifurcation buckling load. The skin may buckle locally, transferring its load to adjacent structural elements. Examples include axially compressed oval cylinders (Fig. 57), the pear-shaped cylinder (Fig. 58), and stiffened panels with oversized stringers (Fig. 243). In view of the brittleness of composite materials, will designs which permit local buckling remain feasible?
- 2) Are cylinders of composite material (with anisotropy and membrane-bending coupling) more or less imperfection sensitive than isotropic cylinders?
- 3) Will the actual size of typical geometric imperfections in practical applications be more or less severe than they are in metal cylinders?
- 4) Do other types of imperfections, such as voids and delaminations affect the buckling load for structures made of composite material?

A number of publications attempt to answer the question of whether cylindrical shells of composite material are more or less sensitive to small geometric imperfections than are isotropic cylinders. Use of a nonlinear analysis [374], Koiter's general theory [375], and Koiter's special theory [376] indicate that in comparison to isotropic cylinders, composite cylinders may be somewhat less sensitive to geometric imperfections. Also, in keeping with

the trend mentioned above, it is clear that cylinders with close to optimum fiber orientation are most sensitive. This is illustrated by Figs. 279 and [280]. Other results for buckling of composite cylinders are shown in Figs. 144- 146.

The possibility remains that composite cylinders, while less sensitive to imperfections, as manufactured display more severe imperfections and therefore possibly more severe knockdown factors. Additional observations of experiments and measurements on practical structures are required before this question can be satisfactorily answered. The possibility must be faced that the composite material plates and shells contain flaws of other types than those that affect isotropic cylinders. It does not seem likely that delaminations will pass undetected through any reasonable inspection if they are large enough to cause the type of separate buckling that is discussed in [377]. However, smaller delaminations will still reduce the stiffness of the shell. Although the results of the bulk of test data seems to be reassuring, the fear that repeated loading can cause a growth of such flaws is not completely dispelled.

A final evaluation of the state of the art must, of course, be based on results from laboratory tests and from the experience acquired by use of composite material in structural applications in the past. Many experimental results on the buckling of composite material plates and shells have been presented over the last few years. In general, they tend to indicate that the theory for composites is approximately on a par with the theory for metal shells with

respect to its reliability. It is prudent to assume, however, that quality control may be better for laboratory test specimens than for mass-produced structural components. The literature scanned during a recent evaluation of the state-of-the-art [378] contains little information about the performance of actual hardware.

In Ref. [34] a procedure is presented for calculation of a lower bound to the buckling load. This procedure, to be described in more detail later, is based on Koiter's special theory [343] and the assumption that cylinders with the same effective radius-to-thickness ratio, $(R/t)_e$, have identical dimensionless amplitudes of axisymmetric imperfections when these imperfections are expressed as a percentage of the wall thickness of an equivalent isotropic shell with the same wall radius of gyration as that of the composite cylinder. Predictions with use of this method were compared in 1970 to the test results on composite cylinders available at that time. All the test specimens failed above the prediction by this lower-bound method. However, a comparison shows that the procedure is only slightly less conservative than direct application of the knockdown factor for the equivalent isotropic cylinder with the same $(R/t)_e$. A similar evaluation of results obtained in later experimental investigations would be of value. As of this writing there is little reason to recommend different knockdown factors for cylinders of composite materials under axial compression than those chosen from charts such as Fig. 258 for the equivalent isotropic cylinder. For cylinders in torsion or external pressure, a knockdown factor of about 0.8 seems to be appropriate (see [172]). For fairly wide cylindrical panels (or local buckling between stiffeners of complete cylinders) the results in Ref. [379]

indicate that knockdown factors similar to those for complete cylindrical shells must be used. Of course, for narrower panels the situation is more favorable, as has just been shown for isotropic panels (Figs. 268, 269): Sufficiently narrow panels of isotropic material are able to carry loads above the critical load. Due to brittleness, such use must be further tested before it can be recommended for the design of panels made of composite materials.

It must be noted that in a few experiments extremely low buckling loads were obtained and were discarded as not being representative. It is possible that similar test results went unreported in other cases. While test results generally support the use of composite materials in stability-critical structural components, some doubts remain and additional research is advisable. This is particularly true if composite materials are to be used at elevated hygrothermal conditions. The effects of the viscoelastic nature of the matrix in these applications appears to be essentially unexplored. Such special problems as nonlinear stress-strain curves for shear or different moduli in tension and compression seem to have little effect on the critical load. However, more research should be devoted to the effects of transverse shear and certainly additional experimental results are most welcome. Finally, the development of methods for nondestructive testing, possibly based on the Southwell plot (see [379], for example), may eventually allow the designer of composite shells to sleep well at night.

Calculation of Load-Carrying Capability Based on Measurements of Imperfections

In the applications described so far the imperfection has been assumed either to be proportional to the buckling mode or to be a known localized disturbance,

usually an axisymmetric dimple of deterministic form. Árbocz, Babcock, Sechler, and their coworkers at the California Institute of Technology [339] have developed techniques for measuring cylindrical shells and generating double Fourier series representations of the imperfections. Figure 281 (a) shows typical imperfection fields measured for a stringer-stiffened shell a ring-stiffened shell, and a monocoque shell. Figure 281 (b) shows the surface condition at axial loads about ten percent below the failure loads. Using a nonlinear analysis based on the Kármán-Donnell equations (104) and (105) with imperfections and incremental normal displacement of the forms given by Eqs. (112) and (113), respectively, Árbocz, et al [339] calculated maximum loads λ_s which generally explain approximately 60% to 80% of the difference between the classical buckling load and the test load. Particularly interesting is the unexpected growth of nonsymmetric deflection patterns with long axial wavelengths in the cases of the ring-stiffened and isotropic shells. It is very likely that extension of the series expansions (112) and (113) would bring test and theory into better agreement.

Árbocz and Williams [380] carefully measured a 10-ft. diameter stiffened cylinder photographed in Fig. 282(a). The measured imperfection field is shown in Fig. 282(b). Calculating collapse loads from the theory given in Eqs. (104) and (105) with Eqs. (112- 118), they concluded that the lowest predicted buckling load compares favorably with values usually recommended for the design of similar shell structures. Unfortunately, no test results are available for the 10-ft. diameter shell.

Almroth, Burns, and Pittner [34] suggest the following semi-empirical method for evaluating designs of practical cylindrical shells which may be pressurized, stabilized by an elastic core (such as a solid propellant rocket motor), stiffened, of laminated composite wall construction, and etc. An effective radius-to-thickness ratio $(R/t)_e$ is first calculated from the formula

$$(R/t)_e = [5.46(\bar{C}_{44} + \bar{C}_{55})C_{22}/(C_{11}C_{22} - C_{12}^2)]^{-1/2} \quad (138)$$

with

$$\begin{aligned} \bar{C}_{44} &= C_{44} - \frac{C_{14}^2}{C_{11}} \\ \bar{C}_{55} &= C_{55} - \frac{C_{25}^2}{C_{22}} \end{aligned} \quad (139)$$

The C_{ij} in Eq. (138) are the coefficients of the integrated constitutive law for the complex shell wall which relate the stress and moment resultants to the reference surface strains, changes in curvature and twist:

$$\begin{pmatrix} N_1 \\ N_2 \\ N_{12} \\ M_1 \\ M_2 \\ M_{12} \end{pmatrix} = \begin{bmatrix} C_{11} & C_{12} & 0 & C_{14} & C_{15} & 0 \\ C_{12} & C_{22} & 0 & C_{24} & C_{25} & 0 \\ 0 & 0 & C_{33} & 0 & 0 & C_{36} \\ C_{14} & C_{24} & 0 & C_{44} & C_{45} & 0 \\ C_{15} & C_{25} & 0 & C_{45} & C_{55} & 0 \\ 0 & 0 & C_{36} & 0 & 0 & C_{66} \end{bmatrix} \begin{pmatrix} e_1 \\ e_2 \\ e_{12} \\ \kappa_1 \\ \kappa_2 \\ 2\kappa_{12} \end{pmatrix} \quad (140)$$

The C_{ij} are given in Ref.[430] by Eqs. (85) for the general case and by Eqs. (205)-(208) for laminated composite shell walls.

Corresponding to the effective radius-to-thickness ratio $(R/t)_e$ calculated from Eq. (138), a knockdown factor ϕ is read from one of the three empirically derived curves in Fig. 258 corresponding to isotropic cylindrical shells. (Almroth, et al recommend the 99% probability curve.)

Buckling loads for the trial complex design in question are then calculated in two ways:

- (1) from a wide-column formula which includes a stabilizing contribution due to the curvature and
- (2) from a computer program based on an extended version of Koiter's Special Theory [343] which is based on the assumption that the imperfection is axisymmetric and which accounts for stiffeners, orthotropic laminated skin, elastic core, and internal pressure.

Critical Load from Wide-Column Theory: The critical axial load/length of circumference calculated from the modified wide-column formula is

$$N_{CR} = N_{WC} + \phi(N_{CL} - N_{WC}) \quad (141)$$

in which the wide-column buckling load N_{WC} is given by

$$N_{WC} = R^2 \bar{C}_{44} (\pi/L)^2 \quad (142)$$

for shells without elastic cores and

$$N_{WC} = 1.19 (R^2 \bar{C}_{44})^{1/3} [E_C / (1 - \nu_C^2)]^{2/3} \quad (143)$$

for shells with an elastic core of modulus E_C and Poisson's ratio ν_C . In Eq. (141) the second term on the right-hand-side represents the contribution due to the curvature. N_{CL} is the classical buckling load calculated from a theory such as that given in Eqs. (81), (82), and (94) with use of Table 26, but extended to include internal pressure and an elastic core. A formula for N_{CL} is given in the appendix of Almroth, Burns, and Pittner's paper [34]. The quantity ϕ in Eq. (141) is the knockdown factor read from the appropriate curve in Fig. 258 corresponding to the $(R/t)_e$ calculated for the trial design from Eq. (138). This knockdown factor is applied to the difference $N_{CL} - N_{WC}$ because only that part of the axial load is sensitive to initial imperfections, the wide-column post-buckling behavior being characterized by the curves shown in Fig. 8(a).

Critical Load from Extended Version of Koiter's Special Theory: The critical axial load/length of circumference computed from the extended version of Koiter's special theory (axisymmetric imperfection) is the lowest real root of the equation

$$N_{CR}^3 + \alpha N_{CR}^2 + \beta N_{CR} + \gamma = 0 \quad (144)$$

in which α , β , and γ are complicated formulas that depend on the geometric and material properties of the shell wall and stiffeners, the core modulus, the internal pressure, the assumed buckling pattern wave numbers in the axial and circumferential directions, and the amplitude μ and axial wavelength λ_{imp} of the axisymmetric imperfection.

The amplitude μ of the axisymmetric imperfection is determined a priori in the following way: A knockdown factor ϕ corresponding to $(R/t)_e$ is read from the appropriate curve of Fig. 258. Corresponding to this value of ϕ the results of Koiter's Special Theory for isotropic shells are used to obtain μ . Thus, the dimensionless imperfection amplitude μ is read from the lowest curve in Fig. 262 for $\lambda_1 = N_{CR}/N_{CL} = \phi$. The actual imperfection amplitude to be used for the Koiter-theory analysis of the trial design is then given by the product μt_e , where t_e is the effective thickness obtained from Eq. (138).

It is assumed in the analysis that the axial wavelength of the buckling pattern is twice the wavelength of the initial imperfection pattern. It is assumed also that the normalized imperfection amplitude μ for the equivalent monocoque cylinder is applicable to any sinusoidal pattern of imperfections whose wavelength λ_{imp} is equal to or larger than the critical wavelength λ_c for axisymmetric buckling of the perfect shell. The computer program in which the extended Koiter-type analysis is implemented first computes λ_c . (In the presence of an elastic core iteration is required.) The critical load N_{CR} is then determined from Eq. (144) for a series of imperfection wavelengths λ_{imp} until a minimum is found. The half-wavelength of the buckling pattern, which is twice that of the imperfection, is not allowed to exceed the shell length. In addition, the critical load N_{CR} is, of course, minimized with respect to the number of circumferential waves.

Formulas for the coefficients α , β , γ in Eq. (144) are given in the appendix of Ref. [34].

Design Philosophy: The design philosophy in Ref. [4.34] is based on the assumption that both the wide-column method and the Koiter theory method are conservative. Consequently, in a particular case the higher of the predictions from the two methods is used as the design critical load. The computer program which generated the results to be described next is listed in Ref. [381].

Numerical Results: In Fig. 283 comparisons between test and theory are shown for more than 250 cylinders of different types. The reference numbers correspond to the references given in the paper by Almroth et al [34]. In Fig. 283(a), the test results are compared with the critical load N_{CL} according to classical theory. Although all the theoretical results are for cylinders with simply supported edges, the test conditions are probably more likely to correspond to clamped edges. For most cases, it is believed that the influence of the edge conditions is insignificant, but there may be instances, especially for stringer-stiffened shells, in which the test results would have been considerably lower if the conditions of simply supported edges could have been realized. This is illustrated in the tables of Ref. [153] for some stringer-stiffened and some filament-wound cylinders, and it explains why three of the test results are above the classical load.

In Figs. 283(b), 283(c), and 283(d), the test results are compared with the higher of the two predictions from the wide-column formula, Eq. (141),

or the Koiter-type theory, Eq. (144). Figure 283(b) corresponds to the use of the 50 per cent probability curve in Fig. 258, while the results in Fig. 283(c) and (d) are based on use of the curves in Fig. 258 corresponding to 90 per cent probability and 99 per cent probability, respectively. It appears from Fig. 283(c) that the results based on 90 percent probability would not be entirely "safe" and that the 99-percent probability curve therefore should be recommended for design.

For pressurized cylinders, a series of test results at different values of the internal pressure was often obtained from the same test specimen. As the format of Fig. 283 is not suitable for such cases, comparisons between tests of this type and the theory summarized here are presented in Fig. 284. Additional results for internally pressurized cylinders appear in Ref. [34].

Conclusions: It is evident that the classical buckling load is not a suitable design limit for any of these classes of axially compressed cylinders.

Although it has sometimes been stated in the literature that for one type of cylindrical shell or another the classical theory would be applicable, the designer is generally more prudent and applies conservative methods. As an example, for stringer-stiffened shells the wide column load, Eq. (142), is sometimes used as a design limit and in other cases a part of the "curvature effect" is added, as recommended in Ref. [382] and given by Eq. (141). The present method is less conservative because the corresponding design critical load is either equal to or higher than that of Eq. (141). For

other cases, it is a common procedure simply to apply to the classical load N_{CL} the same reduction factor ϕ as for the infinite monocoque shell with the same effective radius-to-thickness ratio. In Fig. 285 the predictions of this simple alternative method ($N_{CR} = \phi \cdot N_{CL}$) are compared with those of the method recommended here (N_{CR} obtained from the higher of the predictions from Eq. (141) or Eq. (144)). It is seen that the latter method gives the same or higher values in all cases and that sometimes the difference is substantial.

It is clear, therefore, that the design principles recommended by Almroth, Burns, and Pittner [34] and summarized here will lead to more economic designs than the methods that are generally in use. At the same time, they should be entirely safe, since out of more than 250 test specimens of many different types every one failed at a value above the design load N_{CR} calculated from the higher of Eqs. (141) or (144). It seems that improvements may be possible through minor modifications of the method. The choice of the curves in Fig. 258 and the definition of an effective radius-to-thickness ratio may, for instance, be questioned. Although it is felt that the method recommended in [34] represents a clear advantage over present design practices, it is still an interim solution that is acceptable only because totally satisfactory methods are not available.

Imperfection Sensitivity of Cylinders Under Uniform Hydrostatic Pressure and Torsion

Uniform Hydrostatic Pressure

Monocoque Cylinders: Cylinders under uniform external hydrostatic pressure are not nearly as sensitive to initial imperfections as are cylinders under uniform axial compression. Evidence of this is contained in Fig. 25, which should be compared with Figs. 18 and 19. An asymptotic imperfection sensitivity analysis has been carried out by Budiansky and Amazigo [383]. Results from their analysis are reproduced in Fig. 286. In the upper half of the figure the classical buckling pressure p_C in nondimensional form is plotted as a function of the length parameter Z appropriate for either a simply supported cylinder of length L or a segment of length L of an infinite cylinder reinforced by rings which permit no lateral deflection but allow rotation. As in the case of the axially compressed cylinder, the initial post-buckling behavior is symmetric with respect to the buckling amplitude δ , and therefore the pressure-deflection relation takes the form

$$\frac{p}{p_C} = 1 + b\left(\frac{\delta}{t}\right)^2 + \dots \quad (145)$$

where b is plotted in the lower half of Fig. 286. In this case, the asymptotic relationship between the buckling pressure and the imperfection is

$$\left[1 - \frac{p_S}{p_C}\right]^{3/2} = \frac{3\sqrt{3}}{2} (-b)^{1/2} \left|\frac{\delta}{t}\right| \frac{p_S}{p_C} \quad (146)$$

where $\bar{\delta}$ is the amplitude of the component of the imperfection in the shape of the classical buckling mode. A wide range of test data, collected by Dow [384], is also included in the figure. Measurements of initial deflections were not made in any of these tests, so it is not possible to make a direct comparison of test and theory. On the other hand, the coincidence of the large discrepancy between test and classical predictions within the Z-range in which b is most negative bears out the imperfection-sensitivity predicted.

Hutchinson and Amazigo [345] investigated stiffened cylinders under uniform hydrostatic pressure. Figures 287 and 288 show the normalized classical buckling pressure and post-buckling coefficient b of stiffened and unstiffened cylindrical shells. The classical buckling pressure of the unstiffened cylinder is calculated by Batdorf [169]. (A different buckling parameter is used in Figs. 287 and 288, however.) The associated post-buckling coefficient of the unstiffened shell is given in Fig. 286.

Axially Stiffened Cylinders: Hutchinson and Amazigo [345] conclude that for axially stiffened cylinders under hydrostatic pressure,

"The major effect of axial stiffening is to eliminate imperfection-sensitivity in the lower range of Z. Even very light stiffening significantly diminishes the postbuckling coefficient in the range of Z in which the unstiffened cylinders are most sensitive. When the postbuckling coefficient is positive, in all likelihood, buckling will not be accompanied by

catastrophic collapse and the cylinder may be able to sustain pressures above the classical buckling pressure. The inside-outside effect of stiffening is less prominent in buckling under hydrostatic pressure than under axial compression. Over some of the range of Z , however, there is a definite advantage in outside stiffening. At the same time, the postbuckling coefficient b provides a hint, but little more, that an outside-stiffened cylinder may be more sensitive to imperfections than its inside-stiffened counterpart. Out of all this, the most important result is that the classical buckling load should be a reliable index of buckling strength in the lower range of Z ." [345]

Ring-Stiffened Cylinders: The classical buckling pressure and post-buckling coefficient of a lightly stiffened cylinder are compared with the corresponding quantities for an unstiffened cylinder in Fig. 288. In the lower range of Z the classical buckling load is higher if the rings are attached to the outside whereas the opposite occurs for larger values of Z . Judging from the postbuckling coefficient it would appear that the inside-stiffened cylinder is slightly less imperfection-sensitive in the lower range of Z than an outside-stiffened cylinder, although this effect is not sufficiently pronounced to warrant any general conclusions.

The lightly stiffened cylinder buckles into a mode that has only one half-wavelength over its length. If the amount of stiffening is increased the number of axial half-wavelengths in the classical buckle pattern may exceed

one and, in fact, may be very large depending on the stiffening and the value of Z . Classical buckling loads and imperfection sensitivity are shown for other degrees of ring stiffening in Ref. [345]. For ring-stiffened cylinders Hutchinson and Amazigo conclude in [345] that,

"The results presented (in [345]) fall short of providing anywhere near a complete picture of the initial postbuckling behavior of ring stiffened cylinders in the Z -independent range. On the other hand, it does seem reasonable to conclude that imperfections may result in fairly drastic buckling load reductions."

General Conclusions: As a general conclusion based on their analytical results, Hutchinson and Amazigo emphasize that,

"Under certain circumstances, axial stiffening may be a more efficient means of strengthening against buckling under hydrostatic pressure than ring stiffening. Comparing the results (for axially stiffened shells with those for ring stiffened shells), one notes that an axially stiffened cylinder can have a higher classical buckling pressure than a cylinder with an equivalent amount of ring stiffening. If, in addition, one takes into account the predicted insensitivity of the axially stiffened cylinder in the lower range of Z and the sensitivity of the ring stiffened specimens, then the advantage of axial stiffening is even more pronounced. Probably an optimum choice would lead to a combination of axial and ring stiffening." [345]

Cylinders Under Torsion

As seen from Fig. 27 buckling loads for cylinders under torsion are even less sensitive to initial imperfections than are cylinders under hydrostatic pressure. Budiansky [385] used Koiter's asymptotic theory to calculate initial postbuckling behavior for various boundary constraints and values of the Batdorf parameter Z . Some imperfection sensitivity is found for a range of Z below 1000. The negative postbuckling coefficient b approaches zero for larger values of Z . Comparisons between the theory of Ref. [385] and tests by Yamaki [386] are given in Fig. 289.

Imperfection Sensitivity of Spherical Shells

Introduction

We have already seen many examples of buckling of spherical shells. Figure 28 shows the post-buckled state of a complete spherical shell under uniform pressure with an interior mandrel that limits the growth of the buckles. Figure 29 shows schematically the transition from plate to shallow cap to deep cap behavior. Load-deflection curves are plotted which imply that the deeper the cap the more sensitive is the buckling pressure to initial geometric imperfections. Figure 30 exhibits a comparison of test versus theory for externally pressurized caps of increasing depth parameter $\lambda = 2[3(1 - \nu^2)]^{1/4}(\bar{H}/\bar{h})^{1/2}$, where H is the rise of the cap above its base

and h is the thickness. This comparison reinforces the tentative conclusion that the deeper (more like a complete spherical shell) the cap, the greater its imperfection sensitivity. Figure 37 gives comparisons between test and theory for more carefully fabricated specimens. The trend established by the theory is supported by the test results.

Figures 37 and 63- 68 display behavior of externally pressurized shallow and deep spherical caps with edge rings of various cross-section areas and eccentricity. In particular, Figs. 64 and 65 lead to the implication that the buckling pressure is sensitive to edge ring eccentricity.

Figures 83- 85 show buckling of spherical shell segments under axial tension, and Figs. 86 and 87 give a practical example of such instability - buckling of a large spherical tank for transporting liquid natural gas. Figures 88 and 89 show experimental and theoretical buckling modal displacements of a spherical shell with an outward-directed concentrated load.

Bifurcation buckling loads of complete spherical shells under uniform external pressure were first calculated by Zoelly [387], who assumed axisymmetric deformations throughout his analysis, and van der Neut [388], who included non-symmetric modes. Both analyses lead to a formula for the critical pressure

$$p_{CR} = 2Eh^2/(cR^2) \quad (147)$$

with the parameter c given by

$$c \equiv [3(1 - \nu^2)]^{1/2} \quad (148)$$

Experimental critical pressures, such as those shown in Fig. 30, revealed at an early date that imperfections drastically affect the maximum load-carrying capability. As in the case of early work on the cylindrical shell under axial compression, attempts were made to derive practical formulas for design based on the "minimum post-buckling load" [389, 320]. Low post-buckling loads calculated for axially compressed cylindrical shells, such as plotted in Fig. 20(b) have discouraged further attempts in this direction.

Most papers on spherical shell buckling are applied to clamped shallow spherical caps. Although the prebuckling problem is more difficult for this configuration than for the complete spherical shell, the calculation of bifurcation pressure and nonlinear collapse is easier because the lowest bifurcation load is unique and isolated from higher critical loads, and a reasonable approximation to the nonlinear behavior of imperfect shells can be obtained with fewer, simpler functions than is the case for the complete shell. Kaplan [37] gives a thorough review which will not be repeated here. Surveys are also presented by Fung and Sechler [389], Koiter [390], Hutchinson and Koiter [6] and Tvergaard [7]. The work done on initial postbuckling behavior based on Koiter's general theory [15, 298] is summarized briefly in [6] and [7].

As pointed out in the section on axially compressed cylindrical shells, the ultimate aim of all imperfection sensitivity analyses is to determine the maximum load-carrying capability (λ_s in Figs. 7 and 249; P_S in Fig. 250(a)). In the case of spherical shells the search for λ_s or P_S has been accomplished in the following ways:

- 1) Koiter's general theory [15, 298] has been specialized for the analysis of a complete spherical shell, a shallow spherical cap with a well-defined boundary condition on a parallel circle, and a shallow portion of a complete shell with a rectangular plan form but with unspecified boundary conditions, and a shell of revolution. These approaches have been taken, for example, by Koiter [390], who performed both first and second-order asymptotic post-buckling analyses of complete spherical shells; Fitch [348] and Fitch and Budiansky [391], who used Marquerre's equations [392] in polar coordinates to obtain the factor b in Eqs. (73) and (75) for clamped spherical caps with axisymmetric loads distributed uniformly over a portion of the surface; Hutchinson [393], who used shallow shell equations in Cartesian coordinates to obtain λ_s in a case for which multiple buckling modes exist at the critical load λ_c ; and Tong and Pian [394], who used a mixed finite element method for the post-buckling analysis of shells of revolution.

- 2) An axisymmetric imperfection shape has been assumed and λ_s identified as the lowest load at which either axisymmetric collapse or nonsymmetric bifurcation occurs from the axisymmetrically deformed prebuckled state. This is analogous to the approach taken by Koiter for the axially compressed

cylindrical shell [343]. It was used by Hutchinson [393], Tong and Pian [394] and Bushnell [395], who included nonsymmetric bifurcation buckling in their nonlinear analysis of the axisymmetrically imperfect shells, and by Bushnell [396], Koga and Hoff [397] and Kalnins and Biricikoglu [398], who did not.

3) A general imperfection shape has been assumed and collapse loads calculated from a "brute force" numerical analysis based on two-dimensional discretization of the structure. This is the approach used by Kao and Perrone [399].

Governing Equations for the Asymptotic Post-Buckling Analysis

The purpose in this section is to show how general equations governing the asymptotic behavior of an imperfect structure with simultaneous bifurcation buckling modes are developed. The imperfection is expressed as a series expansion of the buckling modes. Here the derivation of Hutchinson [393] is closely followed. It is based on Koiter's general theory for multimode buckling [15, 298]. The notation used here was introduced by Budiansky and Hutchinson [303] and is used in the papers [304] and [300].

Briefly, the aim of the derivation is to generate a set of simultaneous nonlinear algebraic equations, such as those for the cylindrical shell, Eqs. (110), in which the magnitude of the externally applied load λ is related to the undetermined amplitudes ξ_i , $i = 1, 2, \dots, N$ of the N simultaneous buckling modal displacements and the known amplitudes $\bar{\xi}_i$, $i = 1, 2, \dots, N$

of the N components of the initial imperfection. These equations are asymptotically exact at the bifurcation point of the perfect shell and are reasonably accurate in the early post-buckling regime. The derivation represents an application of the principle of stationary potential energy in which equilibrium of the imperfect structure is determined by setting equal to zero the first variation of the potential energy with respect to each of the independent unknown coefficients, ξ_i .

In the following, σ , ϵ , and u denote stress, strain and displacement fields, respectively. For example, for a shell of revolution σ might represent the vector $[N_1, N_2, N_{12}, M_1, M_2, M_{12}]$ in which N_1, N_2, \dots etc. are the stress and moment resultants; ϵ might represent the vector $[e_1, e_2, e_{12}, \kappa_1, \kappa_2, \kappa_{12}]$ in which e_1, e_2, \dots etc. are the reference surface strains, changes in curvature, and twist; and u might represent the vector $[u, v, w]$, in which u, v , and w are the displacement components tangential and normal to the reference surface of the shell. The magnitude of the applied load is λ , and all loads on the structure are assumed to vary proportionally.

Hutchinson [393] writes the potential energy in the compact form

$$PE = \frac{1}{2}\{\sigma, \epsilon\} - \lambda B_1(u) \quad (149)$$

The $\{\sigma, \epsilon\}$ represents the internal virtual work of the stress field σ acting through a strain field ϵ , and $\lambda B_1(u)$ is the work done on the structure by the applied force field of magnitude λ acting through a displacement field u .

Examples of the expressions of the type (149) specific to shells of revolution are given by Eqs. (79), (87), (98), and (99) in Ref. [430].

Hutchinson [393] considers structures the behavior of which can be adequately described by nonlinear strain-displacement relations of the form

$$\epsilon = L_1(u) + \frac{1}{2} L_2(u) \quad (150)$$

in which L_1 and L_2 are homogeneous operators that are linear and quadratic, respectively, in u . An example for shells of revolution is given by Eqs. (90) with (91) of Ref. [430] and below.

The stress-strain relations are assumed to be linear and may be written symbolically as

$$\sigma = H_1(\epsilon) \quad (151)$$

Equation (140) provides an example of such a relationship applicable to shells of revolution.

Let the initial imperfection be denoted \bar{u} . If there are no residual stresses associated with the initial displacement field \bar{u} , the strain consistent with the relationship (151) may be expressed in the form

$$\epsilon = \epsilon(u + \bar{u}) - \epsilon(\bar{u}) = L_1(u) + \frac{1}{2} L_2(u) + L_{11}(u, \bar{u}) \quad (152)$$

where $L_{11}(u, \bar{u}) = L_{11}(\bar{u}, u)$ is a bilinear operator of u and \bar{u} which appears in the identity

$$L_2(u + \bar{u}) = L_2(u) + 2L_{11}(u, \bar{u}) + L_2(\bar{u}) \quad (153)$$

For example, L_{11} can easily be derived for a shell of revolution with an imperfection having only a normal displacement component \bar{w} . Replacing β and ψ on the right-hand side of Eqs. (90) of Ref. [430] by $\beta + \bar{\beta}$ and $\psi + \bar{\psi}$, we obtain

$$\varepsilon(u + \bar{u}) = \begin{matrix} L_1(u) \\ + \frac{1}{2}L_2(u) \\ + L_{11}(u, \bar{u}) + \varepsilon(\bar{u}) \end{matrix} \quad (154)$$

$$\begin{pmatrix} e_1 \\ e_2 \\ e_{12} \\ \kappa_1 \\ \kappa_2 \\ 2\kappa_{12} \end{pmatrix} = \begin{pmatrix} u' + w/r_1 \\ \dot{v}/r + ur'/r + w/R_2 \\ \dot{u}/r + r(v/r)' \\ \beta' \\ \dot{\psi}/r + r'\beta/r \\ 2(-\dot{\beta}/r + r'\psi/r + v'/R_2) \end{pmatrix} + \frac{1}{2} \begin{pmatrix} \beta^2 + \gamma^2 \\ \psi^2 + \gamma^2 \\ \beta\psi \\ 0 \\ 0 \\ 0 \end{pmatrix} + \begin{pmatrix} \beta\bar{\beta} \\ \psi\bar{\psi} \\ \beta\bar{\psi} + \bar{\beta}\psi \\ 0 \\ 0 \\ 0 \end{pmatrix} + \begin{pmatrix} \bar{e}_1 \\ \bar{e}_2 \\ \bar{e}_{12} \\ \bar{\kappa}_1 \\ \bar{\kappa}_2 \\ 2\bar{\kappa}_{12} \end{pmatrix}$$

in which

$$\begin{aligned} \beta &= w' - u/R_1; & \psi &= \dot{w}/r - v/R_2 \\ \gamma &= \frac{1}{2}(\dot{u}/r - v' - r'v/r) \end{aligned} \quad (155)$$

and

$$\bar{\beta} = \bar{w}'; \quad \bar{\psi} = \dot{\bar{w}}/r; \quad \bar{\gamma} = 0 \quad (156)$$

The last term on the right-hand-side of Eq. (154) is to be dropped because it is assumed that the imperfection is associated with zero residual stress.

Returning to Hutchinson's derivation [393], we assume that the displacement of the structure can be expressed in the form

$$u = \lambda u_0 + \sum_{n=1}^N \xi_n u_c^{(n)} + \tilde{u} \quad (157)$$

in which λu_0 is the prebuckling displacement of the perfect structure at the load λ ; $u_c^{(1)}, u_c^{(2)}, \dots, u_c^{(N)}$ are the N linearly independent buckling modes associated with the lowest critical eigenvalue λ_c ; and \tilde{u} is an additional displacement of the form

$$\tilde{u} = \sum_{n=1}^N \sum_{m=1}^N \xi_n \xi_m u_{nm} + \text{higher order terms} \quad (158)$$

in which \tilde{u} is orthogonal to the buckling modes $u_c^{(1)}, u_c^{(2)}, \dots, u_c^{(N)}$. The orthogonality condition, in the notation given in Eq. (149), is

$$\{\sigma_o, L_{11}(u_c^{(i)}, u_c^{(j)})\} = 0 \quad i \neq j \quad (159)$$

where

$$\sigma_o \equiv H_1[L_1(u_o)] \quad (160)$$

Imperfections are taken in the form of the N critical bifurcation buckling modes

$$\bar{u} = \sum_{n=1}^N \bar{\xi}_n u_c^{(n)} \quad (161)$$

With use of Eqs. (151), (152), (157) and (161) and the orthogonality condition (159), the potential energy expression (149) can be written in the form

$$\begin{aligned} PE = & (\text{constant}) + \frac{1}{2}(\lambda - \lambda_c) \sum \xi_i^2 \{ \sigma_o, L_2(u_c^{(i)}) \} \\ & + \frac{1}{2} \{ \sum \xi_i s_c^{(i)}, L_2(\sum \xi_i u_c^{(i)}) \} + \sum \xi_i \bar{\xi}_i \lambda \{ \sigma_o, L_2(u_c^{(i)}) \} \\ & + \text{terms of order } \xi^4, \bar{\xi}\xi^2, \dots \end{aligned} \quad (162)$$

in which it is assumed that the summations span the N simultaneous critical buckling modes and

$$s_c^{(i)} \equiv H_1[L_1(u_c^{(i)})] \quad (163)$$

The additional displacement \bar{u} [Eq. (158)] does not appear explicitly in Eq. (162) because it contributes to quartic but not cubic terms in the ξ_i . The potential energy in the truncated form (162) leads to accurate prediction of the behavior of the structure provided that the amplitudes of the buckling

modal displacements ξ_i and of the initial imperfections $\bar{\xi}_i$ are sufficiently small as to insure that the terms neglected are small compared to those retained.

Equilibrium equations relating the ξ_i to the load parameter λ follow from the requirement that

$$\delta(PE)/\delta\xi_i = 0 \quad i = 1, 2, \dots, N \quad (164)$$

These equilibrium equations are obtained from Eq. (162) and are given by

$$\begin{aligned} \xi_i (1 - \lambda/\lambda_c) + \{ \sum_n \xi_n s_c^{(n)}, L_{11} (\sum_n u_c^{(n)}, u_c^{(i)}) \} \\ + \frac{1}{2} \{ s_c^{(i)}, L_2 (\sum_n u_c^{(n)}) \} / (-\lambda_c \{ \sigma_o, L_2 (u_c^{(i)}) \}) = (\lambda/\lambda_c) \bar{\xi}_i \\ i = 1, 2, \dots, N \quad (165) \end{aligned}$$

Finally Hutchinson gives an expression for the generalized load-deflection relation for a perfect structure which has multiple critical bifurcation buckling modes:

$$\frac{B_1(u)}{B_1(\lambda_c u_o)} = \frac{\lambda}{\lambda_c} - \frac{1}{2} \sum_n \xi_n^2 \frac{\lambda_c \{ \sigma_o, L_2 (u_c^{(n)}) \}}{\lambda_c^2 \{ \sigma_o, L_1 (u_o) \}} \quad (166)$$

where, from Eq. (149), $B_1(u)$ represents the generalized displacement through which the external loading system acts. For example, for a cylinder under axial compression $B_1(u)$ would be the end shortening and for a clamped spherical

cap $B_1(u)$ would be the volume displaced between the undeformed and the deformed cap. In Hutchinson's shallow shell analysis [393] the generalized displacement $B_1(u)$ is taken as the average normal deflection w_{ave} .

Application to a Shallow Spherical Segment

Classical Buckling Analysis: Hutchinson [393] uses shallow shell equations of the type (81) and (82), simplified for application to isotropic monocoque shell wall construction, to obtain the buckling modes $u_c^{(i)}$, $i = 1, 2, \dots N$. With the assumption of membrane prebuckling behavior, the shallow shell equations in Cartesian coordinates (x,y) yield a critical pressure

$$p_c = \frac{2E}{[3(1 - \nu^2)]^{1/2}} \left(\frac{h}{R}\right)^2 \quad (167)$$

associated with any combination of wave numbers k_x, k_y which satisfy the equation

$$k_x^2 + k_y^2 = q_0^2 \equiv [12(1 - \nu^2)]^{1/2} (R/h) \quad (168)$$

This critical pressure, obtained from shallow shell theory, is the same as that for a complete sphere calculated by Zoelly [387] and van der Neut [388]. It is associated with the modal normal displacement field $w(x,y)$ and stress function $f(x,y)$ given by

$$\begin{aligned} w(x,y) &= \cos(k_x \frac{x}{R}) \cos(k_y \frac{y}{R}) \\ f(x,y) &= -EhR (k_x^2 + k_y^2)^{-1} \cos(k_x \frac{x}{R}) \cos(k_y \frac{y}{R}) \end{aligned} \quad (169)$$

Post-Buckling Equilibrium Patns: Hutchinson [393] investigates the two types of modal interaction that occur in this case. If one of the modes is prismatic (varies in only one coordinate direction) only two modes interact: the prismatic mode and a single two-dimensionally varying mode. Otherwise sets of three two-dimensionally varying modes interact. The two-mode interaction leads to the greatest degree of imperfection sensitivity. Only this type will be described here. The reader is referred to Hutchinson's paper [393] for a description of three-mode interaction.

The general equations (165) can be specialized for application to shallow spherical caps modeled in the Kármán-Donnell or Marguerre W-F notation.

For the two-mode case the first generalized buckling modal vector field

$u_c^{(1)}$ is identified with the prismatic mode

$$w_c^{(1)} = h \cos (q_o x/R) \quad (170a)$$

with the associated stress function

$$f_c^{(1)} = -(ERh^2/q_o^2) \cos (q_o x/R) \quad (170b)$$

Of all the modes that satisfy Eq. (168), Hutchinson [393] shows that

only the mode with $k_x = q_o/2$, and therefore $k_y = \sqrt{3} q_o/2$, will interact with

$w_c^{(1)}, f_c^{(1)}$. Therefore, the second generalized buckling modal vector field

$u_c^{(2)}$ in Eq. (165) is identified with the set $w_c^{(2)}, f_c^{(2)}$ given by

$$\begin{aligned}
 w_c^{(2)} &= h \sin(q_0 x/2R) \sin(\sqrt{3} q_0 y/2R) \\
 f_c^{(2)} &= -(ERh^2/q_0^2) \sin(q_0 x/2R) \sin(\sqrt{3} q_0 y/2R)
 \end{aligned}
 \tag{171}$$

Hutchinson shows that use of Eqs. (170) and (171) in Eq. (165) leads to two equilibrium equations for ξ_1 and ξ_2 in terms of the external pressure p of the form

$$\begin{aligned}
 (1 - p/p_c) \xi_1 - \frac{9}{32} [3(1 - \nu^2)]^{1/2} \xi_2^2 &= (p/p_c) \bar{\xi}_1 \\
 (1 - p/p_c) \xi_2 - \frac{9}{8} [3(1 - \nu^2)]^{1/2} \xi_1 \xi_2 &= (p/p_c) \bar{\xi}_2
 \end{aligned}
 \tag{172}$$

in which the ξ_i in Eq. (172) are dimensionless modal and imperfection amplitudes normalized by the shell wall thickness h .

From Eqs. (172) it is easily seen that the early post-bifurcation state of a perfect shell ($\bar{\xi}_1 = \bar{\xi}_2 = 0$) is governed by

$$\begin{aligned}
 \xi_1 &= \frac{8}{9c} \left(1 - \frac{p}{p_c} \right) \\
 \xi_2 &= \pm \frac{16}{9c} \left(1 - \frac{p}{p_c} \right)
 \end{aligned}
 \tag{173}$$

in which $c \equiv [3(1 - \nu^2)]^{1/2}$. This behavior, sketched in Fig. 290, is characteristic of a "quadratic-type" structure and has been discussed by Koiter [15, 298] for the general case. As with the axially compressed cylindrical shell, the equilibrium load in the postbuckling regime is greatly reduced even where the buckling deflections are only a small fraction of the shell thickness; i.e., ξ_1 and ξ_2 a small fraction of unity. The curves

for the perfect spherical shell are analogous to those in Fig. 259a for the perfect cylindrical shell under uniform axial compression.

The generalized load-deflection relation valid in the initial postbuckling region is calculated with use of Eq. (166). The generalized displacement $B_1(u)$ in this case corresponds to the average normal displacement, w_{avg} , of the shallow section. Equation (166) becomes

$$\frac{w_{avg}}{w_c^0} = \frac{p}{p_c} + \frac{16}{27(1-\nu)} \left(1 - \frac{p}{p_c}\right)^2 \quad (174)$$

in which

$$w_c^0 = - \left(\frac{1-\nu}{3(1+\nu)} \right)^{1/2} h \quad (175)$$

is the prebuckling normal displacement at the bifurcation pressure, p_c .

An imperfect shell deflects in the buckling modes with the first application of external pressure. The behavior for the prismatically imperfect shell ($\bar{\xi}_2 = 0$, $\bar{\xi}_1 > 0$) is also exhibited in Fig. 290. Prior to buckling, the load increases with deflection in the prismatic ξ_1 -mode with

$$\xi_1 = \frac{\bar{\xi}_1 p / p_c}{1 - p / p_c} \quad (176)$$

until the coefficient of ξ_2 in Eq. (172b) vanishes. At this point, bifurcation occurs. Following bifurcation, the equilibrium pressure falls with deflections

occurring in both modes; thus the maximum (buckling) pressure, denoted by p^* , is the bifurcation pressure which satisfies

$$\left(1 - \frac{p^*}{p_c}\right)^2 = \frac{9c}{8} \bar{\xi}_1 \frac{p^*}{p_c} \quad (177)$$

Equation (176) represents behavior for an imperfect structure the perfect version of which is neutrally stable in the early post-bifurcation regime. (See Fig. 8a). It is this behavior upon which the construction of Southwell plots is based, more about which will be written later. The curves displayed in Fig. 290 for the prismatically imperfect shallow region are analogous to that for the axially compressed cylinder shown in Fig. 261 and labeled $\bar{\xi}_1 < 0$, $\bar{\xi}_2 = \bar{\xi}_3 = 0$. As depicted in Fig. 291, small imperfections (relative to the shell thickness) result in large reductions of the buckling pressure.

If $\bar{\xi}_1 = 0$ but $\bar{\xi}_2 \neq 0$, the maximum value of p does not correspond to bifurcation but is a limit load of the type shown in Fig. 260. The limit load p^* is obtained by substitution for ξ_1 in terms of ξ_2 from Eq. (172a) into Eq. (172b) and determination of the value of p such that $dp/d\xi_2 = 0$. One finds

$$\left(1 - \frac{p^*}{p_c}\right)^2 = \frac{27\sqrt{3}c}{32} |\bar{\xi}_2| \frac{p^*}{p_c} \quad (178)$$

This formula is also plotted in Fig. 291, from which it is seen that an imperfection in the form of the ξ_2 -mode causes a slightly greater reduction in

the load-carrying capacity than an equal imperfection in the ξ_1 -mode. Also plotted in Fig. 291 is the imperfection sensitivity curve for the case in which these modes interact. This curve is a plot of the equation

$$(1 - p^*/p_c)^2 = \frac{9c}{16} \bar{\xi}_3(p^*/p_c) \quad (179)$$

which is derived in [393]. Load-generalized-displacement curves for the two types of modal interaction are exhibited in Fig. 292.

Special Theory vs. General Theory: Figure 293 displays imperfection sensitivity curves for the shallow spherical region analogous to the curves in Fig. 262 for the axially compressed cylindrical shell. The curve labeled "General Theory" is plotted from Eq. (177); that labeled "Upper Bound Calculation" is derived from an analysis completely analogous to that described in connection with Eqs. (104-109) and Eqs. (119-122). The results represent an upper bound because the assumed displacement function is kinematically admissible, the compatibility equation is solved exactly, and the resulting expressions for the normal displacement w and the stress function f are used in the equilibrium equation, which is solved approximately by the Galerkin procedure. Hutchinson gives some details in Ref. [393].

Difficulties Encountered in the Asymptotic Analysis of Complete Spherical Shells

Although the prebuckling behavior of a complete spherical shell is simpler than that of a spherical cap, a practical asymptotic post-buckling analysis

according to Koiter's general theory [15, 298] is rendered extraordinarily difficult by the fact that a cluster of buckling modes exists at a critical pressure very slightly above the lowest critical mode. These higher modes interact with the lowest in the early post-buckling regime, leading to a requirement for a higher order asymptotic approximation than that needed for other types of shells. Figure 294 shows load-generalized-displacement curves predicted by Koiter [390] from various asymptotic analyses. The curves labeled "first approximation" are valid only for post-buckling displacements w/t of order $1/n$, where n is the order of the Legendre polynomial corresponding to the critical buckling mode (usually a high number; $n = 16$ for $R/h = 82$). The first-approximation behavior corresponding to axisymmetric post-buckling deformations was computed also by Thompson [400]. Koiter [390] found that a second-order asymptotic approximation with the assumption of an axisymmetric imperfection and axisymmetric post-buckling deformations leads to a load-deflection curve very similar to Hutchinson's two-mode case (Figs. 292, 294), but the sensitivity of the maximum pressure p^* is somewhat less, as shown in Fig. 295.

Nonlinear Numerical Studies

Figure 295 displays, in addition to imperfection-sensitivity curves predicted from asymptotic analyses (Koiter, Hutchinson), several curves generated by nonlinear numerical studies in which spherical shells and caps are assumed to contain axisymmetric imperfections of various geometries. The critical limit loads p^* are calculated by incremental analysis in which the deformations

of the shell in a shallow region are expanded in suitable series or calculated from finite difference or finite element discretization. Kaplan [37] discusses these results in more detail. Figure 296 shows the same kind of data, except that Koga and Hoff's result [397] is compared with a curve from a finite element elastic analysis by Tong and Pian [394] and an asymptotic elastic-plastic analysis by Hutchinson [313].

Figures 297, 298, and 299 show a load-generalized-deflection curve and pre- and post-bifurcation axisymmetric deformations computed by a Ritz method for a shallow cap by Bushnell [401]. The geometry of this cap ($\lambda^2 = 200$) is such that further increases in the cap depth parameter λ would not change the post-buckling behavior much. As seen from Fig. 299, an axisymmetric dimple at the pole grows as the pressure falls on the post-buckling unstable branch. This result was later confirmed by Koiter's second approximation asymptotic analysis [390], results from which are displayed in Fig. 294.

Other Asymptotic Imperfection Sensitivity Analyses

For Doubly-Curved Shells of Revolution

Spherical Caps with Axisymmetric Loading Over Part of the Surface

Results of Fitch and Budiansky [391]: A sketch of the configuration is shown in Fig. 300. Fitch and Budiansky [391], basing their analysis on the nonlinear shallow shell theory of Marguerre [392], used an asymptotic

post-buckling analysis analogous to that developed for the axially compressed, barreled cylindrical shell in Eqs. (81- 103) for which the critical buckling mode is unique. Inclusion of nonlinear and nonuniform axisymmetric prebuckling deformation, as set forth by Fitch [348], Cohen [349], and Hutchinson and Frauenthal [346] [see Eqs. (102) and (103)] is essential for accurate prediction of the initial post-buckling behavior of the perfect shell and hence for accurate prediction of its asymptotic sensitivity to initial imperfections. Fitch and Budiansky [391] calculate post-buckling factors b [Eq. (73)] and slopes α (Fig. 301) of the post-bifurcation load-generalized-deflection path at the bifurcation point of the perfect cap, but they do not give the load-carrying capacity p_s as a function of imperfection amplitude $\bar{\delta}/t$. Figures 302 - 304 show some of their results. Spherical caps with concentrated loads have stable bifurcation behavior, as indicated by positive b in Fig. 302. For a distributed load corresponding to $\bar{\lambda}$ (Fig. 303) less than 2 the post-bifurcation behavior is stable. For $2 < \bar{\lambda} \leq 4.8$ there is no bifurcation; the critical load corresponds to axisymmetric snap-through. For $\bar{\lambda} > 4.8$ bifurcation buckling occurs before axisymmetric collapse, but the coefficient b is negative, indicating sensitivity of the load-carrying capacity to initial imperfections according to Eq. (102), which Fitch [348] gives in the form

$$(1 - p_s/p_c)^{3/2} = \frac{-3(3)^{1/2}}{2} (-b)^{1/2} \left(\frac{\bar{\delta}}{t} \right) \frac{1}{p_c} \frac{\{s_{1,e_1}\}_c}{B_2(u_1)} \quad (180)$$

In Eq. (180), $\{s_{1,e_1}\}$ denotes the same operation as the term in brackets in Eq. (149), subscript c indicates "evaluated at the bifurcation point," and

$$S_1 \equiv H_1(e_1 + L_{11}(\bar{u}, u_1))$$

$$e_1 \equiv L_1(u_1)$$

(181)

$$B_2(u_1) \equiv \{\bar{\sigma}'_c, L_2(u_1)\} + \{2\sigma_1, L_{11}(\bar{u}'_c, u_1)\}$$

$$\sigma_1 \equiv H_1(e_1 + L_{11}(\bar{u}_c, u_1))$$

The H_1 , L_1 , L_2 , and L_{11} appear in Eqs. (150- 154). The terms with subscript one (except for the functionals L_1 , L_{11} , H_1) denote bifurcation buckling modal quantities; the terms with bars $\bar{\sigma}_c$, \bar{u}_c indicate prebuckling quantities evaluated at the critical load p_c ; and (') signifies the derivative of () with respect to the load parameter p . Unfortunately, Eq. (180) is not plotted for any of the examples in Ref. [391]. The critical pressures p_c plotted in Fig. 303 (ordinate for $\bar{\lambda} > 2$) and Fig. 304 are normalized by the buckling pressure of a complete spherical shell, Eq. (147).

In Fig. 303 the asymptotic limit as $\bar{\lambda} \rightarrow \infty$ corresponds to $\bar{\lambda}/\lambda = 0$, whereas in Fig. 304 the limit as $\bar{\lambda} \rightarrow \infty$ corresponds to $\bar{\lambda}/\lambda = 1.0$.

Questions Raised by the Results Shown in Fig. 304: The asymptotic results shown in Fig. 304 raise some significant questions. Superficially it appears from the asymptotic value $b = -1.19$ and the similarity of the formula (180) to that valid for a membrane prebuckling state [Eq. (146)] and the curves sketched in Fig. 250, that the critical external pressure of a spherical cap is just as sensitive to imperfections in the form of an edge buckle (see Fig. 68) as is the complete spherical shell to imperfections in the form of

an axisymmetric dimple or zonal harmonic (Hutchinson [393], Bushnell [395, 396], Koiter [390], Koga and Hoff [397], Kalnins and Biricikoglu [398], Tong and Pian [394]. and Figs. 295, 296). This may be so for extremely small imperfection amplitudes but is probably not the case for actual spherical caps with average imperfections.

Figure 305 is offered as an aid to explain why. The load-deflection curve for perfect complete spherical shells and rather deep caps (large λ) have been established theoretically by Bushnell [401], Koiter [390], and Hutchinson [393]. Such a curve, other examples of which are displayed in Figs. 292, 294, and 297, is indicated by the heavy dashed line in Fig. 305. The post-buckling portion of this curve corresponds in the analyses of Bushnell [401] and Koiter [390] to growth of an axisymmetric dimple as shown in Figs. 298 and 299, and in the analysis of Hutchinson [393] to growth of deformations in two interacting modes given by Eqs. (170a) and (171a). Also shown in Fig. 305 is a postulated post-buckling load-deflection curve of a perfect cap corresponding to growth of the critical nonsymmetric edge buckling mode.

The collapse pressure p_s of imperfect spherical caps thus depend on the shapes of the imperfections. If an imperfection resembles a flat spot or a local dimple which commonly occurs in spherical shells [402], then the value of p_s will be governed by the curve labeled "Imperfect Cap with Initial Local Dimple" in Fig. 305. Even though the bifurcation pressure p_c (cap) corresponding to edge buckling of the perfect cap is about 20% lower than the value p_c (sphere) corresponding to buckling of the perfect cap in the classical Legendre mode (Fig. 68), the collapse pressure p_s of the imperfect cap will be determined by

growth of the dimple, that is, by growth of a deformation field proportional to bifurcation modes higher than the fundamental edge mode.

If the imperfection is proportional to the nonsymmetric edge zone buckling mode, then the value of p_s will be governed by the curve labeled "Cap with Initial Nonsymmetric Edge Zone Imperfection," which displays a much smaller drop from p_c (cap) because of the postulated high minimum post-buckling pressure of the perfect cap "forced" to deform in this edge mode. A general imperfection will contain harmonics of both the dimple and the edge mode type, but it is the dimple component that essentially determines the maximum load-carrying capability p_s .

It may be that for very small imperfections the imperfection sensitivity as calculated from Eq. (180) is as great as that shown by the dashed lines in Fig. 250(b) and by the numerical and asymptotic results displayed in Figs. 295 and 296. Thus, an analyst may calculate maximum pressures p_s from the asymptotic theory of [391] which agree with tests on specimens with large depth parameters λ . However, it is felt that because of the post-buckling behavior hypothesized in Fig. 305, such agreements between test and theory would be fortuitous.

The argument just presented and Fig. 305 might be applied equally well to axially compressed cylindrical shells. With boundary conditions ignored, the asymptotic post-buckling theory leads to a prediction of extreme sensitivity to initial imperfections because of the interaction of the multiple critical modes in the post-buckling regime. However, when boundary effects are included in the model, the lowest eigenvalue becomes unique, and the asymptotic imperfection sensitivity analysis is thus based on the b-factor

method, with early post-buckling deformations being proportional to an edge zone buckling mode similar to that shown in Fig. 62. It is reasonable to expect that even if the post-bifurcation behavior in the immediate neighborhood of the bifurcation point should indicate extreme imperfection sensitivity corresponding to edge zonal buckling, very early in the post-buckling regime other modes corresponding to classical buckling (which are associated with bifurcation points some 8% to 15% higher than the fundamental edge mode) would interact in a nonlinear way with other imperfection components, leading to a substantial reduction in the maximum load-carrying capacity, p_g .

Nonsymmetrically Loaded Spherical Shell

Figures 86 and 87 show large spherical tanks used for marine transport of liquid natural gas and prebuckling and bifurcation buckling behavior of such a tank partially filled with LNG. Buckling is caused by hoop compression that develops as the doubly-curved surface is subjected to axial tension (See Figs. 83- 85). If the ship is rolling at sea, the tension loading due to the weight of the LNG will no longer be axisymmetric, as indicated in Fig. 87, but will be tilted at some angle with respect to the support, as shown in Fig. 306. For this problem Pedersen and Jensen [112] determined for several loading conditions the asymmetric, non-linear prebuckling deformations, an approximate bifurcation mode, and the corresponding initial post-buckling behavior. Good correlation with small-scale tests of such partially filled tanks was obtained by Pedersen and Jensen [403].

Initial Post-Buckling Behavior of Toroidal Segments

Hutchinson [404] applied Koiter's general theory to shells of the geometries shown in Fig. 307 loaded by lateral pressure, hydrostatic pressure, and axial tension. Consideration is restricted to segments which are shallow with respect to the axial coordinate, that is $1/r_x \ll 1$. The analysis is based on shallow shell equations of the type 81- 83 for isotropic shells and the prebuckling state is assumed to be characterized by a linear membrane state N_{x0} , N_{y0} which is uniform over the entire shell. Classical buckling loads, factors b [Eq. (73)], and initial slopes of post-buckling load-generalized-deflection paths of perfect shells are plotted for various ratios r_y/r_x (Fig. 307) as functions of the shell length parameter $Z = (1 - \nu^2)^{1/2} \ell^2/(r_y h)$. Given the imperfection sensitivity parameter b , the load-carrying capacity λ_s or p_s is calculated from Eq. (146), except for the case $r_y/r_x = 1$ and uniform hydrostatic pressure (externally pressurized spherical shell), for which the lowest bifurcation mode is no longer unique. Hutchinson's results are shown in Figs. 308- 310.

Limitations of Asymptotic Imperfection Sensitivity Theory

The analyst should be aware of the following limitations of the theory of imperfection sensitivity just described:

1. It applies only if the imperfections are of small amplitude (less than the shell wall-thickness) and only in the immediate neighborhood of the bifurcation point on the load-deflection curve of the perfect shell.

2. The assumption is made that the growth of the postbuckling displacement distribution is proportional to the lowest buckling mode of the perfect shell, if this mode is unique.

The effects of these limitations have already been illustrated by some examples. In the immediate neighborhood of the bifurcation point the post-buckling behavior of an axially compressed perfect cylinder of elliptic cross section may exhibit the same type of imperfection sensitivity as a circular cylinder. (See Figs. 57, 271, for example.) Hence, the use of the imperfection sensitivity factor b with Eqs. (75) or (146) would lead to a prediction of failure of an imperfect shell well below the bifurcation point A in Fig. 57. In its postbuckled state, however, this shell can carry more load than the bifurcation load. Therefore, a design based on conventional imperfection sensitivity theory, that is, use of the factor b from Fig. 272 in Eq. (146), might be overly conservative.

We have already emphasized a difficulty associated with stability of structures which have a unique critical bifurcation mode and other modes at somewhat higher loads that are more sensitive to imperfections with components proportional to these higher modes (Fig. 305). It seems likely that imperfection components proportional to the lowest buckling mode shape are irrelevant in these cases for determination of the true load-carrying capability of the imperfect structures. Clamped, externally pressurized deep spherical caps (large geometric parameter λ) and axially compressed monocoque cylindrical shells provide common examples of structures for which this problem arises.

Imagine the difficulty of judging the relevance of the lowest buckling loads and modes in a complex practical shell structure! One might have to calculate many buckling modes and associated imperfection sensitivity factors to determine which leads to the minimum peak load of an imperfect shell. More computer time could be involved than in a complete two-dimensional nonlinear analysis.

Bifurcation Buckling with Stable Post-Buckling Behavior

Figure 271(b,c) illustrate two types of bifurcation buckling with stable post-buckling behavior. In one (b) the initial post-bifurcation behavior is unstable, but equilibrium states at higher loads exist in the far-post-buckling regime. In the other (c) the initial post-bifurcation behavior is stable. We have already seen many examples of stable post-buckling behavior, including axially compressed columns (Fig. 9), plates (Fig. 15), and non-circular cylindrical shells (57, 58). Internally pressurized torispherical and ellipsoidal vessel heads are also stable in the far post-bifurcation regime, as described in the discussion associated with Fig. 90, 96, and 103. Additional examples are introduced in this section.

Spherical Shell with an Inward-Directed Point Load

Figures 302 and 303, which are based on nonlinear prebuckling theory and a Koiter-type asymptotic imperfection sensitivity analysis, demonstrate that spherical caps subjected to inward-directed concentrated loads exhibit stable initial post-bifurcation equilibrium paths. This result is confirmed by tests

[405, 406]. Figure 311(c) shows load-deflection curves from test [405] and theory [111] for a spherical cap with an inward-directed point load. There are points on the theoretical primary load-deflection curve labeled "Bifurcation into 4 Waves" and "Bifurcation into 5 Waves". On the test curve loads are identified for which nonsymmetry of the deflection pattern was first observed. It is easy to perform a table-top experiment to confirm qualitatively the results shown in Fig. 311: puncture a ping-pong ball to allow air to enter and leave freely. Then gently push the tip of a rather blunt pencil perpendicularly against some other point. You will notice that for small loads the dimple is axisymmetric but that as you continue to increase the load the growing dimple gradually assumes a triangular pattern. The bifurcation point corresponds to the load for which a nonsymmetric pattern begins to superpose itself on the axisymmetric dimple. By the time you notice the nonsymmetry, the shell is in its postbuckled state. Figure 311(a) illustrates such a state.

Subject to a concentrated load, the spherical shell is stable in the postbuckling regime, just as the axially compressed pear-shaped cylinder shown in Fig. 58 is stable for loads above the lowest bifurcation load. There is no sudden release of stored-up membrane energy because much of the prebifurcation strain energy has been stored in a bending mode. The gradual growth of the nonsymmetrical pattern in the point-loaded spherical cap is due to the gradual building up of the circumferential compressive stresses in a small sector fairly near the load. Predicted axisymmetric prebuckling deformations and the critical bifurcation mode for a very thin spherical shell are displayed in Fig. 311(d).

Stable Post-Buckling Shearing Deformations

Wagner Beam: Figure 312 shows part of a beam consisting of a thin shear web capped by T-shaped flanges and reinforced by vertical angle stiffeners. The beam is supported by blocks at its ends and subjected to vertical loads that cause it to bend, stressing the thin web in shear and causing the formation of diagonal buckles as displayed in Fig. 312(b). The bifurcation buckling stress of the panels between vertical stiffeners is given by

$$\tau_c = KE(t/\bar{b})^2 \quad (182)$$

in which the value of K is dependent upon the panel dimensions and the conditions of edge support, t is the thickness of the web and \bar{b} is its minor dimension. Curvature causes an increase of the critical stress levels. The formula for such cases can be written in the form (182), with the value K now depending on the ratio of \bar{b}^2/Rt where R is the radius of curvature, as well as on the other parameters.

In the design of aircraft structures, in which the requirement of low weight leads to beams with very thin shear webs, the bifurcation stress τ_c given by Eq. (182) corresponds to loads far below that at which the structure fails. Therefore, it is necessary to ascertain the stiffness and strength of the beam with the web in its post-buckled state. In this state the shearing forces at the flanges are reacted in the wrinkled web by diagonal tensile stresses acting parallel to the buckles. This diagonal tension field tends to pull the flanges together. The main purpose of the vertical angle stiffeners is to hold the flanges apart, thus maintaining the moment of inertia required to carry the bending moment in the beam. The beam with

the deeply post-buckled web is called a Wagner beam, after the man who first analyzed such a structure. He modeled the web as if it were replaced by a diagonal tension field [407].

Computerized Analysis of a Complex Stiffened Curved Panel Under Shear: The effective stiffness of buckled shear panels has traditionally been estimated semiempirically [408]. With advanced computer programs it is now possible to calculate the post-buckling behavior of such panels rigorously. Figure

313 shows a curved, stiffened panel which was analyzed with the STAGS computer program [409]. The panel was subjected to imposed displacements at the corners A and B. As the imposed displacements are increased, the six subpanels buckle but continue to carry load. Contour plots of normal displacement are shown in Fig. 313, with solid lines indicating outward and dashed lines inward buckles. The modified Newton method was used, with 198 displacement increments and 35 refactorings of the stiffness matrix being required to reach a displacement slightly in excess of the ultimate imposed displacement, which was provided as a given value. According to this numerical analysis, the effective shear moduli of the buckled subpanels ranges from 36 to 48 percent of that of the unbuckled sheet. The discrete model contained 21 rows and 58 columns, corresponding to a total of 4230 degrees of freedom and a stiffness matrix bandwidth of 478. The computer time required on the CDC 6600 was 3.73 hours.

Wrinkling of an Antenna Membrane: This problem resembles the Wagner beam model in that a diagonal tension field develops in the post-buckled (wrinkled) membrane. During the final stages of deployment of an unfurlable parabolic antenna, such as depicted in Fig. 314, the antenna mesh stretches and causes loads to be applied to the ribs. It is of interest to determine if the loads

in the mesh might cause the mesh to tear, or if the reactions where the mesh is attached to the ribs are sufficient to buckle the ribs, preventing the antenna from reaching its fully deployed state. An adequate analysis of this problem requires accounting for the forces applied by the mesh to the ribs when the mesh is partially wrinkled.

Figure 314 shows a schematic of a ribbed antenna. In the fully deployed state (a) the ribs are perpendicular to the hub. The study described in Ref. [410] treats the case of static deployment from the tangency point (b) to the fully deployed state (a). The problem is solved "backwards" . . . that is, the fully deployed state is the initial condition, and mesh loads are calculated as the ribs rotate about fictitious attachment points on the hub through an angle of 90 deg. Because all of the ribs are assumed to rotate by the same angle β , the analysis of the entire antenna can be effected by the treatment of a single gore bounded by two ribs, denoted "Rib 1" and "Rib 2."

In the fully deployed state, the mesh is prestrained biaxially. Part of the problem involves calculation of the nonuniform prestrain field, given the details about how the mesh is prestressed and cut to fit over the ribs of the fully deployed antenna. A uniform prestress before cutting to fit the deployed antenna ribs becomes nonuniform after cutting and attaching to the ribs because of the relaxation of the mesh along the free circumferences near the hub and at the extreme radius. These "boundary layer" nonuniformities in prestrain can be calculated by application of the Ritz method and linear theory.

After the nonuniformly prestrained initial state has been determined, the rib bending angle, called β , is increased in constant increments to some maximum value. For each increment in β the state of strain and stress in the mesh is determined as follows: A reasonable displacement field is assumed in the mesh, given the displacements at the rigid ribs. Strains are calculated from this displacement field and added to the now known non-uniform prestrains. From this total strain state, stresses are calculated. The principal stresses are determined. At a given radial coordinate on Rib 2, if the smallest principal stress component becomes less than zero, a wrinkle is assumed to form. This wrinkle on forming on Rib 2 is assumed immediately to propagate across the mesh to Rib 1, thereafter acting as an elastic string joining the two adjacent ribs at an angle determined by the principal stress calculation. In the wrinkled regions, the mesh cannot transmit shear stresses nor stresses normal to the axis of the wrinkles. Once a wrinkle forms, it persists for all subsequent increments in β . Furthermore, it is assumed that the wrinkle continues to join the same two points on the adjacent ribs. Thus the uniaxial strain along the wrinkle axis can easily be computed. Given the elastic properties of the equivalent string, the force applied by this wrinkle to the two adjacent ribs can be calculated.

If the smallest principal stress exceeds zero, then no wrinkle forms, and the normal and shear stresses in the mesh at the ribs can be computed. The rib moments, radial forces and shear forces at any radius can then be computed by integration of the wrinkle forces where wrinkles exist and by integration of

the normal stress resultants and shear resultants where the mesh remains smooth. Certain assumptions can be made regarding the load carrying capability of the mesh near the interfaces of smooth and wrinkled regions. Figure 315, plotted by the computer, shows an example of the predicted growth of wrinkled regions as β is increased. This behavior is exhibited by the model photographed in Fig. 316.

The Southwell Method for Determination of Buckling Loads from Non-Destructive Tests

Definition of the Method

Previously in this chapter, measured or postulated imperfections have been used in connection with asymptotic or nonlinear analysis to calculate collapse loads λ_s which are often considerably less than the critical loads λ_c calculated from "classical" theory for perfect shells. The Southwell semi-empirical method is a sort of reverse process: measurements of increasing deflections of actual imperfect shells under increasing load are used to obtain "classical" buckling loads of the perfect idealization of the real test specimen.

Southwell [411] originally proposed this clever method for extracting the theoretical buckling load P_{CR} of a perfect column from experiments on real columns with small initial imperfections. Southwell's argument is as follows: Suppose that an elastic column is not quite straight initially. Let the initial deflection of the neutral axis be denoted by \bar{w} . Then the condition for equilibrium of the bent configuration, based on small deflection theory, is given by

$$\frac{d^2 w}{dx^2} + \frac{P}{EI} (\bar{w} + w) = 0 \quad (183)$$

in which w is the additional deflection, P the axial force, and EI the flexural rigidity of the column.

Both \bar{w} and w can be represented by Fourier sine series with coefficients \bar{w}_n and w_n , respectively. Substitution of these series into the equilibrium equation (183) yields, after rearrangement of terms,

$$w_n = \frac{\bar{w}_n}{\frac{P_n}{P} - 1} \quad (184)$$

in which P_n is the n^{th} critical load for the perfect column, only the smallest of which (P_{CR}) is of practical importance. When P approaches its critical value, the first coefficient w_1 becomes the predominant component of the Fourier series expansion of w , and the deflection δ of the column at its midlength is approximated by

$$\delta \approx w_1 = \frac{\bar{w}_1}{\frac{P_{CR}}{P} - 1} \quad (185)$$

This is the equation of a rectangular hyperbola whose asymptotes are the axis of P and the horizontal line $P = P_{CR}$. Such a hyperbola is shown as the dashed line in Fig. 8(a). In terms of new variables δ and δ/P , Eq. (185) defines the straight line

$$P_{CR} \frac{\delta}{P} = \delta + \bar{w}_1 \quad (186)$$

Thus, by measuring δ and P during a column test, and plotting δ versus δ/P , one can determine the "classical" critical load P_{CR} from the slope of the best straight line fitted to the test points.

It must be emphasized that the Southwell method is based on small-deflection theory: the total deflection w is obtained by superposition of terms in the series

$$w = \sum_i \frac{\bar{w}_i}{(P_{CR}^{(i)}/P - 1)} \quad (187)$$

The use of small-deflection theory, which results from the linearizing assumption that the square of the slope, $(dw/dx)^2$, is negligible in comparison with unity, is justified provided the deflections are small compared with the overall dimensions of the structure. Therefore, the measured deflection, δ , must be small enough so that small-deflection theory remains applicable yet be large enough so that w_1 predominates.

The Southwell procedure works very well if the post-buckling characteristic of the perfect structure represents a neutral equilibrium path, as in Fig. 8(a), and if the buckling loads $P_{CR}^{(i)}$ for the different modes are well separated, as they are for the column and in many cases for flat plates. The only way to obtain disagreement between the classical buckling load for a column and the experimental load determined by the Southwell method is to misjudge boundary conditions or column stiffness EI . It seems that the Southwell plot may be useful to establish actual boundary conditions, for example.

Ariaratnam [412] used the Southwell method for predicting in-plane and out-of-plane buckling of planar frameworks, and Timoshenko and Gere [26] suggest its use in plate buckling experiments, since expressions analogous to Eq. [185] can be obtained. Horton and Cundari [413], Horton and Craig [414], and Horton, Nassar, and Singhal [415] applied the Southwell procedure to a number of shell buckling problems, including cylindrical shells under various types of loading, spherical caps, and complete spherical shells. A more extensive list of references is contained in [413]. Donnell [416] formulated the harmonic analysis outlined in Eqs. (184)-(186) for application to cylindrical shells.

Examples of Application of the Southwell Method

Figures 317- 322 and Tables 28- 30 give results of application of the Southwell method to plate and shell structures. Figures 317- 320 and Tables 28 and 29 apply to structures for which the post-buckling behavior is neutrally stable (imperfection-insensitive) and for which the classical bifurcation buckling modes are well separated. Therefore, the Southwell procedure is ideally suited for prediction of the lowest critical load of the idealized structure. Figures 321 and 322 and Table 30 apply to axially compressed cylinders, for which the post-buckling behavior is symmetrically unstable (imperfection-sensitive, Fig. 8d) and for which the classical bifurcation buckling modes are not well separated. In this case, the applicability of the Southwell method is limited to fairly small loads below the classical load and extremely careful measurements of the deflection at many points on the shell surface are required in order to obtain a good

estimate of the coefficient \bar{w}_n of the harmonic displacement field which corresponds to the critical component of the imperfection. Table 30 demonstrates that if the variation of axial load around the circumference of the cylinders (shown in Fig. 322d) is accounted for, better agreement between test and theory results.

Limitations of the Southwell Method

It is seen from comparison of the Southwell plots of the neutrally stable cases (Figs. 317- 320) with those from the unstable case (Figs. 322a-c) that the former yield more reliable estimates of the classical bifurcation buckling loads than the latter. Roorda [417] explains why:

"In essence, Southwell's method is based on the neutral characteristic. In the nonlinear theory of elastic stability the post-buckling behavior is generally not of the neutral type but takes one of three forms, depending on the nature of the nonlinearities of the system. The possible load-deflection curves are depicted in Figs. 323(b), (c), and (d), and may be described as the asymmetric, stable-symmetric, and unstable-symmetric characteristics, respectively. The corresponding load-deflection curves for an imperfect system are also indicated on the diagram. These are now not rectangular hyperbolas but have the perfect equilibrium curves as asymptotes."

". . .Typical Southwell lines corresponding to the four buckling types, namely neutral, asymmetric, stable symmetric, and unstable symmetric, are drawn in Figs. 324(a), (b), (c), and (d), respectively. The initial slope in each case is $1/P_{CR}$. For the neutral case, this slope is maintained for all values of δ . For the asymmetric case, the slope decreases as δ increases in the positive direction and increases as δ increases in the negative direction. For the stable symmetric and unstable symmetric cases, the slope decreases and increases, respectively, as $|\delta|$ increases."

"On the basis of these diagrams, it is now possible to draw certain conclusions regarding the validity of the Southwell procedure as the measured deflections become large."

"For the neutral buckling characteristic there is no problem. The asymmetric buckling characteristic is the most interesting. If in an experimental structure the imperfections are such that they generate a load-deflection curve with monotonically increasing load [positive deflections in Fig. 323(b)], then the best straight line fitted to the experimental points in a Southwell plot will have a slope which is less than the true slope at zero deflection. Hence, the Southwell procedure would overestimate the critical load. If, on the other hand, the imperfections generate a load deflection curve in which the load reaches a local maximum [i.e., negative deflections in Fig. 323(b)], then the Southwell procedure underestimates the critical load . . . A steep ideal post-buckling curve may give rise to a considerable discrepancy."

"Similarly, in the case of symmetric buckling characteristics (Fig. 323 c,d) the following conclusion is drawn. The Southwell procedure overestimates the critical load for a stable symmetric characteristic and underestimates it for an unstable symmetric characteristic, regardless of the sense of the initial imperfections. . . The sharper the initial curvature in the ideal post-buckling path, the greater the difference between P_{CR} and its estimated value." [417]

From Figs. 321 and 322(a-s) it is seen that application of the Southwell procedure to different harmonic components of the displacement fields of the axially compressed cylindrical shells yield different estimates of the critical load. While in this case it is easy to choose the Southwell line with the highest slope (lowest P_{CR}) as corresponding to the critical load, remember that the curves in Fig. 321 were generated from a rather elaborate test set up involving fairly small, easily managed laboratory specimens. To extract and reduce a similar amount of data for actual shell structures to be used in the field would appear to be impractical. It would be easier to obtain the critical bifurcation load theoretically from one of the many computer programs now available. In some cases, such as that corresponding to Fig. 322(c), the Southwell plot has a very limited linear region. The slope depends on which points the analyst decides to include when he draws the straight line.

An important question in a discussion of the Southwell method is, of what significance is the classical bifurcation load? Figure 325 shows schematically load-deflection curves for perfect and imperfect axially compressed rectangular plates. A very reliable Southwell plot can easily be obtained from

a plate with a large imperfection because the hyperbolic growth of the lateral deflection is easily measured, as seen from Fig. 317, for example. However, the bifurcation load N_{CR} is of little significance because the plate fails due to maximum strain at some axial load not at all related to N_{CR} . The plate with the small imperfection represented in Fig. 325 may fail at a load many times the bifurcation load. For example, Tennyson et al [419] report that shear panels with b/h of about 300 carried loads of at least 8 times the classical buckling loads. Some panels were cycled to five times the the bifurcation load 100 times. Test results reported by Borton [420] on buckling of shear plates with b/h of 100 show ultimate loads between two and three times the classical buckling load. A nonlinear analysis combined with Tsai's fracture criterion [421] predicts reasonably well the ultimate load of these panels; the classical bifurcation load has no significance. Consequently, the design of flat plates, especially those designed as shear webs, is not properly based on the bifurcation buckling analysis, but rather on a nonlinear postbuckling analysis.

In the case of curved shells, the Southwell procedure is most easily applied to configurations for which the load-carrying capability is not sensitive to initial imperfections. However, it often develops that for just these cases the bifurcation load is of little significance because of post-buckling strength, as with the axially compressed pear-shaped cylinder (Fig. 58), which collapses at a load more than twenty times the lowest bifurcation load. The Southwell procedure applied to imperfection-sensitive structures is difficult and probably expensive because of the closely spaced eigenmodes, all of which grow at different rates, necessitating the use of many control points in tests

and associated automated data reduction. It appears to be more practical nowadays to use a computer program to calculate P_{CR} . As mentioned previously, however, it may be beneficial to use the Southwell method in conjunction with computer programs to ascertain certain unknown or doubtful physical characteristics of a complicated structure, such as effective stiffness or boundary conditions. These characteristics would be changed in repeated runs of the computer program until the critical bifurcation load predicted by the program agrees with that from the Southwell plot.

Section 9

BUCKLING OF HYBRID BODIES OF REVOLUTION

Introduction

By "hybrid bodies of revolution" is meant configurations such as shown in Figs. 41 and 42 of Ref. [430], in which some parts of an axisymmetric structure are modeled with use of thin shell theory and other parts with use of isoparametric solid elements of revolution. Bushnell [426] has written a computer program called BOSOR6 for the stress, buckling, and vibration analysis of these configurations. Such a computer program is useful for the analysis of axisymmetric structures with local axisymmetric stress concentrations or the analysis of foam-supported shells.

The stresses and strains for neighborhoods within about one wall thickness of the junction shown in Fig. 41 of Ref. [430] cannot adequately be predicted with thin shell theory. Therefore, a small region is defined in which the domain is discretized in two dimensions. Figure 42 of Ref. [430] shows other examples in which such a hybrid model might be used for accurate prediction of local stresses and strains.

Equations governing the stress stability, and modal vibration of hybrid bodies of revolution are given in Ref. [430] [Eqs. (209) - (329)]. The analysis is applicable to bodies of revolution composed of thin shell segments, thick segments, and discrete rings. The thin shell segments are discretized by the finite difference energy method as shown in Figs. 20 and 21 of Ref. [430], and the thick or solid segments are treated as assemblages of 8-node isoparametric

quadrilateral finite elements of revolution, an example of which is illustrated in Fig. 46 of Ref.[430]. Suitable compatibility conditions are formulated through which these dissimilar segments are joined without introduction of large spurious discontinuity stresses, as described in the discussion associated with Fig. 49 of Ref.[430] . In the formulation on which the EOSOR6 computer program is based plasticity and primary or secondary creep are included. Axisymmetric prebuckling displacements may be moderately large. The nonlinear axisymmetric prebuckling problem is solved in two nested iteration loops at each load level or time step. In the inner loop the simultaneous nonlinear equations corresponding to a given tangent stiffness are solved by the Newton -Raphson method. In the outer loop the plastic and creep strains and tangent stiffness are calculated by a subincremental procedure. The linear response to nonaxisymmetric loading is obtained by superposition of Fourier harmonics (Eqs. (219) of Ref. [430]).

Summary

The purpose of this section is to show some examples in which the hybrid model is used for accurate prediction of critical loads corresponding to axisymmetric collapse or bifurcation buckling. The section opens with a study of ring-stiffened cylindrical shells under uniform hydrostatic pressure p which each ring and small regions on either side are modeled with use of 8-node quadrilaterals of revolution. Results from a hybrid model are compared to predictions such as shown in Fig. 165 in which the rings are treated as discrete line structures attached at specific nodes of the discretized shell

wall reference surface. Next, results are reported for buckling of a spherical shell embedded in an elastic foam. The case represents a model of a flotation material proposed for deep submersible vehicles.

The remainder of the section is devoted to a detailed study of an axially compressed frangible joint in a cylindrical shell and in a rocket interstage consisting of a cylindrical shell joined to the small end of a conical frustrum. These frangible joints are used for the separation of booster stages during launch of a payload into space. The stages when consumed are separated from the remainder of the vehicle at joints designed to fracture under forces generated by the explosion of a primacord contained within a cavity extending around the circumference at the plane of separation. Proper design of these joints is difficult because they must be strong enough to carry the launch loads but weak enough to fracture under the primacord explosion forces. If the separating joint is to fracture reliably, it must contain a circumferential notch or notches at the roots of which fracture initiates. These notches naturally act as stress raisers under launch loads as well. The behavior of the structure in the immediate neighborhoods of the notches cannot be predicted with use of shell theory, and the hybrid model is therefore required to obtain accurate results. Two configurations are investigated, one in which test and theory are compared for frangible joints embedded in a short cylindrical shell and the other in which a frangible joint is embedded in a cylindrical shell a short distance between this shell and a conical frustrum. The effect of a modification of the joint design on the critical axial load is demonstrated in the second case, which represents a realistic rocket interstage.

the problems described in these sections of the chapter are complicated indeed, involving bifurcation buckling, nonlinear geometric effects, elastic-plastic material behavior, and changing points of contact between parts of a specimen. These sections are written in the spirit of a tutorial--a guide-by-example for the modeling and solution of other complex nonlinear problems with similar ingredients. To be effective, such a guide must contain many details and illustrations. The intent here is to demonstrate the applicability of a rather complex but computationally efficient model to a real design problem. Particular attention is given to proper formulation of boundary conditions and contact conditions in both the nonlinear prebuckling and bifurcation phases of the problem.

Ring-Stiffened Cylindrical Shells Under Uniform Hydrostatic Pressure

In 1965 Boichot and Reynolds [212] tested to failure many ring-stiffened aluminum cylinders of the geometry illustrated in Fig. 326. The bottom part of Fig. 326 shows four analytical models of such a cylinder that can be treated with the hybrid program, BOSOR6 [426]. All of the Boichot and Reynolds cylinders failed after some of the material had yielded. Some of them collapsed axisymmetrically and others buckled nonsymmetrically. Comparisons between Boichot and Reynold's tests and predictions obtained with BOSOR5 [47] are shown in Figs. 163 - 167.

One of the specimens, denoted "20-52", buckled nonsymmetrically in a general instability mode with three or four circumferential waves. The dimensions

of this specimen are given in Fig. 326. Buckling pressures corresponding to each of the four analytical models shown in Fig. 326 were obtained with BOSOR6. In every case the predicted buckling pressure is very close to 5200 psi with a buckling mode of 3 or 4 circumferential waves. The hybrid model and prebuckling and buckling modal deformations are shown in Fig. 327. In the test the cylinder failed at 4595 psi. Here the relatively expensive hybrid model is not needed. In fact, a "smeared" ring analysis is sufficient. The discrepancy between test and theory is caused by some other factor, perhaps a nonsymmetric geometric imperfection.

Another of the specimens, denoted "25-88", had very thick rings, as shown in Fig. 328 (a). In the test this specimen collapsed axisymmetrically at a pressure of 9450 psi. At this pressure most of the material was stressed well beyond the proportional limit.

Figure 328 (b) and (c) shows the results of two analyses performed with BOSOR5 [47]. In Model 1 the three rings are treated as discrete and attached at single node points. This model yields a predicted axisymmetric collapse pressure of 8819 psi, underestimating the test pressure by about 7%. Actually the shell wall is not as free to bend axially in the neighborhoods of these ring attachment points as Model 1 allows. In the Model 2 analysis the meridional rotations at the top and bottom faces of each ring are constrained to be equal. The resulting prediction overestimates the test pressure by about 5%. The predicted axisymmetric failure modes for Models 1 and 2 are shown in Fig. 328.

A better approximation of the actual behavior in the neighborhoods of the ring-shell junctures can be obtained with a hybrid model such as shown in Fig. 329. The clamped edge area and the rings with neighboring portions of cylinder are modeled as assemblages of two-dimensional isoparametric 8-node finite elements. These are joined by means of appropriate juncture conditions to the one-dimensional shell segments. With use of this model the predicted collapse pressure is 9520 psi, less than 1% above the test value of 9450 psi. The axisymmetrically deformed shape just before collapse is shown with exaggerated amplitude in Fig. 329.

Spherical Shells Embedded in Structural Foam

Since the 8-node isoparametric element permits the prediction of thin shell behavior, as revealed in Fig. 43 of Ref. [430], problems of the type shown in 330 can be handled with BOSOR6. Figure 330(a) shows buckling of a spherical shell embedded in foam subjected to uniform pressure. Such systems are being considered for high strength, low density buoyancy materials for deep submersible vehicles.

Tests have been performed [327] for failure under external pressure of configurations such as shown in Fig. 330(b). The most likely failure modes are nonaxisymmetric buckling at the equators of the spherical shells (Symmetry Plane AA in Fig. 330(b)) and fracture due to stress concentrations in the neighborhoods where adjacent spherical shells almost touch (Symmetry Plane BB in Fig. 330(b)). Figure 330(c) shows the prebuckling deformations and Fig. 330(d) shows the buckling mode for the section of structure denoted "AA" in Fig. 330(b).

The quality of the models and results are better than they appear to be in Fig. 330 because the element shapes and displacements actually vary quadratically within each 8-node element, not bi-linearly as plotted.

Let p_{cr} be the buckling pressure of the embedded shell and p_{cl} the classical buckling pressure of the shell without the foam. In a test [427]

p_{cr}/p_{cl} was 1.135, very close to the prediction from BOSOR6 of $p_{cr}/p_{cl} = 1.130$.

The failure occurred at the equator of one of the embedded spherical shells.

Elastic-Plastic Instability of Axially Compressed Shells of Revolution with Axisymmetric Frangible Joints

Rockets for launching from earth to space are staged. The stages when consumed are separated from the remainder of the vehicle at joints designed to fracture under forces generated by the explosion of a primacord contained within a cavity extending around the circumference at the plane of separation. Proper design of these joints is difficult because they must be strong enough to carry the launch loads but weak enough to fracture under the primacord explosion forces. If the separating joint is to fracture reliably, it must contain a circumferential notch or notches at the roots of which fracture initiates. These notches act as stress raisers under the launch loads, of course. Instability of the shell with the notched joint embedded in it may result from a complicated interaction of load-path eccentricity and local plastic flow which cannot be predicted accurately unless the regions in the immediate neighborhoods of the notches are modeled with the use of solid elements of revolution. The growth of the regions in which plastic flow

occurs as the axial load is increased cannot be accurately determined from shell theory. This local plastification exacerbates the load path eccentricity caused by the notches. The increased load path eccentricity gives rise to increased local meridional rotations that precipitate axisymmetric collapse similar to that shown in Figs. 59- 61 or nonsymmetric bifurcation buckling similar to that shown in Fig. 81.

In this section two configurations are examined in some detail, one in which test results are available for comparison and the other which represents a real design problem in aerospace technology. The main purpose for inclusion of this detailed discussion of a rather esoteric application is to demonstrate modeling techniques for structural stability problems that involve a complicated interaction of structural parts, plasticity, load-path eccentricity, and configurations in which shell theory alone cannot lead to an accurate prediction of failure. Full details are presented in Refs. [428] and [429].

Comparison of Test and Theory for a Frangible Joint Embedded in a Simple Cylindrical Shell

Test Configuration and BOSOR6 Model: Figure 331 shows an experimental arrangement and joint configuration. The test panels had a nominal radius of curvature of 45 inches and were supported in such a way as to simulate a complete (360°) cylinder. Loading was applied through hydraulic rams, visible at the bottom of Figure 331. The right- and left-hand sets of rams were controlled such that axial strain gages on the inside and outside of the specimen located 2.0 inches from the lower end of the specimen ($z = 2.0$) recorded the same strain. This procedure minimizes the bending that can be

quite substantial in tests of axially compressed curved panels if such control is not used. Each curved panel was mounted on soft aluminum end plates so that the axial load was reasonably uniformly distributed along its circumference.

Three tests were performed in which the frangible joint specimens were loaded in compression to failure. In one of the tests the steel primacord tube shown in Figure 331 was omitted; in the other two tests it was present. The three specimens were all nominally symmetric about a horizontal plane passing through the roots of the two notches.

Figures 332 and 333 show one of the failed specimens and a BOSOR6 axisymmetric hybrid model of the undeformed and deformed specimen. In this particular model, the specimen is assumed to be loaded by different meridional moments, M_a and M_b , at the ends "a" and "b" as well as by axial compression V at the end "b" (Fig. 332). The magnitudes of the end moments are established so as to simulate as well as possible test conditions as measured by inner and outer fiber strain gages at points c and d and the radial deflection at the inside notch as measured by a radial deflectometer. More details on this are given in Ref. [428].

Shell theory can be used to predict the overall deformation of the structure, but not to predict the stresses and strains at and near the roots of the notches. The long solid lines in Figures 332(b) and 333(l) represent the reference surfaces of axisymmetric shell segments. The models are chosen so that shell theory leads to accurate prediction of the behavior at the four interfaces of the thin shell and solid regions shown in Fig. 4.333(b). We

know from principles set forth by St. Venant that these interfaces need be only an order of a shell thickness away from the roots of the notches.

Discretization: The BOSOR6 discretized model shown in Figures 334 and

335 consists of Segments 1 through 6 and 9 through 18, which are treated as thin shell segments and Segments 7 and 8, which are treated as solids of revolution with use of eight-node isoparametric finite elements. At the junctures between the thin shell segments and solid segments, the nodal point displacements are constrained to be related to each other such that the normal to the shell surface remains straight and normal as deformation occurs. An alternative model would be one in which the entire structure is treated with use of solids of revolution and degenerate solids of revolution (Ahmad elements, Ref.[430]). However, use of such a model would result in very high computational costs compared to those associated with the hybrid model shown here, thereby precluding extensive parameter studies.

Pads: The purpose of the very short Segments 4 and 11, shown in Figures

334(c) and 335, is to provide elastic pads which connect the steel primacord tube crowns, Segments 15 and 18, to the main aluminum cylinders, Segments 1 and 14. By changing the elastic modulus E_p of these pads, one can simulate a loose fit (small E_p) or a snug fit (large E_p). For example, if E_p is very small, very little axial load will pass through the tube. Application of axial compression V at the end "b" (Fig. 332) will cause the frangible doublers to pinch together because of the inward load path eccentricity created by the notches, flattening the tube somewhat. On the

other hand, if E_p is set equal to the modulus of Segment 1 (aluminum), more axial load will pass through the tube. In this case, whether the tube is flattened or bulges opposite the doubler notches depends on the relative importance of four forces. Those imposed at the tube crowns by the main cylinders, Segments 1 and 14, tend to cause bulging, and those imposed at the plane of symmetry of the tube [$z = 4.44$ in Fig. 334(c)] by the notched doublers tend to cause flattening.

Material Properties: The discretized model is assumed to be composed of three different materials, aluminum, steel, and a fictitious pad material, the modulus of which is adjusted for the purpose just described. The aluminum is elastic-plastic with the proportional limit at $\sigma_y = 56650$ psi and the stress-strain curve given in Fig. 347. The material of the steel primacord tube is assumed to be elastic and have significant stiffness only in the meridional direction ($E_{1\text{tube}} = 30 \times 10^6$ psi, $\nu_{\text{tube}} = 0$). Small values for the circumferential modulus ($E_{2\text{tube}} = 10^6$ psi) and the shear modulus ($G_{\text{tube}} = 3.8 \times 10^5$ psi) are specified in order to prevent local spurious "zero energy" tube buckling modes. The characterization of the tube material as being orthotropic rather than isotropic is advisable in this case because the test specimens were rather short in the circumferential direction (about 5 to 11 inches) compared to the cylinder radius (about 45 inches). The primacord tube, therefore, does not develop circumferential stresses that vary around its meridian due to distortion of its cross section, which would be the case if the tube formed a complete torus. The same argument cannot be set forth for the aluminum frangible doublers because the area of particular interest in this study includes the notches, the cross-sectional dimensions of which are very small compared to the circumferential dimensions of the test specimens.

Junction and Contact Conditions Between the Primacord Tube and the Cavity

Provided for It: The primacord tube absorbs some of the axial load and, more important, counteracts the tendency of the frangible doublers to pinch together as axial compression is increased. While a conservative joint design from the point of view of load carrying capability would result from an analysis in which the tube is neglected, such a procedure would lead to a notch configuration requiring more energy for separation, with associated higher shock loads due to primacord ignition. For this reason, and for good correlation with test results, it is essential to include the primacord tube in the model.

In the actual frangible joint the steel primacord tube is not fastened to the surrounding structure but is simply inserted into the rectangular cavity provided for it. The snugness of the fit depends on the tolerances on the parts. In the BOSOR6 model the snugness of the axial fit is adjusted as just described. The width of the cross section of the tube is assumed to match that of the cavity, as shown in Figure 335. Since the tube is not fastened to the rest of the structure, it is important to formulate proper contact conditions for stress and bifurcation buckling.

Proper contact conditions for nonlinear stress analysis are formulated in the following way: A BOSOR6 model is first set up in which it is assumed that the frangible doublers contact the thicker cylindrical Segments 1 and 14 only at the bolt center lines shown in Figure 334(b), where they are clamped. The crowns of the tube, Segments 15 and 18, are assumed to contact the pads, Segments 4 and 11, as shown in Figure 335. A small axial compression combined with moments M_a and M_b is applied and the relative

radial displacements w^* of the tube, cylinders, and doublers at points of potential contact are observed. If one segment is observed to move through another, contact is assumed to occur at the point of maximum relative w^* . A new run is made with the new contacts incorporated, and any further contact points are identified as before. Such runs are repeated until there are no further changes in the model.

Figure 335 shows the results of such a procedure. The positions of contact points depend on the snugness of the axial fit. With stiff pads ($E_p = 10^7$ psi), the tube bulges out at the equators of the toroidal tube crowns ($z = 4.16$ in. and $z = 4.72$ in., Fig. 334(c)), contacting the frangible doublers there and preventing these doublers from contacting the end of Segment 1 and the beginning of Segment 14. With soft pads ($E_p = 10^5$ psi), more axial load passes through the frangible doublers, which pinch the tube opposite the notches so that contact occurs at the end of Segment 1 and the beginning of Segment 14 instead of at the equators of the toroidal tube crowns. Figure 336 shows deformation patterns for three cases in which constant end moments M_a and M_b are included.

Bifurcation buckling is a possible mode of failure. If $M_a = M_b = 0$, the prebuckling deformation is symmetrical about a plane through the notch roots, and the critical bifurcation buckling mode corresponds to an axisymmetric deformation ($n = 0$) or nonaxisymmetric deformation ($n > 0$) in a pattern which is antisymmetric about this plane of symmetry. If $M_a \neq M_b$, the prebuckling deformation contains a component of the antisymmetric $n = 0$ bifurcation mode which grows until failure occurs; there is no axisymmetric bifurcation buckling. However, bifurcation buckling for $n > 0$ is still a possibility.

The contact conditions given in Figure 335 for bifurcation buckling are derived from inspection of the post-buckled test specimen shown in Figure 333(a). In order to predict bifurcation buckling failure, it is necessary in this case to impose different contact conditions for the nonlinear prebuckling (equilibrium) problem and the bifurcation buckling (eigenvalue) problem. It is clear from Figure 333(a) that after buckling the primacord tube remains in contact with the rest of the structure only at four points, two diametrically opposed points on each side of the structural plane of symmetry.

A detailed discussion of the boundary conditions at points (a) and (b) [See Fig. 332(b)] for the prebuckling and bifurcation phases of the analysis is given in Ref. [428] and will not be repeated here.

Numerical Results: Table 31 lists the critical axial loads per circumferential arc length for the three specimens tested and numerical results corresponding to nonlinear collapse (limit load behavior) and bifurcation buckling. Load-axial strain curves are shown in Figs. 337 and 338 for the specimens without and with the primacord tube. Also plotted are curves for models in which the notches are omitted. With the notches present, the specimen without the tube is predicted to collapse at 4300 lb/in and that with the tube is predicted to collapse at 5650 lb/in. Both of these results are within about 2% of the test failure loads.

Omission of the notches clearly changes the problem significantly for the case without the primacord tube. However, a very good estimate of the collapse load is obtained for the case with the tube. The notch plays a less important role in nonlinear collapse when the tube is present because the tube resists the tendency of the frangible doublers to pinch together.

Computer runs in which the notches are omitted cost much less than do those with the notches included because the entire model then consists of thin shell segments. Local and global matrices for thin shell segments contain many fewer degrees of freedom and integration points than do those for the eight-node isoparametric solid elements of revolution, and the assembled matrices are more narrowly banded. Therefore, in preliminary design analyses of similar frangible joints the tube should be included in and the notches omitted from the computerized models.

Figure 339 shows the predicted growth of plastic regions in the notches with increasing axial compression for the case in which the end moments $M_a = M_b = 0$ [See Fig. 332(b)]. The maximum effective strains ϵ_e at the notch roots are much less for the specimen with the tube, primarily because the tube resists the pinching motion evident in Figure 336(c) and secondarily because the tube carries approximately 19% of the axial load (with the assumption of "stiff pads").

The linear bifurcation loads listed in Table 31 are calculated for models in which the end moments M_a and $M_b = 0$. For the specimen without the tube, contact is assumed to exist at the four points E, F, G, and H (shown in Figure 337) in the prebuckling phase. As before, the critical bifurcation buckling mode is axisymmetric ($n = 0$) and antisymmetric with respect to the structural plane of symmetry through the notch roots. At $V_{cr} = 6840$ lb./in., the critical axial bifurcation load predicted from linear theory with zero M_a and M_b is much higher than the predicted axisymmetric collapse (limit) load of 4800 lb./in. with non-zero M_a and M_b .

For the specimen with the tube, the bifurcation buckling contact conditions are given in Figure 335. These conditions lead to a prediction of $V_{cr} = 5339 \text{ lb./in.}$, somewhat lower than the nonlinear axisymmetric collapse load of 5650 lb./in. The latter prediction is associated with the existence of more contact points between the tube and the doublers, which undoubtedly causes a significant part of the difference.

The model with the tube gives a lower bifurcation buckling load than that without because the effective free lengths of the doublers, which act as wide columns in axial compression, are apparently greater if the doublers contact the tube crown equators [$z = 4.16$ and 4.72 in Fig. 334(c)] than if they contact the ends of either Segment 1 or Segment 14. This result appears at first to be anomalous. However, remember that the tube is only hinged to Segments 1 and 14. Without the doublers, the two cylindrical segments and the tube, linked as implied in Figure 335, constitute a mechanism. Therefore, the contacts between the tube crown equators at $z = 4.16$ and 4.72 in Figs. 334(c) and 335 represent effective loads on the doublers rather than effective supports, and the free axial lengths of the doublers are thereby increased approximately by the distance from the ends of Segments 1 or 14 at $z = 4.0$ and $z = 4.88$, respectively, to the bolt lines indicated in Fig. 334(b), depending on the contact conditions specified for the bifurcation problem in Fig. 335.

Frangible Joint Embedded in a Complex Shell Structure

The purpose of this section is to demonstrate the applicability of the nonlinear hybrid shell-solid model to a practical aerospace design, and to

show how a proposed design modification affects the ultimate axial load-carrying capability of the joint and surrounding structure. Also demonstrated here are the technique and appropriateness of use of an equivalent axisymmetric axial load to represent a combination of axial compression, shear, and bending loads.

Structural Configuration and Segmented Model: Figure 340 shows the rocket interstage with a frangible joint similar to that displayed in Fig. 337. The manner in which the structure is segmented for analysis with the BOSOR6 program [426] is illustrated in Fig. 341. Segment 1 is an eccentrically stiffened conical frustrum, treated in the BOSOR6 model as a layered shell with layer properties derived as described in Fig. 39 of Ref.[430]. The joint region and contact conditions between the frangible doublers and Segments 5 and 16 are modeled in a manner similar to that shown in Fig. 335, except that the primacord tube is absent. The web of the large ring at the junction between the conical frustrum and the cylindrical shell ($z = 231.6$) is treated as a flexible shell branch, with its flange included as a discrete ring with dimensions indicated in Fig. 341(b). Axial load path eccentricities exist in the upper part of the cylindrical shell, as shown in Fig. 341(a). Segment 20 is made of graphite-epoxy and the rest of the structure is made of aluminum.

Certain geometrical constraints and the location of electrical equipment imposed limitations on the location of the frangible joint. The best compromise resulted in its location within the bending region in the neighborhood of the cylinder-cone junction, as demonstrated in Fig. 342. This behavior necessitates the use of the extensive model shown in Fig. 341. It is not

sufficient to study only the immediate region of the joint or of the notches in the frangible doublers in order to determine accurately the critical axial load. There are nonlinear interaction effects between the overall rotation, bending, and shearing of the joint region and the local bending of the frangible doublers due to the load path eccentricities caused by the notches. The hybrid shell-solid model is ideally suited for this analysis because extensive regions in which shell theory holds can be included in the model with relatively minor increases in computer run costs.

Substitution of Uniform Axial Compression for the Actual Loads: The actual loading on the rocket interstage consists of axial, shear, and bending components, as illustrated in Fig. 340. Figure 343 shows total load components S,M,P applied at an end of a cylindrical shell and how these loads can be converted into trigonometric harmonics of applied axial and shear stress resultants for use as input into BOSOR6. The most critical meridian is that at $\theta = 0$, where the compressive axial load is maximum. The local stresses in the notch areas are predicted very accurately by an axisymmetric analysis in which the axisymmetric compressive axial stress resultant V_0 is set equal to

$$V_0 = P/2\pi r + (M + S\lambda)/\pi r^2 \quad (188)$$

where λ is the distance from the axial station at which S is applied to the axial station at the notch. Figure 344 shows a comparison of the effective (von Mises) stress distributions through the doubler thicknesses at the roots of the notches predicted from nonlinear axisymmetric and linear nonaxisymmetric analyses with $V_0 = 1000$ lb/in, a rather small load compared to the ultimate

load. Clearly an axisymmetric loading model suffices. The advantages of the axisymmetric model are:

1. Nonlinear material and geometric effects are included in this analysis branch of BOSOR6;
2. Far fewer degrees of freedom and hence much less computer time are required for axisymmetric nonlinear analysis than for non-symmetric nonlinear analysis.

Axisymmetric Collapse of the Rocket Interstage: Figures 345 and 346 show exaggerated views of the axisymmetric deformation as the axial compression is increased to the predicted collapse load of 4400 lb./in. Failure is due to an interaction of overall large rotation of the joint region and local collapse of the outboard doubler brought about by plastic flow which at this load has spread through the entire doubler thickness near the notch root. The predicted effective strain at the notch root in this doubler is plotted for various axial loads in Fig. 347.

Effect of a Minor Design Change: Figure 348 shows the difference between an original joint design and the final configuration displayed in Fig. 341. With the original design (a) the axially loaded joint deforms in such a way that approximately 56% of the total axial load passes through the inboard frangible doubler and 44% through the outboard frangible doubler, causing the stresses at the root of the inboard notch to be higher than those at the root of the outboard notch. The changes in Segments 4 and 17 shown in Figure 348 shift more axial load to the outboard member such that the maximum stresses in the outboard member are slightly higher than those of

the inboard member. The original design (a) leads to a predicted collapse load of 4000 lb/in and the redesigned joint (b) leads to a predicted collapse load of 4400 lb/in. The .03-inch outboard shift of Segments 4 and 17 is a bit too much. A .025 shift would probably be better. The deformations in the doublers at the collapse loads of the two configurations are illustrated in Fig. 349 and the growth of the plastified regions is exhibited in Figs. 350(a) and (b).

Effect of a Steel Primacord Tube: Figure 351 shows results from a model in which a 0.035-inch-thick steel primacord tube is added to the model displayed in Fig. 341. The steel tube contacts Segments 5 and 16 in such a way that only axial displacement continuity is enforced (sliding contact). It is represented as a toroidal shell with four segments as plotted in Fig. 335. The predicted axisymmetric collapse load with the tube present is 1000 lb/in higher than with the tube absent. This result is corroborated by experiments, as demonstrated by comparison of Figs. 337 and 338.

REFERENCES

- 1 Galletly, G. D., "Torispherical shells--A caution to designers," Trans. ASME J. Engng. Industry, 81, No. 1, pp 51-66 (Feb. 1959).
- 2 Baltus, R. and Massonnet, C., "Use of computer programs BOSOR4 and 5 in the stability analysis of two civil engineering steel shell structures," in Proc. of conference, Stability of Steel Structures, Liege, Belgium, pp 609-617 (13-15 April 1977).
- 3 Bushnell, D., "Crippling and buckling of corrugated ring-stiffened cylinders," J. Spacecraft & Rockets, 9, No. 2, pp 357-363 (May 1972).
- 4 Brush, D. O., and Almroth, B. O., Buckling of Bars, Plates, and Shells, McGraw-Hill Book Company, New York (1975).
- 5 Roorda, J., "Stability of structures with small imperfections," J. Eng. Mech. Div. ASCE, 91, No. EM1, pp 87-106 (1965).
- 6 Hutchinson, J. W. and Koiter, W. T., "Postbuckling theory," Appl. Mech. Rev., Vol. 23, pp 1353-1356 (1970).
- 7 Tvergaard, V., "Buckling behaviour of plate and shell structures," Proc. 14th Int. Congr. Theor. and Appl. Mech. (W. T. Koiter, ed.) pp 233-247, North-Holland Publishing Co. (1976).
- 8 Bushnell, D., Plastic Buckling, Lockheed Missiles & Space Co., Inc. Report LMSC-D673763, April 1979, to appear in ASME PVP Decade of Progress in (1981).
- 9 Pilkey, W., Saczalski, K., and Schaeffer, H. (eds.), Structural Mechanics Computer Programs: Surveys, Assessments, and Availability, Univ. Press of Virginia, Charlottesville, Va. (1974).
- 10 Bushnell, D., "A computerized information retrieval system," pp 735-80 in [9](1974).
- 11 Cohen, G. A., "User Document for Computer Programs for Ring-Stiffened Shells of Revolution," NASA CR-2086 (1973); "Computer Analysis of Ring-Stiffened Shells of Revolution," NASA CP-2085 (1973); "Computer Program for Analysis of Imperfection Sensitivity of Ring-Stiffened Shells of Revolution," NASA CR-1801 (1971), National Aeronautics and Space Administration, Washington, D.C.

- 12 Kalnins, A., "User's Manual for KSHEL Computer Programs," (1970), available from Dr. Kalnins, Lehigh University, Pa. Also see "Free Vibration, Static and Stability Analysis of Thin Elastic Shells of Revolution," AFFDL-TP-68-144 (March 1969), Wright-Patterson Air Force Base, Ohio.
- 13 Svalbonas, V., "Numerical Analysis of Stiffened Shells of Revolution," NASA CR-2273 (1973), National Aeronautics and Space Administration, Washington, D.C.
- 14 Bushnell, D., "Stress, stability and vibration of complex branched shells of revolution," Computers & Structures, Vol. 4, pp 399-435 (1974).
- 15 Koiter, W. T., "Over de stabiliteit van het elastisch evenwicht," Delft thesis, H. J. Paris, Amsterdam; (English transl.) National Aeronautics and Space Administration, Rep. TTF-10, 1967 (1945).
- 16 Biot, M. H., Mechanics of Incremental Deformation, J. Wiley, N.Y. (1965).
- 17 Fung, Y. C., Foundations of Solid Mechanics, Prentice-Hall, Englewood Cliffs, N.J. (1965).
- 18 Washizu, K., Variational Methods in Elasticity and Plasticity, Pergamon Press, N.Y. (1968).
- 19 Green, A. E., and Zerna, W., Theoretical Elasticity, 2nd Ed. Oxford Univ. Press, London and N. Y. (1968).
- 20 Malvern, L. E., Introduction to the Mechanics of a Continuous Medium, Prentice-Hall, Englewood Cliffs, N.J. (1969).
- 21 Oden, J. T., Finite Elements of Nonlinear Continua, McGraw-Hill, N.Y. (1972).
- 22 Przemieniecki, J. S., Theory of Matrix Structural Analysis, McGraw-Hill, N. Y. (1968).
- 23 Zienkiewicz, O. C., The Finite Element Method in Engineering Science, McGraw-Hill, London (1971).
- 24 Desai, C. S. and Abel, J. F., Introduction to the Finite Element Method, Van Nostrand Reinhold Co., N. Y. (1972).
- 25 Martin, H. C. and Carey, G. F., Introduction to Finite Element Analysis: Theory and Applications, McGraw-Hill, N. Y. (1973).

- 26 Timoshenko, S. P. and Gere, J. M., Theory of Elastic Stability, 2nd ed., McGraw-Hill, N. Y. (1961).
- 27 Van Der Neut, A., Postbuckling behavior of structures, NATO AGARD Report 60 (1956).
- 28 Johnston, B. G. (Ed.), Guide to Design Criteria for Metal Compression Members, 2nd ed., Column Research Council, Wiley, N. Y. (1966).
- 29 Hoff, N. J., "The perplexing behavior of thin cylindrical shells in axial compression," Israel Journal of Technology, Vol. 4, No. 1, pp 1-28 (1966).
- 30 Donnell, L. H. and Wan, C. C., "Effects of imperfections on buckling of thin cylinders and columns under axial compression," J. Appl. Mech., Vol. 17, pp. 73-83 (1950).
- 31 Lorenz, R., "Achsensymmetrische Verzerrungen in dünnwandigen Hohlzylindern," Zeitschrift des Vereines Deutscher Ingenieure, Vol. 52, pp 1707- (1908).
- 32 Timoshenko, S. P., Theory of Elastic Stability, McGraw-Hill Book Co., N. Y. p. 439 (1936).
- 33 Singer, J. and Abramovich, H., "Vibration techniques for definition of practical boundary conditions in stiffened shells," AIAA J., Vol. 17, No. 7, pp 762-769 (1979).
- 34 Almroth, B. O., Burns, A. B., and Pittner, E. V., "Design criteria for axially loaded cylindrical shells," J. Spacecraft & Rockets, Vol. 7, No. 6, pp 714-720 (1970).
- 35 Ekstrom, R. E., "Buckling of cylindrical shells under combined torsion and hydrostatic pressure", Experimental Mech., Vol. 3, pp. 192-197 (Aug. 1963).
- 36 Harris, L. A., Suer, H. S., and Skene, W. T., "Model investigations of unstiffened and stiffened circular shells," Experimental Mechanics, Vol. 1, No. 7, pp 1-9 (1961).
- 37 Kaplan, A., "Buckling of Spherical Shells," from Thin Shell Structures, Theory, Experiment, and Design, Y. C. Fung and E. E. Sechler, eds., Prentice-Hall, Inc., Englewood Cliffs, N. J., pp 248-288 (1974).
- 38 Horton, W. H., Bailey, S. C., and McQuilkin, B. H., An Introduction to Stability, Stanford University Report version of Paper No. 219 presented at ASTM Annual Meeting, Atlantic City, N. J. (June 1966).

- 39 Carlson, R. L., Sendlebeck, R. L., Hoff, N. J., "Experimental studies of the buckling of complete spherical shells, Experimental Mechanics, Vol. 7, pp 281-288 (1967).
- 40 Lee, L. H. N., "Inelastic buckling of initially imperfect cylindrical shells subject to axial compression," J. Aero. Sci., Vol. 29, pp 87-95 (1962).
- 41 Batterman, S. C., "Plastic buckling of axially compressed cylindrical shells," AIAA J. Vol. 3, No. 2, pp 316-325 (Feb. 1965).
- 42 Sobel, L. H. and Newman, S. Z., "Plastic buckling of cylindrical shells under axial compression," Third U. S. Congress on Pressure Vessels and Piping, San Francisco, CA, June 25-29 (1979).
- 43 Sewell, M. J., "A survey of plastic buckling," in Stability (H. Leipholz, ed.), Chap. 5, pp 85-197, Univ. of Waterloo Press, Ontario (1972).
- 44 Ramsey, H., "Plastic buckling of conical shells under axial compression," Int. J. of Mech. Sci., Vol. 19, pp 252-272 (1977).
- 45 Gerard, G., "Compressive and torsional buckling of thin walled cylinders in the yield region," NACA TN 3726 (Aug. 1956).
- 46 Murphy, L. M. and Lee, L. H. N., "Inelastic buckling process of axially compressed cylindrical shells subject to edge constraints," Int. J. Solids Struct., Vol. 7, pp 1153-1170 (Sep. 1971).
- 47 Bushnell, D., "BOSOR5--Program for buckling of elastic-plastic complex shells of revolution including large deflections and creep," Computers & Structures, Vol. 6, pp 221-239 (1976).
- 48 Almroth, B. O., Brogan, F. A., and Stanley, G. M., "Structural analysis of general shells, Vol. II: User Instructions for STAGSC," Lockheed Missiles & Space Co. Rept. LMSC-D633873, Jan. (1979).
- 49 Gellin, S., "Effect of an axisymmetric imperfection on the plastic buckling of an axially compressed cylindrical shell," J. Appl. Mech., Vol. 46, pp 125-131 (1979).
- 50 Hutchinson, J. W., "On the postbuckling behavior of imperfection-sensitive structures in the plastic range," J. Appl. Mech. Vol 39, pp 155-162 (1972).

- 39 Carlson, R. L., Sendlebeck, R. L., Hoff, N. J., "Experimental studies of the buckling of complete spherical shells, Experimental Mechanics, Vol. 7, pp 281-288 (1967).
- 40 Lee, L. H. N., "Inelastic buckling of initially imperfect cylindrical shells subject to axial compression," J. Aero. Sci., Vol. 29, pp 87-95 (1962).
- 41 Batterman, S. C., "Plastic buckling of axially compressed cylindrical shells," AIAA J. Vol. 3, No. 2, pp 316-325 (Feb. 1965).
- 42 Sobel, L. H. and Newman, S. Z., "Plastic buckling of cylindrical shells under axial compression," Third U. S. Congress on Pressure Vessels and Piping, San Francisco, CA, June 25-29 (1979).
- 43 Sewell, M. J., "A survey of plastic buckling," in Stability (H. Leipholz, ed.), Chap. 5, pp 85-197, Univ. of Waterloo Press, Ontario (1972).
- 44 Ramsey, H., "Plastic buckling of conical shells under axial compression," Int. J. of Mech. Sci., Vol. 19, pp 252-272 (1977).
- 45 Gerard, G., "Compressive and torsional buckling of thin walled cylinders in the yield region," NACA TN 3726 (Aug. 1956).
- 46 Murphy, L. M. and Lee, L. H. N., "Inelastic buckling process of axially compressed cylindrical shells subject to edge constraints," Int. J. Solids Struct., Vol. 7, pp 1153-1170 (Sep. 1971).
- 47 Bushnell, D., "BOSOR5--Program for buckling of elastic-plastic complex shells of revolution including large deflections and creep," Computers & Structures, Vol. 6, pp 221-239 (1976).
- 48 Almroth, B. O., Brogan, F. A., and Stanley, G. M., "Structural analysis of general shells, Vol. II: User Instructions for STAGSC," Lockheed Missiles & Space Co. Rept. LMSC-D633873, Jan. (1979).
- 49 Gellin, S., "Effect of an axisymmetric imperfection on the plastic buckling of an axially compressed cylindrical shell," J. Appl. Mech., Vol. 46, pp 125-131 (1979).
- 50 Hutchinson, J. W., "On the postbuckling behavior of imperfection-sensitive structures in the plastic range," J. Appl. Mech. Vol 39, pp 155-162 (1972).

- 63 "MARC-CDC Nonlinear Finite Element Analysis Program," User Information Manual, Vol. 1, Control Data Corp. (1971).
- 64 Zudans, Z., et al, "Theory and User's Manual for EPACA," Franklin Institute Report F-C-30.8 (June 1972).
- 65 Bolt, S. E. and Greenstreet, W. L., "Experimental determination of plastic collapse loads for pipe elbows," ASME Paper 71-PVP-37 (1971).
- 66 Vrillon, B., Montfort, C., and Befre, J., "Experimental analysis of piping components of fast breeder reactors," Third. Int. Conf. on Structural Mechanics in Reactor Technology, Vol. 2, Part F, Paper F3/4, American Elsevier Publishing, Inc., N. Y. (1975).
- 67 Hoffman, A., Livolant, M., and Roche, R., "Plastic analysis of shell by finite element method: global plasticity model for any shapes of shells," 2nd SMiPT Conf., Berlin, Paper L6/2 (1973).
- 68 Sherman, D. R., "Tests of circular steel tubes in bending," ASCE J. of Structural Div., Vol. 102, ST11, pp 2181-2195 (1976).
- 69 Bushnell, D., "Use of BOSOR5 for the Elastic-Plastic Bending and Buckling Analysis of Pipes and Elbows," to be published (1980).
- 70 Sobel, L. H., and Newman, S. Z., "Plastic in-plane bending and buckling of an elbow: comparison of experimental and simplified analysis results," Westinghouse Advanced Reactors Div. Report WARD-HT-94000-2 (Aug. 1979); available from US-DOE Tech. Inf. Ctr.
- 71 Bung, H., Clement, G., Hoffmann, A., and Jakubowicz, H., "Piping benchmark problems--computer analysis with the CEASEMT finite element system," CEASEMT Report EMT/78/61 (Oct. 1978).
- 72 Roche, R., and Hoffmann, A., "Global plastic models for computerized structural analysis," 4th SMiPT, San Francisco, Paper, L5/5 (1977).
- 73 Skogh, J. and Brogan, F., "Collapse analysis of finite-length pipe pipe bends," Lockheed Missiles & Space Co. Rept. , Dec. (1978).
- 74 Remseth, S. N., Holthe, K., Bergan, P. G., and Holand, I., "Tube collapse analysis using finite elements," Computers & Structures, Vol. 8, pp 383-390 (1978).
- 75 Mello, R. M., and Griffin, D. S., "Plastic collapse loads for pipe elbows using inelastic analysis," J. Pressure Vessel Technology, pp 177-183 (Aug. 1974).

- 76 Sobel, L. H., and Newman, S. Z., "Instability analysis of elbows in the plastic range," 4th Int. Conf. on Structural Mechanics in Reactor Technology, Vol. L, Inelastic Analysis of Metal Structures, San Francisco, Paper L3/2 (1977).
- 77 Roche, R., Hoffmann, A., and Vrillon, B., "Piping systems inelastic analysis--A simplified numerical method," 3rd Int. Conf. on Pressure Vessel Technology, ASME, Tokyo, Japan, pp 133-142 (1977).
- 78 Spence, J., and Findlay, G., "Limit load for pipe bend under plane bending," Proc. 2nd Int. Conf. on Pressure Vessel Technology, Vol. 1, ASME, pp 393-399 (1973).
- 79 Spence J., and Findlay, G. E., "Limit moments for noncircular cross section (elliptical) pipe bends," 4th SMiRT Conf., San Francisco, Vol. F, Paper F1/6 (1977).
- 80 Calladine, C. R., "Limit analysis of curved tubes," J. of Mech. Eng. Sci., Vol. 16, No. 2, pp 85-87 (1974).
- 81 Popov, E. P., Sharifi, P., and Nagarajan, S., "Inelastic buckling analysis of pipes subjected to internal pressure, flexure and axial loading," in Pressure Vessels and Piping: Analysis and Computers, edited by I. S. Tuba, R. A. Selby, W. B. Wright, ASME Symposium Vol. pp 11 23 (1974).
- 82 Bushnell, D., "Stress, buckling, and vibration of prismatic shells," AIAA J. Vol 9, No. 10, pp 2004-2013 (1971).
- 83 Sabir, A. B., and Lock, A. C., "The application of finite elements to the large deflection geometrically non-linear behavior of cylindrical shells," in Variational Methods in Engineering (C. A. Brebbia, H. Tottenham, eds.), Southampton University Press, pp 7/66=7/75 (1973).
- 84 Bergan, P. G., Horrigmoe, G., Krækland, B., and Søreide, T. H., "Solution techniques for nonlinear finite element problems," Int. J. Num. Meth. Engng., Vol. 12, pp 1677-1696 (1978).
- 85 Almroth, B. O., and Brogan, F. A., "Bifurcation Buckling as an Approximation of the Collapse Load for General Shells, AIAA J., vol. 10, pp 463-467 (April 1972).

- 86 Okubo, S., Wilson, P. E., and Whittier, J. S., "Influence of concentrated lateral loads on the elastic stability of cylinders in bending," Experimental Mechanics, Vol. 10, No. 9, pp 384-389 (1970).
- 87 Almroth, B. O., and Holmes, A. M. C., "Buckling of Shells with Cutouts, Experiment and Analysis," Intl. J. Solids Structures, Vol. 8, pp 1057-1071 (Aug. 1972).
- 88 Almroth, B. O., Brogan, F. A., and Marlowe, M. B., "Stability of Cylinders with Circular Cutouts," AIAA J., Vol. 11, pp 1582-1584 (Nov. 1973).
- 89 Starnes, J. H., Jr., The Effect of a Circular Hole on the Buckling of Cylindrical Shells, Ph.D. thesis, California Institute of Technology, Pasadena, CA (1970).
- 90 Bushnell, D., Almroth, B. O., and Brogan, F. A., "Finite-difference energy method for nonlinear shell analysis," Computers & Structures, Vol. 1, pp 361-387 (1971).
- 91 Bushnell, D., "Buckling and vibration of ring-stiffened segmented shells of revolution-numerical results," Proc. 1st ASME International Pressure Vessel Conference, Delft, Holland, Part 1: Design and Analysis, pp 255-268 (1969).
- 92 Bushnell, D., "Buckling of spherical shells ring-supported at the edges," AIAA J., Vol. 5, No. 11, pp 2041-2046 (1967).
- 93 Wang, R. L., "Effects of edge restraint on the stability of spherical caps," AIAA J., 4, pp 718-719 (1966).
- 94 Weinitschke, H., "On asymmetric buckling of shallow spherical shells," J. Math. Phys., 44, pp 141-163 (1965).
- 95 Huang, N. C., "Unsymmetrical buckling of thin shallow spherical shells," J. Appl. Mech., 31, pp 447-457 (1964).
- 96 Cohen, G. A., "Buckling of axially compressed cylindrical shells with ring-stiffened edges," AIAA J., 4, 1859-1862 (1966).
- 97 Bushnell, D., "Nonsymmetric buckling of cylinders with axisymmetric thermal discontinuities," AIAA J. Vol. 11, No. 9, pp 1292-1295 (1973).
- 98 Hoff, N. J., "Buckling of the Thin Cylindrical Shell Under Hoop Stresses Varying in the Axial Direction," Journal of Applied Mechanics, Vol. 24, pp 405-412 (1957).

- 99 Johns, D. J., "Local Circumferential Buckling of Thin Circular Cylindrical Shells," Collected Papers on Instability of Shell Structures, TN-D-1510, NASA, pp 267-276 (1962).
- 100 Anderson, M. S., "Thermal Buckling of Cylinders," Collected Papers on Instability of Shell Structures, TN D-1510, NASA, pp 255-265 (1962).
- 101 Chang, L. K., and Card, M. F., "Thermal Buckling in Stiffened Cylindrical Shells," Proceedings of the AIAA/ASME 11th Structures, Structural Dynamics, and Materials Conference, pp 260-272 (April 1970).
- 102 Bushnell, D., "Analysis of Ring-Stiffened Shells of Revolution under Combined Thermal and Mechanical Loading," AIAA J., Vol. 9, No. 3, pp 401-410 (March 1971).
- 103 Bushnell, D., "Effect of Ring Out-of-Plane Bending Stiffness on Thermal Buckling Prediction for Ring-Stiffened Cylinders," AIAA J., Vol. 9, No. 8, pp 1653-1654 (Aug. 1971).
- 104 Ross, B., Hoff, N. J., and Horton, W. H., "The Buckling Behavior of Uniformly Heated Thin Circular Cylindrical Shells," AFOSR 65-0982, SUDAER No. 225, Stanford Univ., Stanford, CA (April 1965); also Experimental Mechanics, Vol. 6, pp 529-537 (1966).
- 105 Hill, D. W., "Buckling of a Thin Circular Cylindrical Shell Heated Along an Axial Strip," SUDAER 88, Stanford Univ., Stanford, CA (Dec. 1959).
- 106 Ross, B., Mayers, J., and Jaworski, A., "Buckling of Thin Cylindrical Shells Heated Along an Axial Strip," Experimental Mechanics, Vol. 5, No. 8, pp 247-256 (Aug. 1965).
- 107 Flügge, W., Stresses in Shells, Springer-Verlag, Berlin, Chap. 5, pp 275-276 (1960).
- 108 Johns, D. J., Houghton, D. S., and Webber, J., "Buckling Due to Thermal Stress of Cylindrical Shells Subjected to Axial Temperature Distribution," Rept. 147, College of Aeronautics, Cranfield, England (May 1961).
- 109 Webber, J. P. H., private communication, Univ. of Bristol, Dept. of Aeronautical Engineering, Bristol, England (Nov. 2, 1972).

- 110 Yao, J. C., "Buckling of a truncated hemisphere under axial tension," AIAA J., Vol. 1, pp 2316-2319 (1963).
- 111 Bushnell, D., "Bifurcation phenomena in spherical shells under concentrated and ring loads," AIAA J., Vol. 5, pp 2034-2040 (1967).
- 112 Pedersen, P. T., and Jensen, J. J., "Buckling of spherical cargo tanks for liquid natural gas," The Royal Institution of Naval Architects, Vol. 5, pp (1975).
- 113 Galletly, G. D., "Stress failure of large pressure vessels -- recommendations resulting from studies of the collapse of a 68 ft. high x 45 ft. dia. pressure vessel," Tech. Rept. No. 45-57, Shell Development Corp., Emeryville, CA (Mar. 1957).
- 114 Drucker, D. C., and Shield, R. J., "Limit analysis of symmetrically loaded thin shells of revolution," Journal of Applied Mechanics, Vol. 26, No. 1, pp 61-68 (Mar. 1959).
- 115 Shield, R. J., and Drucker, D. C., "Design of thin-walled torispherical and toriconical head pressure vessels," Journal of Applied Mechanics, Vol. 28, No. 2, pp 292-297 (1961)
- 116 Gerdeen, J. C., and Hutula, D. N., "Plastic limit analysis of hemispherical and toriconical head pressure vessels," Journal of Applied Mechanics, Vol. 28, No. 2, pp 292-297 (1961).
- 117 Crisp, R. J., and Townley, C. H. A., "The application of elastic and elastic-plastic analysis to the design of torispherical heads," First International Conference on Pressure Vessel Technology, Delft, pp 345-354 (1969).
- 118 Simonen, F. A. and Hunter, D. T., "Elastic-plastic deformations in pressure vessel heads," Welding Research Council Bulletin No. 163 (1971).
- 119 Calladine, C. R., "Lower-bound analysis of symmetrically loaded shells of revolution," First International Conference on Pressure Vessel Technology, Delft., pp 335-344 (1969).
- 120 Savé, M., "Verification experimentale de l'analyse limite plastique des plaques et des coques en acier doux," Centre de Recherches Scientifiques et Techniques de L'Industrie des Fabrications Metalliques, Brussels, Belgium (Feb. 1966).

- 121 Use of Computer in Pressure Vessel Analysis, ASME, Papers and Discussion from ASME Computer Seminar, Dallas, Texas (Sept. 25, 1968) (1969).
- 122 Gerdeen, J. C., "Use of the computer in the plastic limit analysis of pressure vessels," ibid, pp 37-49.
- 123 Mescall, J. F., "Large deflections and stability of shells of revolution," ibid, pp 1-25.
- 124 Marcal, P. V., "Elastic-plastic analysis of pressure vessel components," ibid, pp 71-81.
- 125 Esztergar, E., "Development of design rules for dished pressure vessel heads," Welding Research Council Bulletin, 215 (April 1976).
- 126 Fino, A., and Schneider, R. W., "Wrinkling of a large, thin code head under internal pressure," Welding Research Council Bulletin, No. 69 (June 1961).
- 127 Mescall, J., "Stability of thin torispherical shells under uniform internal pressure," NASA TN D-1510, Collected Papers on Instability of Shell Structures, pp 671-692 (Dec. 1962).
- 128 Adachi, J., and Benicek, M., "Buckling of torispherical shells under internal pressure," Experimental Mechanics, Vol. 4, No. 8, pp 217-222 (Aug. 1964).
- 129 Thurston, G., and Holston, A. A., Jr., "Buckling of cylindrical shell end closures by internal pressure," NASA CR-540 (July 1966).
- 130 Brown, K. W., and Kraus, H., "Stability of internally pressurized vessels with ellipsoidal heads," presented at 2nd National Congress on Pressure Vessels and Piping Technology, San Francisco (June 23-27, 1975).
- 131 Bushnell, D., and Galletly, G. D., "Comparisons of test and theory for nonsymmetric elastic-plastic buckling of shells of revolution," Int. J. Solids Struct., Vol. 10, pp 1271-1286 (1974).
- 132 Bushnell, D., and Galletly, G. D., "Stress and buckling of internally pressurized elastic-plastic torispherical vessel heads--comparisons of test and theory," ASME J. Pressure Vessel Technology, Vol. 99, pp 39-53 (Feb. 1977).

- 133 Lagae, G., and Bushnell, D., "Elastic-plastic buckling of internally pressurized torispherical vessel heads," Nuclear Engineering and Design, Vol. 48, pp 405-414 (1978).
- 134 Galletly, G. D., "Internal pressure buckling of very thin torispherical shells--a comparison of experiment and theory," 3rd SMiRT Conf., London, Paper G2/3 (1975).
- 135 Galletly, G. D., "Elastic and elastic-plastic buckling of internally-pressurized 2:1 ellipsoidal shells," ASME Paper 78-PVP-47 (June 1978).
- 136 Kirk, A. and Gill, S. S., "The failure of torispherical ends of pressure vessels due to instability and plastic deformation-an experimental investigation," Int. J. Mech. Sci., Vol. 17, pp 525-544 (1975).
- 137 Patel, P. R. and Gill, S. S., "Experiments on the buckling under internal pressure of thin torispherical ends of cylindrical pressure vessels," Int. J. Mech. Sci., Vol. 20, pp 159-175 (1978).
- 138 Bushnell, D., "Nonsymmetric buckling of internally pressurized ellipsoidal and torispherical elastic-plastic pressure vessel heads," ASME J. of Pressure Vessel Technology, Vol. 99, pp 54-63 (Feb. 1977).
- 139 Galletly, G. D., "Buckling and collapse of thin internally pressurized dished ends," Univ. of Liverpool Report A/Q3/79, Liverpool, UK (1979).
- 140 Vandepitte, D., "Model Investigation of the Collapse of a Steel Water Tower," Proc. of Conference on Stability of Steel Structures, Liege, Belgium, pp 599-607 (April 1977).
- 141 Other Vandepitte/Lagae work in Belgium from which Fig. 105(a) and (c) come. Letter dated 8 Aug., 1978 from Guy Lagae Laboratorium voor Modelonderzoek Rijksuniversiteit-Gent, Belgium, to D. Bushnell.
- 142 Bushnell, D., "Effect of Cold Bending and Welding on Buckling of Ring-Stiffened Cylinders," Computers & Structures, Vol. 12, pp. 291-307 (1980)
- 143 Faulkner, D., "Effects of Residual Stresses on the Ductile Strength of Plane-Welded Grillages and of Ring-Stiffened Cylinders," J. Strain Anal. & Eng. Design, Vol. 12, pp. 130-139 (April 1977).

- 144 von Mises, R., "Der kritische Aussendruck für allseits belastete zylindrische Röhre (Fest Zurn 70 Beburstag von Prof. A. Stodola, pp. 418-430, Zurich) (1929).
- 145 Nash, W. A., "Buckling of thin cylindrical shells subject to hydrostatic pressure," J. Aeronaut. Sci., 21, pp 354-355 (1954).
- 146 Galletly, G. D., and Bart, R., "Effects of boundary conditions and initial out-of-roundness on the strength of thin-walled cylinders subject to external hydrostatic pressure," J. Appl. Mech., 23, pp 351-358 (1956).
- 147 Singer, J., "The effect of axial constraint on the instability of thin cylindrical shells under external pressure," J. Appl. Mech., pp 737-739 (1960).
- 148 Sobel, L.H., "Effects of boundary conditions on the stability of cylinders subject to lateral and axial pressures," AIAA J. 2, 1437-1440 (1964).
- 149 Nachbar, W. and Hoff, N.J., "The buckling of a free edge of an axially compressed circular cylindrical shell," Quart. Appl. Math., XX, pp 267-277 (1962).
- 150 Stein, M., "The effect on the buckling of perfect cylinders of prebuckling deformations and stresses induced by edge support," Collected Papers on Instability of Shell Structures--1962, NASA TN D-1510, pp 217-228 (1962).
- 151 Fischer, G., "Über den Einfluss der gelenkigen Lagerung auf die Stabilität dünnwandiger Kreiszyinderschalen unter Axiallast und Innendruck," A. Flugwissenschaften. 11, 111-119 (1963).
- 152 Almroth, B.O., "Influence of edge conditions on the stability of axially compressed cylindrical shells," AIAA J., 4, pp 134-140 (1966).
- 153 Almroth, B.O., Bushnell, D., "Computer Analysis of Various Shells of Revolution," AIAA J. 6, pp. 1848-1855 (Oct. 1968).
- 154 Galletly, G.D., Aylward, R.W., Bushnell, D., "An Experimental and Theoretical Investigation of Elastic and Elastic/Plastic Axisymmetric Buckling of Cylinder Cone Combinations Subjected to Uniform External Pressure," Ingenieur-Archiv. Vol. 43, pp. 345-358 (1974).
- 155 Aylward, R.W., Galletly, G.D., Moffat, D.G., "Buckling Under External Pressure of Cylinders with Toriconical or Pierced Torispherical Ends: A Comparison of Experiment with Theory," J. Mech. Eng. Sci., Vol. 17, 11-18 (1975).
- 156 Weller, T, Singer, J., Batterman, S.C., "Influence of Eccentricity of Loading on Buckling of Stringer-Stiffened Cylindrical Shells," Thin-Shell Structure, Theory, Experiment and Design, Y.C. Fung and E. E. Sechler (Eds.), Prentice-Hall, Englewood Cliffs, N.J., pp. 305-324 (1974).

- 157 Singer, J., and Rosen, A., "Influence of Boundary Conditions on the Buckling of Stiffened Cylindrical Shells," Buckling of Structures, Proceedings of IUTAM Symposium, Harvard University, Cambridge, Mass., June 1974; Springer-Verlag, Berlin, pp 227-250 (1976).
- 158 Singer, J., and Abramovich, H., "Vibration techniques for definition of practical boundary conditions in stiffened shells," AIAA J., 17, No. 7, pp 762-769 (July 1979).
- 159 Block, D. L., Influence of discrete ring stiffeners and prebuckling deformations on the buckling of eccentrically stiffened orthotropic cylinders, NASA TN D-4283 (1968).
- 160 Baruch, M., and Singer, J., "Effect of Eccentricity of Stiffeners on the General Instability of Stiffened Cylindrical Shells under Hydrostatic Pressure," Journal of Mechanical Engineering Science, 5, No. 1, pp 23-27 (March 1963).
- 161 Stuhlman, C. E., DeLuzio, A., and Almroth, B., "Influence of Stiffener Eccentricity and End Moment on Stability of Cylinders in Compression," AIAA J. 4, pp 872-877 (May 1966).
- 162 Budiansky, B., and Hutchinson, J. W., "A Survey of Some Buckling Problems," AIAA J. 4, No. 9, pp 1505-1510 (Sept. 1966).
- 163 Lo, H., Crate, H., and Schwartz, E. B., Buckling of Thin-Walled Cylinder Under Axial Compression and Internal Pressure, NACA TN 2021 (January 1950).
- 164 Harris, L. A., Suer, H. S., Skene, W. T., and Benjamin, R. J., "The Stability of Thin-Walled Unstiffened Circular Cylinders Under Axial Compression Including the Effects of Internal Pressure," J. of Aeronautical Sciences, 24, No. 8, pp 587-596 (Aug 1957).
- 165 Suer, H. S., Harris, L. A., Skene, W. T., and Benjamin, R. J., "The bending stability of thin-walled unstiffened circular cylinders including the effects of internal pressure," J. Aero. Sci., 25, No. 5, pp 281-287 (May 1958).
- 166 Flügge, W., Die Stabilität der Kreiszylinderschale, Ing-Archiv, Bd III, Heft 5, pp 463-506 (Dec. 1932).
- 167 Crate, H., Batdorf, S. B., and Baab, G. W., "The Effect of Internal Pressure on the Buckling Stress of Thin-Walled Circular Cylinders Under Torsion," NACA L4E27 (May 1944)

- 168 Hopkins, H. C., and Brown, E. H., "The effect of internal pressure on the initial buckling of thin-walled circular cylinders under torsion," British Aeronautical Research Council, R&M No. 2423 (Jan. 1950).
- 169 Batdorf, S. B., "A simplified method of elastic-stability analysis for thin cylindrical shells," NACA Report 374 (1947).
- 170 Tennyson, R. C., "The effect of shape imperfections and stiffening on the buckling of circular cylinders," in Buckling of Structures, B. Budiansky, ed., Springer-Verlag, New York, pp. 251-273 (1976).
- 171 Eushnell, D., "Buckling of elastic-plastic shells of revolution with discrete elastic-plastic ring stiffeners," Int. J. Solids Structures, Vol. 12, pp. 51-66, (1976).
- 172 Tennyson, R. C., "Buckling of laminated composite cylinders: a review," Composites (U.K.) pp. 17-24, Vol. 6, No. 1 (Jan. 1975).
- 173 March, H. W. et al., "Buckling of thin-walled plywood cylinders in torsion", Forest Products Lab, Madison, Wisc., Report 1529 (June 1945).
- 174 Thielemann, W. F., Schnell, W. and Fischer, G., "Buckling and post-buckling behaviour of orthotropic circular cylindrical shells subjected to combined axial and internal pressure", Zeitschrift Flugwiss, 8 Heft 10/11 (1960).
- 175 Cheng, S. and Ho, B. P. C., "Stability of heterogeneous aeolotropic cylindrical shells under combined loading", AIAA Journal, 1 No. 7, pp. 892-898 (April 1963).
- 176 Ho, B. P. C. and Cheng, S., "Some problems in stability of heterogeneous aeolotropic cylindrical shells under combined loading", AIAA Journal, 1, No. 7, pp. 1603-1607 (July 1963).
- 177 Tasi, J., "Effect of heterogeneity on the stability of composite cylindrical shells under axial compression", AIAA Journal, 4, No. 6 (June 1966).
- 178 Holston, A., Jr., "Buckling of inhomogeneous anisotropic cylindrical shells by bending", AIAA Journal, 6, No. 10 (Oct. 1968).
- 179 Holston, A., Jr., "Buckling of filament-wound cylinders by axial compression", AIAA Journal, 6, No. 5 (May 1968).

- 180 Lei, M. M. and Cheng, S., "Buckling of composite and homogeneous isotropic cylindrical shells under axial and radial loading", J. Applied Mech, Trans. ASME (Dec. 1969).
- 181 Jones, R. M., "Buckling of circular cylindrical shells with multiple orthotropic layers and eccentric stiffeners", AIAA Journal, 6, No. 12 (Dec. 1968).
- 182 Jones, R. M., "Buckling of circular cylindrical shells with different moduli in tension and compression", AIAA J. Vol. ,
- 183 Card, M. F. and Peterson, J. P., "On the instability of orthotropic cylinders", NASA TN D-1510 ("Collected Papers on Instability of Shell Structures", Dec. 1962).
- 184 Card, M. F., "Experiments to determine the strength of filament-wound cylinders loaded in axial compression", NASA TN D-3522 (Aug. 1966).
- 185 Ravenhall, R., "Stiffness and buckling in filament-wound motors", AIAA Journal of Spacecraft and Rockets, 1, No. 3 (1964).
- 186 Tasi, J., Feldman, A., and Stang, D. A., "The buckling strength of filament-wound cylinders under axial compression", NASA Cr-266 (July 1965).
- 187 Khot, N. S. Venkayya, V. B., and Berke, L., "Buckling and post-buckling behavior of initially imperfect orthotropic cylindrical shells under axial compression and internal pressure", presented at IUTAM Conference "Instability of continuous systems" (Herrenalb, West Germany, Sept. 1969).
- 188 Khot, N. S., "Buckling and postbuckling behavior of composite cylindrical shells under axial compression," AIAA Journal, Vol. 8, pp. 229-235 (Feb. 1970).
- 189 Card, M. F., "The sensitivity of buckling of axially compressed fiber-reinforced cylindrical shells to small geometric imperfections", NASA TMX-61914 (June 1969).
- 190 Tennyson, R. C. and Muggeridge, D. B., "Buckling of laminated anisotropic imperfect circular cylinders under axial compression," Journal of Spacecraft and Rockets, Vol. 10, pp. 143-148 (Feb. 1973).

- 191 Jones, R. M. and Hennemann, J. C. F., "Effect of prebuckling deformations on buckling of laminated composite circular cylindrical shells", Proceedings of AIAA 19th Structures, Structural Dynamics and Materials Conference, Bethesda, Md., (April 1978), AIAA J., Vol. 18, pp 110-115(1980).
- 192 Booton, M. and Tennyson, R. C., "Buckling of imperfect anisotropic circular cylinders under combined loading", AIAA J., Vol 17, No. 3, pp. 278-287 (March 1979).
- 193 Tennyson, R. C., Booton, M., and Chan, K. H., "Buckling of short cylinders under combined loading", Journal of Applied Mechanics, Transactions of ASME, Vol. 45 (Sept. 1978).
- 194 Stricklin, James A., Haisler, Walter E., Von Reisemann, Walter A., Leick, Roger D., Hunsaker, Barry, and Saczalski, Kenneth J., "Large deflection elastic-plastic dynamic response of stiffened shells of revolution", TEES-RPT-72-25 and SLA-73-0128, Texas A&M University, Texas (December 1972).
- 195 Klein, S., "SABOR/DRASTIC 6 - user's manual", The SABOR Manual, Vol. III, Poulter Laboratory Technical Report, Stanford Research Institute, Menlo Park, California (1974).
- 196 Ball, R. E., "A program for the nonlinear static and dynamic analysis of arbitrarily loaded shells of revolution", Computers and Structures, Vol. 2, pp. 141-162 (1972).
- 197 Underwood, P. G., "User's guide to the SHORE code", LMSC-D244589, Lockheed Missiles & Space Company, Palo Alto, California (November 1971).
- 198 Huffington, N. J., Jr., "Large deflection elastoplastic response of shell structures", U.S. Army Ballistic Research Laboratories, Report No. 1515, Aberdeen Proving Ground, Maryland (1970).
- 199 Hubka, W. F., Windholz, W. M., and Karlsson, T., "A calculation method for the finite deflection, anelastic dynamic response of shells of revolution", Kaman Sciences Corporation, Report KN-69-660(R), Kaman Sciences Corporation, Colorado Springs, Colorado (January 1970).
- 200 Bushnell, David and Smith, Strether, "Stress and buckling of nonuniformly heated cylindrical and conical shells", AIAA Journal, Vol. 9, No. 12, pp. 2314-2321 (1971).

- 201 Hoff, N. J., "Buckling at high temperature", Journal of the Royal Aeronautical Society, Vol. 61, pp. 756-774 (1957).
- 202 Anderson, M. S., "Combinations of temperature and axial compression required for buckling of a ring-stiffened cylinder", TN D-1224, NASA (April 1962).
- 203 Abir, D. and Nardo, S. Y., "Thermal buckling of circular cylindrical shells under circumferential temperature gradients", Journal of the Aeronautical Sciences, Vol. 26, pp. 803-808 (1959).
- 204 Anderson, M. S. and Card, M. F., "Buckling of ring-stiffened cylinders under a pure bending moment and a nonuniform temperature distribution", TN D-1513, NASA (Nov. 1962).
- 205 Holmes, A., "Measurement of thermal stresses in ring-stiffened cylinders", LMSC/Y1-69-66-1, Lockheed Missiles & Space Co., Palo Alto, CA (Dec. 1966).
- 206 Holmes, A., "An experimental investigation of cylinder buckling under axial load and thermal stress due to asymmetrical heating", LMSC/Y1-69-66-2, Lockheed Missiles & Space Co., Palo Alto, CA (Dec. 1966).
- 207 Lu, S. Y. and Chang, L. K., "Thermal buckling of conical shells", AIAA Journal, Vol. 5, No. 10, pp. 1877-1882 (Oct. 1967).
- 208 Chang, L. K. and Lu, S. Y., "Nonlinear thermal elastic buckling of conical shells", Nuclear Engineering and Design, Vol. 7, pp. 159-169 (1968).
- 209 Bendavid, D., and Singer, J., "Thermal buckling of conical shells heated along a generator", SUDAAR 258, Stanford Univ., Stanford, CA (Feb. 1966).
- 210 Smith, S., "An experimental investigation of the thermal buckling of conical shells", thesis, Dept. of Aeronautics and Astronauts, Stanford Univ., CA (May 1964).
- 211 Blumenberg, W. F., "The effect of intermediate heavy frames on the elastic general instability strength of ring-stiffened cylinders under external hydrostatic pressure", David Taylor Model Basin Report 1844, (Feb. 1965).

- 212 Boichot, L. and Reynolds, T. E., "Inelastic buckling tests of ring-stiffened cylinders under hydrostatic pressure", David Taylor Model Basin Report 1992, Washington, D.C. (May 1965).
- 213 Lunchick, M. E., "Plastic general instability of ring-stiffened cylindrical shells", David Taylor Model Basin Report 1587, Washington, D.C. (Sept. 1963).
- 214 Krenzke, M. A. and Kiernan, T. J., "Structural development of a titanium oceanographic vehicle", David Taylor Model Basin Report 1675, Washington, D.C. (Sept. 1963).
- 215 Reynolds, T. E., Private communication (June 1974).
- 216 Lee, L. H. N., "Inelastic asymmetric buckling of ring-stiffened cylindrical shells under external pressure", AIAA J. 12, 1051-1056 (1974).
- 217 Gerard, G. "Plastic theory of stiffened cylinders under hydrostatic pressure, J Ship Res., 6, 1 (1962).
- 218 Ketter, R. L., "The influence of residual stresses on the strength of structural members", Welding Research Council Bulletin #44, (Nov. 1958).
- 219 Almen, J. O. and Black, P. H., Residual Stresses and Fatigue in Metals, McGraw Hill, Chapter 5, pp 46-47 (1963).
- 220 Queener, C. A. and De Angelis, R. J., "Elastic springback and residual stresses in sheet metal formed by bending", ASM Transactions Quarterly, Vol. 61, pp. 757-768 (Dec. 1968).
- 221 Lunchick, M. E., "Influence of residual rolling stresses on the strength of cylindrical pressure vessels under external loading", J. Eng. Ind., Trans. ASME, Vol. 92, pp. 275-280 (May 1970).
- 222 Shama, M. A., "Cold forming residual stresses and their effect on the accuracy of post-forming operations", European Shipbuilding, Vol. 19 No. 2, pp. 23-26 (1970).
- 223 Tacey, R. K., "A computer program for calculation of the residual stress distribution and the effective stress-strain curve of cold-formed structural members", David W. Taylor Naval Ship Research and Development Center, Bethesda, Md., Report 76-0141 (November 1976).

- 224 Numerical Modeling of Manufacturing Processes, PVP-PB-025, ASME, NY (R. F. Jones, Jr., H. Armen, and J. T. Fong, ed.) presented at ASME Winter Annual Meeting, Atlanta, GA (1977).
- 225 Masubuchi, K., "Numerical modeling of thermal stresses and metal movement during welding", pp. 1-17 of Reference 4.224 (1977).
- 226 Friedman, E., "Numerical simulation of the gas tungsten-arc welding process", pp. 35-47 of Reference 4.224 (1977).
- 227 Lobitz, D. Q., McClure, J. D., and Nickell, R. E., "Residual stresses and distortions in multi-pass welding", pp. 81-88 of Reference 4.224 (1977).
- 228 Hsu, M. B., "Analysis of welds by the finite element method", pp. 97-115 of Reference 4.224 (1977).
- 229 Rybicki, E. F., Schmueser, D. W., Stonesifer, R. B., Greom, J. J. and Mishler, H. W., "A finite element model for residual stresses in girth-butt welded pipes", pp. 131-142 of Refer 4.224 (1977).
- 230 DeYoung, R. M., and Chin, S. S., "Some applications of numerical methods to practical welding problems", pp. 143-156 of Reference 4.224 (1977).
- 231 Masubuchi, K., "Report on current knowledge of numerical analysis of stresses, strains, and other effects produced by welding", Welding in the World, Vol. 13, No. 11/12, pp. 271-288 (1975).
- 232 Hibbitt, H. D., and Marcal, P. V., "A numerical thermomechanical model for the welding and subsequent loading of a fabricated structure", Computers & Structures, Vol. 3, pp. 1145-1174 (1973).
- 233 Nickell, R. E. and Hibbitt, H. D., "Thermal and mechanical analysis of welded structures", Nuclear Engineering and Design, Vol. 32, No. 1, pp. 110-120 (April 1975).
- 234 Friedman, E., "Thermomechanical analysis of the welding process using the finite element method", ASME J. of Pressure Vessel Technology, pp. 206-213 (August 1975).
- 235 Bushnell, D., BOSOR5 - A Computer Program for Buckling of Elastic Plastic Complex Shells of Revolution Including Large Deflections and Creep, Vol. 1: User's Manual, Input Data, LMSC-D407166; Vol. II: User's Manual, Test Cases, LMSC-D407167; Vol. III: Theory and Comparisons with Tests, LMSC-D407168, Lockheed Missiles & Space Co., Sunnyvale, CA (Dec. 1974).

- 236 Chen, W. F. and Ross, D. A., "Axial strength and behavior of cylindrical columns", Proc. 8th Annual Offshore Technology Conference, Houston, TX, Vol. 3, pp. 741-754 (May 1976).
- 237 Faulkner, D., "Effects of residual stresses on the ductile strength of plane welded grillages and of ring-stiffened cylinders", J. Strain Anal. & Eng. Design, Vol. 12, pp. 130-139 (April 1977).
- 238 Krenzke, M. A., "Effect of initial deflections and residual welding stresses on elastic behavior and collapse pressure of stiffened cylinders subjected to external hydrostatic pressure", David Taylor Model Basin Report 1327 (April 1960).
- 239 Kirstein, A. F., and Slankard, R. C., "An experimental investigation of the shell-instability strength of a machined, ring-stiffened cylindrical shell under hydrostatic pressure (Model BR-4A)", David Taylor Model Basin, Washington, D.C., Report 997 (April 1956).
- 240 Slankard, R. C., "Tests of the elastic stability of a ring-stiffened cylindrical shell, Model BR-4 subjected to hydrostatic pressure", David Taylor Model Basin, Washington, D.C., Report 876 (Feb. 1955).
- 241 Bushnell, D., "A strategy for the solution of problems involving large deflections, plasticity, and creep", Int. J. Num. Math. in Engng., Vol. 11, pp. 683-708 (1977).
- 242 Bushnell, D., PANEL - Computer Program for Optimization of Stiffened Cylindrical Panels by Simultaneous Buckling Criterion, LMSC-D676240, Lockheed Missiles & Space Co., Inc., Palo Alto, CA (June 1979).
- 243 Bushnell, D., PANEL/CONMIN - Computer Program for Optimization of Stiffened Cylindrical Panels by Mathematical Programming Method, LMSC-D676309, Lockheed Missiles & Space Co., Inc., Palo Alto, CA (July 1979).
- 244 Costello, M. G., "A computer program to determine the elastic instability of ring frames", Rept. 3285, Naval Ship Research and Development Center, Washington, D.C. (Jan. 1970).
- 245 Informal communication with personnel at the David Taylor Model Basin about 1970.

- 246 Leonard, R. W., Anderson, M.S., and Heard, W. L., Jr., Design of a Mars Entry Aeroshell, Buckling of Structures IUTAM Symposium, Cambridge, USA, (1974). Springer-Verlag Berlin Heidelberg, New York (1976) pp. 346-364.
- 247 Bushnell, D., "BOSOR4: Program for stress, buckling, and vibration of complex shells of revolution", Structural Mechanics Software Series-Vol. 1, N. Perrone and W. Pilkey, Eds., University Press of Virginia, Charlottesville, pp. 11-143 (1977).
- 248 Kempner, J. and Chen, Y. N., "Postbuckling of an Axially Compressed Oval Cylindrical Shell", Applied Mechanics Proceedings of the Twelfth International Congress of Applied Mechanics, Stanford Univ., pp. 246-256, Springer-Verlag, (1969).
- 249 Hutchinson, J. W., "Buckling and initial postbuckling behavior of oval cylindrical shells under axial compression", ASME Journal of Applied Mechanics, Vol. 35, No. 1 pp. 66-72 (March 1968).
- 250 Almroth, B. O., Brogan, F. A., and Marlowe, M. B., "Collapse Analysis for Elliptic Cones", AIAA Journal, Vol. 9, No. 1, pp. 32-36 (Jan. 1971).
- 251 Yao, J. C. and Jenkins, W. C., "Buckling of elliptic cylinders under normal pressure", AIAA Journal, Vol. 8, No. 1, pp. 22-27 (Jan. 1970).
- 252 Liaw, B. D., "A survey of the stability of cylindrical and conical shells of oval cross section", Brown Engineering Rept. RL-NXDO-610, Brown Univ. (April 1969).
- 253 Almroth, B. O., "Buckling of a cylindrical shell subjected to nonuniform external pressure", ASME Journal of Applied Mechanics, Vol. 29, No. 4, pp. 675-682 (Dec. 1962).
- 254 Plank, P. P., Sakata, I. F., Davis, G. W., and Richie, C. C., Hypersonic Cruise Vehicle Wing Structure Evaluation, Vol. 3, Sec. 27, Lockheed Missiles & Space Co., Sunnyvale, CA (1970).
- 255 Shang, J. C., Marulic, W. J., and Sturm, R. G., "Buckling of longitudinally stiffened cylinders", ASCE Journal of the Structural Division, Vol. ST5, pp. 161-195 (Oct. 1964).

- 256 Egle, D. M. and Sewall, J. L., "An analysis of free vibration of orthogonally stiffened cylindrical shells with stiffeners treated as discrete elements", AIAA Journal, Vol. 6, No. 3, pp. 518-526 (March 1968).
- 257 McDonald, D., "A problem in the free vibrations of stiffened cylindrical shells", AIAA Journal, Vol. 8, No. 2, pp. 252-258 (Feb. 1970).
- 258 Flügge, W., Stresses in Shells, 2nd ed., Springer Verlag, Berlin, Chap. 7, pp. 424-425 (1962).
- 259 Marlowe, M. B. and Brogan, F. A., "Collapse of elliptic cylinders under uniform external pressure", AIAA Paper 71-146, New York (1971).
- 260 Viswanathan, A. V., Soong, T. C., and Miller, R. E., Jr., "Buckling analysis for axially compressed flat plates, structural sections, and stiffened plates reinforced with laminated composites", CR-1887, NASA (1971).
- 261 Wittrick, W. H., "A unified approach to the initial buckling of stiffened panels in compression", The Aeronautical Quarterly, pp. 265-283 (Aug. 1968).
- 262 Agarwal, B. and Davis, R. C., "Minimum-weight designs for hat-stiffened composite panels under uniaxial compression", NASA TN D-7779 (Nov. 1974).
- 263 Williams, F. W., "Computation of natural frequencies and initial buckling stresses of prismatic plate assemblies", Journal of Sound and Vibration, Vol. 21, No. 1, pp. 87-106 (1972).
- 264 Przemieniecki, J.S., "Finite-element structural analysis of local instability", AIAA Journal, Vol. 11, No. 1, pp. 33-39 (Jan. 1973).
- 265 Carri, R. L. and Herring, W. H., "Compressive strength of titanium alloy skin-stringer panels selectively reinforced with boron-aluminum composite", AIAA Paper 72-359, San Antonio, Texas (1972).
- 266 Libove, C., "Survey of recent work on the analysis of discretely attached corrugated shear webs", AIAA Paper 72-354, San Antonio, Texas (1972).

- 267 Wittrick, W. H. and Williams, F. W., "Buckling and vibration of anisotropic or isotropic plate assemblies under combined loadings", International Journal of Mechanical Sciences, Vol. 16, pp. 209-239 (April 1974).
- 268 Williams, J. G. and Stein, M., "Buckling behavior and structural efficiency of open-section stiffened composite compression panels", AIAA Journal, Vol. 14, pp. 1618-1626 (Nov. 1976).
- 269 Anderson, M. S. and Stroud, W. J., "General panel sizing computer code and its application to composite structural panels", AIAA J., Vol. 17, No. 8, pp. 892-897 (1979).
- 270 Vanderplaats, G. N. and Moses, F., "Structural optimization by methods of feasible directions", Computers and Structures, Vol. 3, pp. 739-755 (July 1973).
- 271 Timoshenko, S., Theory of Elastic Stability, McGraw-Hill, New York, Chap. 7, pp. 329 and 345 (1936).
- 272 Holmes, A. M. C., "Compression tests on small panels having corrugated reinforcement", Rept. F-70-69-1, Lockheed Missiles & Space Co., Palo Alto, CA (May 1969).
- 273 Bushnell, D., "Evaluation of various analytical models for buckling and vibration of stiffened shells", AIAA J., Vol. 11, No. 9, pp. 1283-1291 (Sept. 1973).
- 274 Bushnell, D., "Effect of fastening method on stiffness and stability of semi-sandwich corrugated panels and shells", LMSC Report D352079, Lockheed Missiles & Space Co., Palo Alto, CA (1973).
- 275 Tvergaard, V., "Buckling behavior of plate and shell structures", in Theoretical and Applied Mechanics, W. T. Koiter, editor, North-Holland Publishing Co., pp. 233-247 (1976).
- 276 Bijlaard, P. P. and Fisher, G. P., "Column strength of H-sections and square tubes in postbuckling range of component plates," NACA TN 2994 (1953).
- 277 Koiter, W. T. and Skaloud, M., "Interventions," in Comportement Postcritique des plaques utilisées en construction métallique. Colloque intern. à l'Université de Liège, Mémoires de la Société Royale des Sciences de Liège, 5^{me} série, tome VIII, fasc. 5, pp. 64-68, 103, 104 (1962).

- 278 Neut, A. van der, "The interaction of local buckling and column failure of thin-walled compression members," Proceedings of the Twelfth International Congress of Applied Mechanics, edited by Hetenyi, M. and Vincenti, W. G., Springer, Berlin, pp. 389-399 (1969).
- 279 Thompson, J. M. T. and Lewis, G. M., "On the optimum design of thin-walled compression members", Journal of the Mechanics and Physics of Solids, Vol. 20, pp. 101-109 (1972).
- 280 Crawford, R. F. and Hedgepeth, J. M., "Effects of initial waviness on the strength and design of built-up structures", AIAA J., Vol. 13, No. 5, pp. 672-675 (1975).
- 281 Maquoi, R., Massonnet, C., "Interaction between local plate buckling and overall buckling in thin-walled compression members, Theories and Experiment, 365-382, Buckling of Structures, (edited by B. Budiansky), Springer-Verlag (1976).
- 282 Graves Smith, T. R., "The effect of initial imperfections on the strength of thin-walled box columns", Int. J. Mech. Sci., Vol. 13, pp. 911-925 (1971).
- 283 Tvergaard, V., "Imperfection-sensitivity of a wide integrally stiffened panel under compression," Int. J. Solids Structures 9, 177-192 (1973).
- 284 Tvergaard, V., "Influence of post-buckling behavior on optimum design of stiffened panels," Int. J. Solids Structures 9, 1519-1534 (1973).
- 285 Koiter, W. T. and Pignataro, M., "An alternative approach to the interaction between local and overall buckling in stiffened panels", Buckling of Structures (edited by B. Budiansky), Springer-Verlag, pp. 133-148 (1976).
- 286 van der Neut, A., "Mode interaction with stiffened panels," Buckling of Structures, (edited by B. Budiansky), Springer-Verlag, pp. 117-132 (1976).
- 287 Thompson, J. M. T., Tulk, J. D., Walker, A. C., "An experimental study of imperfection-sensitivity in the interactive buckling of stiffened plates", Buckling of Structures, (edited by B. Budiansky), Springer-Verlag, pp. 149-159 (1976).

- 288 Tvergaard, V., Needleman, A., "Mode interaction in an eccentrically stiffened elastic-plastic panel under compression, Buckling of Structures, (edited by B. Budiansky), Springer-Verlag, pp. 160-171 (1976).
- 289 Tvergaard, V. and Needleman, A., "Buckling of eccentrically stiffened elastic-plastic panels on two single supports or multiply supported", Int. J. Solids Struct., Vol. II, pp. 647-663 (1975).
- 290 Byskov, E. and Hutchinson, J. W., "Mode interaction in axially stiffened cylindrical shells", AIAA J., Vol. 15, No. 7, pp. 941-948 (1977).
- 291 van der Neut, A., "The sensitivity of thin-walled compression members to column axis imperfection", Int. J. Solids and Structures 9, pp. 999-1011, (1973).
- 292 Reissner, E., "The effect of transverse shear deformation on the bending of elastic plates", J. Appl. Mech., Vol. 12, pp. A69-A77 (June 1945).
- 293 Mindlin, R. D., "Influence of rotary inertia and shear on flexural motions of isotropic elastic plates", J. Appl. Mech., Vol. 18, pp. 31-38 (June 1945).
- 294 Srinivas, S., and Rao, A. K., "Buckling of thin rectangular plates," AIAA J., Vol. 7, pp. 1645-1646 (August 1969).
- 295 Noor, A. K., "Stability of multilayered composite plates", Fibre Science and Technology, Vol. 8, pp. 81-89 (1975).
- 296 Sharifi, P., "Nonlinear buckling analysis of composite shells," AIAA J., Vol. 13, No. 6, pp. 729-734 (1975).
- 297 Sharifi, P., and Yates, D. N., "Nonlinear thermo-elastic-plastic and creep analysis by the finite element method", AIAA Journal, Vol. 12, pp. 1210-1215 (Sept. 1974).
- 298 Koiter, W. T., "Elastic stability and postbuckling behavior," Proc. Symp. Nonlinear Problems, R. E. Langer, editor, 257-275, Univ. of Wisconsin Press, Madison, (1963).
- 299 Budiansky, B. and Hutchinson, J. W., "Buckling: Progress and Challenge", Trends in Solid Mechanics, , editor, Delft Univ. Press, pp. , (1979).

- 300 Budiansky, B., "Theory of buckling and post-buckling behavior of elastic structures", in Advances in Applied Mechanics, Vol. 14, Academic Press, 1-65 (1974).
- 301 Seide, P., "A reexamination of Koiter's theory of initial post-buckling behavior and imperfection-sensitivity of structures", Thin Shell Structures, Theory, Experiment, Design (Y. C. Fung and E. E. Sechler, editors), Prentice-Hall, pp. 59-80, (1974).
- 302 Masur, E. F., "Buckling of shells - general introduction and review", ASCE National Structural Engineering Meeting, April 9-13, 1973, San Francisco, Preprint 2000.
- 303 Budiansky, B., and Hutchinson, J. W., "Dynamic buckling of imperfection-sensitive structures," Proc. XI Internat. Congr. Appl. Mech., Munich, 1964, Julius Springer-Verlag, Berlin, pp. 636-651 (1966).
- 304 Budiansky, B., "Dynamic buckling of elastic structures: criteria and estimates", Dynamic Stability of Structures, Proc. of an Internat. Conf., Northwestern Univ., Evanston, Illinois, 1965, G. Herrmann, editor, Pergamon Press, pp. 83-106 (1967).
- 305 Budiansky, B. and Hutchinson, J. W., "A survey of some buckling problems", AIAA J., 4, 1505-1510 (1966).
- 306 Koiter, W. T., "The nonlinear buckling problem of a complete spherical shell under uniform external pressure", I, II, III and IV, Proc. Kon. Ned. Ak. Wet., B72, pp. 40-123 (1969).
- 307 Hutchinson, J. W., "Plastic buckling", Advances in Applied Mechanics (C. S. Yih, ed.), Vol. 14, Academic Press, pp. 67-144 (1974).
- 308 Hill, R., "A general theory of uniqueness and stability in elastic/plastic solids", J. Mech. Phys. Solids, Vol. 6, pp. 236-249 (1958).
- 309 Hill, R., "Some basic principles in the mechanics of solids without a natural time", J. Mech. Phys. Solids, Vol. 7, pp. 205-225 (1959).
- 310 Hutchinson, J. W., "Post-bifurcation behavior in the plastic range," J. Mech. Phys. Solids, Vol. 21, pp. 163-190 (1973).

- 311 Tvergaard, V., "Buckling of elastic-plastic oval cylindrical shells under axial compression," Int. J. Solids Structures, Vol. 12, pp. 683-691 (1976) [see also Errata, *ibid.* Vol. 14, p. 329 (1978)].
- 312 Tvergaard, V. and Needleman, A., "On the buckling of elastic-plastic columns with asymmetric cross-sections," Int. J. Mech. Sci., Vol. 17, pp. 419-424 (1975).
- 313 Hutchinson, J. W., "On the postbuckling behavior of imperfection-sensitive structures in the plastic range," J. Appl. Mech., Vol. 39, pp. 155-162 (1972).
- 314 Hutchinson, J. W., "Imperfection sensitivity in the plastic range," J. Mech. Phys. Solids, Vol. 21, pp. 191-204 (1973).
- 315 Hutchinson, J. W. and Budiansky, B., "Analytical and numerical study of the effects of initial imperfections on the inelastic buckling of a cruciform column", Buckling of Structures (B. Budiansky, ed.), Springer-Verlag, pp. 98-105 (1976).
- 316 Needleman, A. and Tvergaard, V., "An analysis of the imperfection-sensitivity of square elastic-plastic plates under axial compression," Int. J. Solids Structures, Vol. 12, pp. 185-201 (1976).
- 317 Tvergaard, V., "Buckling of elastic-plastic cylindrical panel under axial compression," Int. J. Solids Structures, Vol. 13, pp. 957-970 (1977).
- 318 Donnell, L. H., "A new theory for the buckling of thin cylinders under axial compression and bending," Trans. ASME, Vol. 56, pp. 795-806 (1934).
- 319 Von Kármán, Th., and Tsien, H. S., "The buckling of thin cylindrical shells under axial compression," Journal of the Aeronautical Sciences, Vol. 8, pp. 303-312, (1941).
- 320 Tsien, H. S., "A theory for the buckling of thin shells," Journal of the Aeronautical Sciences, Vol. 9, pp. 373-384, (1942).

- 321 Leggett, D. M. A., and Jones, R. P. N., "The behavior of a cylindrical shell under axial compression when the buckling load has been exceeded," Aeronautical Research Council Reports and Memorandum, 2190 (August 1942).
- 322 Michielsen, H. F., "The behavior of thin cylindrical shells after buckling under axial compression," Journal of the Aeronautical Sciences, Vol. 15, pp. 738-744 (1948).
- 323 Kempner, J., "Postbuckling behavior of axially compressed circular cylindrical shells," Journal of the Aeronautical Sciences, Vol. 21, pp. 329-342 (1954).
- 324 Almroth, B. O., "Postbuckling behavior of axially compressed circular cylinders", AIAA Journal, Vol. 1, pp. 630-633 (1963).
- 325 Hoff, N. J., Madsen, W. A., and Mayers, J., "Postbuckling equilibrium of axially compressed circular cylindrical shells", AIAA Journal, Vol. 4, pp. 126-133 (1966).
- 326 Ohira, H., "Local buckling theory of axially compressed cylinders", Proceedings of the Eleventh Japan National Congress of Applied Mechanics, p. 37, Tokyo, Japan (1961).
- 327 Hoff, N. J., and Rehfield, L. W., "Buckling of axially compressed circular cylindrical shells at stresses smaller than the classical critical value," Journal of Applied Mechanics, Vol. 32, p. 533 (1965).
- 328 Stein, M., "The influence of prebuckling deformations and stresses on the buckling of perfect cylinders", Report No. TR-190, National Aeronautics and Space Administration (February 1964).
- 329 Almroth, B. O., "Influence of edge conditions on the stability of axially compressed cylindrical shells," Report No. CR 161, National Aeronautics and Space Administration (February 1965).
- 330 Hoff, N. J., and Soong, T. C., "Buckling of circular cylindrical shells in axial compression," SUDAER No. 204, Stanford, Calif., (August 1964).

- 331 Almroth, B. O., "Influence of imperfections and edge constraint on the buckling of axially compressed cylinders," NASA CR-432, (April 1966).
- 332 Shanley, F. R., "Simplified analysis of general instability of stiffened shells in pure bending," Journal of Aeronautical Sciences, Vol. 16, pp. 590-592 (1949).
- 333 Peterson, J. P., and Dow, M. B., "Compression tests on circular cylinders stiffened longitudinally by closely spaced Z-section stringers", Memorandum 2-12-59L, National Aeronautics and Space Administration (1959).
- 334 Burns, A. B., and Almroth, B. O., "Structural optimization of axially compressed, ring-stringer stiffened cylinders," Journal of Spacecraft & Rockets, Vol. 3, No. 1, pp. 19-25 (January 1966).
- 335 Almroth, B. O., and Brush, D. O., "Postbuckling behavior of pressure- or core-stabilized cylinders under axial compression," AIAA Journal, Vol. 1, pp. 2338-2341 (1963).
- 336 Almroth, B. O., "Postbuckling behavior of orthotropic cylinders under axial compression," Report No. 6-90-63-65, Lockheed Missiles & Space Company, Sunnyvale, Calif. (June 1963).
- 337 Smith, G. W., and Spier, E. E., "Study of stability of unpressurized shell structures under static loading," Report No. GDC DDG 67-005, General Dynamics, San Diego, Calif. (1967)
- 338 Koiter, W. T., "On the stability of elastic equilibrium," translated by E. Riks, Tech. Report AFFDL TR 70-25, Wright-Patterson Air Force Base (February 1970).
- 339 Árbocz, J., "The effect of initial imperfections on shell stability," Thin-Shell Structures: Theory, Experiment, and Design, Y. C. Fung & E. E. Sechler, eds., Prentice-Hall, New Jersey, pp. 205-245 (1974).
- 340 Hutchinson, J. W., "Axial buckling of pressurized imperfect cylindrical shells," AIAA J., Vol. 3, pp. 1461-1466 (1965).

- 341 Árbocz, J., Babcock, C. D., "The effect of general imperfections on the buckling of cylindrical shells," J. Appl. Mech., Vol. 36, pp. 28-38, (1969).
- 342 Árbocz, J. and Sechler, E. E., "On the buckling of stiffened imperfect cylindrical shells," AIAA J., Vol. 14, pp. 1611-1617 (1976).
- 343 Koiter, W. T., "The effect of axisymmetric imperfections on the buckling of cylindrical shells under axial compression," Koninkl. Ned. Akad. Wetenschap. Proc., B66, pp. 265-279 (1963).
- 344 Tennyson, R. C. and Muggeridge, D. B., "Buckling of axisymmetric imperfect circular cylindrical shells under axial compression," AIAA Journal, Vol. 7, No. 11, pp. 2127-2131 (Nov. 1969).
- 345 Hutchinson, J. W. and Amazigo, J. C., "Imperfection sensitivity of eccentrically stiffened cylindrical shells," AIAA J., Vol. 5, pp. 392-401, (1967).
- 346 Hutchinson, J. W. and Frauenthal, J. C., "Elastic postbuckling behavior of stiffened and barreled cylindrical shells," J. Appl. Mech., Vol. 36, pp. 784-790 (1969).
- 347 Amazigo, J. C. and Budiansky, B., "Asymptotic formulas for the buckling stresses of axially compressed cylinders with localized or random axisymmetric imperfections," J. Appl. Mech., Vol. 39, pp. 179-184, (1972).
- 348 Fitch, J. R., "The buckling and postbuckling behavior of spherical caps under concentrated load," Int. J. Solids and Structures, Vol. 4, pp. 421-446 (1968).
- 349 Cohen, G. A., "Effect of a nonlinear prebuckling state on the post-buckling behavior and imperfection-sensitivity of elastic structures", AIAA Journal, 6, pp. 1616-1620 (1968). See also AIAA Journal, 7, pp. 1407-1408 (1969).
- 350 Potters, M. L., "A matrix method for the solution of a second order difference equation in two variables," Mathematisch Centrum, Amsterdam, Report MR 19 (1955).

- 351 Singer, J., Árbocz, J., and Babcock, C. D., "Buckling of imperfect stiffened cylindrical shells under axial compression", AIAA J., Vol. 9, No. 1, pp. 68-75 (1971).
- 352 Budiansky, B. and Hutchinson, J. W., "Buckling of circular cylindrical shells under axial compression", in Contributions to the Theory of Aircraft Structures, Rotterdam Univ. Press, pp. 239-259 (1972).
- 353 Pedersen, P. T., "Buckling of unstiffened and ring-stiffened cylindrical shells under axial compression", Int. J. Solids Structures, Vol. 9, pp. 671-691 (1973).
- 354 Pedersen, P. T., "On the collapse load of cylindrical shells", in Buckling of Structures, B. Budiansky, editor, Springer-Verlag, pp. 27-39 (1976).
- 355 Hutchinson, J. W., Tennyson, R. C., and Muggeridge, D. B., "Effect of a local axisymmetric imperfection on the buckling behavior of a circular cylindrical shell under axial compression", AIAA J., Vol. 9, No. 1, pp. 48-52 (1971).
- 356 Amazigo, J. C. and Fraser, W. B., "Buckling under external pressure of cylindrical shells with dimple-shaped initial imperfections", Int. J. Solids Struct., Vol. 7, pp. 883-900 (1971).
- 357 Fersht, P. S., "Buckling of cylindrical shells with random imperfections" in Thin Shell Structures: Theory, Experiment, and Design, Y. C. Fung and E. E. Sechler, editors, Prentice-Hall, New Jersey, pp. 325-341 (1974).
- 358 Amazigo, J. C., "Asymptotic analysis of the buckling of externally pressurized cylinders with random imperfections", Quarterly of Applied Mathematics, Vol. 31, pp. 429-442 (1974).
- 359 Roorda, J. and Hansen, J. S., "Random buckling in axially loaded cylindrical shells with axisymmetric imperfections", J. Spacecraft, Vol. 9, pp. 88-91 (1972).

- 360 Hansen, J. S. and Roorda, J., "On a probabilistic stability theory for imperfection sensitive structures", Int. J. Solids Struct., Vol. 10, pp. 341-359 (1974).
- 361 Augusti, G. and Baratta, A., "Reliability of slender columns" comparison of different approximations", in Buckling of Structures, B. Budiansky, editor, Springer-Verlag, pp. 183-198 (1976).
- 362 Johns, K. C., "Some statistical aspects of coupled buckling structures", in Buckling of Structures, B. Budiansky, editor, Springer-Verlag, pp. 199-207, (1976).
- 363 Amazigo, J. C., "Buckling of stochastically imperfect structures," in Buckling of Structures, B. Budiansky, editor, Springer-Verlag, pp. 172-182 (1976).
- 364 Weingarten, V. I., Morgan, E. J., and Seide, P., "Elastic stability of thin-walled cylindrical and conical shells under combined internal pressure and axial compression," AIAA J., 3, pp. 1118-1125 (1965).
- 365 Thielemann, W. F., "New developments in the non-linear theories of the buckling of thin cylindrical shells," Aeronautics and Astronautics (Pergamon Press, New York), pp. 76-121 (1960).
- 366 Koiter, W. T., "Buckling and post-buckling behavior of a cylindrical panel under axial compression," National Aeronautical Research Institute, Amsterdam, Rept. S.476, (May 1956).
- 367 Stephens, W. B., "Imperfection sensitivity of axially compressed stringer reinforced cylindrical panels under internal pressure", AIAA J., Vol. 9, pp. 1713-1719 (1971).
- 368 Kempner, J., and Chen, Y. N., "Large deflections of an axially compressed oval cylindrical shell," Proceedings of the Eleventh International Congress of Applied Mechanics, Munich, Springer-Verlag, Berlin, pp. 299-306 (1966).
- 369 van der Neut, A., "General instability of stiffened cylindrical shells under axial compression," Natl. Luchtraartlab., the Netherlands, 13, Rept. S314 (1947).

- 370 Card, M. F., and Jones, R. M., "Experimental and theoretical results for buckling of eccentrically stiffened cylinders," N'SA TN D-3639 (1966).
- 371 Stein, M., "Recent advances in the investigation of shell buckling," AIAA Journal, Vol. 6, pp. 2339-2346 (1968).
- 372 Singer, J., Baruch, M., and Harari, O., "On the stability of eccentrically stiffened cylindrical shells under axial compression," Int. J. Solids Structures, Vol. 3, pp. 445-470 (1967).
- 373 Singer, J., "The influence of stiffener geometry and spacing on the buckling of axially compressed cylindrical and conical shells," Proceedings of the 2nd IUTAM Symposium on the Theory of Thin Shells, Copenhagen, (1967), edited by F. I. Niordson, Springer-Verlag (1969).
- 374 Khot, N. S., "On the influence of initial geometric imperfections on the buckling and postbuckling behavior of fiber-reinforced cylindrical shells under uniform axial compression, AFFDL-TR-68-136, (October 1968).
- 375 Khot, N. S., and Venkayya, V. B., "Effect of fiber orientation on initial postbuckling behavior and imperfection sensitivity of composite cylindrical shells," AFFDL Rept. TR-70-125 (1970).
- 376 Tennyson, R. C., Chan, K. H. and Muggeridge, D. B., "Effect of axisymmetric shape imperfections on the buckling of laminated anisotropic circular cylinders," Transactions Canadian Aeronautics and Space Institute, Univ. of Toronto, Canada, Vol. 4, pp. 131-139 (September 1971).
- 377 Kulkarni, S. V. and Frederick, D., "Buckling of partially debonded layered cylindrical shells, AIAA/ASME/SAE 14th SDM Conf., Williamsburg, Va. (March 1973).
- 378 Almroth, B. O., "Design of composite material structures for buckling", Lockheed Missiles & Space Co., Palo Alto, CA., Rept. LMSC-D681425 (Dec. 1979).
- 379 Wilkins, D. J., "Compression buckling tests of laminated graphite-epoxy curved panels," AIAA 12th Aerospace Sci. Meeting, Washington, D.C., (30 January - 1 February 1974).

- 380 Árbocz, J., and Williams, J. G., "Imperfection surveys on a 10-ft-diameter shell structure," AIAA J., Vol. 15, pp. 949-952 (1977).
- 381 Almroth, B. O., Burns, A. B., and Pittner, E. V., "Design criteria for axially loaded cylindrical shells," Report No. 6-78-69-22, Lockheed Missiles & Space Company, Palo Alto, CA (April 1969).
- 382 Peterson, J. P. and Dow, M. B., "Compression tests on circular cylinders stiffened longitudinally by closely spaced Z-section stringers," NASA Memo 2-12-59L, (March 1959).
- 383 Budiansky, B., and Amazigo, J. C., "Initial postbuckling behavior of cylindrical shells under external pressure," J. Math. Phys., 47, pp. 223-235 (1968).
- 384 Dow, D. A., "Buckling and postbuckling tests of ring stiffened cylinders loaded by uniform pressure," NASA TN D-3111, (November 1965).
- 385 Budiansky, B., "Post-buckling behavior of cylinders in torsion," in Theory of Thin Shells, F. I. Niordson, editor, pp. 212-233 (1969).
- 386 Yamaki, N., "Experiments on the postbuckling behavior of circular cylindrical shells under torsion", in Buckling of Structures, B. Budiansky, editor, Springer-Verlag, pp. 312-330 (1976).
- 387 Zoelly, R., "Ueber ein Knickungsproblem an der Kugelschale", Dissertation, Zurich, (1915).
- 388 van der Neut, A., "De elastische stabiliteit van den dunwandigen bol," Thesis, Delft, H. J. Paris, Amsterdam (1932).
- 389 Fung, Y. C. and Sechler, E. E., "Instability of thin elastic shells," Structural Mechanics, Proc. First Symp. Naval Struct. Mech., edited by J. N. Goodier and N. J. Hoff, Pergamon Press, 115 (1960).
- 390 Koiter, W. T., "The nonlinear buckling problem of a complete spherical shell under uniform external pressure," I, II, III and IV Proc. Kon. Ned. Ak. Wet., B72, 40-123, (1969).
- 391 Fitch, J. R., and Budiansky, B., "The buckling and postbuckling of spherical caps under axisymmetric load," AIAA Jour., 8, pp. 686-692, (1970).

- 392 Marguerre, K., "Zur Theorie der gekrummten Platte grosser Formanderung", Proceedings of 5th International Congress of Applied Mechanis, p. 93, (1938).
- 393 Hutchinson, J. W., "Imperfection-sensitivity of externally pressurized spherical shells", Jour. Appl. Mech., 34, pp. 49-55 (1967).
- 394 Tong, P. and Pian, T. H. H., "Postbuckling analysis of shells of revolution by the finite element method" in Thin Shell Structures, Y. C. Fung and E. E. Sechler, editors, Prentice-Hall, pp. 435-452 (1974).
- 395 Bushnell, D., "Symmetric and non-symmetric buckling of finitely deformed eccentrically stiffened shells of revolution, AIAA J., 5, pp. 1455-1462, (1967).
- 396 Bushnell, D., "Nonlinear axisymmetric behavior of shells of revolution, AIAA J., 5, pp. 432-439 (1967).
- 397 Koga, T. and Hoff, N., "The axisymmetric buckling of initially imperfect complete spherical shells," Intern. J. Solids Structures, 5, pp. 679-697, (1969).
- 398 Kalnins, A. and Biricikoglu, V., "On the stability analysis of imperfect spherical shells, J. Appl. Mech., 37, pp. 629-634 (1970).
- 399 Kao, R. and Perrone, N., "Asymmetric buckling of spherical caps with asymmetrical imperfections", J. Appl. Mech., Vol. , pp. 172-178 (March 1971).
- 400 Thompson, J. M. T., "The rotationally-symmetric branching behavior of a complete spherical shell," Koninklijke Nederland Akademie van Wetenschappen, Proceedings, Series B, Vol. 67, pp. 295-311 (1964).
- 401 Bushnell, D., Some problems in the theory of thin shells, Chap. 1, "Axisymmetric deformation of a shallow spherical cap clamped at the eage and submitted to uniform external pressure," Ph.D. Thesis, Stanford University (1965).

- 402 Krenzke, M. A., Kiernan, T. J., "Elastic stability of near-perfect shallow spherical shells, AIAA J., pp. 2855-2857 (1963).
- 403 Pedersen, P. T. and Jensen, J. J., "Correlation between experimental buckling loads and theoretical predictions for spherical cargo tanks for LNG", Proc. Steel Plated Structures Conference, Imperial College, (1976), Crosby Lockwood, pp. (197).
- 404 Hutchinson, J. W., "Initial post-buckling behavior of toroidal shell segments," Int. J. Solids & Structures, Vol. 3, pp. 97-115, (1967).
- 405 Penning, F. A. and Thurston, G. A., "The stability of shallow spherical shells under concentrated load," NASA-CR-265 (July 1965).
- 406 Penning, F. A., "Experimental buckling modes of clamped shallow shells under concentrated load," J. Appl. Mech., Vol. 33, pp. 297-304 (1966).
- 407 Wagner, H., Ebene Blechwandtrager mit sehr dünnem Stegblech, Z. Flugtech. Motorluft schiffahrt, Vol. 20, pp. 200, 227, 256, 279, and 306 (1929).
- 408 Kuhn, P., Stresses in Aircraft and Shell Structures, McGraw-Hill, New York (1956).
- 409 Skogh, J. and Stern, P., "Postbuckling behavior of a section representative of the B-1 aft intermediate fuselage," AFFDL-TR-73-63, Air Force Flight Dynamics Laboratory, Wright-Patterson Air Force Base, Ohio (May 1973).
- 410 Bushnell, D., "Prediction of loads on antenna ribs due to mesh deployment," Proc. 21st AIAA Structures, Structural Dynamics, and Material Conference, Seattle, WA, pp. (1980).
- 411 Southwell, R. V., "On the analysis of experimental observations in problems of elastic stability," Proceedings, Royal Society, London, Series A, Vol. 135, pp. 601-616 (1932).
- 412 Ariaratnam, S. T., "The Southwell method for predicting critical loads of elastic structures," Quarterly Journal of Mechanics and Applied Mathematics, Vol. 14, Part 2, pp. 137-153 (1961).
- 413 Horton, W. H., and Cundari, F. L., "On the applicability of the Southwell plot to the interpretation of test data from instability studies of shell bodies," Proceedings, of the AIAA/ASME 8th Structural Dynamics, and Materials Conference, Palm Springs, CA, pp. 651-660, (1967).

- 414 Hortor, W. H. and Craig, J. I. "Experimental studies of the effect of general imperfections on the elastic stability of thin shells," Israel J. of Technology, Vol. 7, No. 1-2, pp. 91-103 (1969).
- 415 Horton, W. H., Nassar, E. M., and Singhal, M. K., "Determination of the critical loads of shells by nondestructive methods," Experimental Mechanics, Vol. 17, No. 4, pp. 154-160 (1977).
- 416 Donnell, L. H., "On the application of Southwell's method for the analysis of buckling tests," Stephen Timoshenko 60th Anniversary Volume, MacMillan Book Co., pp. 27-38 (1938).
- 417 Roorda, J., "Some thoughts on the Southwell plot," ASCE J. Eng. Mech. Div., Vol. EM6, pp. 37-48, (Dec. 1967).
- 418 Mandell, J. F., "An experimental investigation of anisotropic fiber reinforced plastic plates, AFML TR-68-281 (1968).
- 419 Tennyson, R. C., Muggeridge, D. B., and Chan, K. H., "Buckling of fiber-reinforced circular cylinders under axial compression," AFFDL TR-72-102, (August 1972).
- 420 Booton, M., "Buckling of imperfect anisotropic cylinders under combined loading," Institute for Aerospace Studies, Univ. of Toronto, UTIAS Rept. No. 203, (August 1976).
- 421 Tsai, S. W., "Strength characteristics of composite materials, NASA CR-224, (April 1965).
- 422 Sturm, R. G., "A study of the collapsing pressure of thin-walled cylinders," University of Illinois, Engineering Experiment Station Bulletin No. 329, (before 1956).
- 423 Galletly, G. D. and Reynolds, T. E., "A simple extension of Southwell's method for determining the elastic general instability of ring stiffened cylinders subjected to external pressure," Proceedings SESA, Vol. 13, No. 2, pp. 141-151 (1956).
- 424 Kendrick, S., "The buckling under external pressure of circular cylindrical shells with evenly spaced equal strength circular ring frames," Part I, NCRE/R No. 211, Naval Construction Research Establishment, Dumfurline, Scotland, (1953).

- 425 Banks, M. H., "The effect of fiber direction on the stability of single-layer resin impregnated glass cloth cylinders under torsion", Engineer's Thesis, Stanford University, (1966).
- 426 Bushnell, D., "Stress, buckling, and vibration of hybrid bodies of revolution," Computers & Structures, Vol. 7, pp. 517-537 (1977).
- 427 Unpublished test results, Lockheed Missiles & Space Co., Inc. (1976).
- 428 Bushnell, D., Holmes, A.M.C., and Loss, E.J., "Failure of axially compressed frangible joints in cylindrical shells," Proc. 20th AIAA/ASME Structures, Structural Dynamics, and Materials Symposium, pp. 145-157 (April 1979); to appear Computers & Structures (1980).
- 429 Bushnell, D. and Yamamura, T. T., "BOSOR6 analysis of the IUS interstage super-zip joint", Lockheed Missiles & Space Co., Inc., Palo Alto, CA, Report LMSC-D626721 (July 1978).
- 430 Bushnell, D., "Computerized analysis of shells - Governing equations," Air Force Wright Aeronautical Laboratories, Wright Patterson Air Force Base, Ohio, AFWAL-TR-81-3048, Dec. 1981.

TABLE 1 COMPARISON OF TEST AND THEORY FOR AXIALLY COMPRESSED CYLINDERS

Model	R/t	Test (Lee [1962]) Load (lb)	BOSOR5 Prediction ^a	Highest Test BOSOR5	Lowest Test BOSOR5
A300	46.1	5400	5202	1.038	—
A110	29.2	9090	8923	1.019	0.884
A210		8680			
A310		7890			
A120	19.4	14500	14328	1.036	1.005
A220		14840			
A320		14400			
A130	9.4	35000	33200	1.087	1.054
A230		36100			
A330		36000			

^aAxisymmetric collapse predicted in all cases

TABLE 2 COMPARISON OF TEST AND THEORY FOR AXIALLY COMPRESSED CYLINDERS TESTED BY PATTERMAN [1965]

Model	R/t	Test Stress (psi)	BOSOR5 Prediction ^a (Clamped Edges)	Test BOSOR5
9	116.61	31770	44643	0.712
8	114.56	33030		
10	113.60	35600	43478	0.820
17	89.33	43950		
26	85.95	43690	45063	0.970
16	56.52	51380	52282	0.983
25	54.93	50640		
15	44.69	55490		
24	44.19	53380	55663	0.959
4	26.61	58200		
3	26.56	58200		
2	26.44	57100		
1	26.18	58600		
5	25.94	59570		
6	25.88	58760	57422	1.023
14	19.71	61580	59175	1.041
23	19.66	61480		
13	14.02	64110		
22	13.93	63790	62886	1.014
18	9.76	70000		
19	9.76	69320		
20	9.76	69840	71225	0.980
12	9.70	69630		
27	9.70	69230		

^aAxisymmetric collapse predicted in all cases

TABLE 3 CALCULATED BUCKLING LOADS $p_{cr} = p/p_{cl}$ FOR RING-SUPPORTED SPHERICAL SHELLS; RADIUS-TO-THICKNESS RATIO, $a/t = 100^a$

α	A^*	0	0.4	1.6	6.4	25.6	∞	Hinged
0.22		0.139 (0)	0.222 (0)	0.399 (0)	0.499 (0)	0.545 (0)	0.568 (0)	^b
0.33		0.171 (0)	0.265 (0)	0.511 (2)	0.675 (2)	0.740 (2)	0.770 (2)	
0.495		0.190 (3)	0.278 (3)	0.490 (4)	0.668 (4)	0.740 (4)	0.772 (4)	
0.88		0.206 (6)	0.302 (7)	0.488 (9)	0.690 (10)	0.760 (10)	0.795 (10)	
1.20		0.0253 (2)	0.0340 (2)	0.128 (2)	0.755 (13)	0.776 (13)	0.798 (13)	
1.57		0.0069 (2)	0.0085 (2)	0.0293 (2)	0.328 (2)	0.805 (15)	0.810 (15)	
1.91		0.0052 (2)	0.0067 (2)	0.0259 (2)	0.261 (2)	0.839 (15)	0.810 (15)	
2.26		0.0064 (2)	0.0093 (2)	0.0418 (2)	0.364 (2)	0.860 (14)	0.816 (14)	
2.65		0.0147 (2)	0.0294 (2)	0.140 (2)	1.000 (-)	0.865 (10)	0.838 (10)	
2.92		0.0590 (2)	0.181 (2)	0.600 (2)	1.000 (-)	0.875 (6)	0.863 (6)	

^a Numbers in parentheses are numbers of circumferential waves in the buckle pattern.

^b These dividing lines separate the various classes of buckling discussed in the text.

α is the angle in radians from the apex of the cap to the edge.

A^* is the edge ring area parameter $A^* = (A/at)(a/t)^{1/2}$.

Table 4 Critical loads $r_1 V_{cr}(1 - \nu^2)/Et^2$ for spherical segments in tension

α_1^a	$R/t = 100$				$R/t = 455$				$R/t = 1600$			
	n	Eq. (4.32)	Linear	Non-linear	n	Eq. (4.32)	Linear	Non-linear	n	Eq. (4.32)	Linear	Non-linear
1.16					38	0.580	0.574	0.578	71	0.552	0.532	0.539
1.0					37	0.518	0.513	0.522				
0.9	18	0.543	0.540		35	0.463	0.468	0.480	63	0.426	0.423	0.430
0.8					33	0.405	0.414	0.430				
0.7	16	0.448	0.442	0.488	30	0.348	0.353	0.371	53	0.305	0.308	0.315
0.6					27	0.285	0.289	0.310				
0.5	13	0.326	0.309	0.381	24	0.224	0.226	0.250	41	0.183	0.188	0.197
0.4					21	0.167	0.166	0.191				
0.3	10	0.205	0.170	0.269	17	0.115	0.110	0.137	28	0.0845	0.0853	0.0940
0.25					15	0.0910	0.0856	0.112				
0.20	8	0.149	0.107	0.225	13	0.0698	0.0632	0.0903	20	0.0467	0.0457	0.0545
0.20	9	0.149	0.112	0.222								
0.15					10	0.0518	0.0432	0.0728				
0.15					11	0.0518	0.0434	0.0714				
0.15					12	0.0518		0.0723				
0.10	4	0.0990	0.0638		7	0.0360	0.0273	0.0682	11	0.0193	0.0173	
0.10	5	0.0990	0.0526		8	0.0360	0.0262	0.0592	12	0.0193	0.0169	0.0254
0.10	6	0.0990	0.0539		9	0.0360	0.0269	0.0567	13	0.0193	0.0171	0.0253
0.10	7	0.0990	0.0605	0.196	10	0.0360		0.0572	14	0.0193	0.0176	0.0258
0.10	8	0.0990	0.0703	0.193								
0.10	9	0.0990		0.199								
0.05	3	0.0775	0.0377		5	0.0230	0.0127		7	0.0100	0.0074	
0.05	4	0.0775	0.0297		6	0.0230	0.0126	0.0580	8	0.0100	0.0072	0.0169
0.05	5	0.0775	0.0331		7	0.0230	0.0139	0.0496	9	0.0100	0.0075	0.0162
0.05	6	0.0775	0.0406		8	0.0230		0.0479	10	0.0100		0.0164
0.05	7	0.0775	0.0510	0.188	9	0.0230		0.0489				
0.05	8	0.0775		0.188								
0	8	0.0580		0.185	8	0.0128		0.0456	8	0.0033		0.0133

^a With $\alpha_1 = 1.16$, $\alpha_2 = 1.57$. These cases were treated experimentally and analytically by Yao (1963). For all other α_1 , with $R/t = 100$: $\alpha_2 = \alpha_1 + 1.0$ rad. With $R/t = 455$ and 1600 $\alpha_2 = \alpha_1 + 0.5$ rad. The nonlinear results were obtained with an early version of BOSOR (see AIAA J, 5, pp. 1455-1462, 1967).

Table 5 BUCKLING LOADS PR/Et^3 FOR SPHERICAL SHELLS
WITH OUTWARD-DIRECTED CONCENTRATED LOADS.

R/t	n	PR/Et^3
3040	8	148
1600	8	147
455	8	144
100	8	129
50	8	113

TABLE 6 INTERNALLY PRESSURIZED TORISPHERICAL HEADS

Specimen	Tested By	Material	Geometry						Buckling Test Results ⁶ (p _{cr} /E)×10 ⁶	BOSOR5 Buckling Predictions			
			Elastic-Plastic							Elastic			
			t _n (mm)	R _c / t _n	R _t / t _n	R _s / t _n	L _c / R _c	Flow Theory		Deformation Theory	Linear	Nonlinear	
A1	Galletly	Aluminum	0.127	540	220	1080	0.6	8.25	8.93 (45) (a)	8.93 (45)	5.7 (50)	13.7 (50)	
A2	Galletly	Aluminum	0.254	270	110	540	0.6	20.87	21.36 (21)	20.90 (25)			
A3	Galletly	Aluminum	0.254	270	110	540	0.6	21.84	22.91 (25)	21.34 (29)	24.0 (37)	No buckling	
MS1	Galletly	Mild Steel	0.127	540	220	1080	0.6	4.23	1.47 (30-40)		4.0 (55)	6.9 (55)	
MS2	Galletly	Mild Steel	0.127	540	220	1080	0.6	2.60	1.17 (30-40)		1.67 (65)	4.3 (55)	
MS3	Galletly	Mild Steel	0.127	540	220	1080	0.6	2.73	2.00 (27)	1.73 (27)	5.01 (50)	10.77 (50)	
MS4	Galletly	Mild Steel	0.127	540	220	1080	0.6	2.50	1.77 (28)		3.4 (55)	3.3 (50)	
4A	Kirk & Gill	Aluminum	0.254	266	40	531	1.0	3.44 (75)	5.13 (40)	4.28 (35)	11.4 (75)	15.3 (65)	
4B	Kirk & Gill	Aluminum	0.254	266	60	531	1.0	5.40 (62)	6.85 (40)	5.70 (35)	12.8 (60)	19.7 (50)	
4C	Kirk & Gill	Aluminum	0.254	266	90	531	1.0	10.81 (49)	10.48 (28)	9.41 (40)	14.3 (45)	34.8 (45)	
1	Patel & Gill	Aluminum	0.254	266	30	531	1.0	4.20	4.17 (45)	3.70 (80)	--	--	
2	Patel & Gill	Aluminum	0.254	266	40	531	1.0	6.20 (54)	7.56 (35)	6.01 (60)	--	--	
3	Patel & Gill	Aluminum	0.254	266	50	531	1.0	6.87	6.48 (45)	5.71 (55)	--	--	
4	Patel & Gill	Aluminum	0.254	266	60	531	1.0	6.34	6.94 (45)	6.48 (50)	--	--	
5	Patel & Gill	Aluminum	0.254	266	70	531	1.0	9.49	9.26 (35)	8.95 (40)	--	--	
6	Patel & Gill	Aluminum	0.254	266	80	531	1.0	11.06	12.65 (30)	12.04 (35)	--	--	
7	Patel & Gill	Aluminum	0.254	266	90	531	1.0	12.5	11.88 (35)	11.42 (35)	--	--	
8	Patel & Gill	Aluminum	0.254	266	100	531	1.0	10.56	10.03 (35)	9.72 (35)	--	--	
9	Patel & Gill	Aluminum	0.254	266	110	531	1.0	No buckling	17.75 (20)	16.98 (25)	--	--	
10	Patel & Gill	Aluminum	0.254	266	120	531	1.0	No buckling	No buckling	No buckling	--	--	

(a) Numbers in parentheses indicate circumferential waves, n_{cr} .

TABLE 7 PREDICTED FAILURE OF STEEL WATER TOWER

Model	Critical Hydrostatic Pressure Factor ^a
Hydrostatic Pressure Only	$1.9 < \lambda_{cr} < 2.0$
Welding + Pressure	$1.8 < \lambda_{cr} < 1.9$
Cold Bending + Pressure	$1.7 < \lambda_{cr} < 1.75$
Mismatch #1 + Pressure	$2.0 < \lambda_{cr} < 2.1$
Mismatch #2 + Pressure	$1.8 < \lambda_{cr}$

^aFailure mode is axisymmetric collapse in all cases.

TABLE 8 NOMENCLATURE FOR BOUNDARY CONDITIONS ON
CYLINDRICAL SHELLS UNDER AXIAL COMPRESSION
OR UNIFORM EXTERNAL HYDROSTATIC PRESSURE^a

Case S1 when $M_x = 0$	$u = 0$	$v = 0$
Case S2 when $M_x = 0$	$N_x = 0$	$v = 0$
Case S3 when $M_x = 0$	$u = 0$	$N_{xy} = 0$
Case S4 when $M_x = 0$	$N_x = 0$	$N_{xy} = 0$
Case C1 when $w_{,x} = 0$	$u = 0$	$v = 0$
Case C2 when $w_{,x} = 0$	$N_x = 0$	$v = 0$
Case C3 when $w_{,x} = 0$	$u = 0$	$N_{xy} = 0$
Case C4 when $w_{,x} = 0$	$N_x = 0$	$N_{xy} = 0$

^a $w = 0$ at the boundary in all 8 cases
In the work of Singer et al. [33] SS3 = S2 and SS4 = S1

TABLE 9 CRITICAL HYDROSTATIC PRESSURES ($p_{cr} a/Eh$) $\times 10^3$, $a/h = 100^a$

	Analysis of Sobel										Galletly and Bart	Nash
	$N_x = 0, w = 0$					$u = 0, w = 0$						
	②	③	④	⑤	⑥	⑦	⑧	⑨	⑩	⑪		
L/a	S_2 $M_x = 0$ $w, x = 0$ $v = 0$	C_2 $w, x = 0$ $v = 0$	S_4 $M_x = 0$ $N_{xy} = 0$	C_4 $w, x = 0$ $N_{xy} = 0$	S_3 $M_x = 0$ $N_{xy} = 0$	C_3 $w, x = 0$ $N_{xy} = 0$	S_1 $M_x = 0$ $v = 0$	C_1 $w, x = 0$ $v = 0$			$w, x = 0$ $v = 0$	
0.5	2.106(11) ^b	2.652(12)	1.930(10)	2.632(11)	2.078(10)	2.798(12)	2.366(11)	2.851(12)	2.912(12)	2.930(12)		
0.6	1.715(10)	2.068(11)	1.599(9)	2.065(11)	1.771(10)	2.239(11)	1.976(11)	2.282(11)	2.349(11)	2.366(11)		
0.75	1.344(9)	1.557(10)	1.268(9)	1.557(10)	1.455(9)	1.743(10)	1.599(10)	1.774(10)	1.846(10)	1.862(10)		
1.0	0.9838(8)	1.104(8)	0.9416(8)	1.103(8)	1.146(8)	1.289(9)	1.224(9)	1.306(9)	1.372(9)	1.388(9)		
1.5	0.6417(7)	0.6981(7)	0.6290(7)	0.6889(7)	0.8094(7)	0.8636(8)	0.8446(8)	0.8688(8)	0.9075(8)	0.9213(8)		
2.0	0.4744(6)	0.5023(6)	0.4657(6)	0.5020(6)	0.6250(7)	0.6520(7)	0.6441(7)	0.6552(7)	0.6833(7)	0.6971(7)		
3.0	0.3132(5)	0.3255(5)	0.3097(5)	0.3251(5)	0.4342(6)	0.444(6)	0.4412(6)	0.4444(6)	0.4580(6)	0.4708(6)		
4.0	0.2395(4)	0.2479(4)	0.2350(4)	0.2478(4)	0.3273(5)	0.3340(5)	0.3333(5)	0.3351(5)	0.3466(5)	0.3608(5)		
5.0	0.1878(4)	0.1920(4)	0.1867(4)	0.1917(4)	0.2764(5)	0.2783(5)	0.2779(5)	0.2785(5)	0.2830(5)	0.2946(5)		
6.0	0.1679(4)	0.1703(4)	0.1676(4)	0.1700(4)	0.2246(4)	0.2281(4)	0.2281(4)	0.2288(4)	0.2364(4)	0.2520(4)		
7.0	0.1378(3)	0.1407(3)	0.1361(3)	0.1407(3)	0.1923(4)	0.1938(4)	0.1936(4)	0.1940(4)	0.1978(4)	0.2109(4)		
8.0	0.1158(3)	0.1177(3)	0.1151(3)	0.1176(3)	0.1751(4)	0.1757(4)	0.1756(4)	0.1758(4)	0.1779(4)	0.1897(4)		
9.0	0.1038(3)	0.1051(3)	0.1035(3)	0.1050(3)	0.1653(4)	0.1656(4)	0.1655(4)	0.1656(4)	0.1669(4)	0.1780(4)		
10.0	0.09678(3)	0.09776(3)	0.09662(3)	0.09762(3)	0.1423(3)	0.1440(3)	0.1442(3)	0.1445(3)	0.1492(3)	0.1677(3)		

^a Results taken from Sobel [4.148]

^b Numbers in parentheses indicate the number of circumferential waves

TABLE 10 CRITICAL VALUES OF NORMALIZED AXIAL COMPRESSION N_{cr}/N_{cl} FOR MONOCOQUE CYLINDRICAL SHELLS^a

r/t	L/r	N_{cr}/N_{cl} and (Number of Waves)							
		S1	S2	S3	S4	C1	C2	C3	C4
10^4 ↓	0.07	0.872(85)	0.805(79)	0.507(2)	0.499(2)	0.908(83)	0.862(82)	0.908(83)	0.862(82)
	0.16	.864(86)	.846(84)	.504(2)	.501(2)	.926(88)	.914(86)	.926(88)	.913(86)
	0.24	.868(86)	.843(79)	.503(2)	.501(2)	.927(87)	.908(78)	.927(87)	.906(78)
	10^4	.867(84)	.844(82)	.503(2)	.501(2)	.926(86)	.910(82)	.926(86)	.908(82)
10^3 ↓	0.222	.874(27)	.807(25)	.507(2)	.500(2)	.907(27)	.863(25)	.907(27)	.861(26)
	0.506	.863(27)	.846(27)	.505(2)	.501(2)	.927(27)	.914(27)	.927(27)	.913(27)
	0.760	.867(27)	.842(25)	.503(2)	.502(2)	.930(28)	.908(25)	.930(28)	.906(25)
	10^3	.867(27)	.844(26)	.503(2)	.502(2)	.926(27)	.910(26)	.926(27)	.908(26)
10^2 ↓	0.7	.876(9)	.806(8)	.513(2)	.508(2)	.910(9)	.863(8)	.910(9)	.862(8)
	1.6	.858(8)	.849(8)	.512(2)	.511(2)	.929(9)	.917(9)	.929(9)	.916(9)
	2.4	.868(9)	.843(8)	.511(2)	.511(2)	.930(9)	.908(8)	.930(9)	.903(8)
	10^2	.868(9)	.844(8)	.510(2)	.510(2)	.928(9)	.911(8)	.928(9)	.909(8)

^a $N_{cr}/N_{cl} = N_{cr}/(2\gamma Et)$, with $\gamma \equiv (t/r)/[12(1-\nu^2)]^{1/2}$

TABLE 11 EXPERIMENTAL AND THEORETICAL BUCKLING PRESSURES OF CONE-CYLINDER VESSELS TESTED UNDER EXTERNAL PRESSURE BY GALLETT [131]

Case	Description of Model	Buckling Pressures (psi)			
		Cone Angle→	45°	60°	75°
1.	Experimental results		559	410	185
2.	Elastic-Plastic model [Fig. 120(c)]		553(6) ^a	397(3)	184(2)
3.	Elastic model with no hinge between Segments ② and ③		598(6)	473(4)	213(2)
4.	Elastic with hinge between Segments ② and ③ in both prebuckling and instability analyses		509(6)	327(4)	113(2)
5.	Elastic with hinge between Segments ② and ③ in stability analysis only		564(6)	434(4)	185(2)

^a Numbers in parentheses are the number of circumferential waves corresponding to the lowest predicted bifurcation buckling pressure

TABLE 12 EXPERIMENTAL AND THEORETICAL BUCKLING PRESSURES FOR THE
TORISPHERICAL HEADS WITH AXISYMMETRIC NOZZLES TESTED UNDER
EXTERNAL PRESSURE BY GALLETTY [131]

Case	Description of Model	Spec. Designation	Buckling Pressures (psi)			
			A3	A4	A5	A6
1.	Experimental results		177	208	168	215
2.	Elastic-plastic model [Fig. 121(b)]		182	205	160	206
3.	Elastic model with no hinge between Segments ② and ③		217	221	228	269
4.	Same as Case 3, except with hinge at nozzle-head junction in both prebuck- ling and stability analyses		128	123	115	112
4.	Same as Case 3, except with hinge at nozzle-head junction in the stability analysis only		181	184	174	197

TABLE 13 DIMENSIONS AND PROPERTIES OF AB CYLINDRICAL SHELLS TESTED
UNDER AXIAL COMPRESSION BY SINGER ET AL. [33]

Shell ^a	h, mm	L, mm	R/h	L/R	Z ^b	d, mm ^c	b/h ^c
AB1	0.257	110	467	0.92	377	1.779	34.63
AB2	0.253	110	475	0.92	384	1.758	35.18
AB3	0.253	154	475	1.28	742	1.748	35.18
AB4	0.253	154	475	1.28	742	1.742	35.18
AB5	0.252	130	477	1.08	531	1.700	35.32
AB6	0.254	130	473	1.08	526	1.485	35.04

R = 120.1 (mm), b = 8.9 (mm), t_s = 0.9 (mm), except Shell AB5 where t_s = 0.8 (mm)
E = 7500 (kg/mm²), ν = 0.3
Material: Aluminum alloy 7075-T6

- ^a All shells are stiffened by integral stringers; h = thickness, L = length, R = radius
^b Z = $(1-\nu^2) \frac{1}{2} (L/R)^2 (R/h)$
^c d = stringer height, t_s = stringer thickness, b = stringer spacing

TABLE 14 THEORETICAL AND EXPERIMENTAL BUCKLING LOADS AND (MODES)

Shell	Experiment		SS3 ^a	SS4	Clamped
	P _{exp} , kg	P _{post} , kg ^b	P _{cr} , kg	P _{cr} , kg	P _{cr} , kg
AB1	4700 (9)	4150	4996 (12)	6554 (12)	9300 (12)
AB2	4900 (9)	4040	4828 (12)	6358 (12)	8990 (12)
AB3	3400 (8)	2970	3967 (10)	5942 (11)	7230 (12)
AB4	3615 (8)	3038	3955 (10)	5929 (11)	7204 (12)
AB5	3580 (8)	3000	3833 (11)	5574 (12)	7044 (12)
AB6	4025 (9)	2250	3687 (11)	5425 (12)	6489 (12)

^a SS3 denotes $v = w = N_x = M_x = 0$ at the edges
SS4 denotes $v = w = u_x = M_x = 0$ at the edges

^b P_{post} = post buckling load-carrying capability

TABLE 15 BUCKLING LOADS (MILLIONS OF LBS) FOR
AXIALLY COMPRESSED ECCENTRICALLY
STIFFENED ALUMINUM CYLINDRICAL SHELLS

Boundary Condition Code No. ^a		Internal Stiffening	External Stiffening
Nonlinear prebuckling analysis	1	1.670 (18) ^b	3.770 (19)
	2	1.250 (20)	4.350 (17)
	3	3.580 (14)	1.235 (26)
	4	4.540 (20)	9.620 (15)
Membrane prebuckling analysis	1,2,3	1.520 (18)	2.700 (21)
	4	3.670 (21)	6.060 (22)

^a Boundary condition code: Axial load applied at 1) neutral surface, 2) shear center, 3) centroid of stiffener, 4) shell clamped

^b Numbers in parentheses indicate number of circumferential waves in buckle pattern

TABLE 16 COMPARISON OF "KNOCKDOWN" FACTORS FOR UNIFORMLY AXIALLY COMPRESSED CYLINDERS WITH RESULTS OF ANALYSIS

	Anderson and Card Tests [204]	Smith Tests [210]	Hill Tests [105]
Effective radius/thickness	320	450-650	640
Typical knockdown factors for uniform axial compression [34]	0.5-1.0	0.4-0.5	0.2-0.35
Knockdown factors determined by this analysis	0.71	0.66-0.89	0.74-0.87
Comments	Short cylinder: effective length/diameter = 0.25, because of ring-stiffen- ers. Heating on very wide axial strip.		
	Conical shells heated on axial strips of medium width		
	Very thin long cylinders heated on very narrow axial strips		

TABLE 17 COMPARISON OF TEST AND THEORY FOR RING-STIFFENED ALUMINUM CYLINDERS SHOWN IN FIGURES 160(a,b).

Model Number- Frame Number	Test Results lb/in. ² (Ref. [18])	Theory	
		Clamped Ends	Free Ends With Large End Rings
<u>Group 1</u> <i>a, b</i>			
1-1	240(2) ^c	281(2)	210(2)
2-2	299(2)	351(2)	280(2)
3-3	407(2)	445(2)	374(2)
4-4	464(2)	517(2)	446(2)
5-5	555(2)	601(2)	530(2)
6-6	795(2)	850(2)	781(2)
7-7	777(2)	838(2)	768(2)
8-8	913(2)	990(2)	921(2)
9-9	963(2)	1058(2)	989(2)
10-10	1055(4)	1120(4)	1117(4)
11-11	1020(4)	1133(4)	
<u>Group 2</u>			
12-1	480(3)	516(3)	395(2)
13-3	785(3)	846(3)	547(2)
14-5	948(3)	1037(3)	695(2)
15-6	1048(4)	1100(4)	933(2)
<u>Group 3</u>			
16-1	621(3)	715(3)	631(3)
17-2	797(3)	900(3)	800(3)
18-3	967(3)	1085(3)	967(3)
19-4	1063(3)	1198(3)	1114(3)
20-5	1075(4)	1189(4)	1152(4)
<u>Group 4</u>			
21-5	758(2)	834(2)	753(2)
22-7	1115(2)	1237(2)	1100(2)
23-9	1471(2)	1611(2)	1537(2)
24-10	1704(5)	1913(2) 1924(5) ^d	1843(2)

^aGroup geometries shown in Figure 160(a).

^bFrame (ring) geometries shown in Figure 160(b).

^cNumbers in parentheses refer to circumferential waves.

^dCorresponds to displacements antisymmetric with respect to symmetry plane.

TABLE 18 EFFECTS OF AXIAL RESTRAINT ON BUCKLING LOADS
OF BLUMENBERG* CYLINDERS 12-15

Model Number- Frame Number	Test Results lb/in. ² (Ref. [18])	Theory				
		Clamped Ends	Ends with Large Rings			
			Axial Restraint u = 0		No Restraint	
12-1	480(3)	516(3)	698(2)	512(3)	395(2)	499(3)
13-3	785(3)	846(3)	856(2)	842(3)	547(2)	832(3)
14-5	948(3)	1037(3)	1006(2)	1035(3)	695(2)	1027(3)
15-6	1048(4)	1100(4)	1245(2)	1096(4)	933(2)	1089(4)

* See Figures 160(a,b) for geometry of shell and frames (rings).

TABLE 19 CONVERGENCE OF CRITICAL LATERAL PRESSURE
PARAMETER^a, $P_{cr} = p_{cr} a/Et$

b , in.	$L/a = 0.6$ $a = 5.236$ in.		$L/a = 6.0$ $a = 0.5236$ in.	
	$P_{cr}^{(10)b}$	$P_{cr}^{(11)b}$	$P_{cr}^{(4)b}$	$P_{cr}^{(6)b}$
10			0.26141	0.38559
25	1.8467	1.9949	0.19387	0.33774
50	1.7790	1.9090	0.17486	0.33036
100	1.7415	1.8815	0.16668	0.32789
500	1.7129	1.8664	0.16085	0.32648
1,000	1.7095	1.8649	0.16017	0.32634
5,000	1.7068	1.8638	0.15964	0.32623
10,000	1.7065	1.8637	0.15957	0.32620
∞	1.7024 \leftarrow (Flügge)		0.15943 \leftarrow (Flügge)	

^a With increasing toroidal radius b for shells with $a/t = 100$, $E = 10^6$ psi, $\nu = 0.3$

^b Superscripts in parentheses represent the total number of waves around the circumference of the cylinder.

TABLE 20 MESH POINT CONVERGENCE STUDY FOR SIMPLY-SUPPORTED CIRCULAR CYLINDER^a

Number of mesh points per half-wave	$L/a = 0.6$ $a = 5.236$ in. $P_{cr}^{(10)}$	$L/a = 6.0$ $a = 0.5236$ in. $P_{cr}^{(4)}$
2	2.0467	0.21976
4	1.7886	0.17209
6	1.7409	0.16491
8	1.7242	0.16250
10	1.7164	0.16141
14	1.7097	0.16046
19	1.7065	0.16002
25	...	0.15979
35	...	0.15964
48	...	0.15957
∞	1.7024	0.15943

^a Analyzed as portion of torus with radius $b = 10,000$, $a/b = 100$, $E = 10^6$ psi, $\nu = 0.3$. Critical lateral pressure parameter $P_{cr} = p_{cr} a/Et$

TABLE 21 MESH POINT CONVERGENCE STUDY FOR SIMPLY-SUPPORTED CIRCULAR CYLINDER ANALYZED AS A CYLINDER^a

Number of axial mesh points	Critical lateral pressure, P_{cr}
5	1.7146
10	1.7063
20	1.7035
30	1.7029
50	1.7025
80	1.7024
97	1.7024

^a $P_{cr} = p_{cr} a/Et$, $a/t = 100$, $E = 10^6$ psi, $\nu = 0.3$, $L/a = 0.6$, $a = 5.236$ in

(All from Bushnell [82])

TABLE 22 BUCKLING PRESSURES OF ELLIPTICAL CYLINDERS WITH
A/B = 2 AND VARIOUS LENGTHS AND THICKNESSES^a

		Buckling pressures, psi				
Thickness <i>t</i> , in.	Length <i>L</i> , in	Theory		Test		Test/ BOSOR
		BOSOR <i>p_{cr}</i> ¹	BOSOR with <i>x₀</i> = 0 <i>p_{cr}</i> ²	Yao and Jenkins <i>p_{cr}</i> ³	Yao and Jenkins <i>p_{cr}</i> ^T	<i>p_{cr}</i> ^T / <i>p_{cr}</i> ¹
0 019	2	0 730	0 797	0 714	0 613	0 84
	4	0 368	0 381	0 331	0 324	0 88
	6	0 246	0 252	0 217	0 239	0 97
	8	0 189	0 203	0 166	0 189	1 00
	10	0 150	0 170	0 133	0 140	0 93
0 029	2	2 16	2 47	2 23	1 88	0 87
	4	1 11	1 16	1 00	0 877	0 79
	6	0 739	0 788	0 661	0 665	0 90
	8	0 567	0 621	0 499	0 533	0 94
	10	0 437	0 502	0 390	0 411	0 94
0 051	2	10 0	11 5	10 12		
	4	4 71	5 13	4 33	3 10	0 66
	6	3 20	3 53	2 82	2 21	0 69
	8	2 26	2 64	2 03	1 54	0 68
	10	1 63	2 15	1 63	1 14	0 70
0 091	2	57 2	57 6	50 5		
	4	20 5	24 4	20 1		
	6	13 4	15 9	12 5	7 77	0 58
	8	9 23	12 2	9 42	5 81	0 63
	10	5 87	10 6	8 23	4 46	0 76

^a *E* = 470,000 psi, *ν* = 0.37, *A* = 4.0 in., *B* = 2.0 in.

TABLE 23 BUCKLING PRESSURES OF ELLIPTICAL CYLINDERS WITH
A/B = 1.5 AND VARIOUS LENGTHS AND THICKNESSES^a

		Buckling pressures, psi				
Thickness <i>t</i> , in.	Length <i>L</i> , in	Theory		Test		Test/ BOSOR
		BOSOR <i>p_{cr}</i> ¹	BOSOR with <i>x₀</i> = 0 <i>p_{cr}</i> ²	Yao & Jenkins <i>p_{cr}</i> ³	Yao & Jenkins <i>p_{cr}</i> ^T	<i>p_{cr}</i> ^T / <i>p_{cr}</i> ¹
0 019	2	0 706	0 768	0 683	0 600	0 85
	4	0 345	0 349	0 316	0 300	0 87
	6	0 228	0 231	0 207	0 214	0 94
	8	0 172	0 176	0 155	0 167	0 97
	10	0 138	0 143	0 125	0 131	0 95
0 029	2	2 08	2 36	2 15	1 60	0 77
	4	1 34	1 05	0 952	0 874	0 84
	6	0 678	0 691	0 621	0 610	0 90
	8	0 511	0 525	0 466	0 496	0 97
	10	0 408	0 424	0 371	0 403	0 99
0 049	2	8 60	9 76	9 45		
	4	3 99	4 14	3 96	3 07	0 77
	6	2 64	2 71	2 54	2 22	0 84
	8	1 97	2 04	1 89	1 69	0 86
	10	1 60	1 69	1 51	1 38	0 86
0 090	2	50 7	52 7	49 7		
	4	18 6	20 8	19 1		
	6	12 7	13 4	12 0	9 52	0 75
	8	9 66	10 3	8 88	7 63	0 79
	10	7 51	8 21	7 01	5 86	0 78

^a *E* = 470,000 psi, *ν* = 0.37, *A* = 5.3333 in., *B* = 3.5777 in.

(both from Bushnell [82])

TABLE 24 CONVERGENCE OF ELLIPTICAL CYLINDER BUCKLING PRESSURES (psi)^a

t	1 term	3 terms	5 terms	9 terms
0.019	0.152	0.151	0.150	0.150
0.029	0.449	0.442	0.438	0.437
0.051	1.73	1.65	1.63	1.63
0.091	6.97	6.32	6.05	5.87

^a With increasing numbers of terms in the Fourier sine series expansion of uniform pressure: $A/B = 2$, $L = 10$ in.

TABLE 25 INFLUENCE OF BOUNDARY CONDITIONS AND PREBUCKLING BEHAVIOR ON THE BUCKLING LOAD OF AXIALLY COMPRESSED CYLINDRICAL SHELLS (from Arbocz and Babcock [341])

Boundary Conditions	λ_{crit}	
	Hoff and Soong [330] (Membrane Prebuckling)	Almroth [152] (Rigorous Prebuckling)
$w = w_{,xx} = \sigma_x = \tau_{xy} = 0$	0.5	0.502
$w = w_{,xx} = u = \tau_{xy} = 0$	0.5	0.503
$w = w_{,xx} = \sigma_x = v = 0$	1.0	0.844
$w = w_{,xx} = u = v = 0$	1.0	0.867
$w = w_{,x} = \sigma_x = \tau_{xy} = 0$	1.0	0.908
$w = w_{,x} = u = \tau_{xy} = 0$	1.0	0.926
$w = w_{,x} = \sigma_x = v = 0$	1.0	0.910
$w = w_{,x} = u = v = 0$	1.0	0.926

TABLE 26 COEFFICIENTS FOR STIFFENED SHELLS USED IN THE DERIVATION BY HUTCHINSON AND FRAUENTHAL [346]

$$\{D_{xx}, D_{xy}, D_{yy}\} = \frac{Et^3}{12(1-\nu^2)} \{\bar{D}_{xx}, \bar{D}_{xy}, \bar{D}_{yy}\}; \quad \{Q_{xx}, Q_{xy}, Q_{yy}\} = t\{\bar{Q}_{xx}, \bar{Q}_{xy}, \bar{Q}_{yy}\}$$

$$\{H_{xx}, H_{xy}, H_{yy}\} = \frac{1}{Et} \{\bar{H}_{xx}, \bar{H}_{xy}, \bar{H}_{yy}\}; \quad \{B_{xx}, B_{xy}, B_{yx}, B_{yy}\} = Et^2 \{\bar{B}_{xx}, \bar{B}_{xy}, \bar{B}_{yx}, \bar{B}_{yy}\}$$

$A_{xx} = \nu \alpha_s / \alpha_o$	$A_{yy} = \nu \alpha_r / \alpha_o$	$A_{xy} = (1 + \alpha_r) / \alpha_o$	$A_{yx} = (1 + \alpha_s) / \alpha_o$
$\bar{B}_{xx} = \alpha_s \gamma_s (1 + \alpha_r) / \alpha_o$	$\bar{B}_{yy} = \alpha_r \gamma_r (1 + \alpha_s) / \alpha_o$	$\bar{B}_{xy} = \nu \alpha_s \alpha_r \gamma_r / \alpha_o$	$\bar{B}_{yx} = \nu \alpha_r \alpha_s \gamma_s / \alpha_o$
$\bar{D}_{xx} = 1 + \beta_s +$ $+ [12(1-\nu^2) \alpha_s (1 + \alpha_r) \gamma_s^2] / \alpha_o$	$\bar{D}_{yy} = 1 + \beta_r +$ $+ [12(1-\nu^2) \alpha_r (1 + \alpha_s) \gamma_r^2] / \alpha_o$	$\bar{D}_{xy} = 1 +$ $+ [12(1-\nu^2) \nu \alpha_s \alpha_r \gamma_s \gamma_r] / \alpha_o$	$\bar{D}_{yx} = \bar{D}_{xy}$
$\bar{H}_{xx} = [1 + \alpha_s (1 - \nu^2)] / \alpha_o$	$\bar{H}_{yy} = [1 + \alpha_r (1 - \nu^2)] / \alpha_o$	$\bar{H}_{xy} = (1 + \nu) - \nu / \alpha_o$	$\bar{H}_{yx} = \bar{H}_{xy}$
$\bar{Q}_{xx} = \nu \alpha_s \gamma_s / \alpha_o$	$\bar{Q}_{yy} = \nu \alpha_r \gamma_r / \alpha_o$	$\bar{Q}_{xy} = -[\alpha_s \gamma_s (1 + (1 - \nu^2) \alpha_r) +$ $+ \alpha_r \gamma_r (1 + (1 - \nu^2) \alpha_s)] / 2 \alpha_o$	$\bar{Q}_{yx} = \bar{Q}_{xy}$

$$\alpha_s = A_s / d_s t, \quad \beta_s = EI_s / D d_s, \quad \gamma_s = e_s / t$$

$$\alpha_r = A_r / d_r t, \quad \beta_r = EI_r / D d_r, \quad \gamma_r = e_r / t$$

$$\alpha_o = (1 + \alpha_s) (1 + \alpha_r) - \nu^2 \alpha_s \alpha_r$$

s - stringers

r - rings

$$D = Et^3 / [12(1 - \nu^2)]$$

TABLE 27 BIFURCATION AND IMPERFECTION SENSITIVITY OF
AXIALLY COMPRESSED, AXIALLY STIFFENED BARRELED
CYLINDRICAL SHELLS (from Hutchinson and Frauenthal [346])

Length Parameter: $Z = \{L^2/ah\}^{1/2}$	Stringer Eccentricity	Load Eccentricity	Barreling Parameter	Critical Axial Load Ratio	Circumferential Wave Parameter	Imperfection Sensitivity Parameter, Membrane Prebuckling	Imperfection Sensitivity Parameter, Rigorous Prebuckling	Initial Slope of Postbuckling Path	Slope of Prebuckling Path at Bifurcation Load
Z	$\frac{e}{r_s}$	$\frac{q}{r_s}$	$\frac{ZR}{R_x}$	$\frac{(P_C)_{stiff.}}{(P_C)_{unstiff.}}$	$\frac{nL}{R}$	b	\bar{b}	θ^+	θ_C^{0+}
500	6	*	0	10.44	10.45	-0.056	-0.064	-135	45
1000	6	*	0	6.07	17.0	-0.046	-0.040	-135	45
2000	6	*	0	4.48	22.0	-0.036	-0.032	-135	45
3000	6	*	0	3.96	24.3	-0.024	-0.024	-135	45
5000	6	*	0	3.50	27.2	-0.016	-0.016	-135	45
500	-6	*	0	4.33	11.3	-0.0065	-0.0077	-125	45
1000	-6	*	0	2.64	14.7	-0.0094	-0.0098	-130	45
2000	-6	*	0	1.96	18.8	-0.013	-0.013	-133	45
3000	-6	*	0	1.79	21.8	-0.013	-0.013	-133	45
5000	-6	*	0	1.71	26.3	-0.012	-0.012	-134	45
1000	6	*	10	7.44	15.7	-0.046	-0.033	-135	45
1000	6	*	20	8.64	15.0	-0.044	-0.026	-135	45
1000	6	*	30	9.58	14.5	-0.040	-0.020	-135	45
1000	6	*	50	10.89	13.9	-0.033	-0.013	-135	45
1000	6	*	70	11.79	13.4	-0.026	-0.0088	-135	44
1000	6	*	90	12.46	12.8	-0.022	-0.0058	-135	44
1000	-6	*	10	3.28	14.2	-0.016	-0.017	-133	45
1000	-6	*	20	4.15	13.7	-0.021	-0.022	-134	45
1000	-6	*	30	5.20	13.3	-0.023	-0.023	-135	45
1000	-6	*	40	6.18	13.4	-0.020	-0.020	-134	45
1000	-6	*	50	6.85	14.6	-0.012	-0.012	-133	45
1000	-6	*	60	7.31	15.2	-0.0086	-0.0083	-131	45
300	6	0	0	8.79	6.5	-0.012	-0.0042	-142	36
500	6	0	0	5.04	10.6	-0.029	-0.013	-136	43
750	6	0	0	3.75	13.1	-0.034	-0.021	-135	44
1000	6	0	0	3.25	14.3	-0.030	-0.023	-135	45
300	-6	0	0	1.18	9.9	0.	0.011	20	45
500	-6	0	0	1.04	11.1	-0.0024	-0.0025	- 17	45
750	-6	0	0	0.996	12.5	-0.0059	-0.0062	- 90	45
1000	-6	0	0	0.978	13.5	-0.0094	-0.0099	-109	45
300	-6	-6	0	4.08	7.6	-0.020	-0.027	-134	44
500	-6	-6	0	2.35	9.4	-0.015	-0.015	-132	45
750	-6	-6	0	1.72	11.2	-0.014	-0.014	-131	45
1000	-6	-6	0	1.48	12.6	-0.014	-0.014	-131	45

* Clamped boundary conditions

† Given to closest degree

TABLE 28

BUCKLING OF A RING-STIFFENED CYLINDRICAL SHELL
UNDER HYDROSTATIC PRESSURE: COMPARISON OF MULTIPLE
OBSERVATIONS ON A SINGLE SPECIMEN (Test data from
[423], theory of [424]).

Station No.	Southwell Load	Station No.	Southwell Load
1	172	12	171
2	171	13	172
3	173	14	174
4	171	15	173
5	173	16	169
6	169	17	168
7	171	18	174
8	178	19	174
9	174	20	168
10	173	21	174
11	174		
Mean value of load		172.2	
Theoretical value (Kendrick)		173	
Ratio of $\frac{\text{mean value}}{\text{theoretical value}} = .995$			

TABLE 29

BUCKLING OF RING-STIFFENED CYLINDRICAL SHELLS
UNDER HYDROSTATIC PRESSURE: COMPARISON OF
SINGLE OBSERVATIONS ON A RANGE OF SPECIMENS
(Test data from [423], theory of [424])

Specimen No.	<u>Southwell Load</u> Theoretical Load
1	1.011
2	1.022
3	.861
4	1.076
5	.882
Average	.970

TABLE 30^a

BUCKLING LOADS OF PERFECT MONOCOQUE CYLINDRICAL SHELLS
OBTAINED FROM SOUTHWELL PLOTS OF DATA OF ARBOCZ AND
BABCOCK [341]

<i>Cylinder</i>	$\alpha = \frac{\text{max. load}}{\text{mean load}}$	$P \text{ (Southwell)}$	P
		P_{cl}	$\alpha \frac{P}{P_{cl}}$
A7	1.16	0.87	1.009
A8	1.12	0.90	1.008
A9	1.06	0.91	0.964

^a from Horton and Craig [414]

TABLE 31 COMPARISON OF FAILURE LOADS FROM TESTS AND BOSOR6 MODELS

Specimen Number	Primacord Tube Present?	Critical Test Axial Load V_{cr} (lb./in.)	Critical Axial Load V_{cr} from BOSOR6 (lb./in.)	
			Nonlinear Collapse ^a	Bifurcation ^b
1	No	4708	4800	6841
2	Yes	5788	5650	5339
3	Yes	5513	5650	5339

^aCorrespond to stiff pads. Specimens 2 and 3 were nominally identical.

^bCalculated from linear analysis with $M_a = M_b = 0$. The lowest bifurcation buckling load corresponds to $n = 0$.



Fig. 1 Buckling is a somewhat mystifying phenomenon (Courtesy St. Regis Paper Co.)

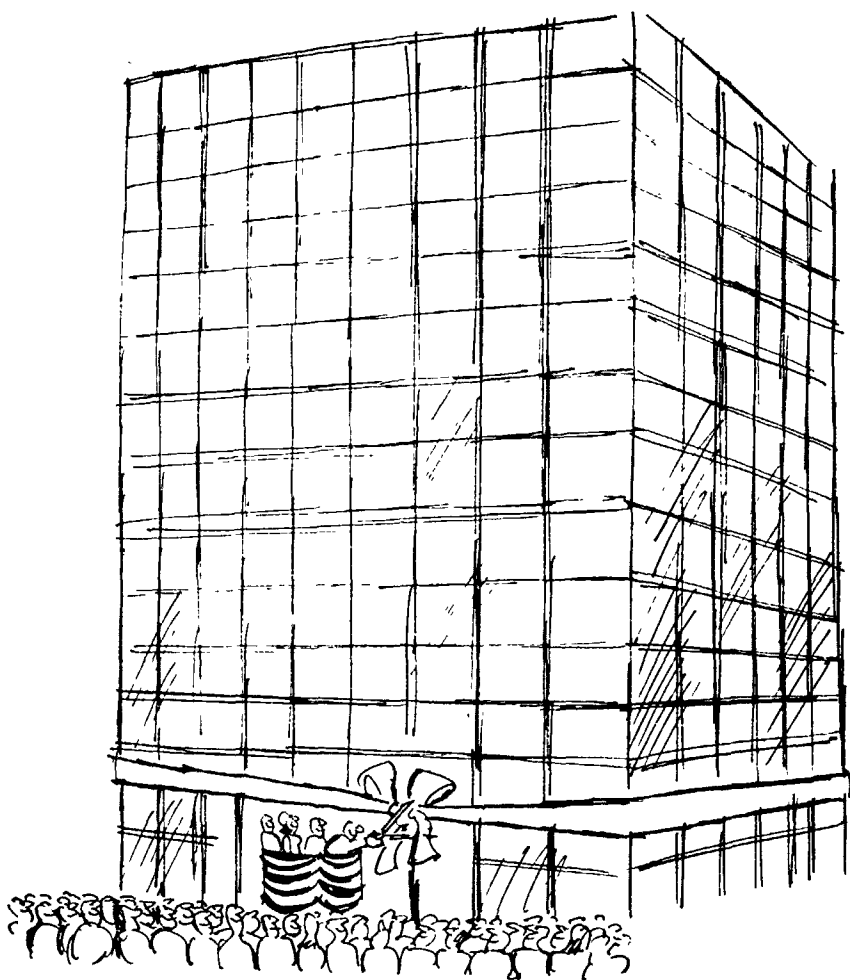


Figure 2(a) Structures have been built with ...
(courtesy New Yorker Magazine, April 29, 1974)

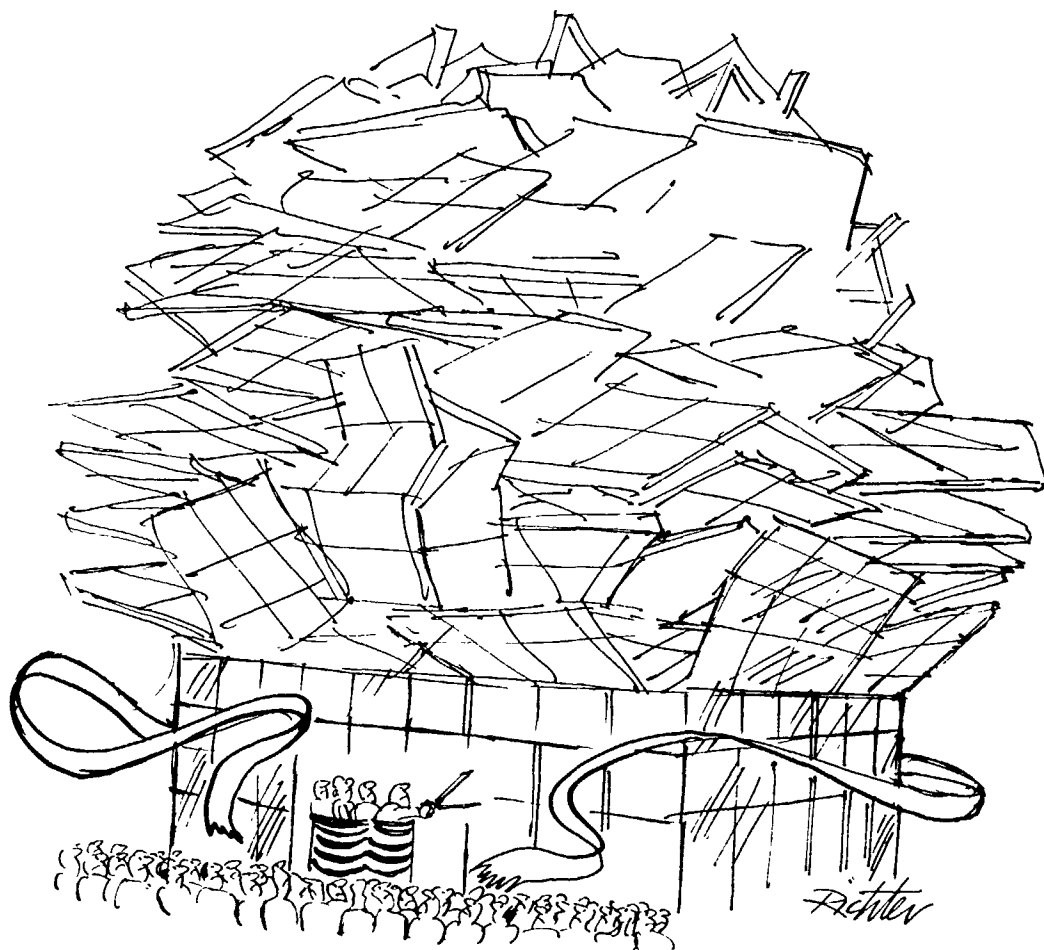


Figure 2(b) ... insufficient margins of safety.
(courtesy New Yorker Magazine, April 29, 1974)

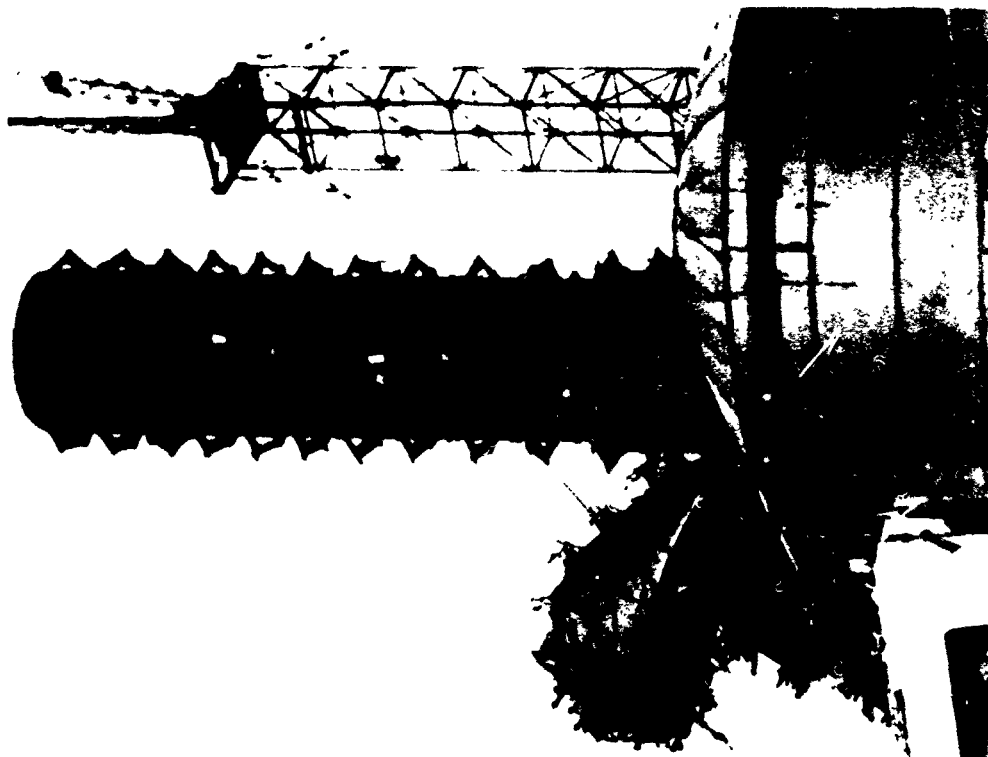


Fig. 3(a) Failure of a large (15m dia.) vessel due to buckling of the bottom torispherical end under internal pressure.



Fig. 3(b) Fragments of the bottom torispherical end (from Harding, A.G., and Ehmke, R.F., Proc. Am. Petrol. Inst., Vol. 42, Sect. 3, p. 107, 1962).



(a)

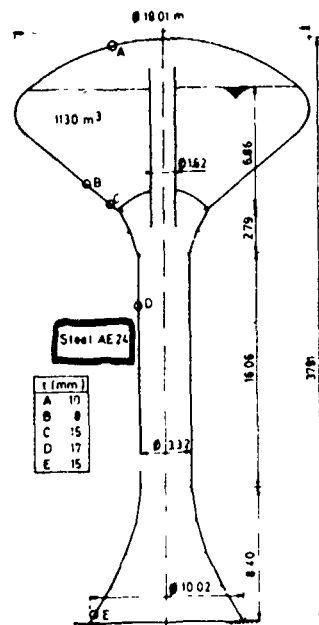


(b)

(a) Photograph of collapsed structure

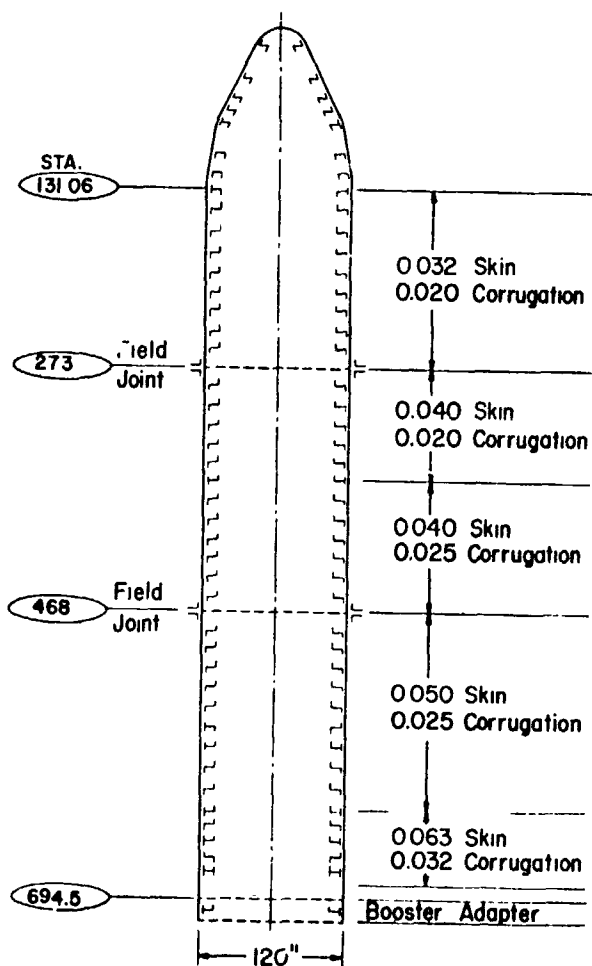
(b) This weak zone interior view after collapse shows a weld along the actual deformed meridian

(c) Dimensions of the damaged watertower

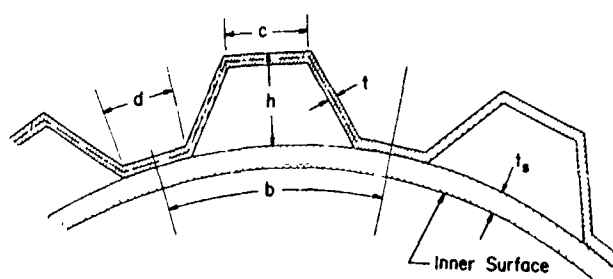


(c)

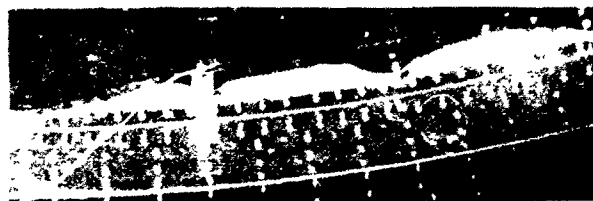
Figure 4 Collapse of a large steel watertower upon being filled for the first time. Failure was caused by local buckling near the deepest water level in the conical portion of the tank (from Baltus and Massonet [2]).



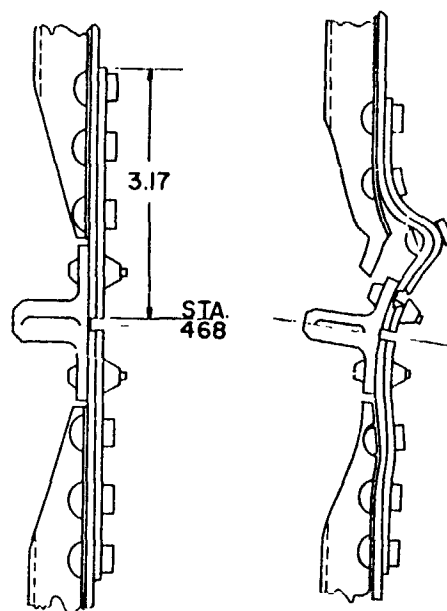
(a) Typical ring-stiffened rocket payload shroud configuration.



(b) Corrugated wall construction.



(c) Interior view of portion of complete shroud buckled locally next to field joint at station 468 [see (a)]. Three waves are visible.



(d) Field joint geometry and buckle configuration.

Figure 5 Local failure of a large payload shroud under axial compression and bending. Buckling is caused by the narrow band of circumferential compression arising from the inward excursion of the axial load path near the field joint at station 468 (from Bushnell [3]).

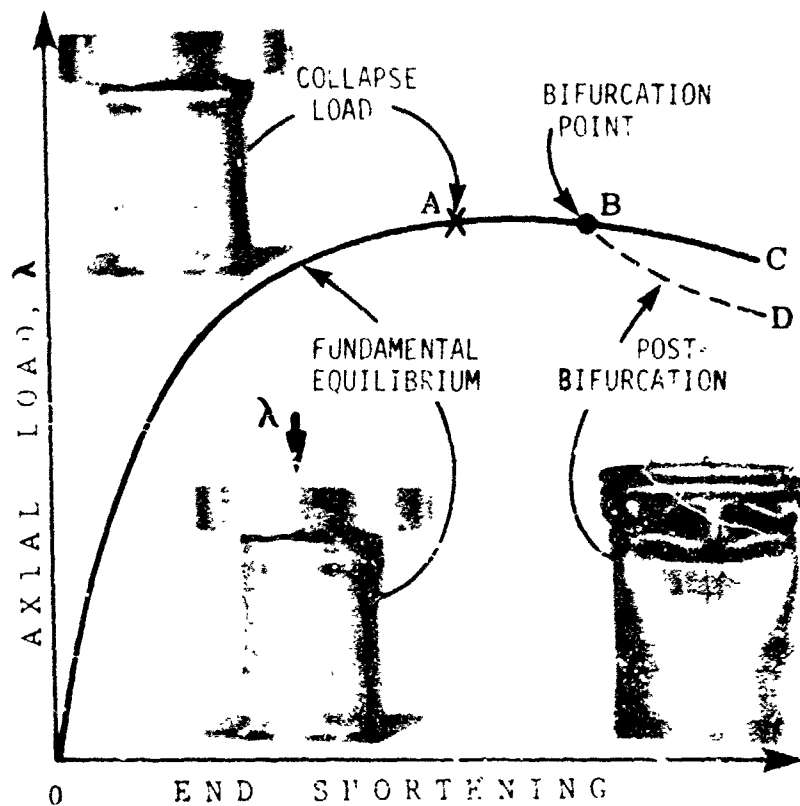


Figure 6 Load-end shortening curve with limit point A, bifurcation point B, and post-bifurcation equilibrium path, BD (photographs courtesy Sobel and Newman [42]).

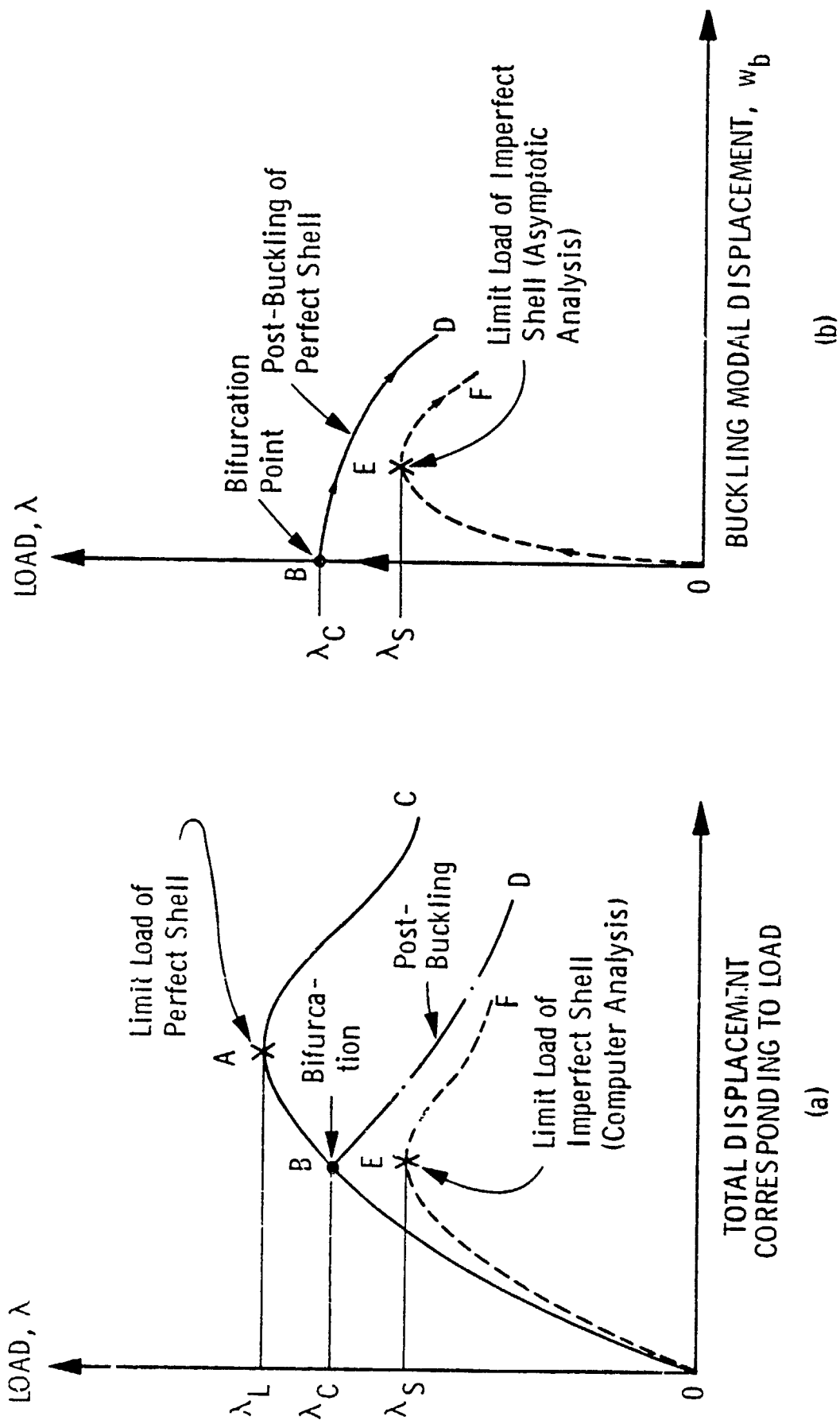
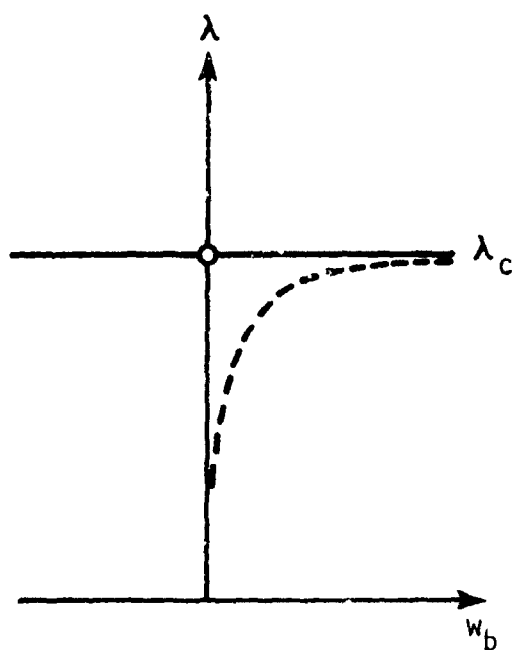
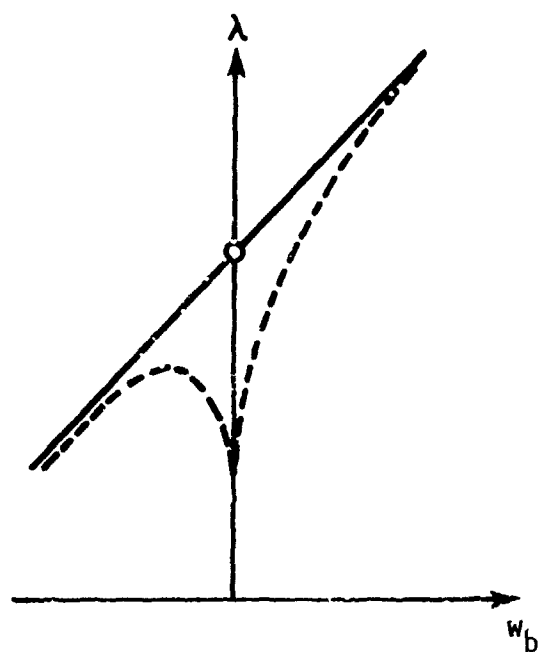


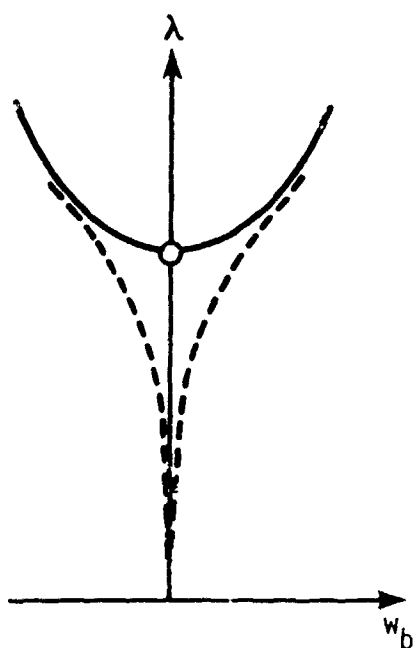
Figure 7 Load-deflection curves showing limit and bifurcation points.
(a) general nonlinear analysis, (b) asymptotic analysis.



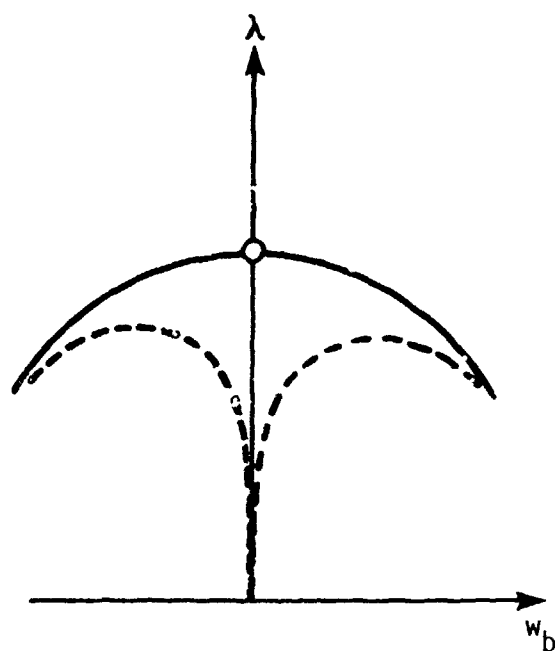
(a) NEUTRAL POSTBUCKLING



(b) UNSYMMETRIC POSTBUCKLING



(c) STABLE POSTBUCKLING



(d) UNSTABLE POSTBUCKLING

————— PERFECT STRUCTURE
 - - - - - IMPERFECT STRUCTURE

Figure 8 Different types of load-displacement relations. λ is the load; w_b is the buckling modal displacement.

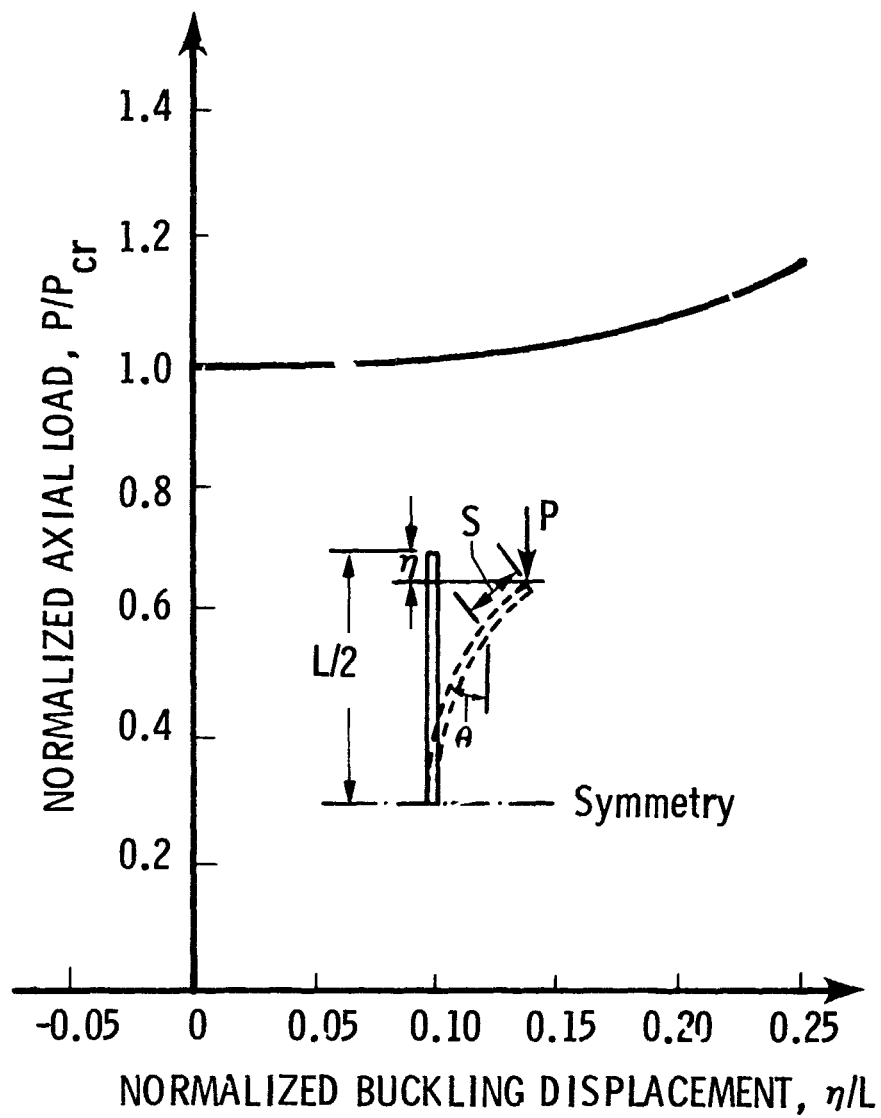


Figure 9 Post-buckling load-deflection curve for a column.

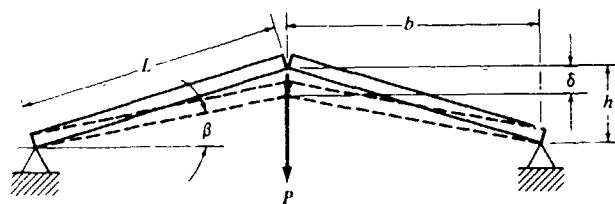


Figure 10 Two-column structure (from Brush and Almroth [4]).

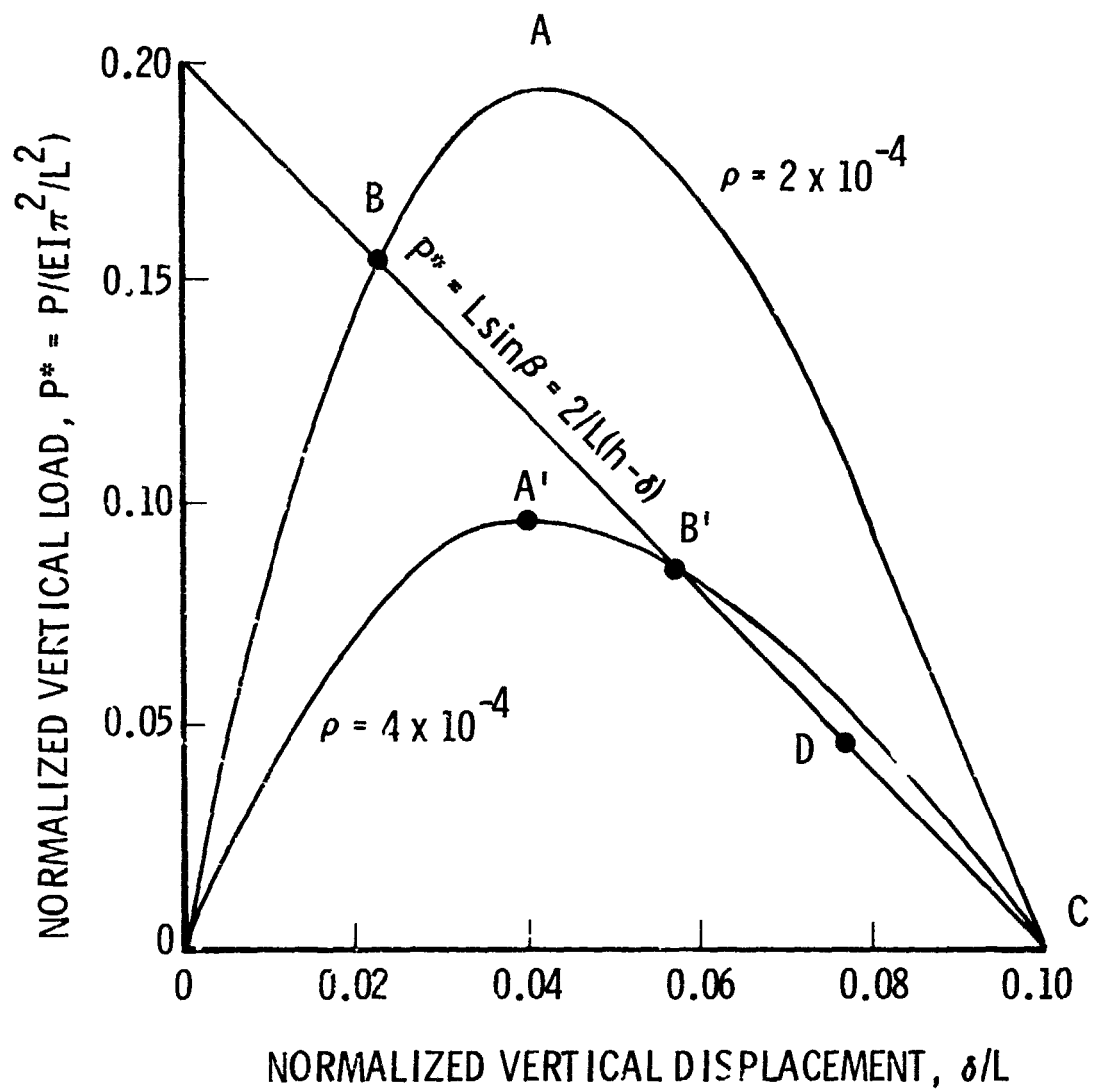


Figure 11 Load-displacement diagrams for two-column structure with $h/L = 0.1$. The quantity $\rho = I/[A(\pi/L)^2]$. (Adapted from Brush and Almroth [4])

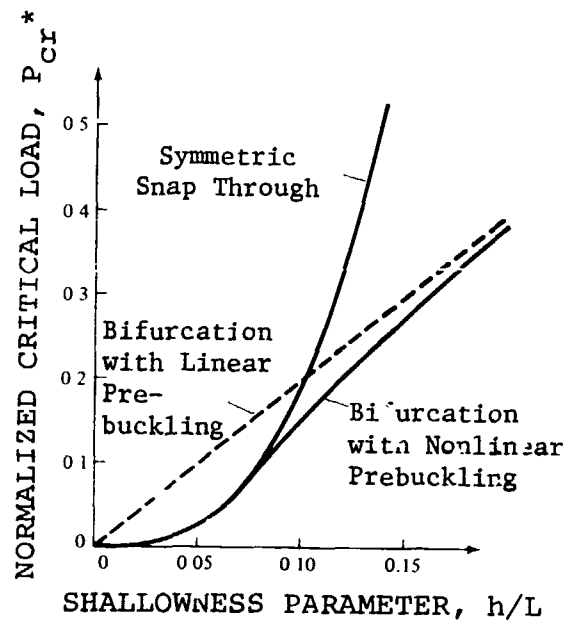


Figure 12 Critical load of two-column structures as function of h/L (adapted from Brush and Almroth [4]).

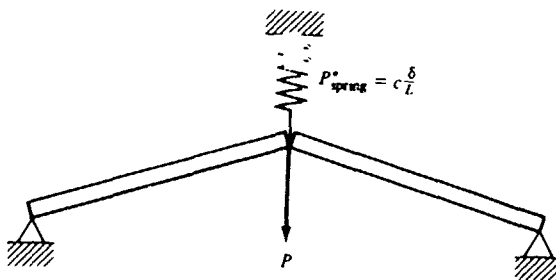


Figure 13 Two-column structure with spring (from Brush and Almroth [4]).

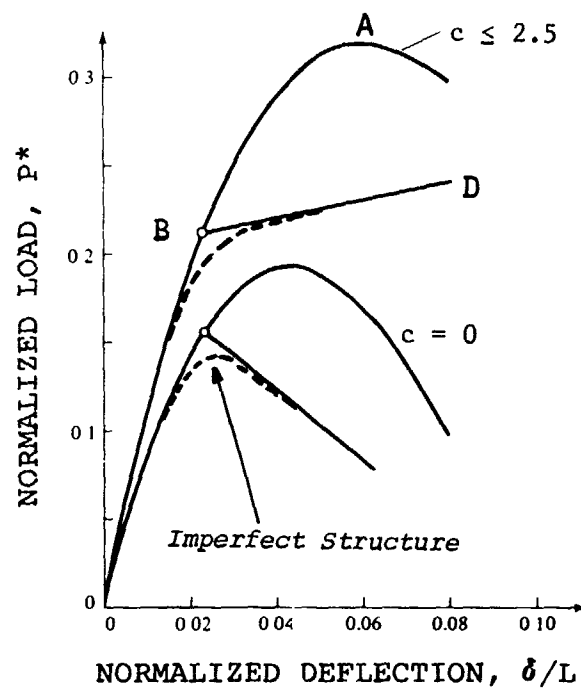


Figure 14 Load-displacement diagram for two-column structure with spring ($h/L = 0.1$) (adapted from Brush and Almroth [4]).

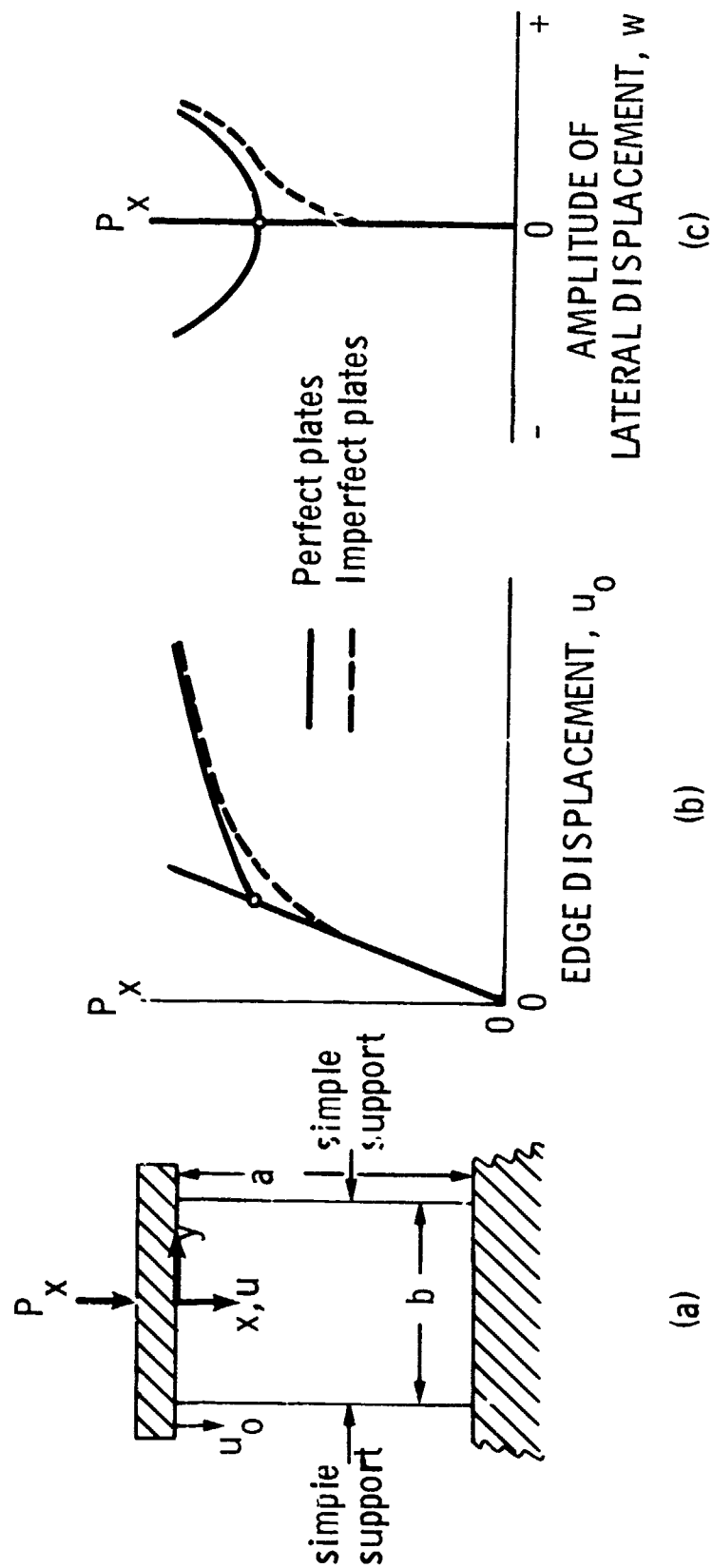


Figure 15 Equilibrium paths for initially perfect plates subjected to uniform end shortening (adapted from Brush and Almroth [4]).

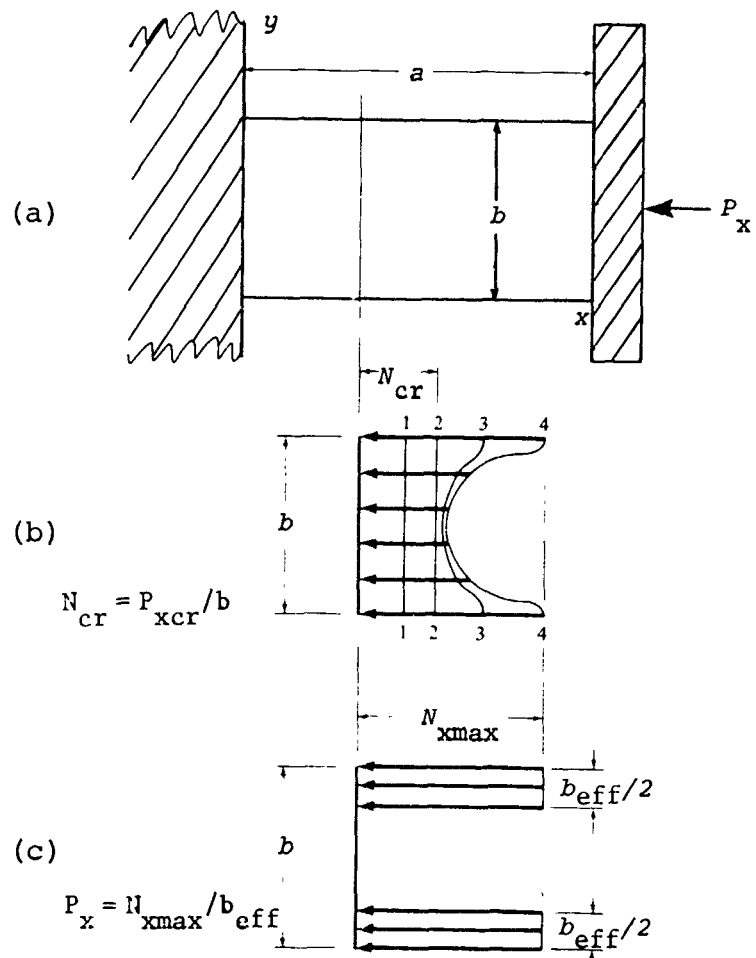


Figure 16 Stress distribution in plate before and after buckling (adapted from Brush and Almroth [4]).



Figure 17 Cylinder with completely developed elastic buckle pattern
(from Horton et. al. [4.38])

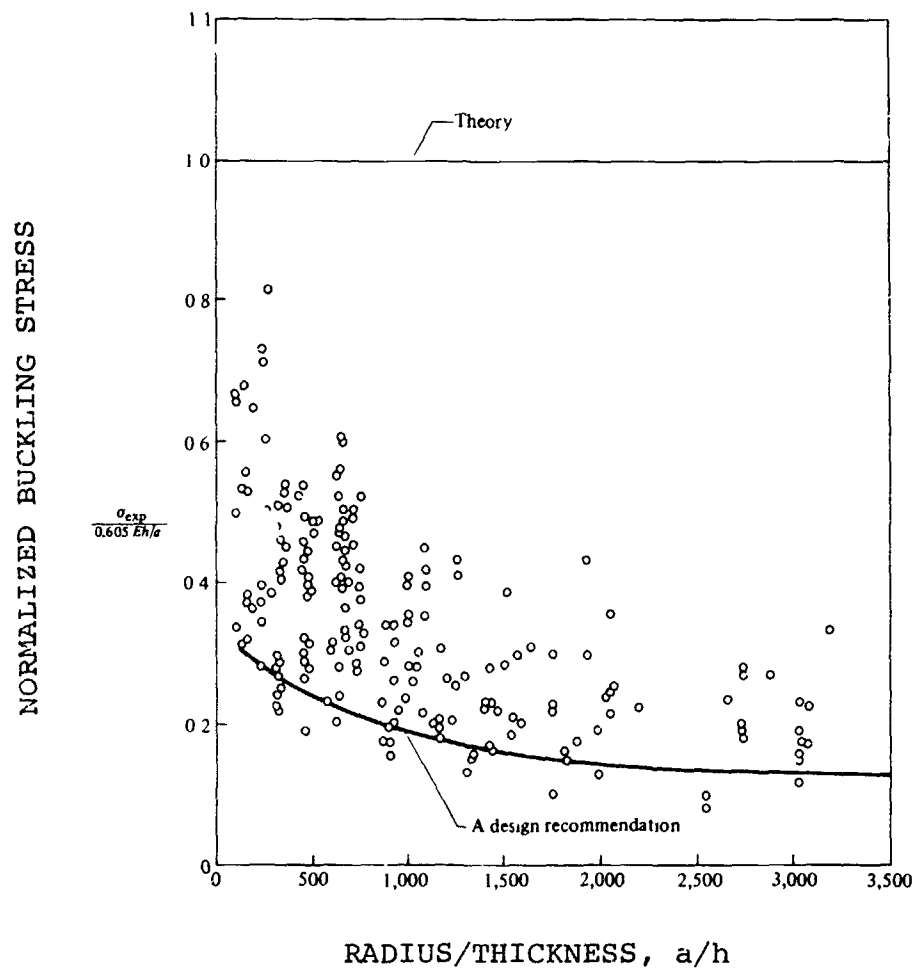
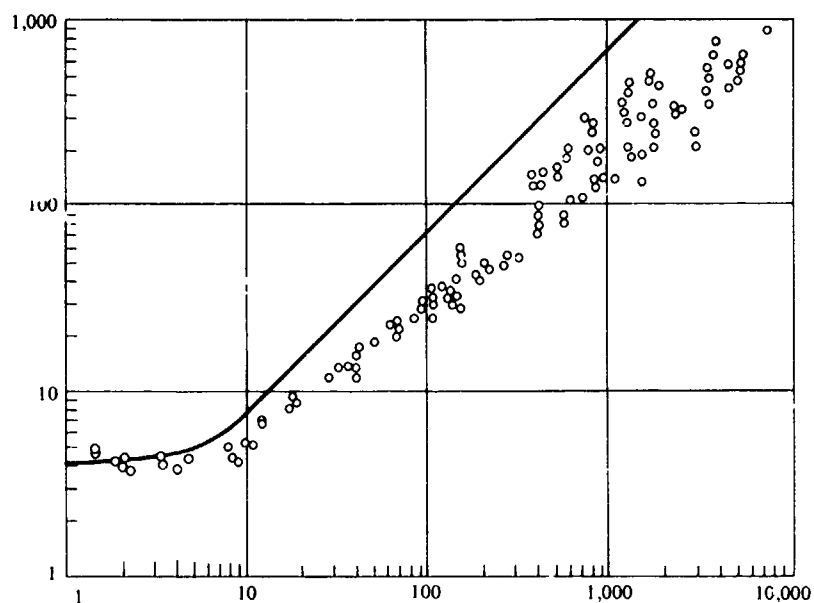


Figure 18 Distribution of test data for cylinders subjected to axial compression (from Brush and Almroth [4]).

AXIAL BUCKLING COEFFICIENT

$$k_a = (L^2/r^2D) \sigma_{cr}$$



$$z = \frac{L^2}{ah} (1 - \nu^2)^{1/2}$$

Figure 19 Comparison of theoretical and experimental values for cylinders subjected to axial compression (D = flexural rigidity) (from Brush and Almroth [4]).

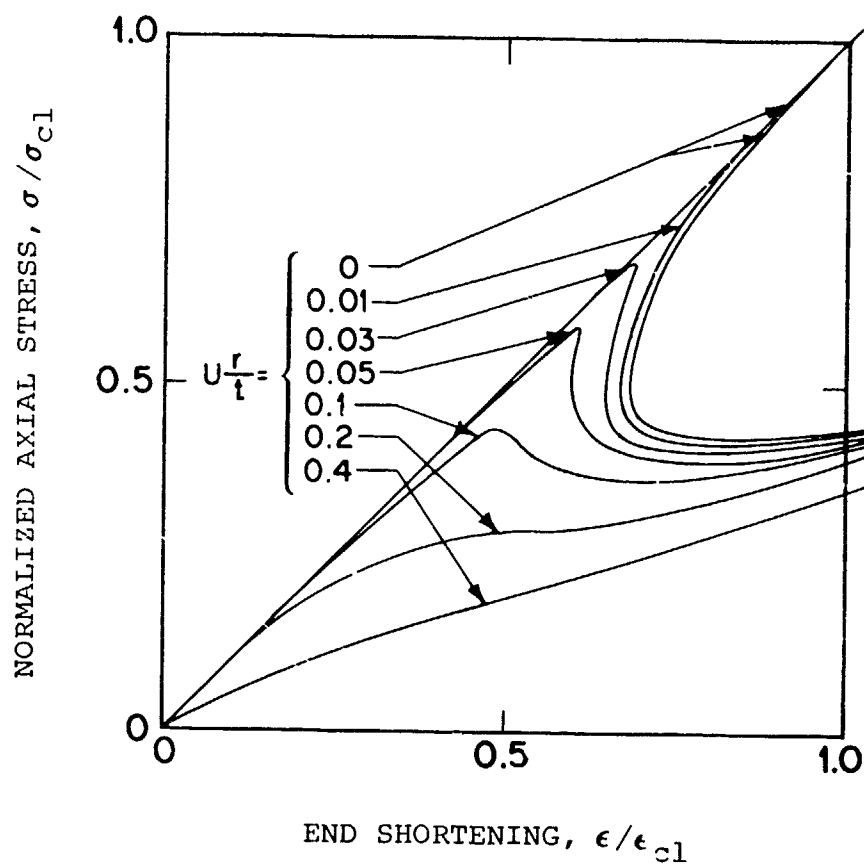


Figure 20(a) Effect of imperfections on load-deflection curve for axially compressed monocoque cylinder (from Donnell and Wan [30]).

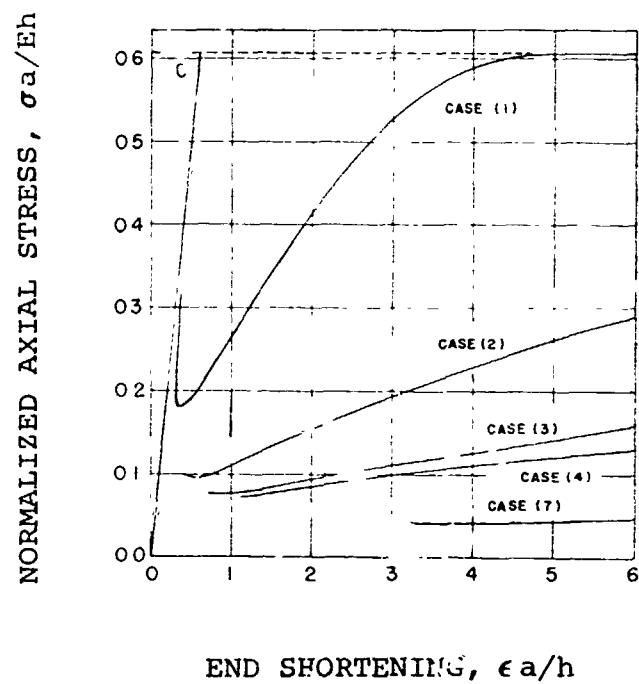


Figure 20(b) Postbuckling curves for axially compressed monocoque cylinder calculated with use of various trigonometric series to express the post-buckling deflection pattern (from Hoff [29]).



Figure 21 Typical postbuckling pattern of axially compressed stiffened cylindrical shell (from Singer and Abramovich [158]).

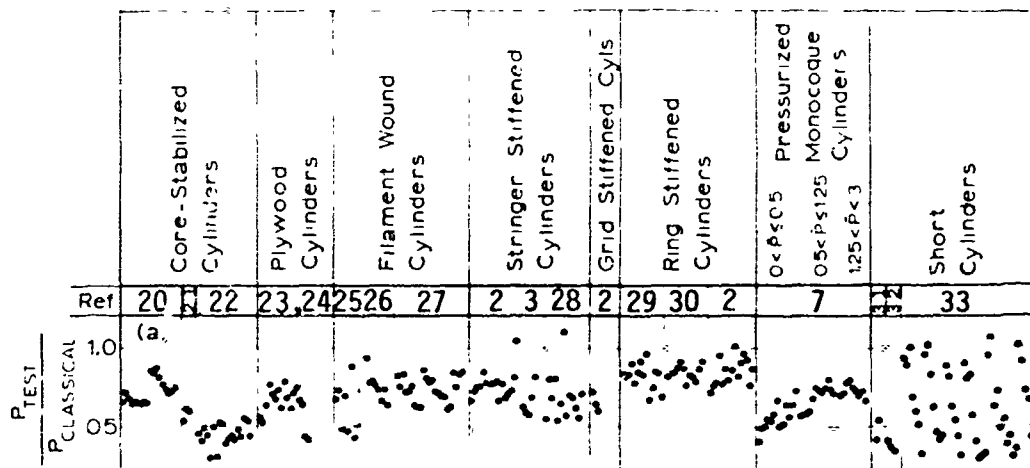


Figure 22 Comparison of test and theory for buckling of axially compressed cylindrical shells with various wall constructions (from Almroth et al. [34]).



Figure 23 Typical post-buckled pattern for long cylindrical shell under external hydrostatic pressure (from Ekstrom et al [35]).



Figure 24 Typical post-buckled pattern for medium-length cylindrical shell under external hydrostatic pressure (from Harris et al. [36]).

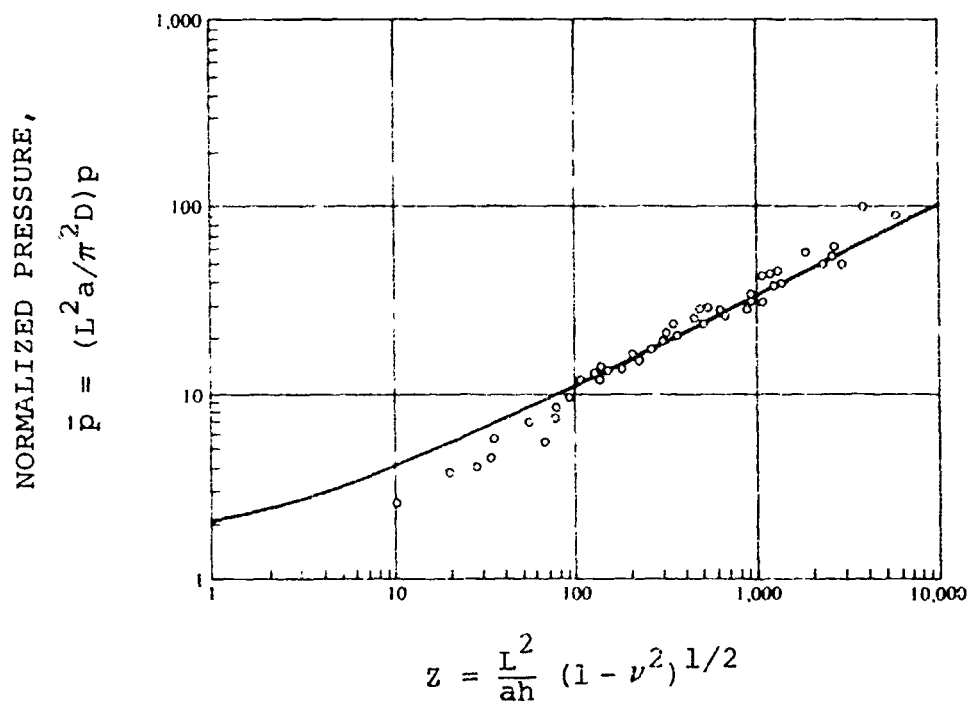
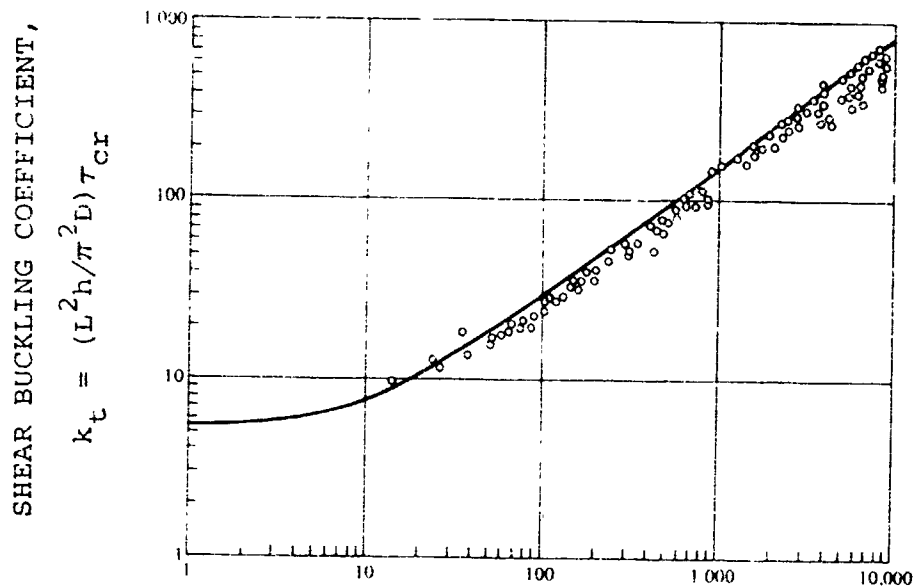


Figure 25 Comparison of theoretical and experimental values for cylinders subjected to external hydrostatic pressure (D = flexural rigidity) (from Brush and Almroth [4]).



Figure 26 Typical post-buckled pattern for unpressurized cylinder in torsion (from Harris et al. [36])



$$z = \frac{L^2}{ah} (1 - \nu^2)^{1/2}$$

Figure 27 Comparison of theoretical and experimental buckling loads for cylinders subjected to torsion (from Brush and Almroth [4]).

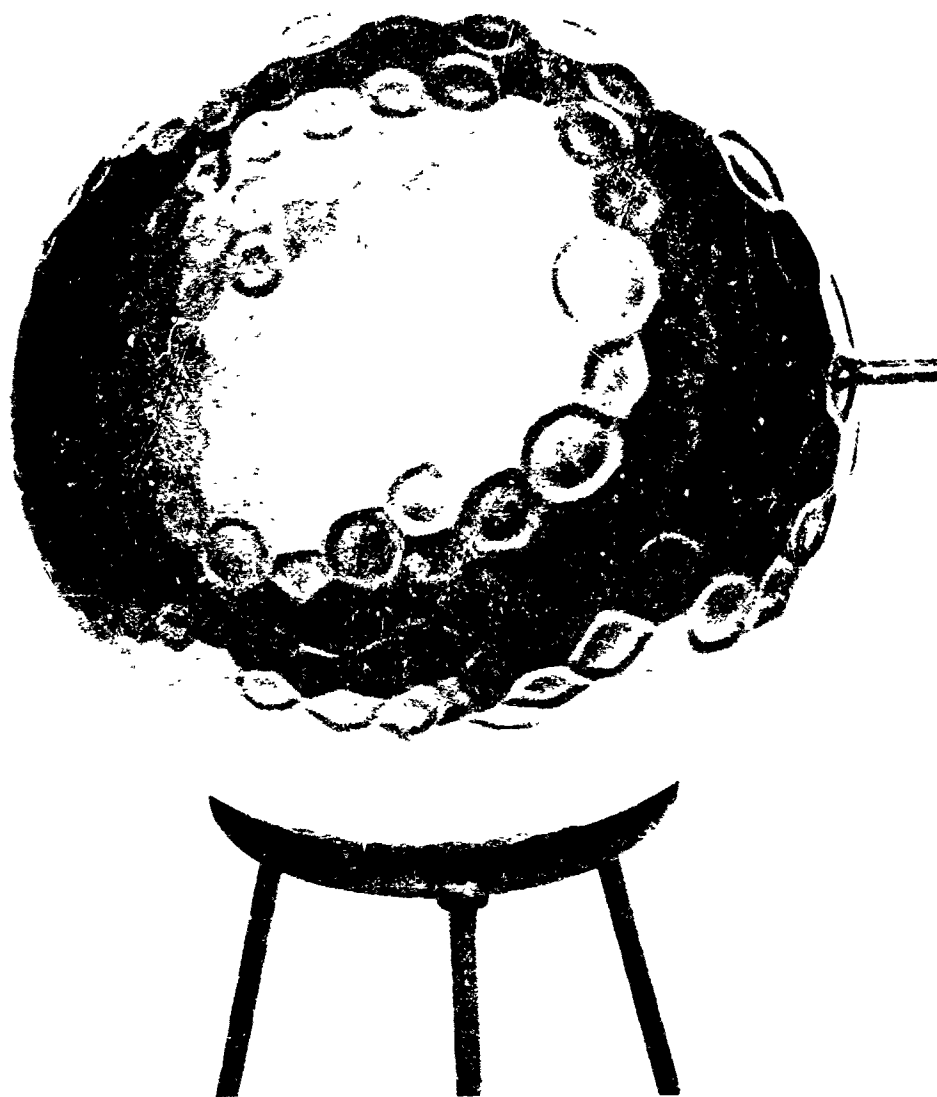


Figure 28 Post-buckled state of a thin-walled spherical shell under uniform external pressure. Buckling motion is restrained by an interior mandrel (from Carlson et al. [39]).

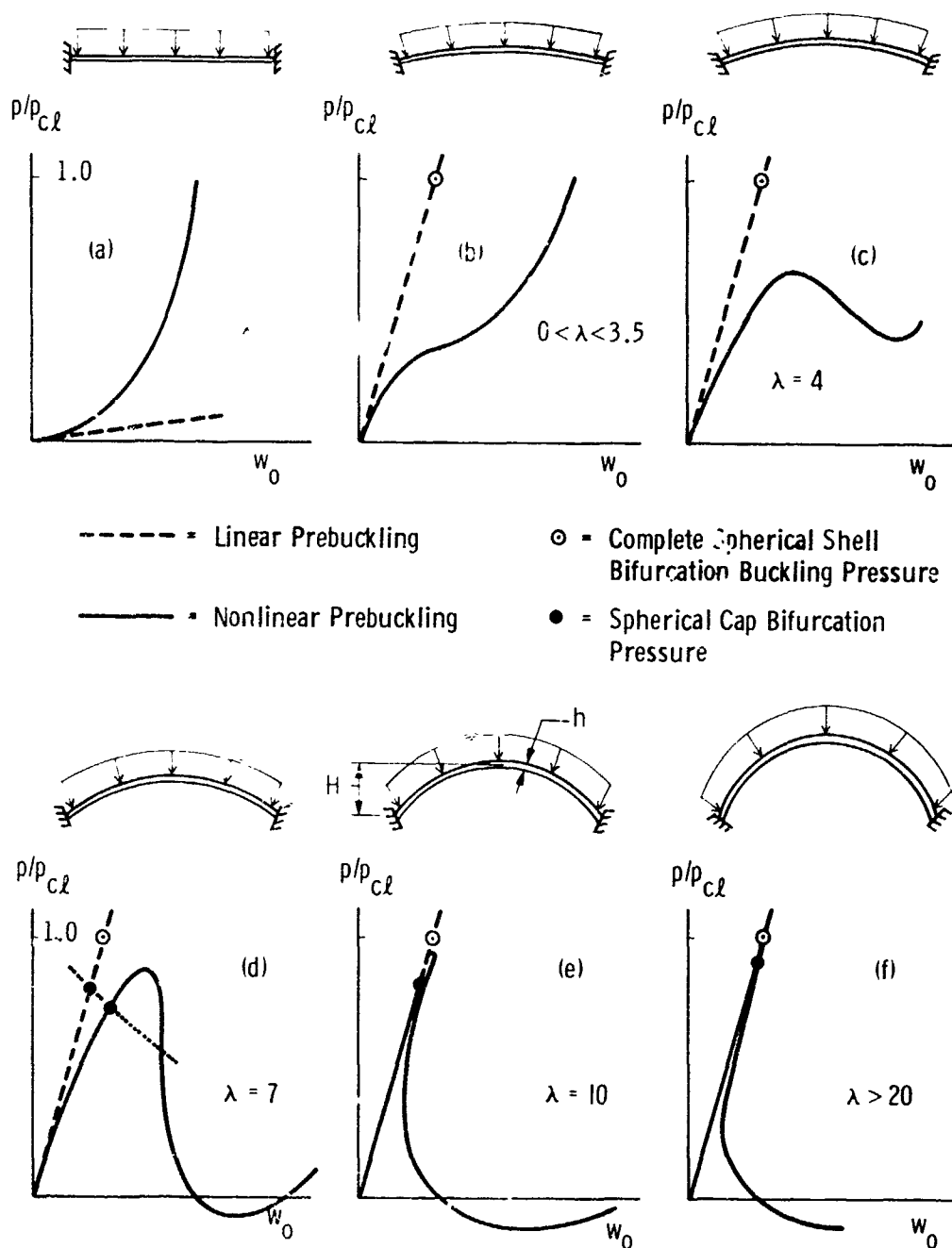


Figure 29 Load-deflection curves and bifurcation buckling of spherical caps with various values of the shallowness parameter $\lambda = 2[3(1-\nu^2)]^{1/4}(H/h)^{1/2}$.

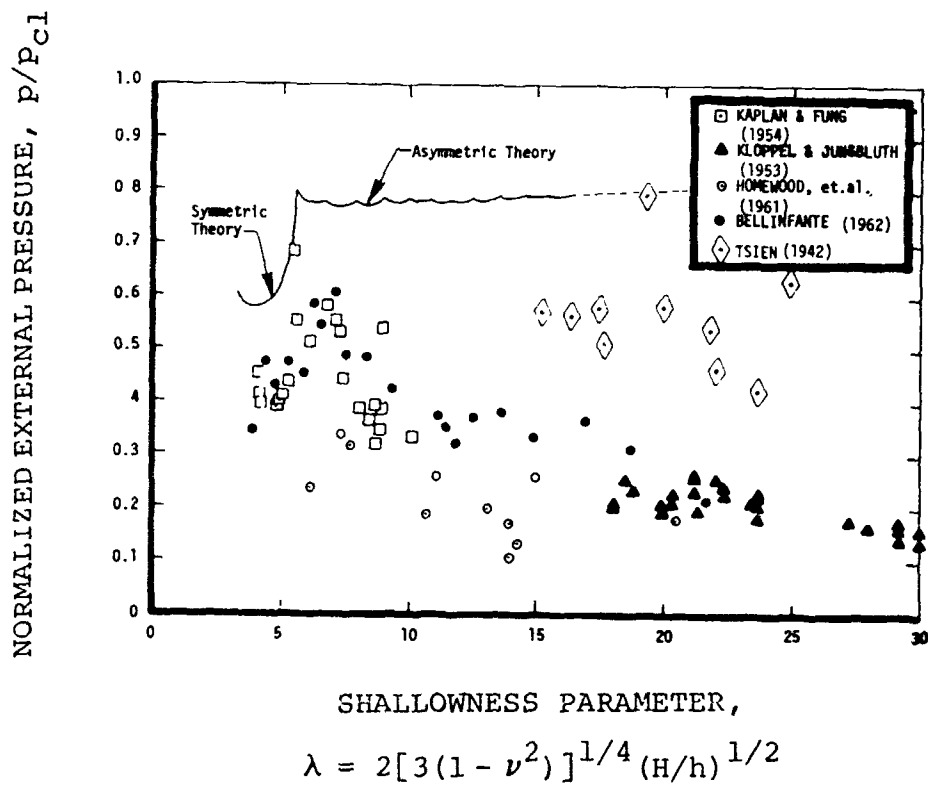


Figure 30 Early experimental results for clamped spherical caps under external pressure (from Kaplan [37]). H is the rise of the apex of the cap above its base plane.

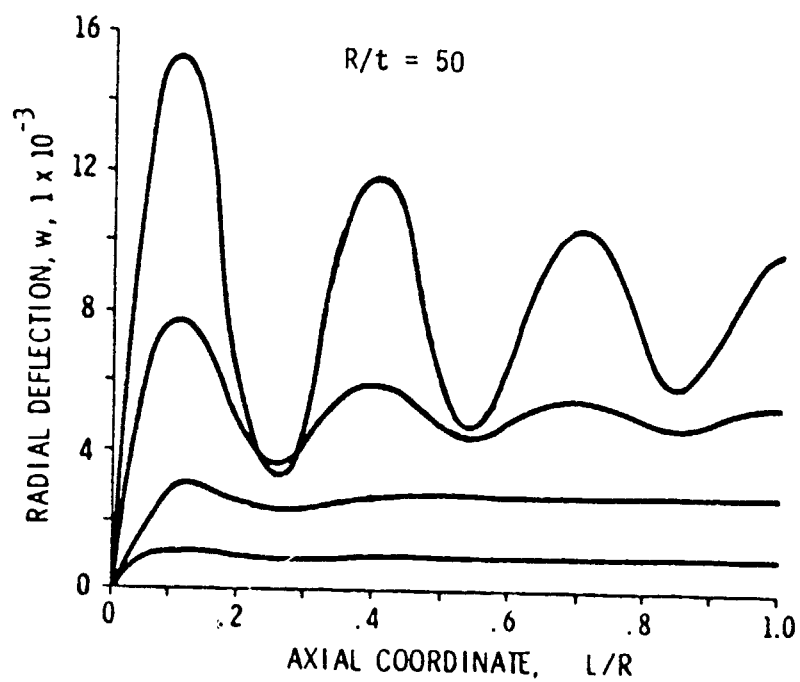


Figure 31 Radial deflection profiles for cylinder under increasing axial load (from Murphy and Lee [46]).

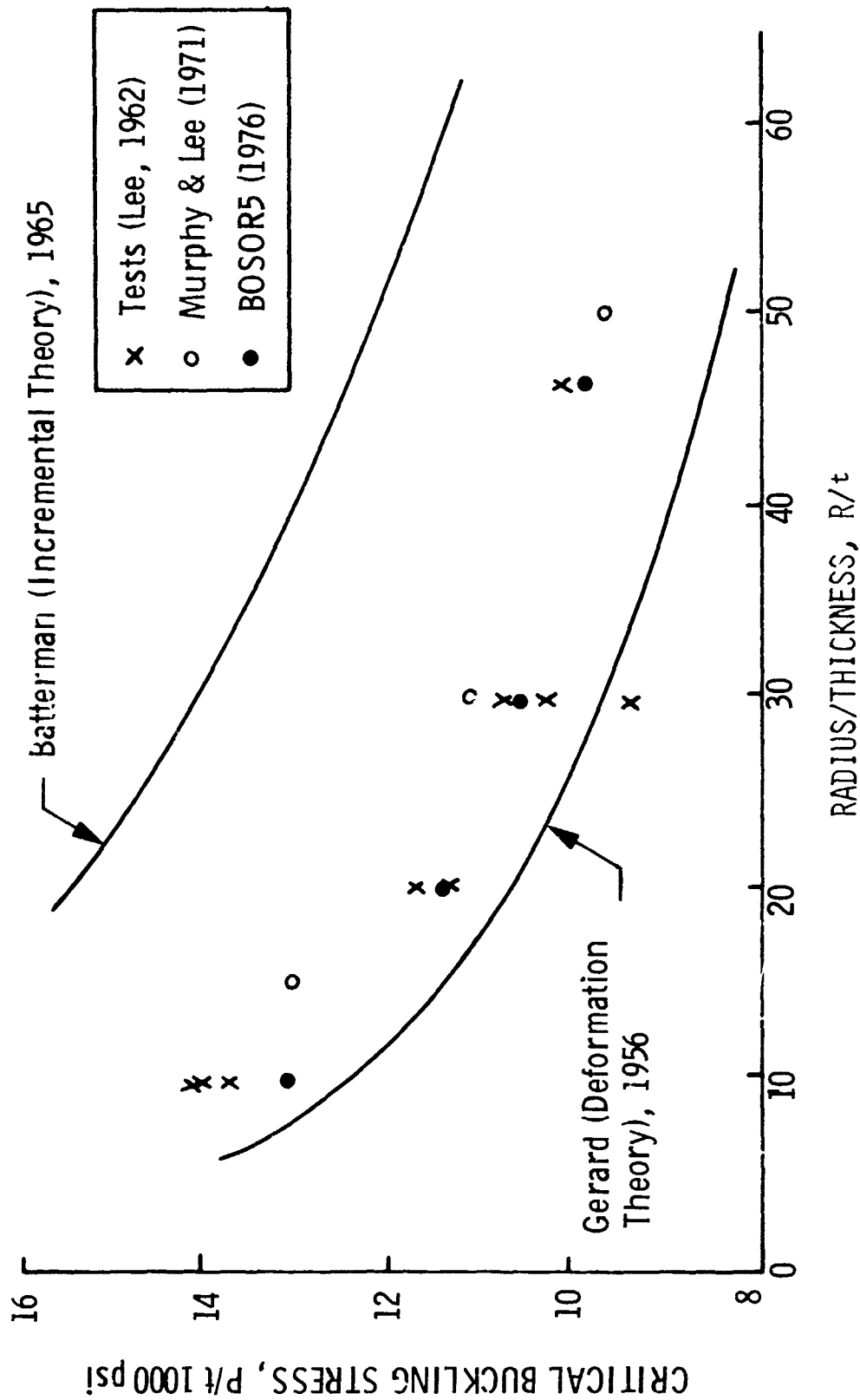


Figure 32 Comparison of test and theory for plastic buckling of axially compressed cylinders (adapted from: Murphy and Lee [46]).



Figure 33 Symmetric ultimate collapse pattern in plastic buckling of axially compressed cylindrical shells (from Lorton et al. [38]).

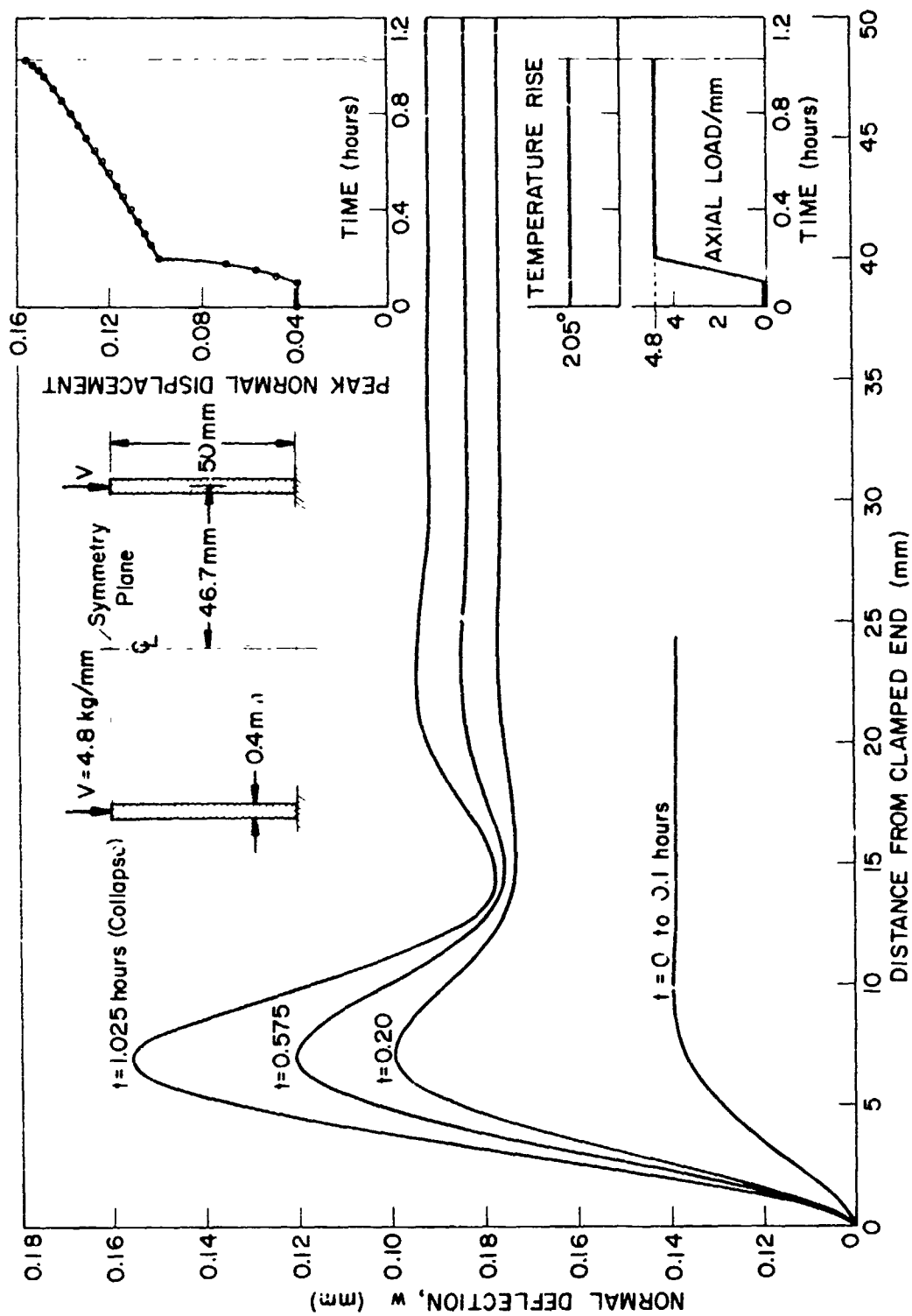


Figure 34 Axisymmetric creep buckling of axially compressed cylindrical shell (from Bushnell [47]).

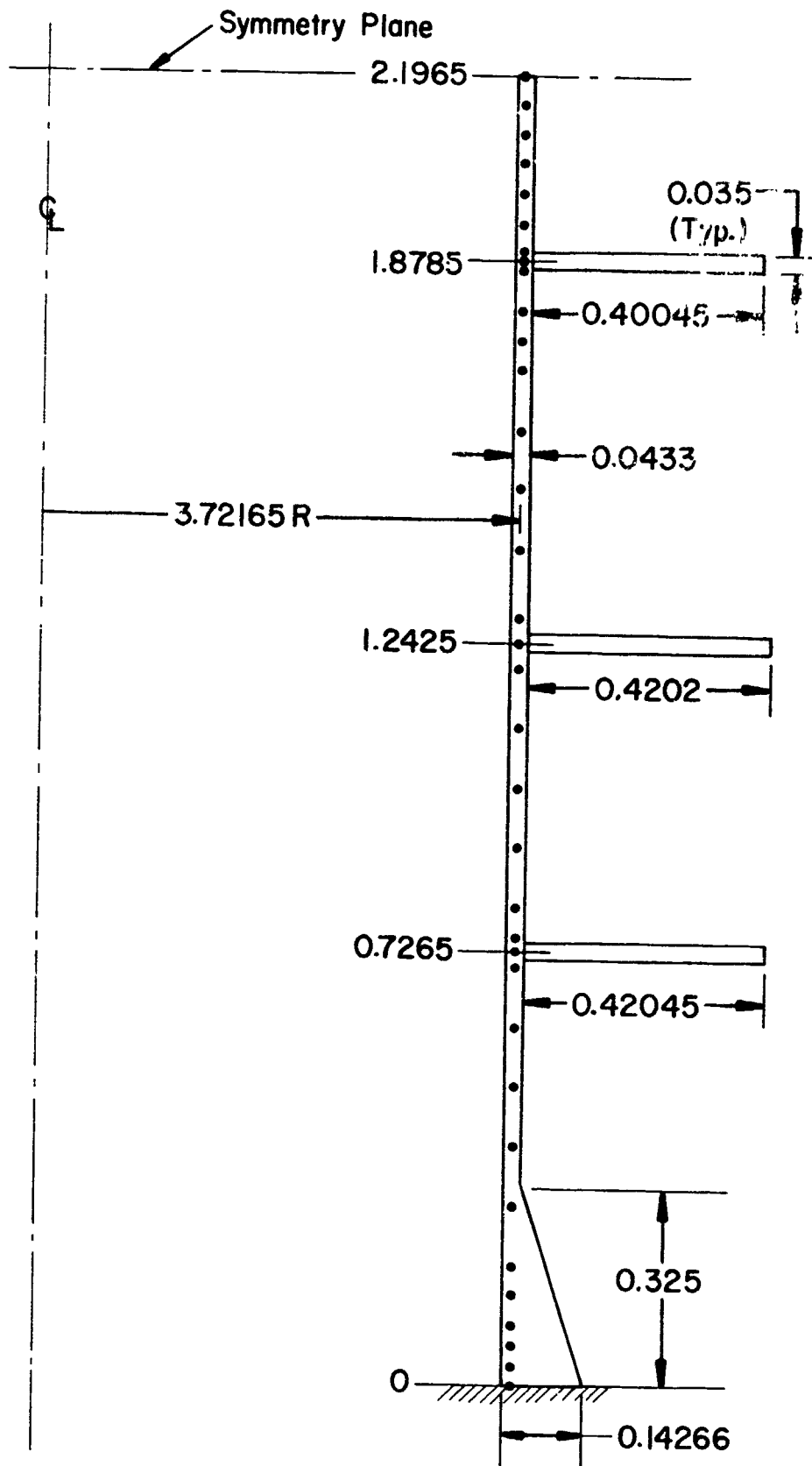


Figure 35(a) Ring-stiffened titanium cylinder under external hydrostatic pressure with nodal points used in the BOSOR5 analysis indicated (from Bushnell [47]).

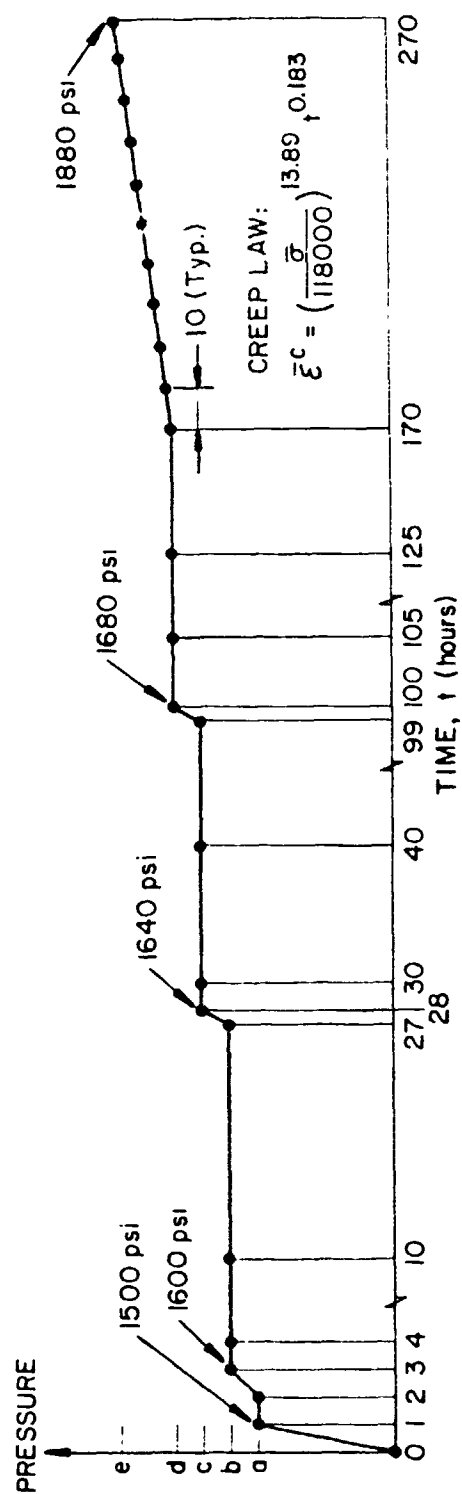


Figure 35(b) Loading schedule for titanium ring-stiffened cylinder (from Bushnell [47]).

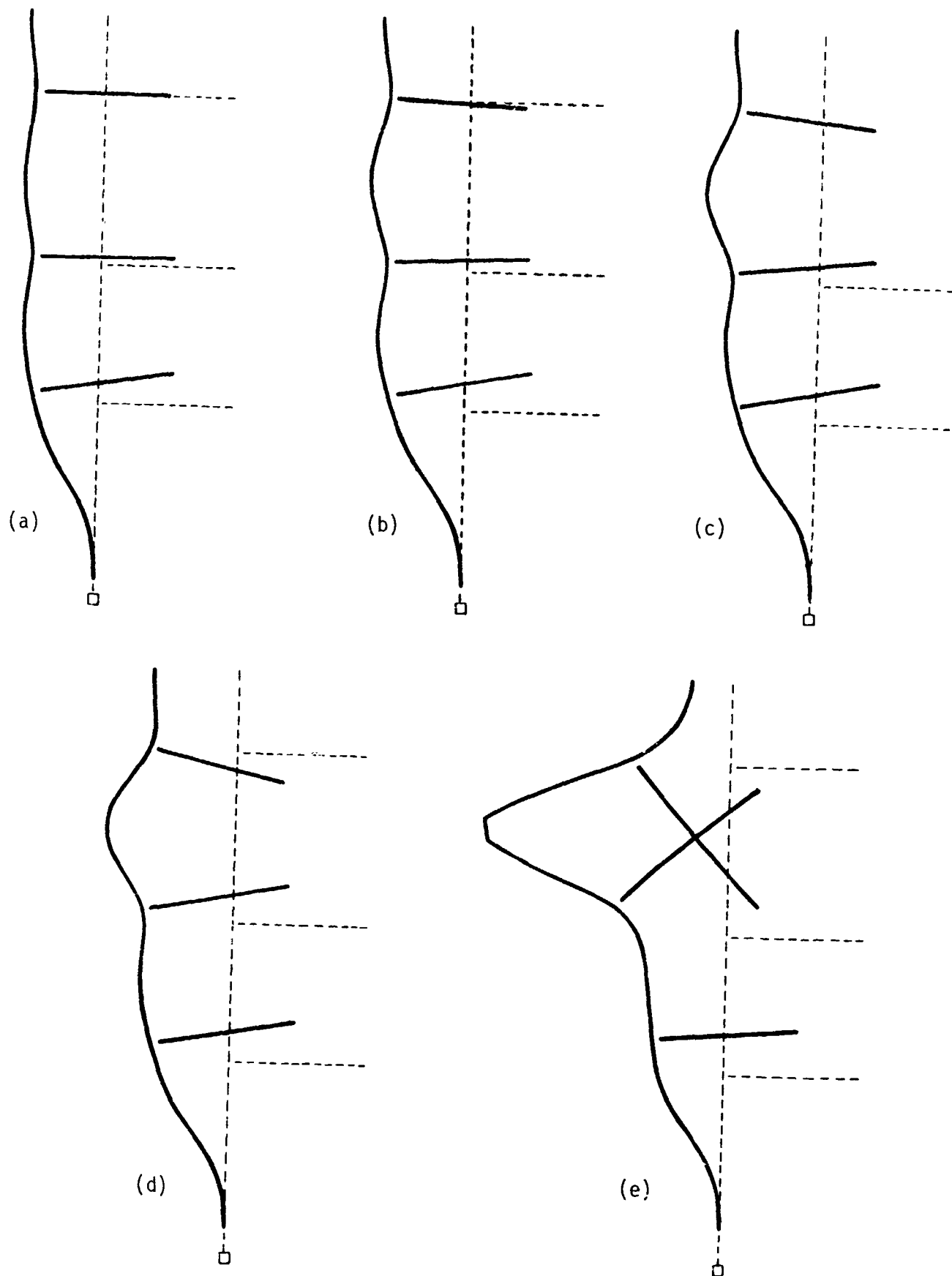


Figure 36 (a) Axisymmetric collapse of ring-stiffened cylinder with creep included in the analysis (from Bushnell [47]).

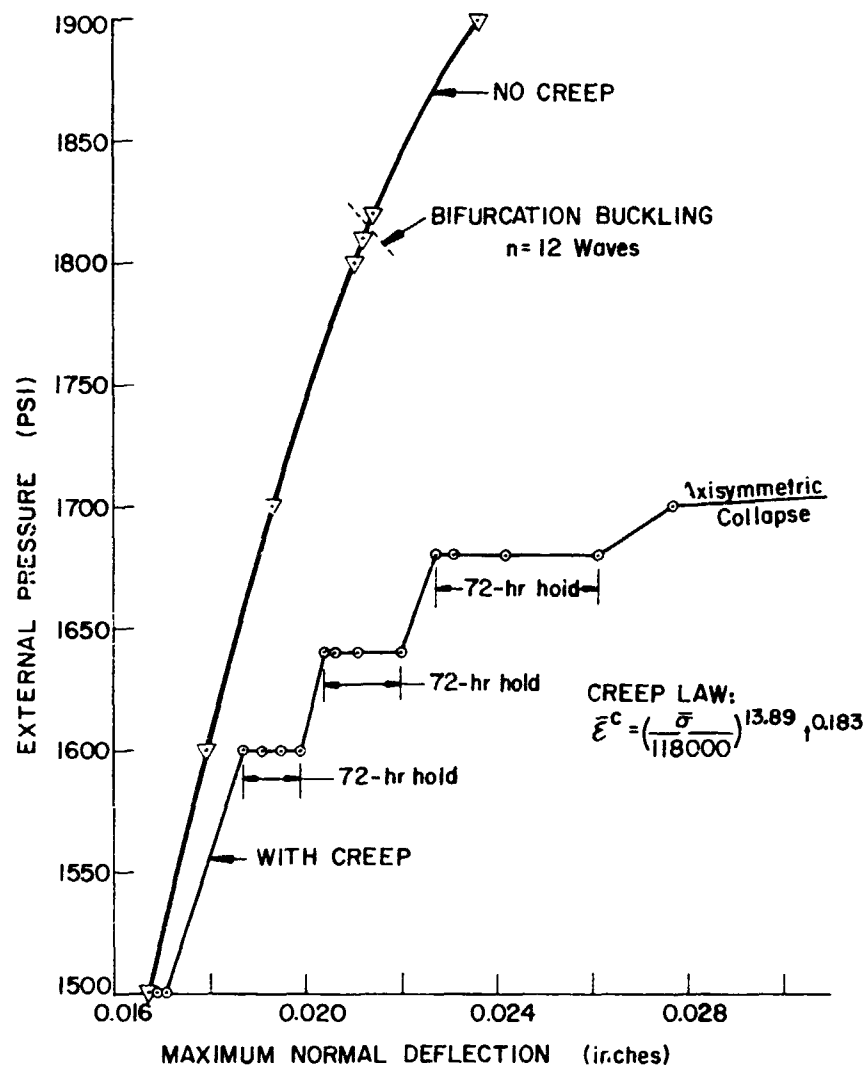


Figure 36(b) Load-deflection curves for externally pressurized ring-stiffened cylinder with and without primary creep included in the analysis (from Bushnell [47]).

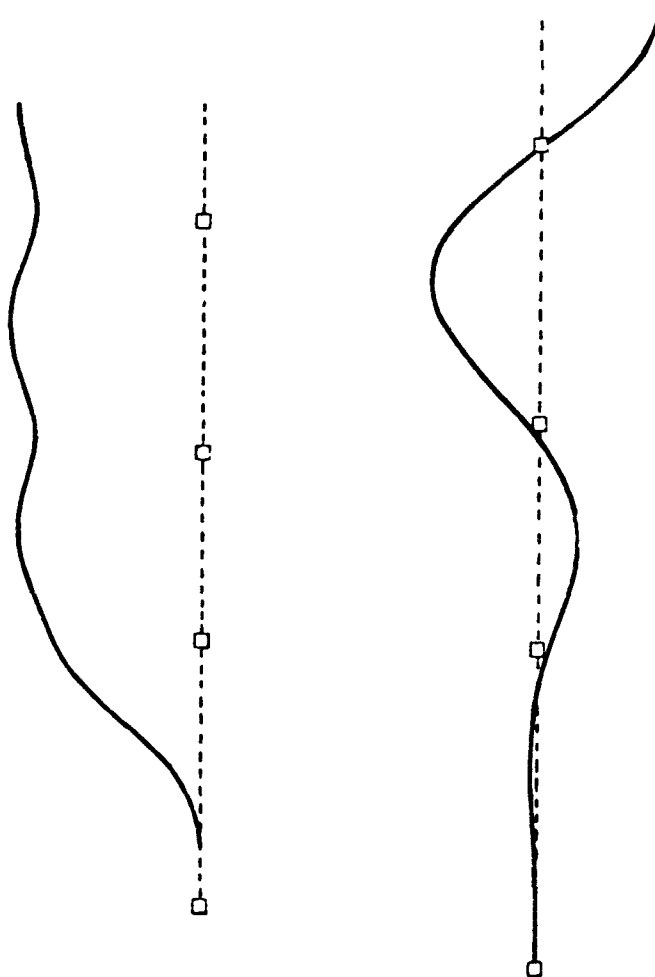


Figure 36(c) Prebuckling deflected shape at the bifurcation pressure and the bifurcation buckling mode for ring-stiffened cylinder with creep neglected in the analysis (from Bushnell [47]).

CRITICAL PRESSURE

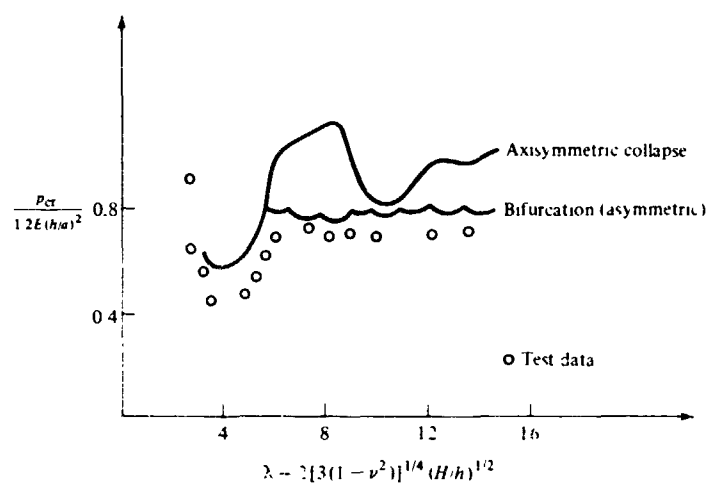
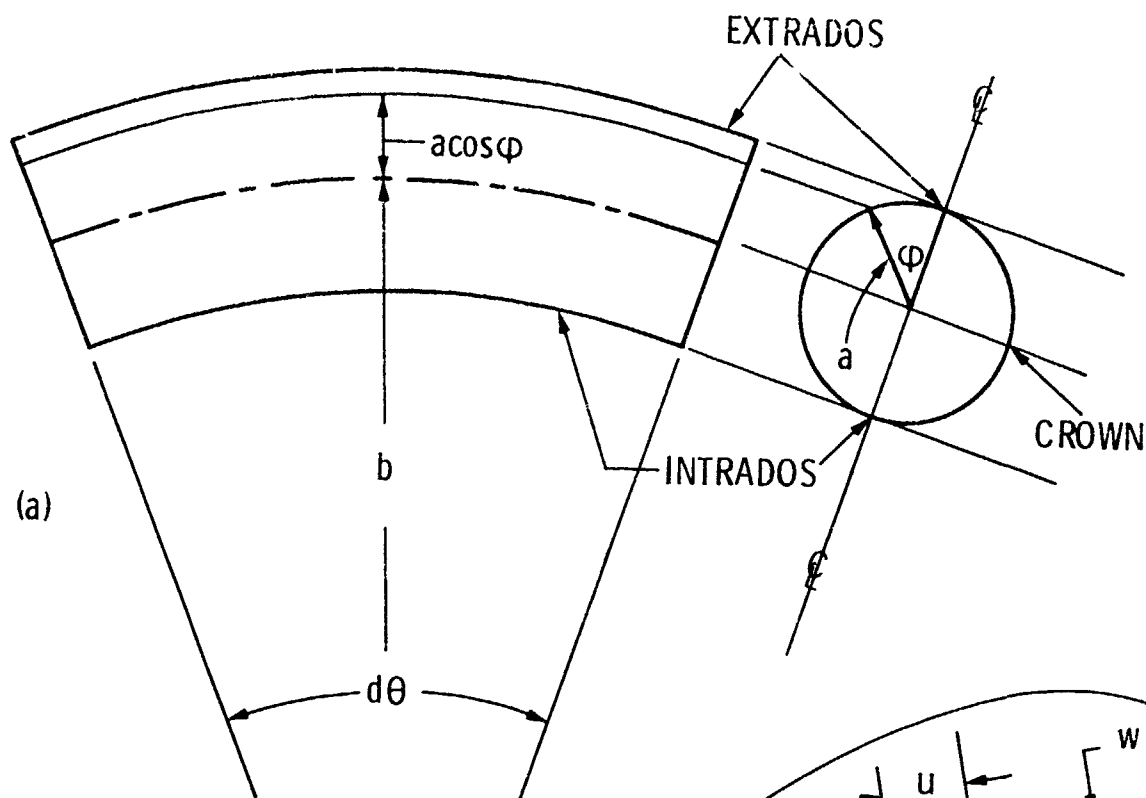


Figure 37 Comparison of more recent tests with theory for clamped spherical caps under uniform external pressure (from Brush and Almroth [4]).



Assume that:

$$R dY = b d\theta$$

$$k \equiv 1/R - 1/b$$

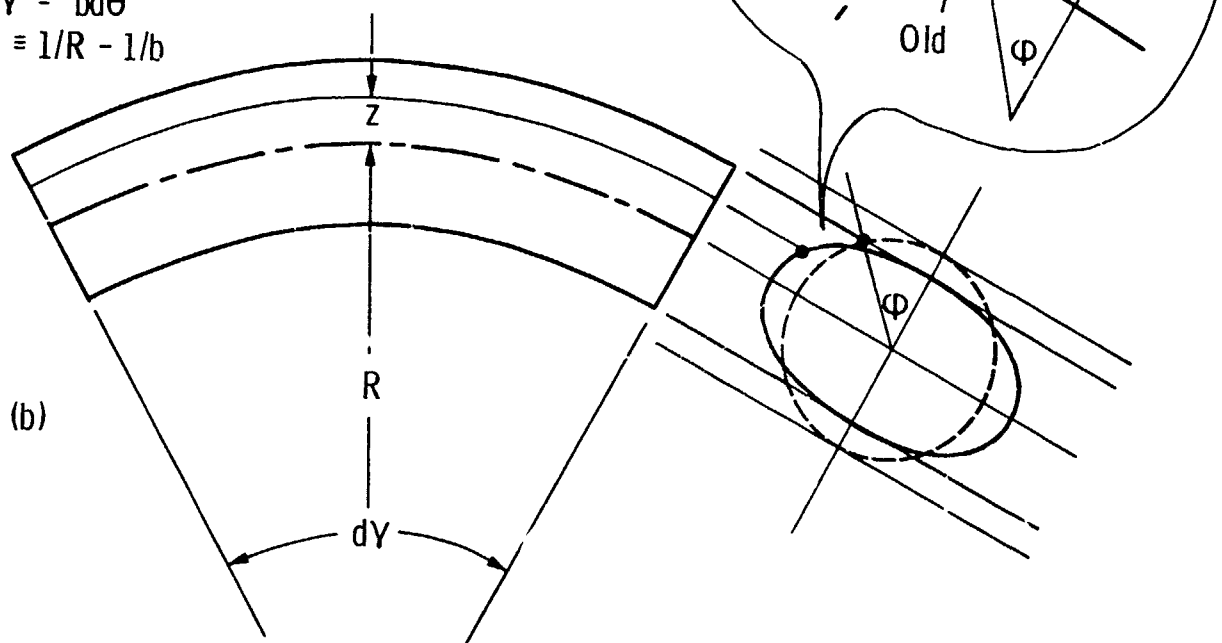


Figure 38 In-plane bending of curved pipe:
(a) initial configuration
(b) uniformly bent configuration

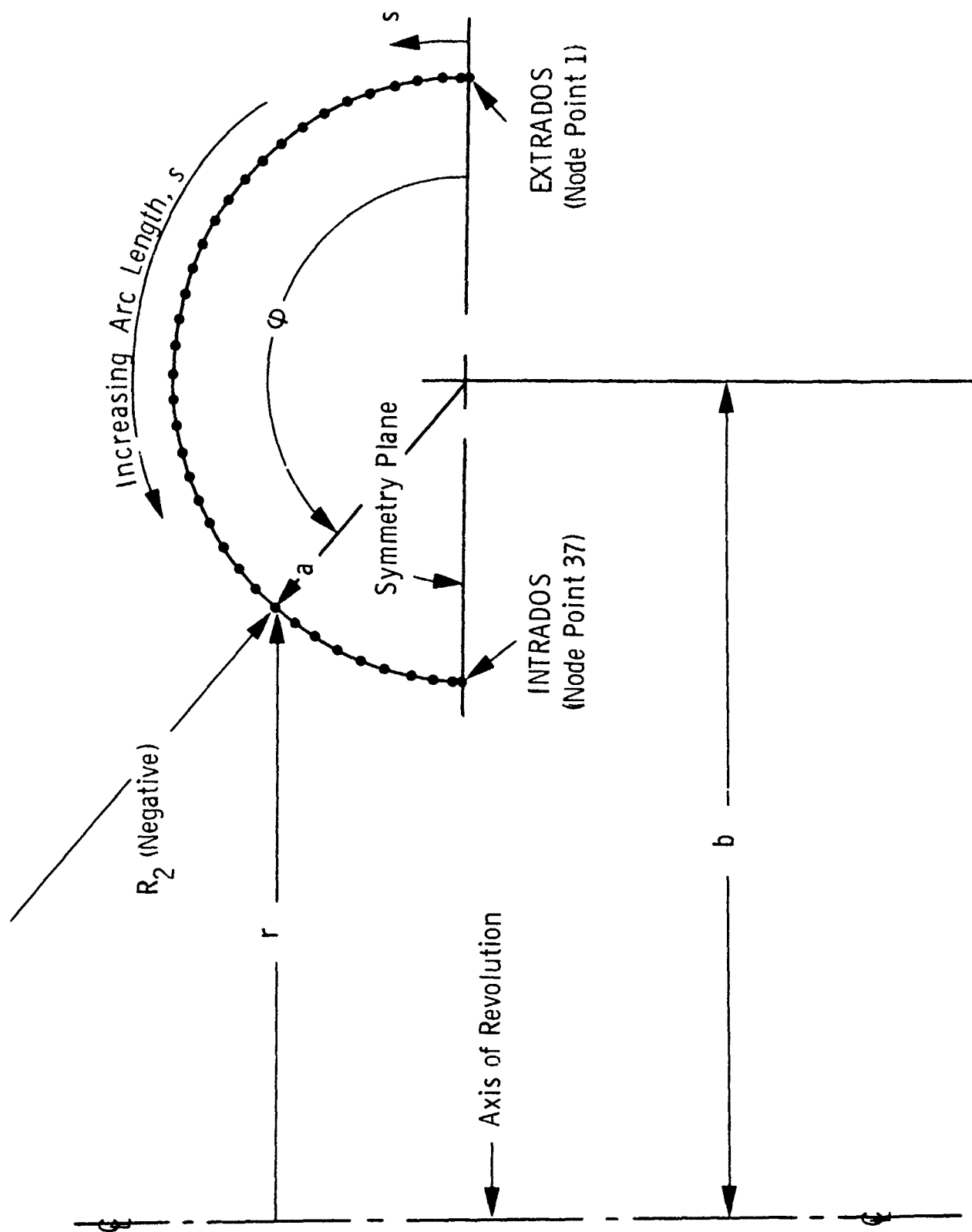


Figure 38(c) Discretization of pipe modeled as toroidal segment.

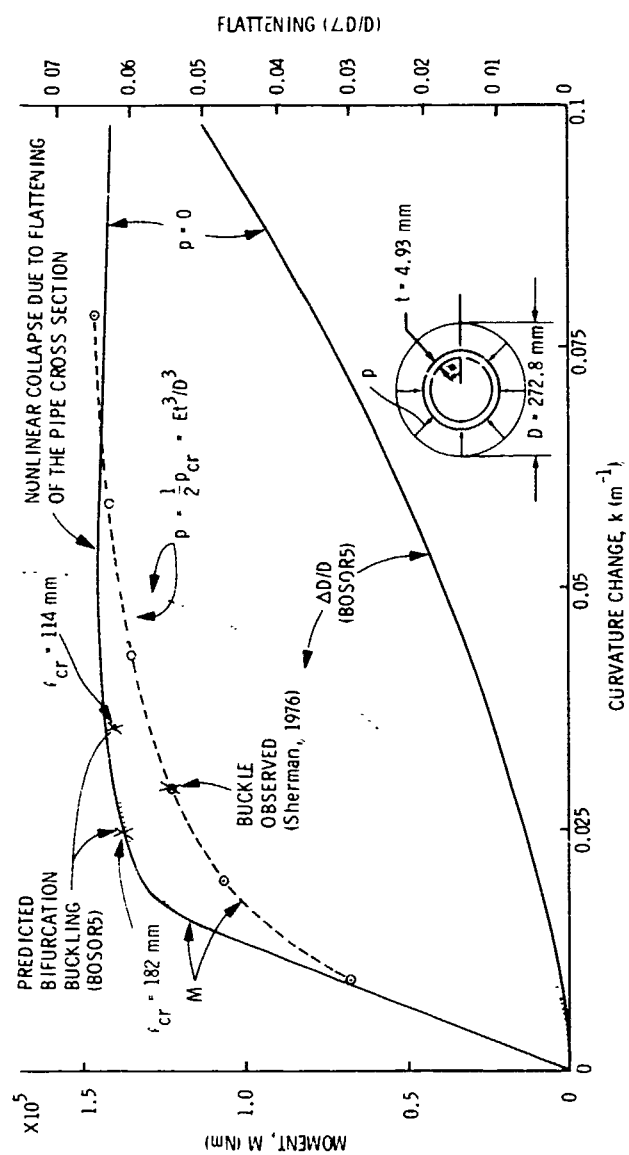
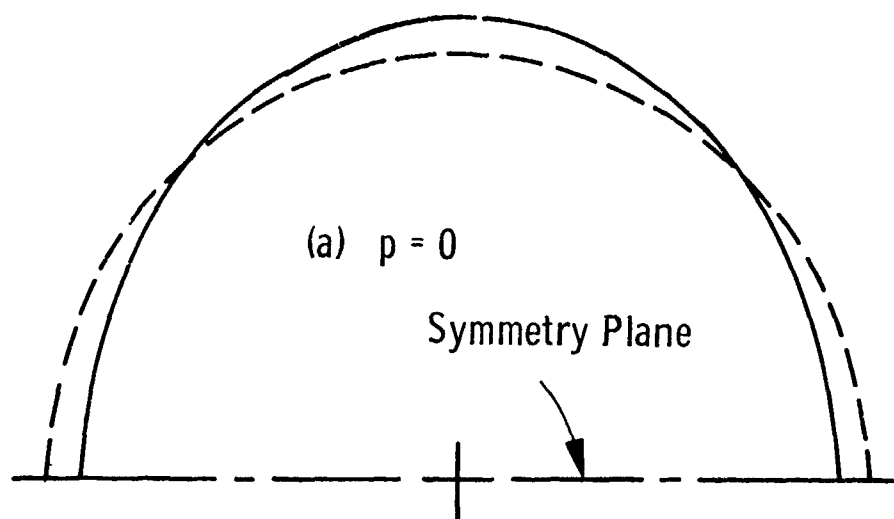


Figure 39 Bending of straight pipe with and without external pressure.



$$k = 0.0432 \text{ m}^{-1}$$

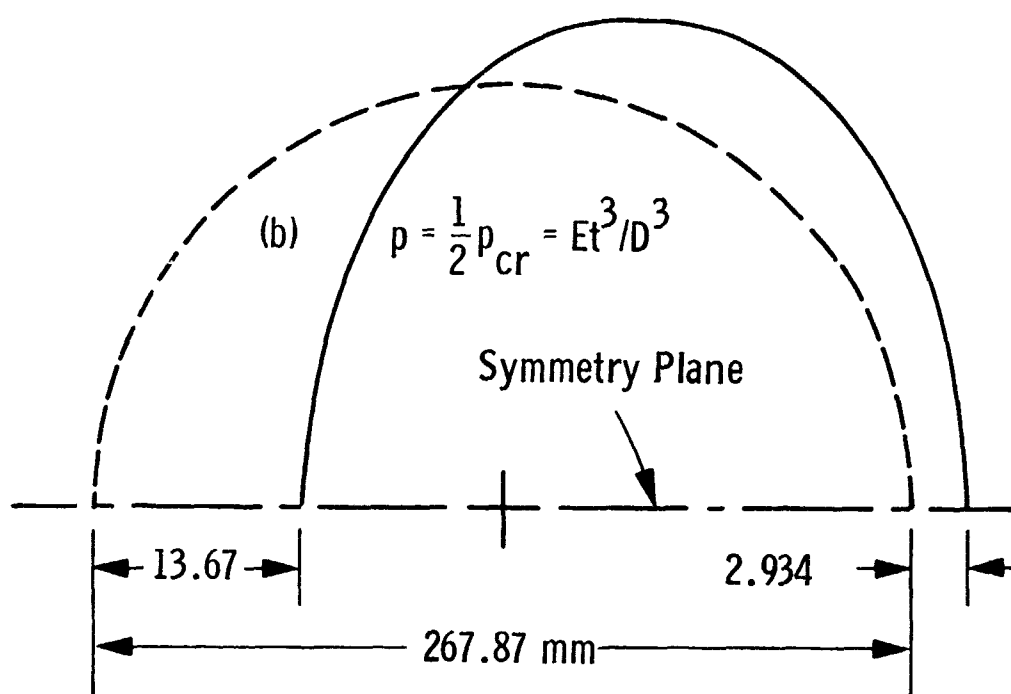


Figure 40 Ovalization of straight pipe with and without external pressure under imposed curvature $k = 0.0432 \text{ m}^{-1}$.

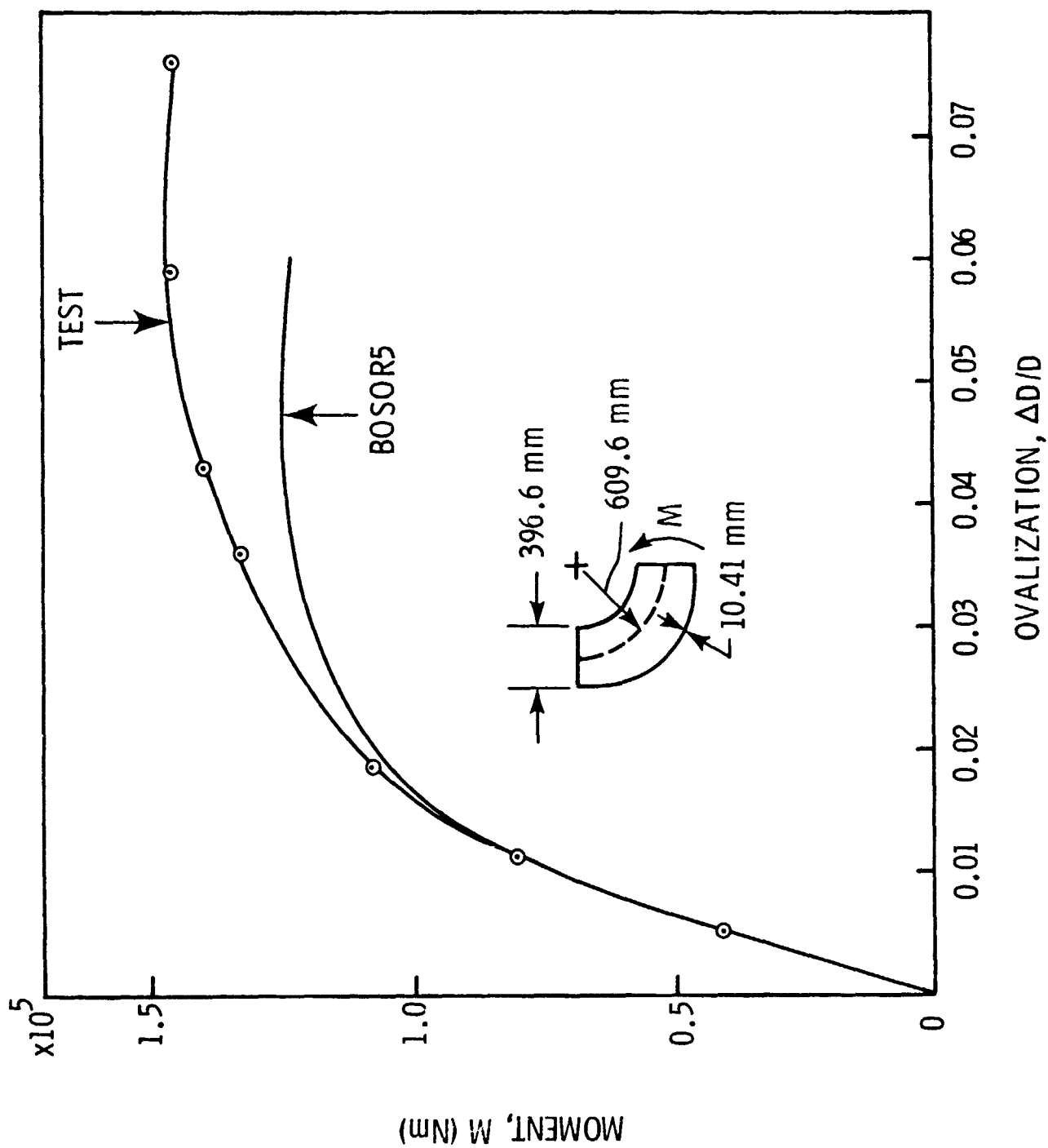


Figure 41 Comparison of test and theory for elastic-plastic bending of 90° elbow.

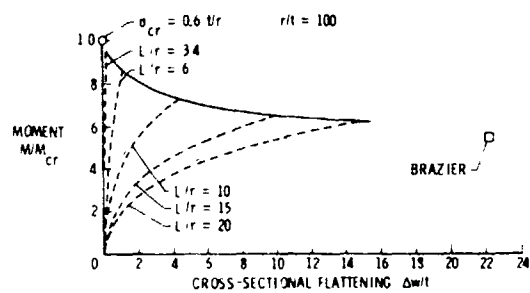


Figure 42(a) Load-deflection curves and maximum moment for bending of unpressurized straight cylindrical shells with various L/r . The ends are constrained to remain circular (from Stephens et al. [58]).

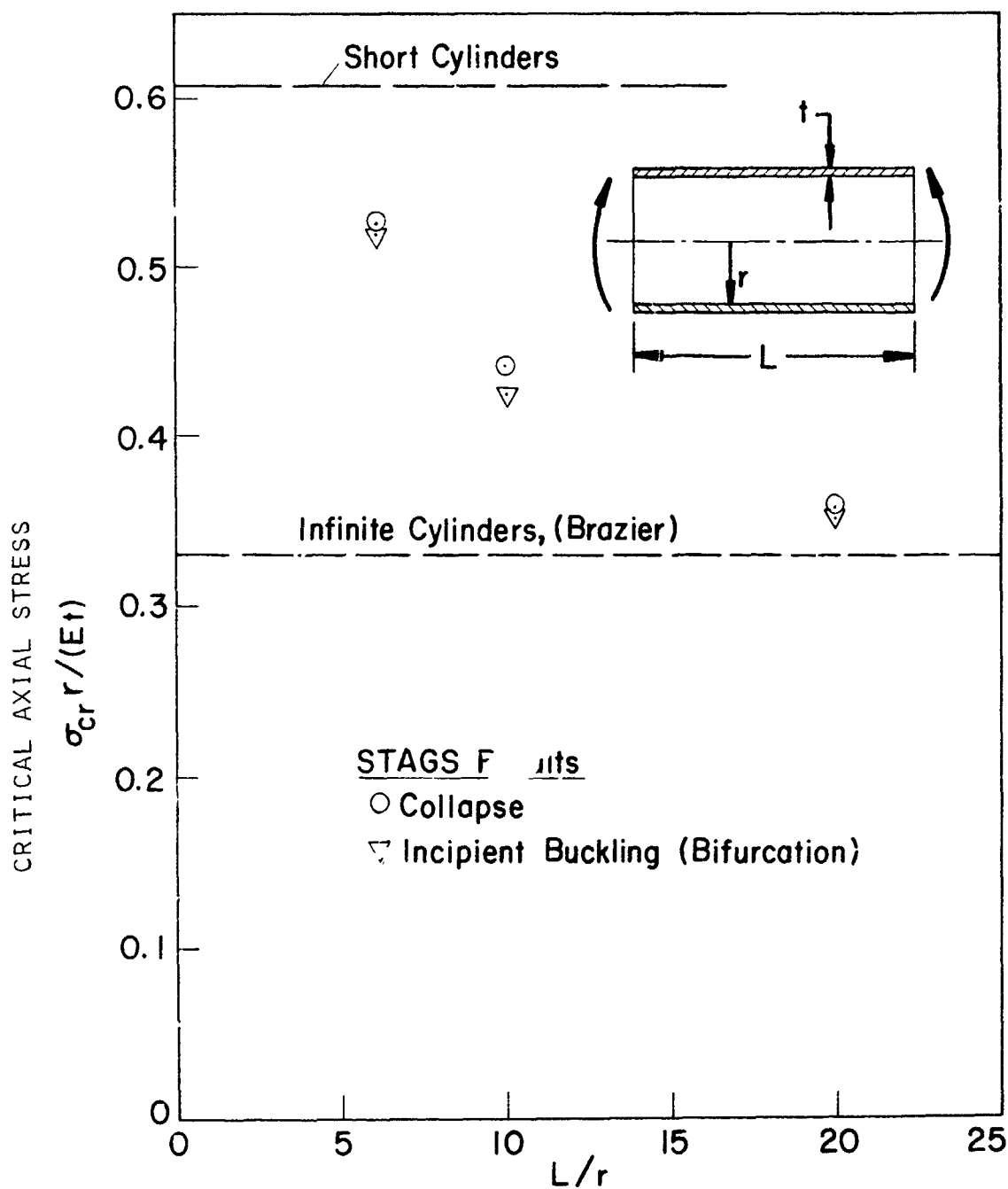


Figure 42(b) Collapse due to cross section ovalization and short-axial-wavelength bifurcation of cylindrical shells subjected to bending. The ends are constrained to remain circular (from Stephens et al. [58]).

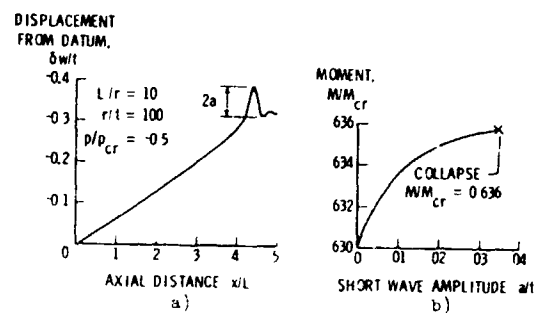


Figure 4.43 Determination of collapse load for the axial short-wave wrinkling mode of failure in cylindrical shell in bending: a) axial distribution of displacement; b) moment-deflection curve for wrinkling component "a" of total displacement, w (from Stephens et al. [58]).

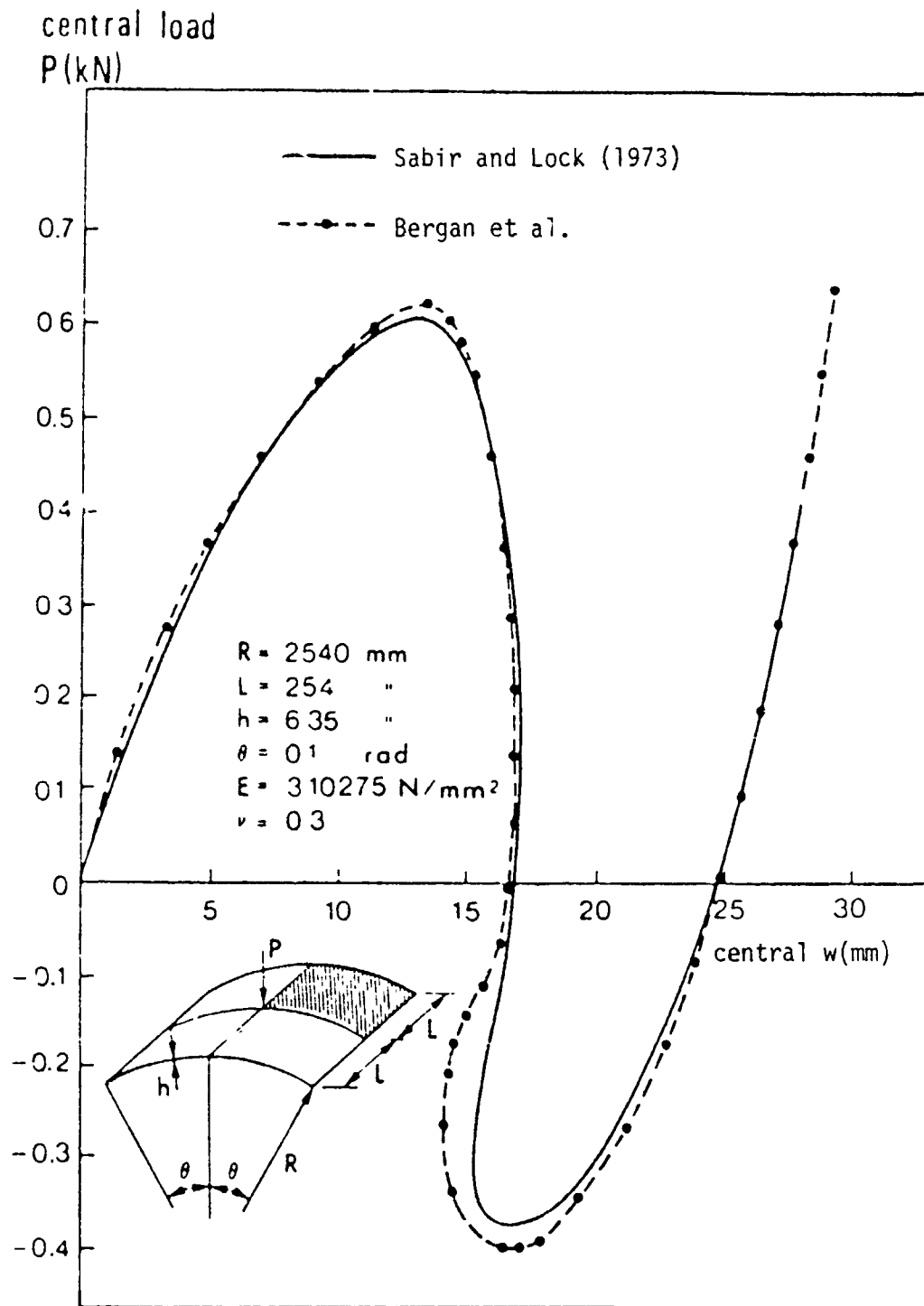


Figure 44 Load-deflection curves for hinged cylindrical panel (from Bergan et al. [84]).

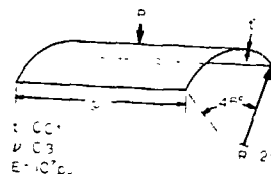
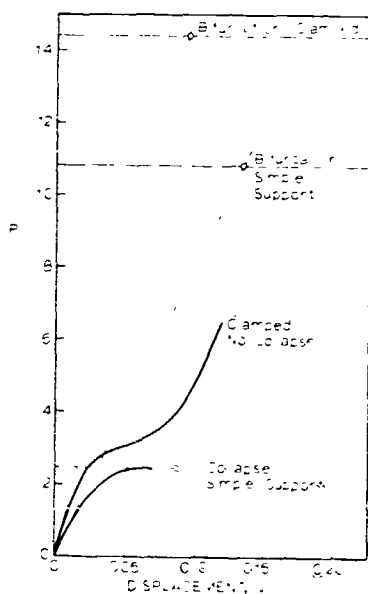


Figure 45 Load-deflection curves for a cylindrical panel with bifurcation buckling loads predicted from linear theory. These results demonstrate the inadequacy of a linear bifurcation model (from Almroth and Brogan [85]).

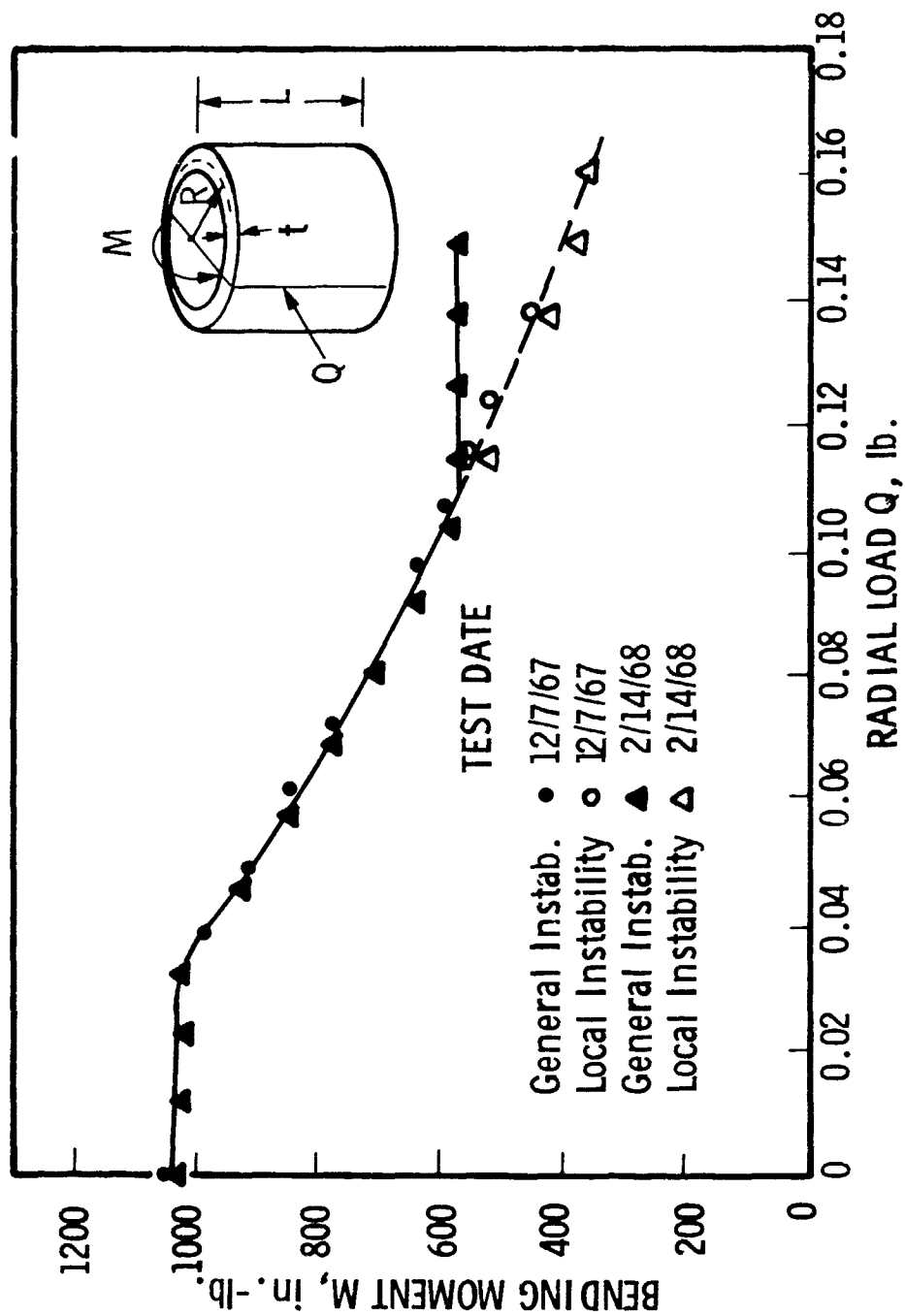


Figure 46 Experimental critical bending moment vs. radial concentrated load for cylindrical shell with $L/r = 2.33$, $R/t = 371$, $t = 0.014$ in., $E = 625,000$ psi (from Akubo et al. [86]).



Figure 47 Initial buckling of axially compressed aluminum cylinder with rectangular cutout (from Almroth and Holmes [87]).



Figure 48 Post-buckled state of axially compressed cylinder with rectangular cutout (from Almroth and Holmes [37]).

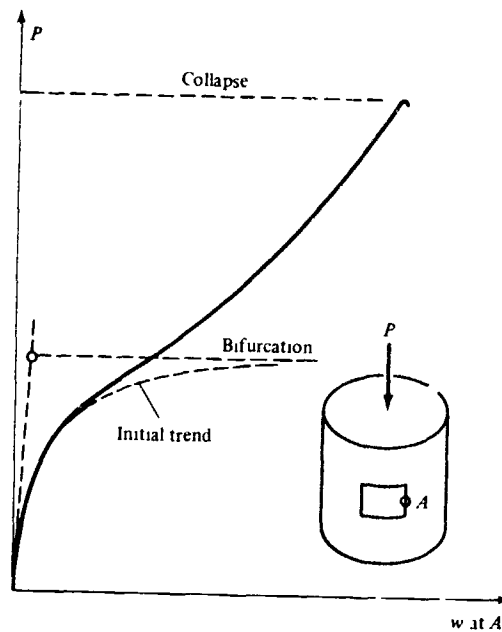


Figure 49 Equilibrium paths for axially compressed cylindrical shell with two diametrically opposed cutouts (from Brush and Almroth [4]).

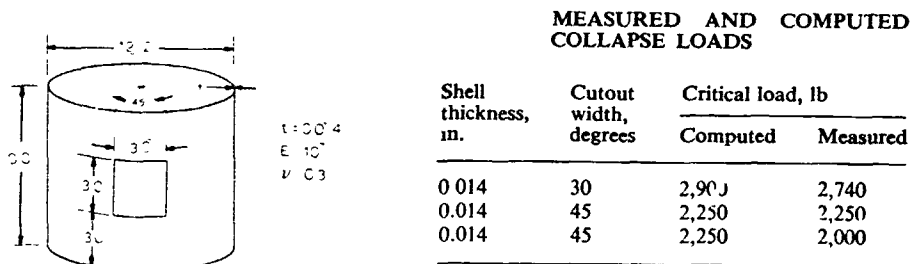


Figure 50 Comparison of test and theory for buckling of axially compressed cylinder with two diametrically opposed rectangular cutouts.

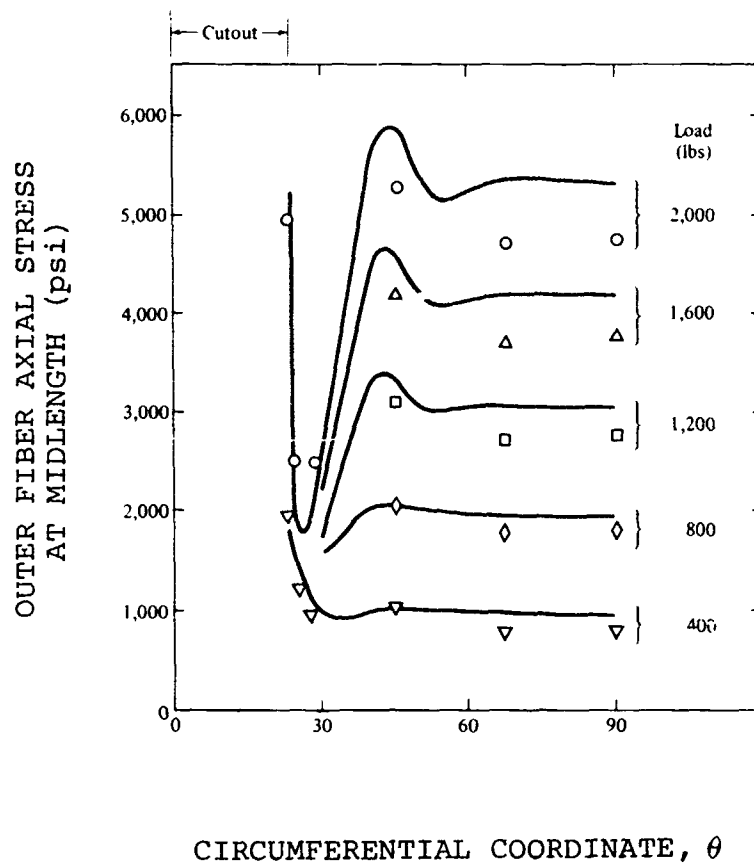


Figure 51 Outer fiber axial stress at midlength of axially compressed cylindrical shell with rectangular cutouts (from Brush and Almroth [4]).

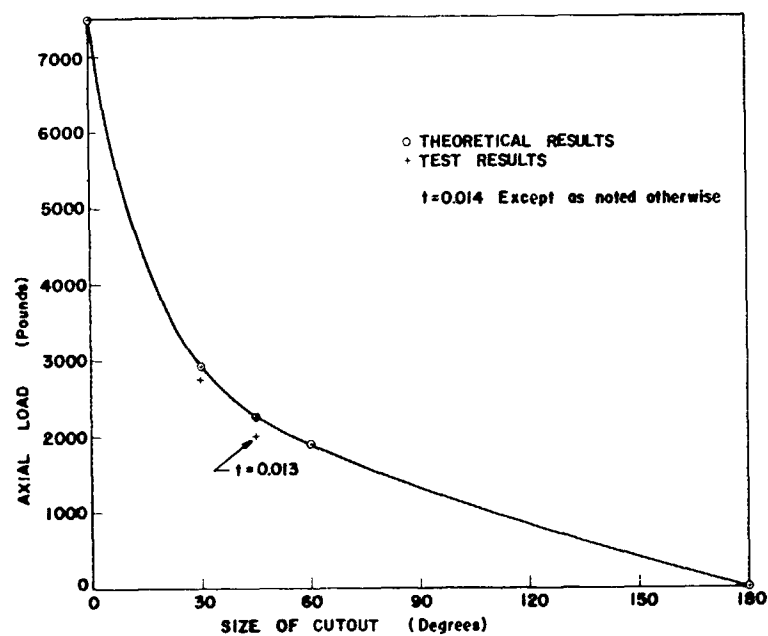


Figure 52 Critical load vs. cutout angle for axially compressed cylindrical shell with two diametrically opposed rectangular cutouts (from Almroth and Holmes [87]).

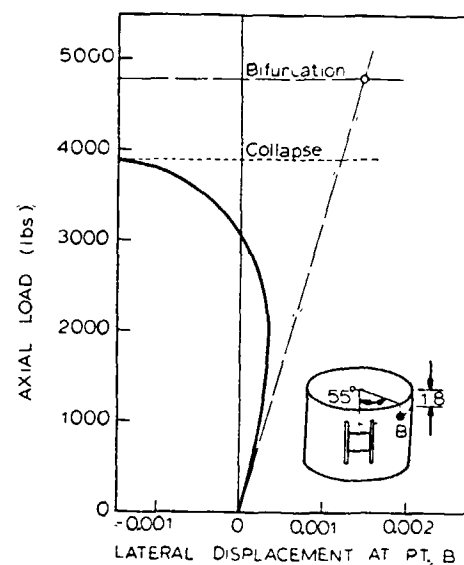
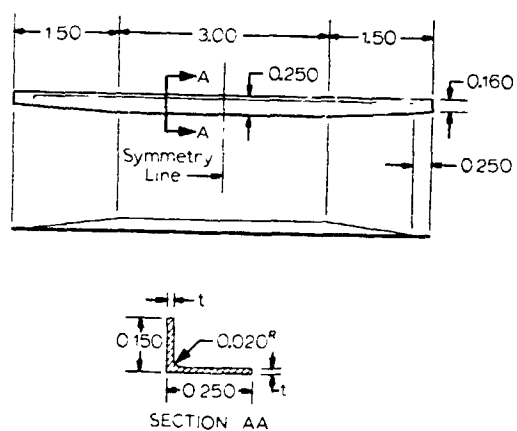


Figure 53 Collapse of axially compressed cylindrical shell with diametrically opposed reinforced cutouts (from Almroth and Holmes [87]).

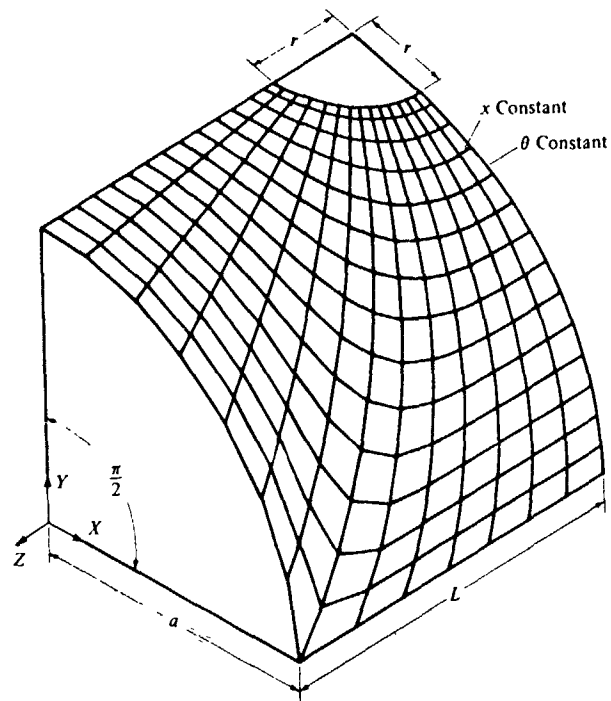


Figure 54 Finite element grid for cylinder with circular cutout (from Brush and Almroth [4]).

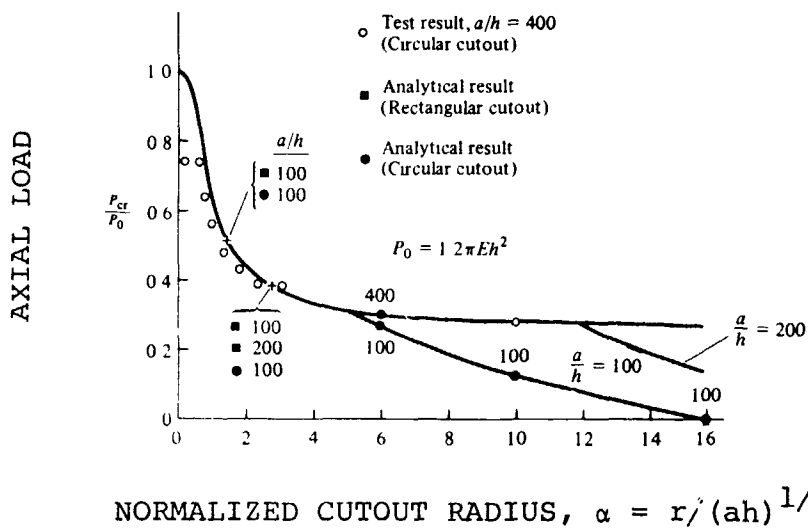


Figure 55 Comparison of test and theory for critical axial loads of cylinders with cutouts (from Brush and Almroth [4]).

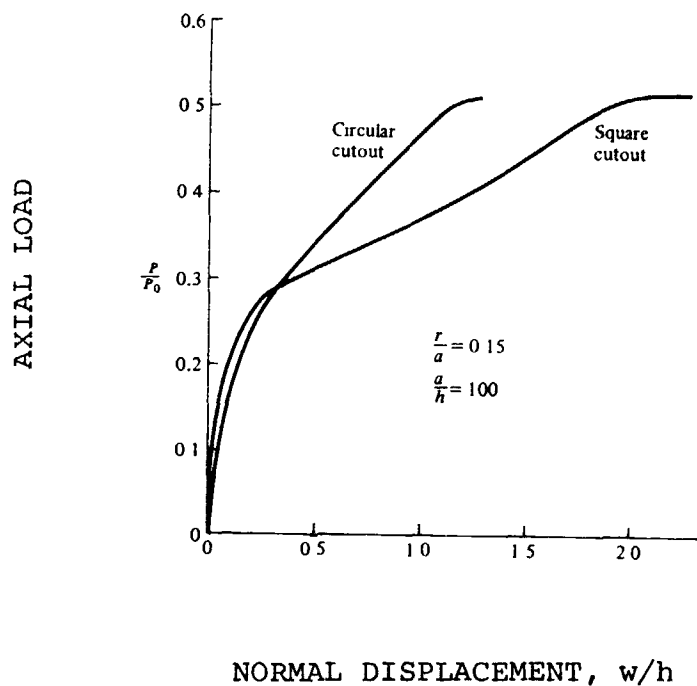
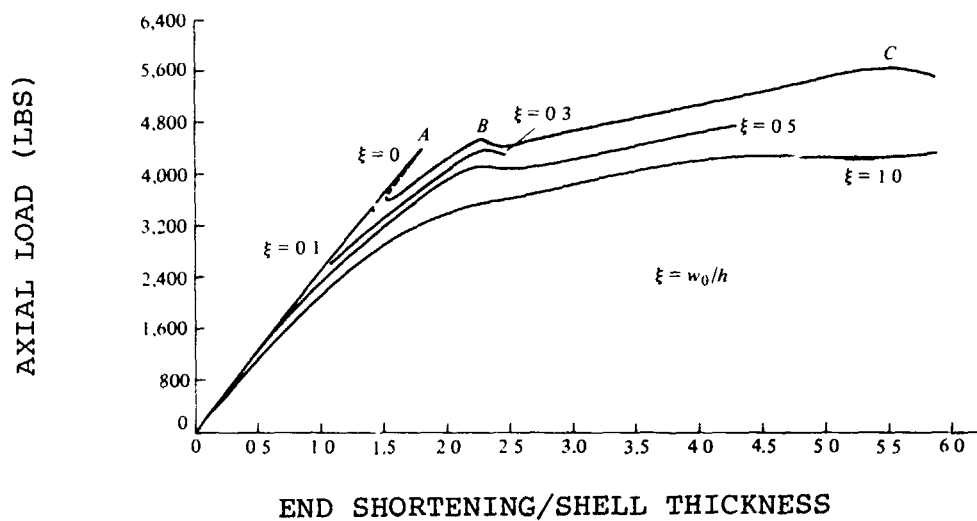
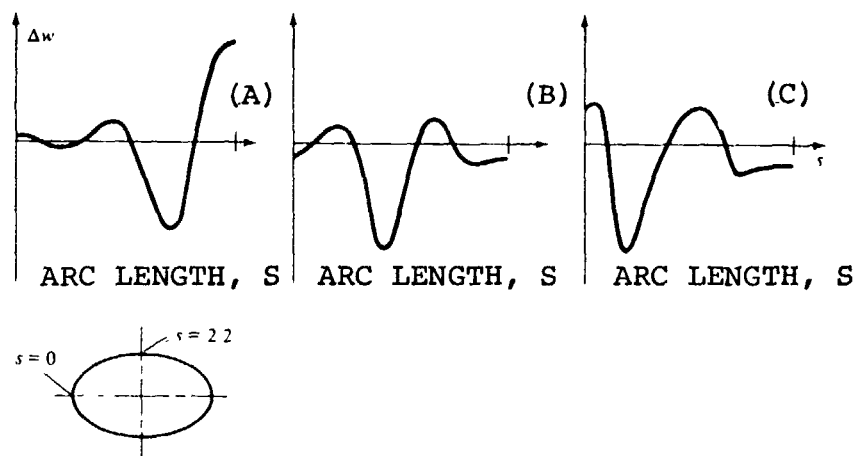


Figure 56 Equilibrium paths for cylinders with cutouts, $\alpha = 1.5$. w is the outward displacement at the midlength of the cylinder at the edge of the cutout (from Brush and Almroth [4]).



(a)



(b)

Figure 57 (a) Load-deflection curves for axially compressed perfect and imperfect cylinders with elliptical cross section;
(b) Fastest growing component of normal displacement at A, B, C.

(from Brush and Almroth [4])

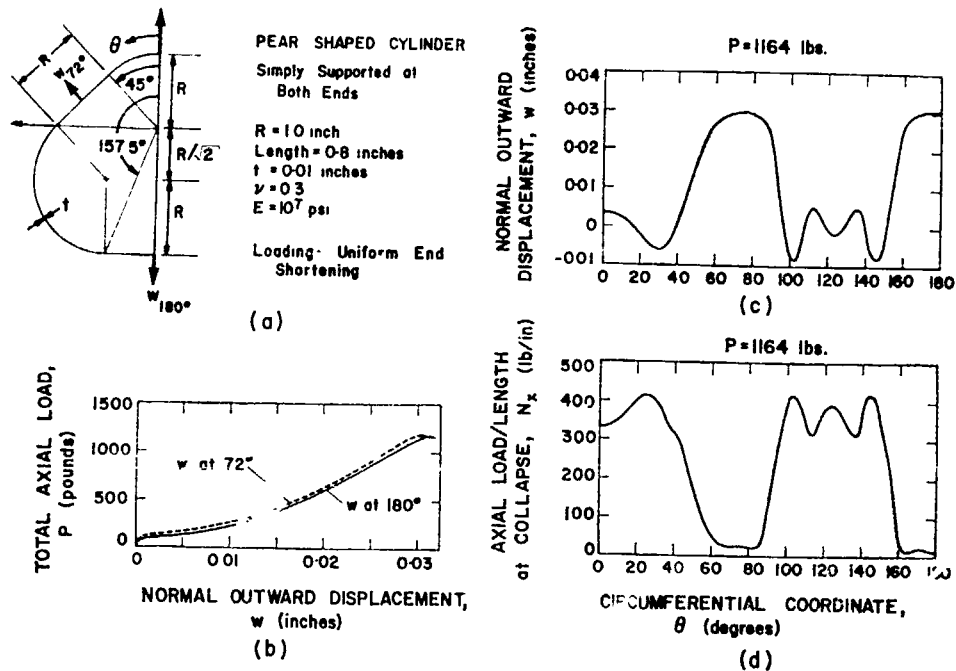


Figure 58 "Pear-shaped" cylinder under uniform end shortening.

(a) Cylinder geometry

(b) Load-deflection curves

(c) Normal displacement at midlength at collapse

(d) Axial line load at midlength at collapse

(Total axial load refers to load on the half of the cylinder shown.)

(from Bushnell et al. [90])

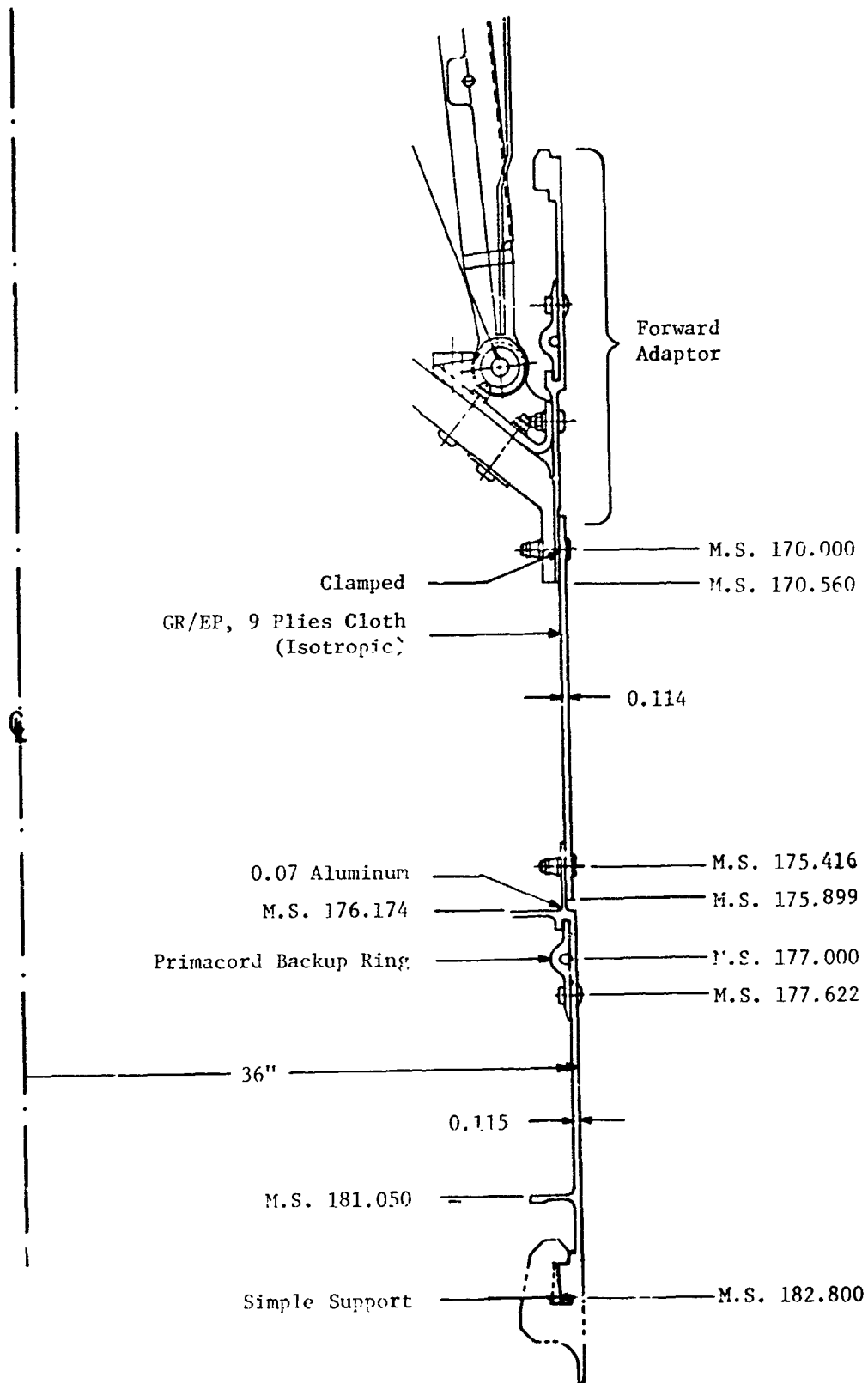


Figure 59 Complex rocket interstage subjected to axial compression during launch. Stability problems arise from the load path eccentricity at Missile Station 175.9.

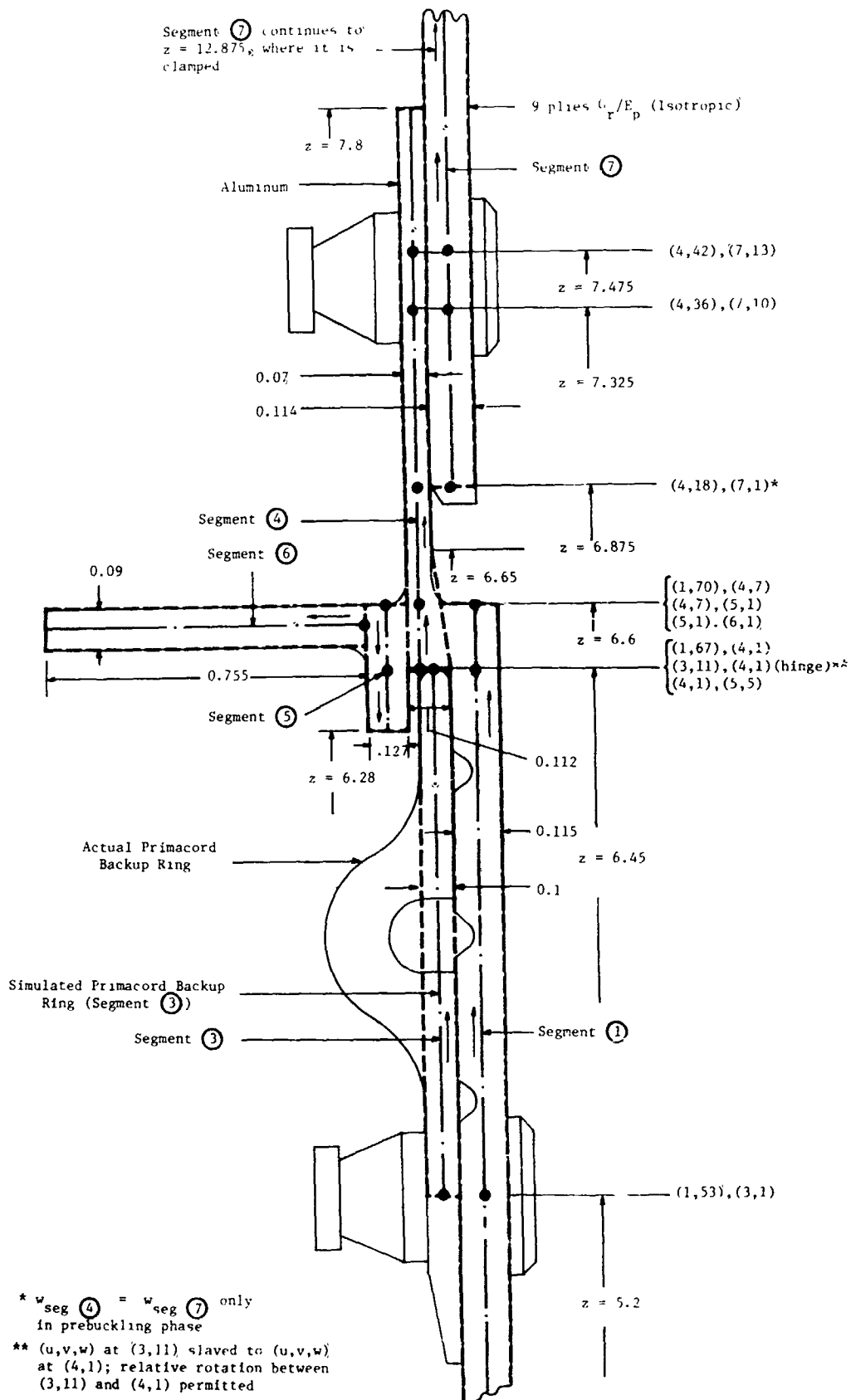


Figure 60 Enlarged view of the rocket interstage surrounding the area where the load path eccentricity occurs.

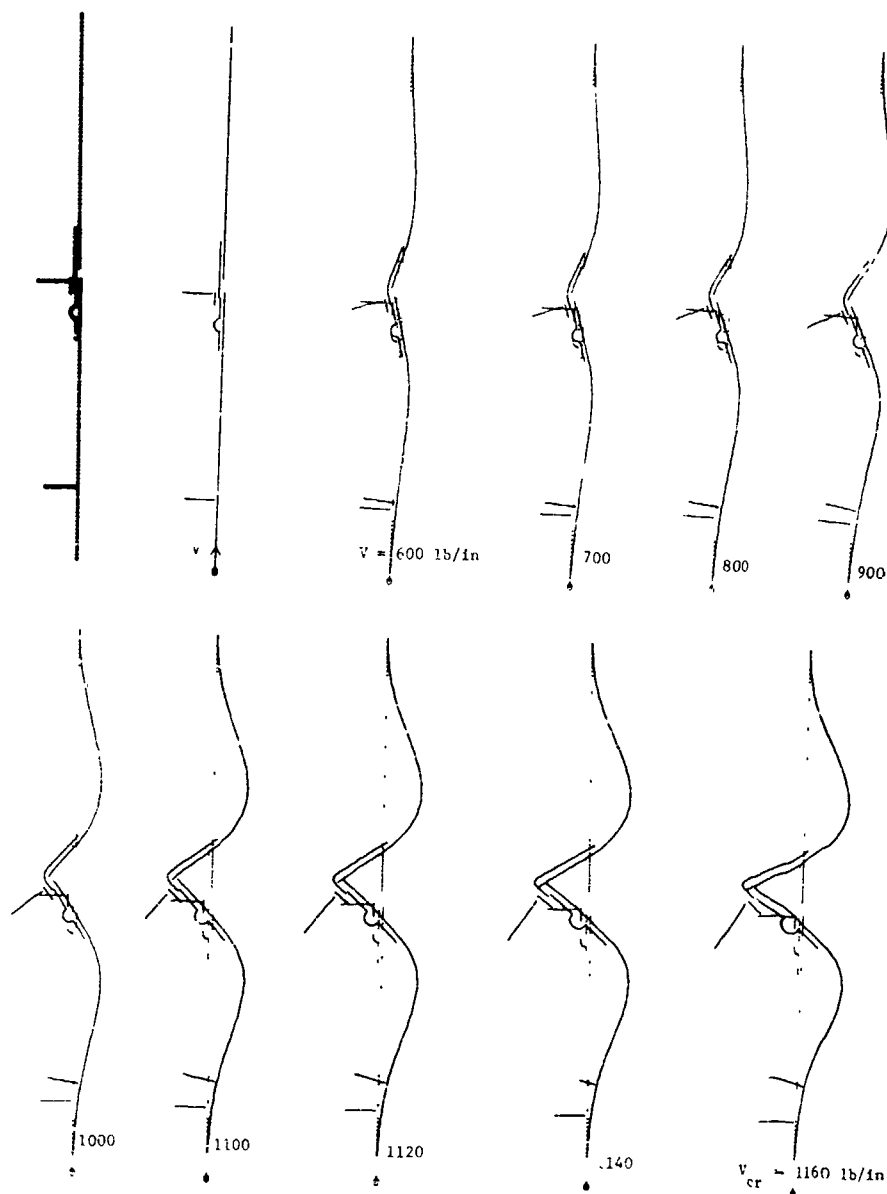


Figure 61 Deformed profiles of the axially compressed rocket interstage with increasing axial compression, V .

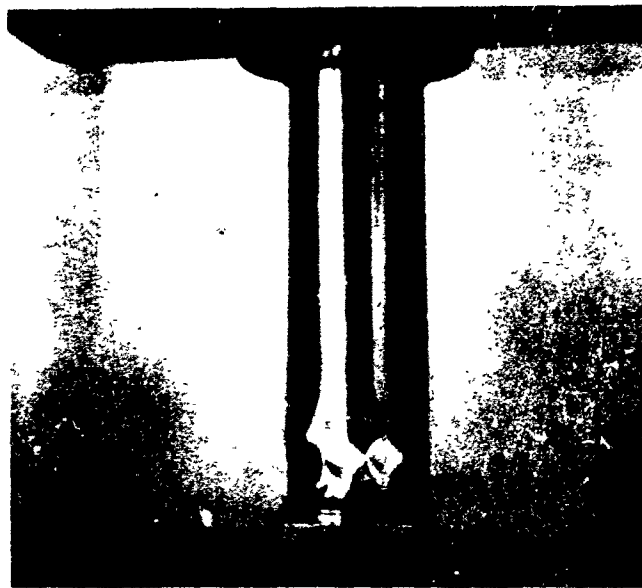


Figure 62(a) Edge buckling mode in thin monocoque circular cylindrical shell under uniform axial compression (from Horton et al. [38]).

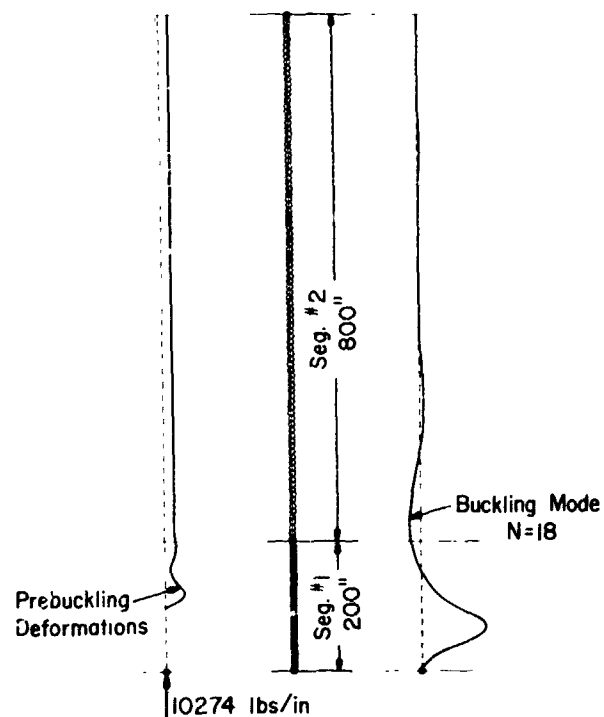


Figure 62(b) Prediction of edge buckling in axially compressed monocoque cylindrical shell (from Bushnell [14]).

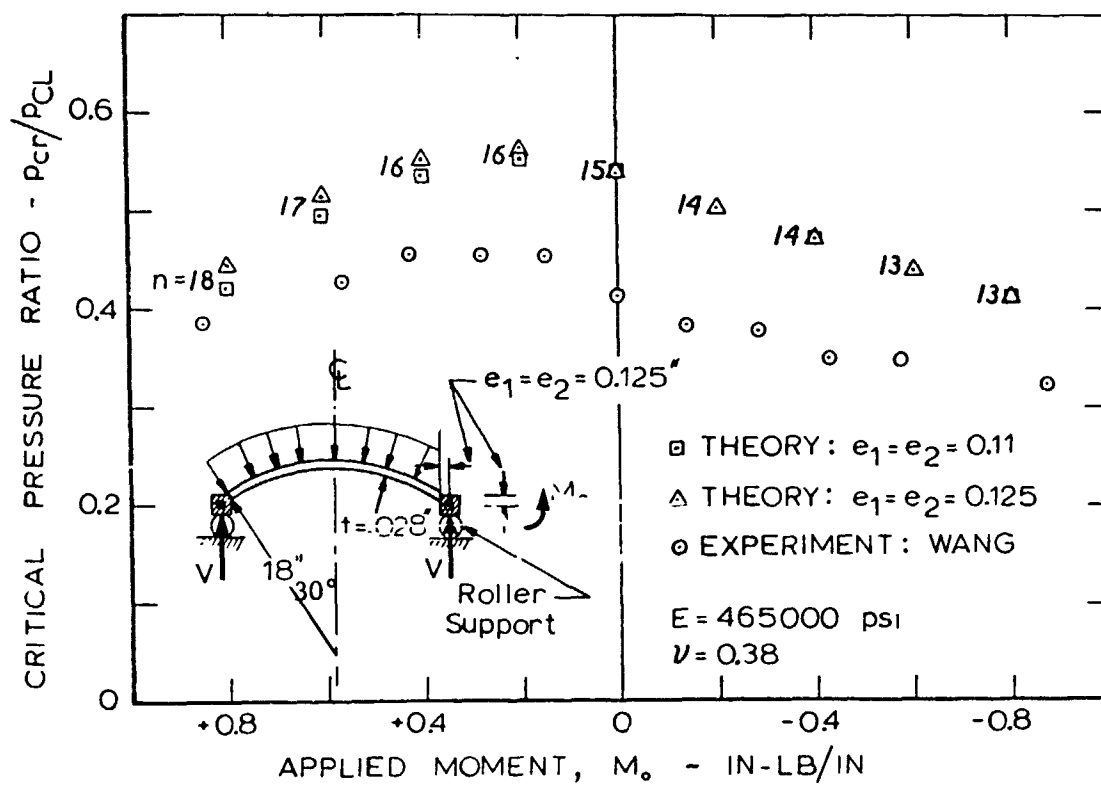


Figure 63 Comparison between test and theory for ring-supported spherical caps with external pressure and applied edge moment, M_o (from Bushnell [91]).

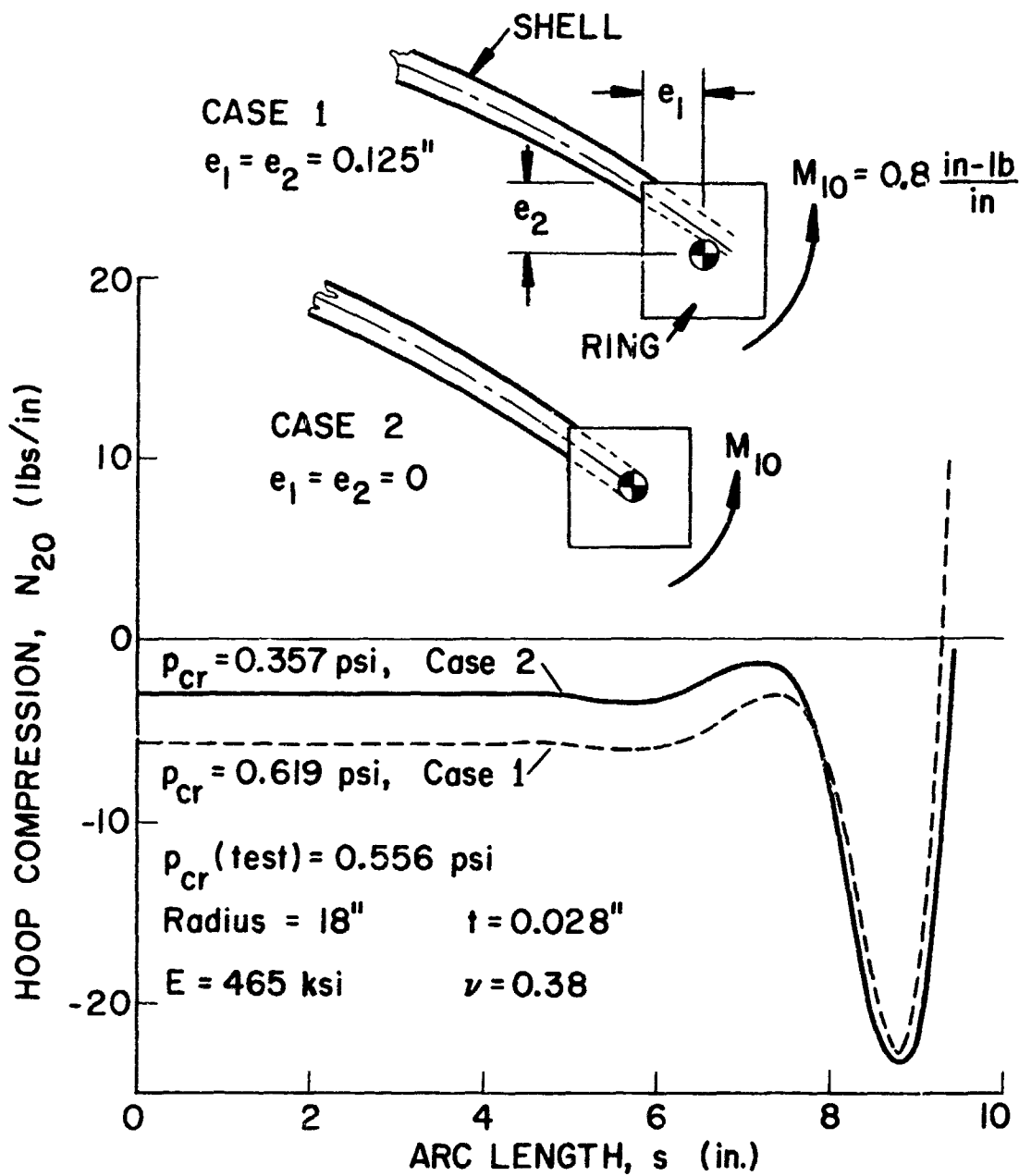


Figure 64 Effect of edge ring eccentricity on predicted buckling pressures of cap (from Bushnell [91]).

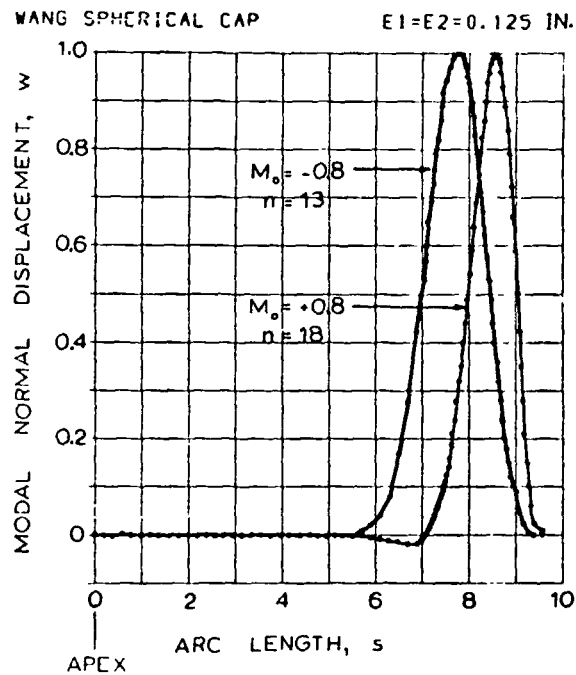


Figure 65 Modal normal displacement w for ring-supported spherical caps with external pressure and applied edge moments, M_o (from Bushnell [91]).

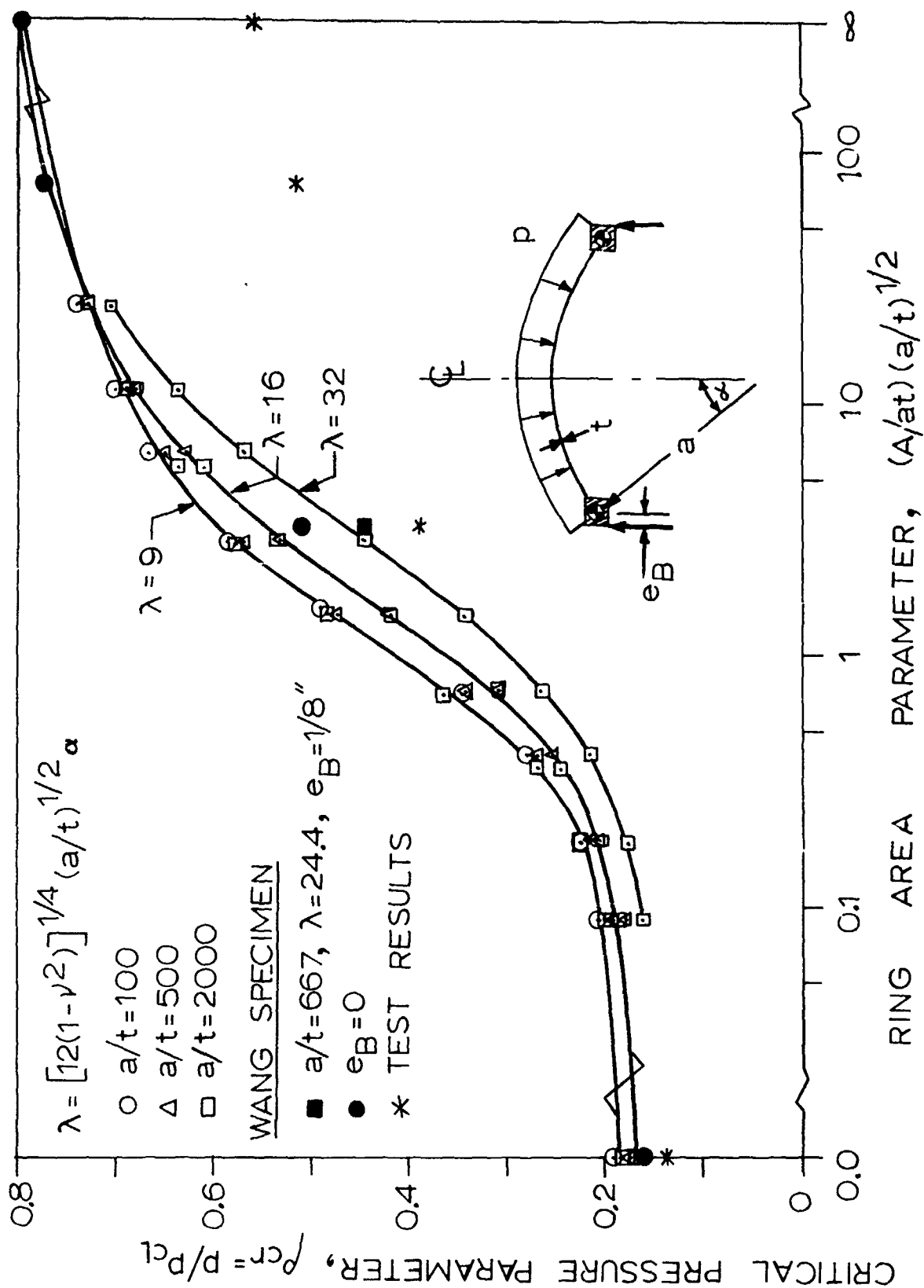


Figure 66 Buckling pressure vs. edge ring size for spherical caps. λ is the shallowness parameter (from Bushnell [92]).

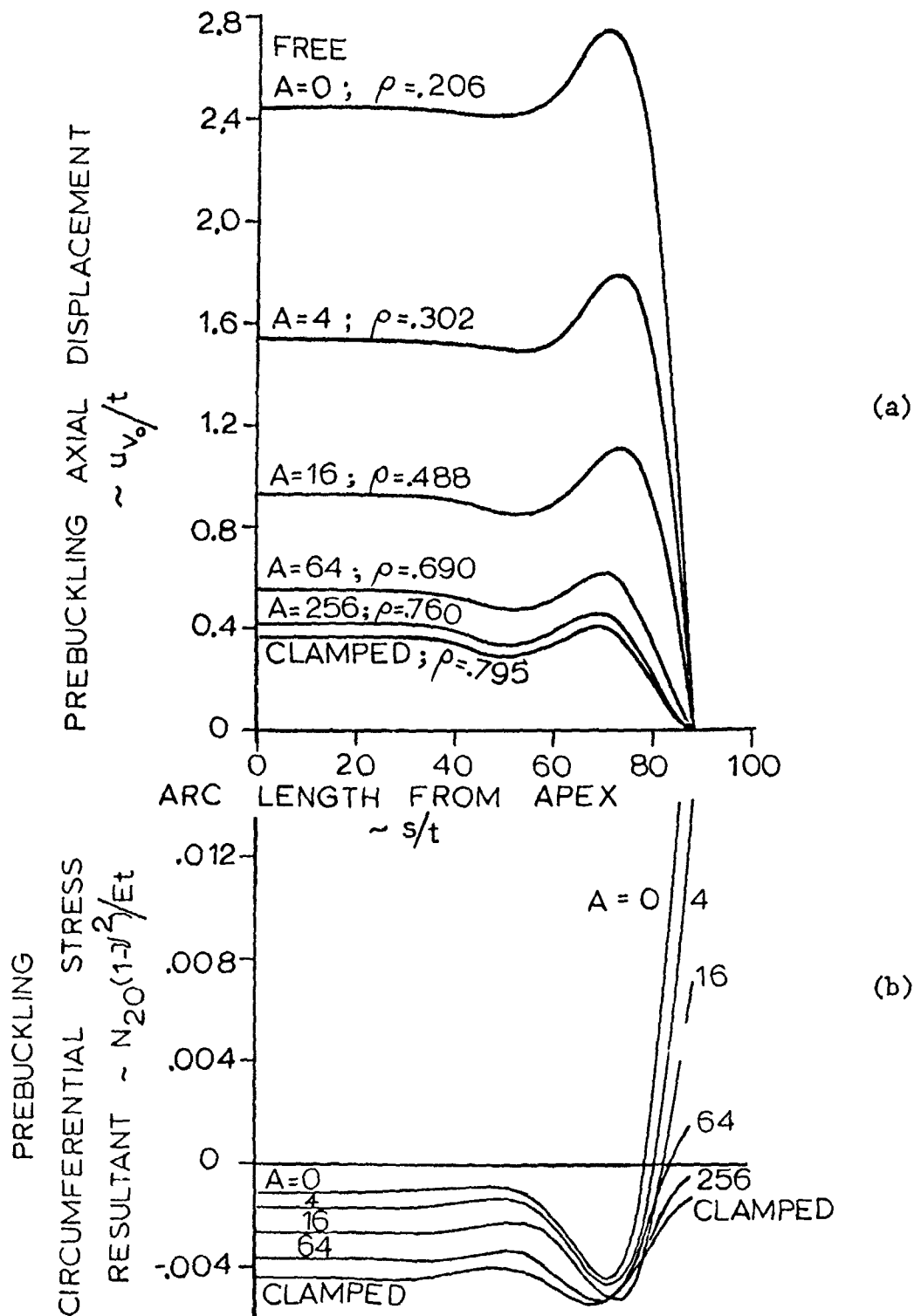
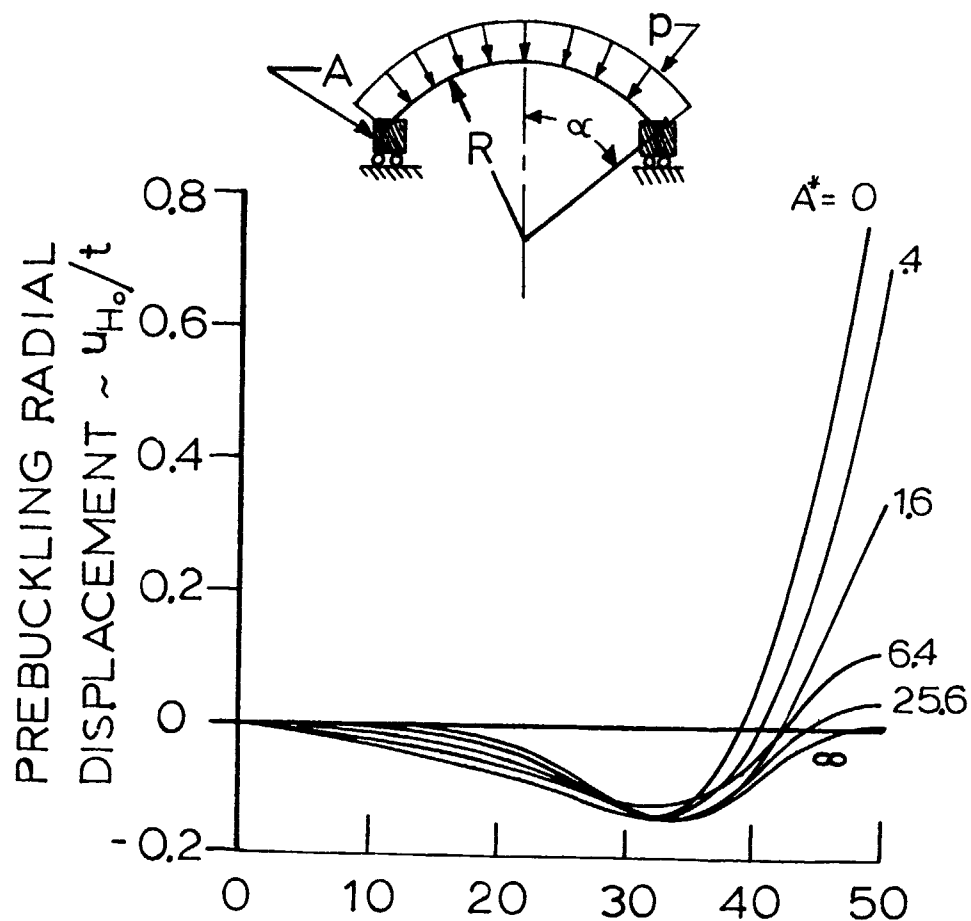
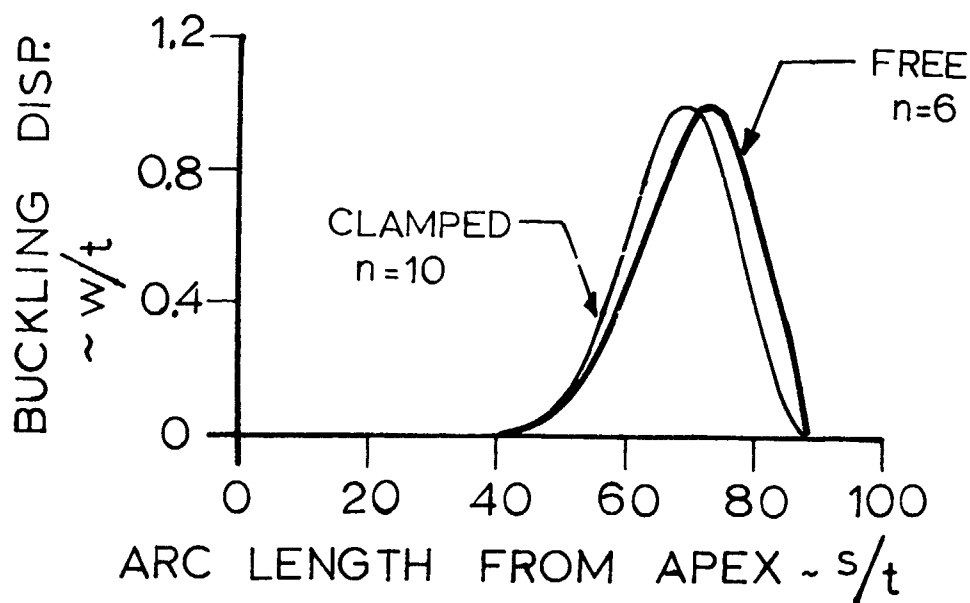


Figure 67(a,b) Prebuckling axial displacement and circumferential stress for ring-supported spherical shells with $\lambda = 16$, $a/t = 100$ (from Bushnell [92]).



(c)



(d)

Figure 67(c,d) Prebuckling radial displacement and buckling mode shape for the same geometry, the results of which are shown in Figure 67(a,b) (from Bushnell [92]).

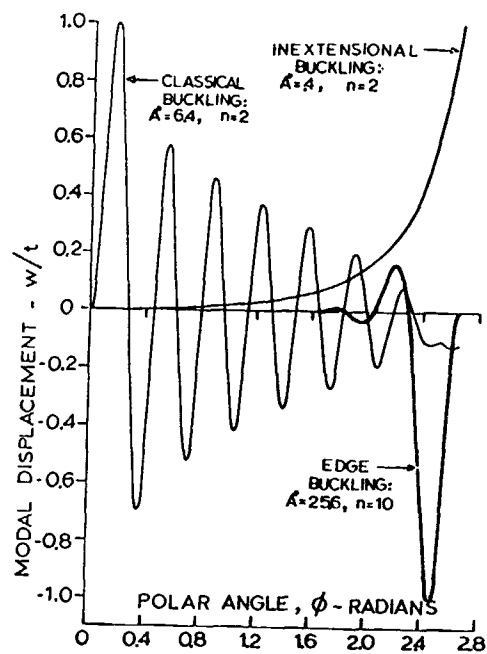
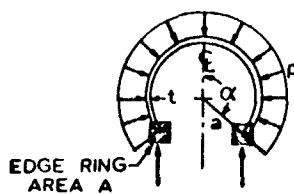


Figure 68 Buckling modes for ring-supported spherical shells with $\alpha = 2.65$ rad, $a = 100$, and $t = 1.0$ (from Bushnell [92]).

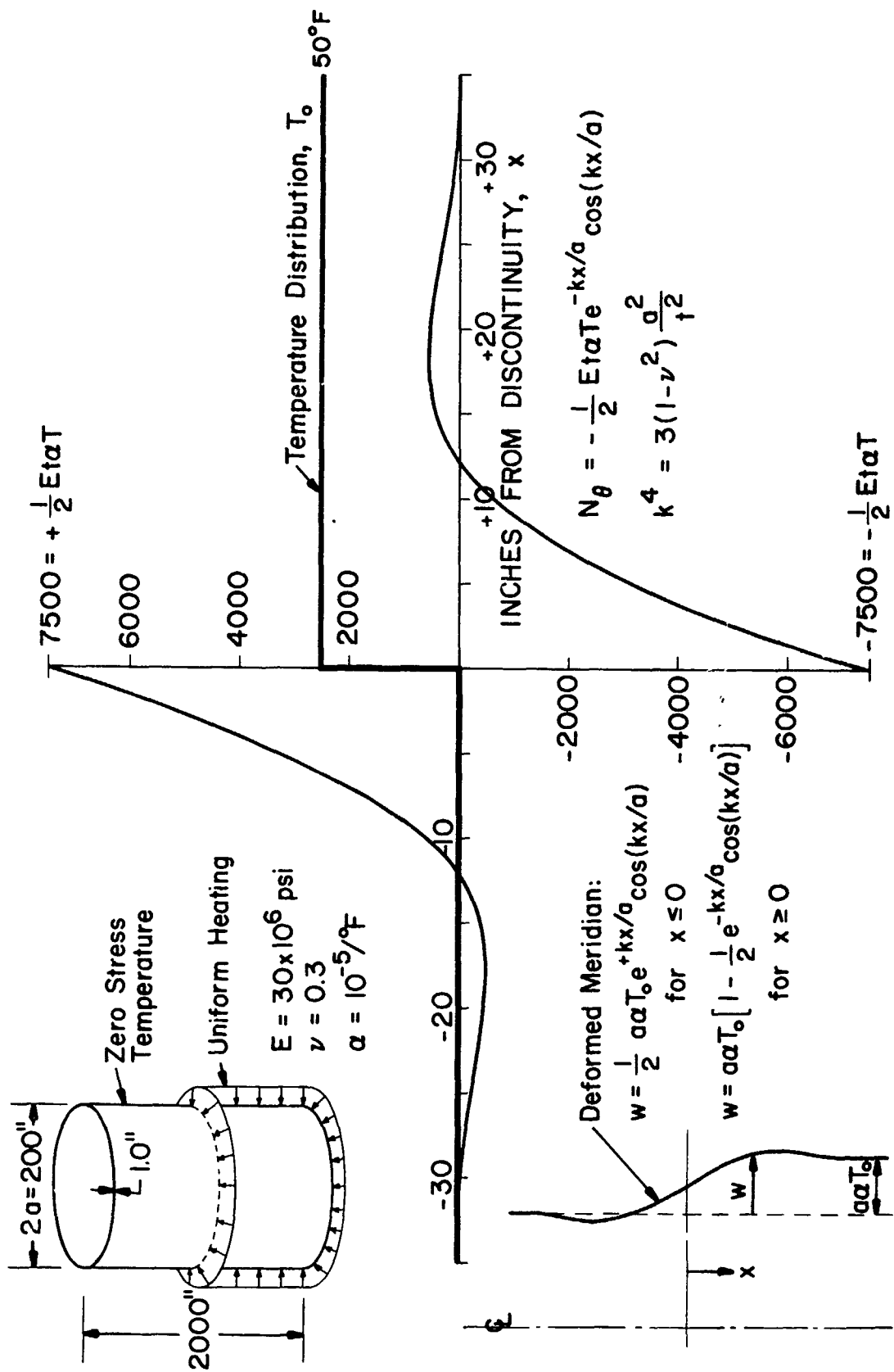


Figure 69 Hoop stress resultant in cylindrical shell with thermal discontinuity (from Bushnell [97]).

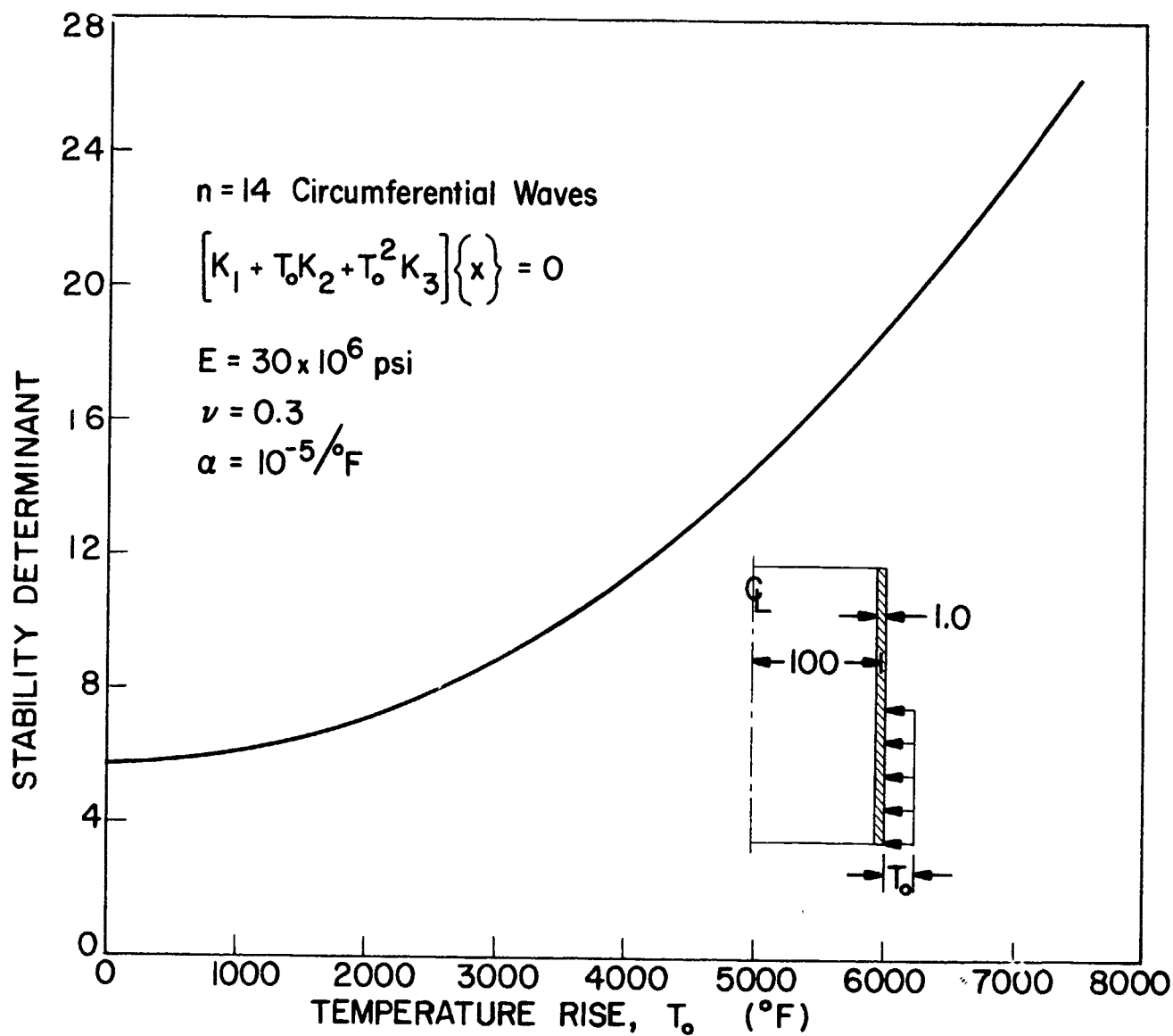


Figure 70 Stability determinant vs. temperature amplitude with prebuckling rotation β_0 included (from Bushnell [97]).

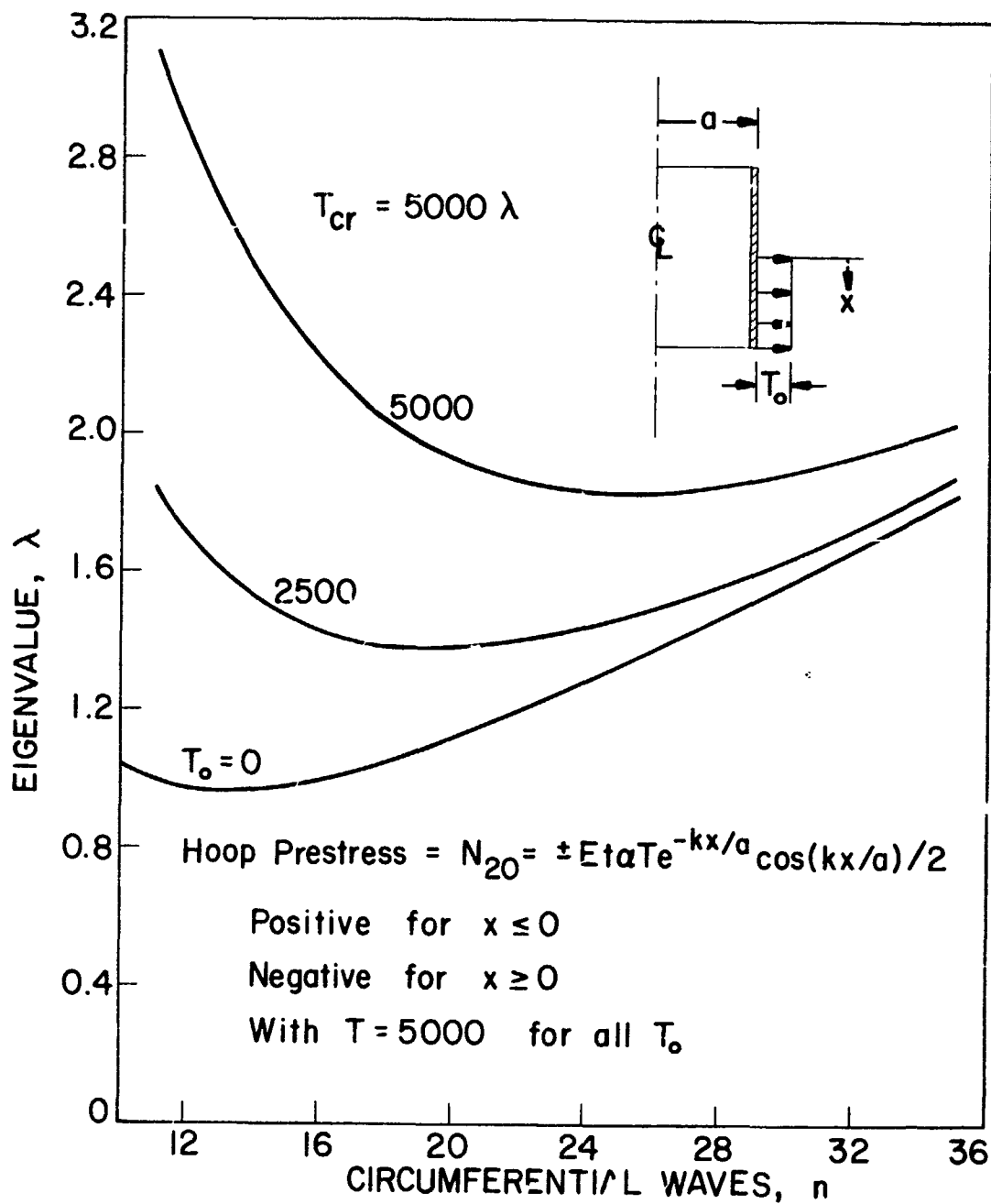


Figure 71 Buckling temperatures for three amplitudes of fixed "imperfection". Imperfection shape given by the expressions for w in Figure 69 (from Bushnell [97]).

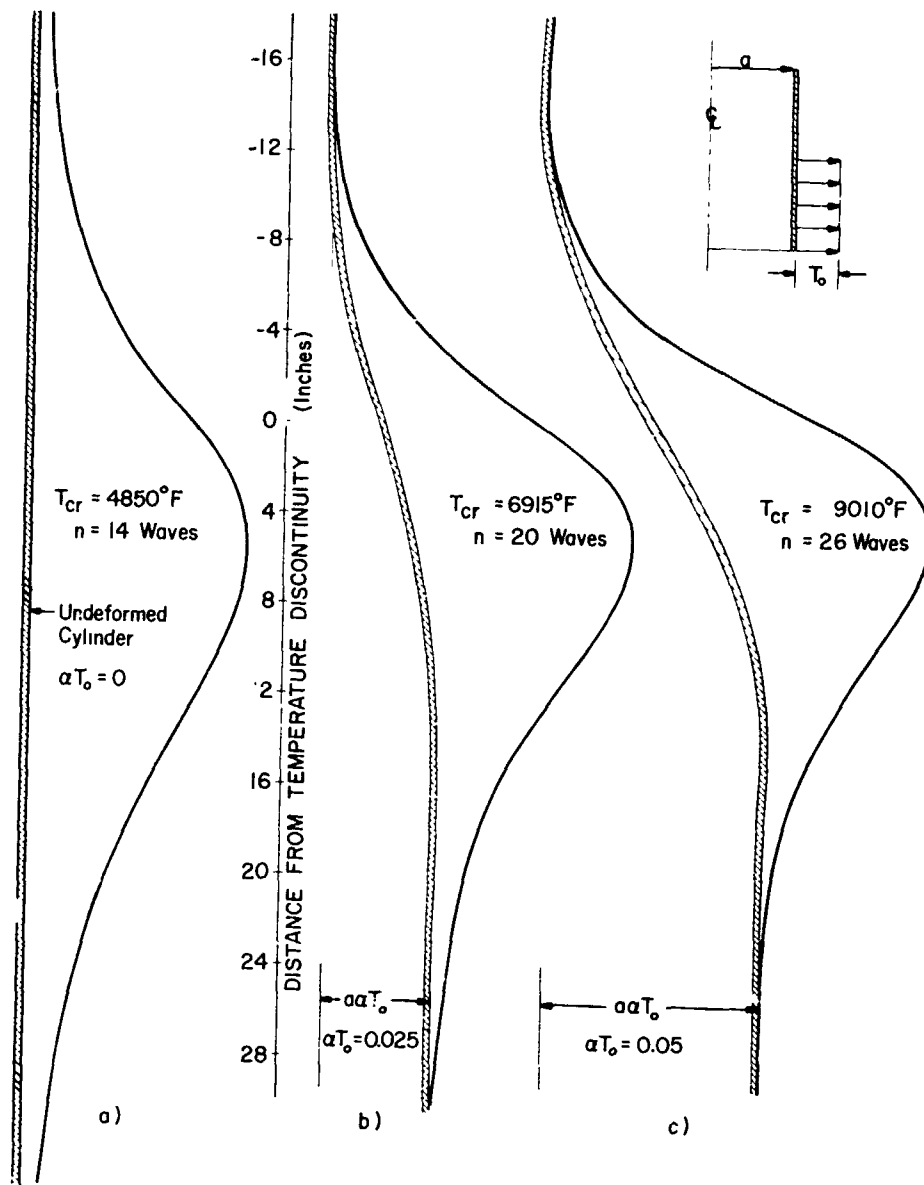


Figure 72 Buckling modes for three amplitudes of fixed "imperfections" (from Bushnell [97]).

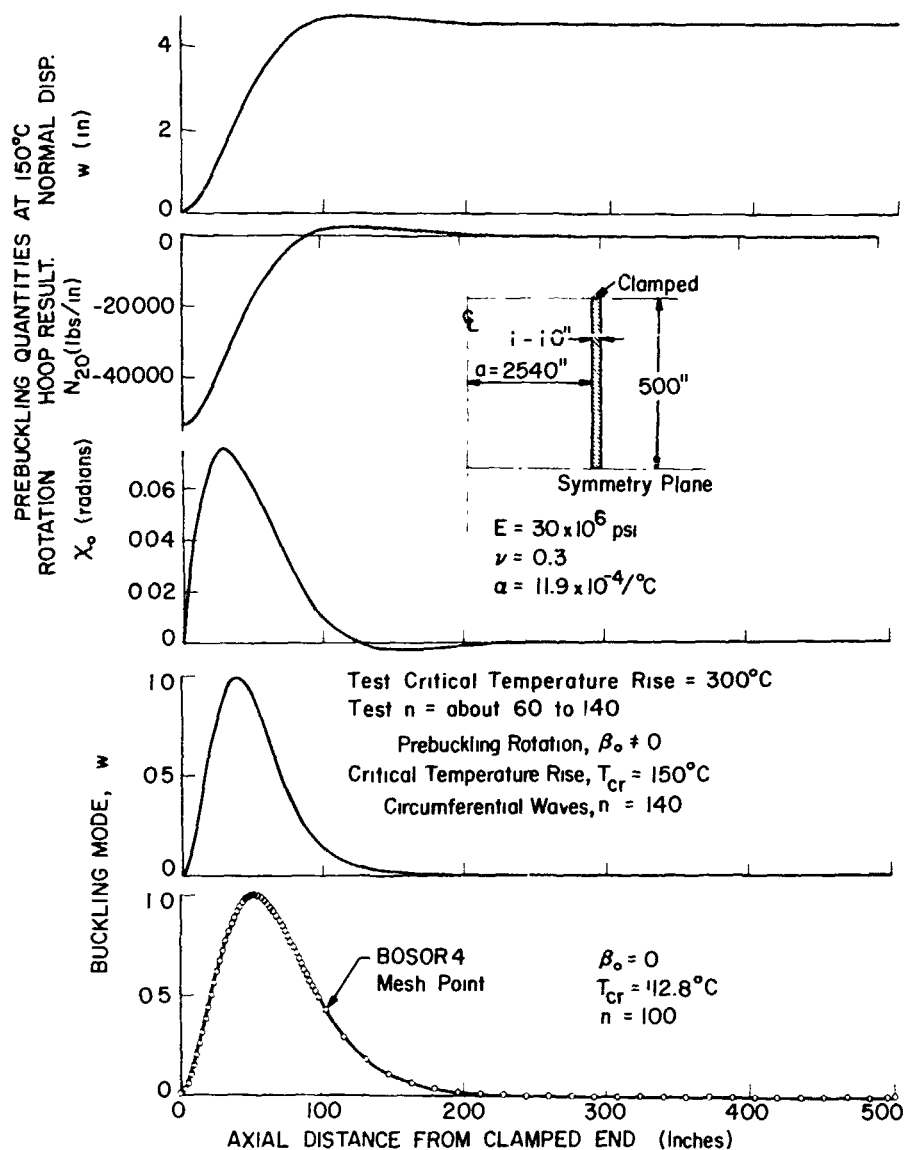


Figure 73 Prestress state and buckling modes with and without prebuckling rotation effect for clamped uniformly heated cylinder (from Bushnell [97]).

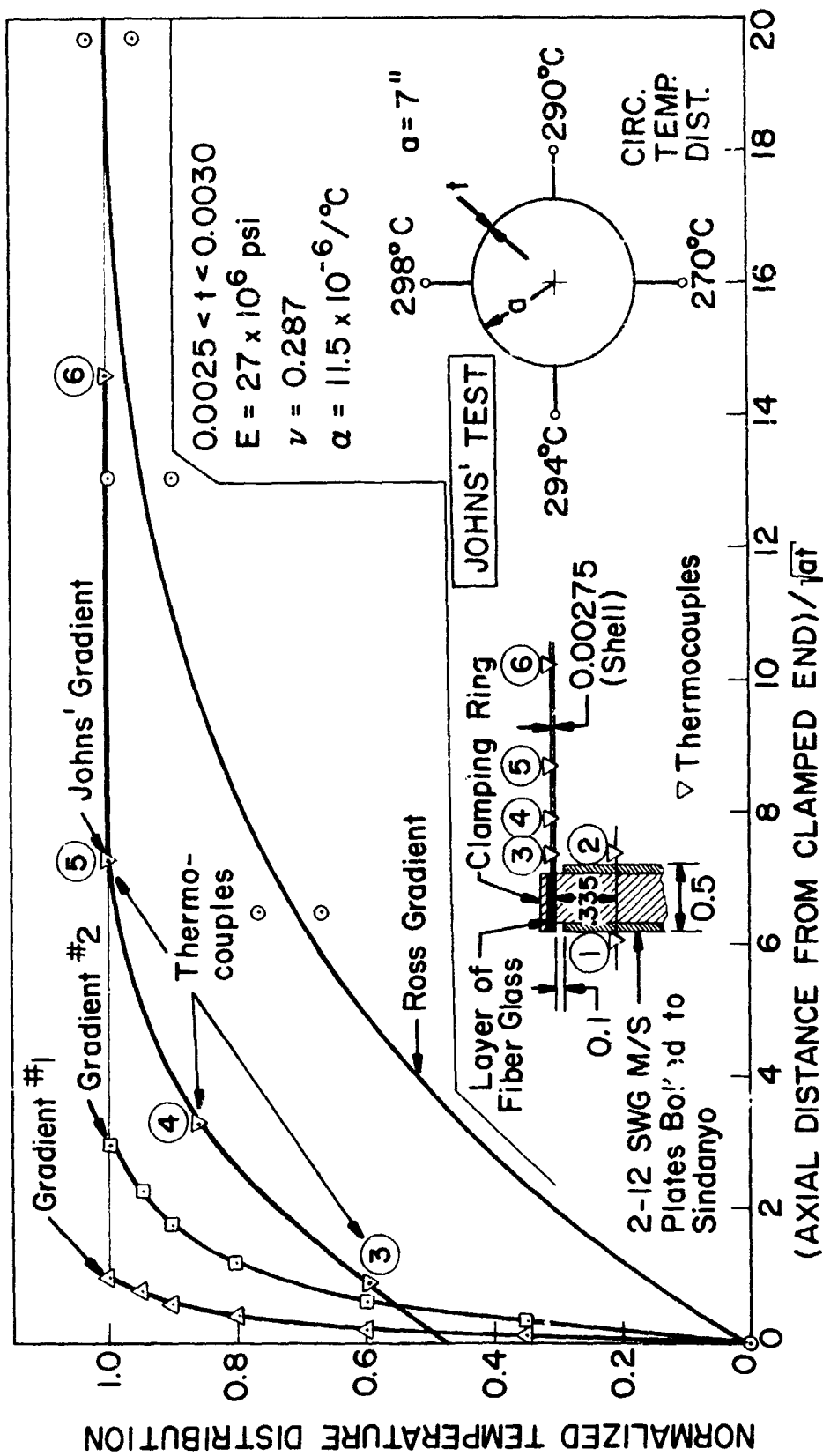


Figure 74 Edge thermal gradients for clamped cylinder (from Bushnell [97]).

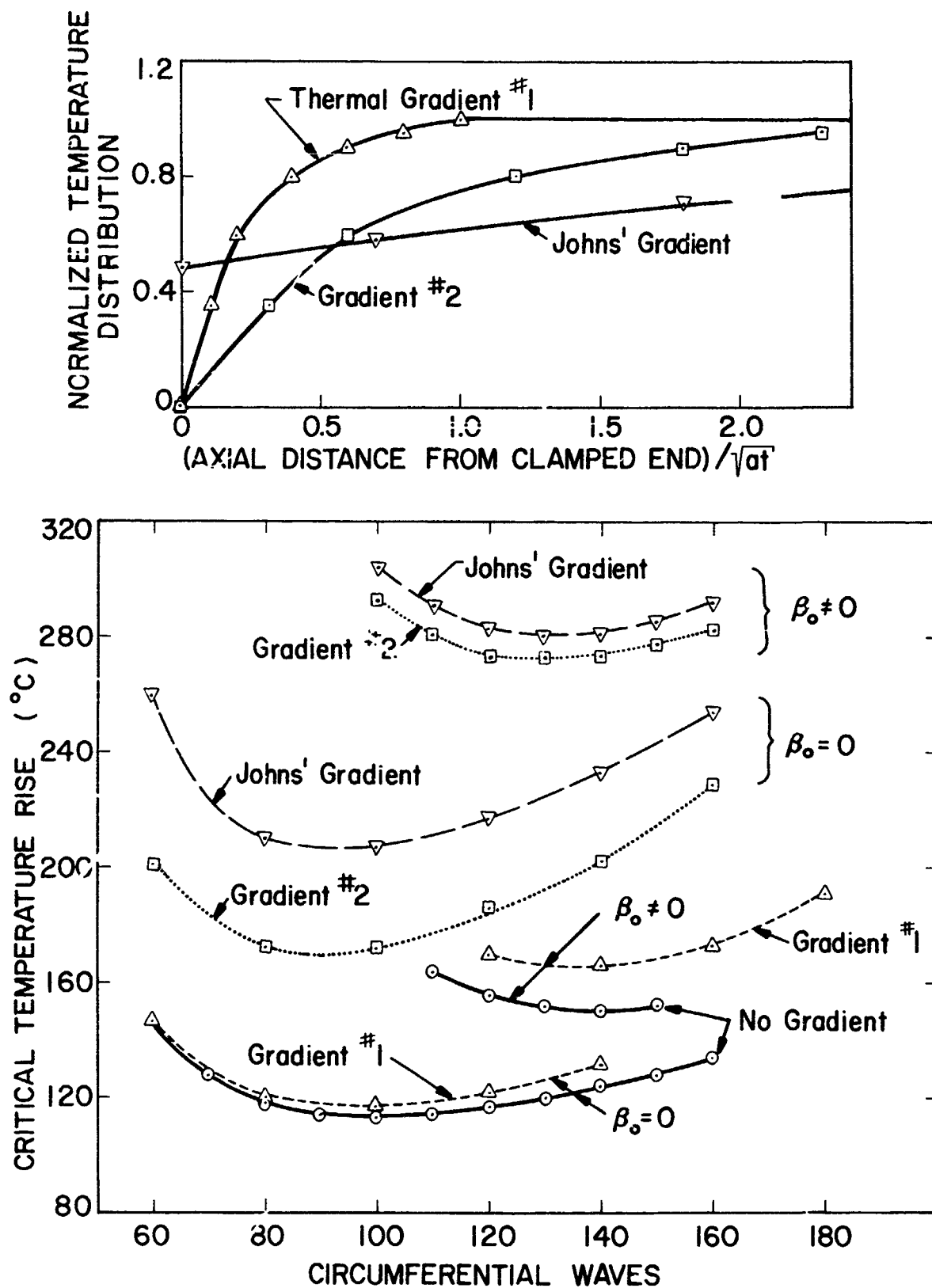


Figure 75 Critical temperatures for various edge gradients with and without prebuckling rotation effect (from Bushnell [97]).

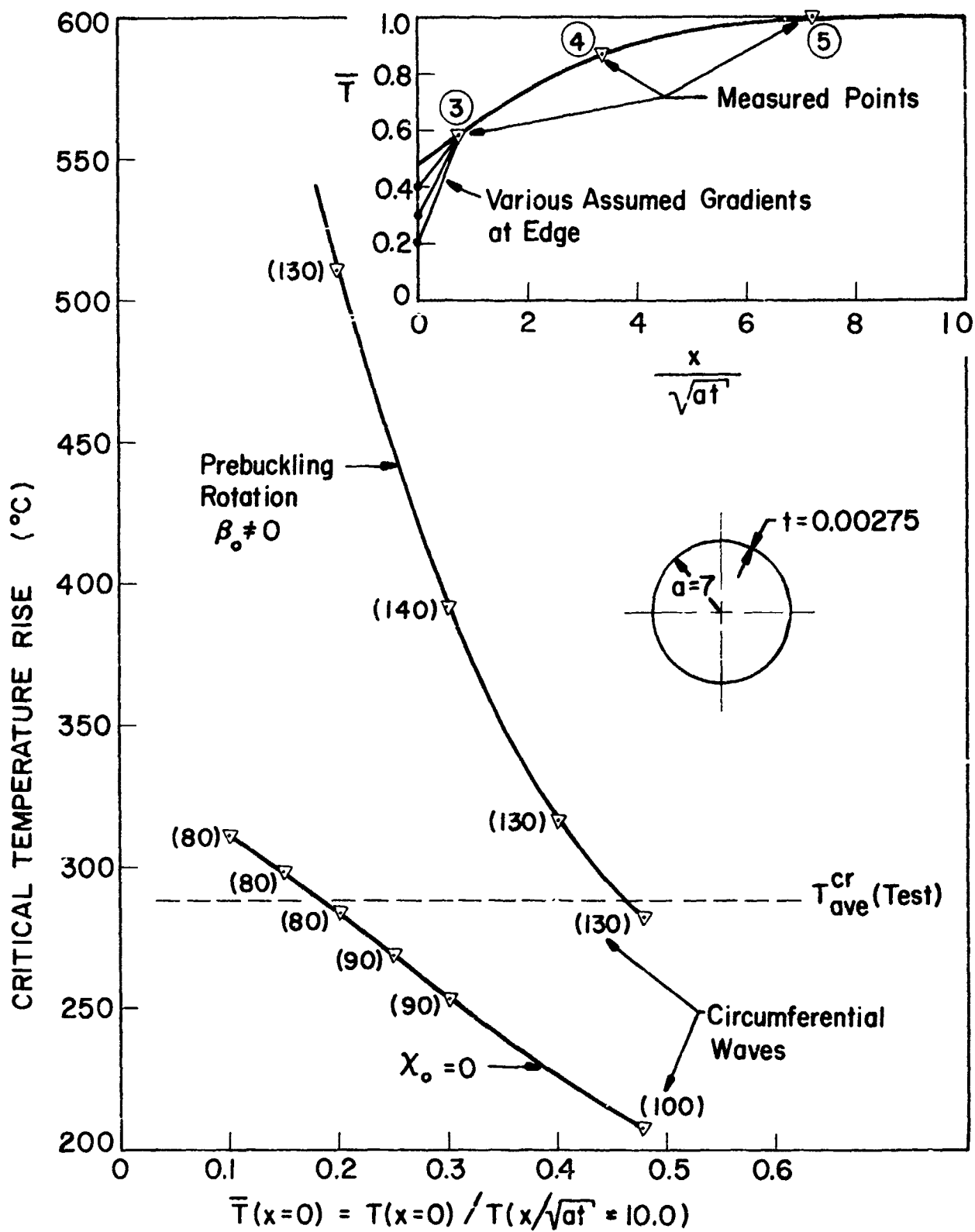


Figure 76 Sensitivity study of critical temperature vs. temperature at edge with and without prebuckling rotation effect (from Bushnell [97]).

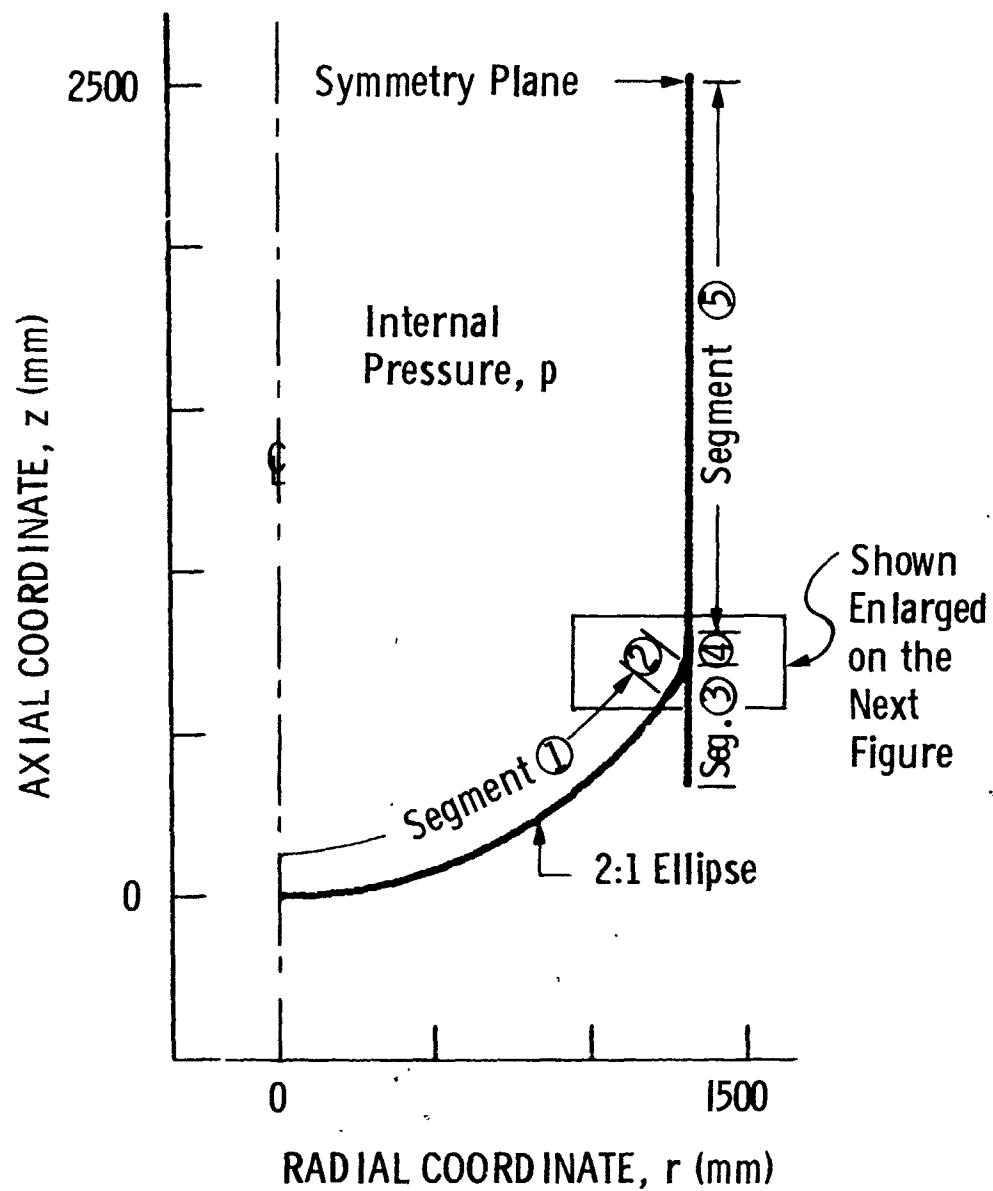


Figure 77 Bottom part of rocket fuel tank as modeled for input to the BOSOR4 computer program.

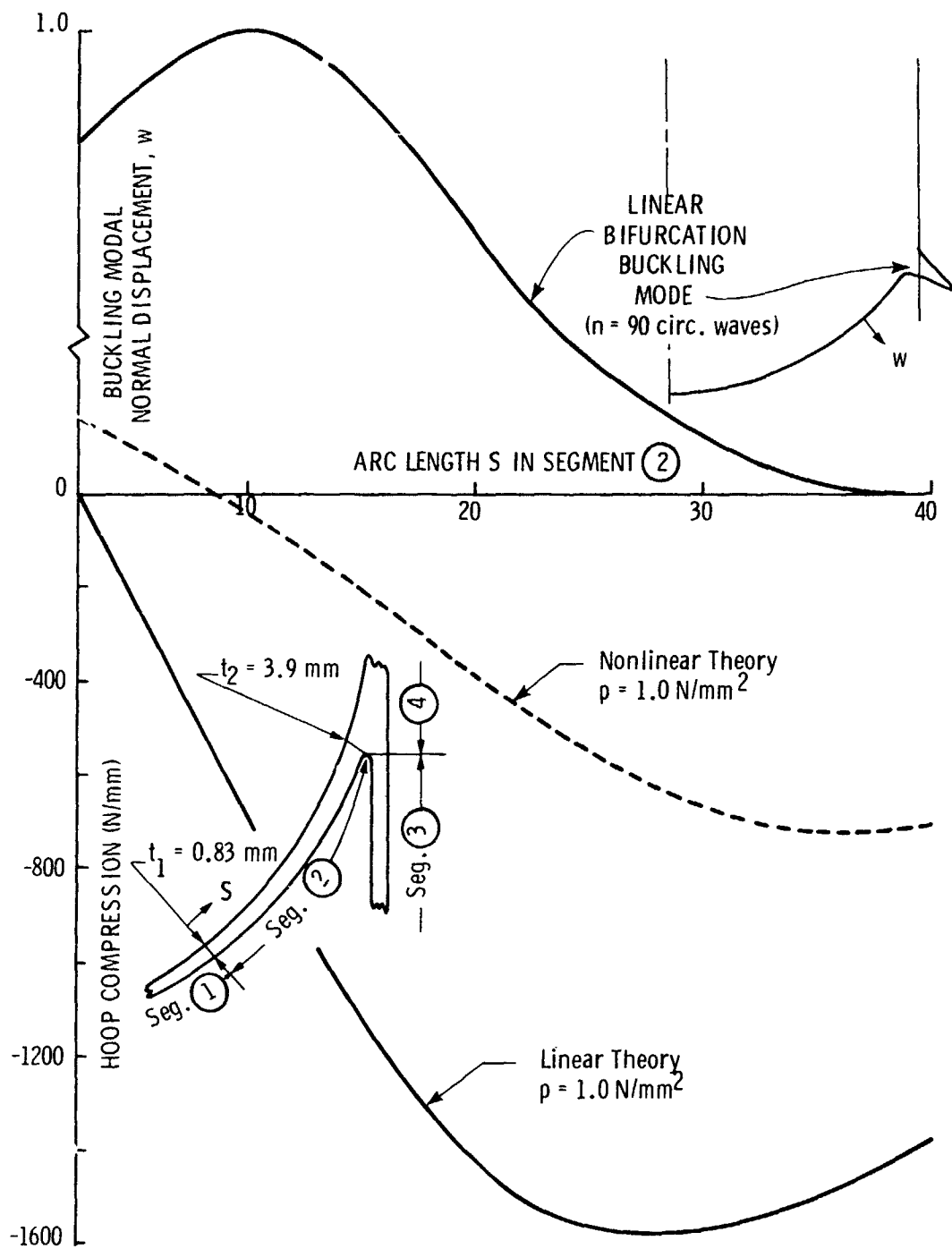
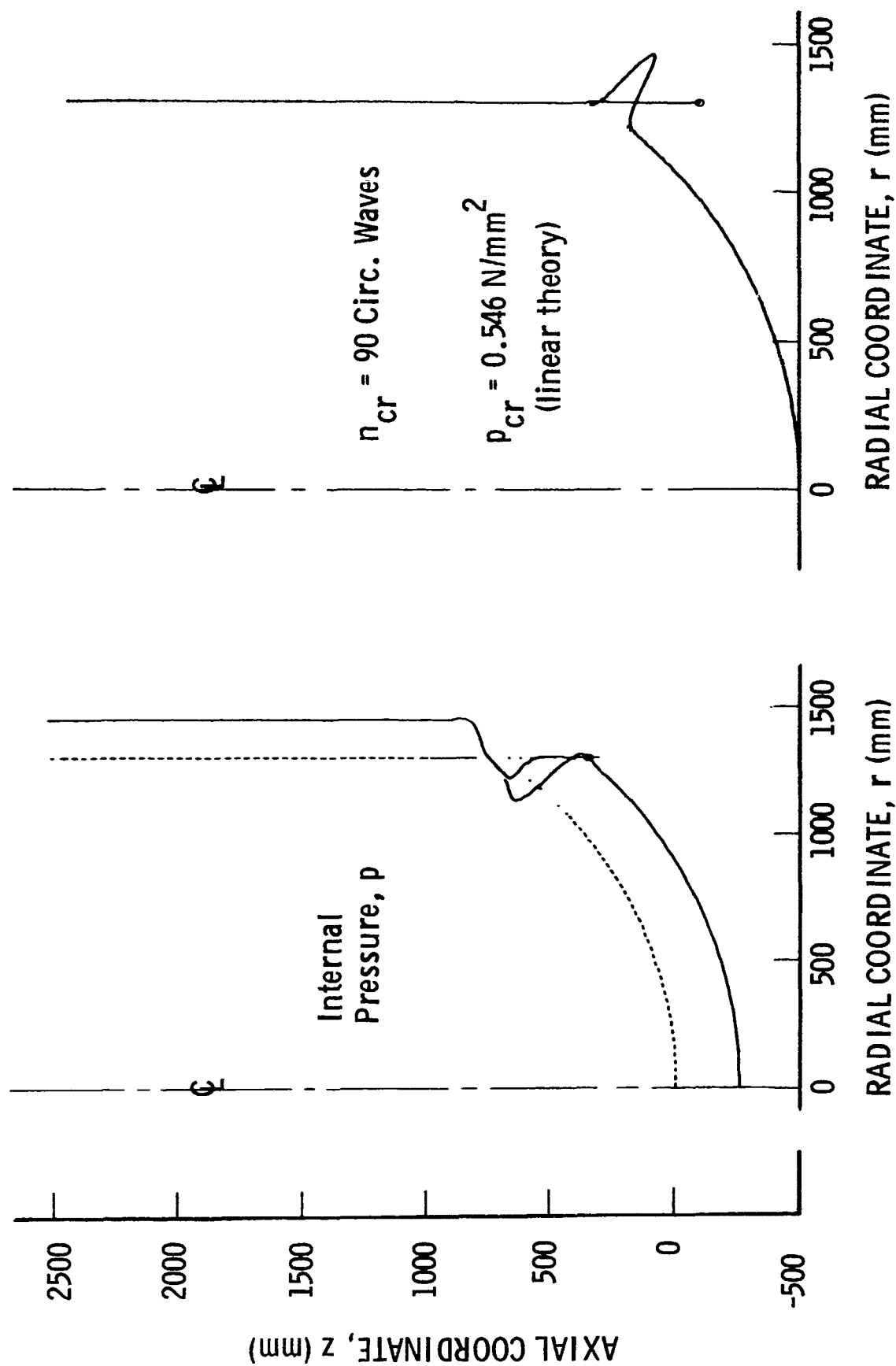
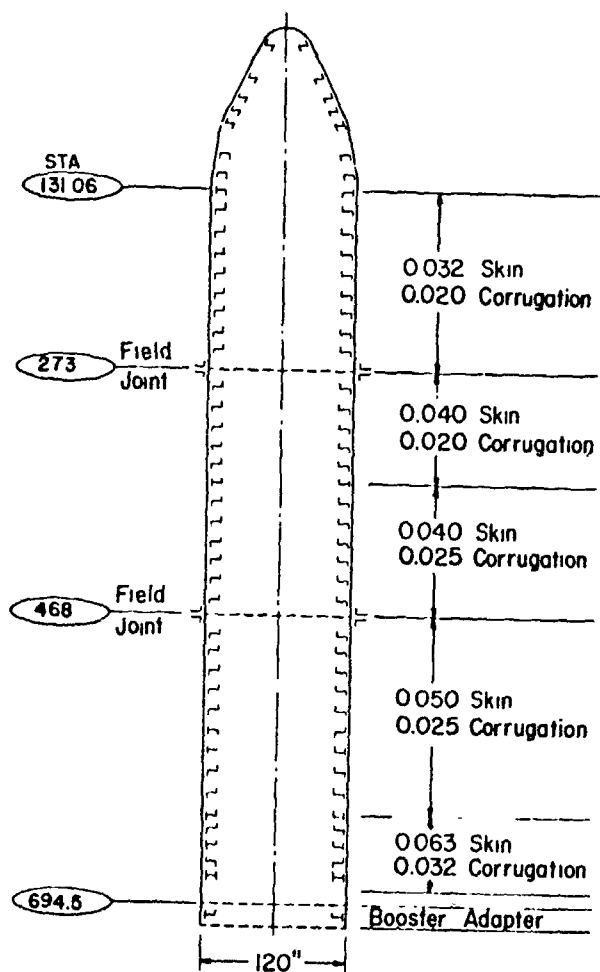


Figure 78 Nonsymmetric buckling mode (top) and hoop resultants (bottom) for the part of the internally pressurized rocket motor indicated in Figure 77.

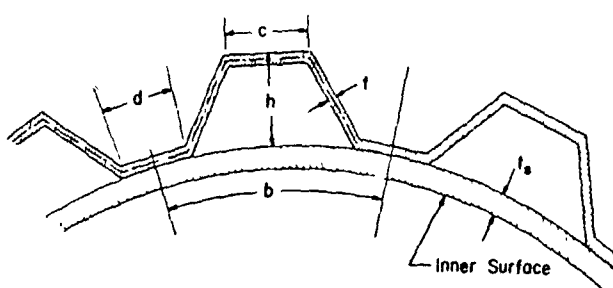


(a) Prebuckling (linear theory) (b) Linear Bifurcation Buckling Mode

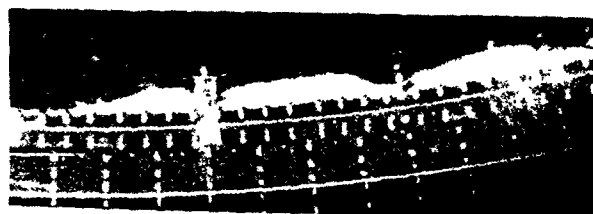
Figure 79 Prebuckling deflection and linear bifurcation buckling mode.



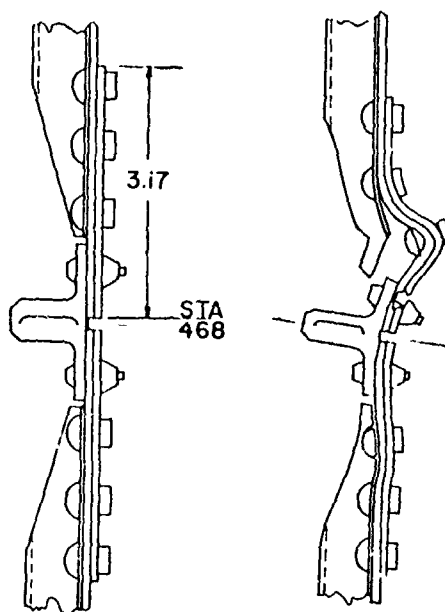
(a) Typical ring-stiffened rocket payload shroud configuration.



(b) Corrugated wall construction.

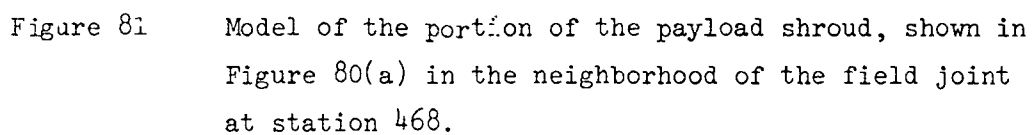


(c) Interior view of portion of complete shroud buckled locally next to field joint at station 468 [see (a)]. Three waves are visible.



(d) Field joint geometry and buckle configuration.

Figure 80 Local failure of a large payload shroud under axial compression and bending. Buckling is caused by the narrow band of circumferential compression arising from the inward excursion of the axial load path near the field joint at station 468 (from Bushnell [3]).



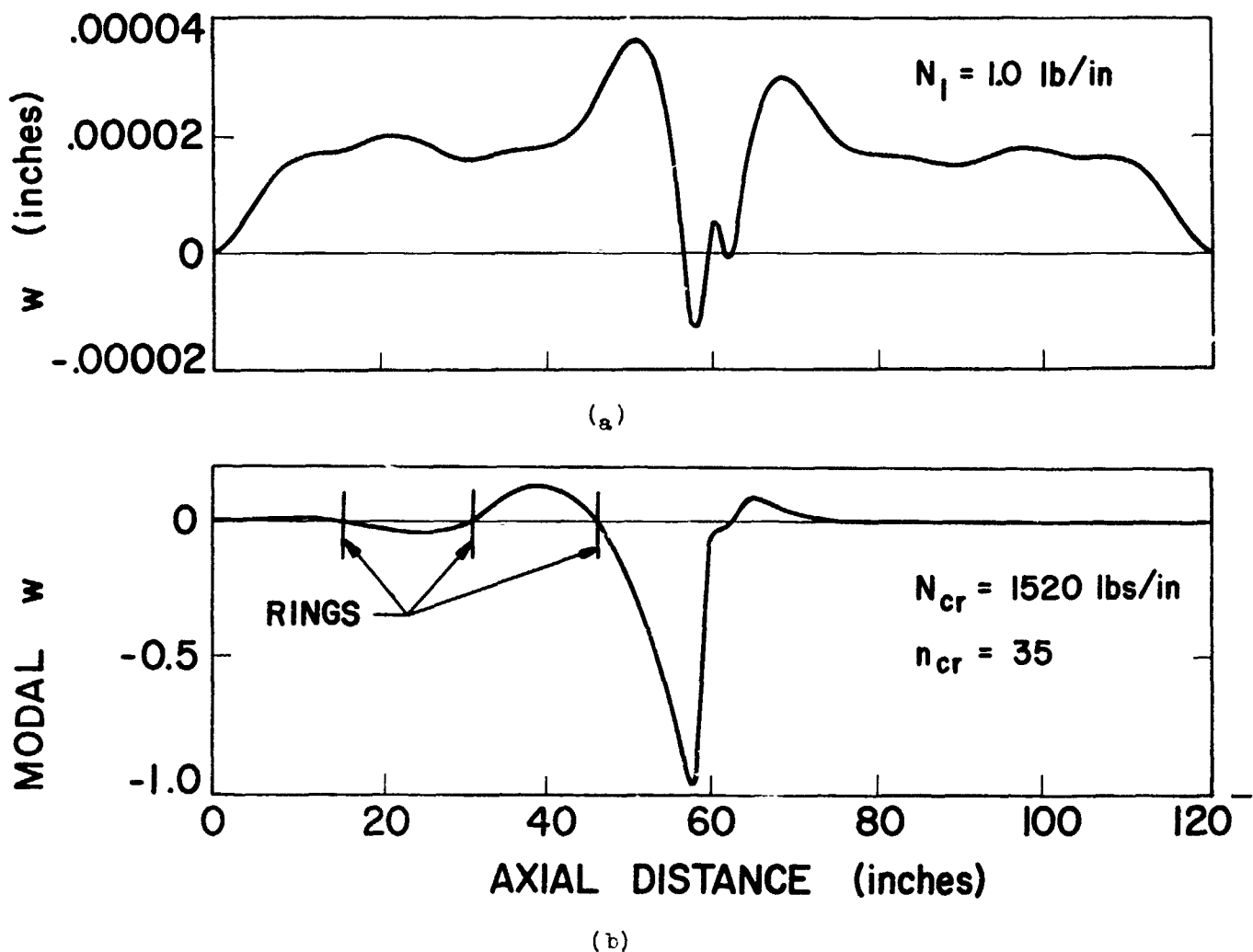
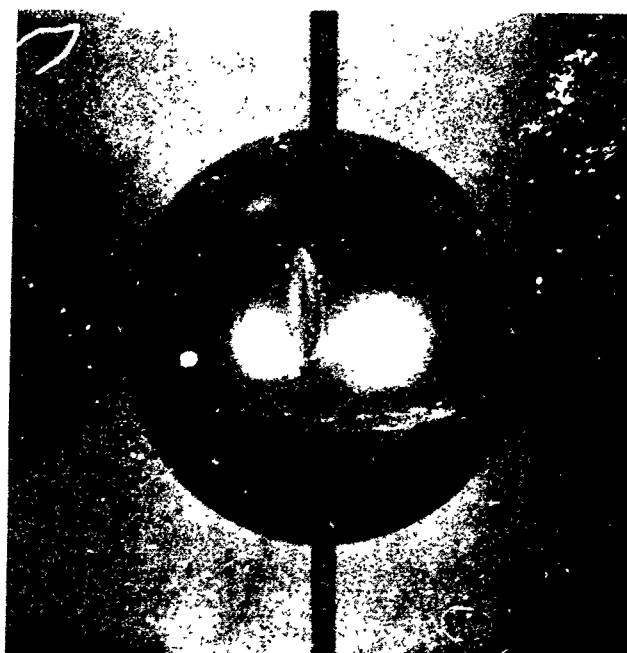


Figure 82 Axially compressed payload shroud: (a) Predicted axisymmetric prebuckling normal displacement distribution corresponding to $N_1 = 1.0 \text{ lb/in}$ compression; (b) Nonsymmetric bifurcation buckling mode (from Bushnell [3]).



(a)

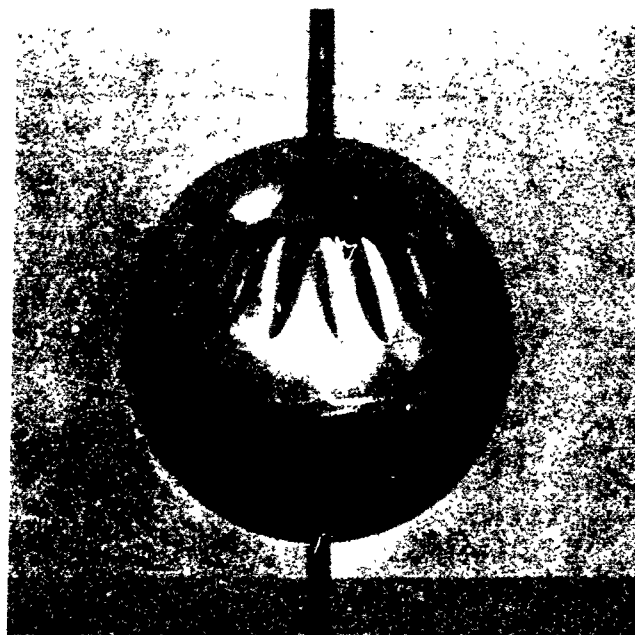
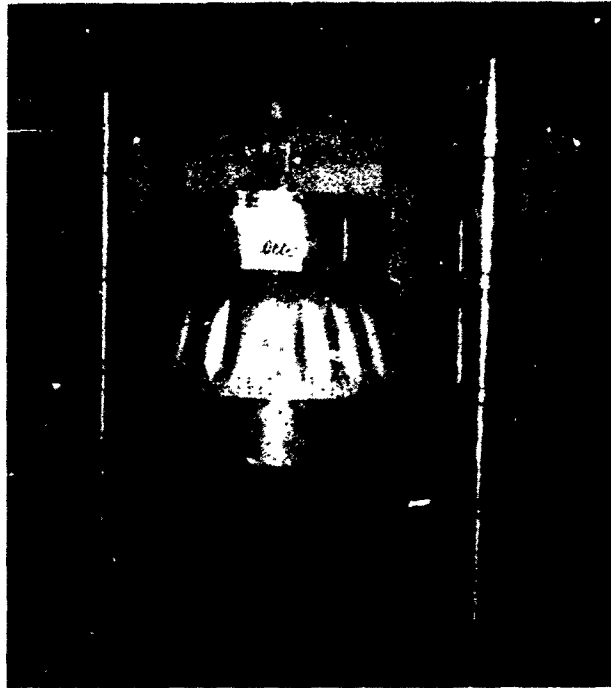
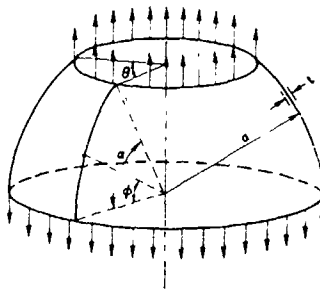


Figure 83 Buckling pattern for a thin-walled spherical shell with a solid bottom half and tension applied by means of an internal rigid spherical mandrel extending approximately 45° from the top pole (from Horton et al. [38]).



(a)



(b)

Figure 84 (a) Truncated hemisphere buckled by axial tension;
 (b) Shell geometry and load (from Yao [110]).

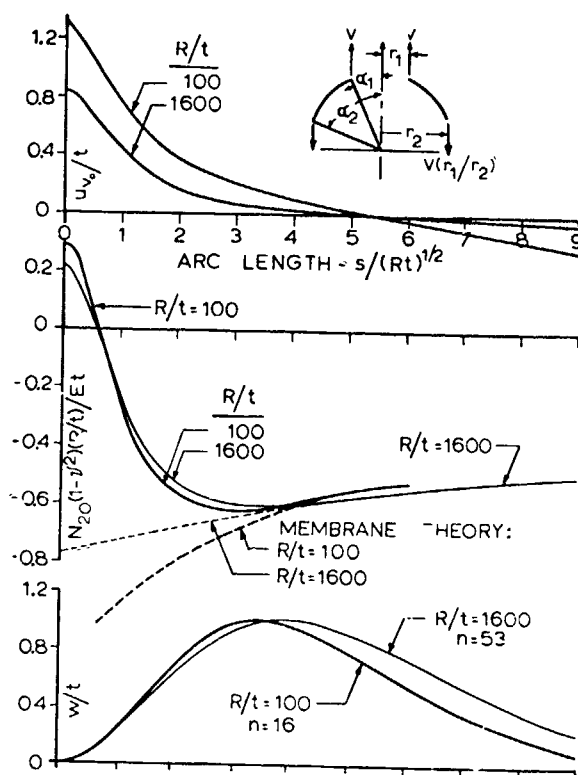
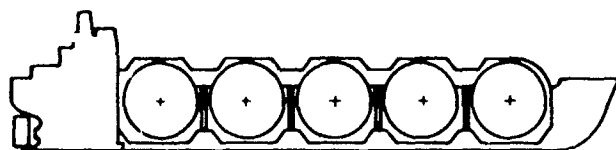
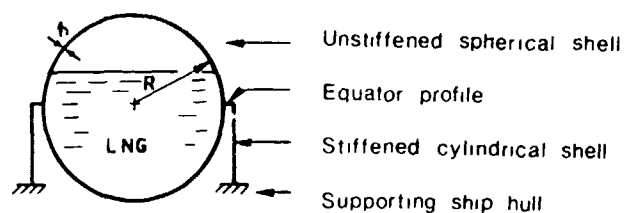


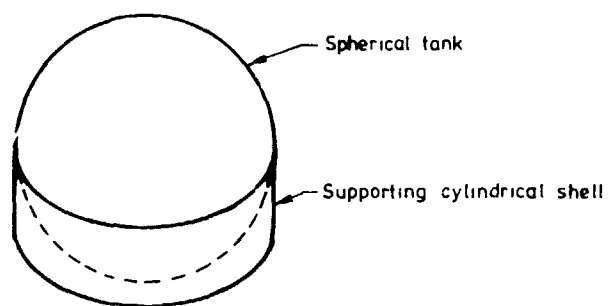
Figure 85 Normalized prebuckling axial displacements and circumferential stress resultants and normalized modal displacements for spherical segments in axial tension, $\alpha_1 = 0.7$ rad (from Bushnell (111)).



(a) Liquid natural gas (LNG) carrier with spherical cargo tanks.

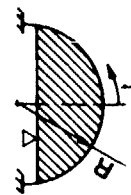
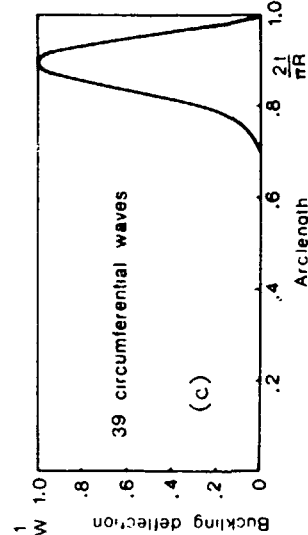
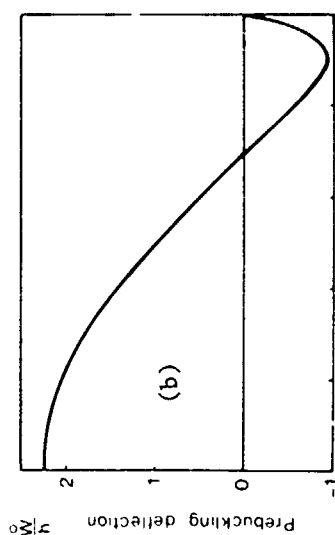
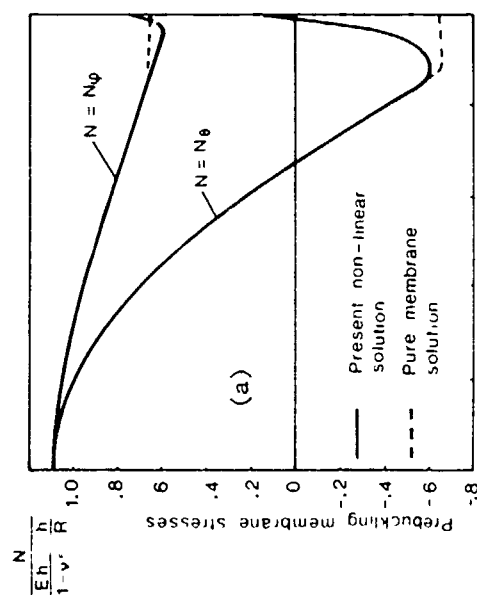


(b) Spherical tank design for LNG.

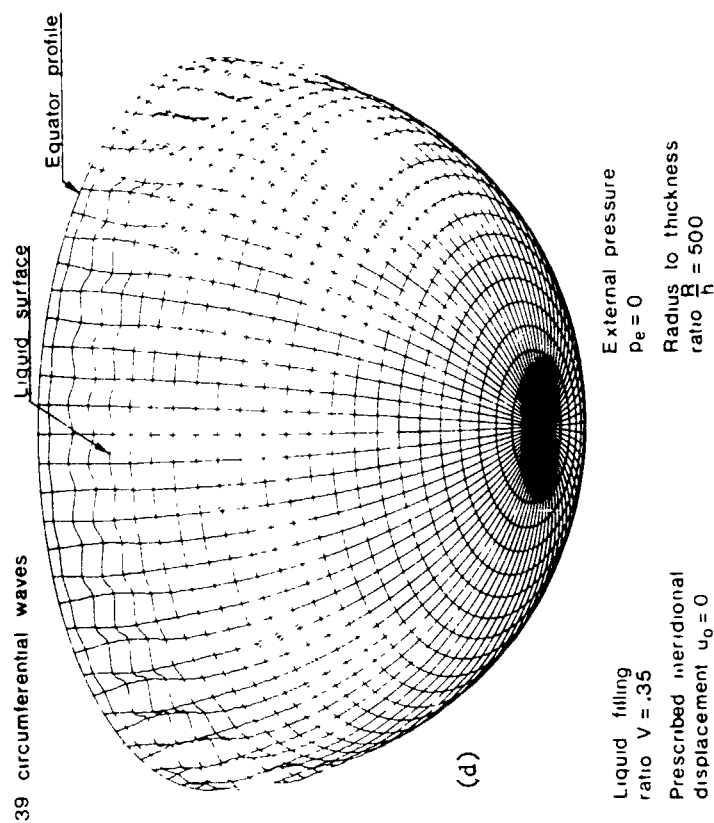


(c) Supporting cylindrical skirt.

Figure 86 Very large spherical tanks for transportation of liquid natural gas (from Pederson and Jensen [112]).



Liquid filling ratio $V = .35$
 Prescribed meridional displacement $u_0 = 0$
 External pressure $p_e = 0$
 Radius to thickness ratio $\frac{R}{h} = 500$



Liquid filling ratio $V = .35$
 Prescribed meridional displacement $u_0 = 0$
 External pressure $p_e = 0$
 Radius to thickness ratio $\frac{R}{h} = 500$

Figure 87 (a) Prebuckling membrane stresses, (b) prebuckling deflection, (c) buckling deflection, and (d) buckling pattern for a partially filled tank (from Pederson and Jensen [112]).

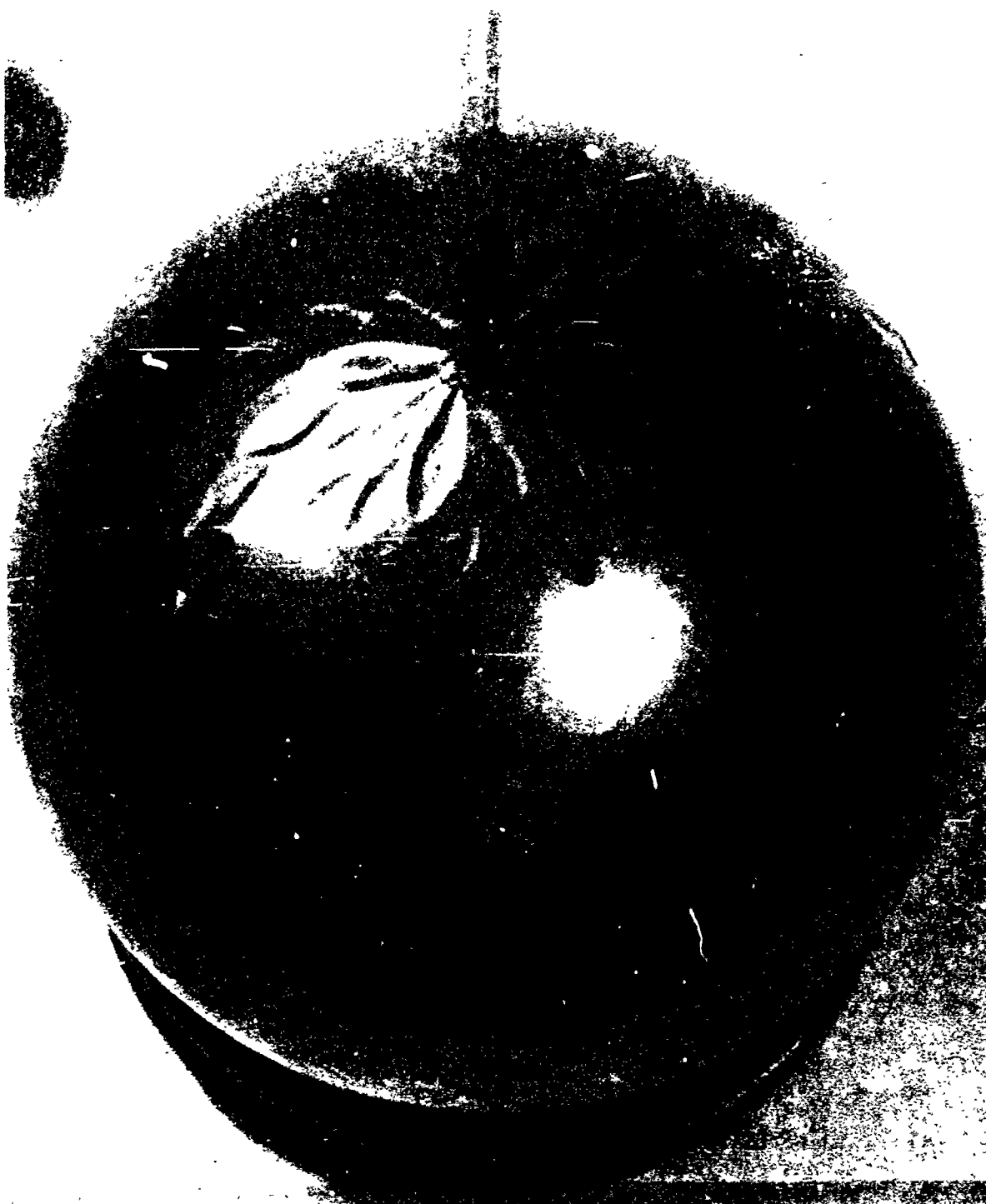
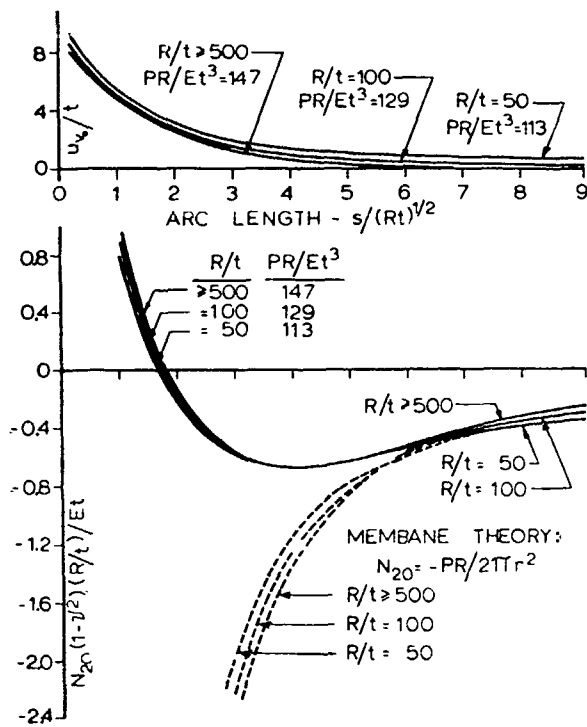
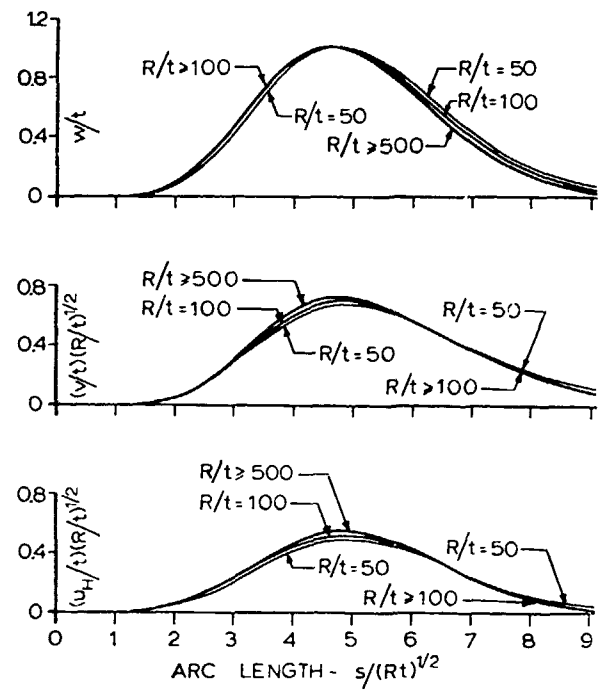


Figure 88 Buckling pattern for a thin spherical shell subjected to axial tension. Buckling motion is restrained by an interior mandrel (from Horton [38]).



(a)



(b)

Figure 89 (a) Normalized prebuckling axial displacement and circumferential stress resultant for spherical shells with outward-directed concentrated loads, (b) normalized mode shapes corresponding to bifurcation into 8 circumferential waves for spherical shells with outward-directed concentrated loads (from Bushnell [11]).

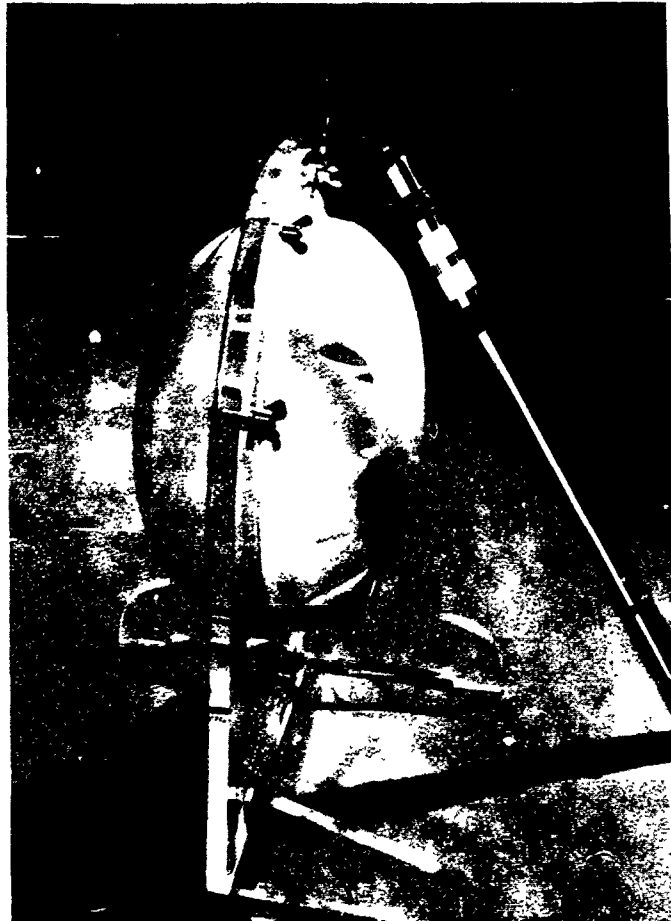


Figure 90 Simple rig to demonstrate nonsymmetric buckling under internal pressure (from Gellately [4.13^o]).

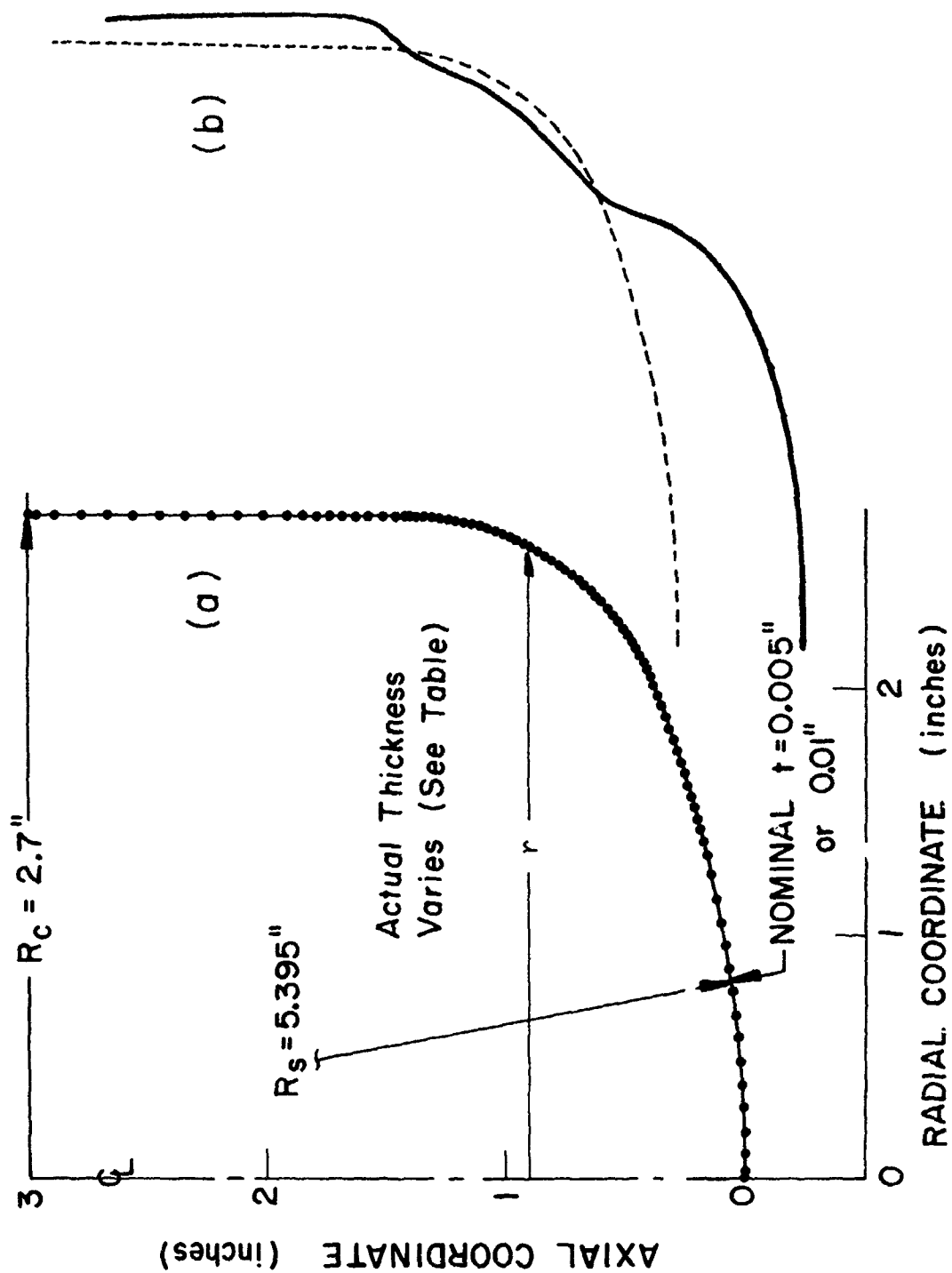


Figure 91 Aluminum or mild steel torispherical head tested under internal pressure by Galletly at the University of Liverpool: (a) BOSOR5 discrete model, (b) exaggerated view of prebuckling deflected shape at the bifurcation buckling pressure (from Bushnell and Galletly [132]).

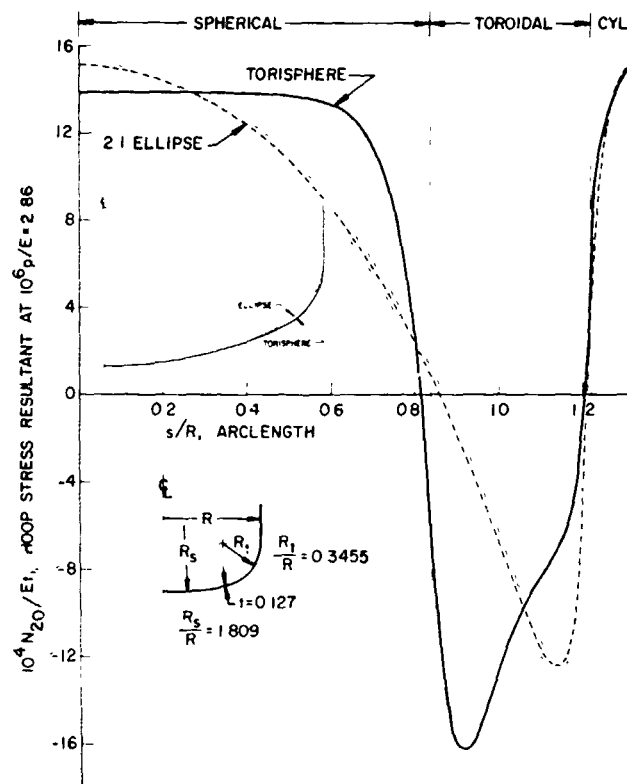
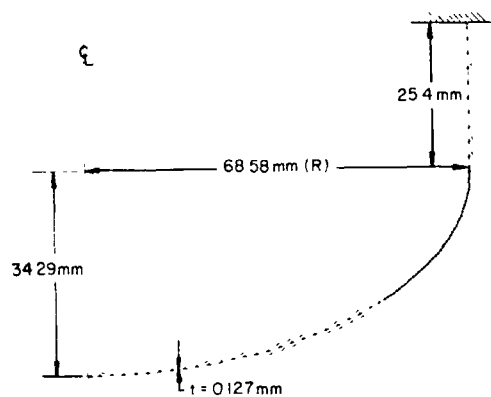
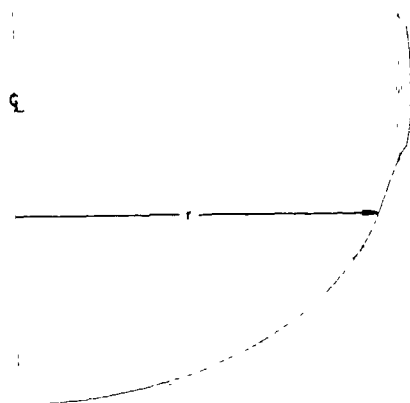


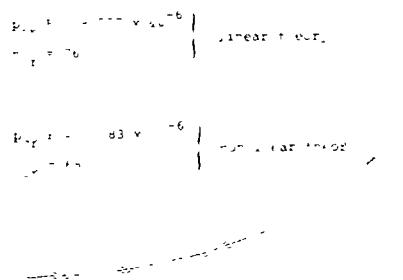
Figure 92 Hoop stress resultant at $p/E = 2.86 \times 10^{-6}$ for elastic 2:1 torispherical and ellipsoidal heads (from Bushnell [138]).



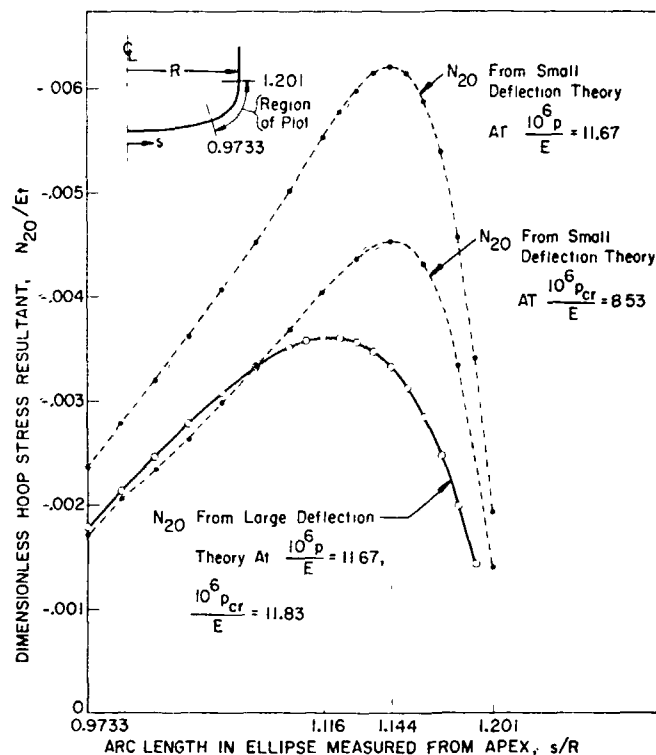
(a) Discretized model of 2:1 ellipsoidal head.



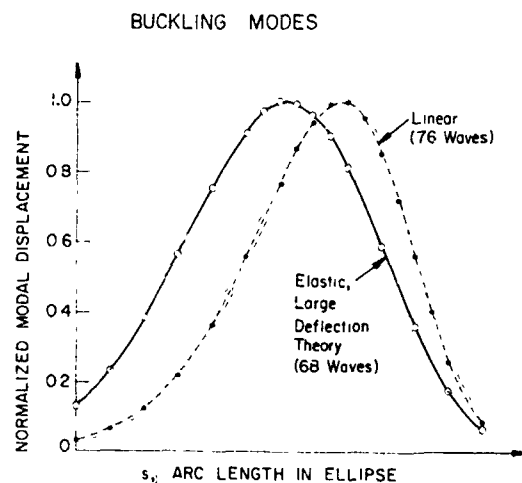
(b) Ellipsoidal head as deformed axisymmetrically under internal pressure.



(c) Nonsymmetric buckling mode from linear elastic analysis.

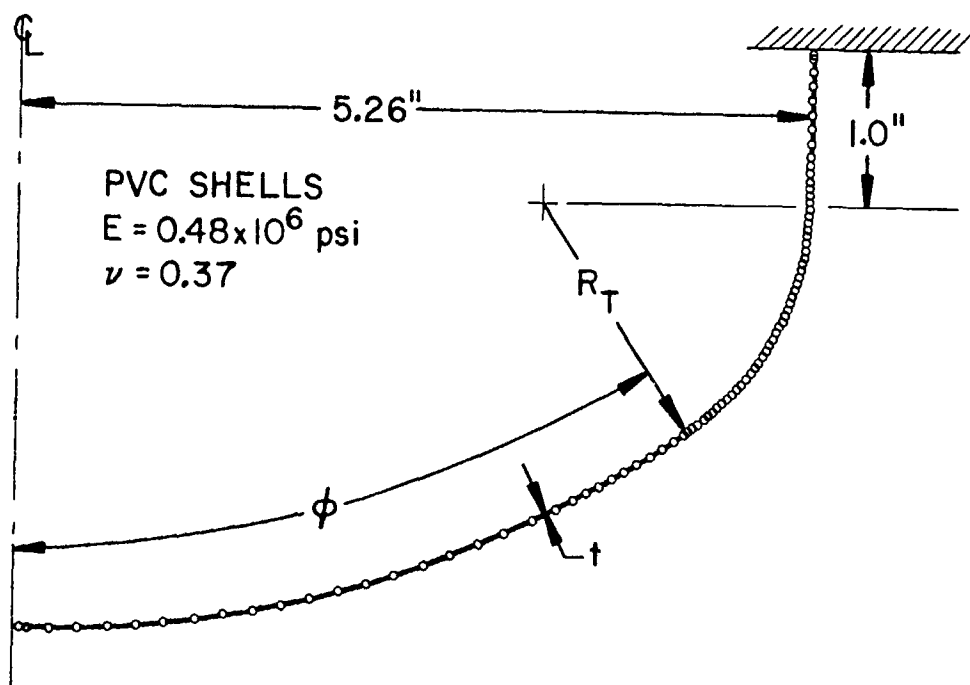


(d) Prebuckling hoop resultants in region of buckle predicted from elastic small deflection theory and elastic large deflection theory.

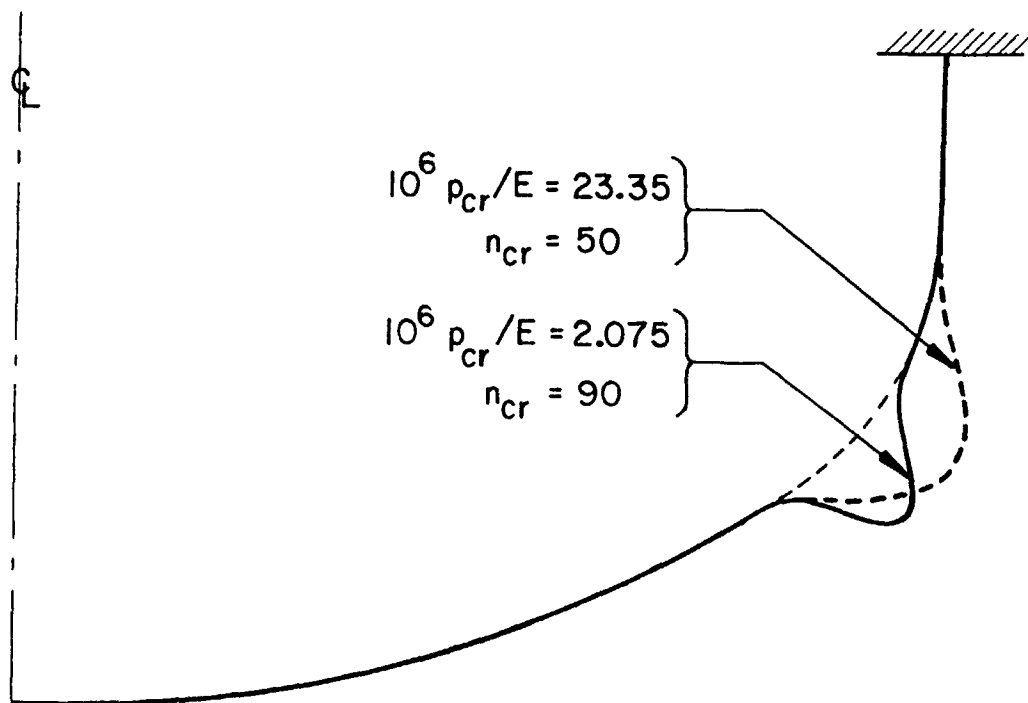


(e) Buckling modes predicted from elastic small deflection theory and elastic large deflection theory.

Figure 93 Linear and nonlinear prebuckling behavior and bifurcation buckling of elastic internally pressurized ellipsoidal vessel head (from Bushnell [138]).



(a) DISCRETIZED MODEL



(b) BIFURCATION BUCKLING MODES FOR TWO SPECIMENS

Figure 94 Discretized model of torispherical vessel head and predicted critical internal pressure and nonsymmetric buckling modes for two of Adachi and Benicek's elastic specimens (from Bushnell [138]).

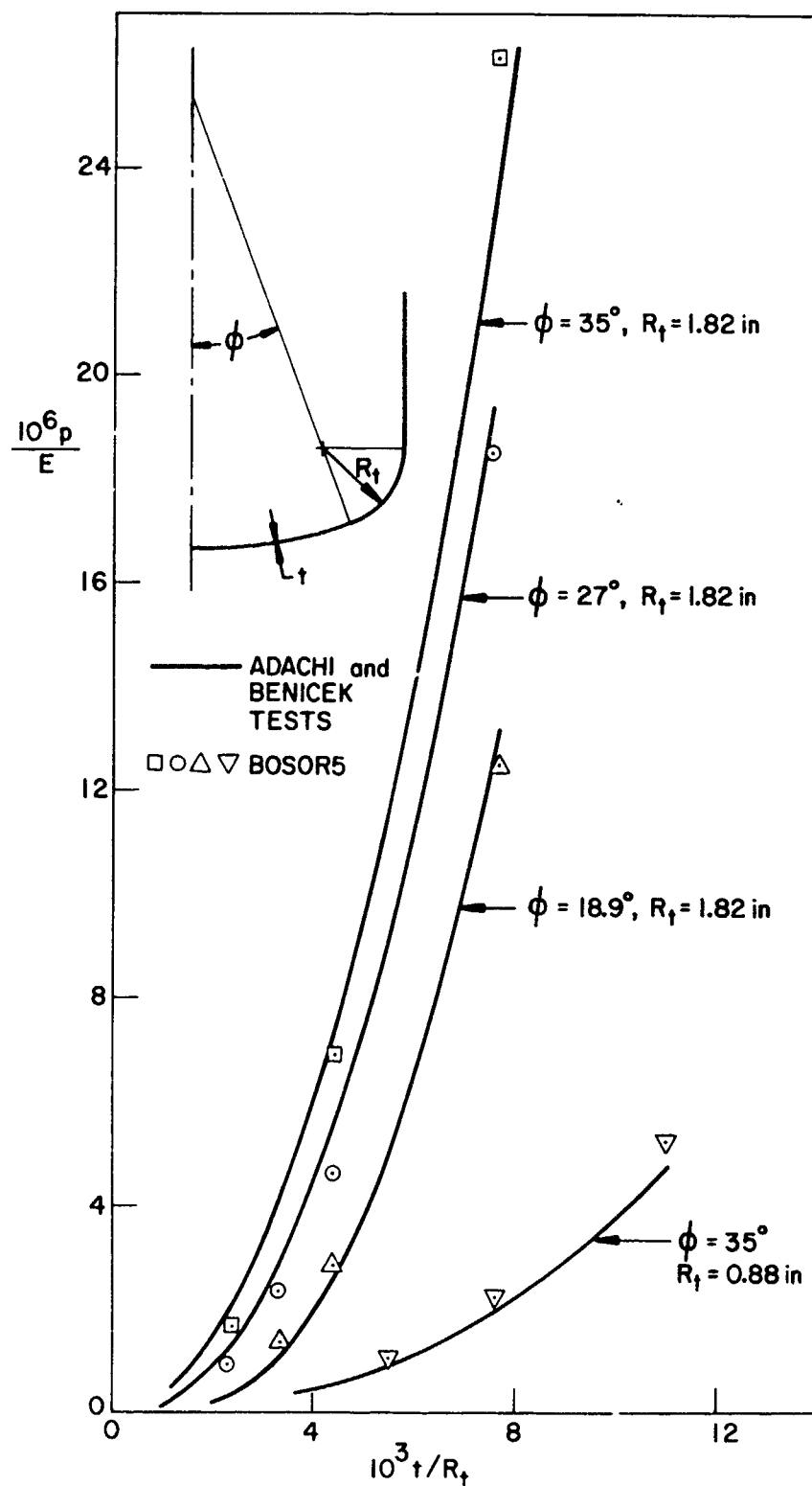
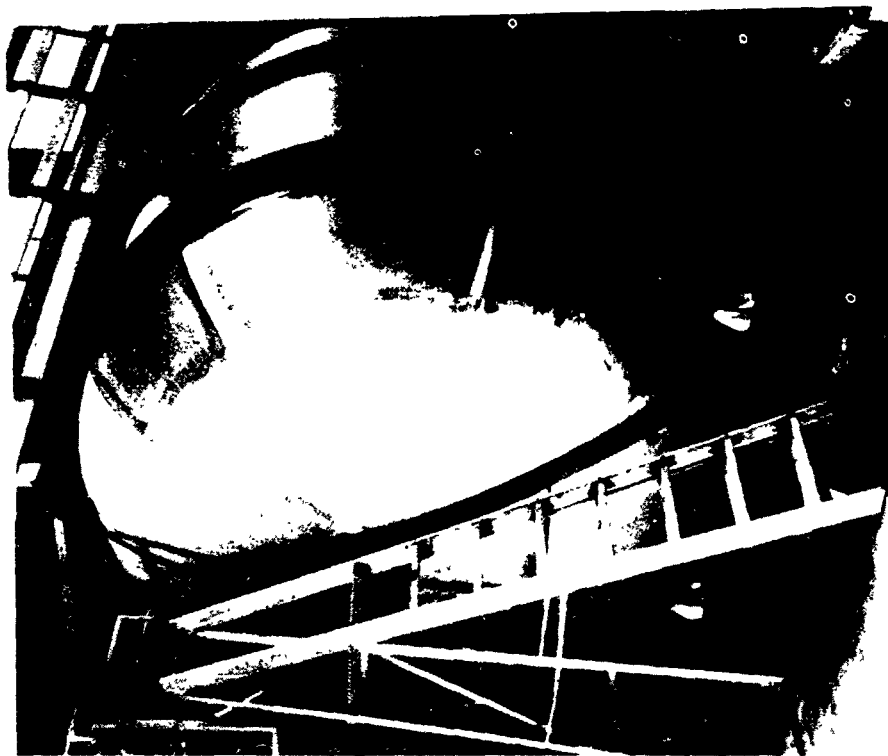


Figure 95 Comparison of test and theory for nonsymmetric buckling of elastic torispherical vessel heads (from Bushnell and Galletly [132]).



(a)

(b)

Figure 96 Examples of elastic-plastic circumferential buckling due to internal pressure: (a) 0.137 m diameter machined aluminum torispherical model (from Galletly [139]); (b) 3 m diameter 'as manufactured' stainless steel pressure vessel with torispherical ends (courtesy P. Stanley, University of Nottingham, England).

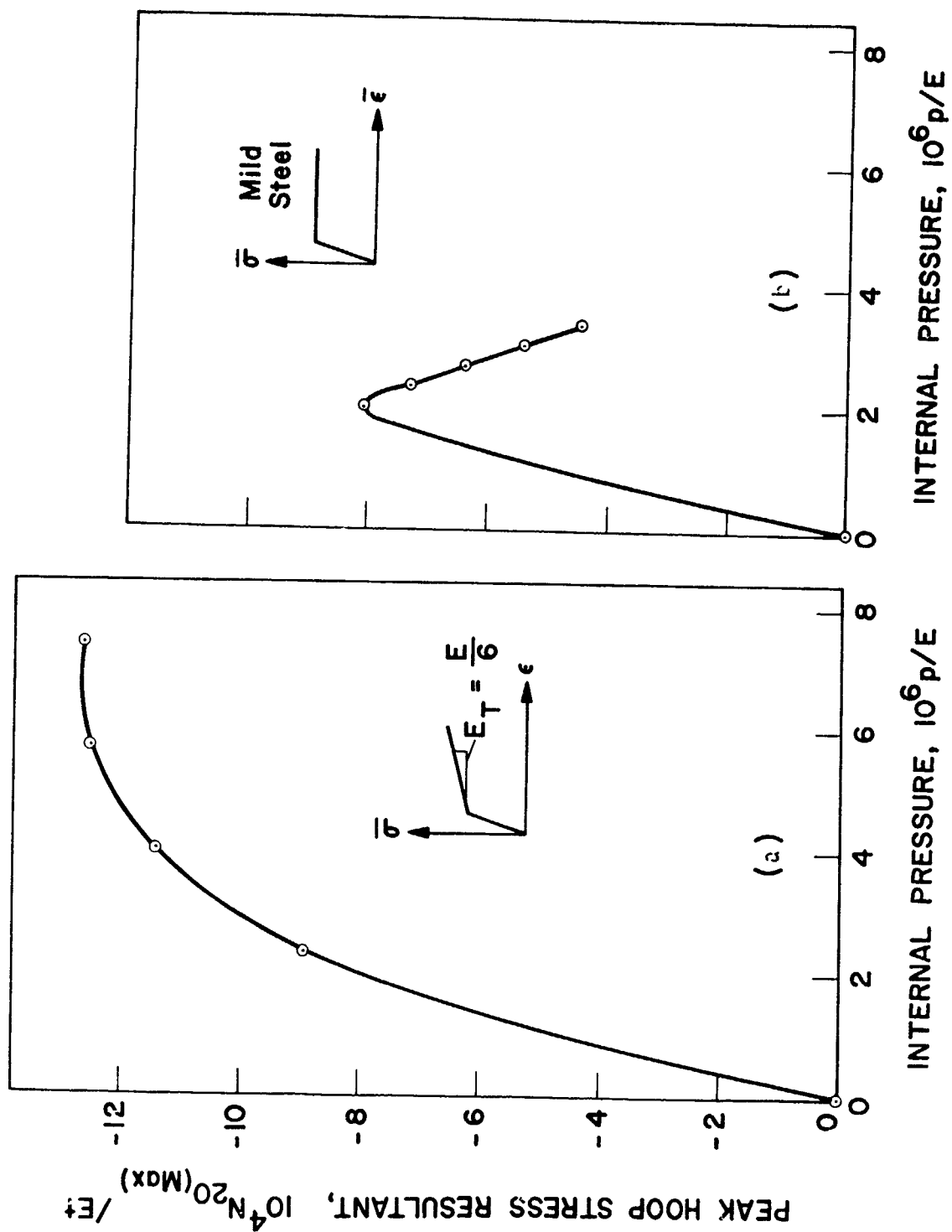


Figure 97 Nonlinear relationship of peak compressive hoop resultant in torispherical head to internal pressure: (a) material with considerable strain hardening; (b) elastic perfectly plastic material.

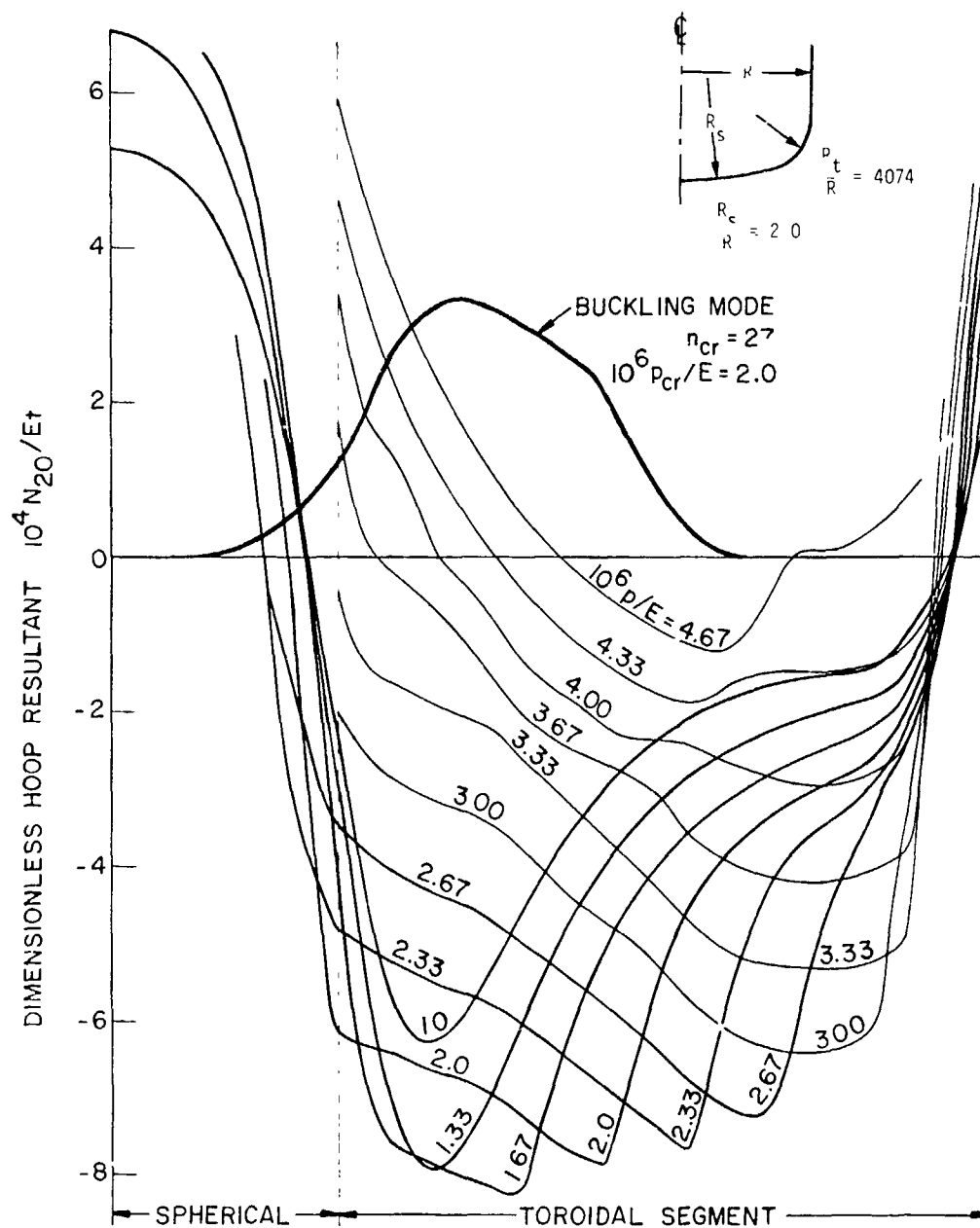
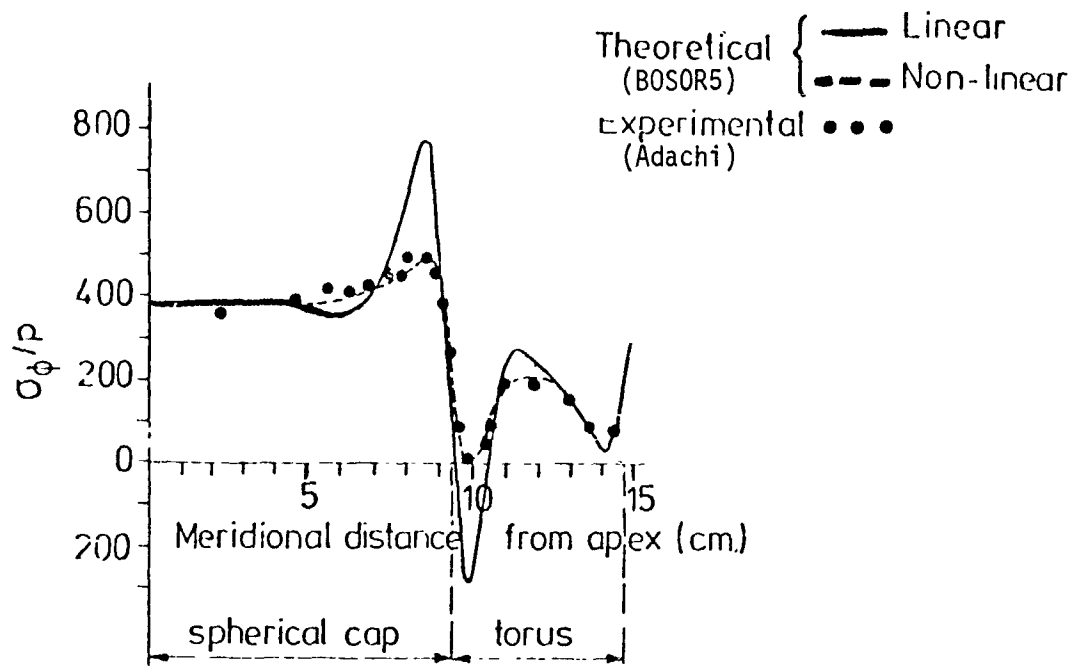
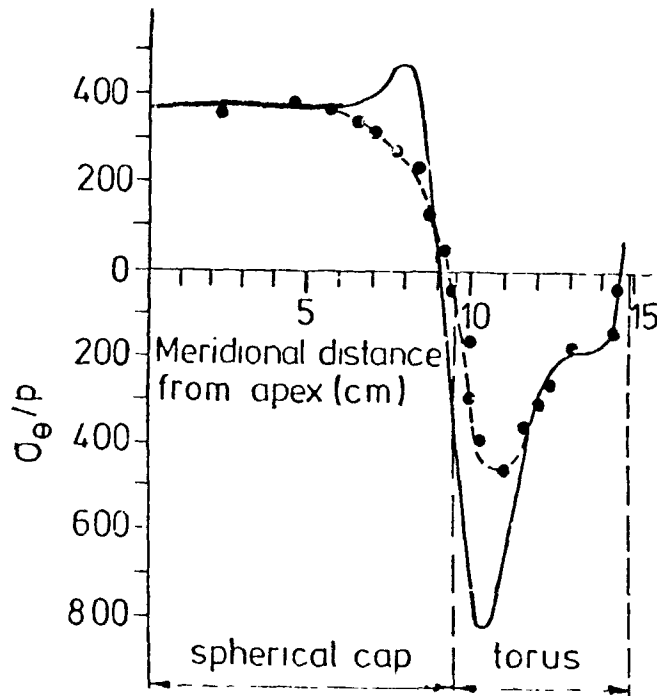


Figure 97(c) Predicted buckling mode and hoop stress resultant distributions as functions of internal pressure for Galletly's mild steel specimen MS3 (Table 6) (from Bushnell and Galletly [132]).



(a) Meridional stresses on outside surface, $p = 414$ kPa.



(b) Circumferential stresses on outside surface, $p = 414$ kPa.

Figure 98 Experimental and theoretical results for an elastic machined aluminum torispherical head subjected to internal pressure (from Galletly [139]).

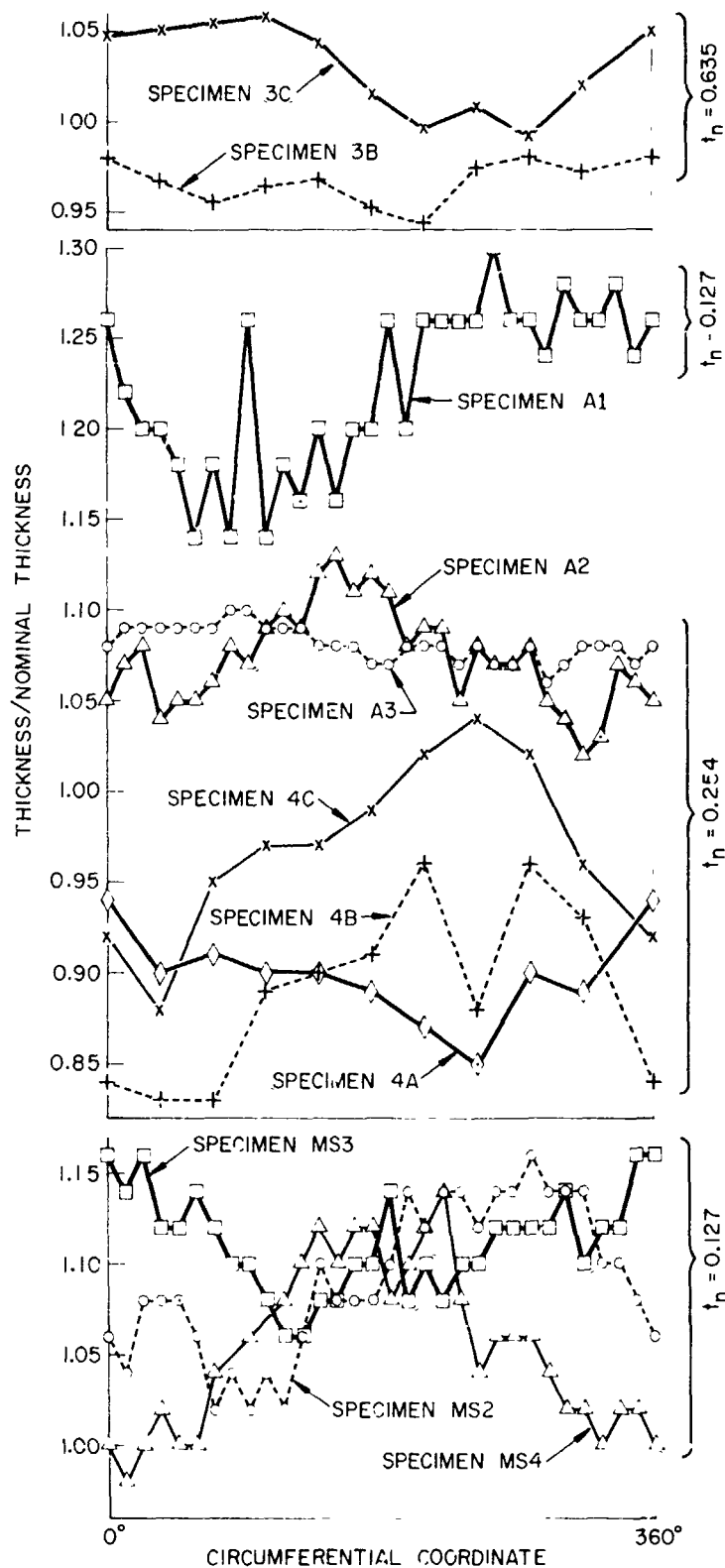


Figure 99 Measured thickness around the circumferences of the torispherical heads at the latitudes where the maximum normal buckling modal displacement is predicted to occur (from Rushnell and Galletly [132]).

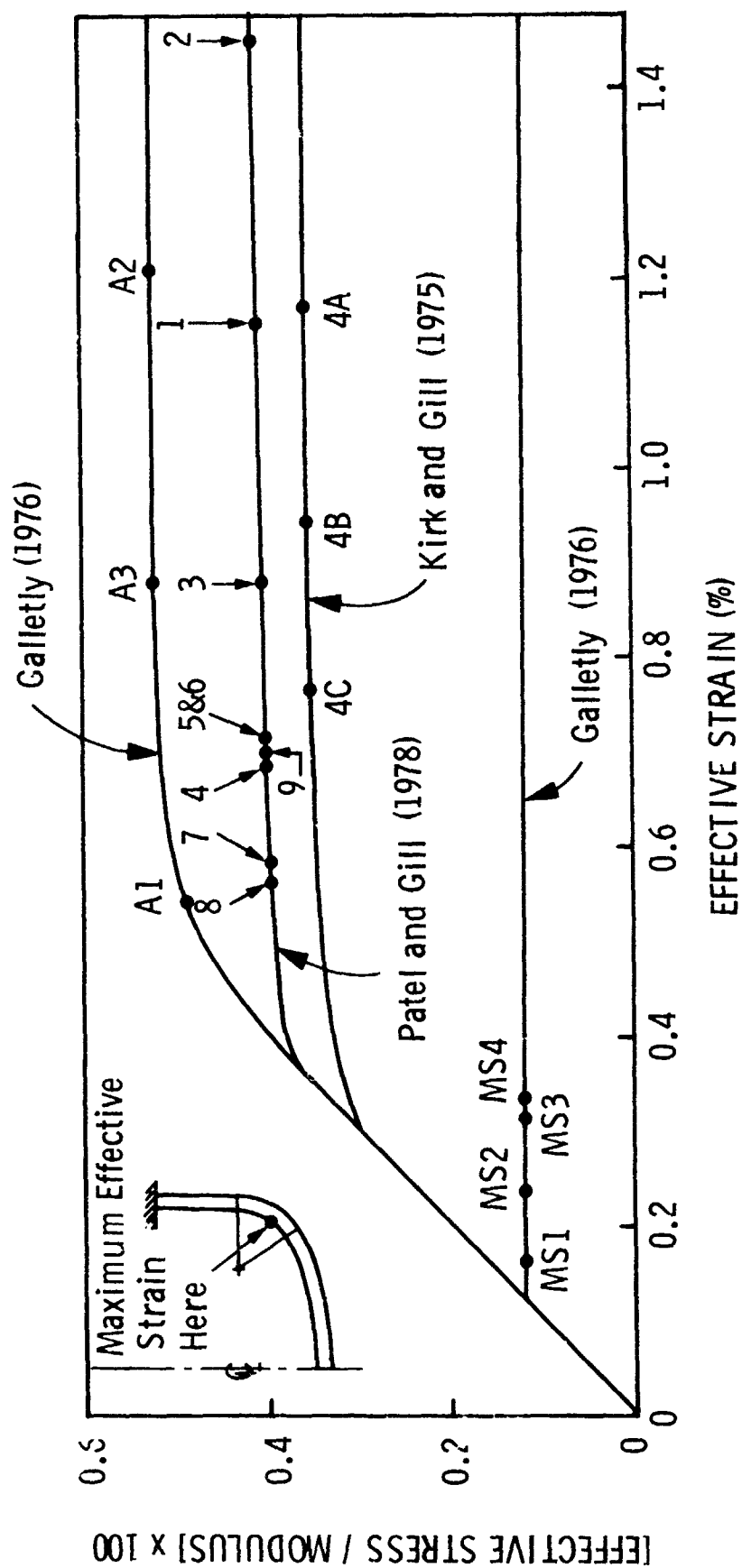


Figure 100 Maximum effective strain at buckling for Kirk and Gill's, Patel and Gill's, and Gilletly's specimens (adapted from Bushnell and Gilletly [132]).

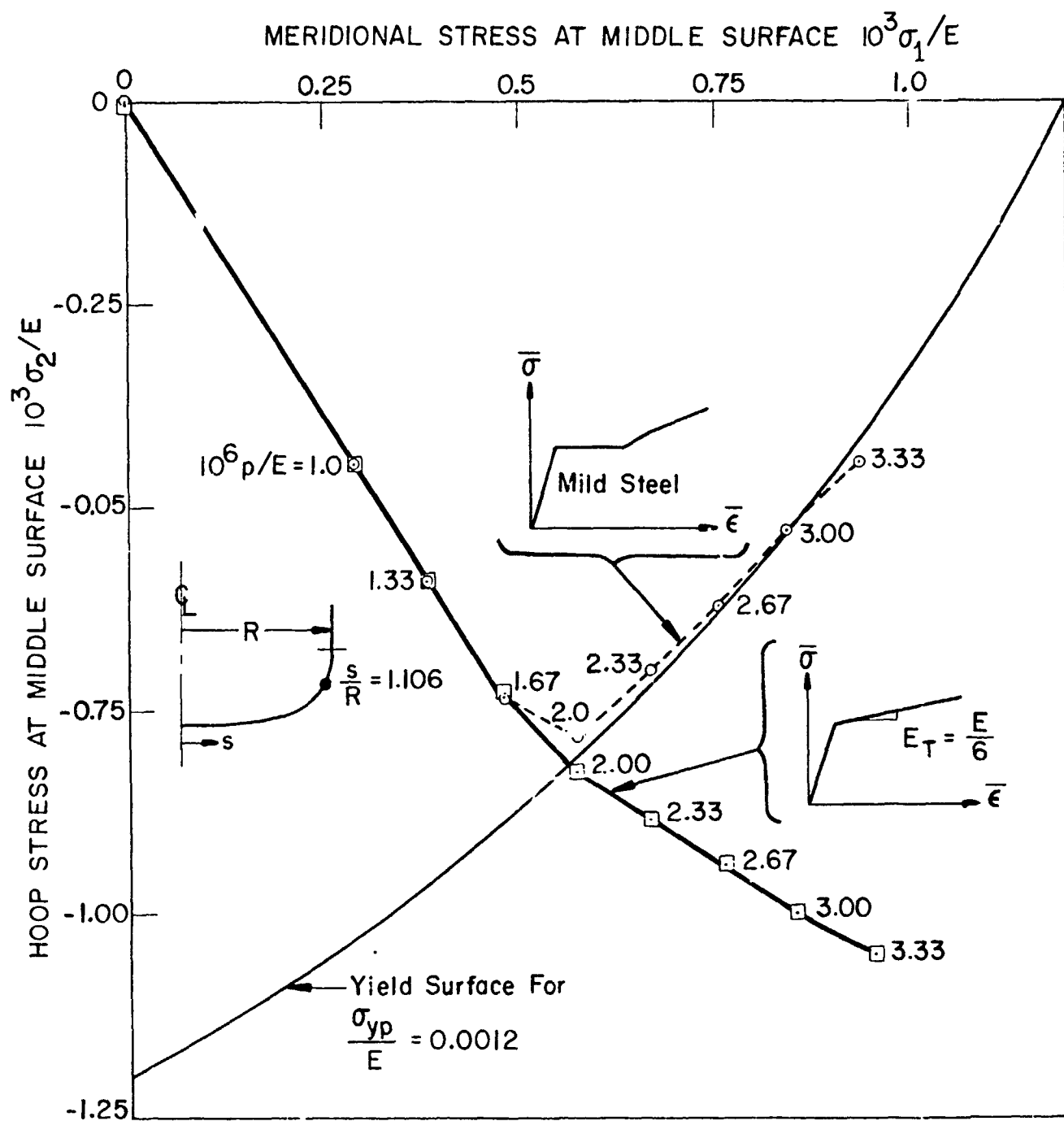
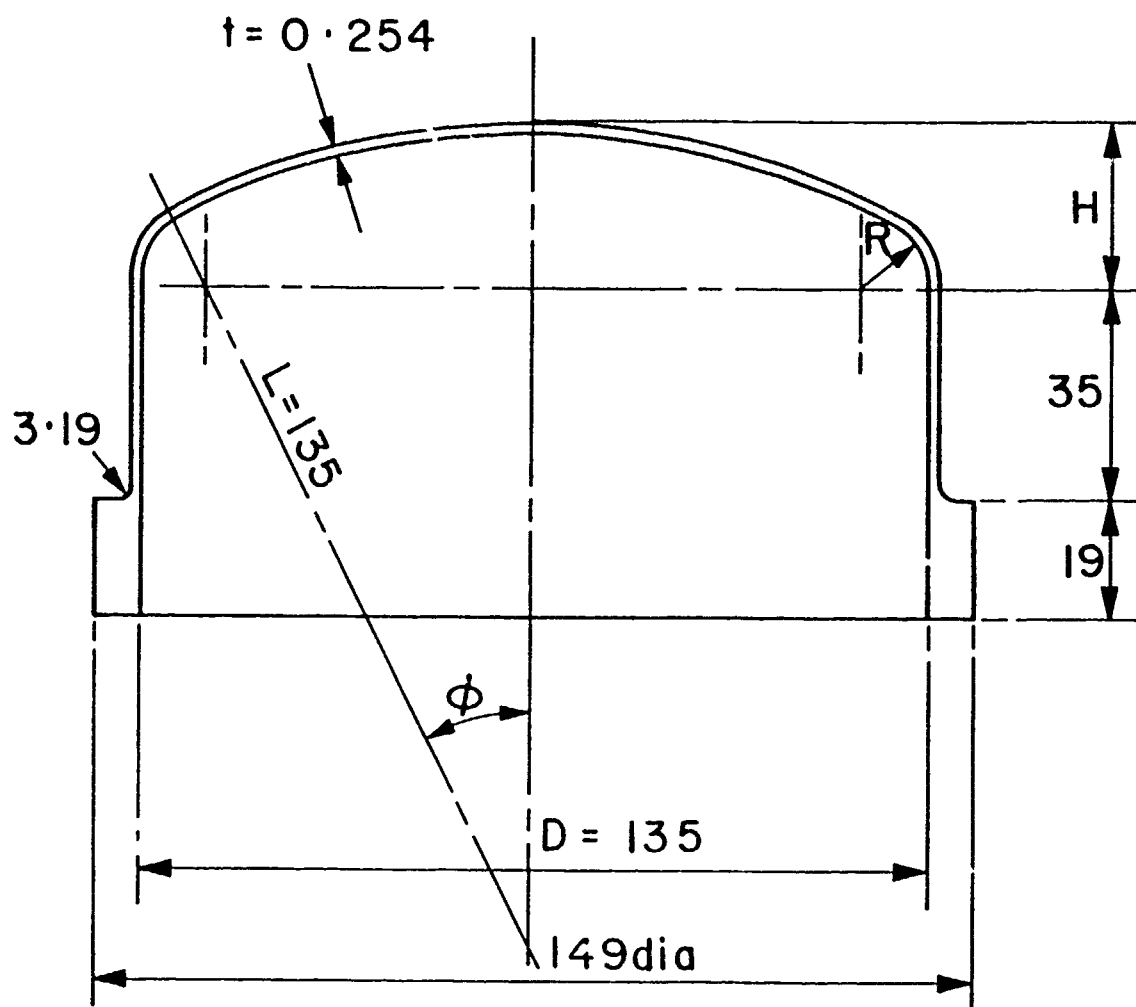


Figure 101 Comparisons of paths in stress space for a point at $s/R = 1.106$ with use of two different stress-strain curves (from Bushnell [138]).



(Dimensions in mm)

Figure 102(a) Test specimen nominal geometry (from Patel and Gill [137]).

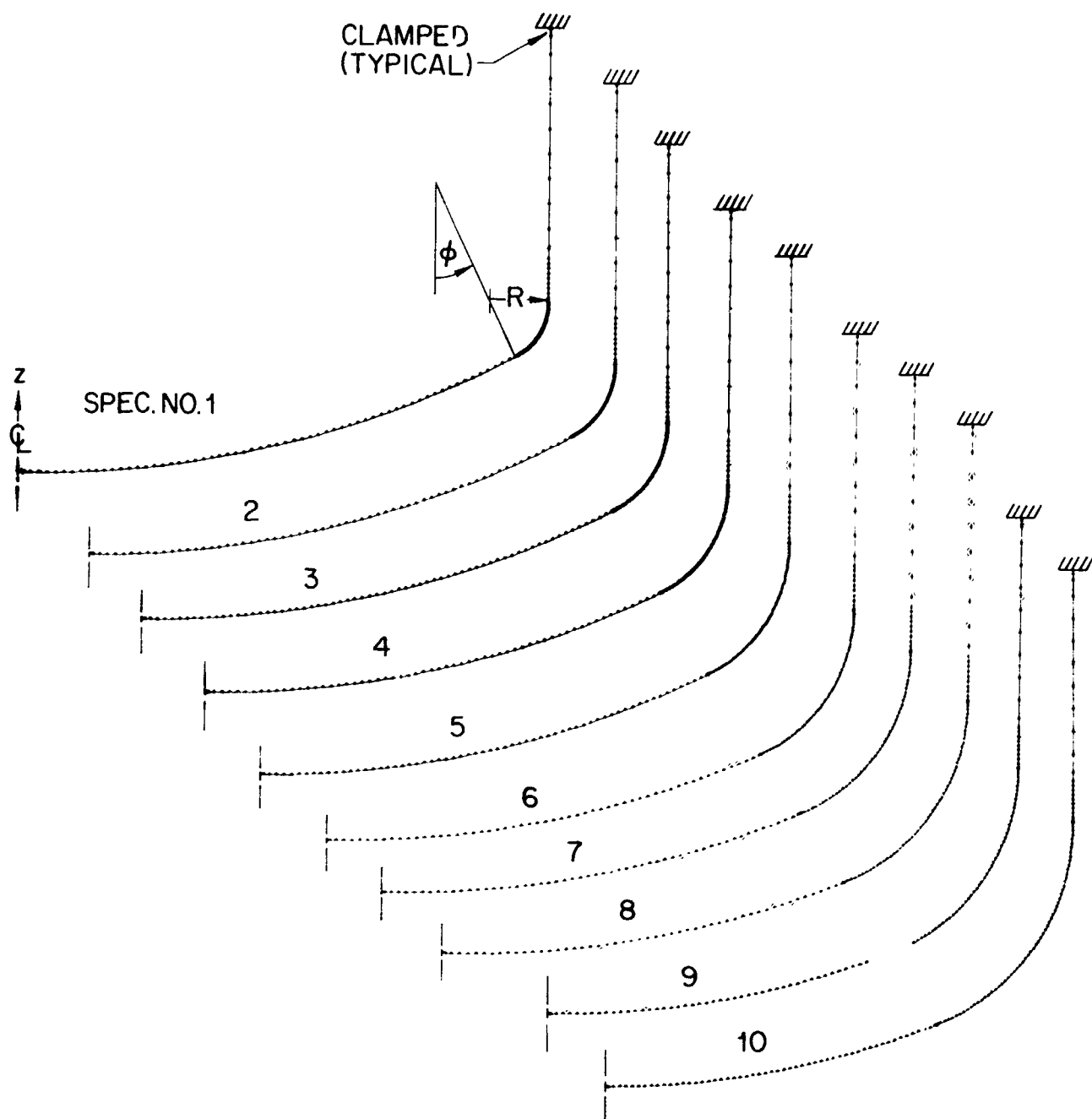


Figure 102(b) Discretized models for the BOSOR5 analysis (from Lagae and Bushnell [133]).

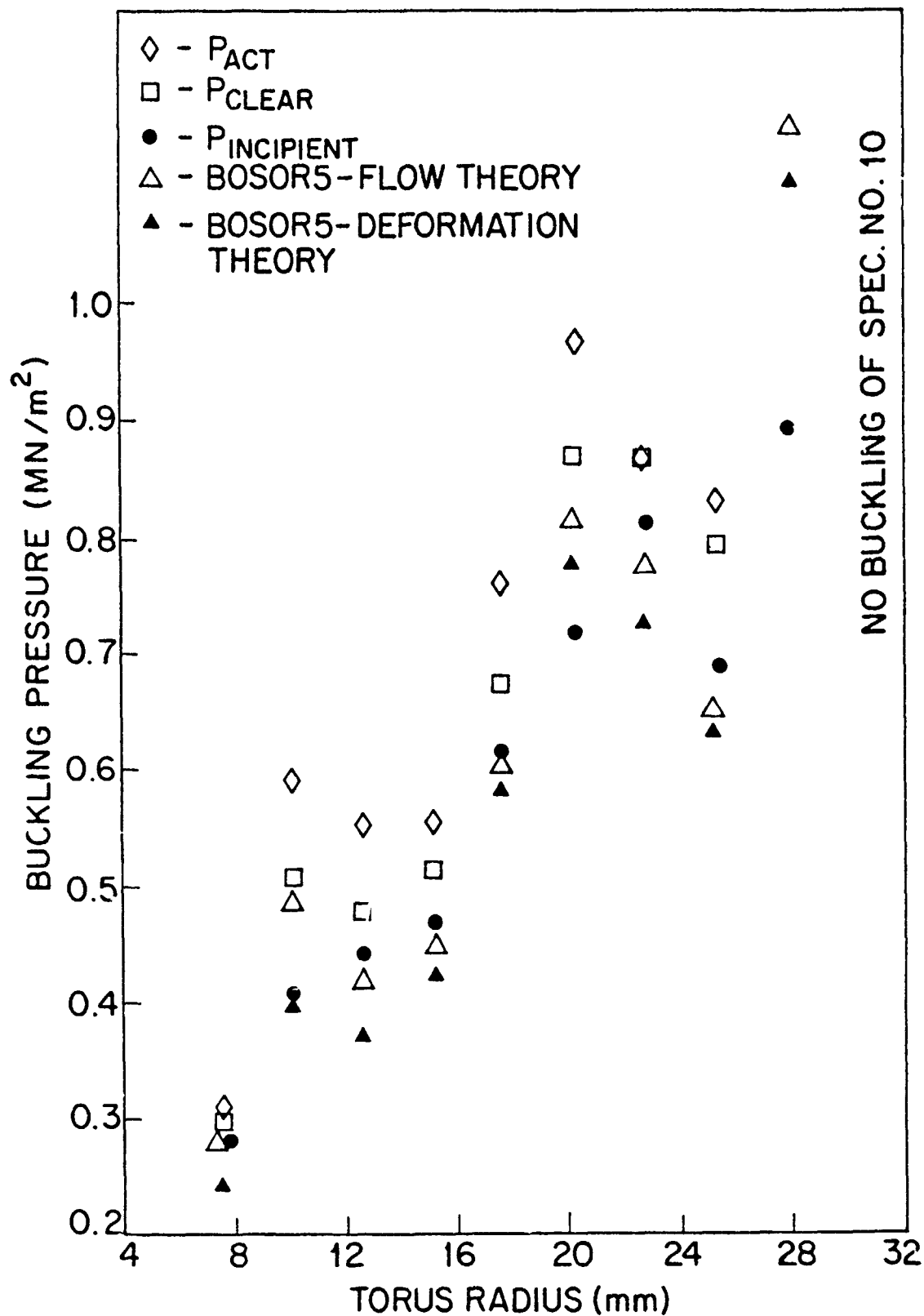
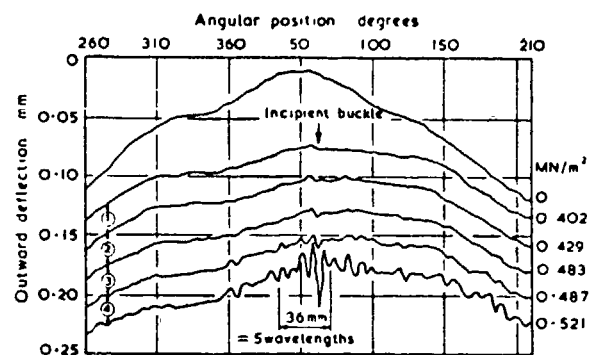
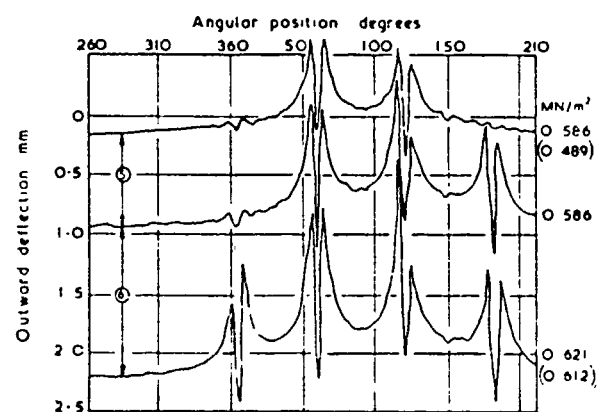


Figure 103 Variation in buckling pressure with radius of toroidal knuckle: comparisons of test results of [37] with BOSOR5 predictions for incipient buckling (from Lagae and Bushnell [133]).

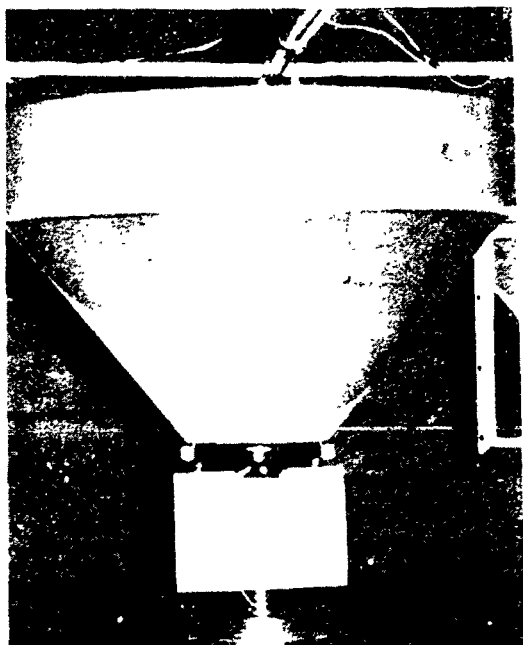


(a)

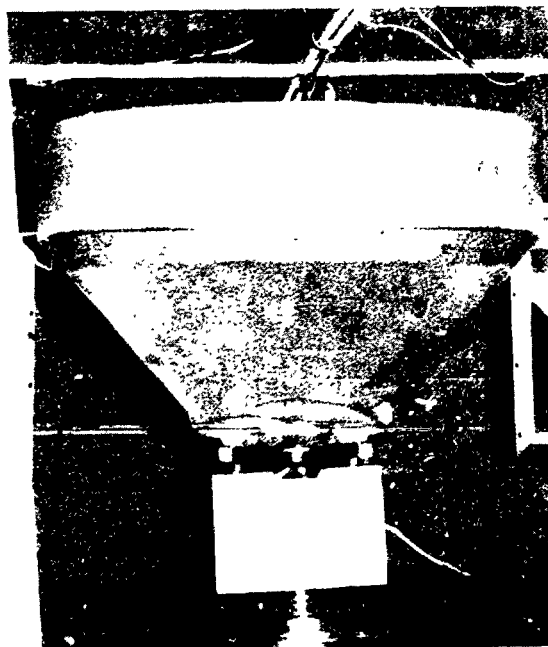


(b)

Figure 104 Development of buckles at sphere/torus junction in specimen 2D (from Patel and Gill [137]).



(a)

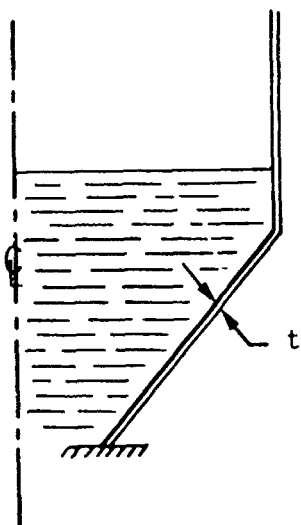


(c)

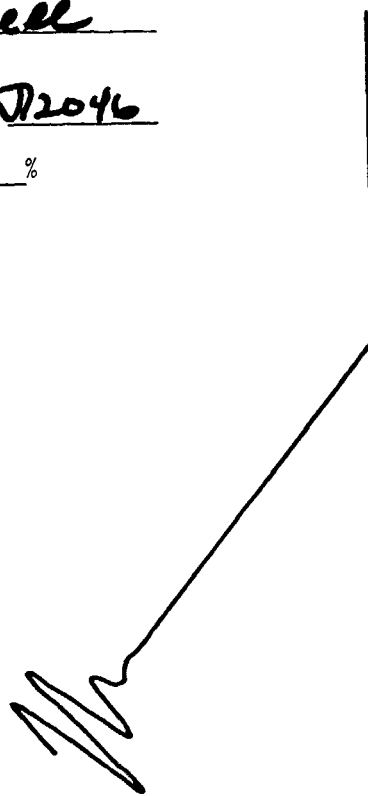
AUTHOR Bushnell

FIG. NO. 1.5 a, c LOG NO. D2046

REDUCE TO 50 %



(b)



(d)

Figure 4.105 Elastic buckling of conical water tank: (a) before buckling; (b) tank geometry and water level; (c) post-buckled model; and (d) predicted bifurcation buckling load factor and mode from linear theory (photographs courtesy of Dr. Guy Lagae, Univ. of Gent, Belgium).

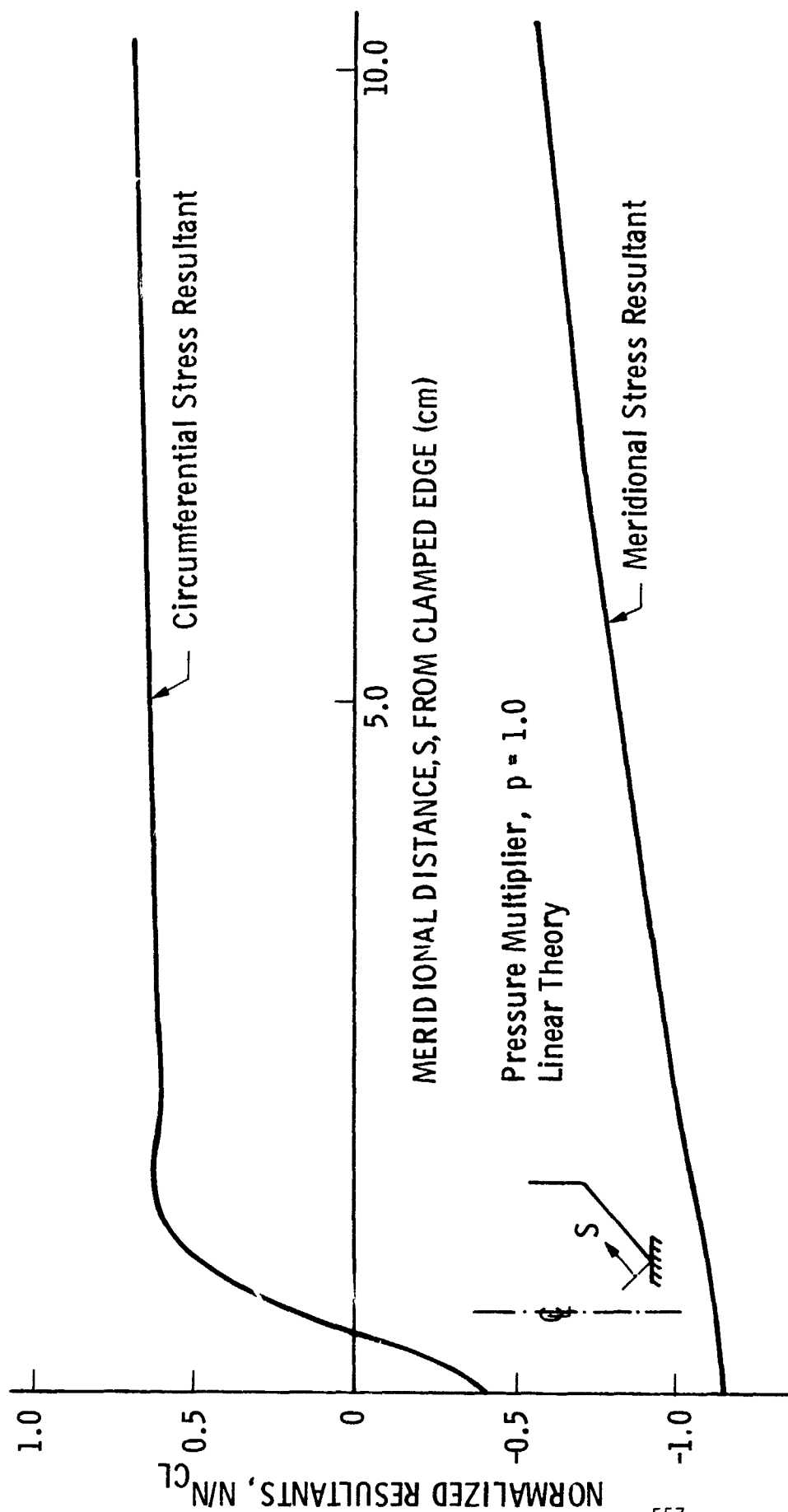


Figure 106 Stress resultants from linear theory at a load factor $p = 1.0$ ($N_{CL} = 0.6 Et^2/R_{normal}$; $R_{normal} = 13/\cos 40^\circ$ - see next figure).

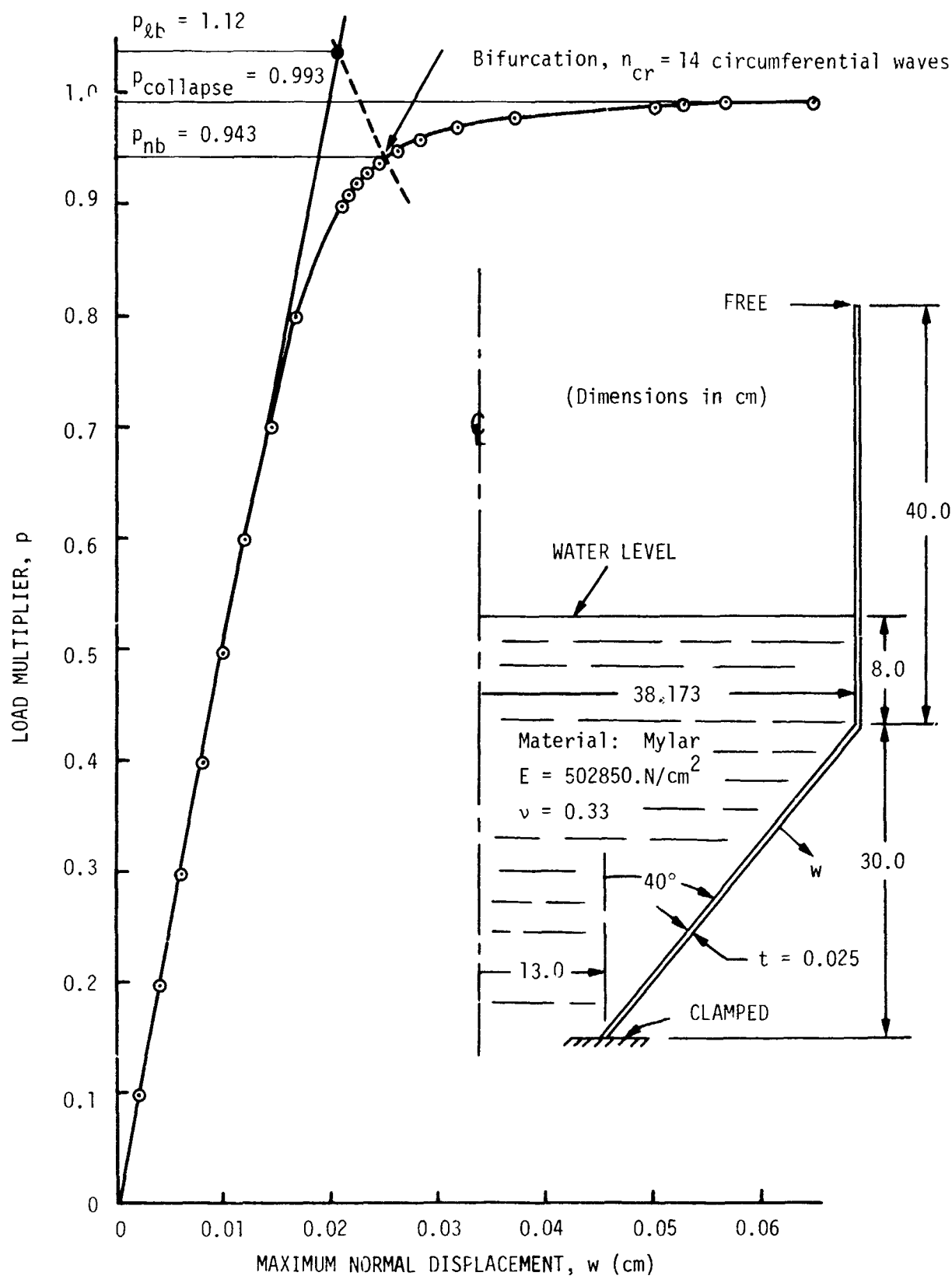


Figure 107 Load-maximum normal deflection curve with bifurcation points from linear and nonlinear prebuckling theory and axisymmetric collapse load factor.

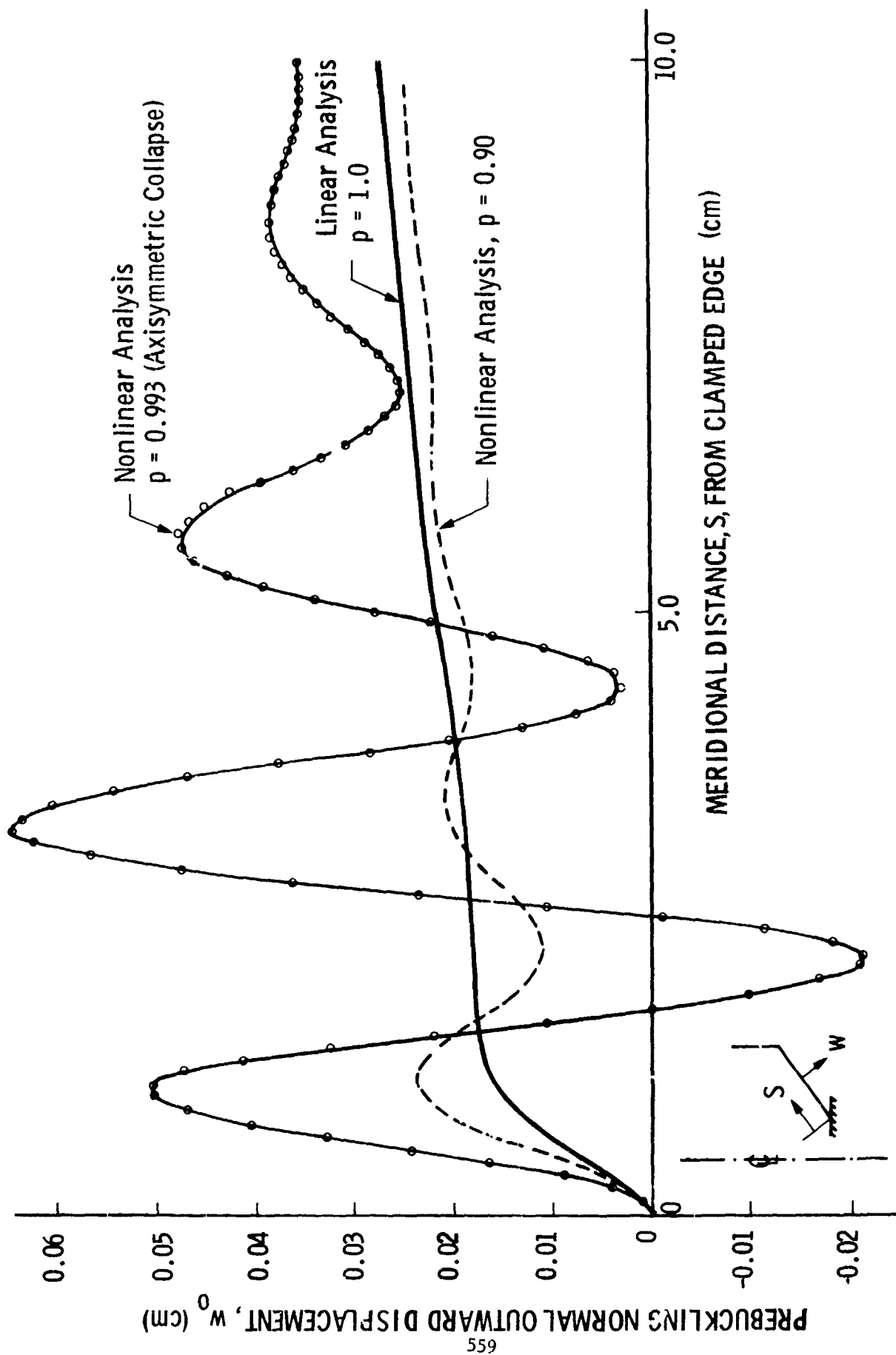


Figure 108 Growth of axisymmetric wrinkles near clamped base of conical water tank model.

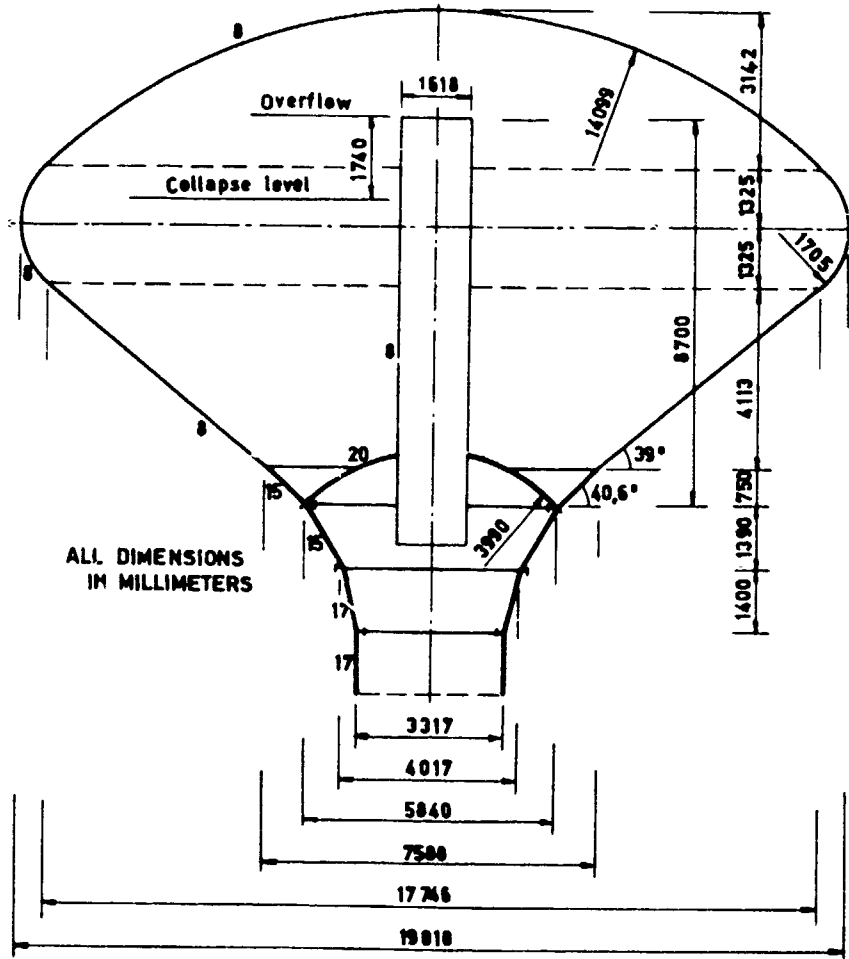


Figure 109(a) Geometry of large steel watertower that failed in Belgium in 1972 (from Vandepitte [140]).

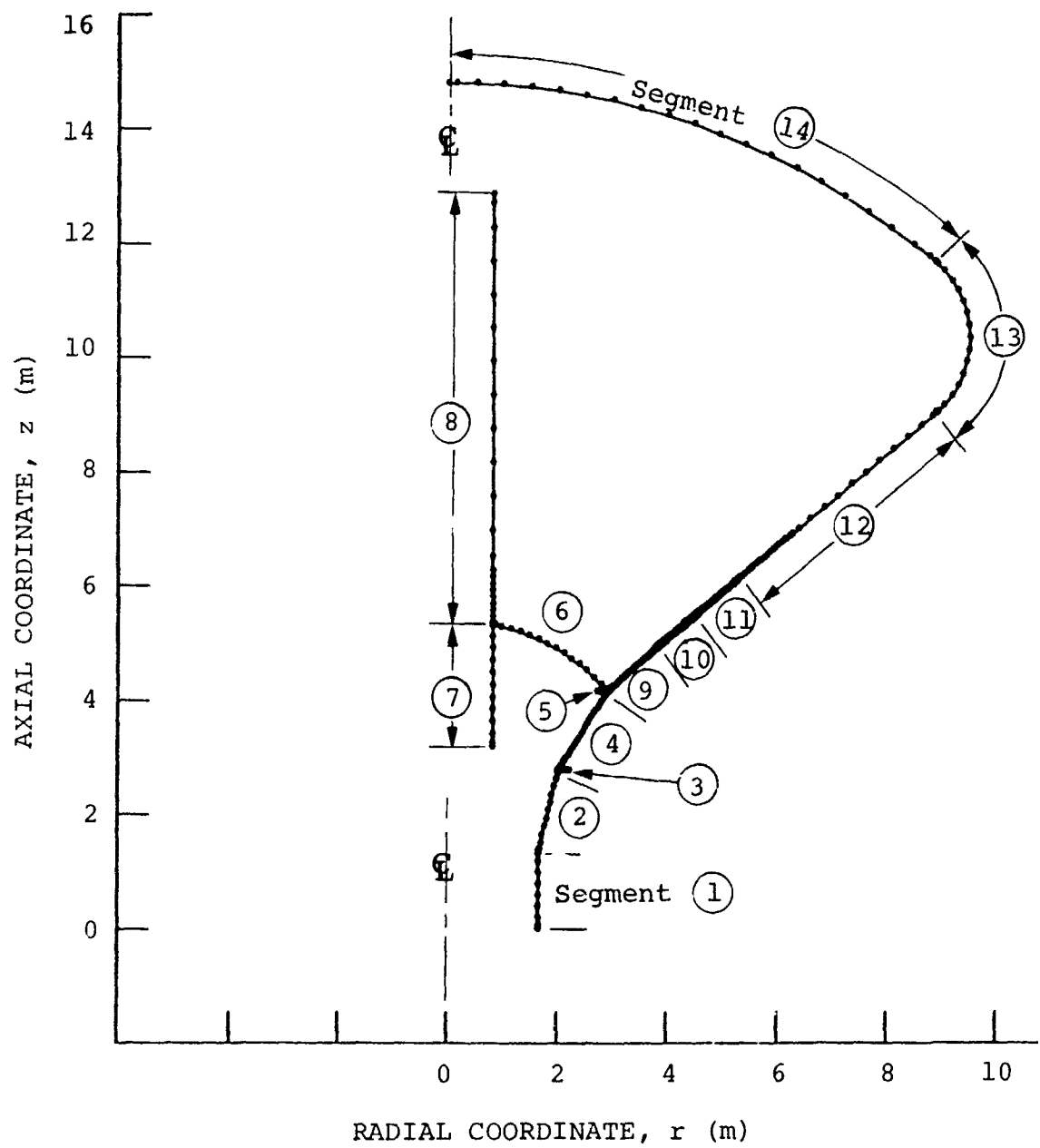


Figure 109(b) Segment numbering and discretization for BOSOR5 analysis of large steel water tank.

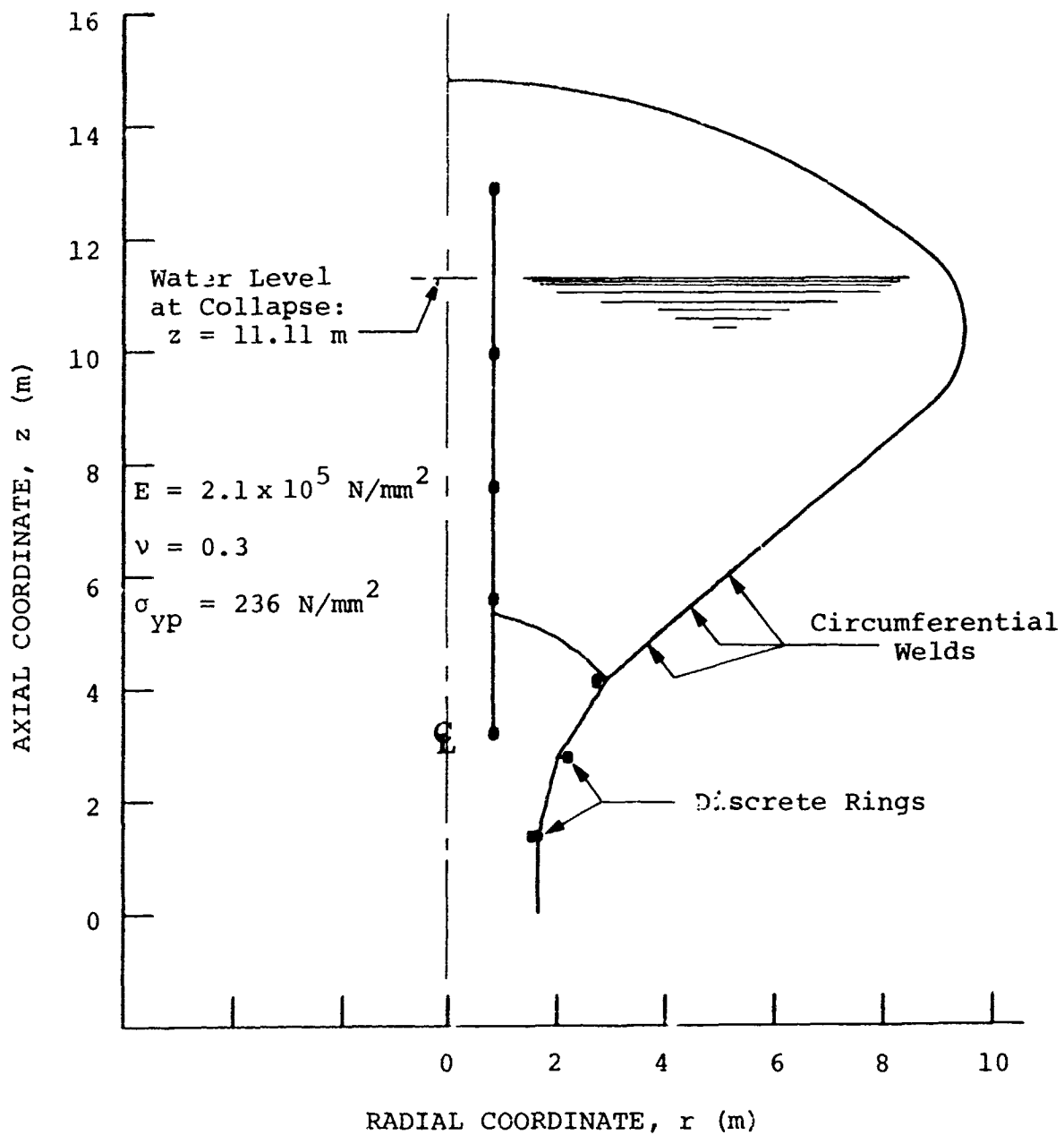


Figure 109(c) BOSOR5 model of watertank showing locations of axisymmetric welds and discrete rings.

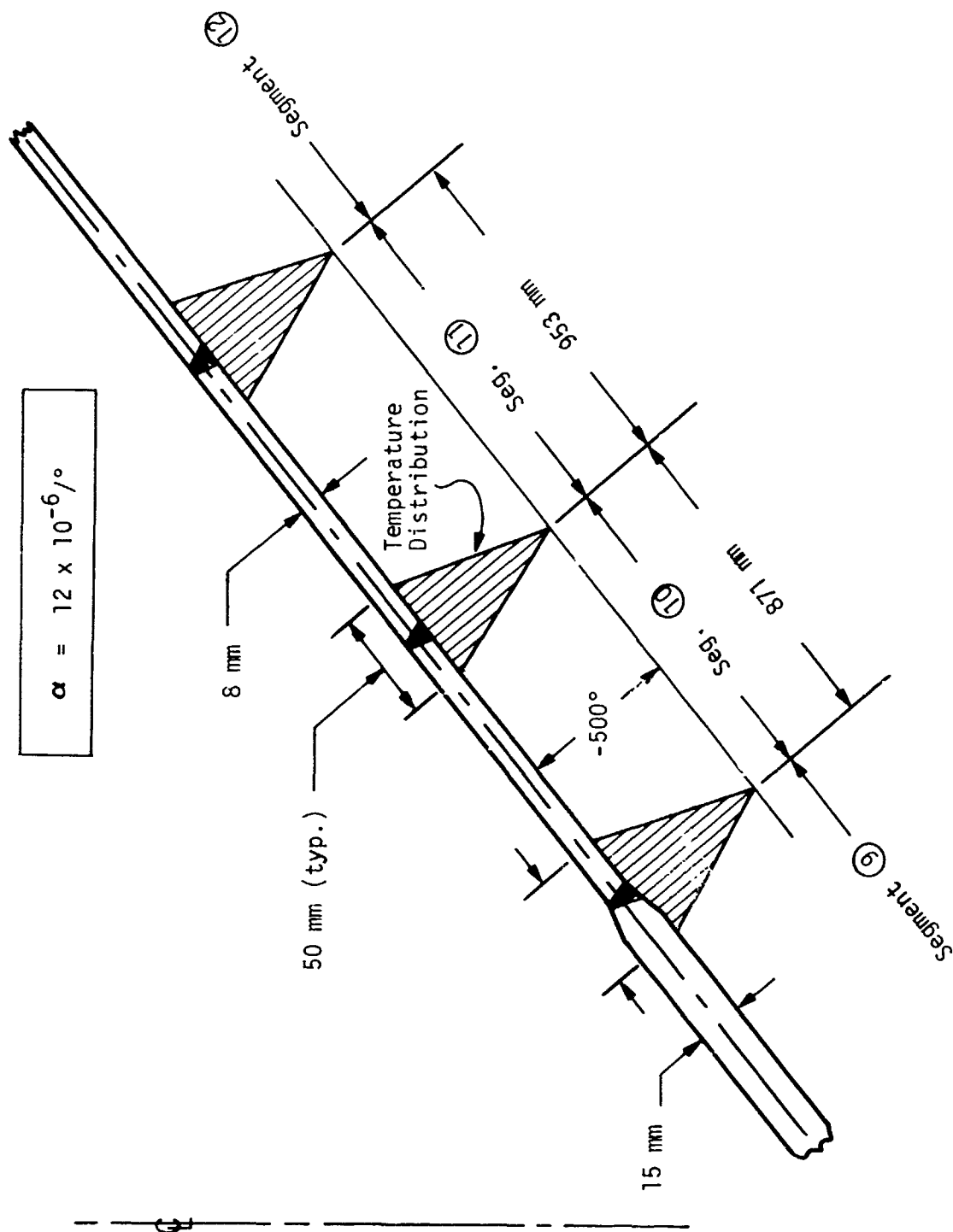


Figure 11C(a) Effect of welding is simulated by local cooling around welds to produce axisymmetric weld sinkage of the approximate amplitude.

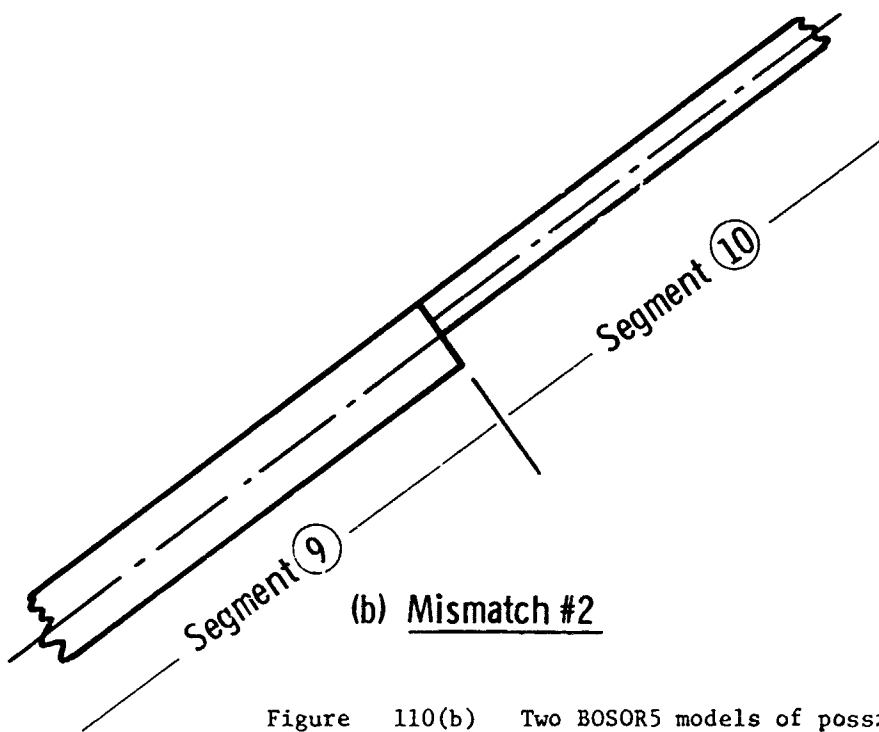
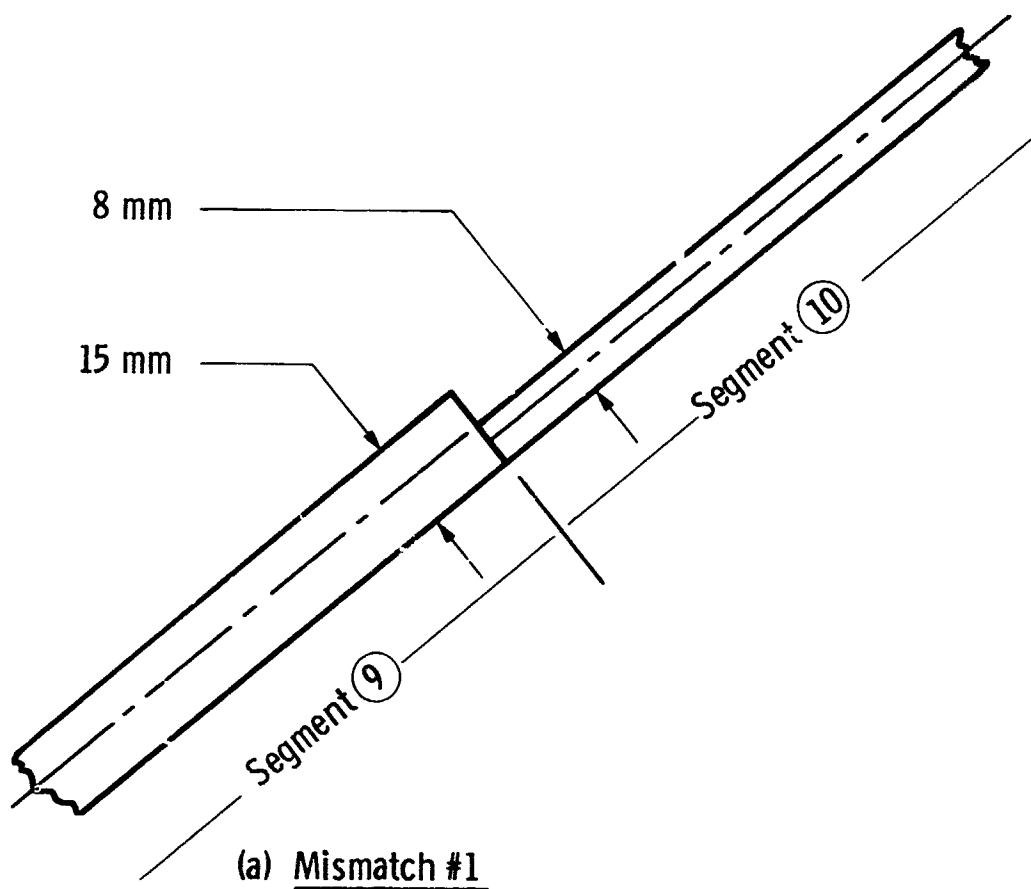


Figure 110(b) Two BOSOR5 models of possible axisymmetric mismatch between Segments ⑨ and ⑩.

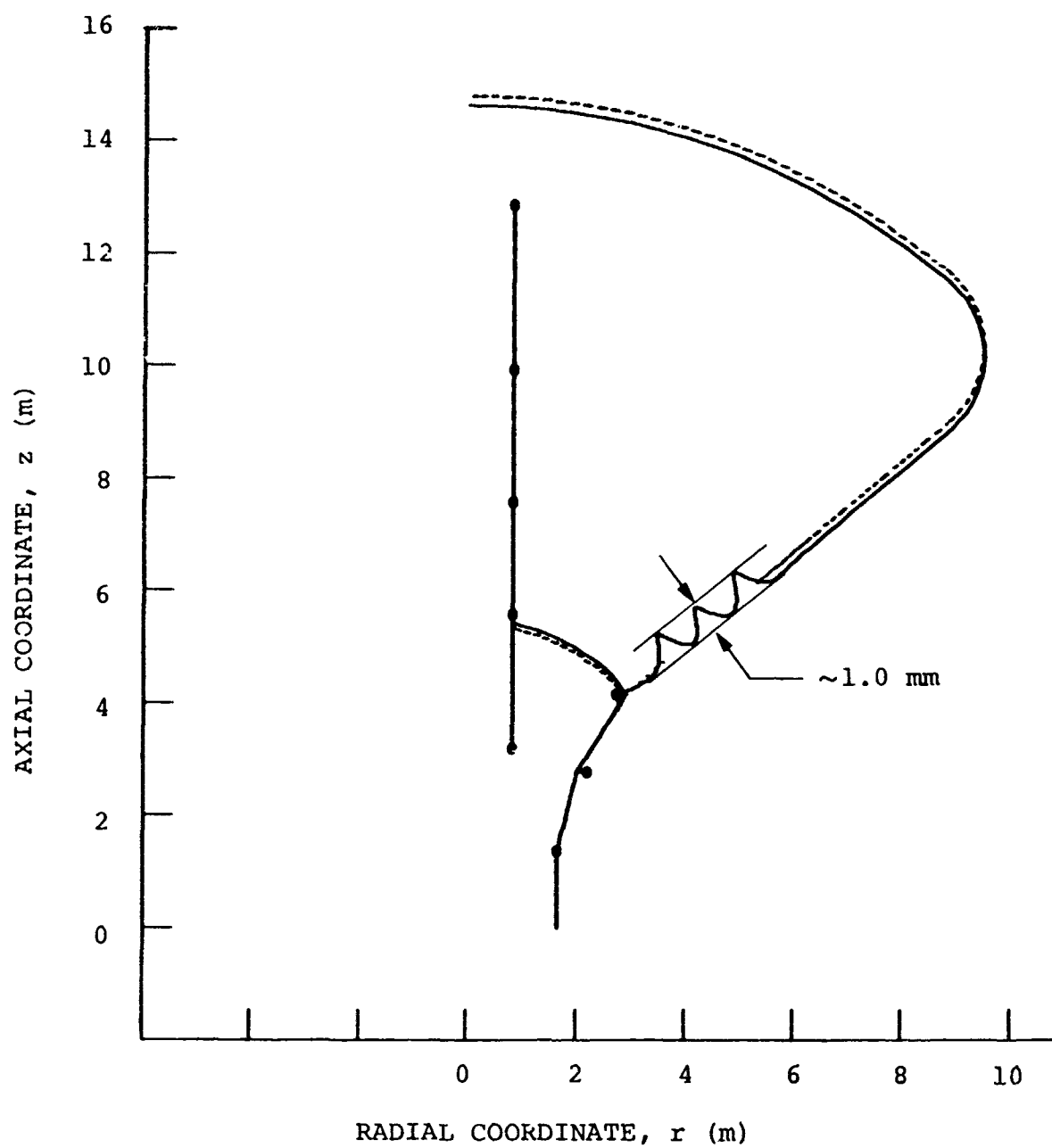


Figure 111 Local axisymmetric shrinkage due to cooling down of welds.

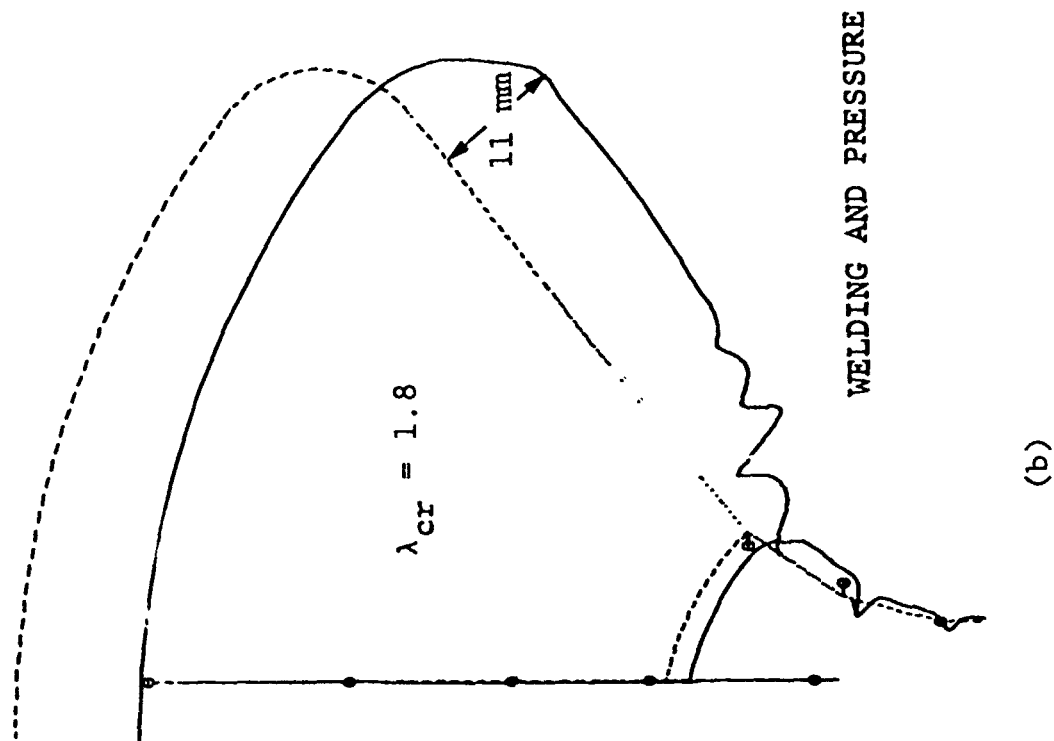
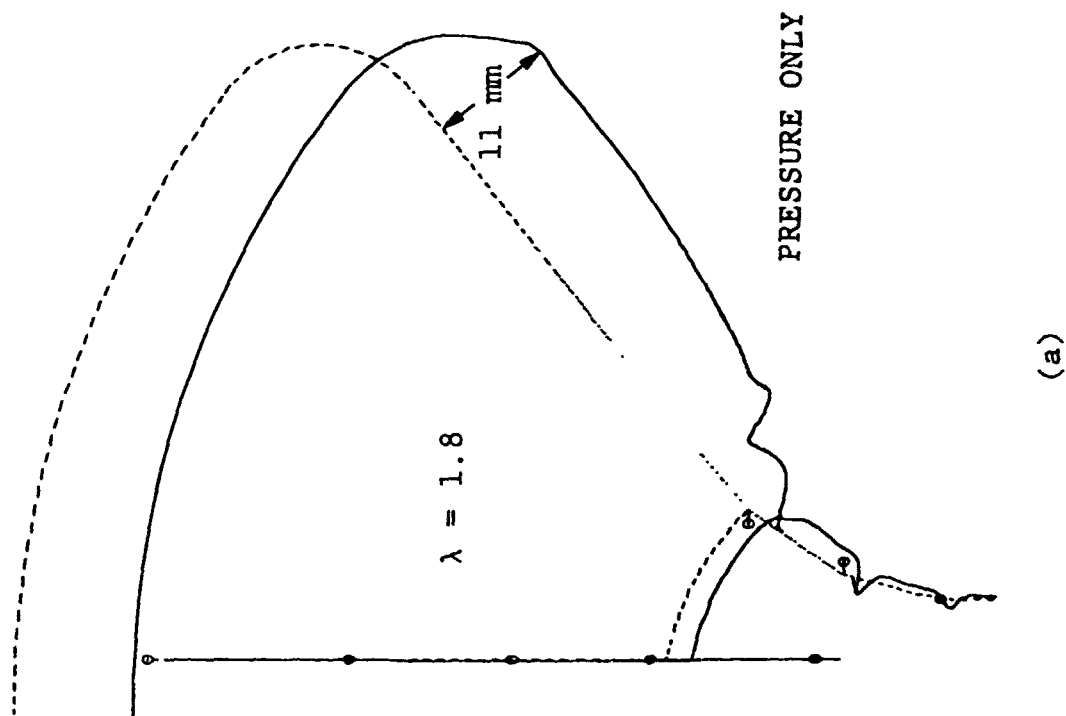
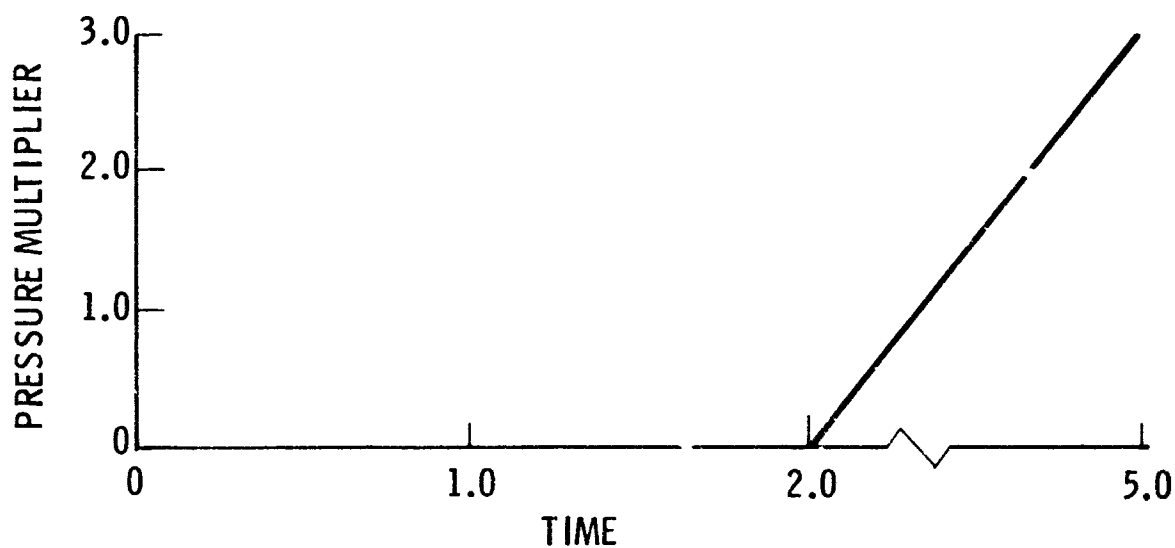
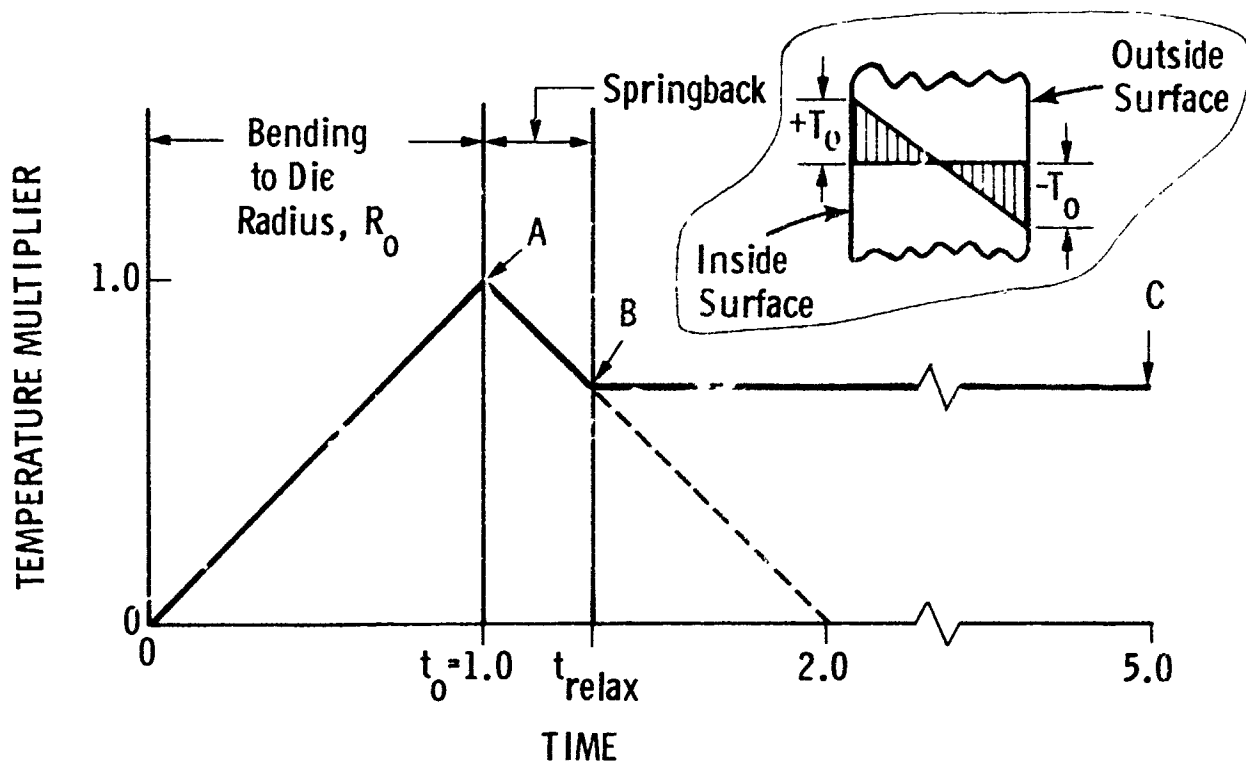


Figure 112 Predicted axisymmetrically-deformed tank at load factor $\lambda = 1.8$: (a) with internal hydrostatic pressure only; (b) internal hydrostatic pressure plus welding effects. Influence of circumferential welds on predicted collapse load factor is small.



Segment	T_0	t_{relax}
1	1094	1.136
2	1045	1.142
4	739	1.201
7,8	558	1.265
9	642	1.225
10	199	1.663
11	191	1.700
12	180	1.731

Figure 113 Cold bending model: time variations of thermal and pressure loading.

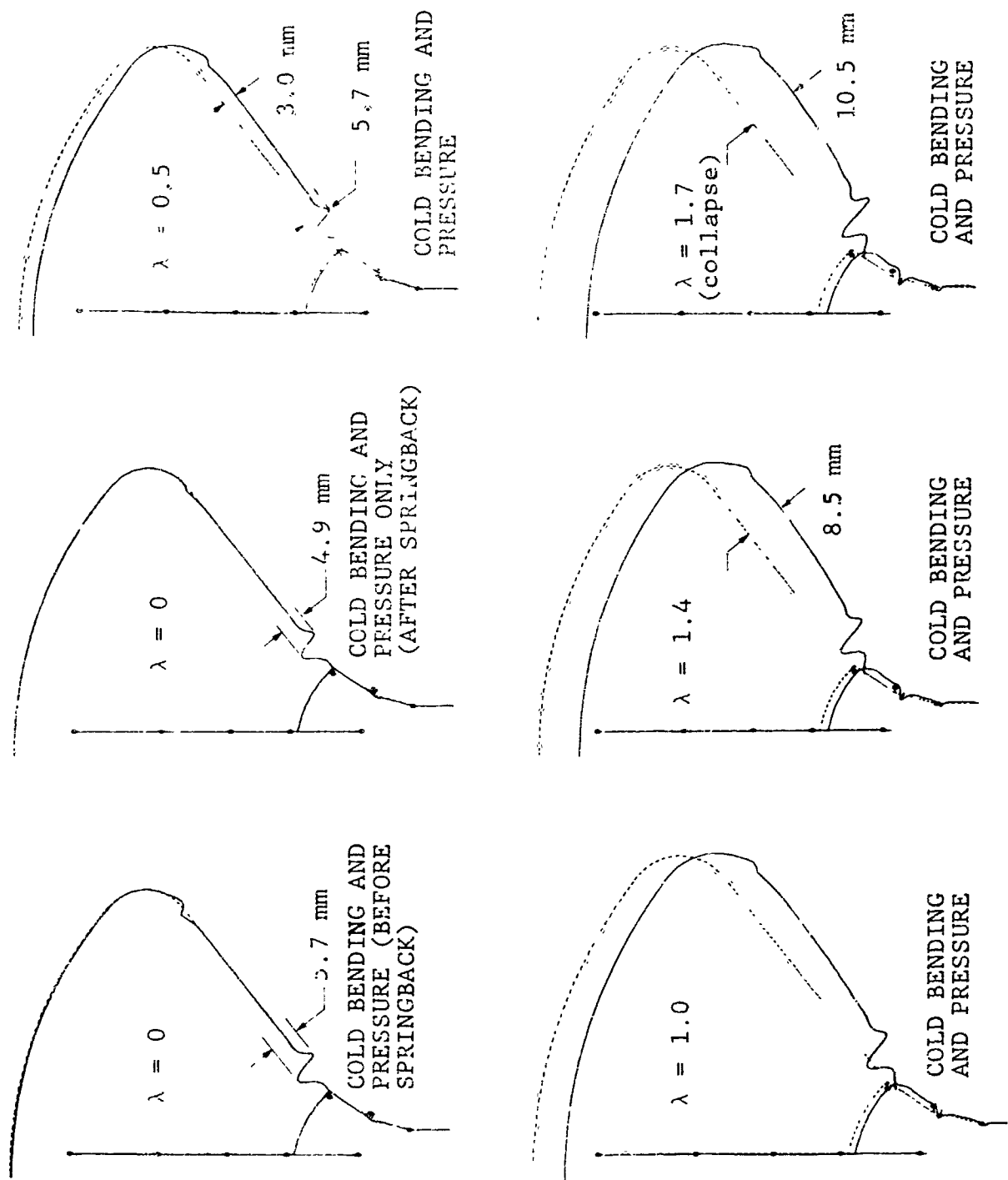
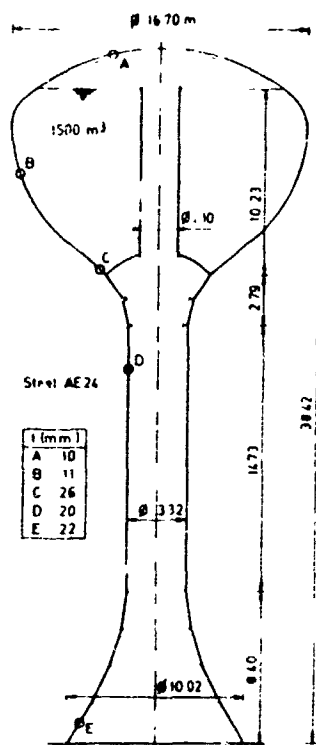
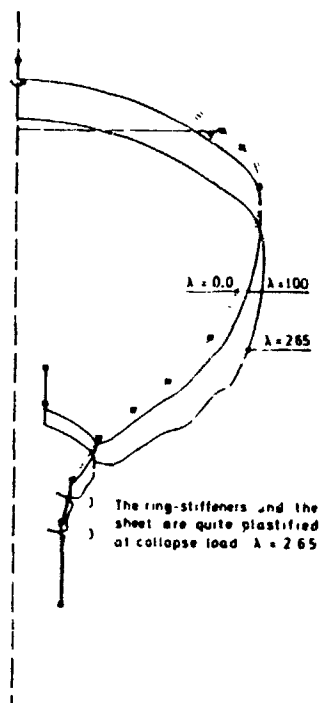


Figure 114 Deformation of watertank during cold bending and application of hydrostatic pressure.



(a)

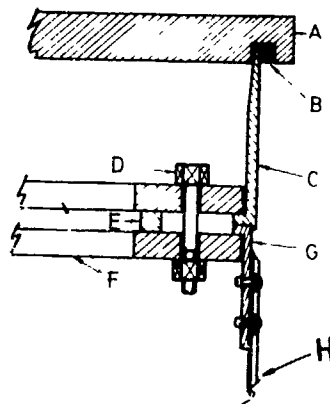


(b)

Figure 115 (a) New design of the watertower; (b) deformations under increasing loads (from Baltus and Massonnet [2]).

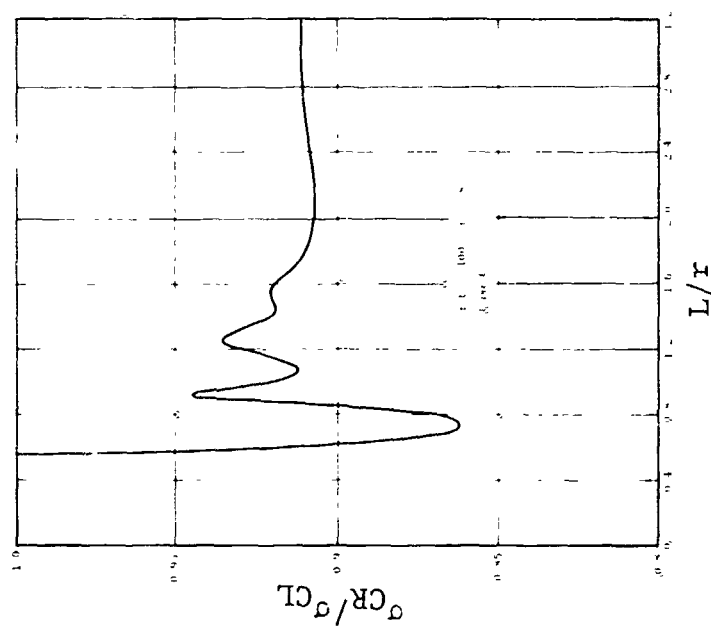


(a) Stringer-stiffened shell with ends simulating a practical aerospace joint.

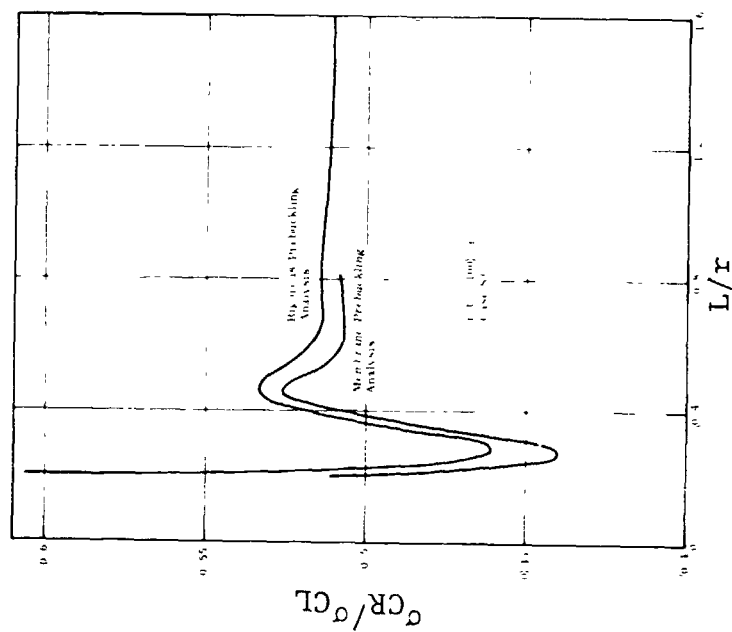


(b) Details of "practical" boundary conditions for axially compressed cylindrical shells.

Figure 116 Stiffened cylindrical shell and simulation of practical end condition used in experiments by Singer et al (from Singer and Abramovich [33]).



(a) Influence of shell length for clamped cylinders.



(b) Influence of shell length for simply supported cylinders with $N_{xy} = 0$ (v free).

Figure 117 Normalized critical stress of axially compressed monocoque cylinders as function of length-to-radius ratio, L/r (from Almroth [152]).

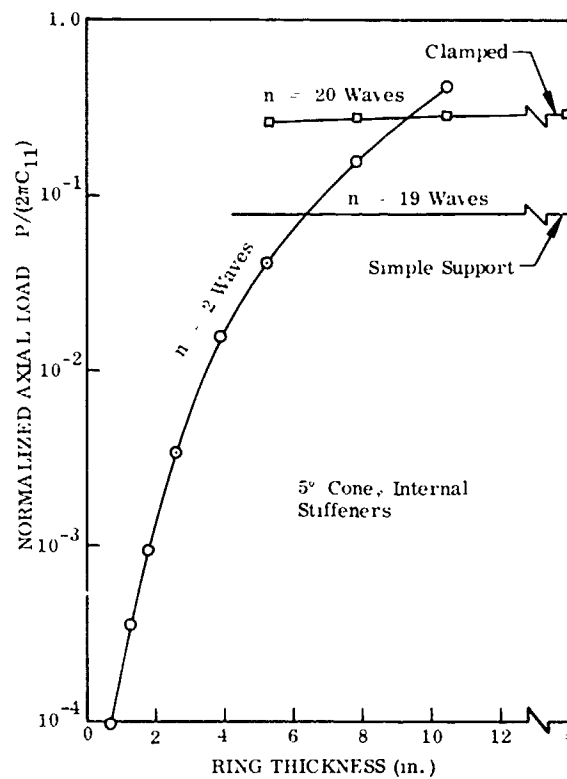


Figure 118

Critical axial load as a function of ring thickness for cones supported at the edges by rings of square cross section [C_{11} is given in Eq. (85) of Ref.[430] (from Almroth and Bushnell [153]).

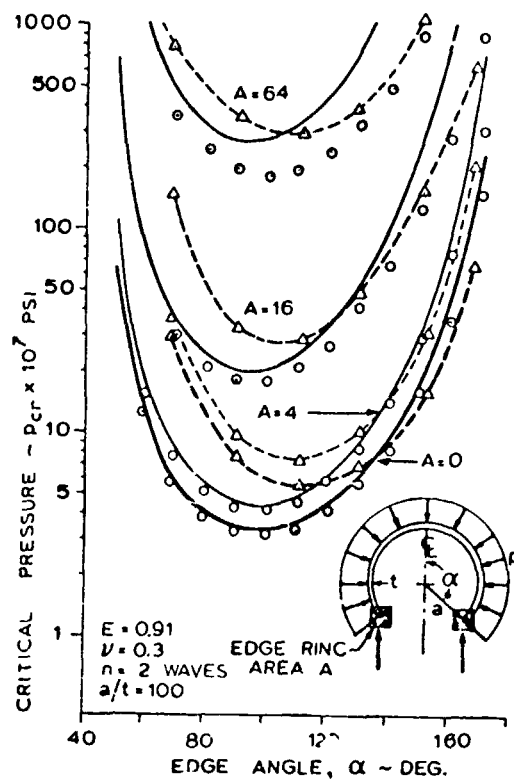


Figure 119 Buckling loads for spherical shells with edge rings of square cross section:

- = BOSOR 4
- = Inextensional [AIAA J., 6, 361-364, 1968]
- Δ-- = Donnell theory [92]

(from Bushnell [91]).

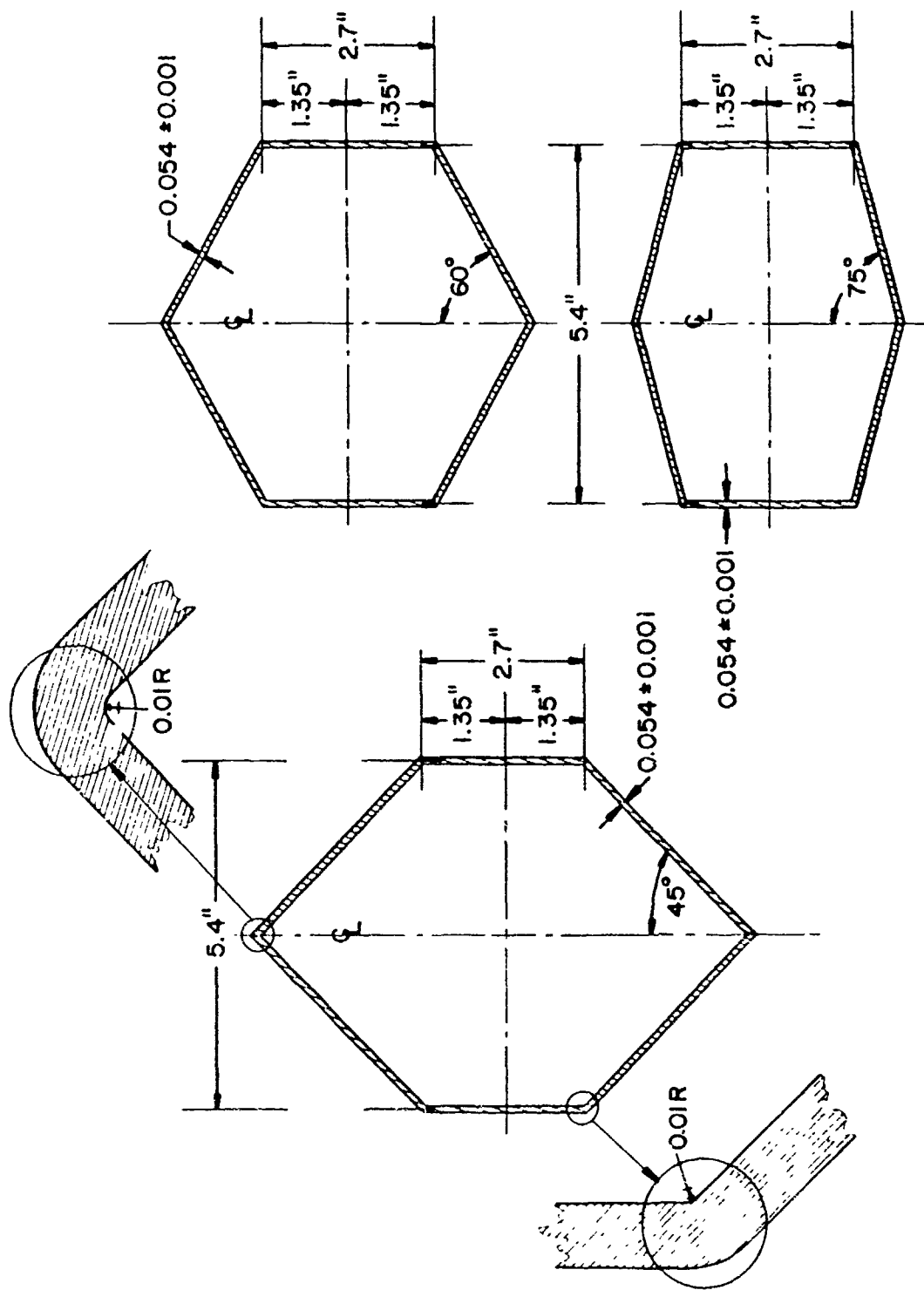


Figure 120(a) Cone-cylinder specimens tested under external pressure by Galletly [131].



Figure 120(b) Post-buckled state of specimen with 75° conical end (courtesy G. D. Galletly [154]).

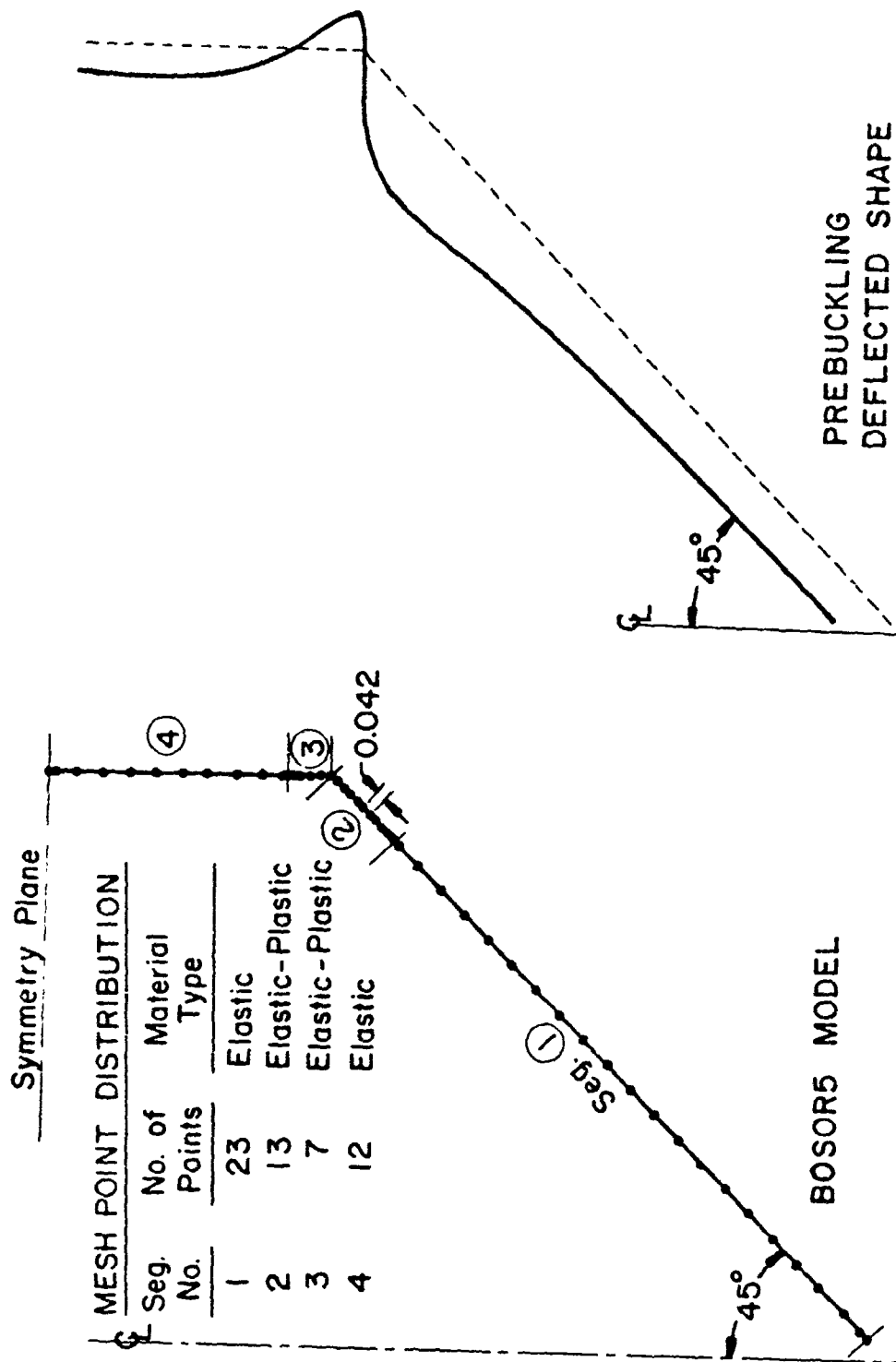


Figure 120(c) Discrete model of the 45° cone-cylindrical specimen and exaggerated view of the pre-buckling deflected shape at the buckling pressure (from Bushnell and Gooch, 1974)

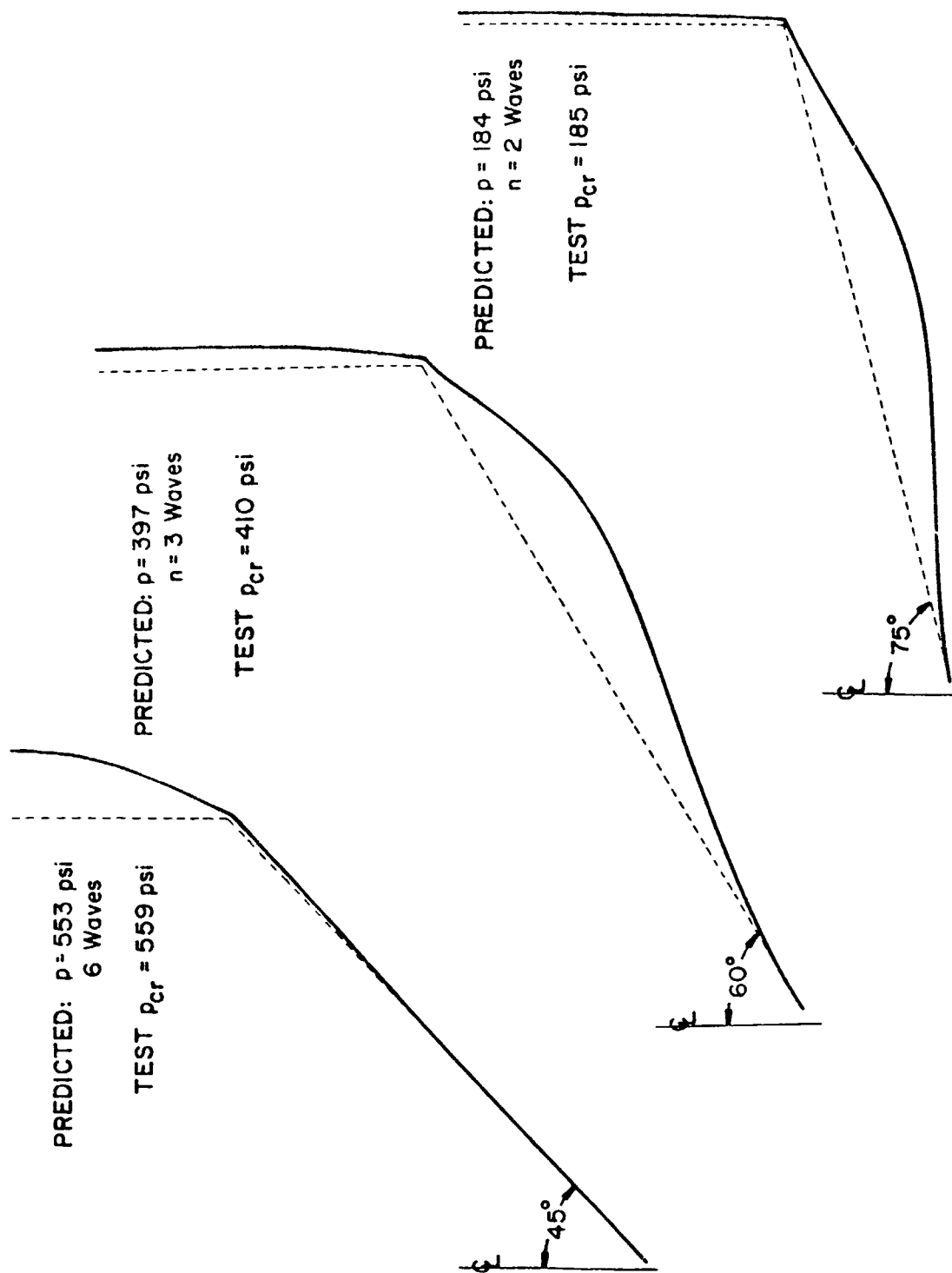


Figure 120(d) Bifurcation buckling modes and comparison with test results (from Bushnell and Galletly [131]).

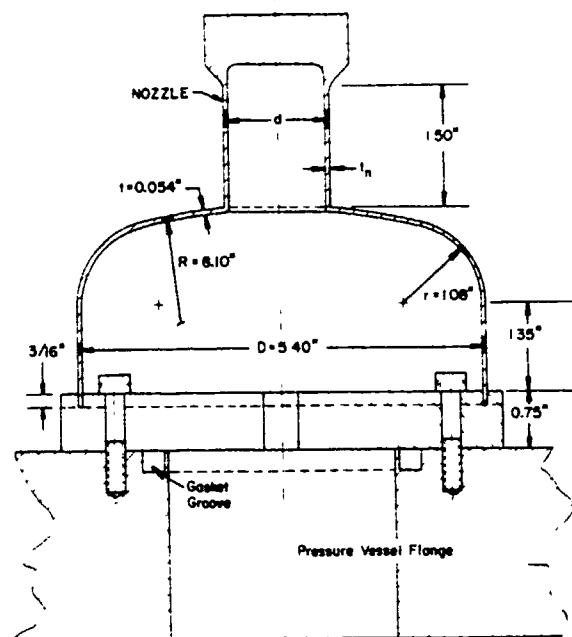


Figure 121(a) Aluminum torispherical head with axisymmetric nozzle tested under external pressure by Galletly at the University of Liverpool (from Bushnell and Galletly [131]).

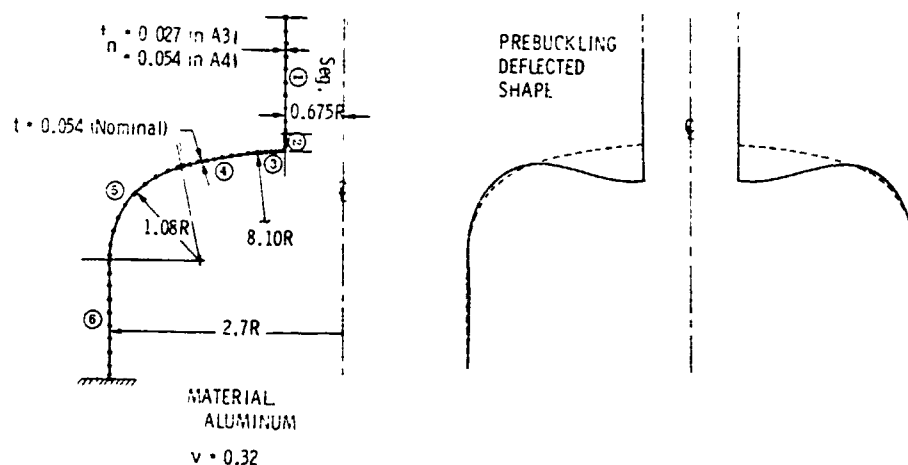


Figure 121(b) Discrete model of one of the torispherical specimens with exaggerated view of the prebuckling deflected shape at the buckling pressure (adapted from Bushnell and Galletly [131]).

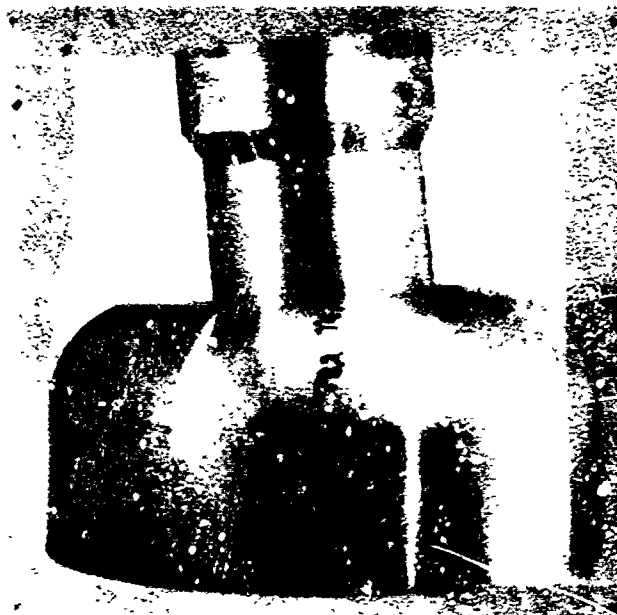
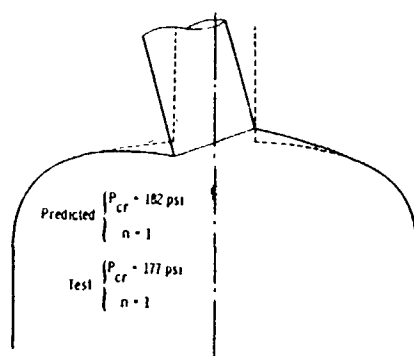
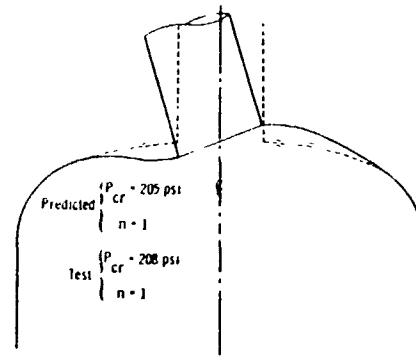


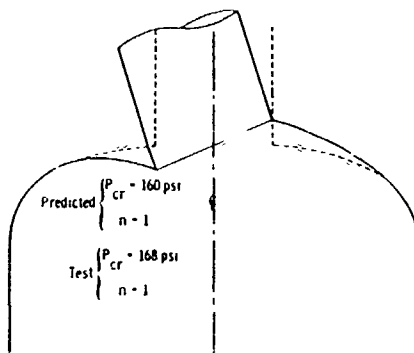
Figure 121(c) Galletly's buckled specimens (courtesy G. D. Galletly [155]).



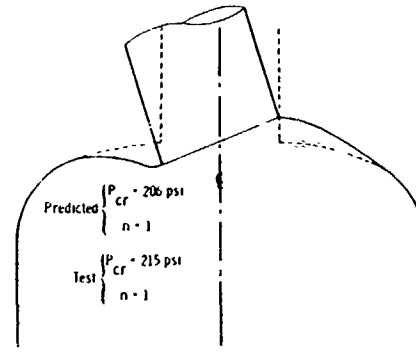
Specimen A3



Specimen A4



Specimen A5



Specimen A6

Figure 121(d) Bifurcation buckling modes and comparison with Galletly's test results (adapted from Bushnell and Galletly [131]).

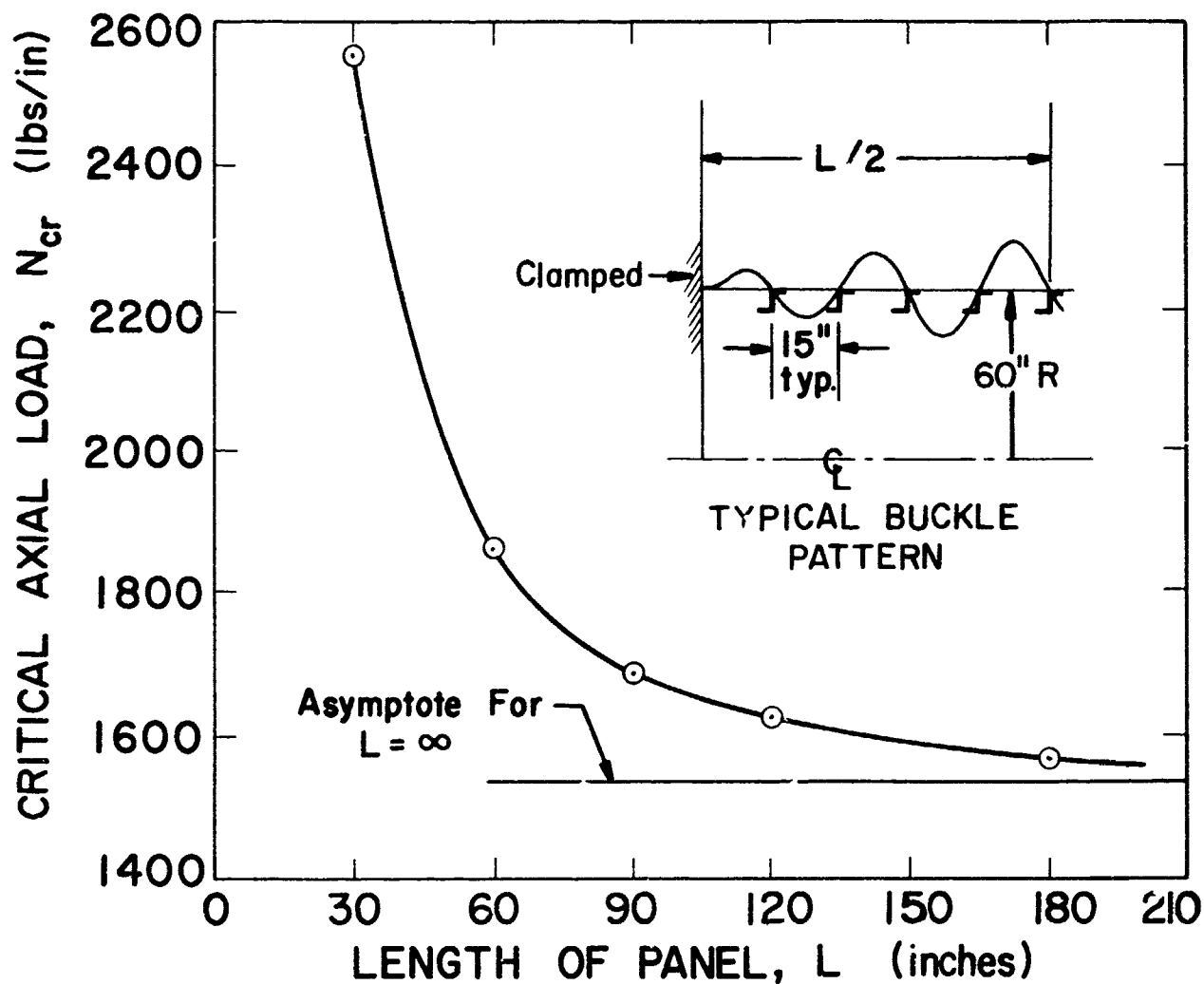


Figure 122(a) Theoretical buckling loads obtained with the BOSOR4 computer program for clamped corrugated cylinders of various lengths with discrete rings on 15-in. centers [$t = 0.020$ in., $t_s = 0.32$ in. (see Figure 122(b)) (from Bushnell [3]).

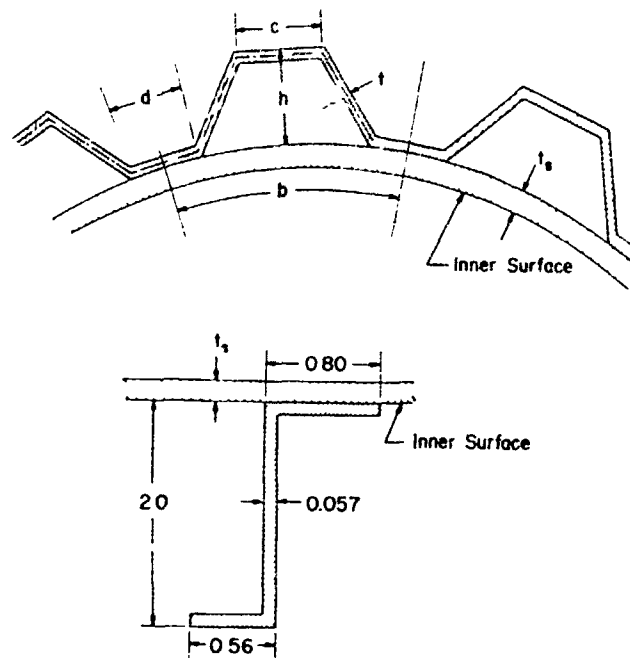


Figure 122(b) Geometry of semisandwich, corrugated wall and internal discrete rings (from Bushnell [3]).

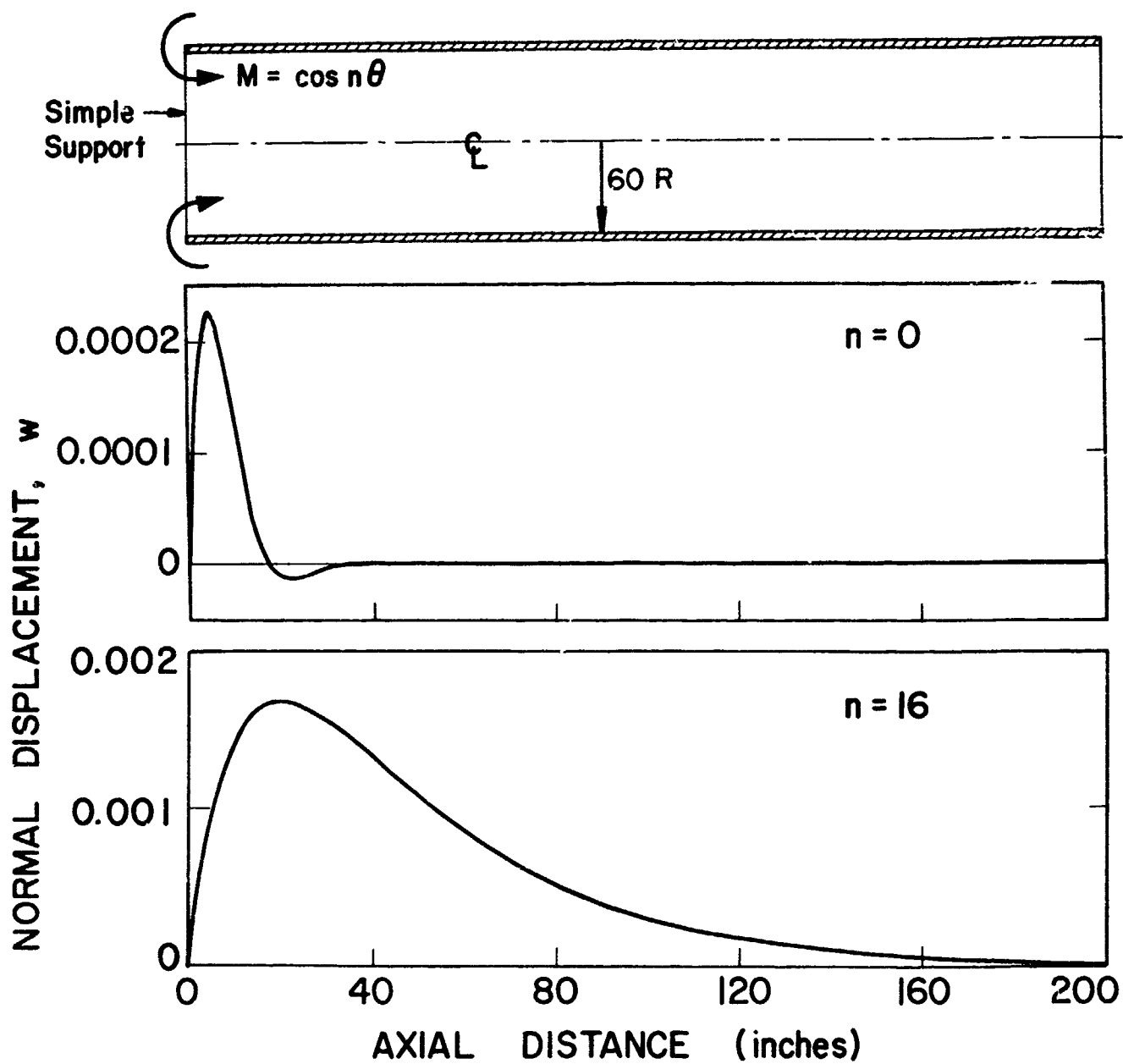
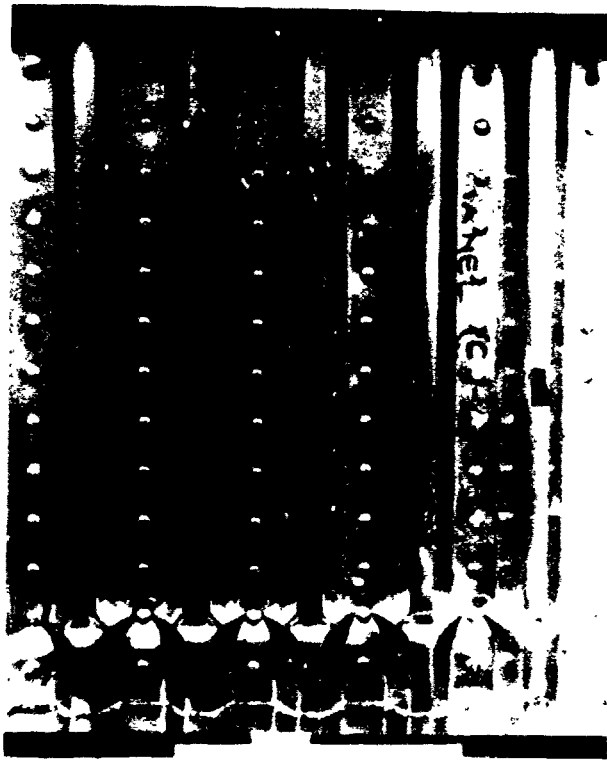


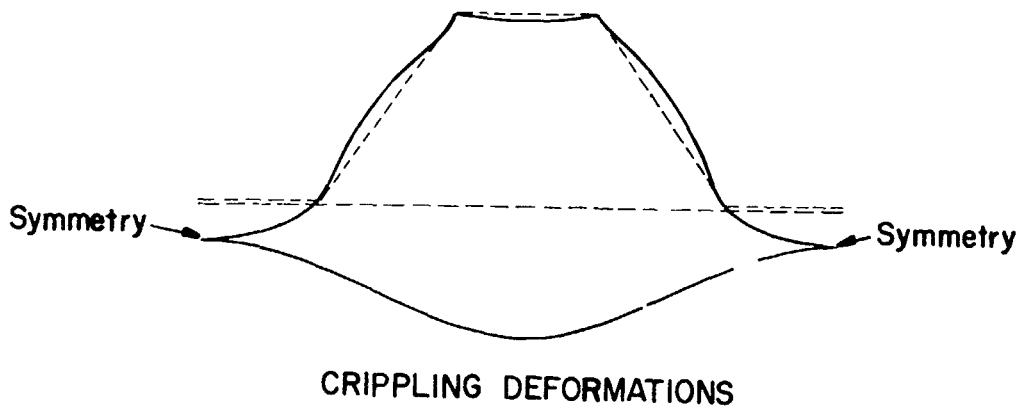
Figure 122(c) Decay of normal displacement for corrugated cylinder with harmonically varying edge moment (from Bushnell [3]).



Figure 123(a) 60-in. radius x 52-in. long curved, ring-stiffened panel with $t = 0.25$ in., $t_s = 0.040$ in. buckled at $N_{xcr} \approx 2550$ lb/in. in a general instability mode (from Bushnell [3]).



(a) Crippling observed in a test of a riveted panel under axial compression.



(b) Predicted crippling deformations for axially compressed riveted semisandwich flat corrugated panel.

Figure 124 Local crippling instability. This buckling mode is associated with very short axial wavelengths.

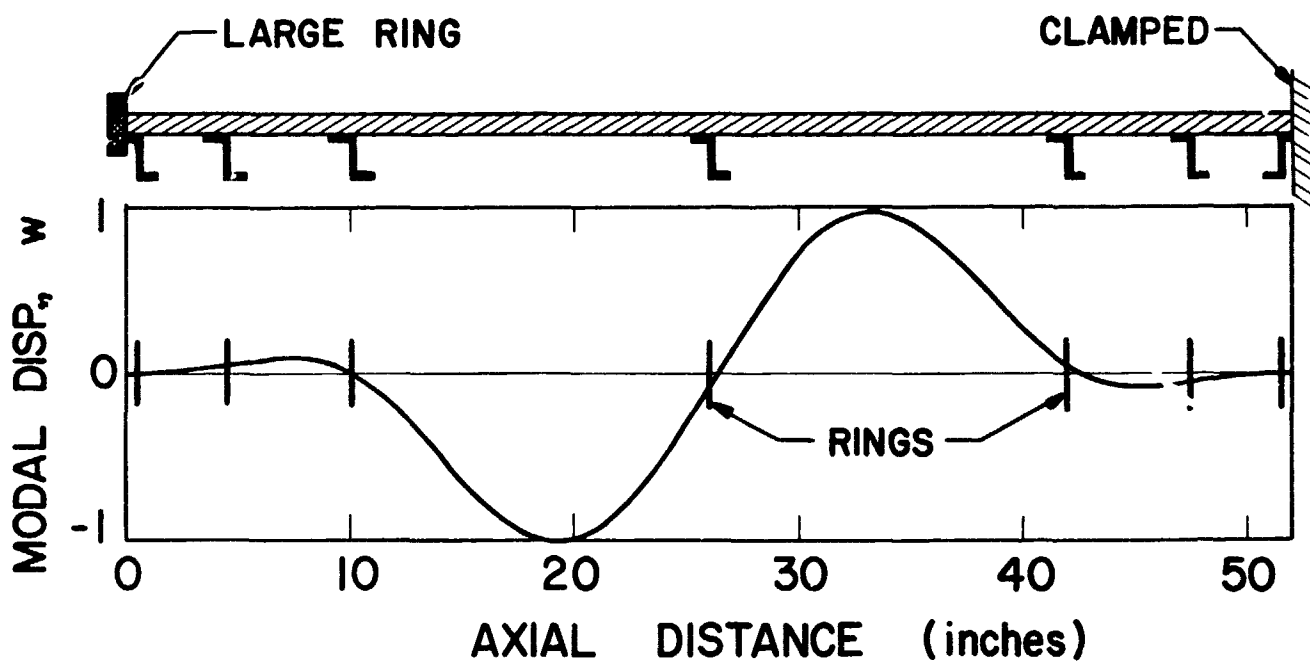


Figure 123(b) Theoretical buckling mode for specimen photographed in previous figure corresponding to $n_{cr} = 13$ circumferential waves at $N_{cr}(\text{BOSOR4}) = 2800 \text{ lb/in.}$ (from Bushnell [3]).

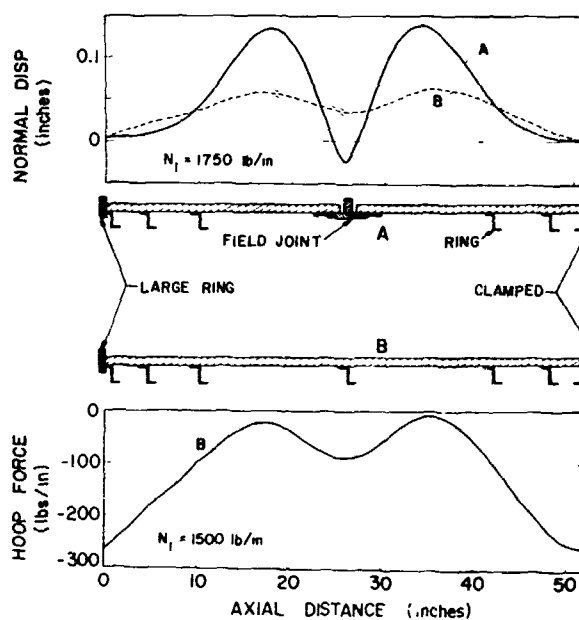
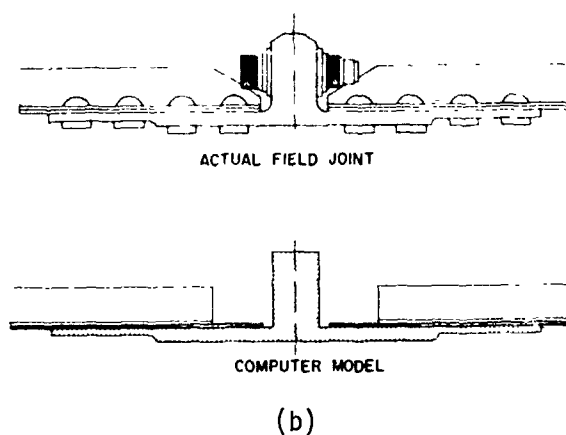
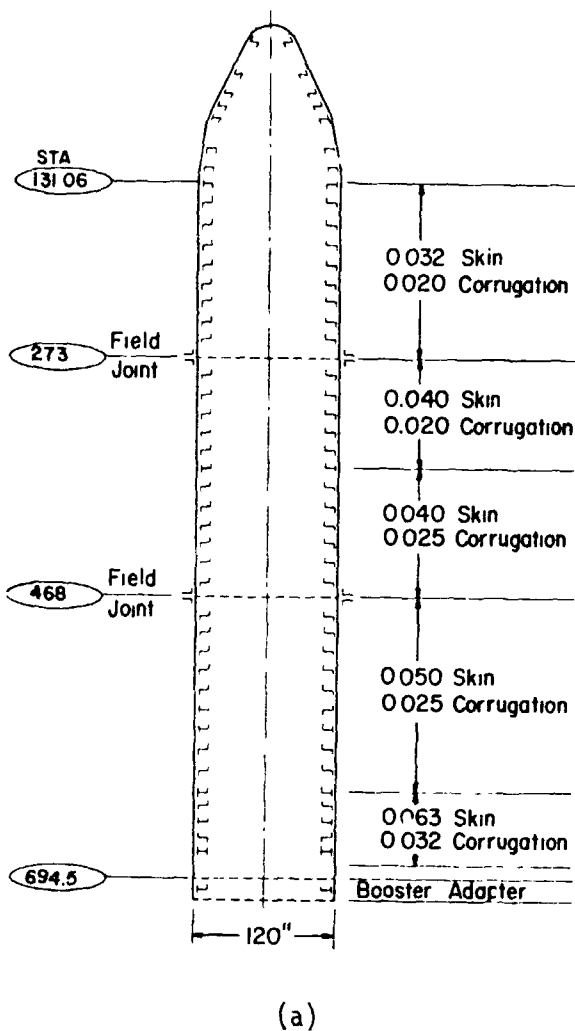
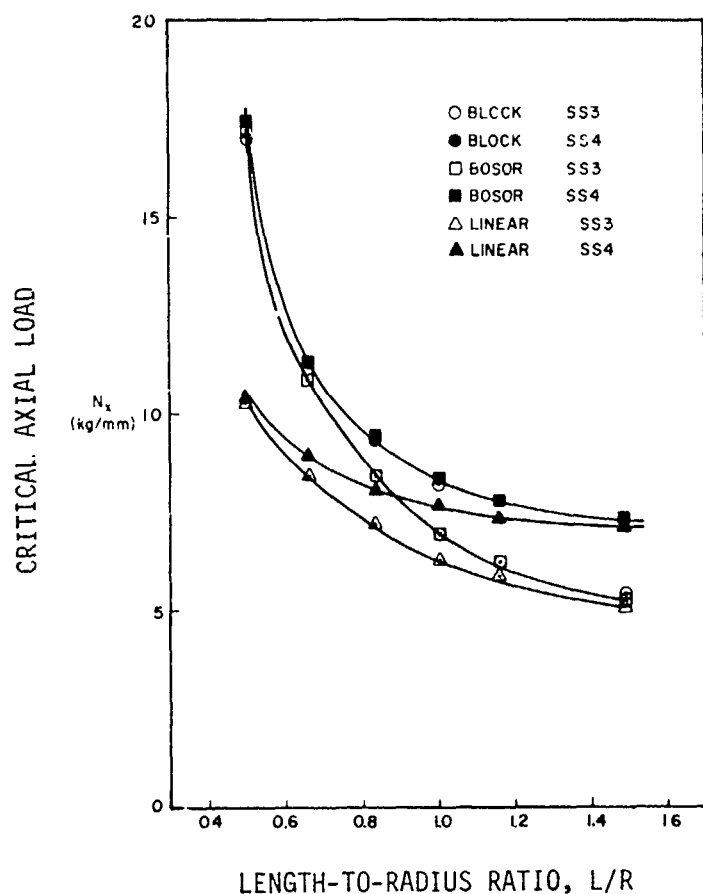


Figure 125 (a) Typical ring-stiffened shroud configuration.
 (b) Actual typical field joint geometry and simplified computer model.
 (c) 60-in.-radius x 52-in.-long panel with field joint and $t = 0.020$ in., $t_s = 0.032$ in. crippled near the bottom under uniform axial compression. $N_{cr} = 1620$ lb/in.
 (d) Theoretical prebuckling behavior of 60-in.-radius x 52-in.-long curved panels with and without a field joint.



Stiffened Cylinder Dimensions, Boundary Conditions, Material Properties:

$$h = 0.235 \text{ mm (shell wall thickness)}$$

$$R/h = 513$$

$$e_1/h = 3.76 \text{ (stringer eccentricity)}$$

$$A_1/bh = 0.779 \text{ (stringer area parameter)}$$

$$\text{SS3} = v = w = N_x = M_x = 0$$

$$\text{SS4} = v = w = u = M_x = 0$$

Material: Al 7075-T6

$$E = 0.75 \times 10^4 \text{ kg/mm}^2$$

$$\nu = 0.3$$

$$b = \text{stringer spacing}$$

Figure 126 Effect of length on buckling of axially compressed stringer stiffened cylindrical shell (from Weller, Singer and Batterman [156]).

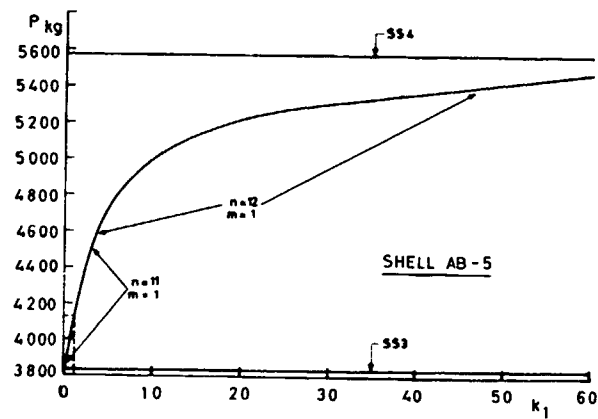


Figure 127 Influence of elastic axial restraint k_1 on the buckling load of shell AB5 (from Singer and Abramovich [33]).

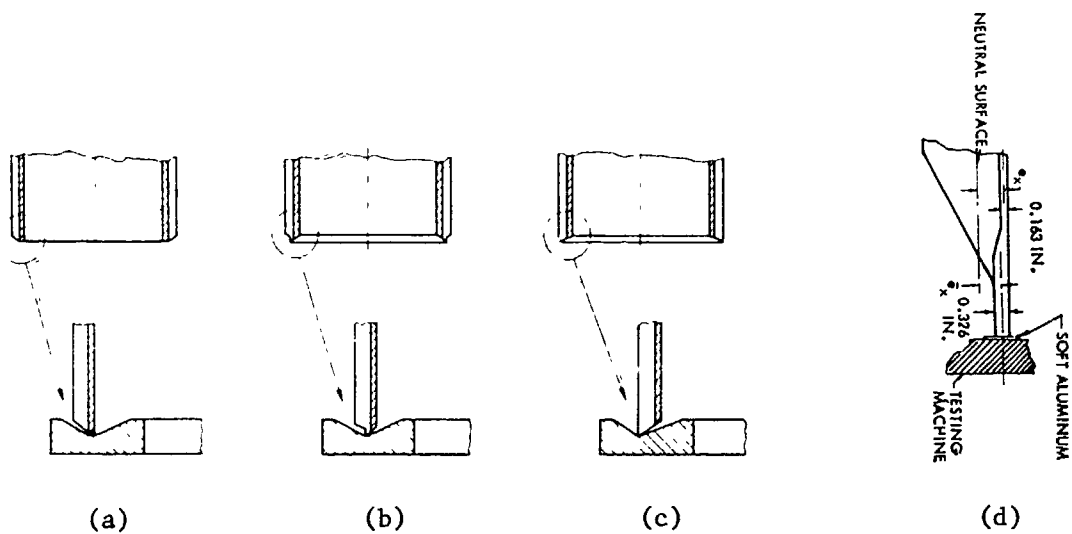
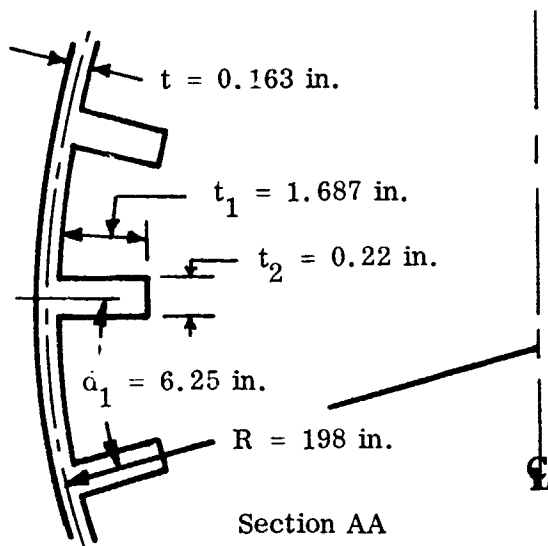


Figure 128 How eccentric loading of axially compressed, stringer-stiffened cylindrical shells is induced in tests:

- (a) load applied through midskin
- (b) load applied through intermediate point
- (c) load applied through stringer tips
- (d) typical test specimen end

(adapted from Singer and Rosen [157] and Stuhlman et al. [161]).



$$E = 10^7 \text{ psi}$$

$$\nu = 0.3$$

Length: 95 in. unless otherwise specified

Boundary Conditions: S2 (Table 8) unless otherwise specified.

Figure 129 Geometry of cylindrical shell wall.

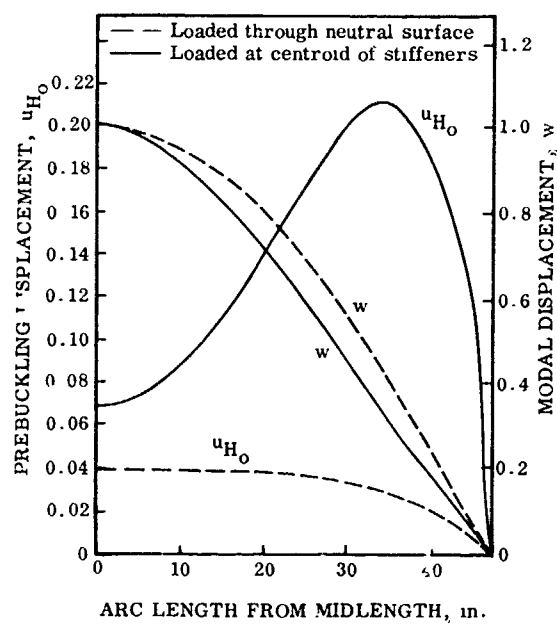


Figure 130 Prebuckling and buckling displacements of an internally-stiffened, simply-supported, axially-compressed cylinder.

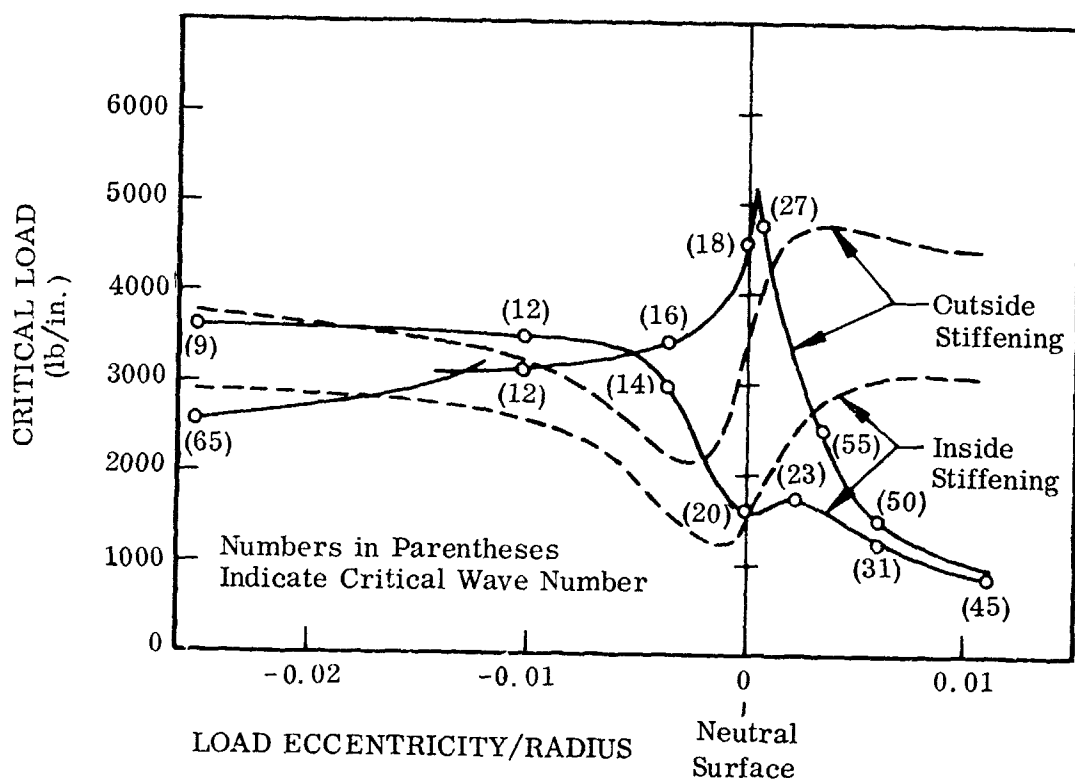


Figure 131 Critical loads for axially-compressed, stiffened cylinders with eccentrically-applied load and S1 (SS4) boundary conditions (dotted curves for membrane prebuckling theory).

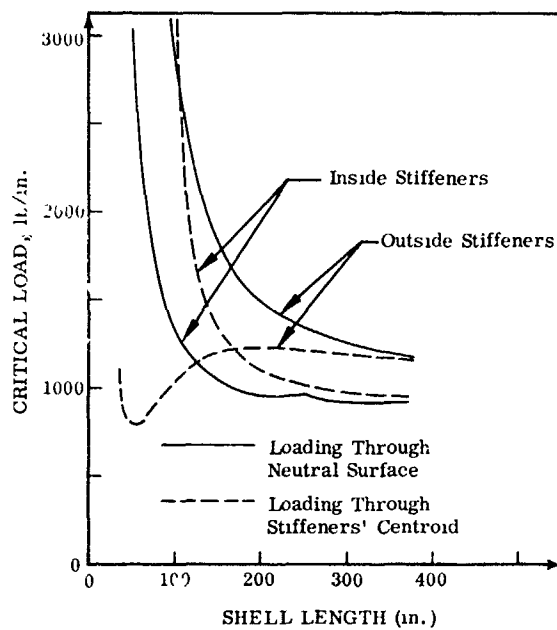


Figure 132 Critical load vs. length for axially-compressed, stiffened cylinders with S2 boundary conditions.

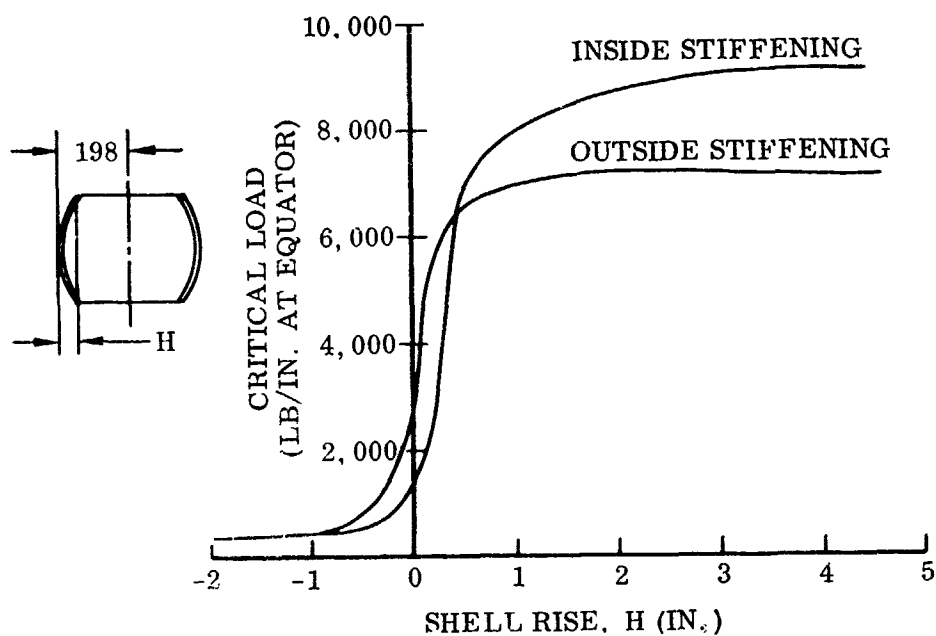


Figure 133 Critical axial load for shallow toroidal shell segments as a function of shell rise H.



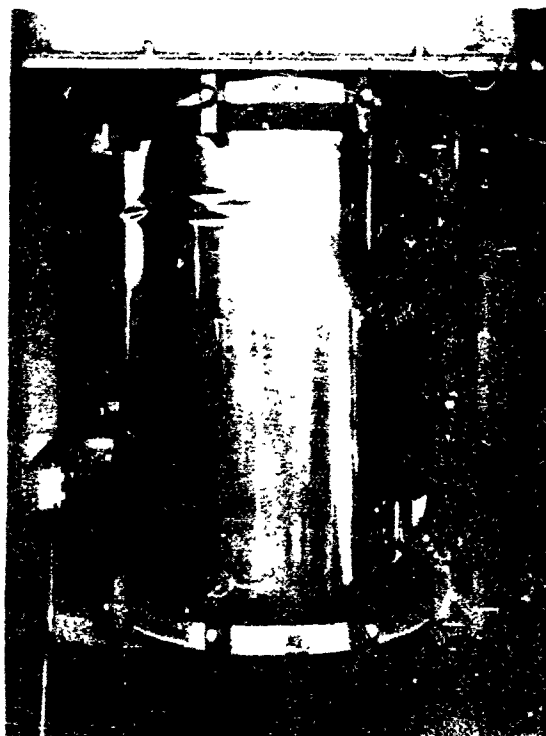
(a)



(b)

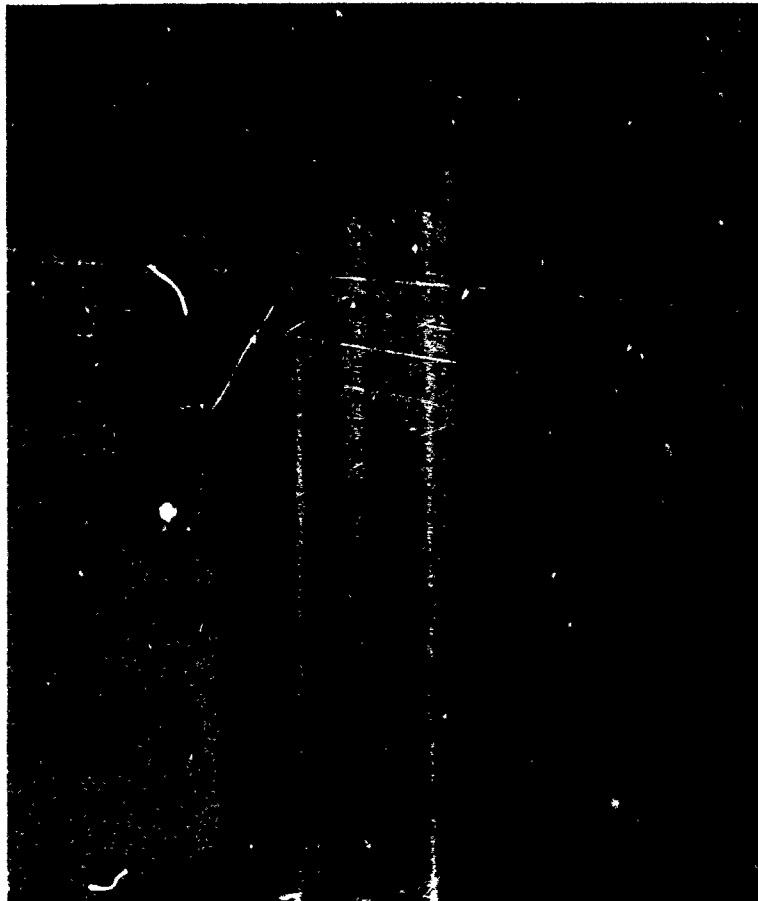


(c)



(d)

Figure 13-(a-d) Post-buckled states of axially compressed cylinders with (a) no, (b) low, (c) moderate, and (d) high internal pressure ((a,b,d) from Suet et al [165], (c) from Harris et al. [166]).

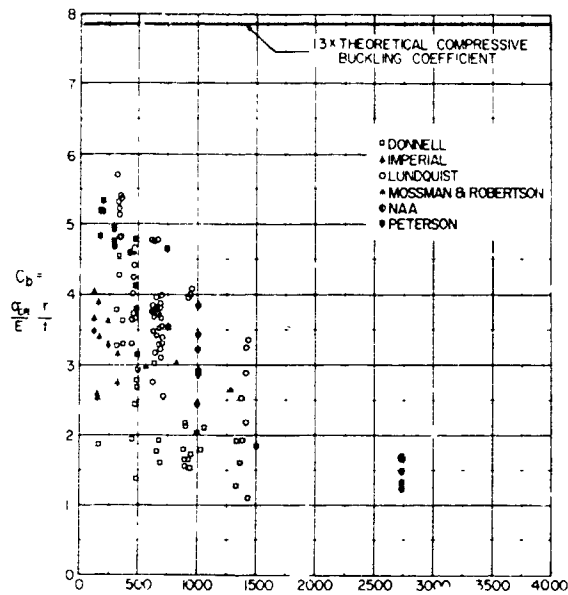


(e)

(from Horton et al. [38])

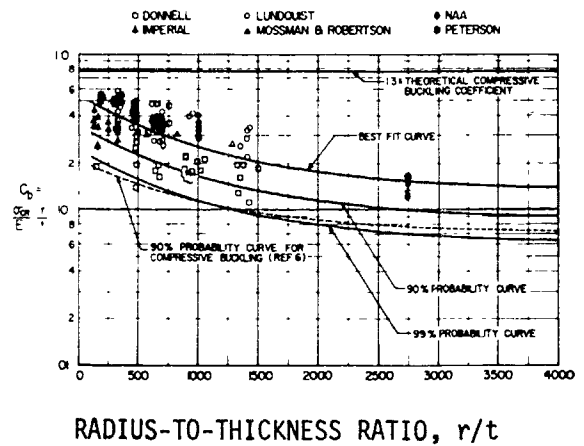
Figure 134 (cont'd) Post-buckled state of axially compressed cylinder with very high internal pressure. Unlike examples a-d, buckling in this case is elastic-plastic, which results in a protruding rather than in indenting buckle. [Compare with 134(d). Also, compare Figures 90 and 96 for differences between elastic and elastic-plastic buckling.]

BUCKLING AXIAL STRESS COEFFICIENT



RADIUS-TO-THICKNESS RATIO, r/t

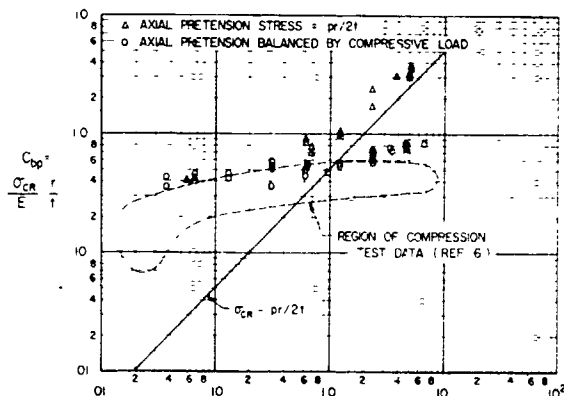
(a)



RADIUS-TO-THICKNESS RATIO, r/t

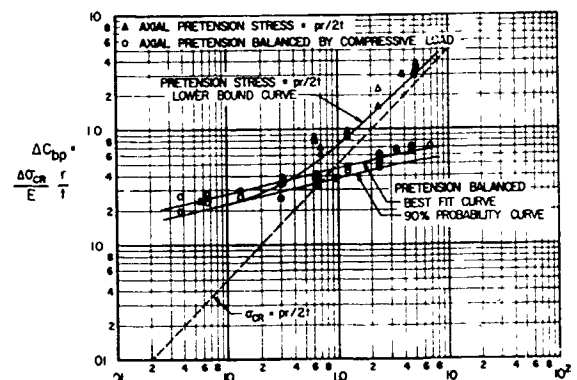
(b)

BUCKLING AXIAL STRESS COEFFICIENT



INTERNAL PRESSURE, $p/E(r/t)^2$

(c)

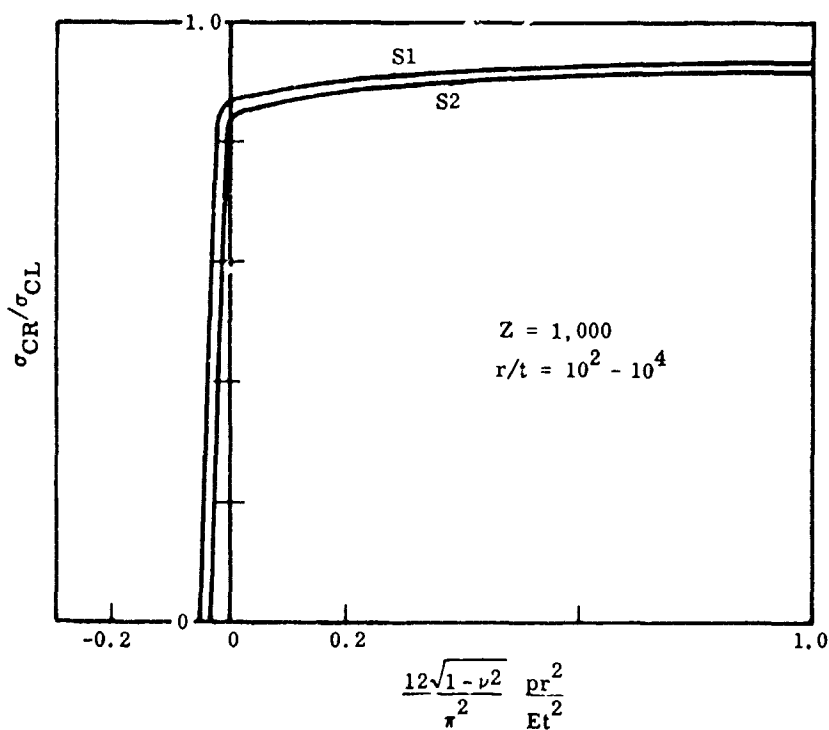
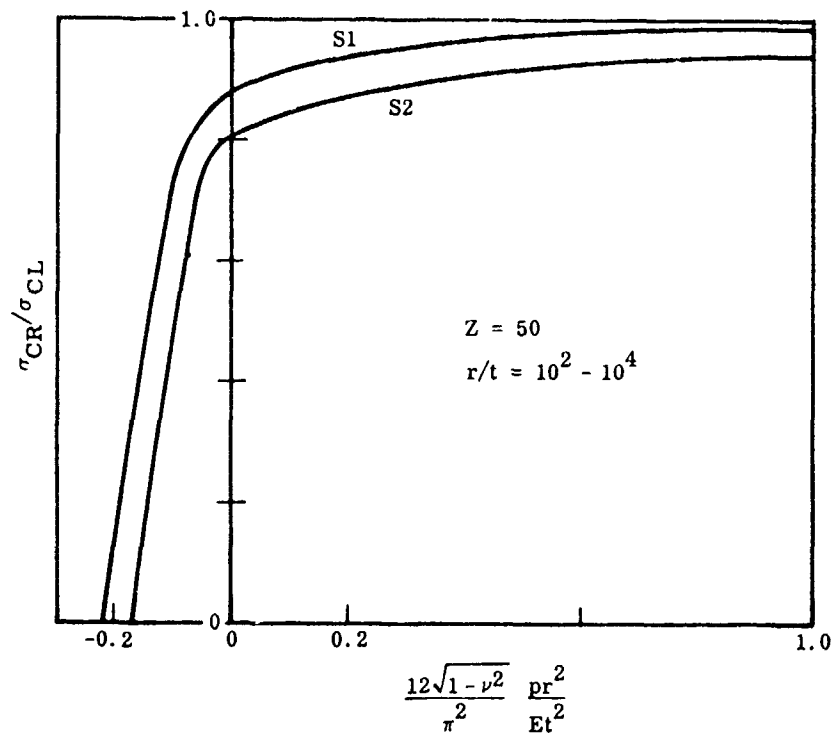


INTERNAL PRESSURE, $p/E(r/t)^2$

(d)

Figure 135 Test results and buckling probability curves for monocoque cylindrical shells under combined bending and internal pressure: (a) unpressurized bending buckling stress coefficients as a function of r/t ; (b) unpressurized bending buckling stress coefficients as a function of r/t with buckling probability curves; (c) bending buckling stress coefficients for pressurized circular cylinders; and (d) increase in bending buckling stress coefficients ΔC_{bp} due to internal pressure (from Suer et al. [165]).

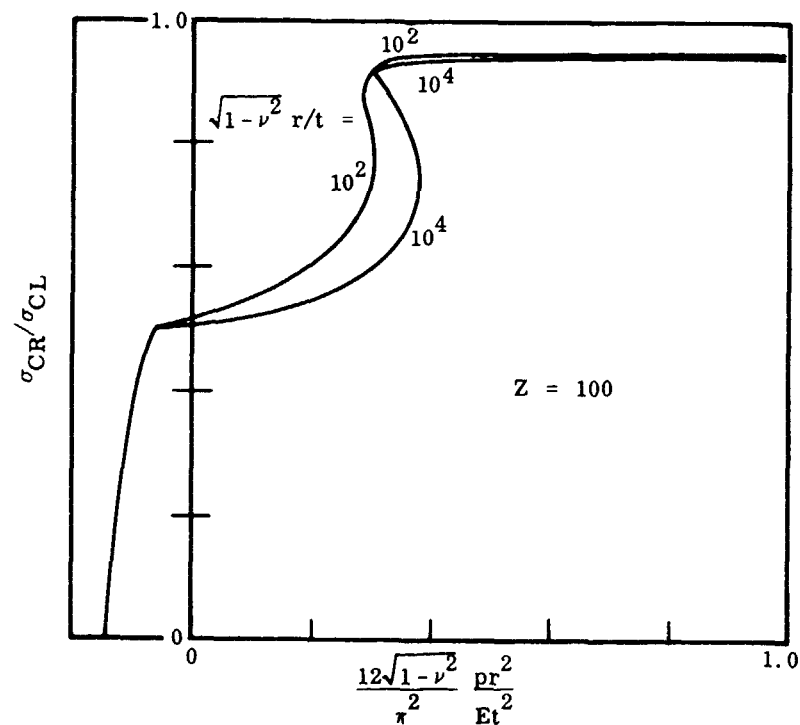
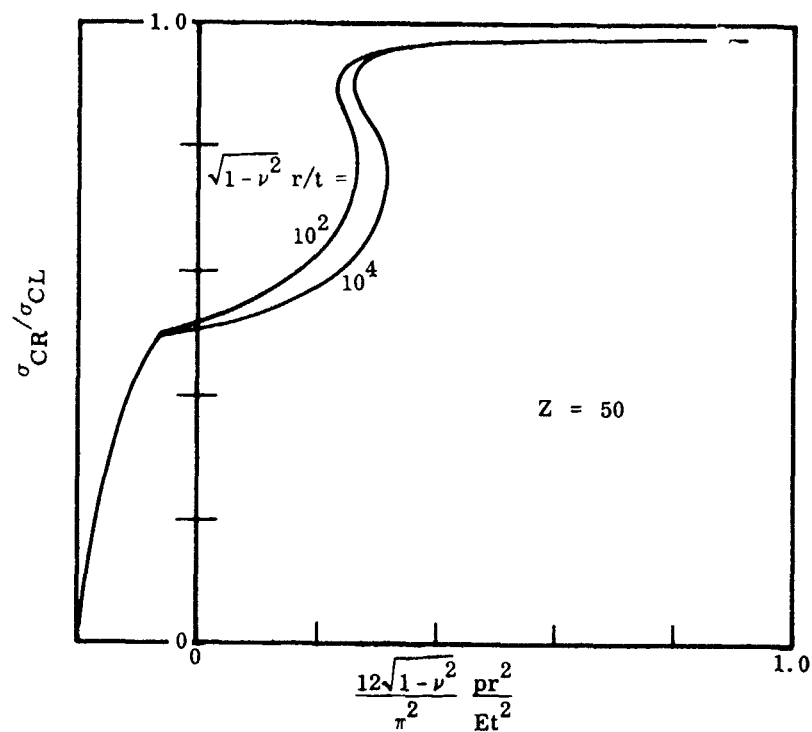
CRITICAL AXIAL STRESS



LATERAL PRESSURE

Figure 136 Interaction curves for simply-supported ($\nu=0$) monocoque cylindrical shells with combined axial compression and lateral pressure (S1 and S2 boundary conditions; see Table 8) (from Almorth [152]).

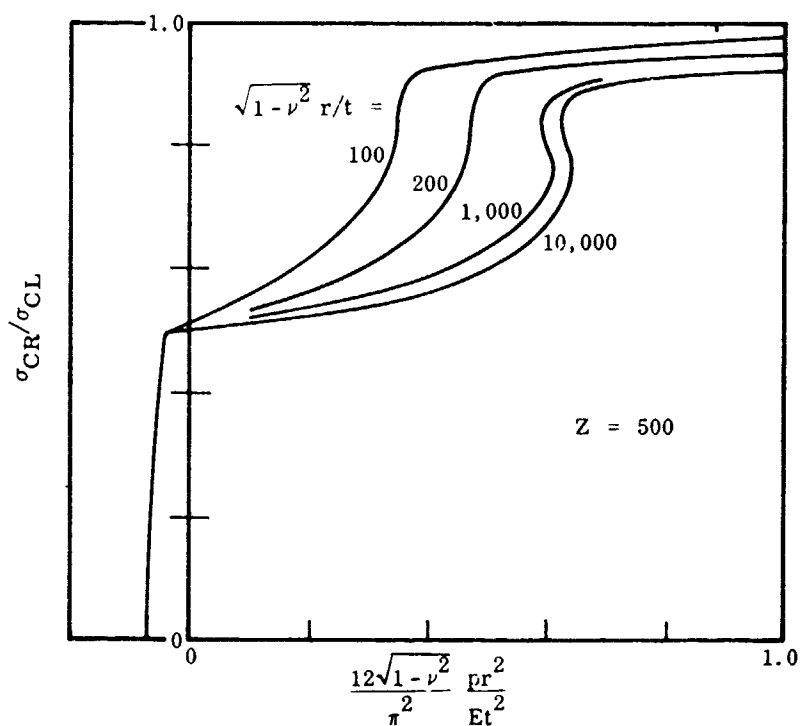
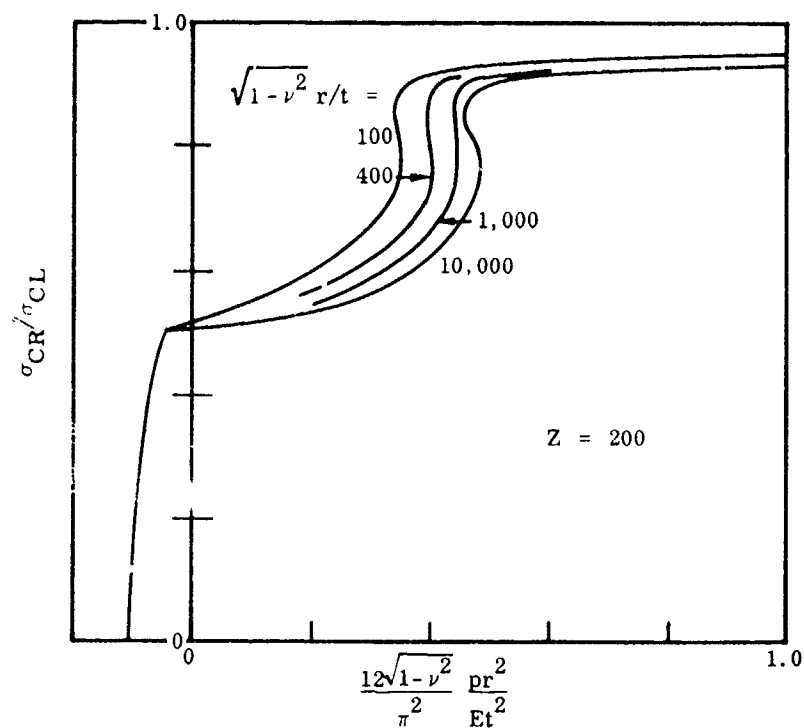
CRITICAL AXIAL STRESS



L A T E R A L P R E S S U R E

Figure 137(a) Interaction curves for simply-supported ($u=0$, $v=\text{free}$) monocoque cylindrical shells with combined axial compression and lateral pressure (S3 boundary conditions) (from Almroth [152]).

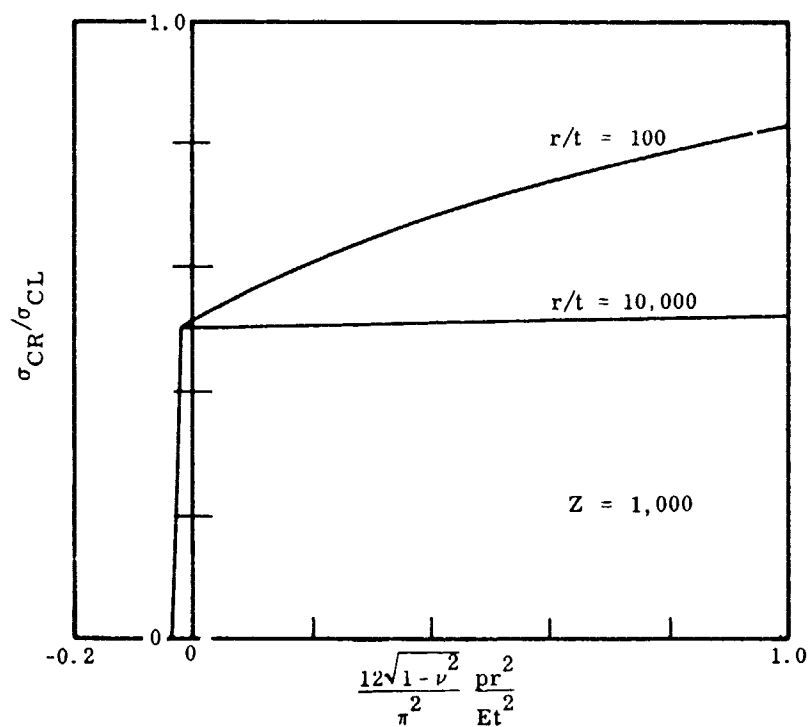
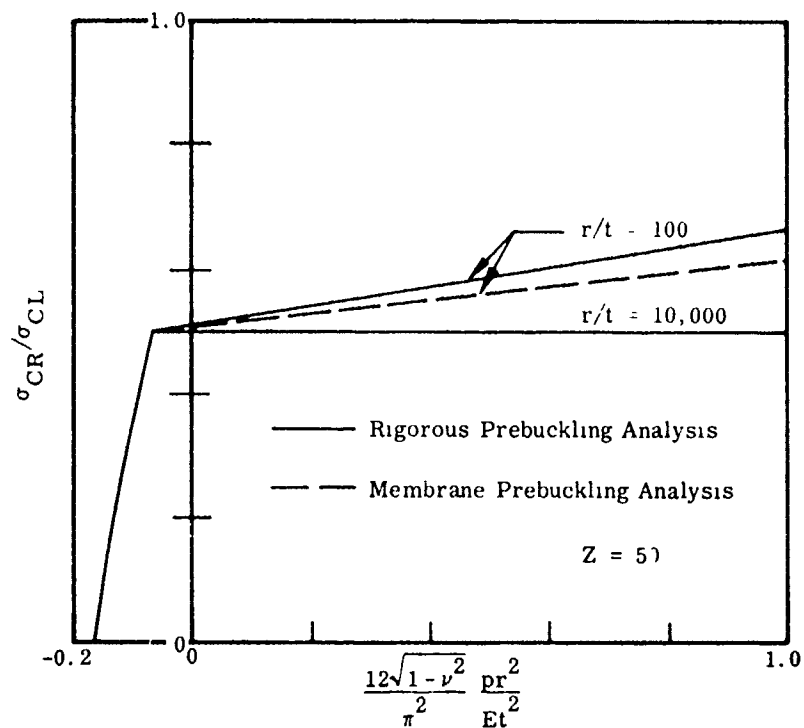
CRITICAL AXIAL STRESS



LATERAL PRESSURE

Figure 137(b) Interaction curves for simply-supported ($u=0, v=\text{free}$) monocoque cylindrical shells with combined axial compression and lateral pressure (S3 boundary conditions) (from Almroth [152]).

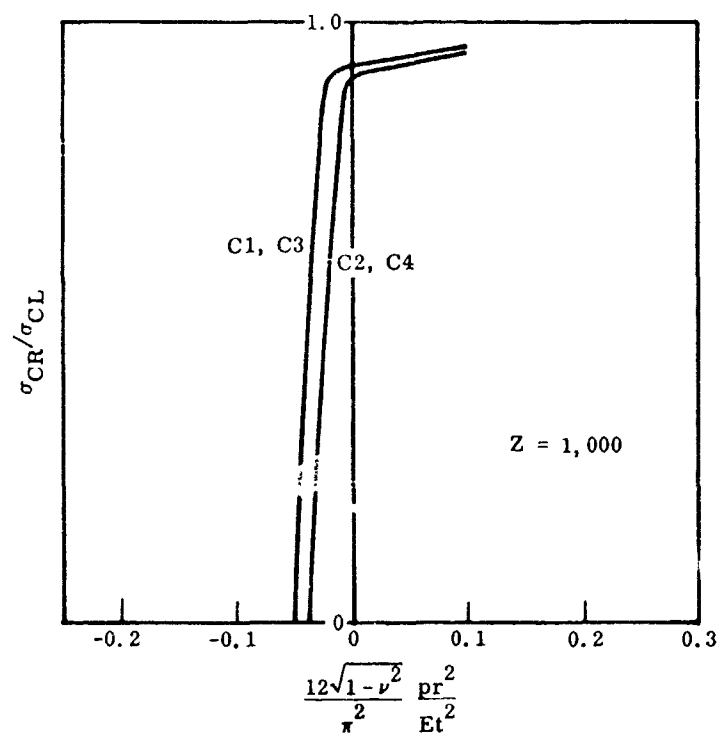
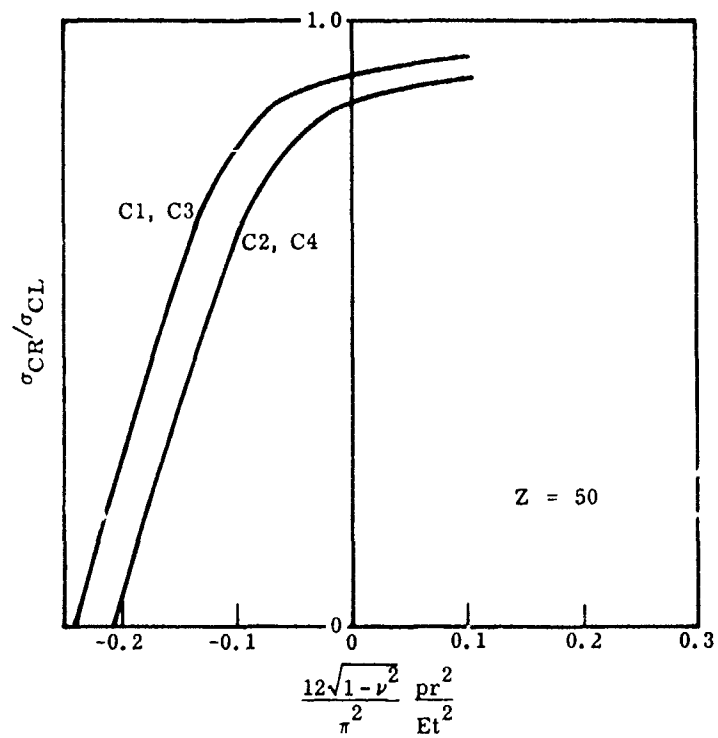
CRITICAL AXIAL STRESS



L A T E R A L P R E S S U R E

Figure 138 Interaction curves for simply-supported (u =free, v =free) monocoque cylindrical shells with combined axial compression and lateral pressure (S4 boundary conditions) (from Almroth [152]).

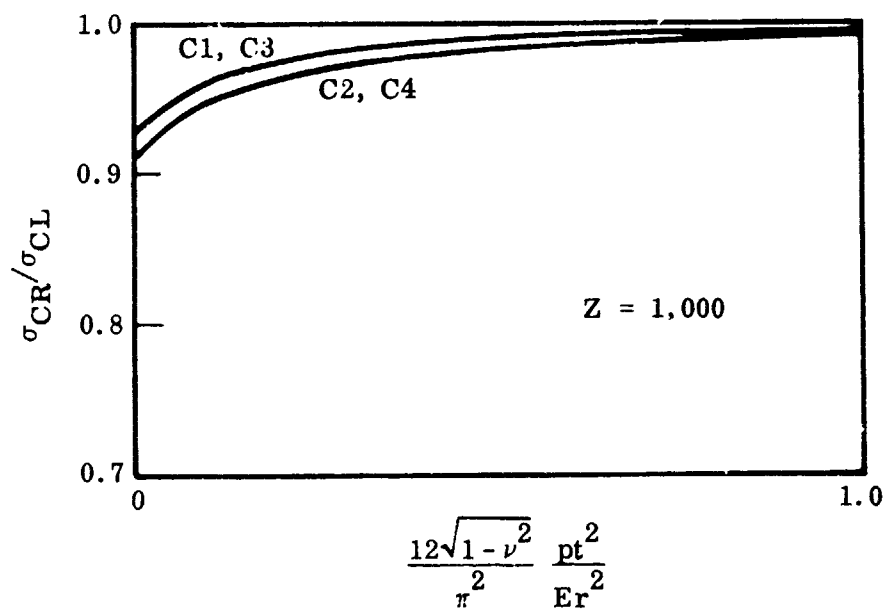
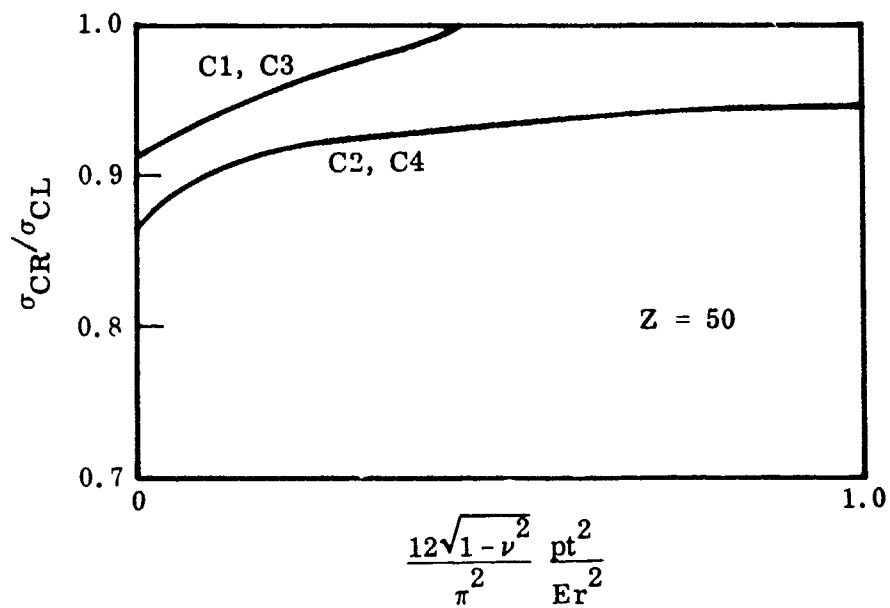
CRITICAL AXIAL STRESS



L A T E R A L P R E S S U R E

Figure 139(a) Interaction curves for clamped monocoque cylinders with combined axial compression and external lateral pressure. Radius-to-thickness $10^2 \leq r/t \leq 10^4$ (from Almroth [152]).

CRITICAL AXIAL STRESS



L A T E R A L P R E S S U R E

Figure 139(b) Interaction curves for clamped monocoque cylinders with combined axial compression and internal lateral pressure. Radius-to-thickness $10^2 \leq r/t \leq 10^4$ (from Almroth [152]).



(a)



(b)

Figure 140 Post-buckled patterns for cylinders under torsion: (a) no internal pressure; (b) with internal pressure (from Harris et al. [36]).

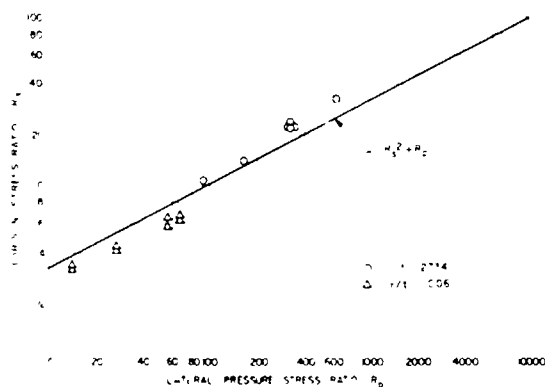
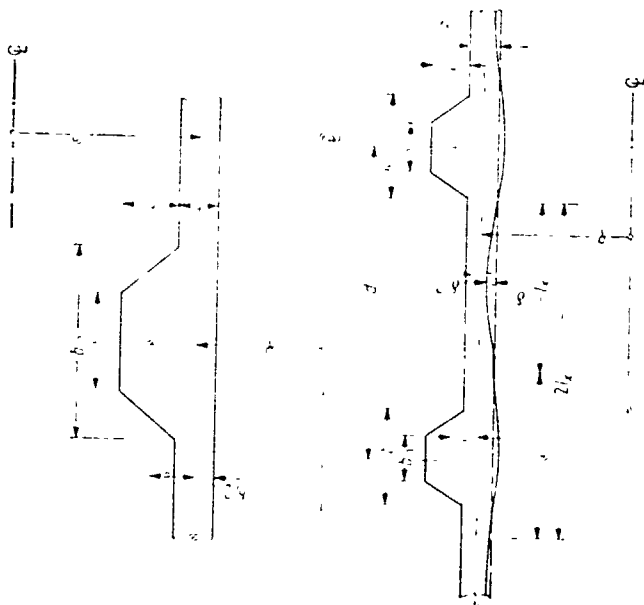
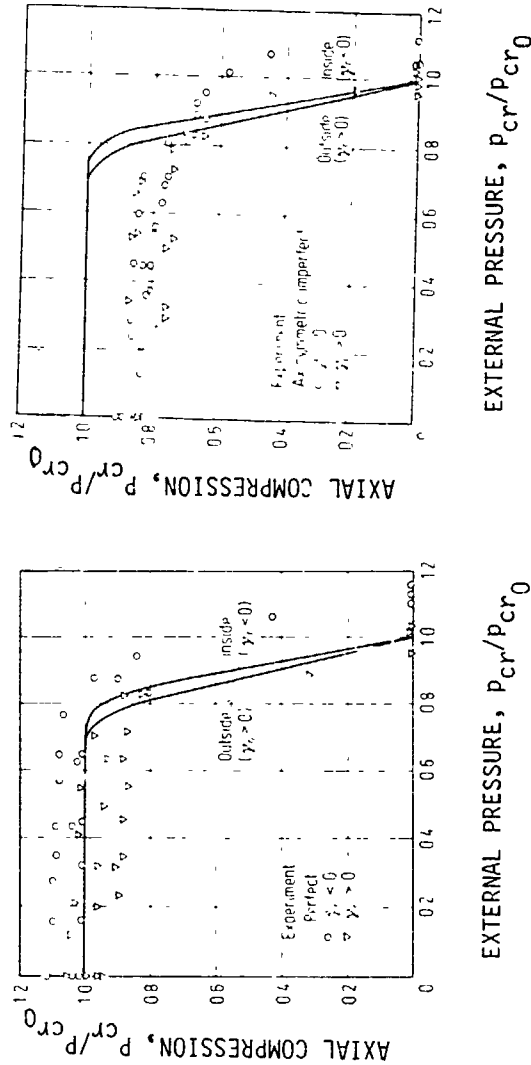


Figure 141 Interaction curve for monocoque cylinders in torsion with lateral internal pressure (from Harris et al. [36]).



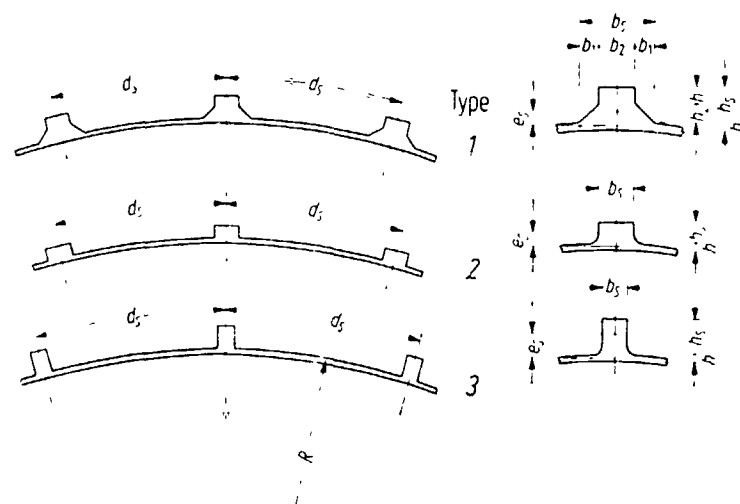
(a) Details of ring geometry.



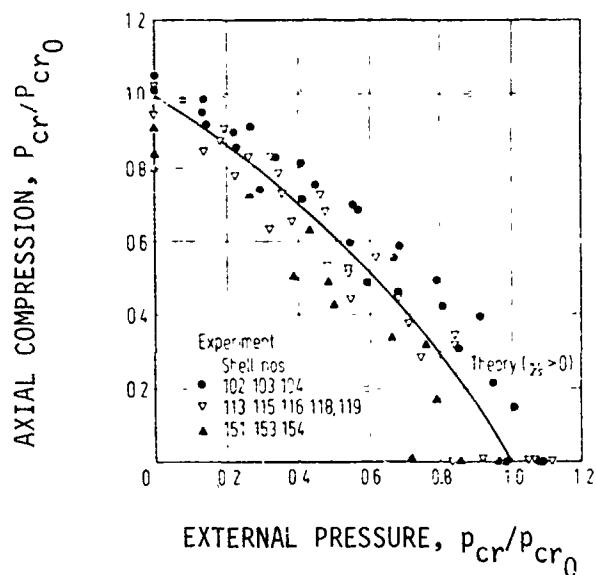
(b) "Perfect" specimens (P_{cr0} and p_{cr0} represent respectively critical axial load with no pressure and critical pressure with no axial load).

(c) Axisymmetrically imperfect specimens.

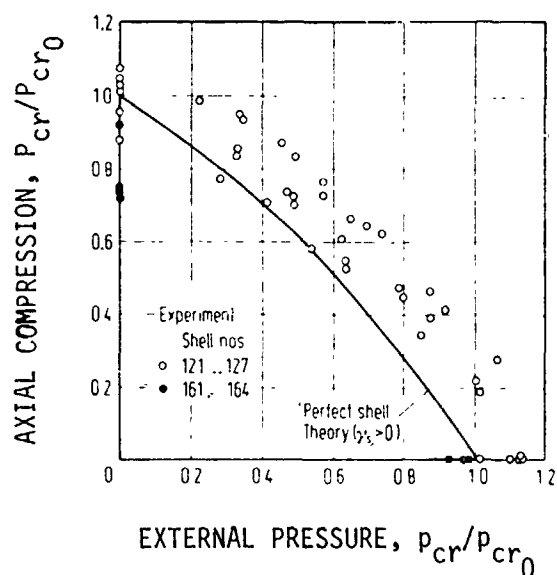
Figure 142 Comparison of test and theory for elastic buckling of "perfect" and axisymmetrically imperfect ring-stiffened, clamped cylindrical shells under combined axial compression and external hydrostatic pressure (from Tennyson [130]).



(a) Details of stringer geometry.

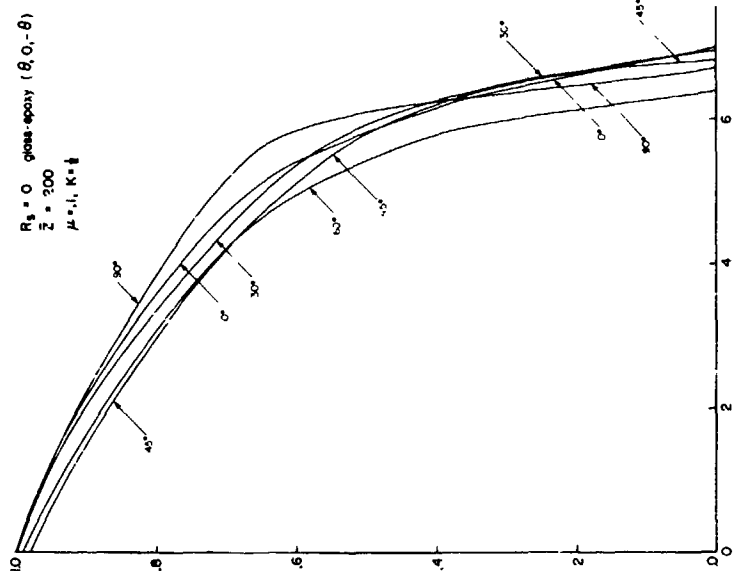


(b) "Perfect" specimens.



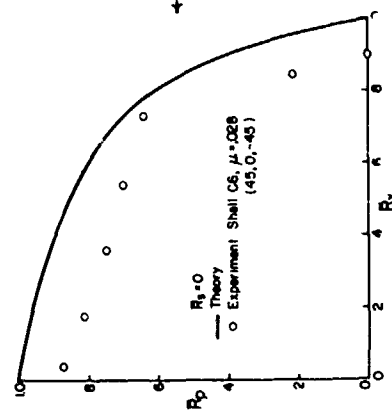
(c) Imperfect specimens (open circles represent axisymmetrically imperfect specimens).

Figure 143 Comparison of test and theory for elastic buckling of "perfect" and imperfect stringer-stiffened, clamped cylindrical shells under combined axial compression and external hydrostatic pressure (from Tennyson [170]).



AXIAL COMPRESSION RATIO, $R_x = P_{cr}/P_{cr0}$
 (a) Perfect cylinders (theory)

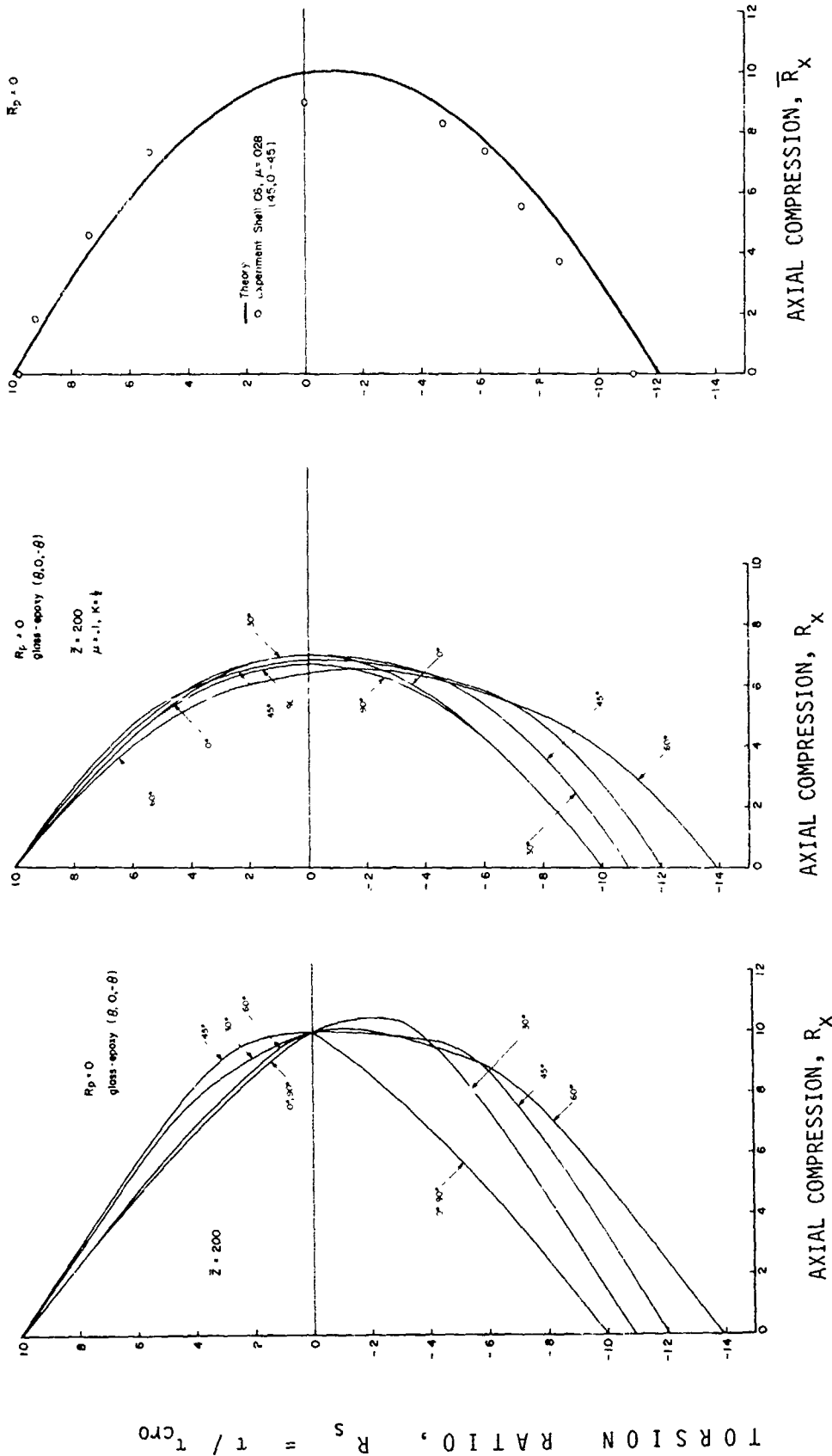
AXIAL COMPRESSION RATIO, $R_x = P_{cr}/P_{cr0}$
 (b) Axisymmetrically imperfect cylinders (theory)



(c)

Comparison of test and theory for imperfect cylinders. $\bar{R}_x = \bar{P}_{cr}/\bar{P}_{cr0}$, in which the bars indicate critical loads for the imperfect cylinders.

Figure 144 Interaction curves for 3-layered $(\theta, 0, -\theta)$ composite glass-epoxy cylindrical shells under combined external pressure and axial compression (from Booton and Tennyson [192]).

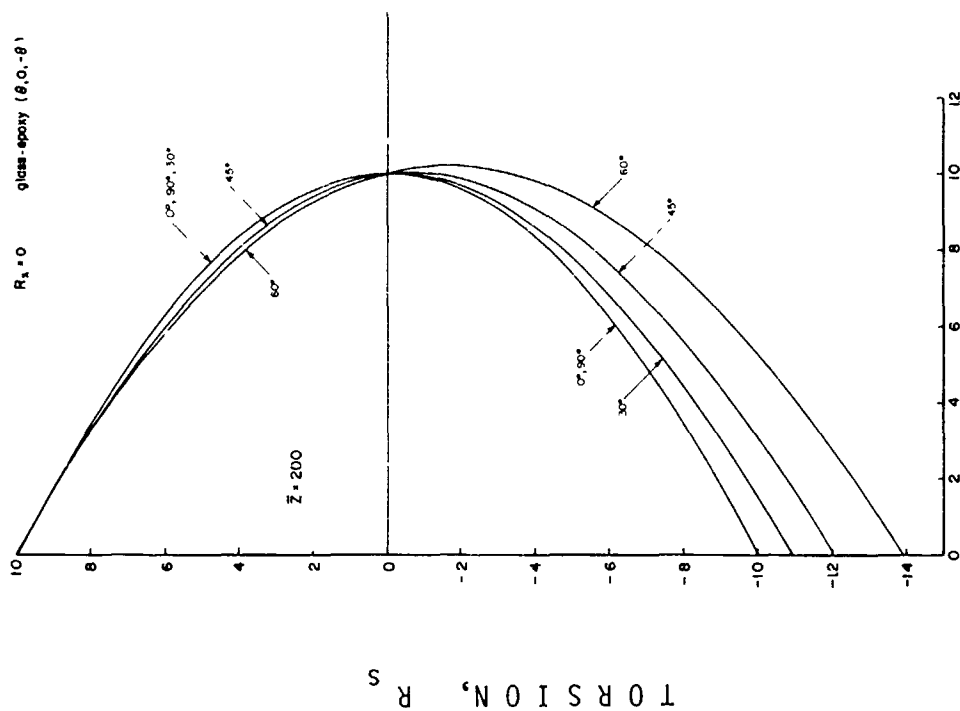


(a) perfect cylinders (theory)

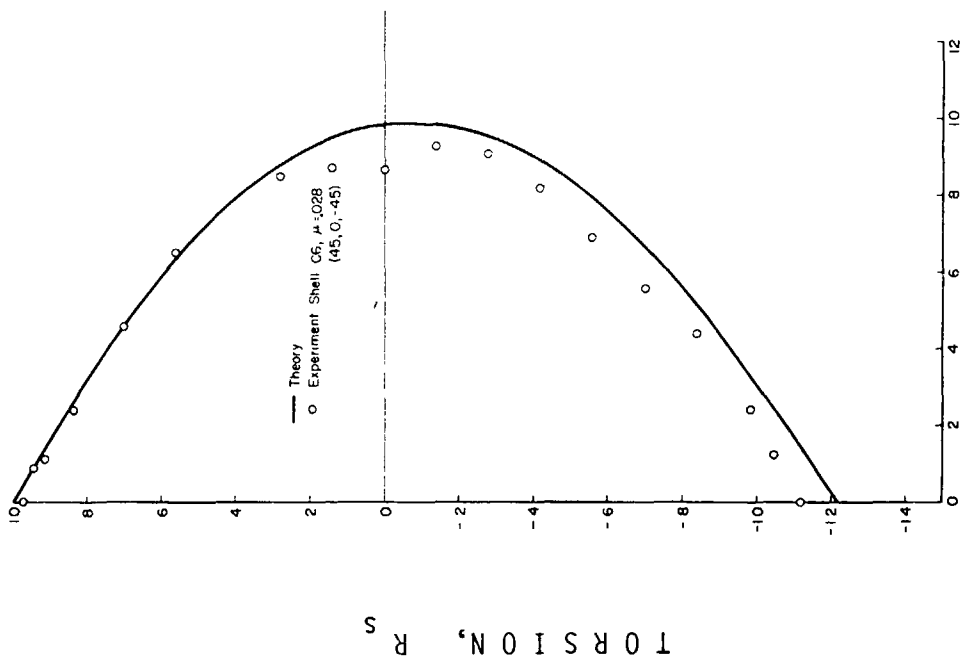
(b) axisymmetrically imperfect cylinders (theory)

(c) Comparison of test and theory for imperfect cylinders. R_x is defined in Figure 144(c).

Figure 145 Interaction curves for 3-layered (0,0,-0) composite glass-epoxy cylindrical shells under combined torsion and axial compression (from Booton and Tennyson [192]).



(a) Perfect cylinders (theory)



(b) Comparison of test and theory for imperfect cylinders

Figure 146 Interaction curves for 3-layered $(\theta, 0, -\theta)$ composite glass-epoxy cylindrical shells under torsion and external pressure (from Booton and Tennyson [192]). $\bar{R}_p = \bar{p}_{cr}/p_{cr0}$, where the bars indicate critical pressures of imperfect cylinders.

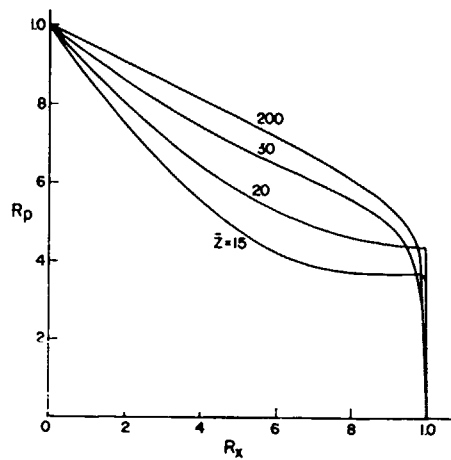


Figure 147 Effect of $Z = L^2/rt$ on interactive buckling behavior for 3-layered laminated cylinder [glass/epoxy, (45 deg., 0 deg., -45 deg.), $R/t = 100$] (from Booton and Tennyson [192]).

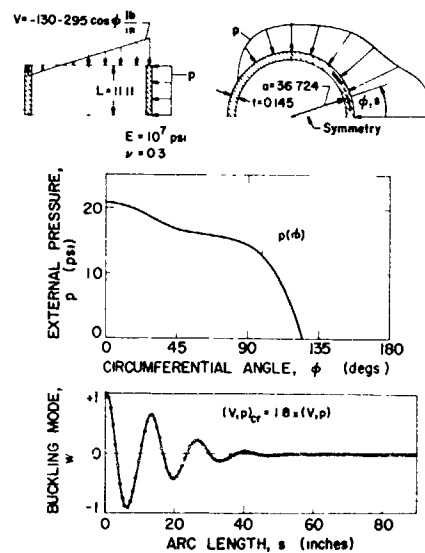


Figure 148 Buckling mode of nonuniformly-loaded, simply-supported, circular cylinder. Critical load = 1.8 times the load distribution shown. Cylinder analyzed as very slender toroidal segment (from Bushnell [82]).

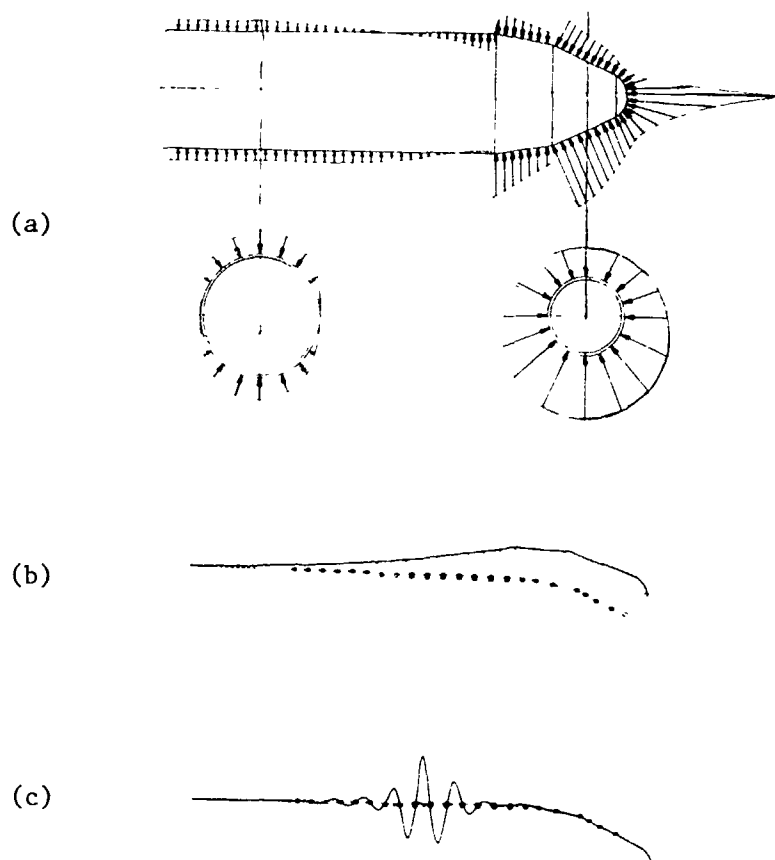


Figure 149 (a) Nonsymmetric pressure distribution on a payload shroud; (b) prebuckling beam-type deflection; (c) nonsymmetric buckling mode ($n_{cr} = 13$ circumferential waves) (from Bushnell [14]).

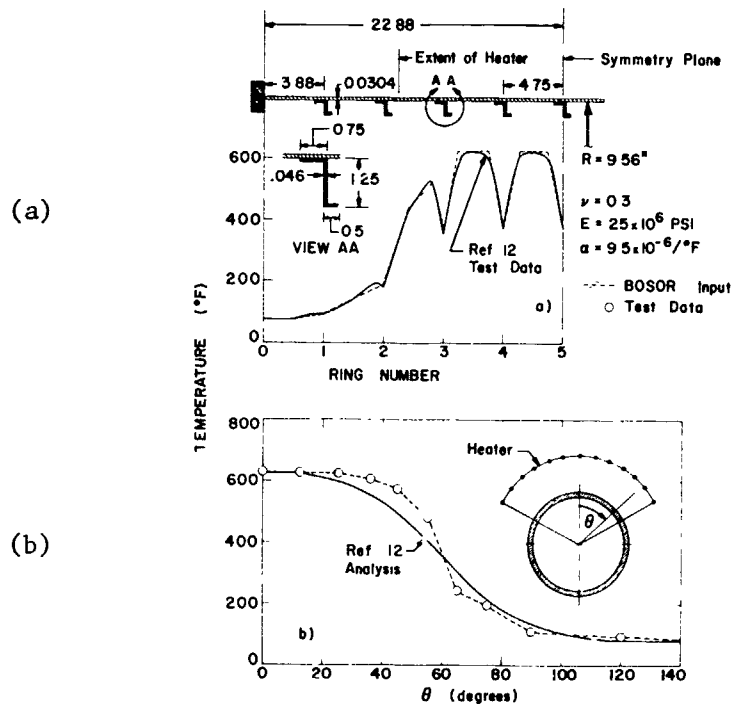


Figure 150 Critical temperature distributions for one of Anderson and Card's tests [204] on ring-stiffened cylinders under combined bending and nonuniform heating: (a) axial distribution at $\theta = 0$; (b) circumferential distribution halfway between rings 4 and 5 (adapted from Bushnell and Smith [200]).

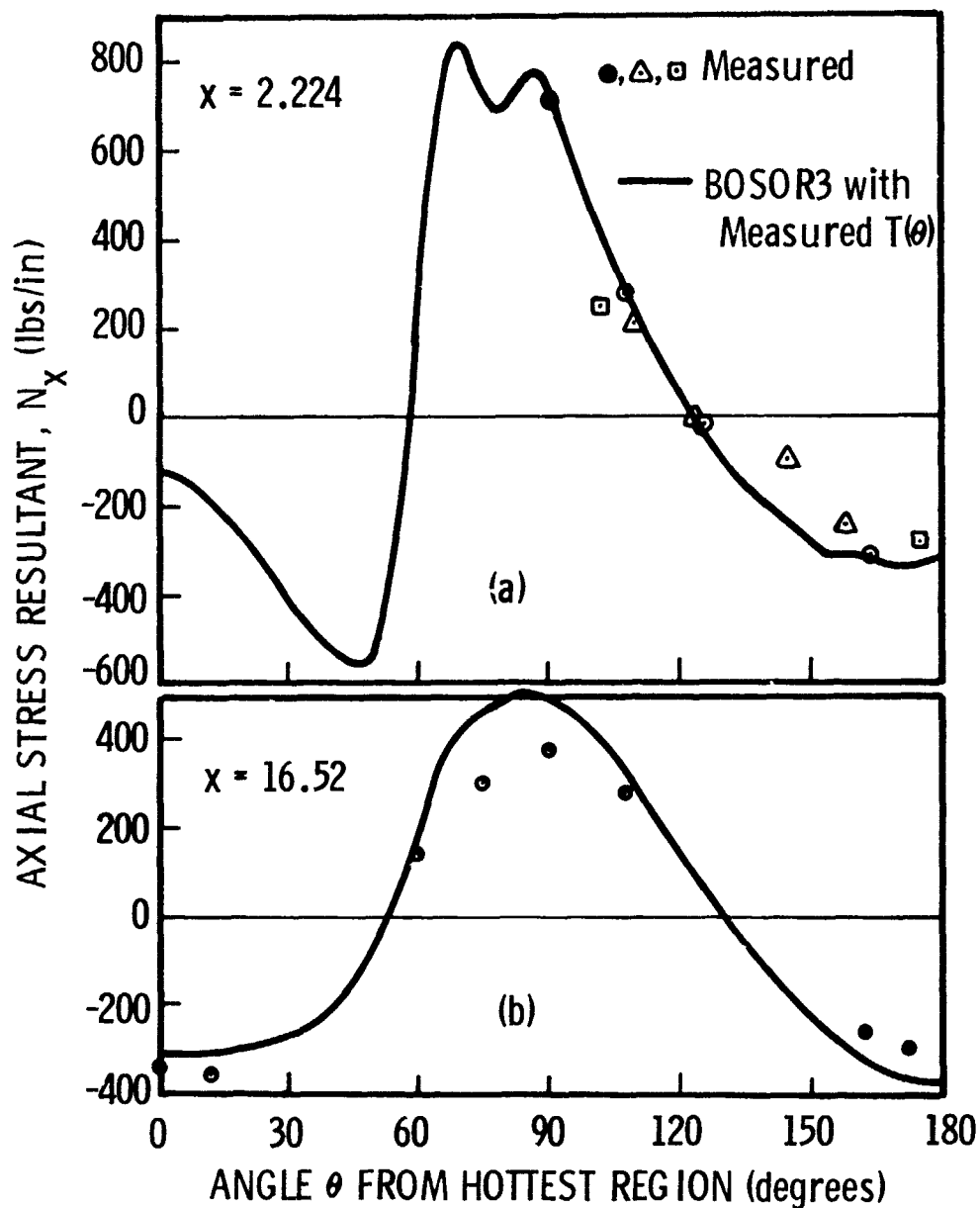


Figure 151 Axial stress resultant at (a) $x = 2.224$ and (b) $x = 16.52$ in. from symmetry plane, corresponding to cylinder and ring geometry and $T(x, \theta)$ given in Figure 150 (adapted from Bushnell and Smith [200]).

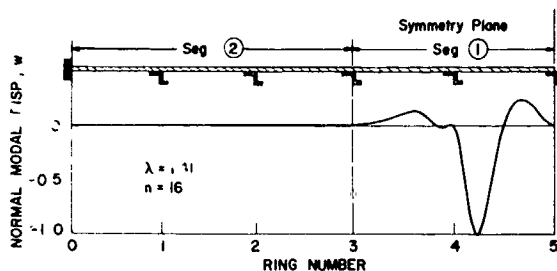


Figure 152 Bifurcation buckling mode with $n_{cr} = 16$ circumferential waves for ring-stiffened cylinder under combined bending and nonuniform heating. The predicted critical load combination is $\lambda = 1.41$ times that measured in a test by Anderson and Card [204]. In the BOSOR analysis the prebuckling membrane stress state at circumferential station $\theta = 40^\circ$ was used in the stability phase of the problem. The total prebuckling axial compression N_x on this meridian was $N_x = -19.1 \cos 40^\circ + N_x$ (thermal at $\theta = 40^\circ$) (from Bushnell and Smith [200]).

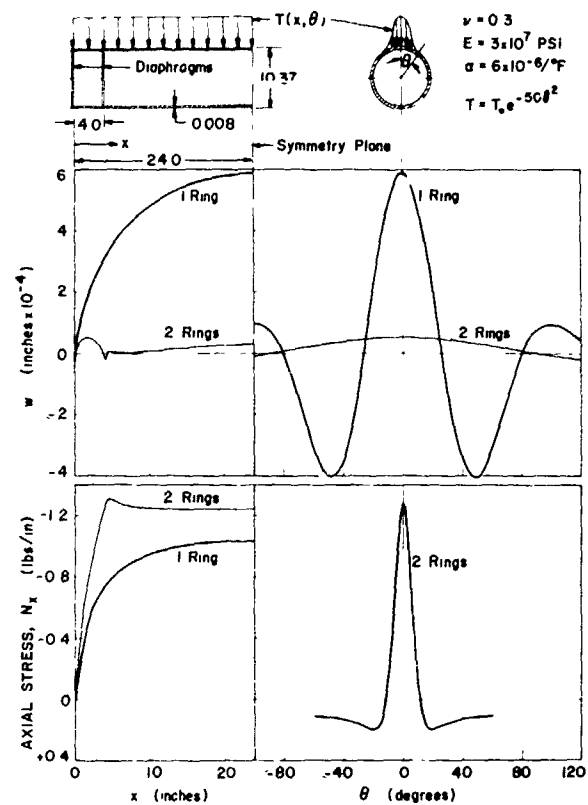


Figure 153 Theoretical axial and circumferential distributions of normal outward displacement and axial stress resultant for cylinders heated on a narrow axial strip with one and two diaphragms ("rings") at each end. $T_0 = 1^\circ\text{F}$ (from Bushnell and Smith [200]).

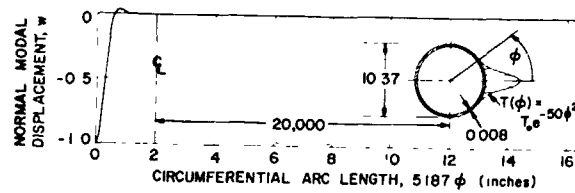


Figure 154(a) Circumferential variation of buckling mode corresponding to critical temperature rise $T_0 = 194^\circ\text{F}$. Axial half-wavelength of buckles is 0.34 in. Cylinder analyzed as slender torus with radius of 20,000 in. (from Bushnell and Smith [200]).

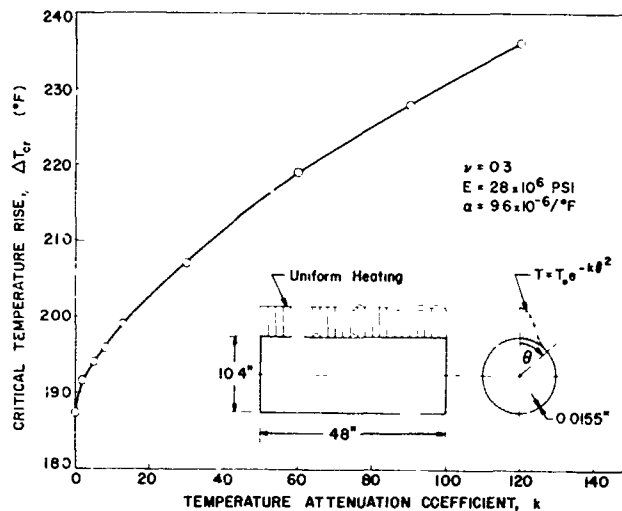


Figure 154(b) Theoretical critical temperature rise vs. width of uniformly heated strip for clamped cylinders (from Bushnell and Smith [200]).

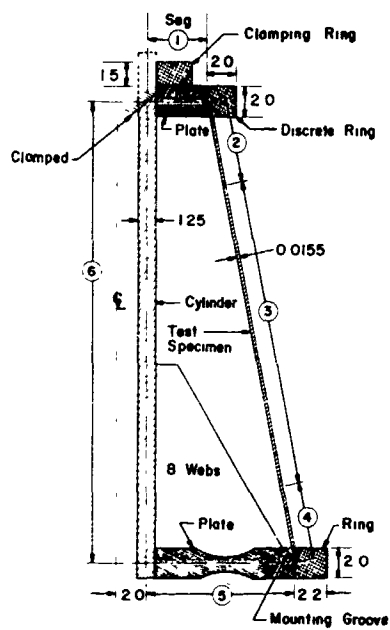


Figure 155(a) Schematic of conical shell in test rig, analyzed with the BOSOR4 program as a six-segment structure. In tests by Smith [210] the conical shell was heated along a narrow axial strip (from Bushnell and Smith [200]).

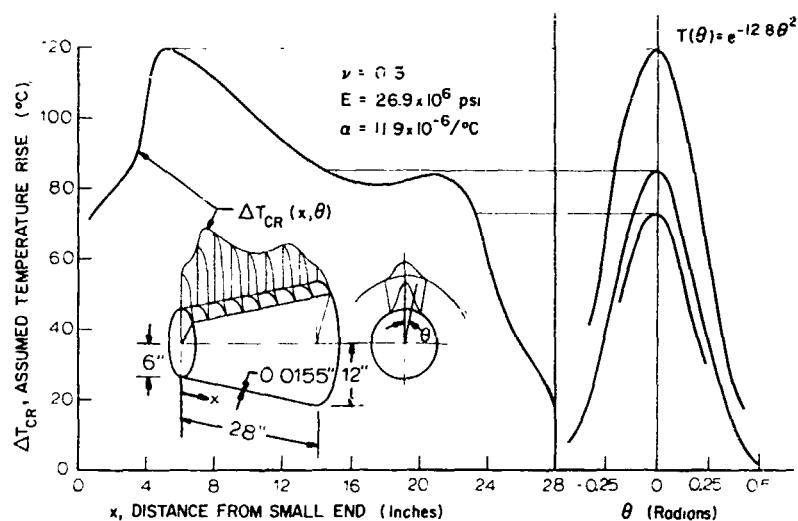


Figure 155(b) Axial and circumferential temperature distributions at buckling for one of Smith's tests (from Bushnell and Smith [200]).

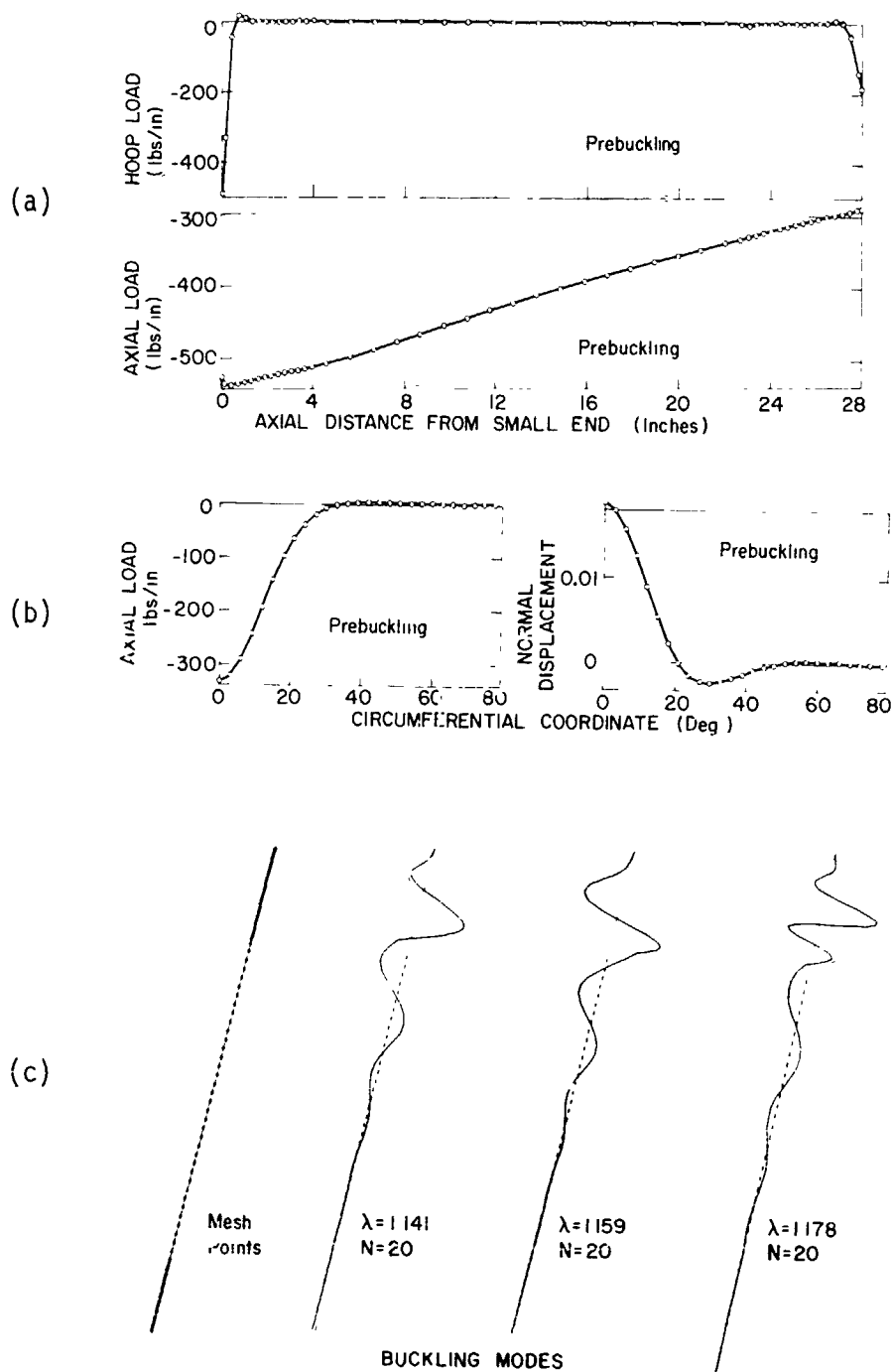


Figure 155(c) Buckling of thin conical shell heated along a narrow axial strip: (a) prebuckling membrane resultants along the "worst" meridian ($\theta=0$); (b) circumferential variation of prebuckling state; (c) discretized model of generator and three bifurcation buckling modes corresponding to $n_{cr} = 20$ circumferential waves (from Bushnell [14]).

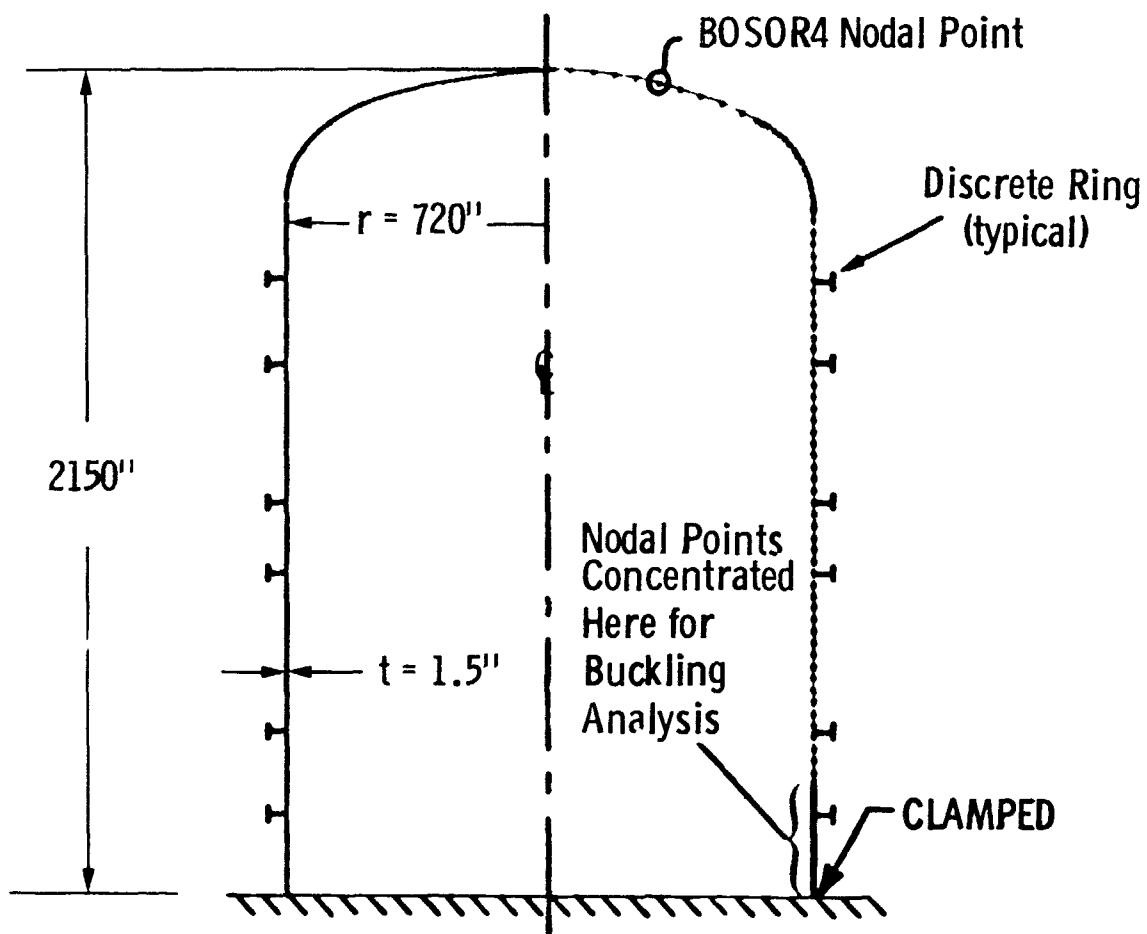


Figure 156(a) Steel containment vessel for nuclear reactor.

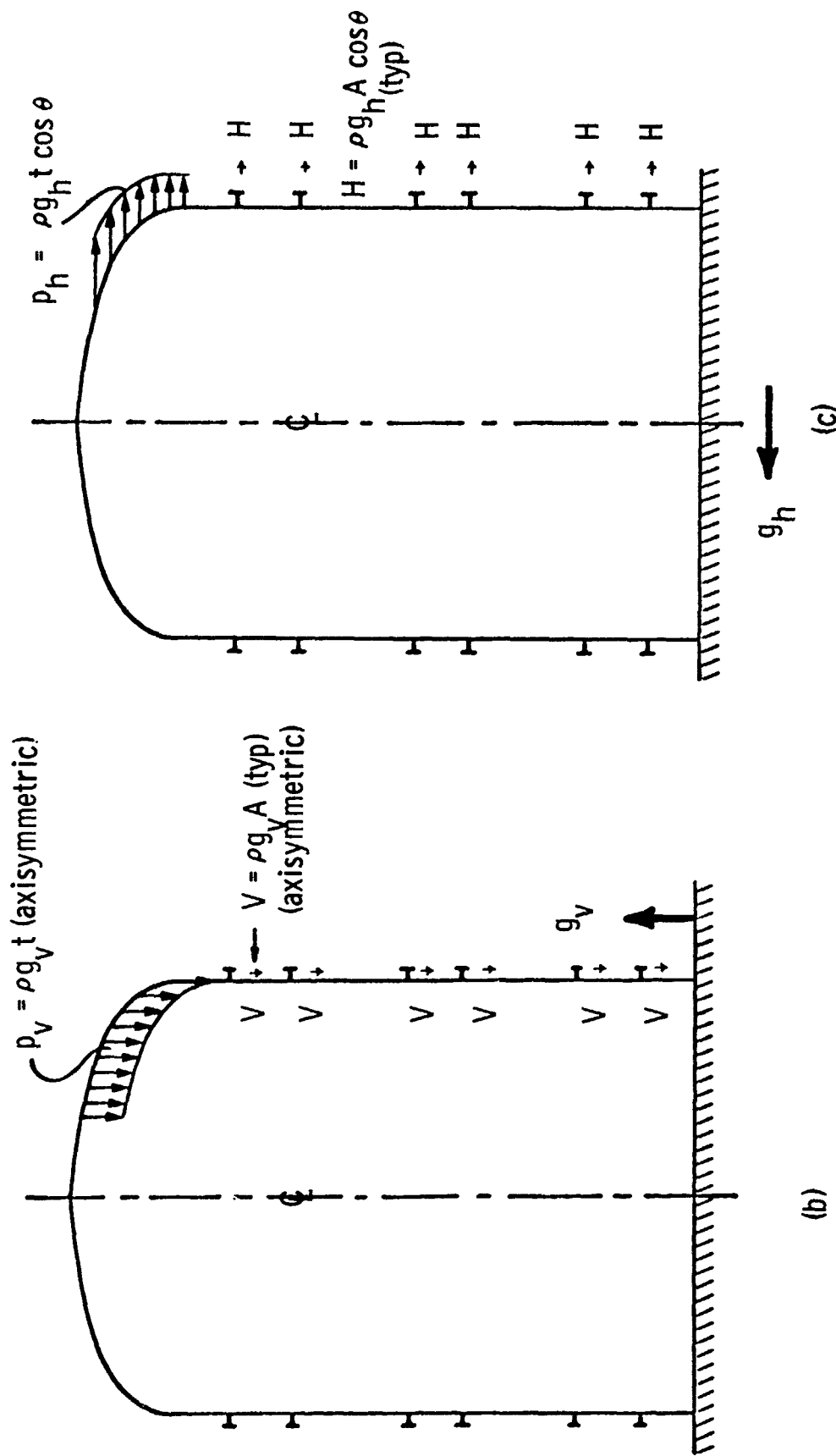


Figure 156(b,c) Body forces in containment shell due to (b) vertical and (c) horizontal components of ground acceleration during an earthquake.

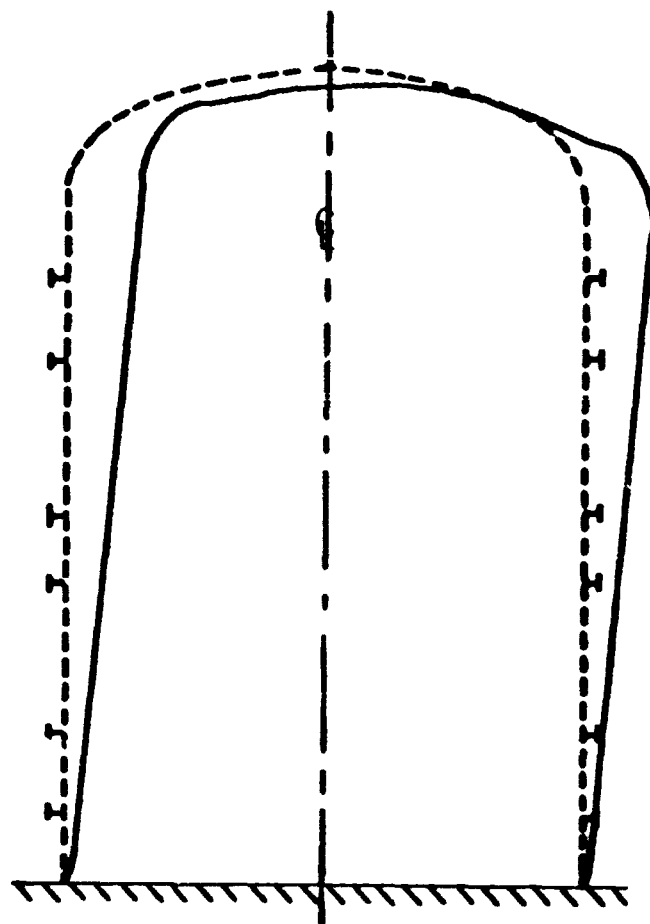


Figure 157 Steel containment vessel as deformed by body forces due to 1 g vertical and 1 g horizontal ground acceleration components.

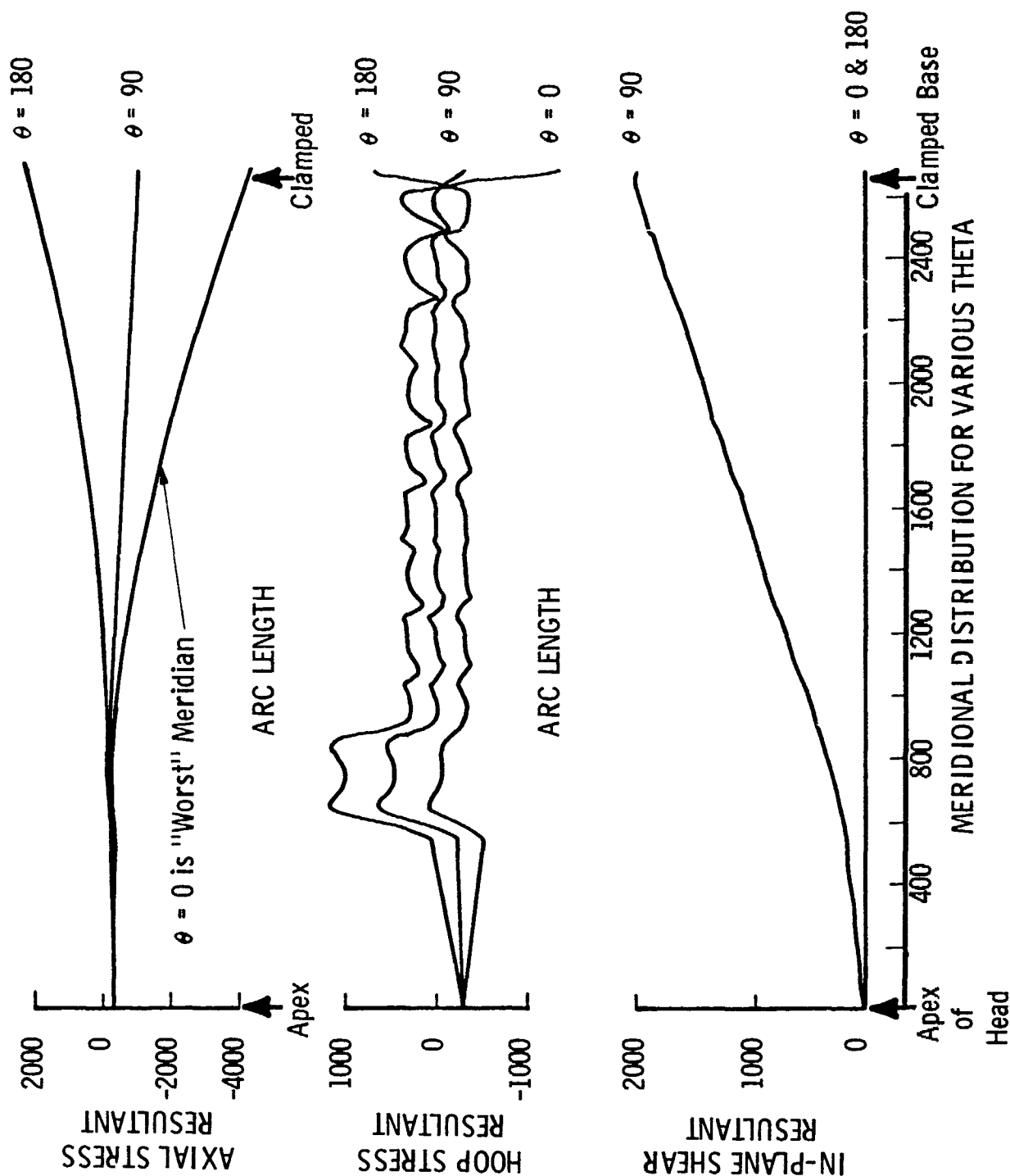


Figure 158 Prebuckling stress resultants in containment vessel under vertical and horizontal ground acceleration: $g_v = g_h = 1.0$.

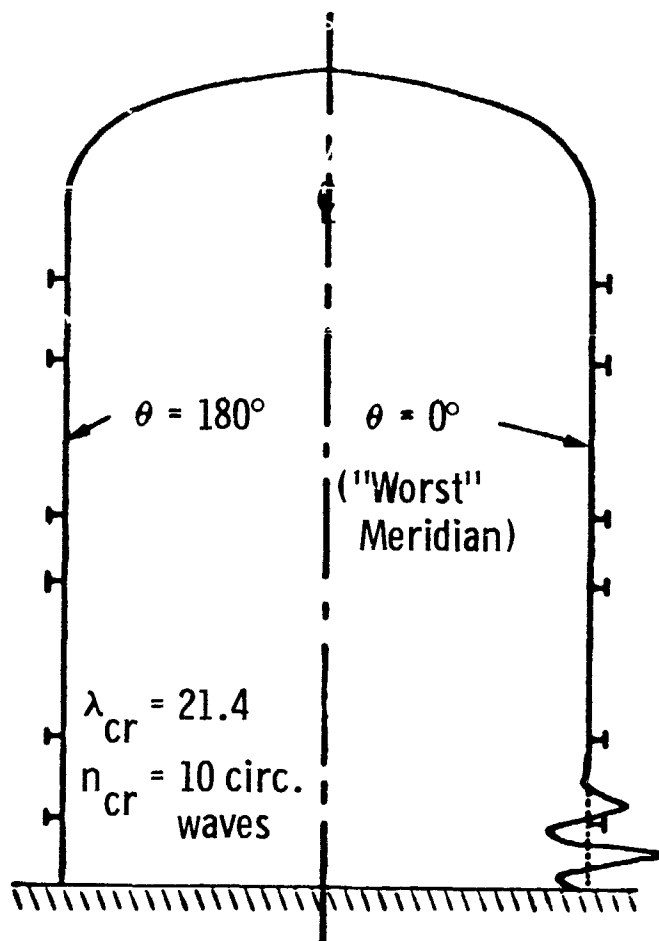
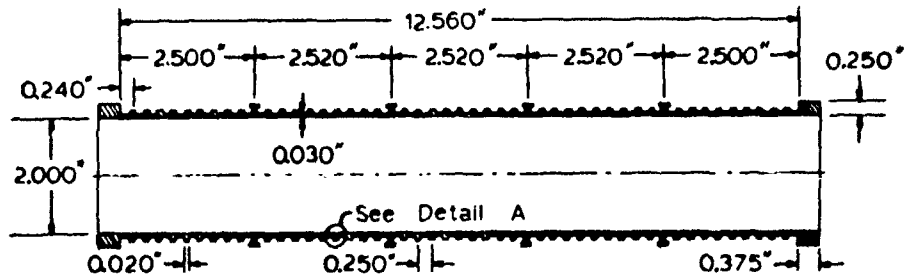
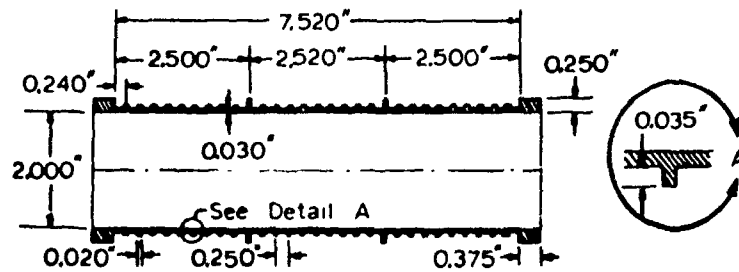


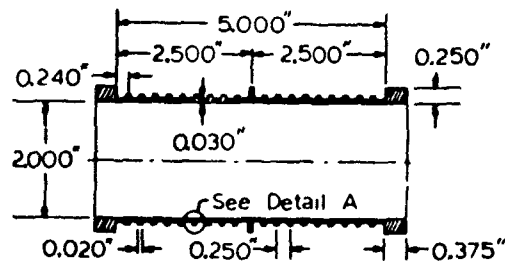
Figure 159 Buckling mode and load factor λ_{cr} for steel containment vessel under 1 g vertical and 1 g horizontal ground acceleration. The membrane stress distribution along the meridian at $\theta = 0^\circ$ was assumed to be axisymmetric in the stability analysis.



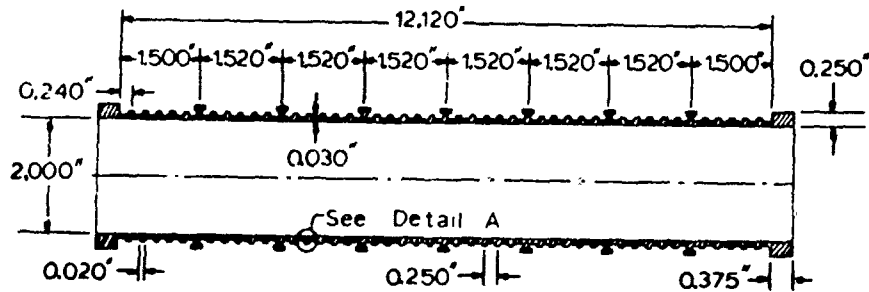
GROUP 1



GROUP 2



GROUP 3



GROUP 4

Figure 160(a) Axial sections of ring-stiffened cylinders with intermediate heavy frames (from Blumenberg [211]).

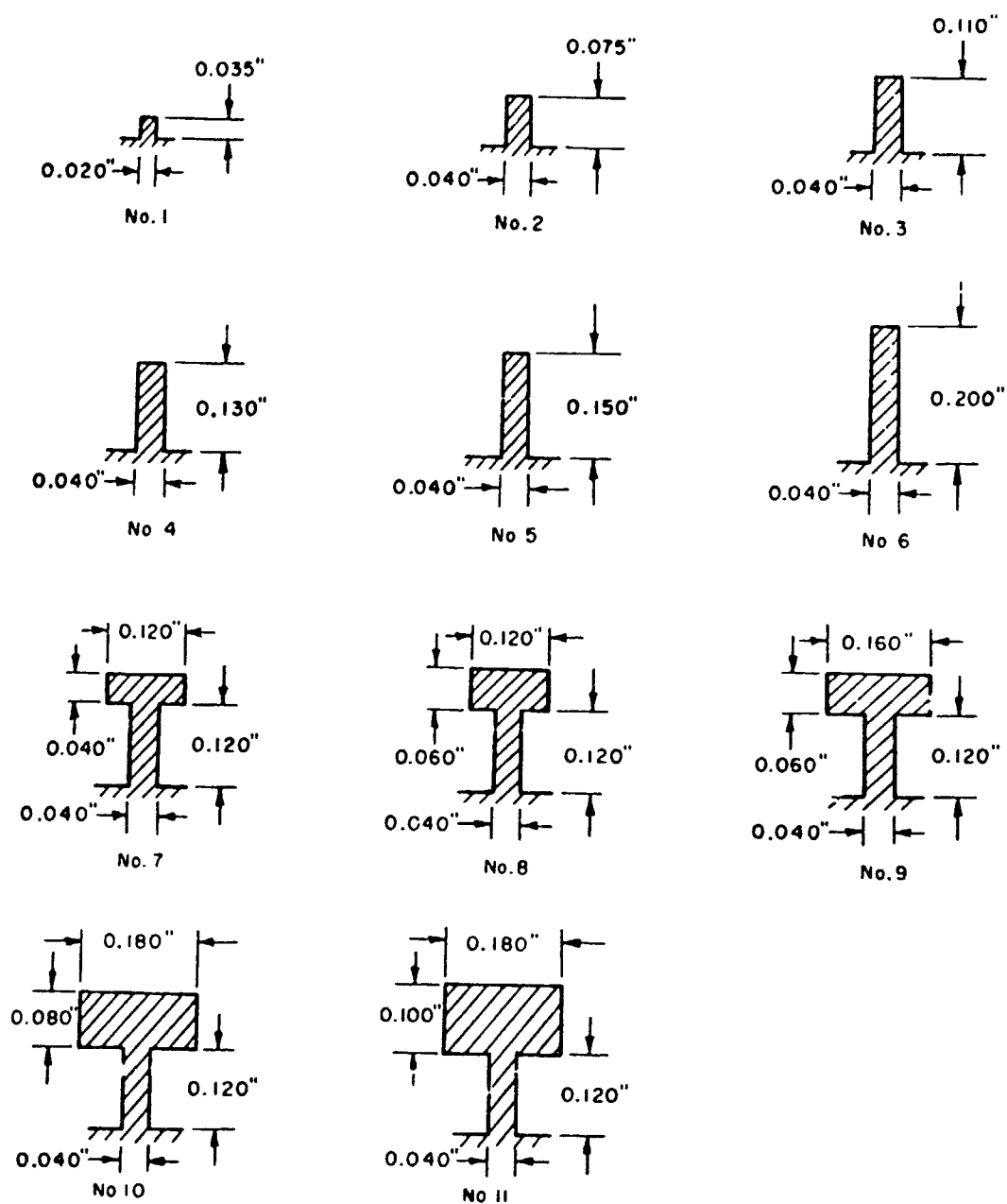
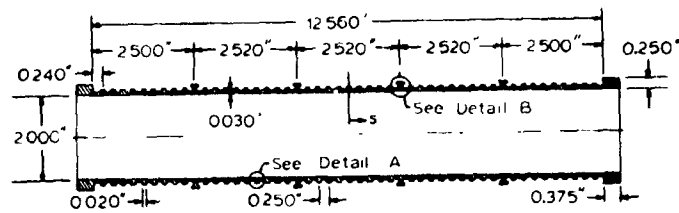
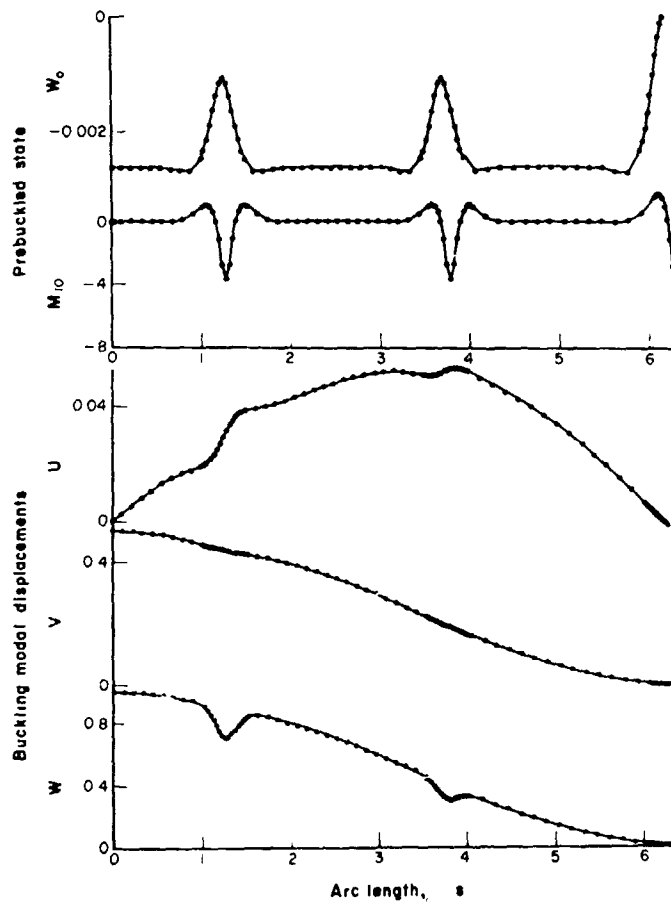
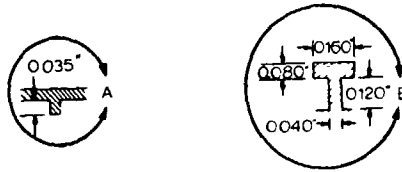


Figure 160(b) Heavy-frame sections for stiffened cylinders (see Table 17) (from Blumenberg [211]).



(a)



(b)

(c)

Figure 161 (a) Group 1 cylinder tested under uniform external hydrostatic pressure by Blumenberg [211]; (b) axisymmetric prebuckling normal deflection w_0 and meridional moment M_{10} ; (c) bifurcation buckling mode corresponding to $n_{cr} = 2$ circumferential waves. The dots are nodal points in the discretized BOSOR model [14].

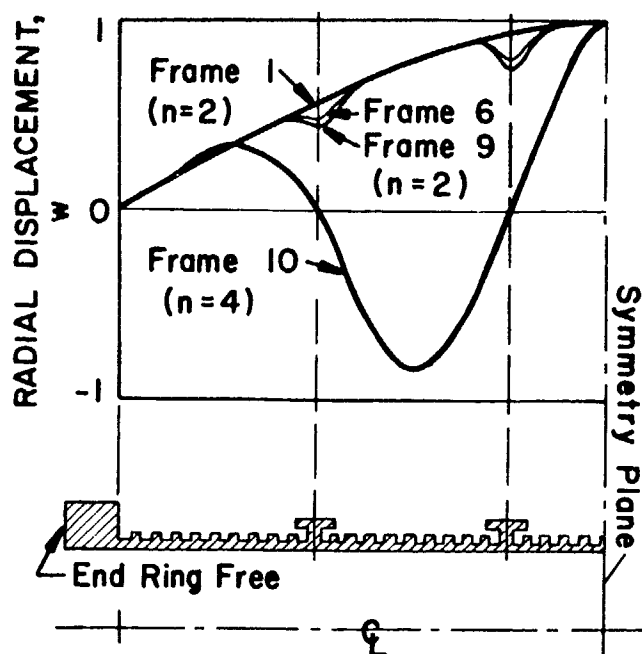


Figure 162 Local ($n=4$) and general ($n=2$) instability of four of the hydrostatically compressed cylindrical shells in Group 1. Buckling pressures are given in Table 17 and cylinder and frame (ring) geometries are displayed in Figure 160(a,b).

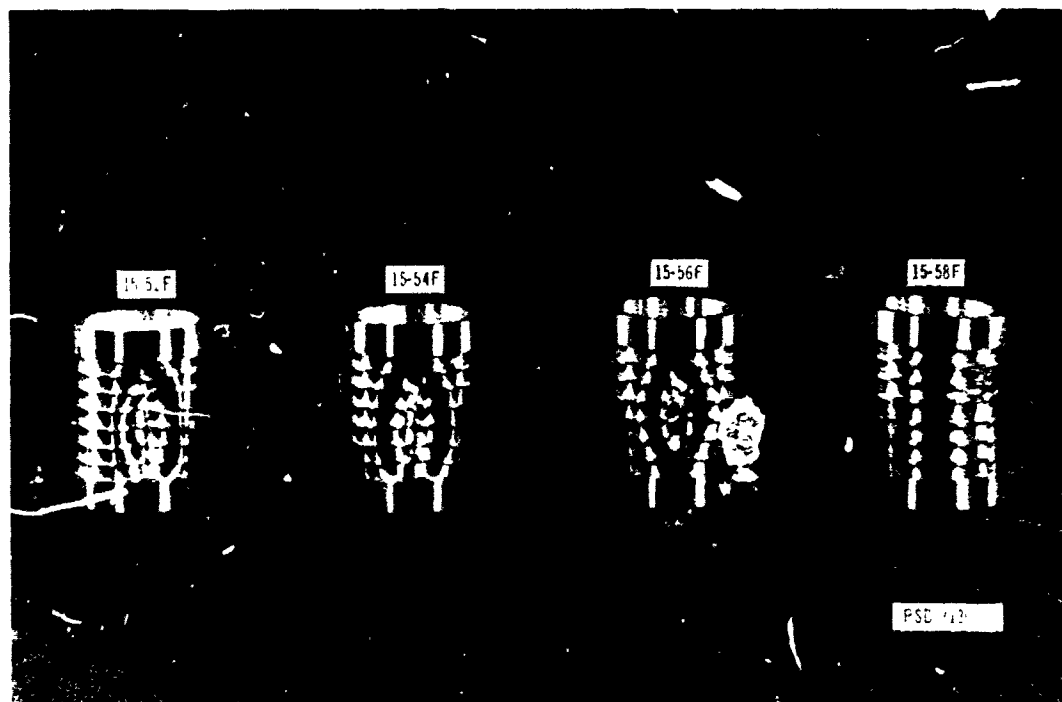
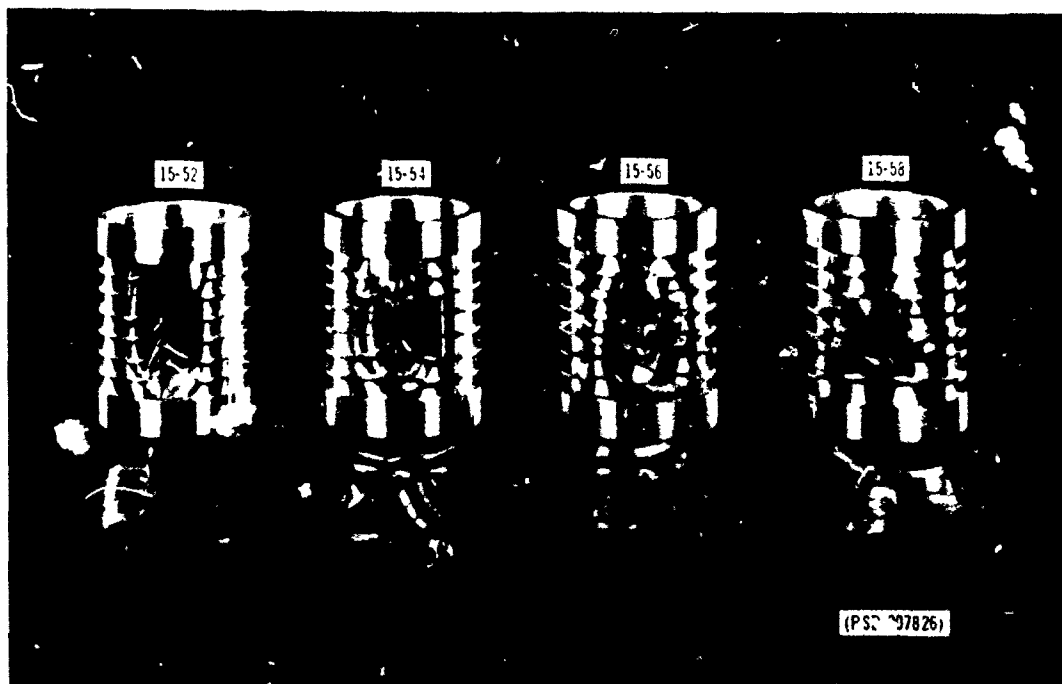


Figure 163 Some of the buckled ring-stiffened aluminum cylinders tested under hydrostatic pressure by Boichot and Reynolds (1965). Top four specimens are without fillets and show evidence of fracturing; bottom four specimens are of similar geometry but have fillets (from Boichot and Reynolds [212]).

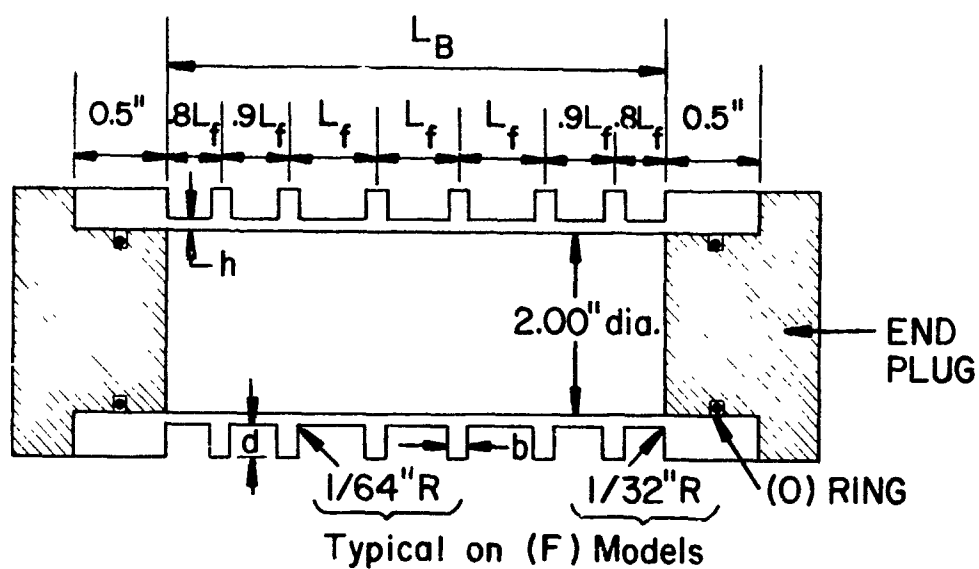


Figure 164 Aluminum ring-stiffened cylinder tested under external pressure by Boichot and Reynolds in 1965 at the Naval Ship Research and Development Center, Maryland (from Bushnell [171]).

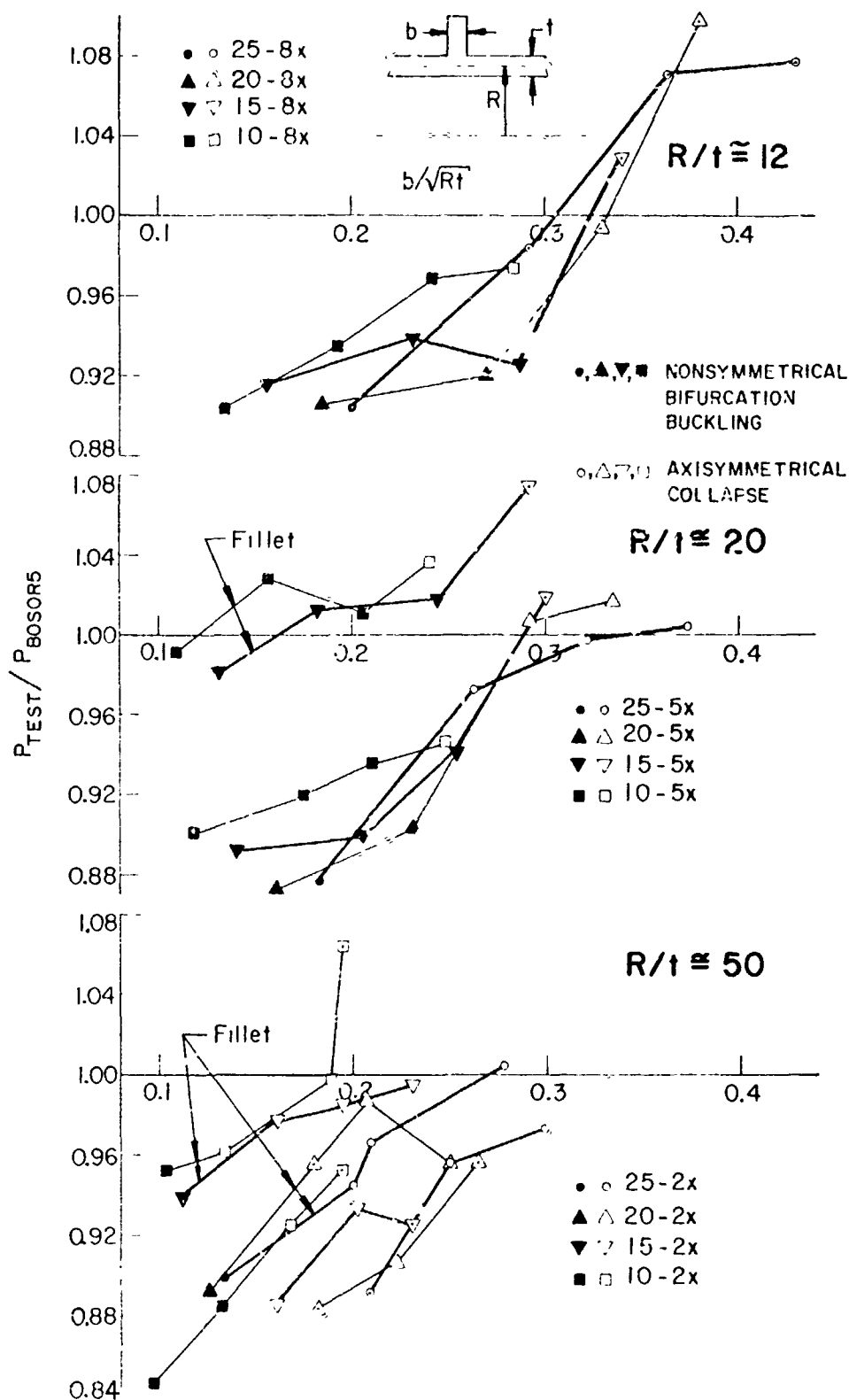


Figure 165 Comparison of test and theory (BOSOR5) for buckling of externally pressurized ring-stiffened cylinders plotted as function of ring thickness parameter b/\sqrt{Rt} (from Businell [171]).

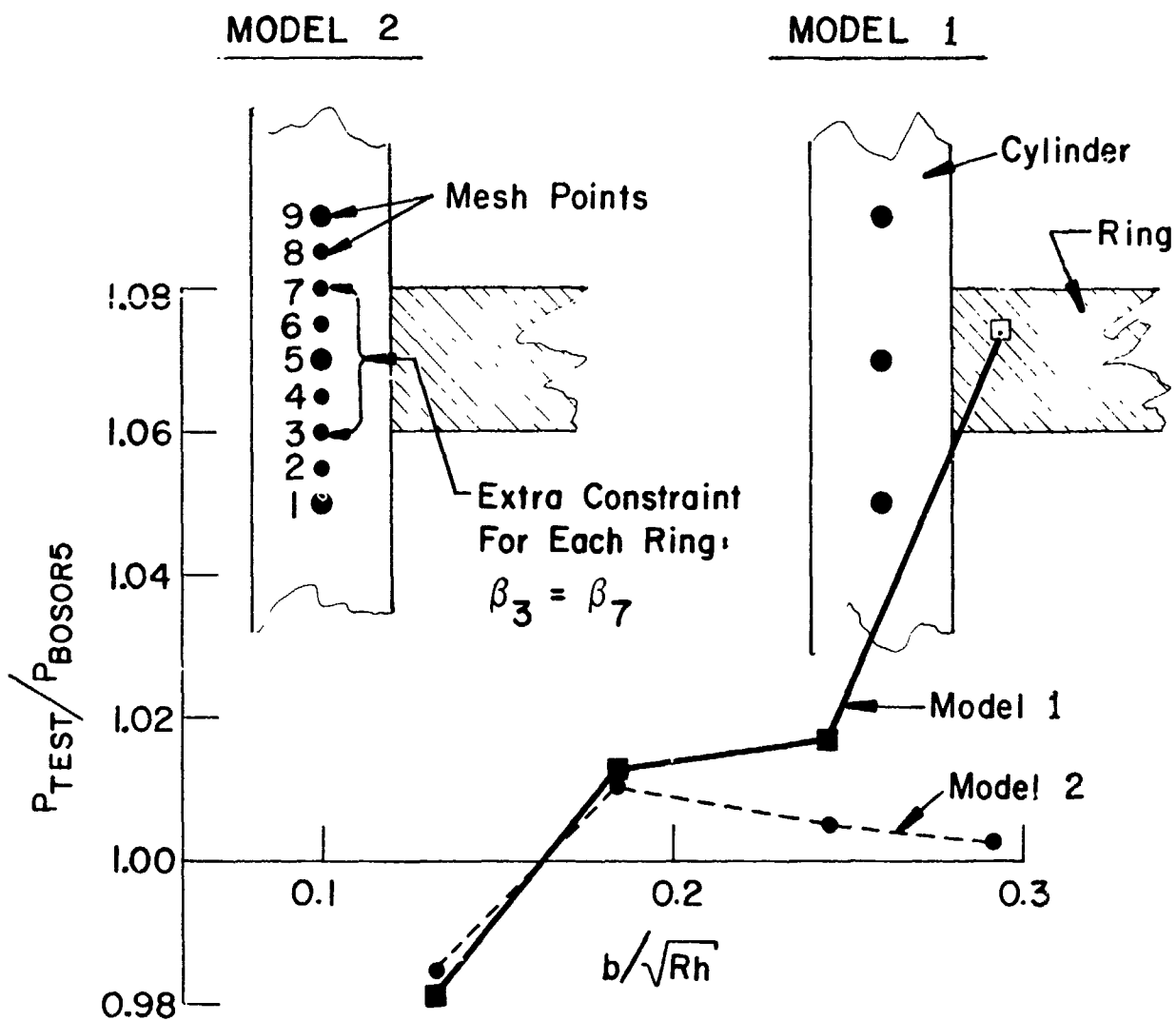


Figure 166 Comparison of test and theory for specimens 15-5XF neglecting and including ring thickness effect (from Bushnell [171]).

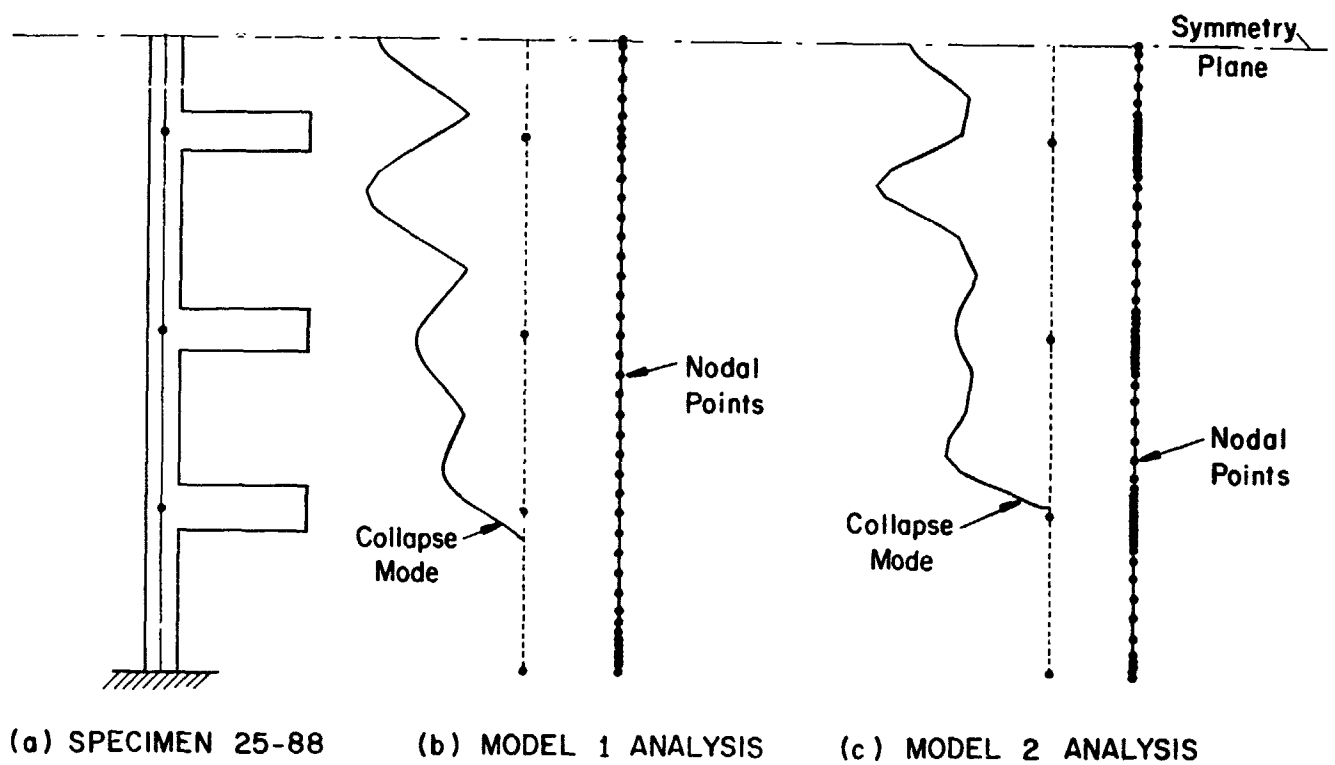
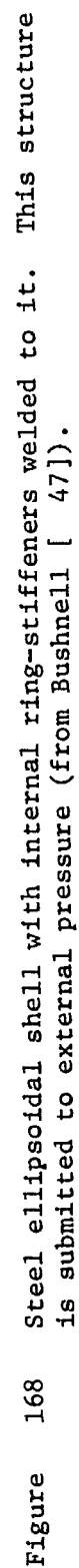
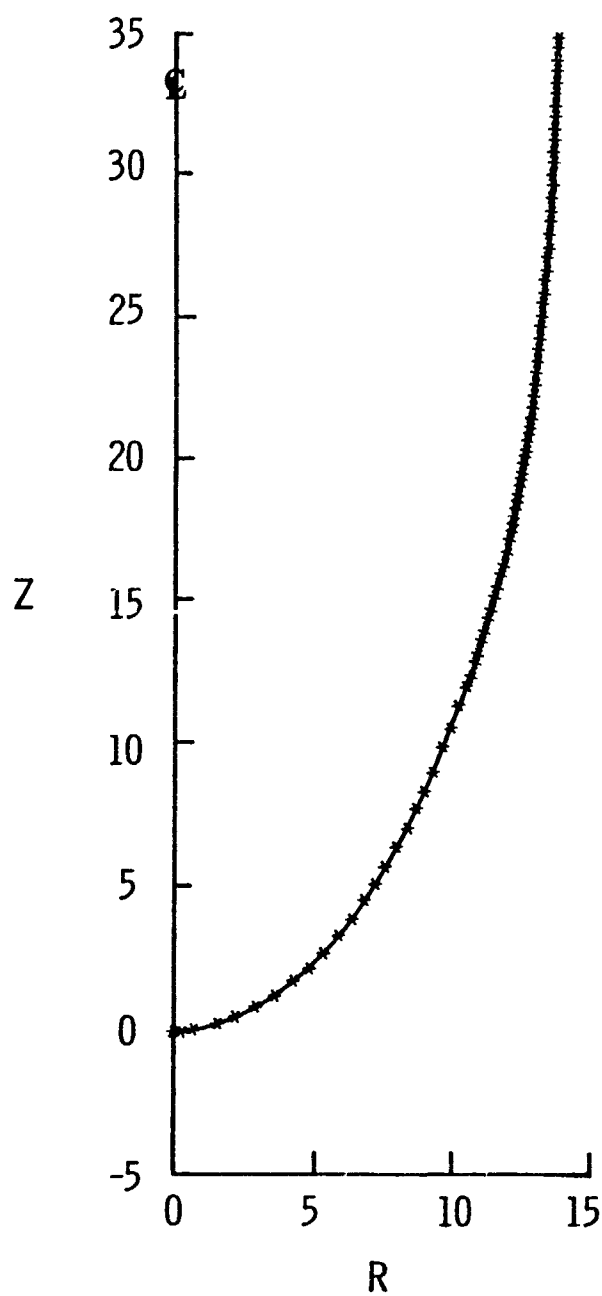
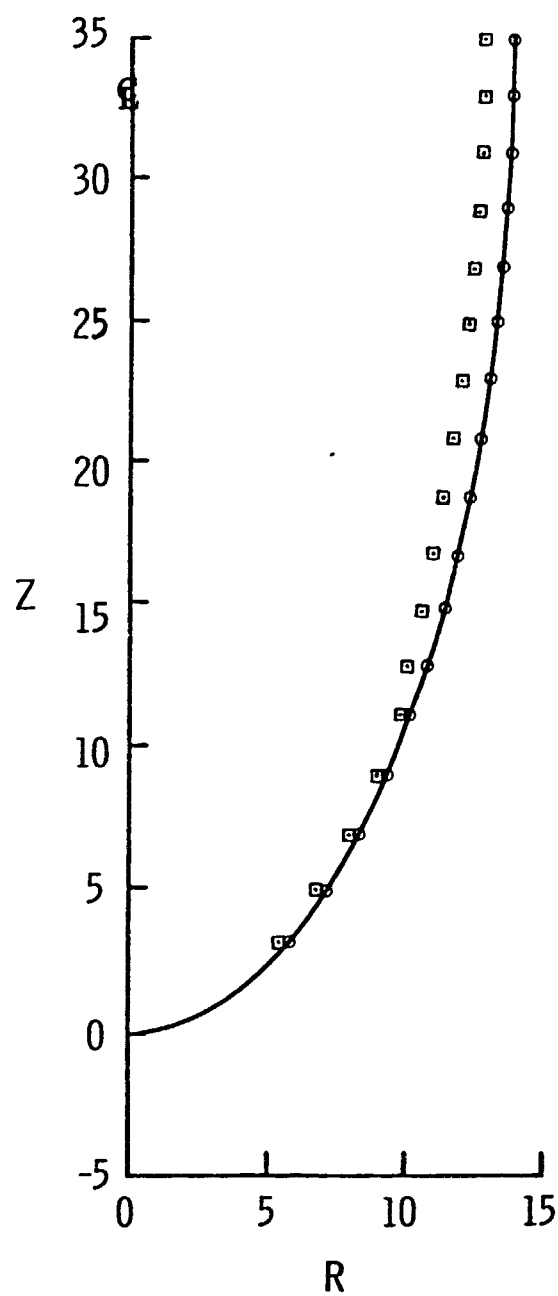


Figure 167 Predicted axisymmetric collapse model of specimen 25-88: (a) specimen geometry; (b) neglecting ring thickness effect; and (c) including ring thickness effect (from Bushnell [171]).





(a)



(b)

Figure 169 BOSOR5 model of the ring-stiffened ellipsoidal shell:
 (a) nodal points; (b) locations of discrete ring
 attachment points and centroids (from Bushnell [47]).

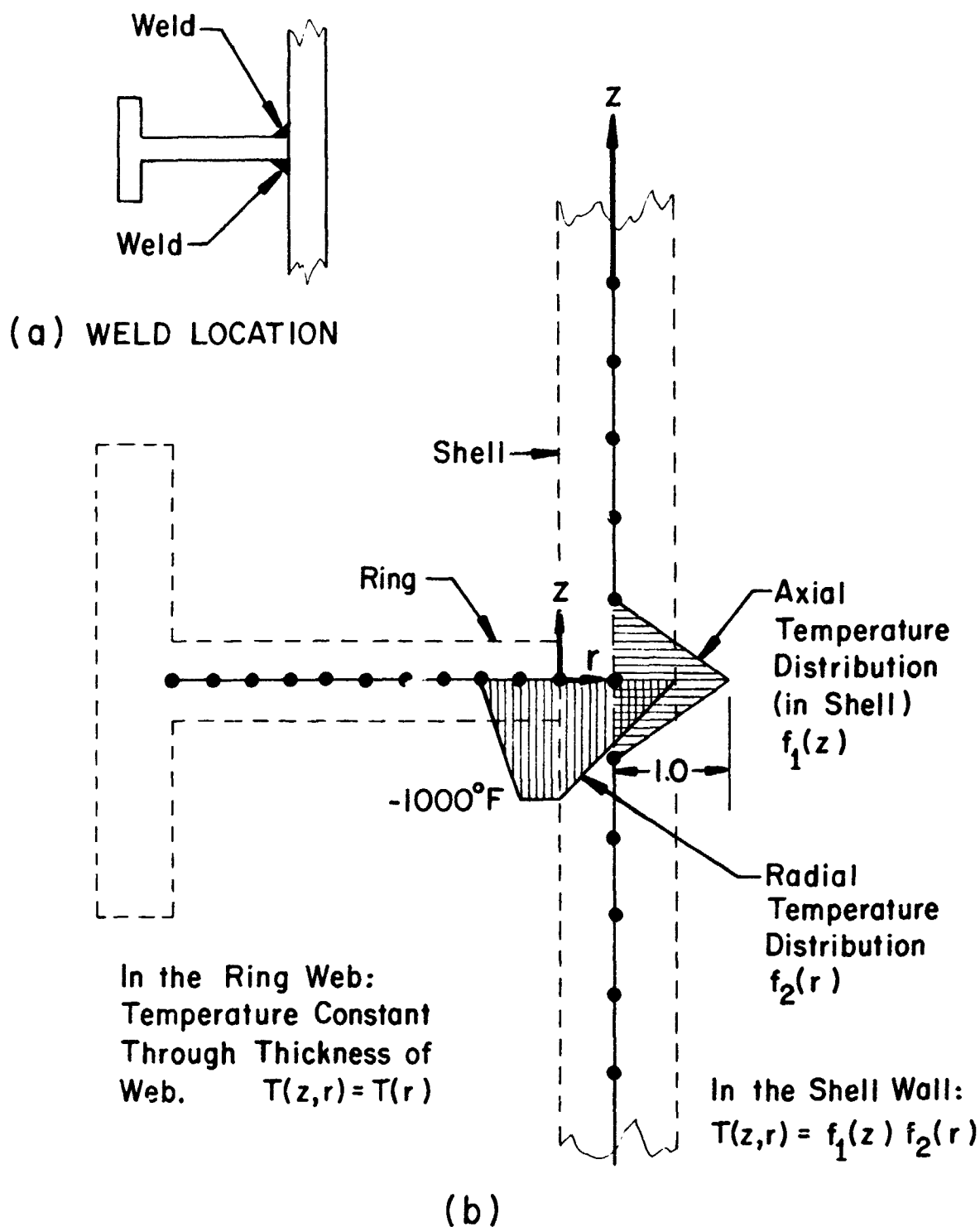


Figure 170 Weld locations and simulation of weld thermal effect by local cooling (from Bushnell [47]).

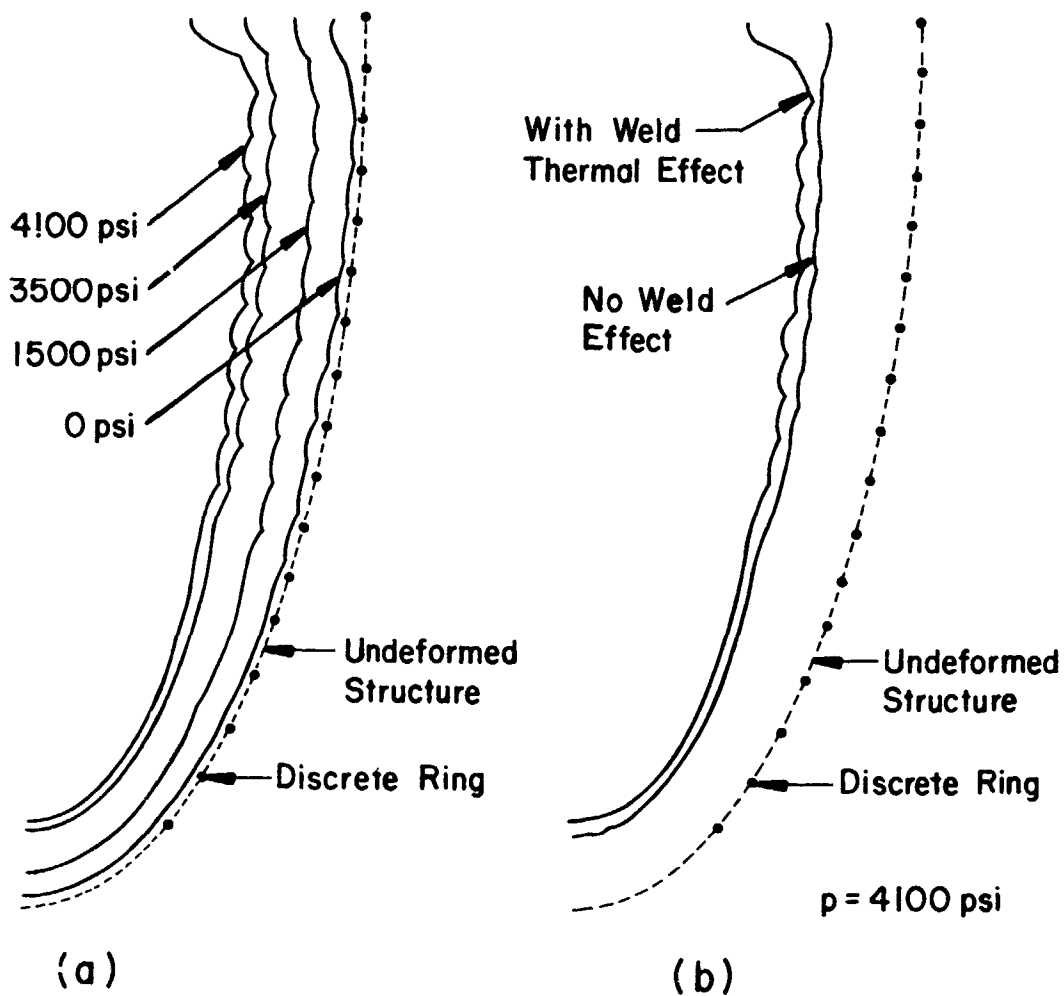


Figure 171 Prebuckling deflections with increasing pressure and comparison with and without the weld cool-down effect (from Bushnell [47]).

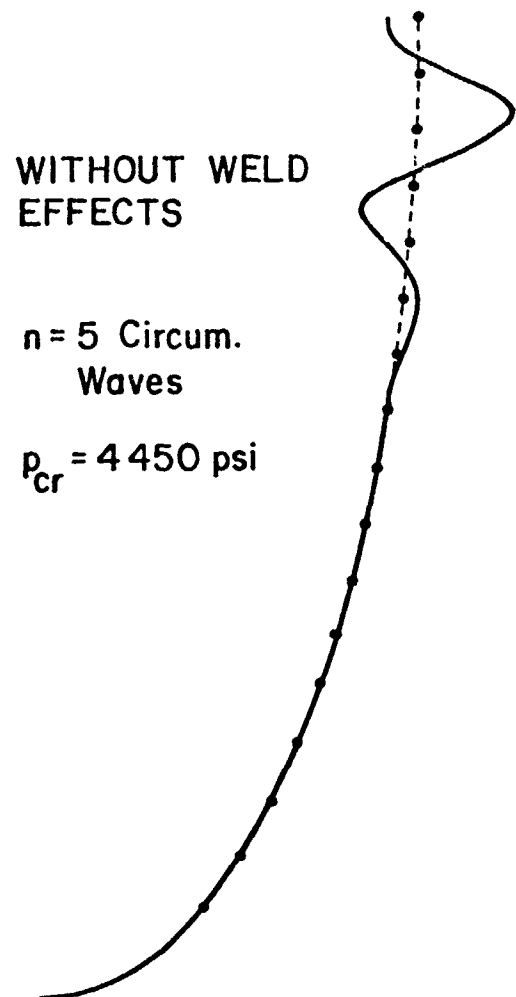
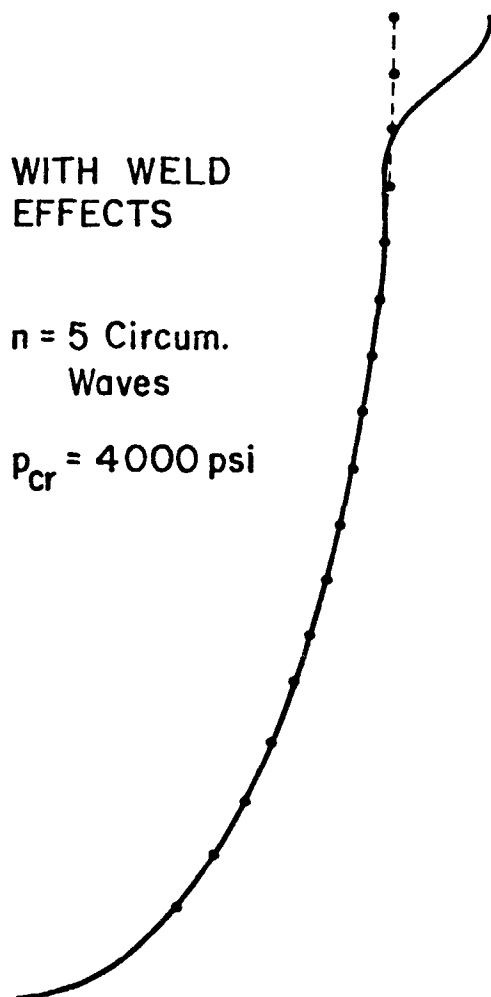


Figure 172 Predicted bifurcation buckling modes and pressures with and without the weld cool-down effect included in the analysis (from Bushnell [47]).

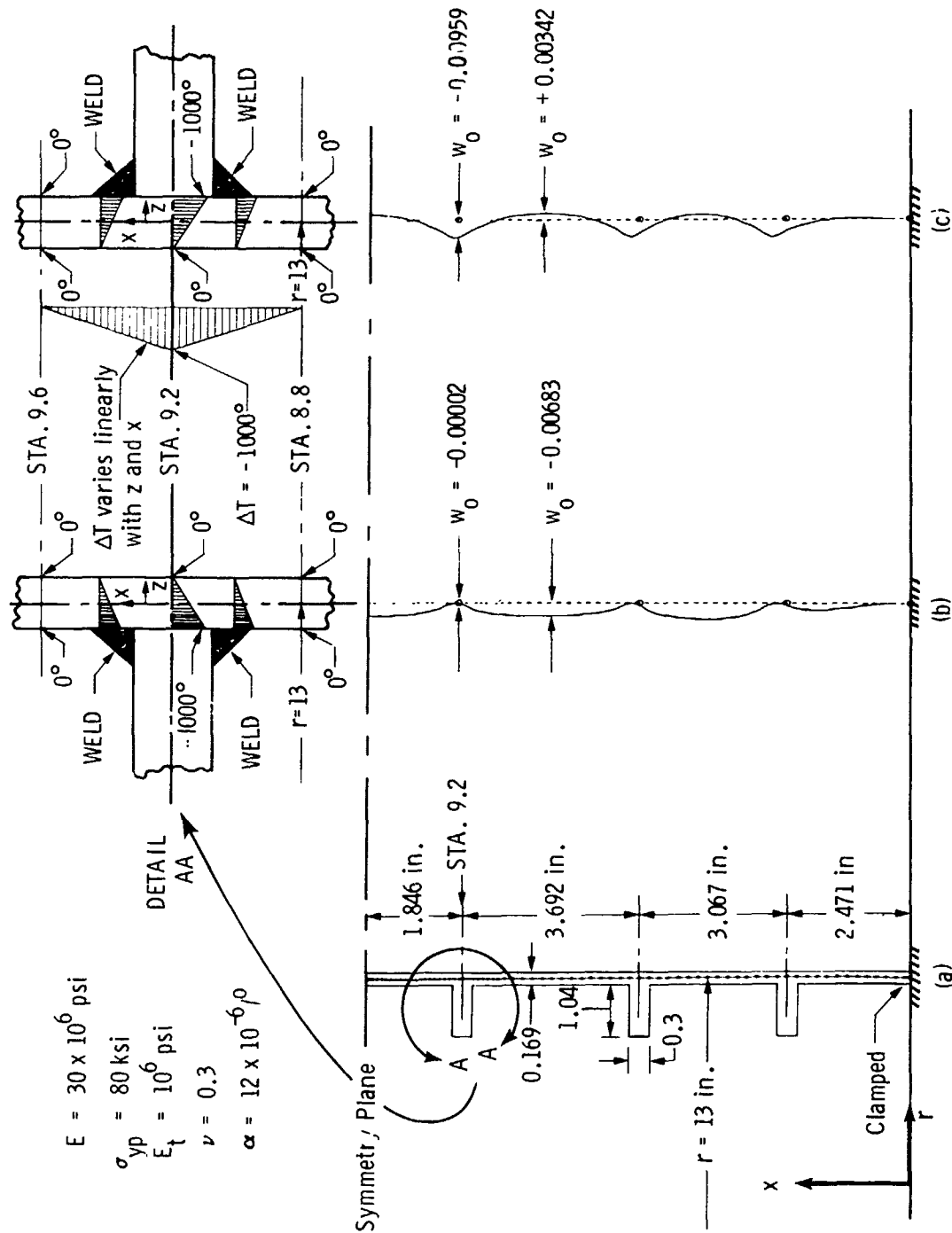
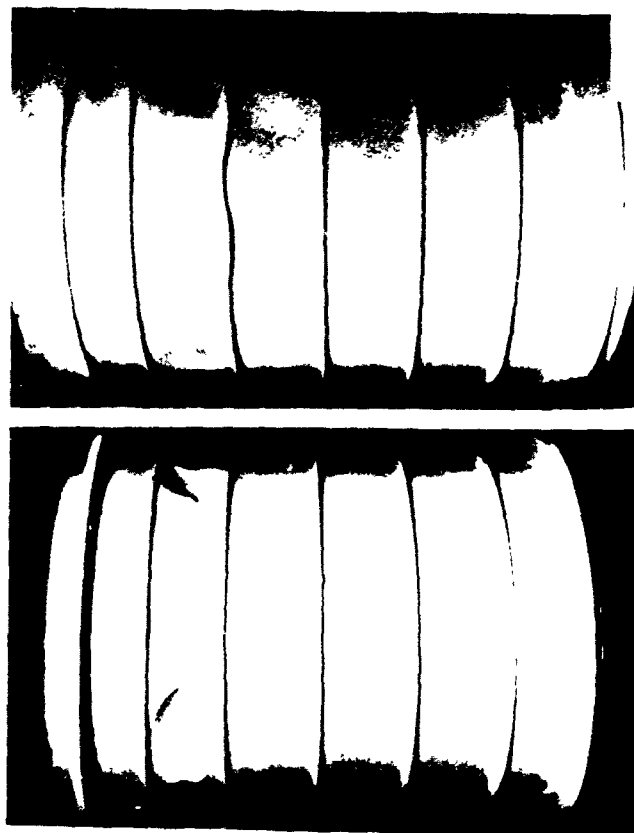


Figure 173 Cylinder with welded internal and external rings: (a) dimensions and BOSOR5 discretized reference surface; (b) predicted residual deformations after welding and before loading of Specimen M1 (internal rings); (c) predicted residual deformations after welding and before loading of Specimen M2 (external rings).



BR-4 (a)

BR-4A (b)

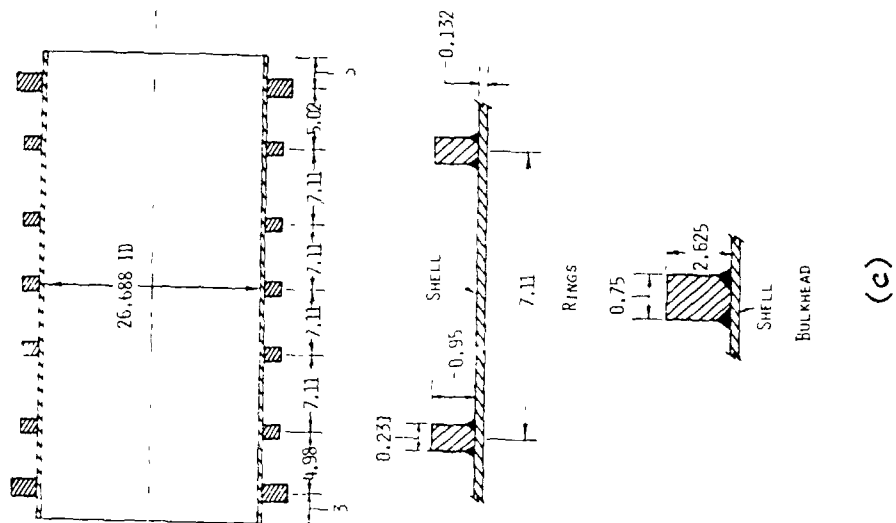


Figure 174 Buckling patterns in: (a) the cold bent and welded specimen BR-4 ($p_{cr} = 390$ psi)
 (b) the machined specimen BR-4A ($p_{cr} = 540$ psi)
 (c) Dimensions of specimens BR-4 and BR-4A (from Bushnell [142]).

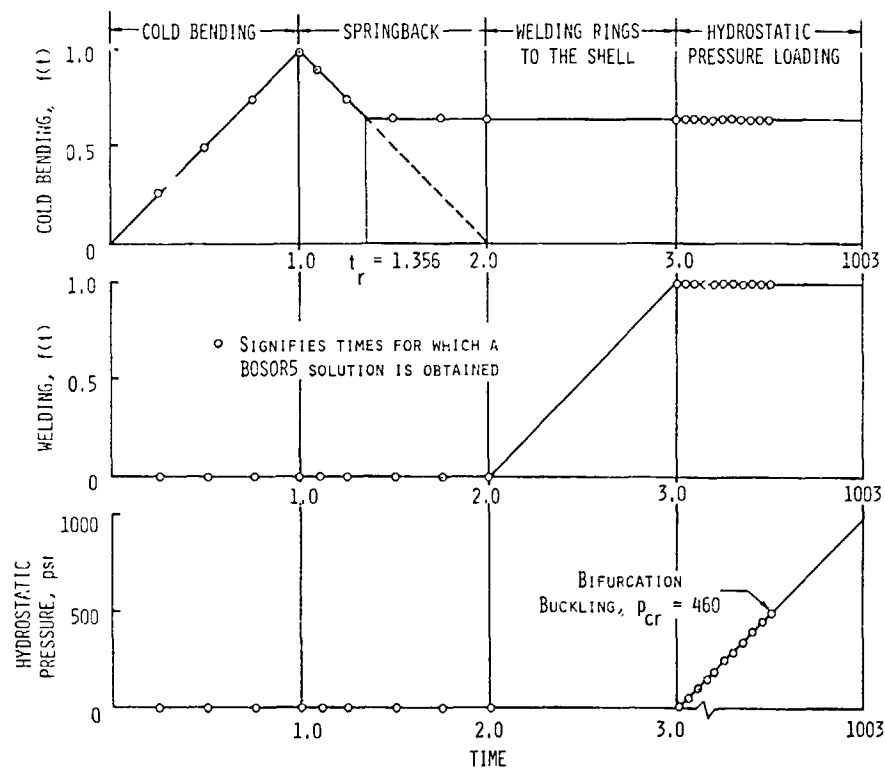


Figure 175 Loading functions of "time" for BOSOR5 analysis of Specimen BR-4.

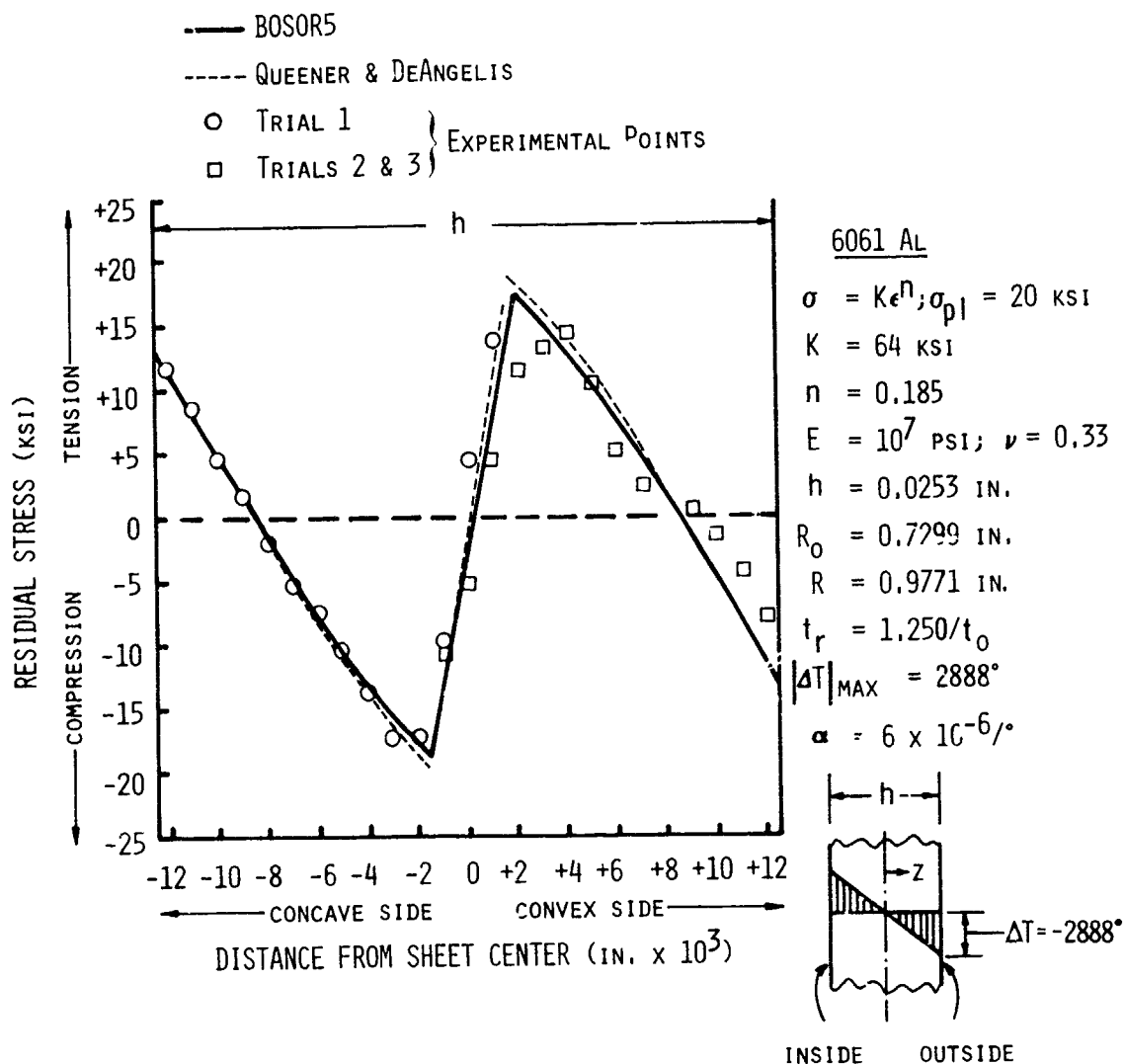


Figure 176 Comparison of BOSOR5 results with test and theory of Queener and DeAngelis for residual stresses in cold bent 6061 aluminum specimen.

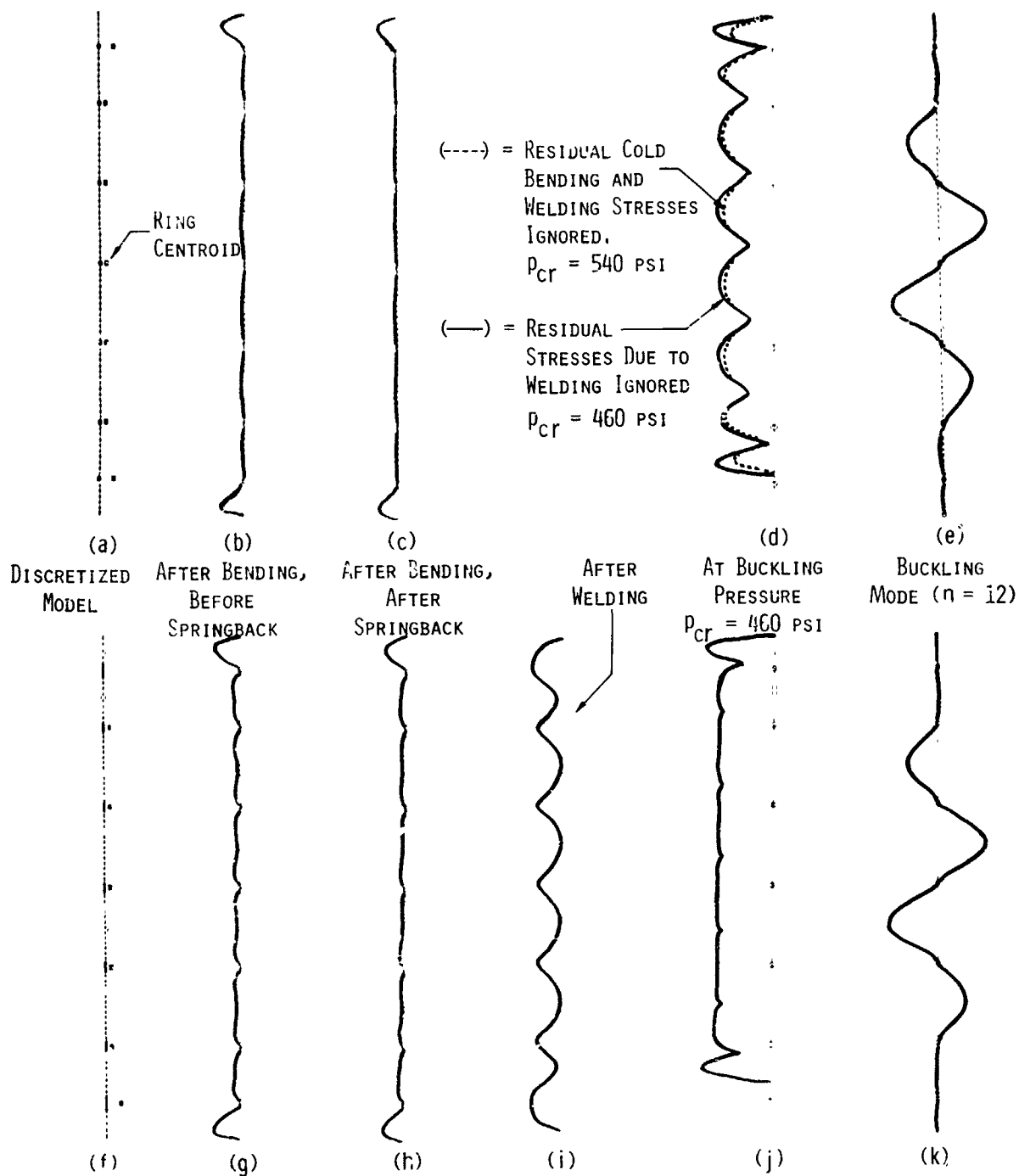


Figure 177 Two BOSOR5 models of Specimen BR-4 showing deformed generator at various stages in the manufacturing process and at the buckling pressure: (a)-(e) Model in which the welding process is ignored, (f)-(k) Model in which the welding process is included.

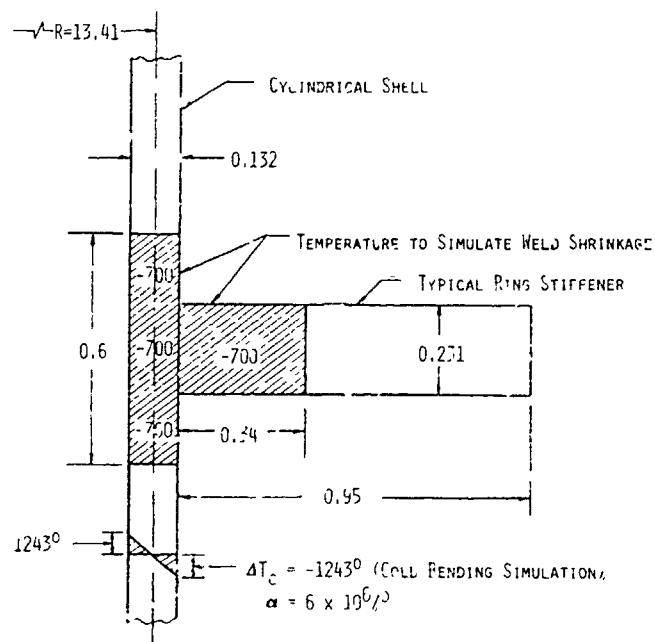


Figure 17C Thermal simulation of cold bending and welding processes in Specimen BR-4.

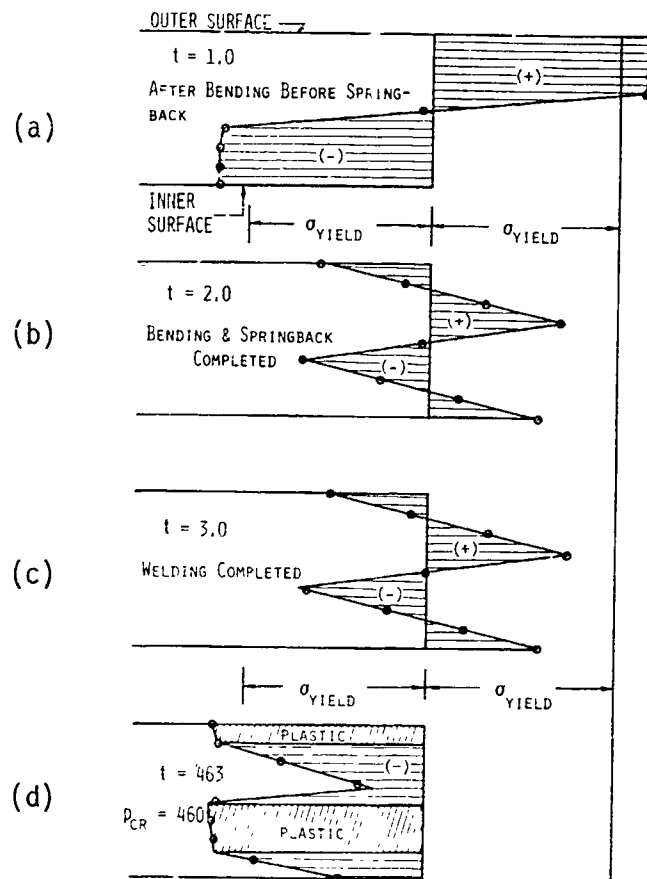


Figure 179 Stress distributions through BR-4 shell wall midway between rings.

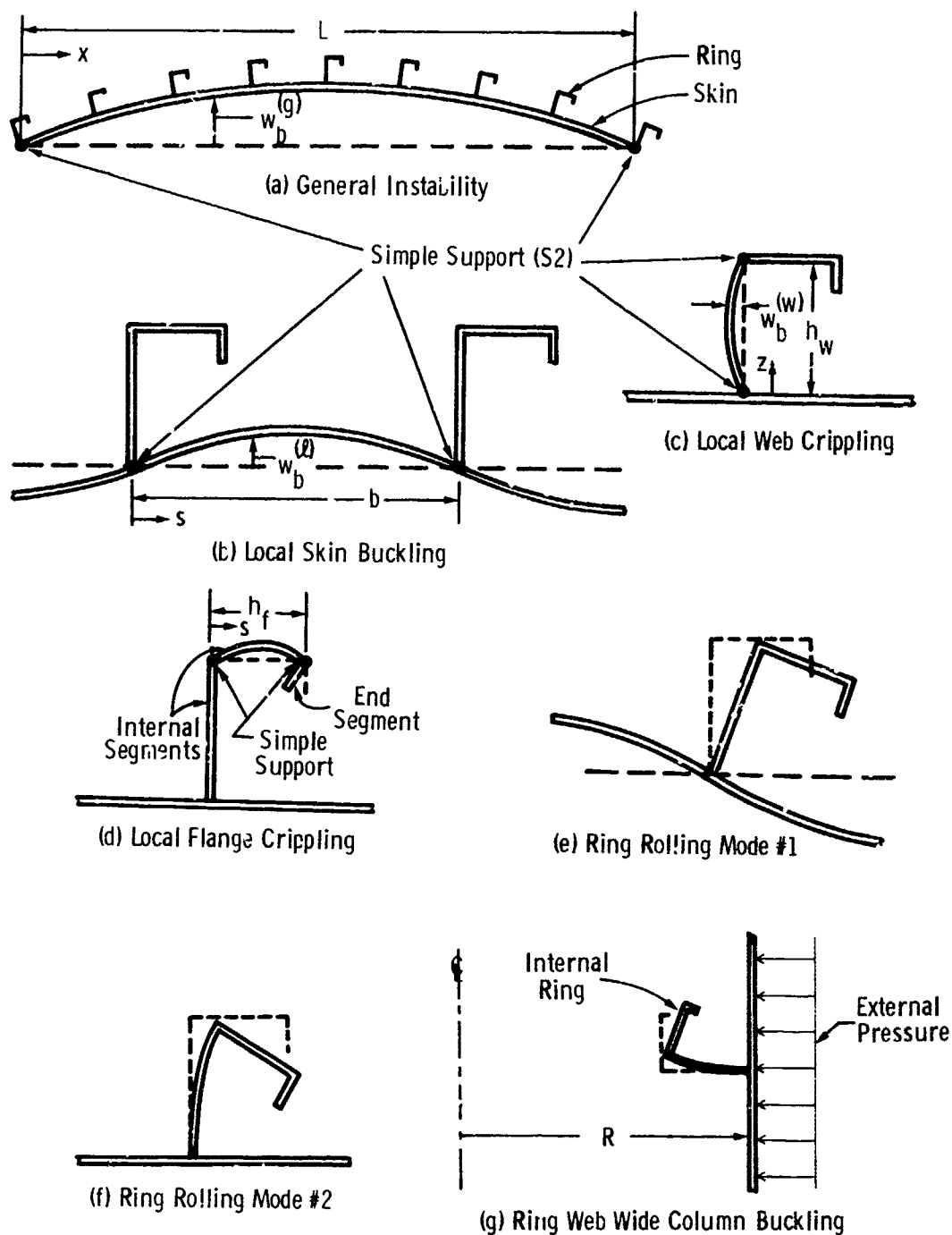


Figure 180 General and local bifurcation buckling modes for a ring-stiffened cylindrical shell.

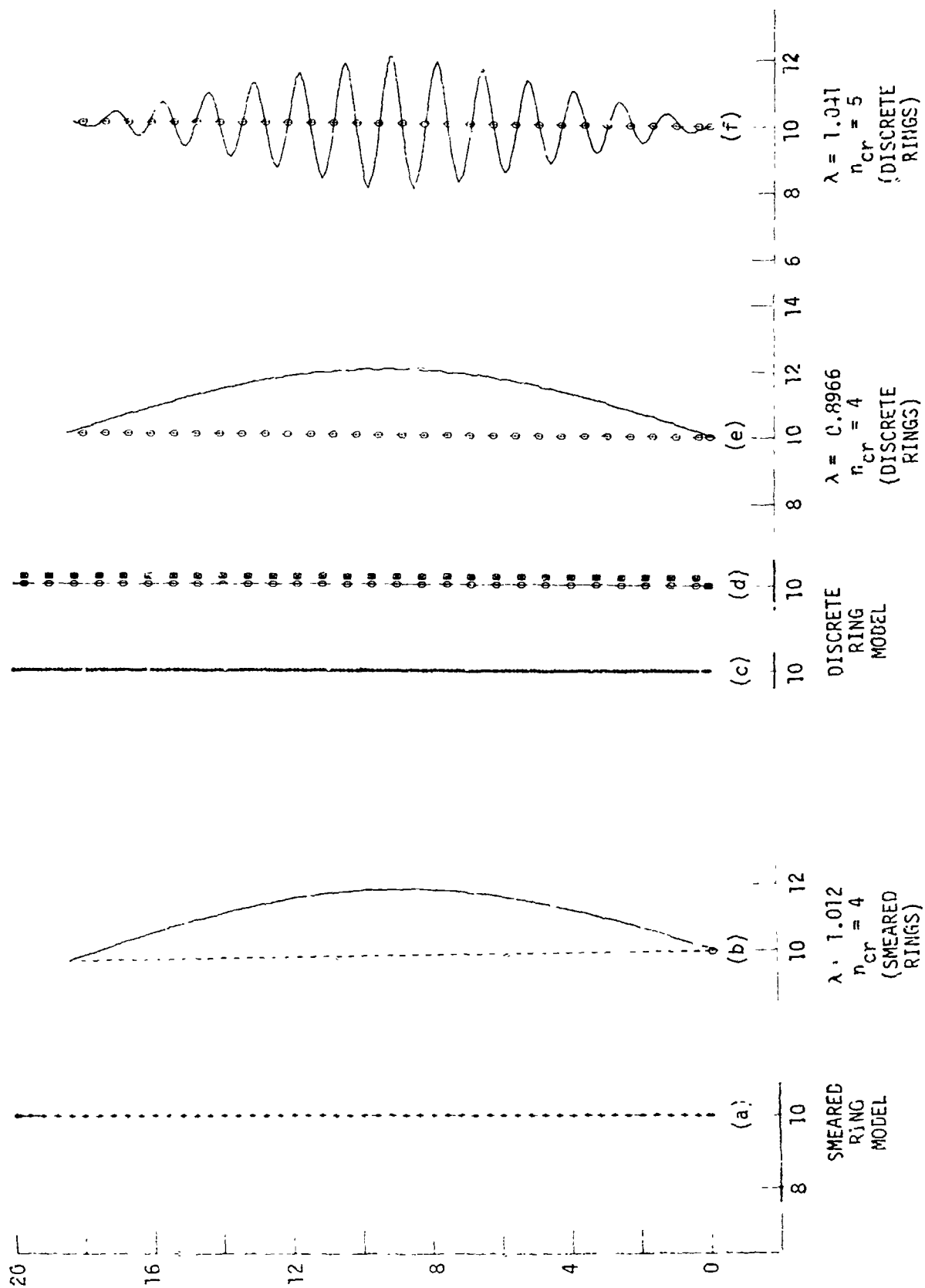


Figure 181 BCSOR4 models and buckling modes of previously optimized ring-stiffened cylindrical shell under external hydrostatic pressure.

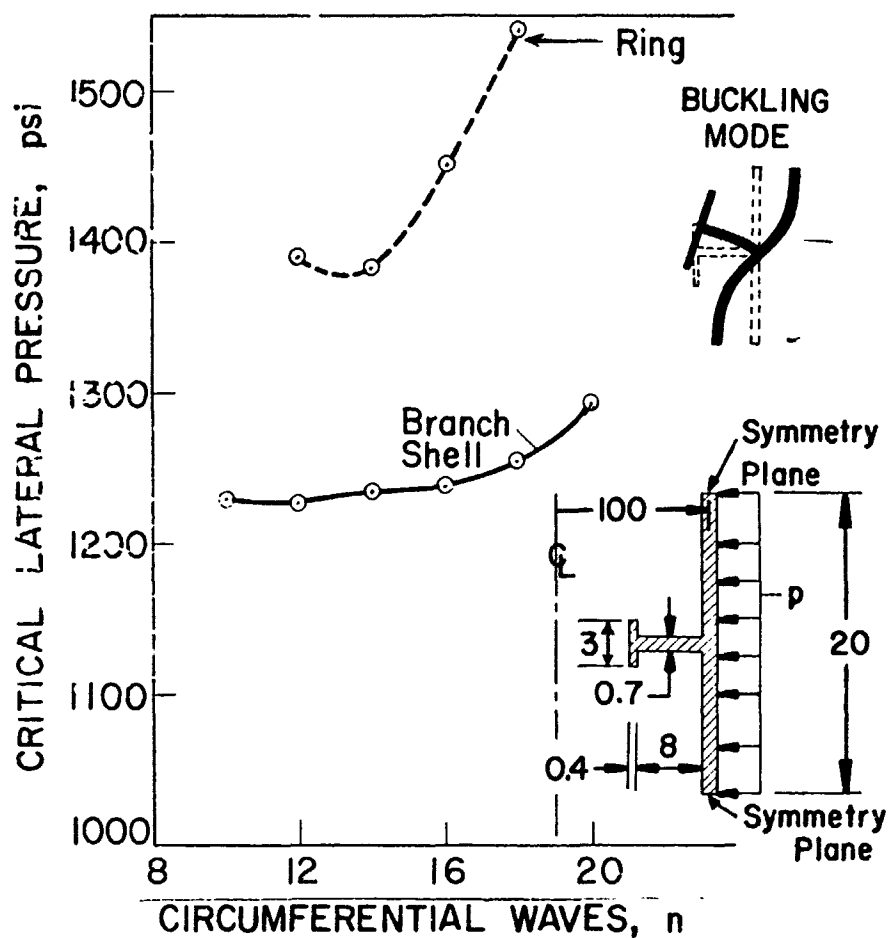


Figure 182 Critical pressures corresponding to local buckling modes from two different discretized models of ring-stiffened cylindrical shell (from Bushnell [247]).

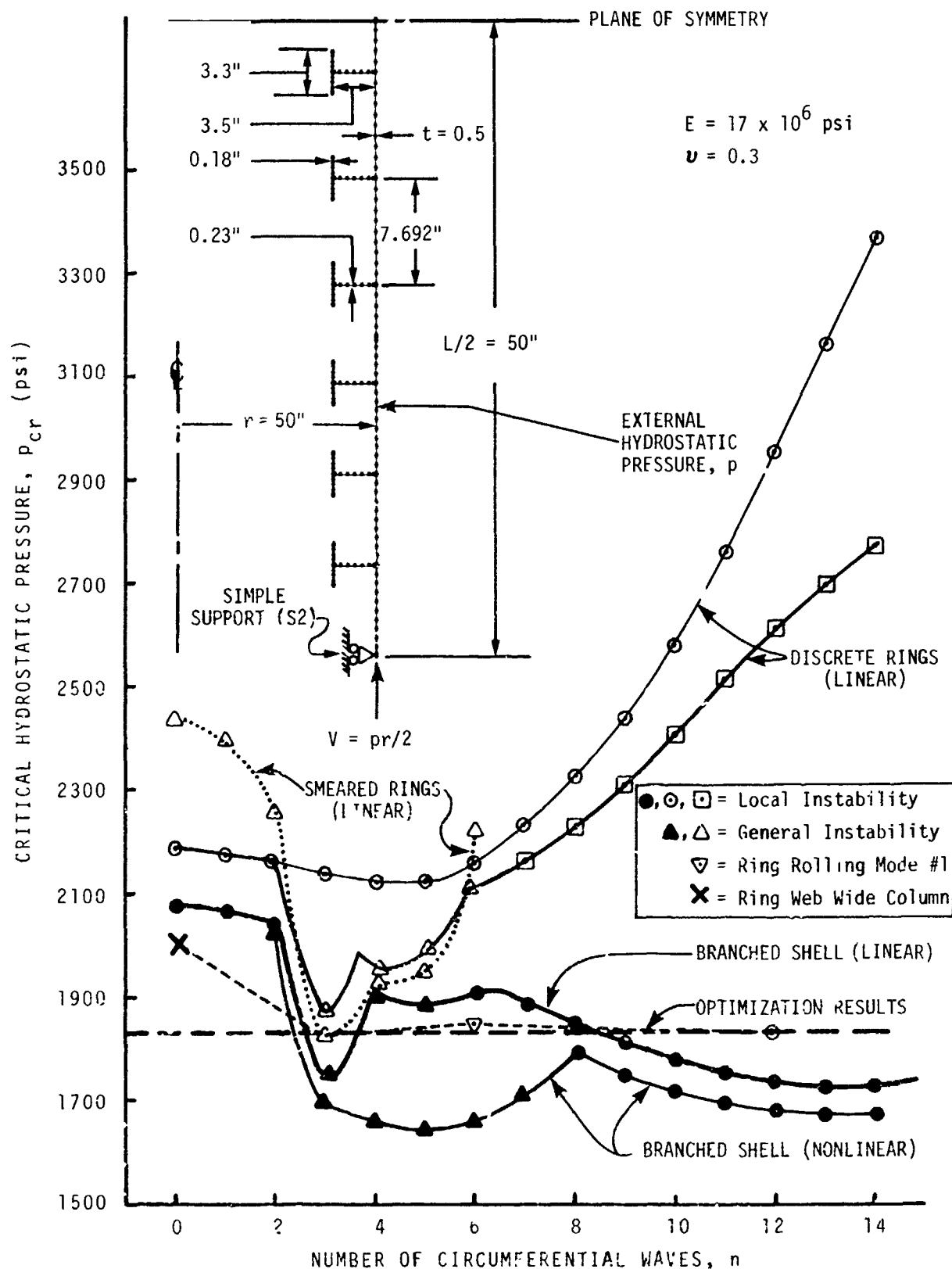


Figure 183 Predicted buckling pressures from various discretized models of ring-stiffened cylinder which had been previously optimized with use of simple formulas.

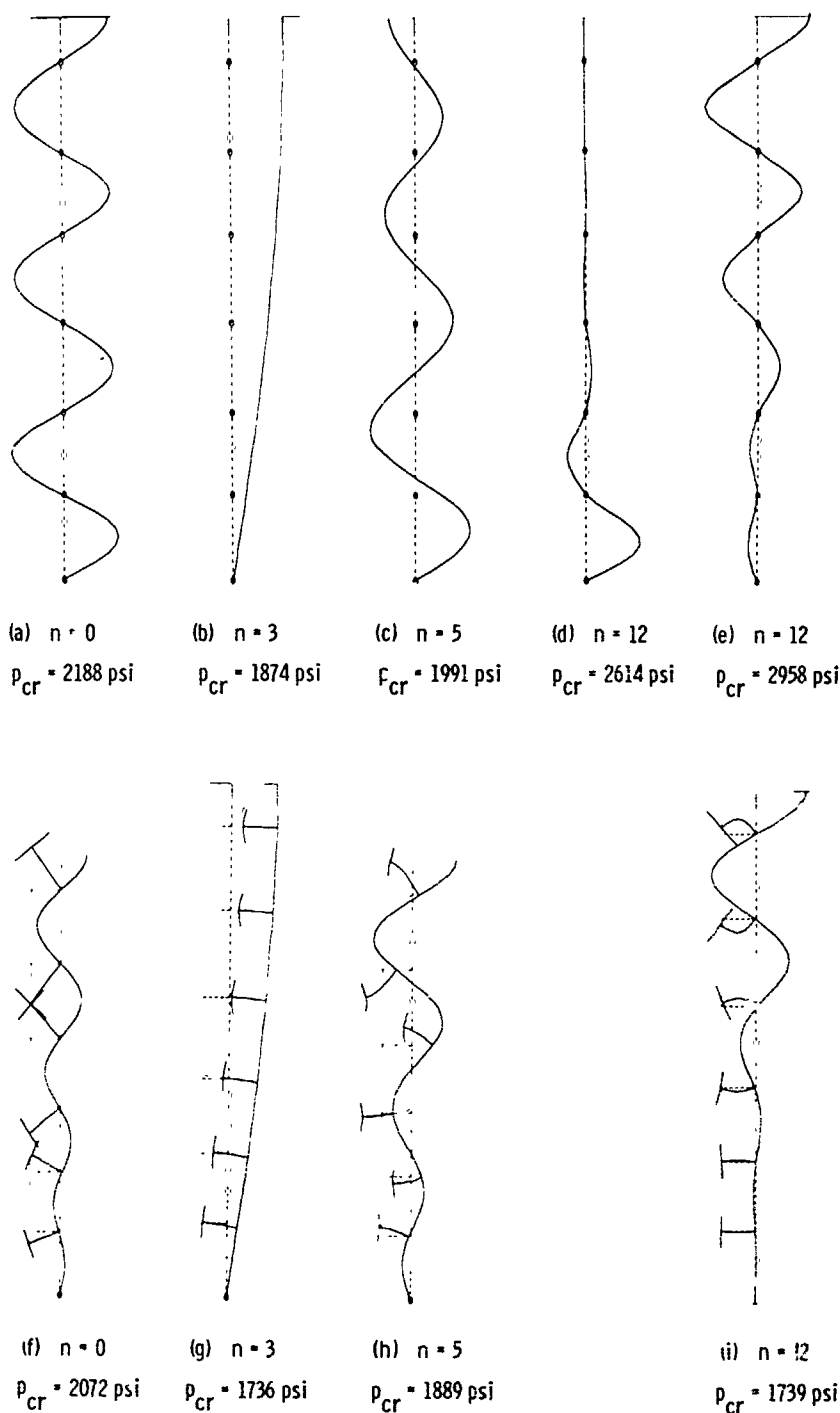


Figure 184 Predicted buckling pressures of internally ring-stiffened cylindrical shell: (a-e) T-shaped rings treated as discrete (cross sections cannot deform); (f-i) T-shaped rings treated as flexible shell segments (cross sections are deformable).

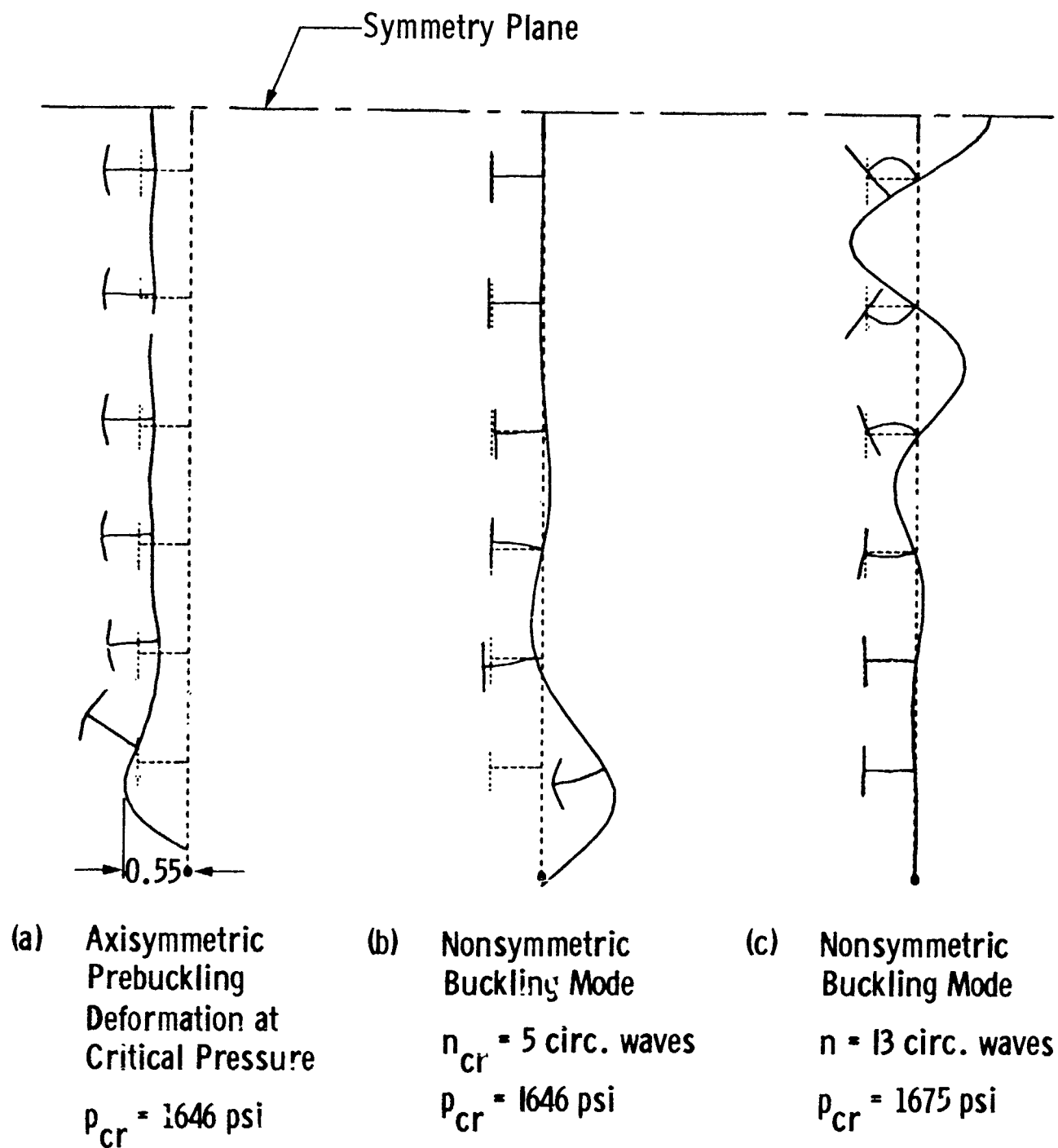
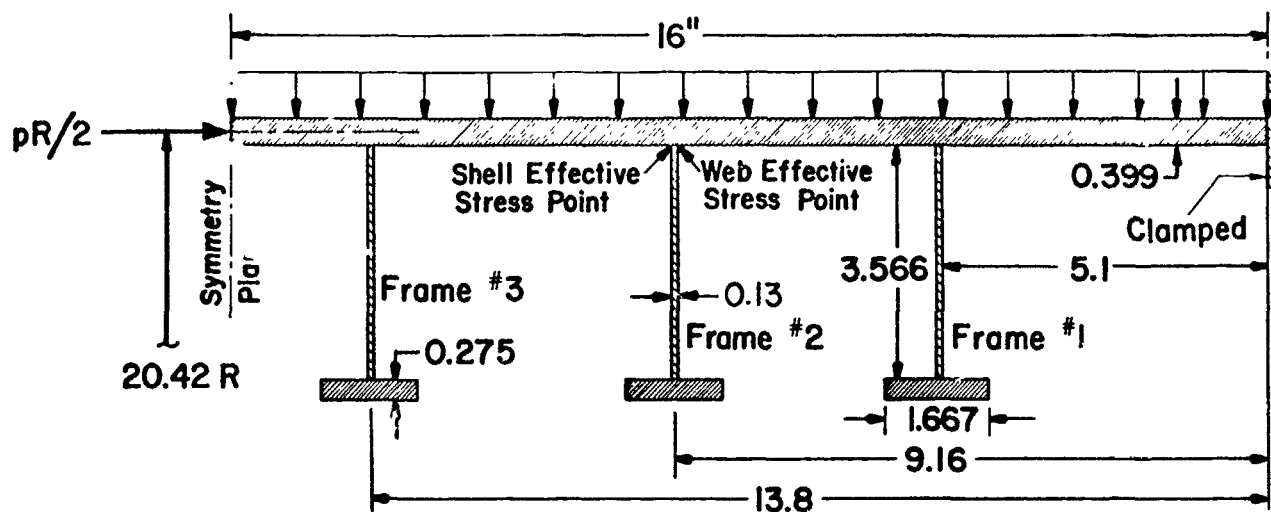
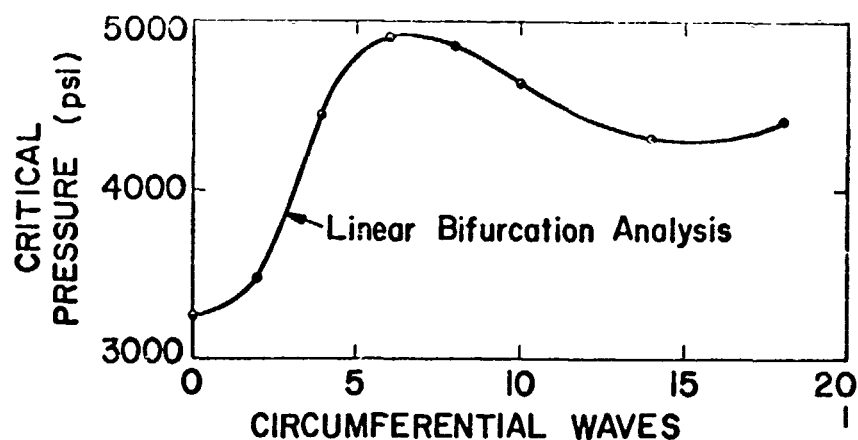


Figure 185 Bifurcation buckling of internally ring-stiffened cylindrical shell shown in Figure 183 including nonlinear prebuckling effects.



(a)



(b)

Figure 187 An externally pressurized ring-stiffened cylindrical shell that failed by axisymmetric sidesway of the deep rings: (a) geometry; (b) results of a linear bifurcation analysis on a branched shell model (from Bushnell [14]).

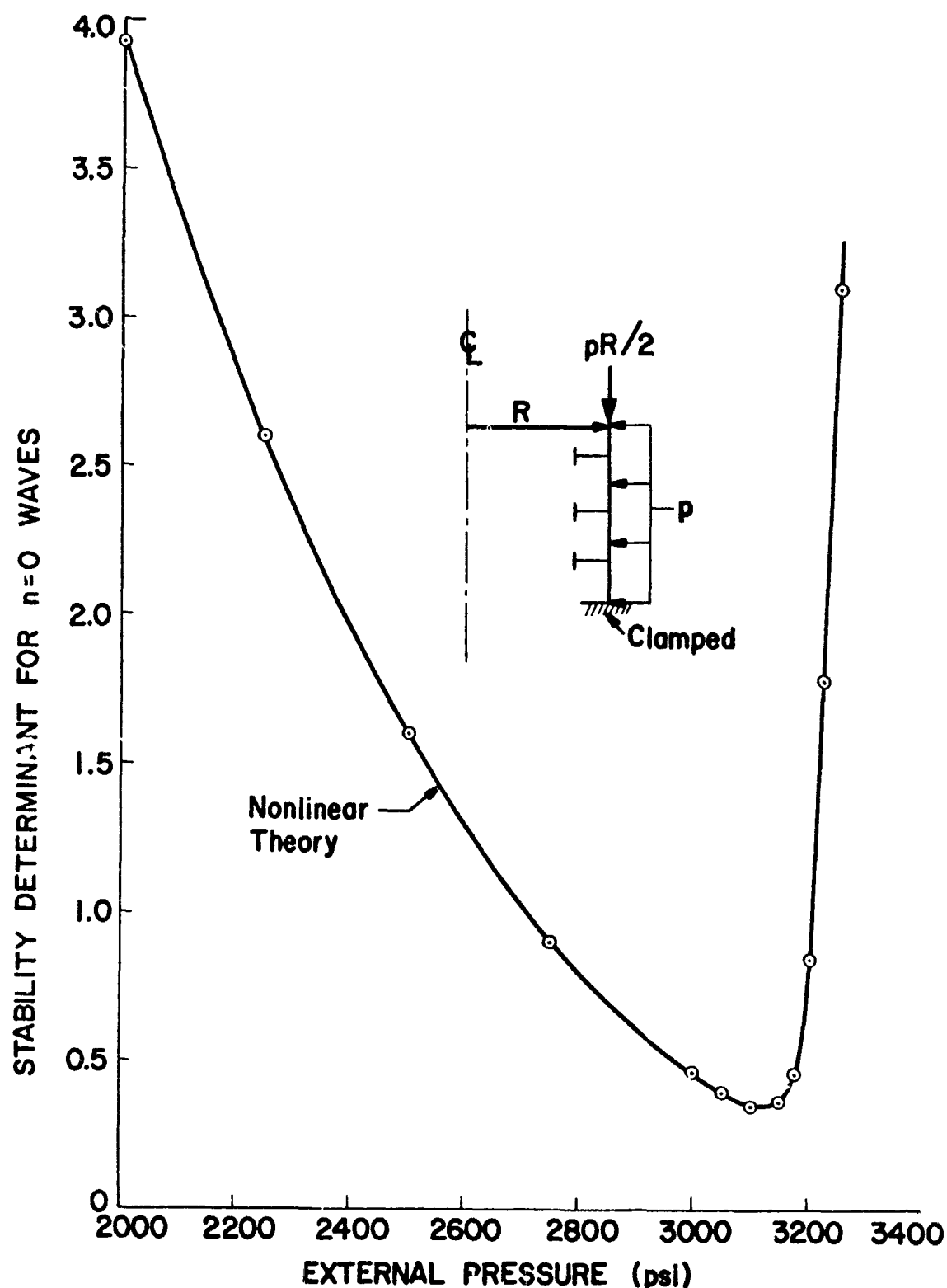


Figure 188 Stability determinant corresponding to axisymmetric ($n = 0$) bifurcation as a function of pressure. The determinant $|K_1(p, n=0)|$ reaches a minimum at the pressure corresponding to linear bifurcation buckling [Figure 187(b)] (from Bushnell [14]).

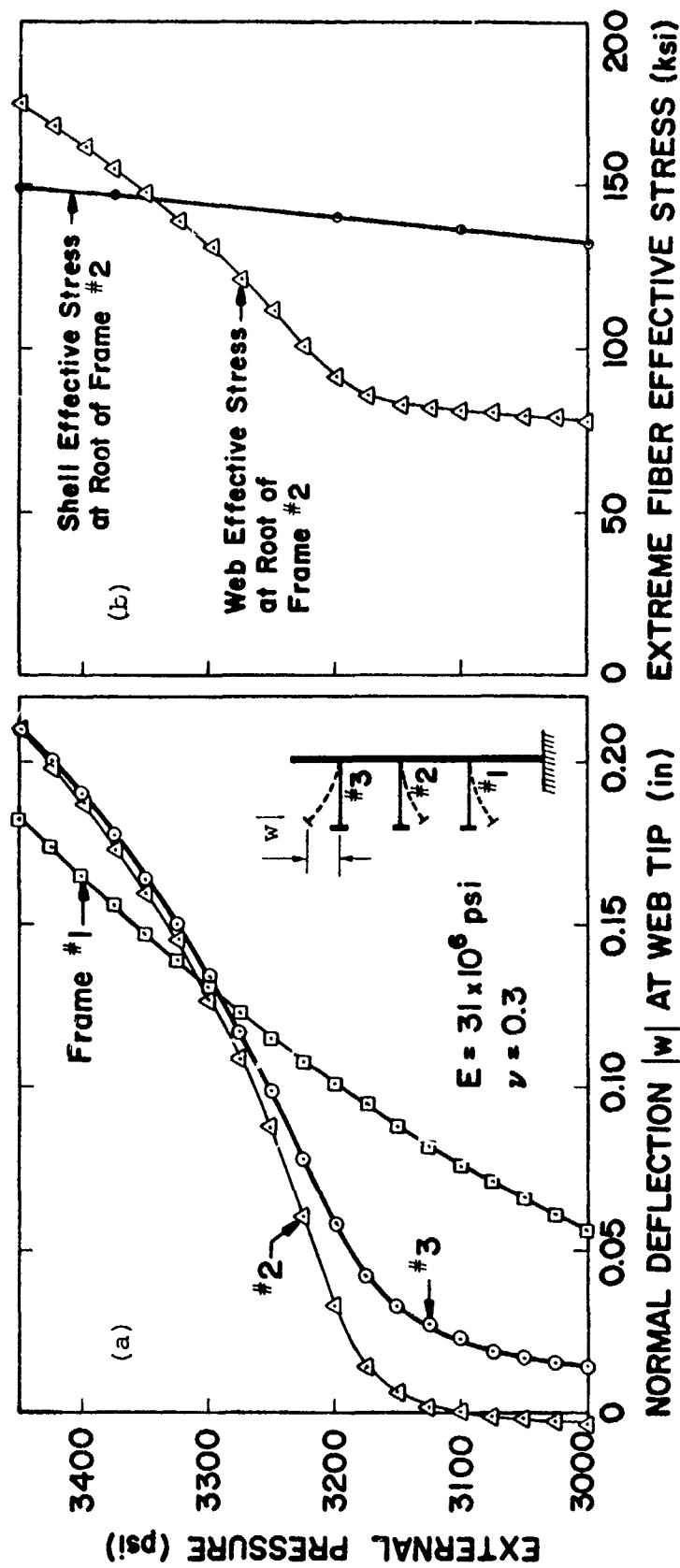
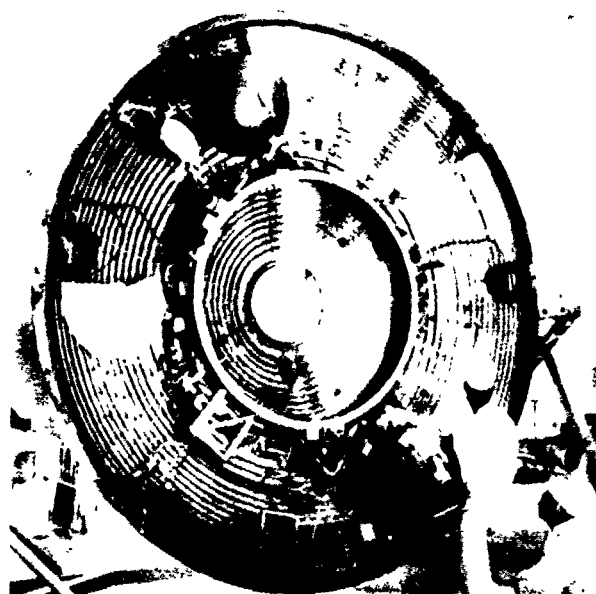
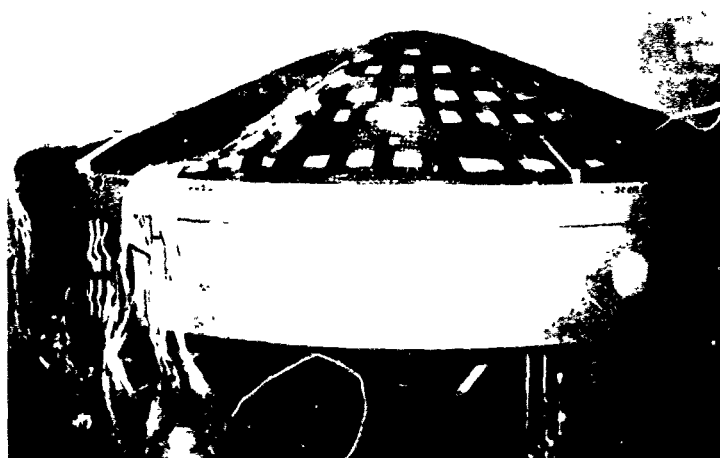


Figure 189 Asymmetric wide column post-buckling behavior of webs: (a) tip deflection; (b) maximum effective stress (from Bushnell [14]).

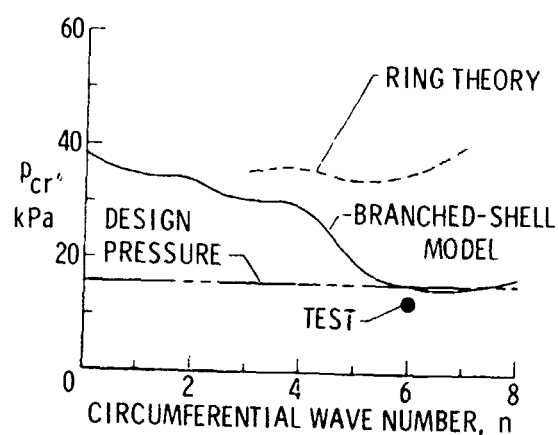


UNIFORM PRESSURE, p
SUPPORT REACTION

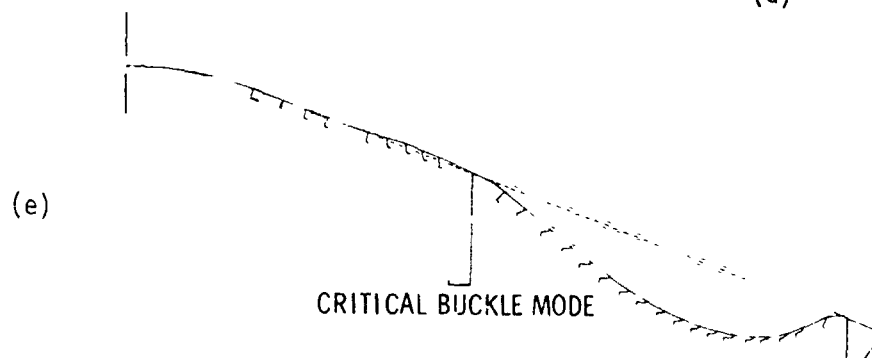
(b)



(c)



(d)



(e)

Figure 190 Lightweight ring-stiffened shallow conical shell designed by NASA for accelerating a payload in the Martian atmosphere: (a) inside the shell; (b) loading; (c) test specimen buckled under uniform external pressure; (d) comparison of test and predictions from two analytical models [11]; and (e) buckling mode from branched shell model (from Leonard et al. [246]).

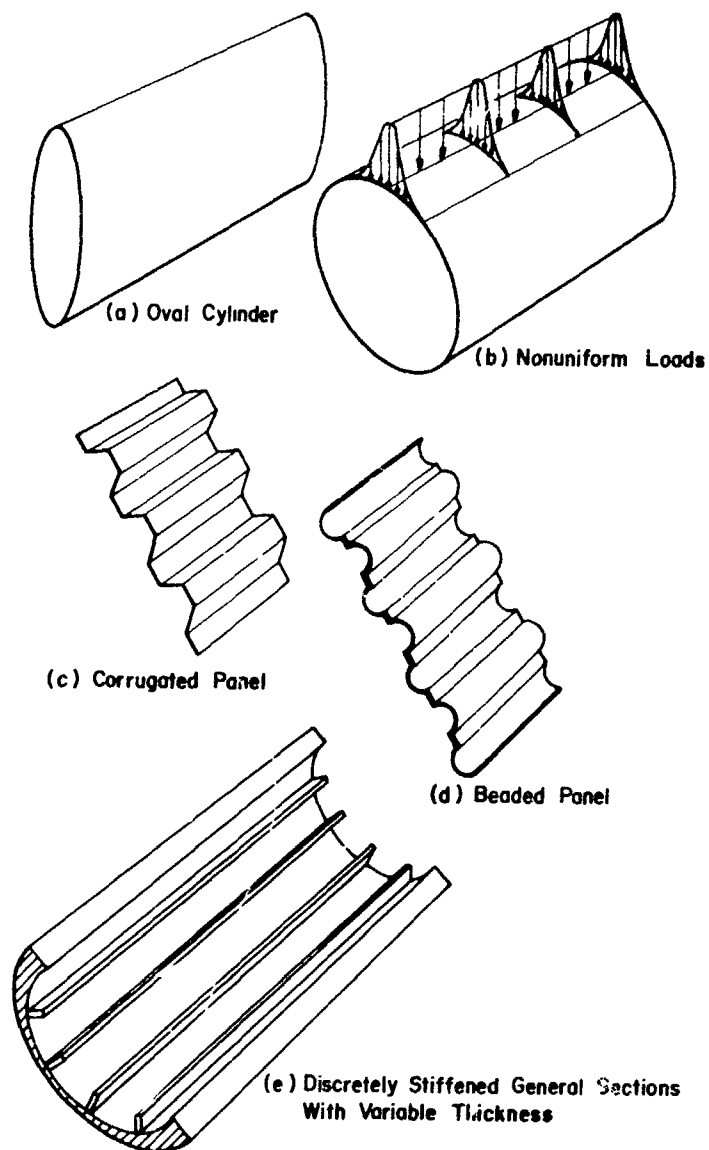


Figure 191 Some typical prismatic shell structure (from Bushnell [82]).

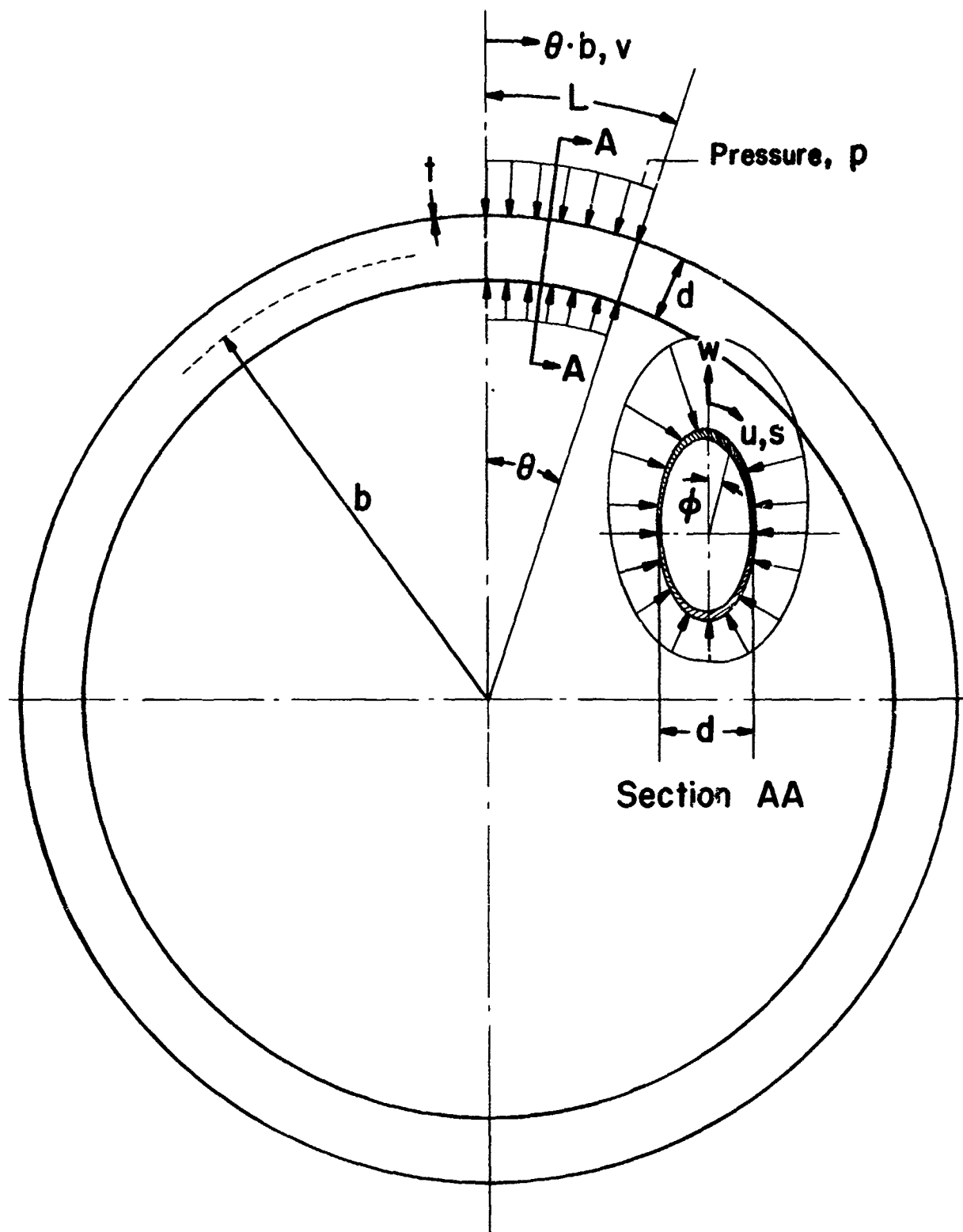


Figure 192 Noncircular cylinder treated as portion of torus with large radius b and length $L = \theta \cdot b$ (from Bushnell [82]).

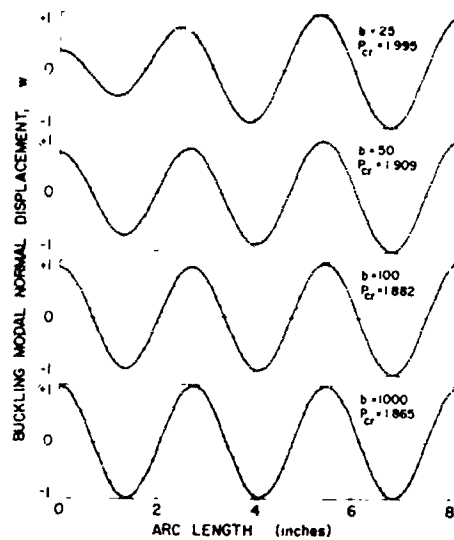


Figure 193 Analysis of simply supported circular cylinder as portion of torus with radius b . Convergence study with increasing b . $P_{cr} = p_{cr}a/Et$, $L/a = 0.6$, $a/t = 100$, $a = 5.236$ in. One Quarter of circumference covered (from Bushnell [82]).

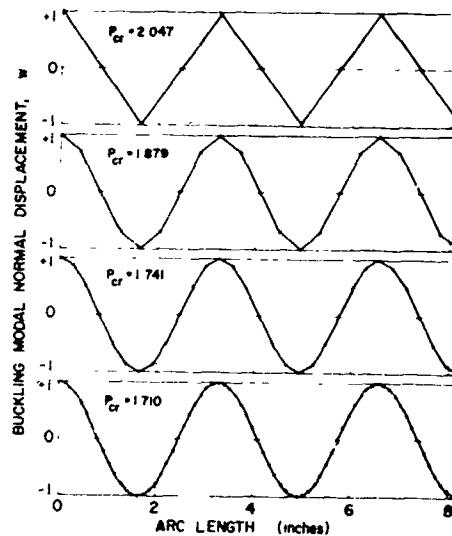


Figure 194 Analysis of circular cylinder as torus. Nodal point convergence study (from Bushnell [82]).

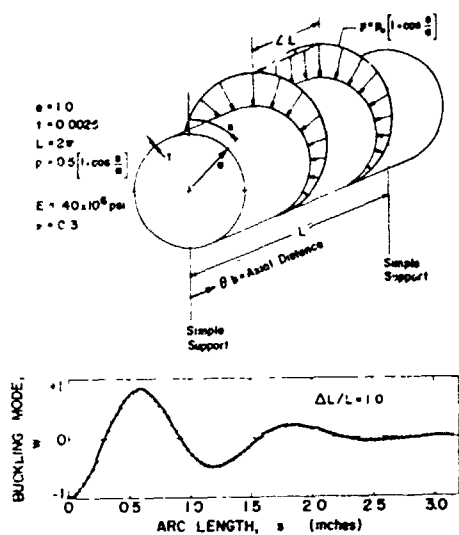


Figure 195 Buckling mode for nonsymmetrically loaded cylinder with $p_{cr}a/Et \times 10^5 = 2.292$, $\Delta L/L = 1.0$ (from Bushnell [82]).

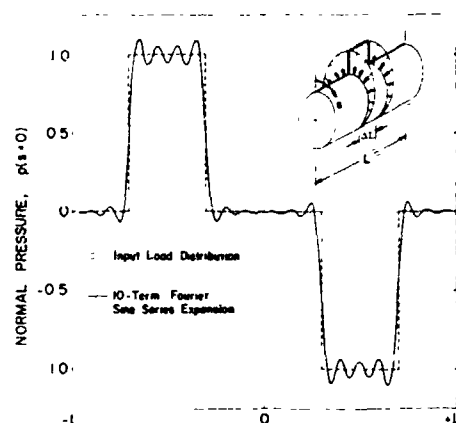


Figure 196 Pressure distribution on cylinder for $\Delta L/L = 0.4$. Cylinder modeled in BOSOR4 as portion of torus (see Figure 192) (from Bushnell [82]).

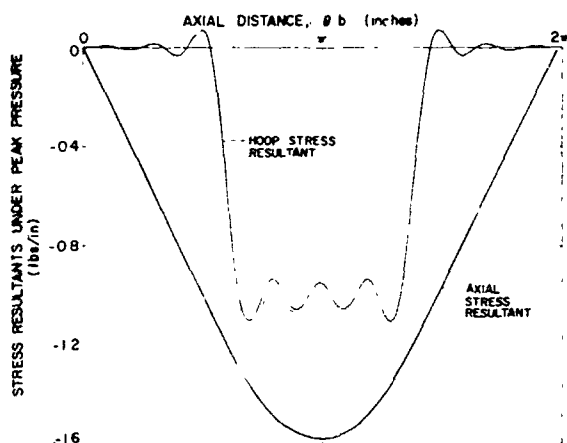


Figure 197 Axial distribution of stress resultants for cylinder under band pressure load ($\Delta L/L = 0.4$) (from Bushnell [82]).

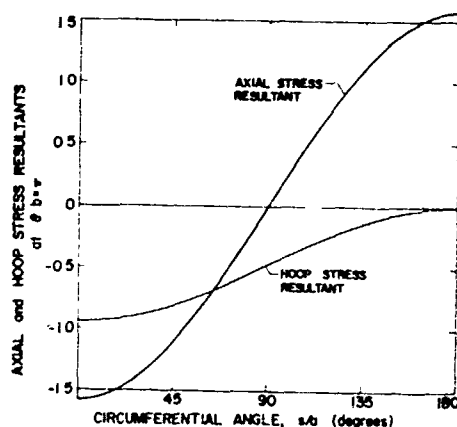


Figure 198 Circumferential distributions of stress resultants at cylinder midlength $\theta \cdot b = \pi$ inches (from Bushnell [82]).

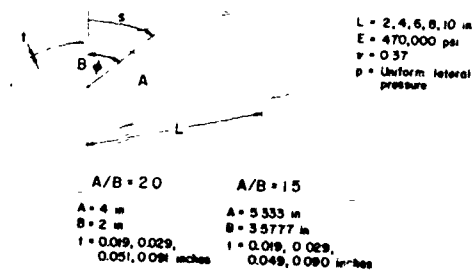


Figure 199 Simply-supported elliptic cylinder configurations.

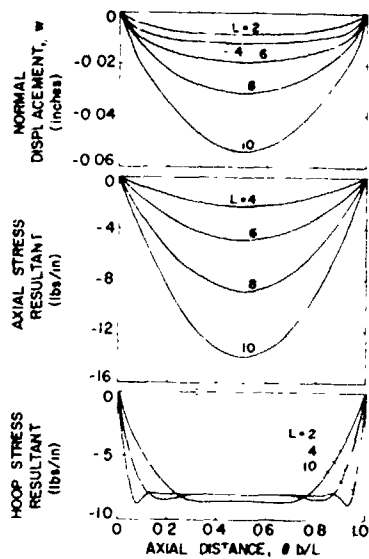


Figure 200 Displacement w and stress resultants at $s = 0$ for 1 psi; external pressure on elliptic cylinder with $A/B = 2$, $t = 0.019$.

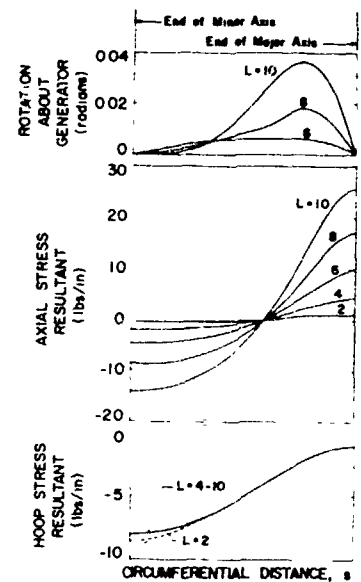


Figure 201 Rotation and stress resultant distributions at midlength of elliptic cylinder with $A/B = 2$, $t = 0.019$.

(all from Bushnell [82])

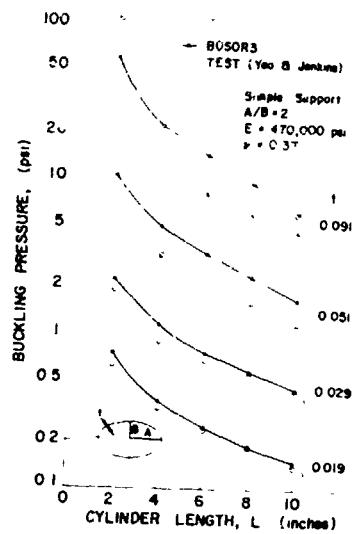


Figure 202 Buckling loads for elliptic cylinders with $A/B = 2$ (from Bushnell [82]).

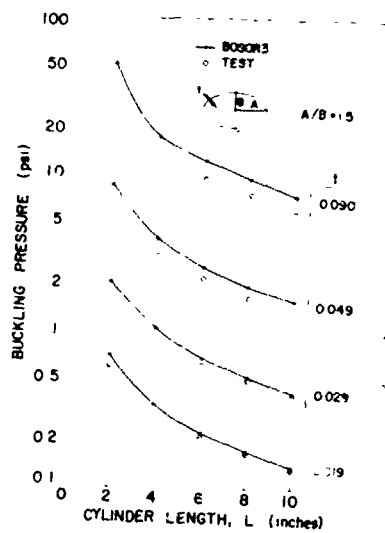


Figure 203 Buckling loads for elliptic cylinders with $A/B = 1.5$ (from Bushnell [82]).

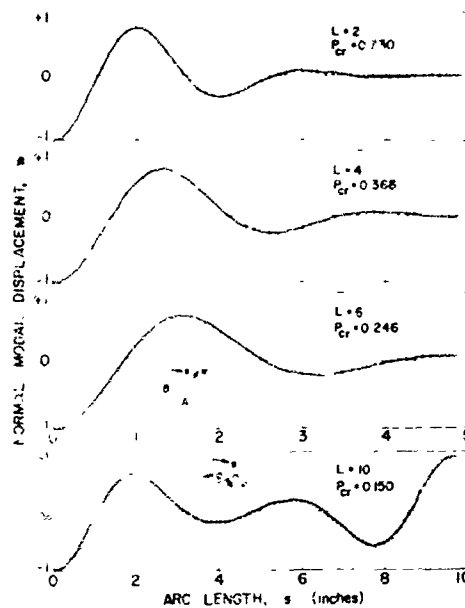


Figure 204 Buckling modes of elliptic cylinders with $A/B = 2$, $t = 0.019$ in., and $L = 2, 4, 6$, and 10 in. (from Bushnell [82]).

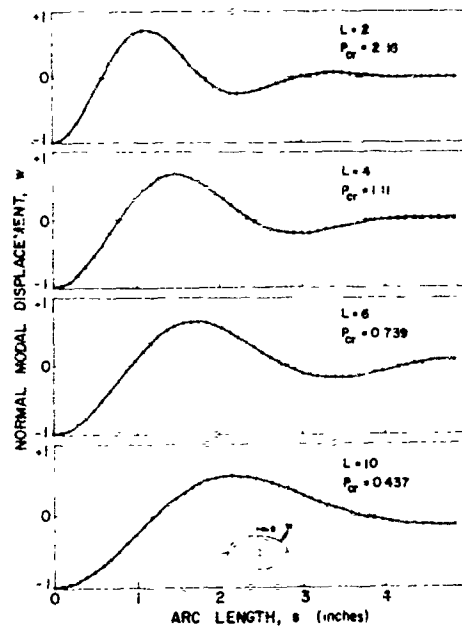


Figure 205 Buckling modes of elliptic cylinders with $A/B = 2$, $t = 0.029$ in., and $L = 2, 4, 6$, and 10 in. (from Bushnell [82]).

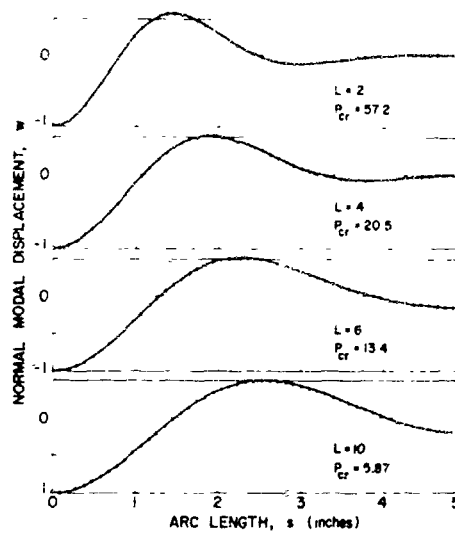


Figure 206 Buckling modes of elliptic cylinders with $A/B = 2$, $t = 0.091$ in., and $L = 2, 4, 6$, and 10 in. (from Bushnell [82]).

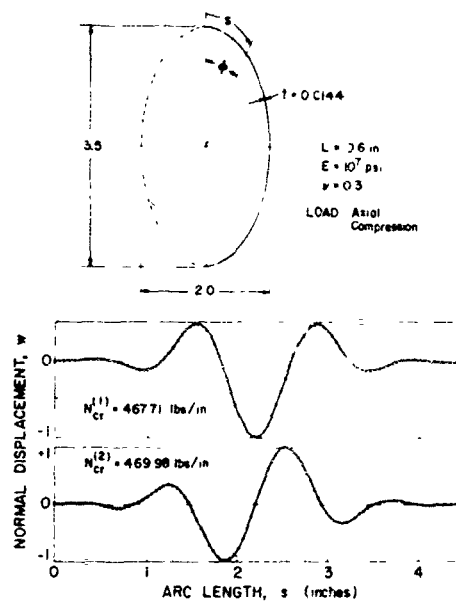


Figure 207 Buckling modes for elliptic cylinder under axial compression (from Bushnell [82]).

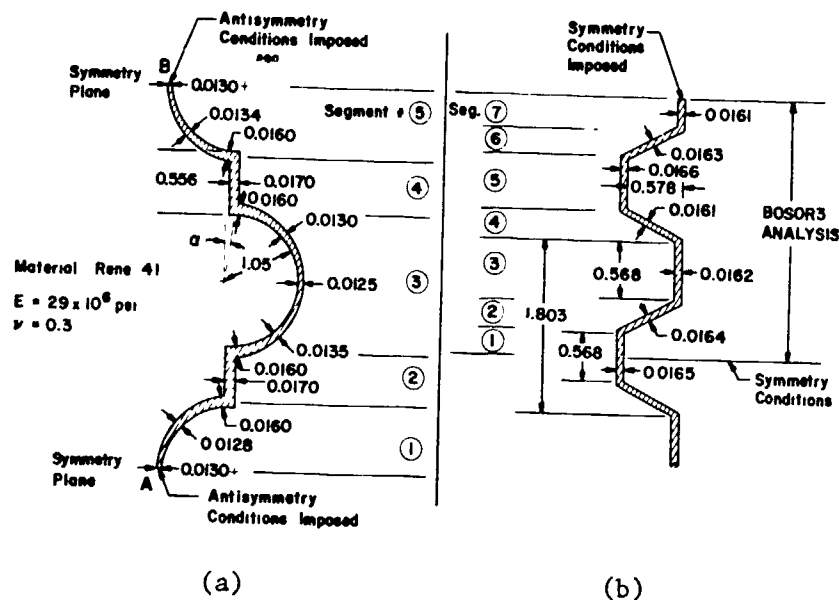


Figure 210 Variable thickness beaded and corrugated panel configurations (from Bushnell [82]).

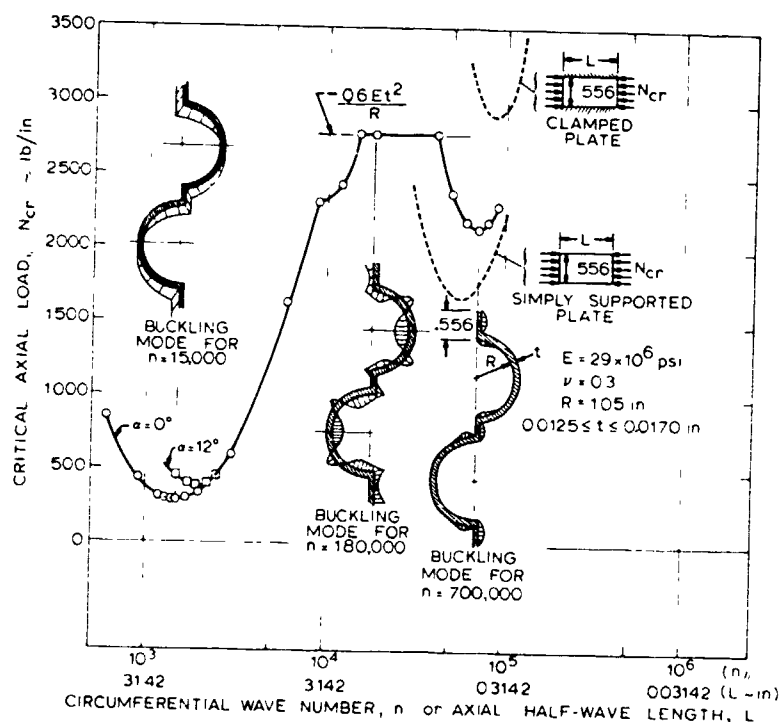


Figure 211 Buckling loads vs. length of beaded panel (from Bushnell [82]).

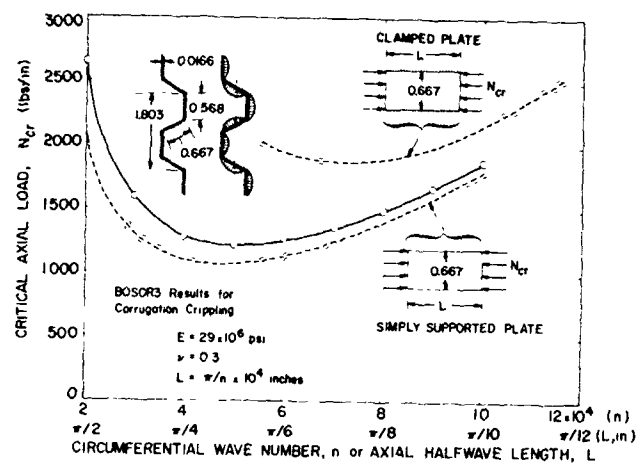


Figure 212 Crippling loads vs. length for a trapezoidal corrugated sheet (from Bushnell [82]).

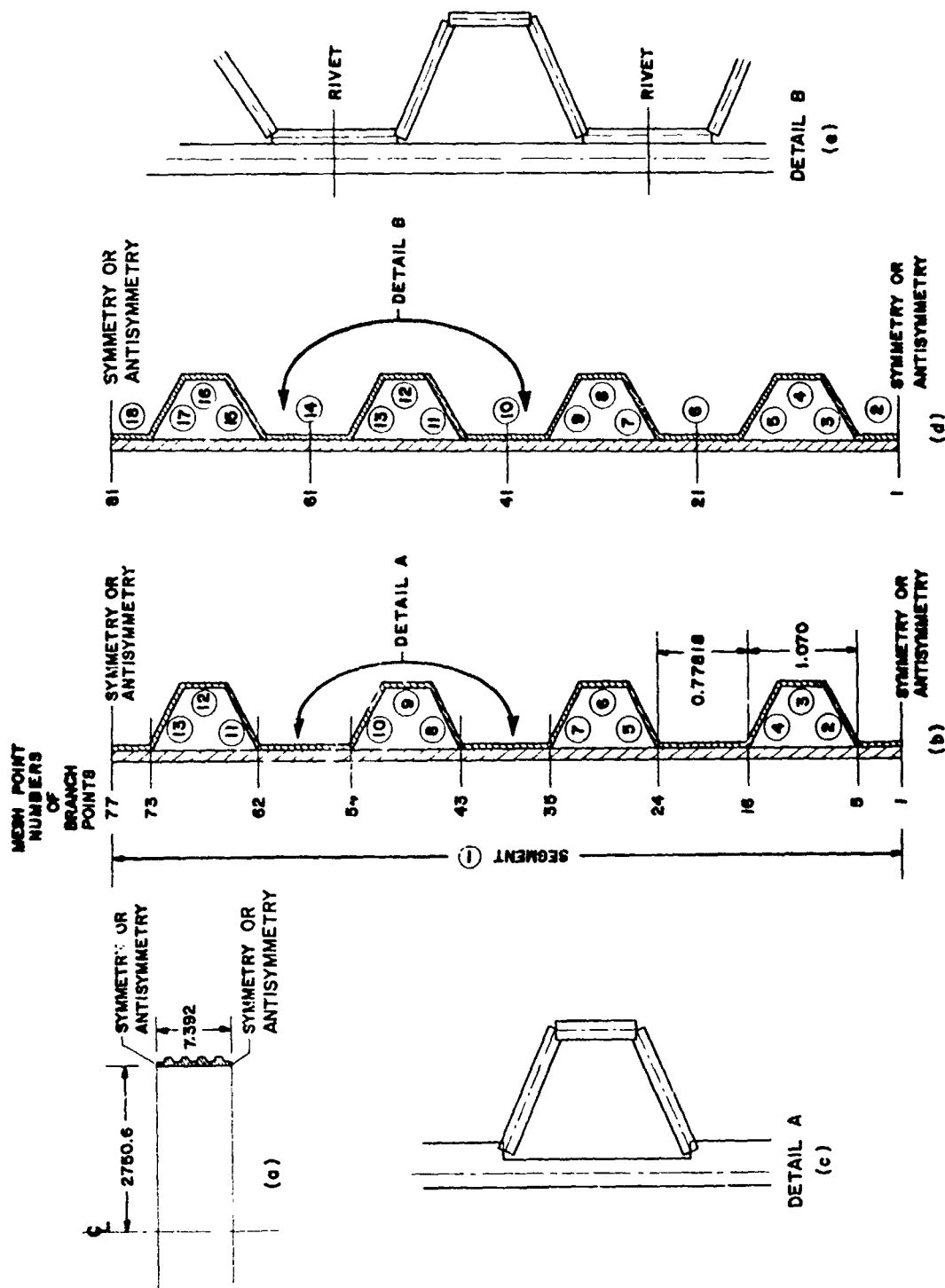


Figure 213 Corrugated panel model: (a) cylinder with large radius; (b) segmented bonded model; (c), detail of branches, bonded model; (d) segmented riveted model; and (e) branches, riveted model.

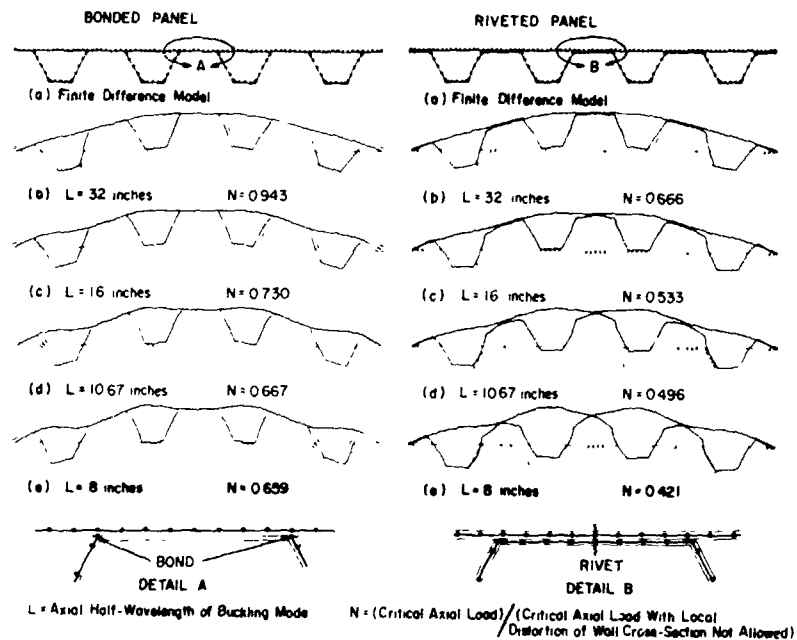


Figure 214 Buckling modes and normalized loads of axially compressed semisandwich corrugated riveted and bonded panels (from Bushnell [273]).

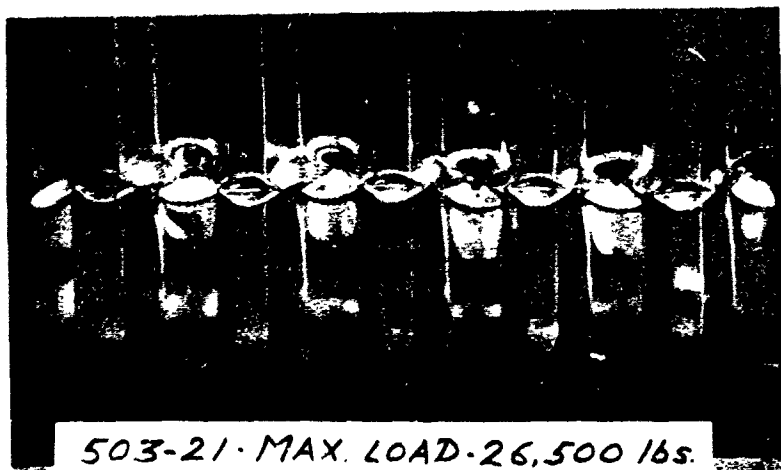


Figure 215 Aluminum corrugated semisandwich bonded panel crippled under axial compression at a load/length of 2867 lb/in (from Bushnell [3]).

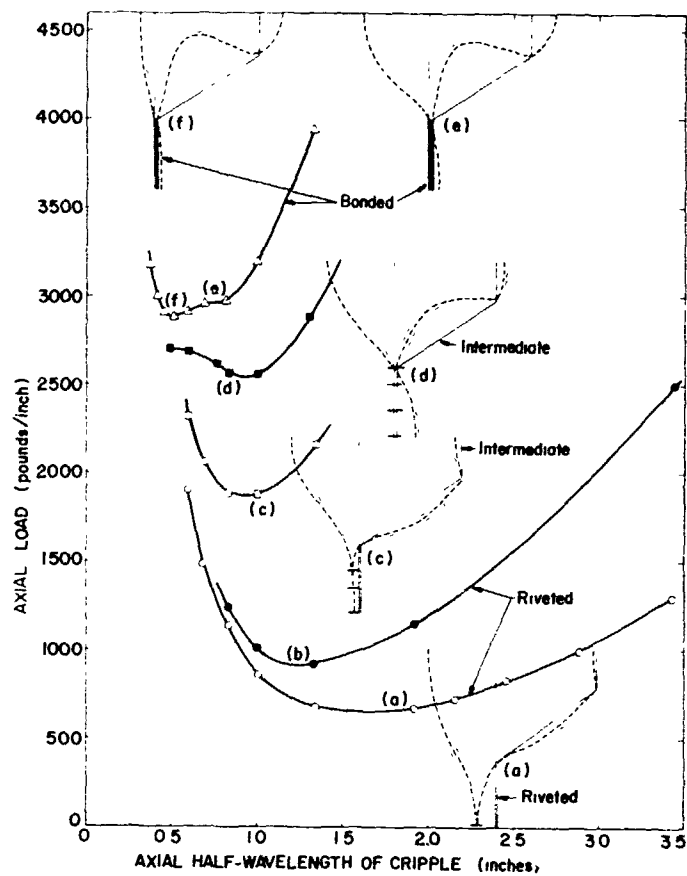


Figure 216 Crippling of axially compressed semisandwich corrugated panel as function of degree of matching of displacements between skin and trough of corrugation (from Bushnell [273]).

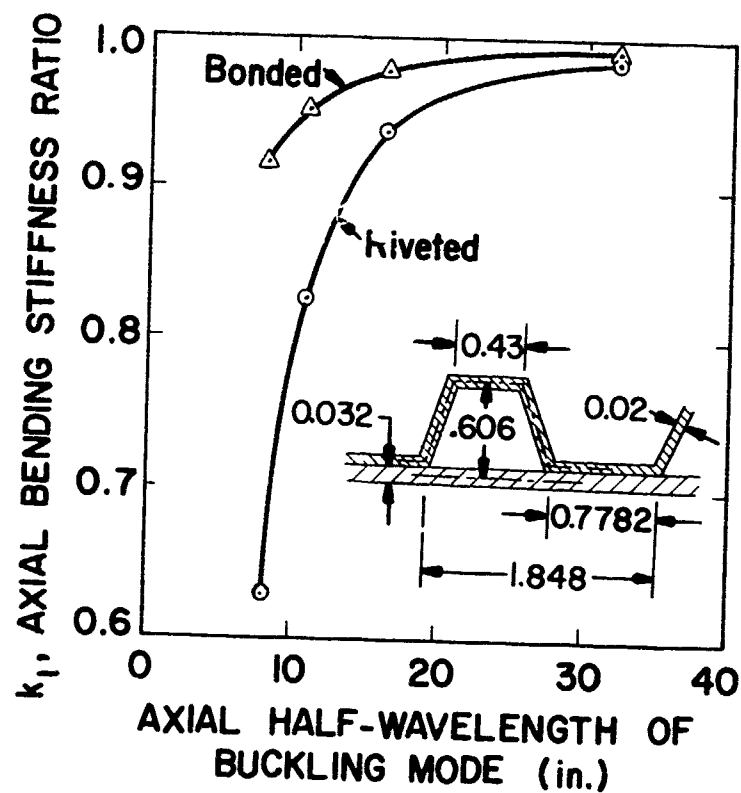


Figure 217 Degradation of axial bending stiffness with decreasing axial wavelength of buckle (from Bushnell [273]).

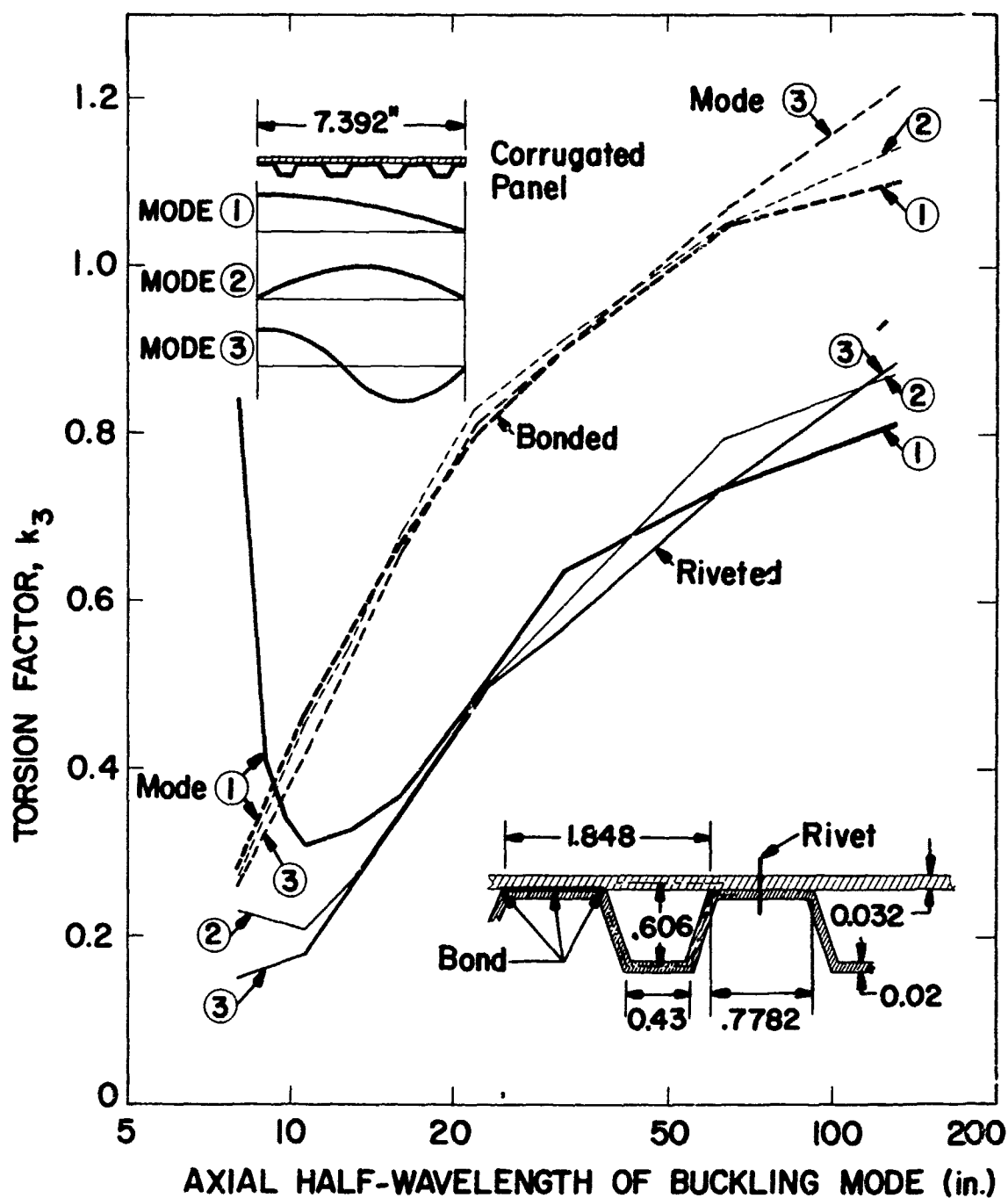


Figure 218 Degradation of torsional stiffness with decreasing axial wavelength of buckle (from Bushnell [273]).

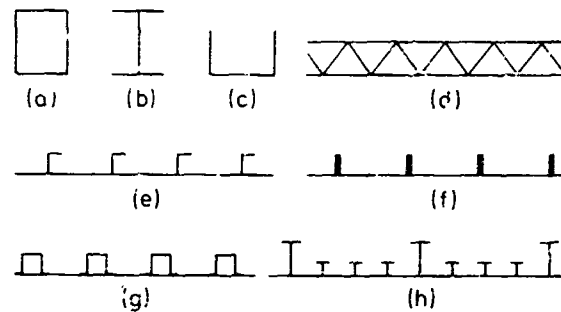


Figure 219 Cross-sectional shapes of various built-up plate structures. (a-c) thin-walled columns, (d) truss-core sandwich panel, (e-h) eccentrically stiffened panels (from Tvergaard [275]).

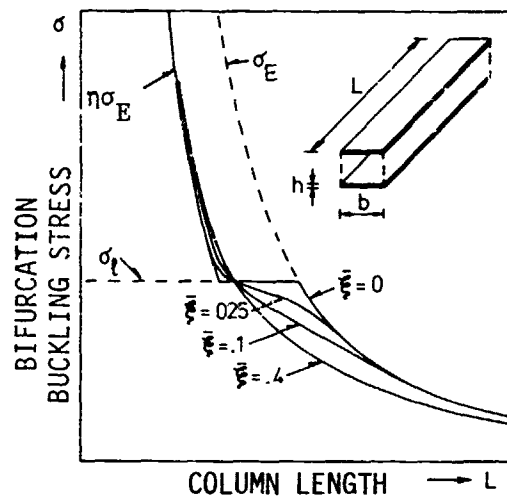


Figure 220 Column buckling load for two-flange model of given cross-section as function of column length and flange imperfection amplitude. This configuration was studied by van der Neut [278] and Thompson and Lewis [279] (from Tvergaard [275]).

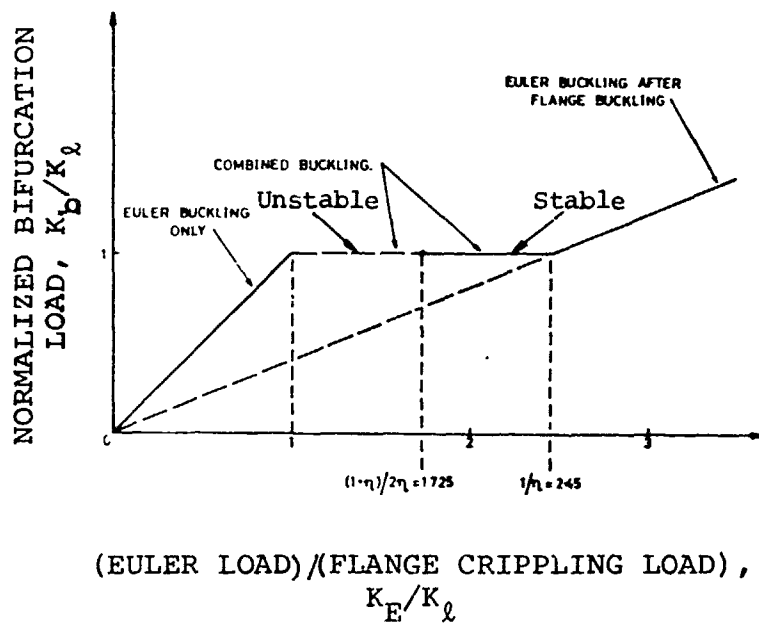
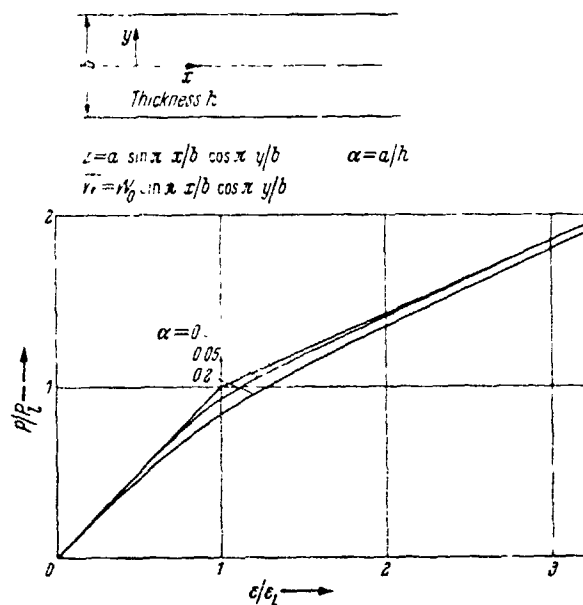


Figure 222 A convenient dimensionless summary of the response of the perfect two-flanged column (from Thompson and Lewis [279]).

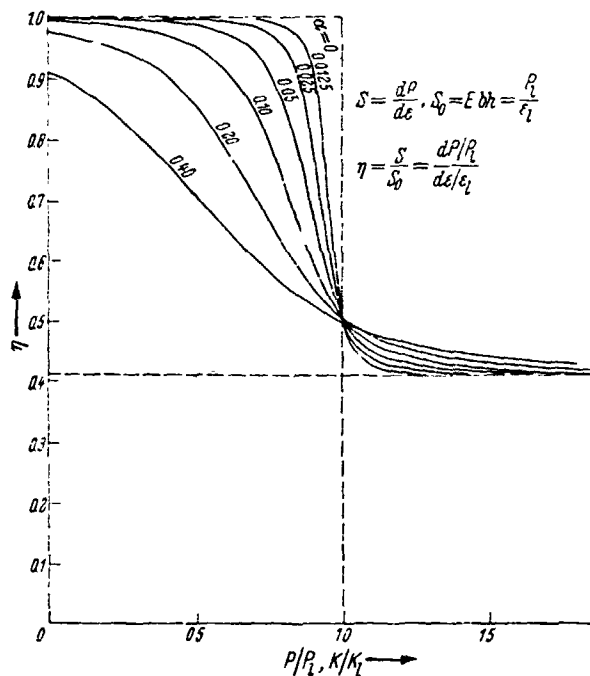
FLANGE AXIAL LOAD RATIO



COMPRESSIVE STRAIN RATIO

Figure 223 Load-strain curve of imperfect simply-supported plate strip under axial compression $[(P_c, \epsilon_c) = \text{flange compressive (load, strain) at bifurcation of the perfectly flat simply-supported flange}]$ (from van der Neut [278]).

AXIAL STIFFNESS REDUCTION FACTOR



NORMALIZED AXIAL FLANGE OR COLUMN LOAD

Figure 224 Reduction of the stiffness of the axially compressed plate strip due to initial waviness α (from van der Neut [278]).

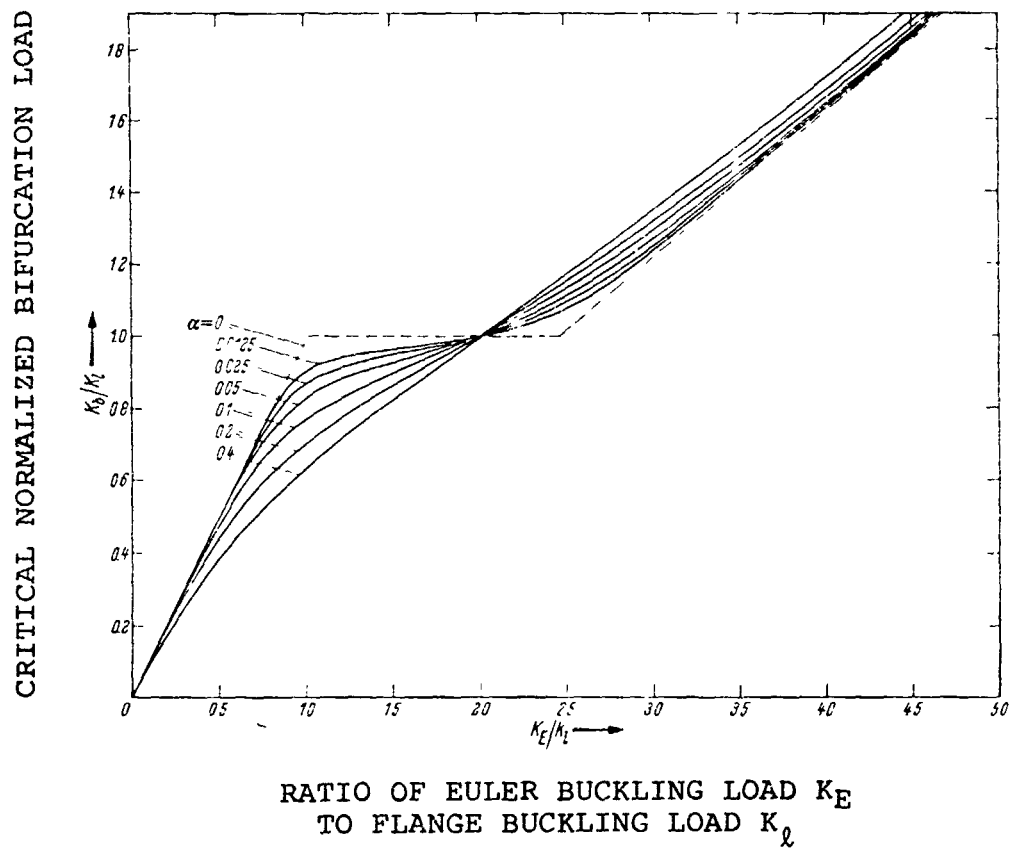


Figure 225 Bifurcation buckling curves of columns with imperfect flanges (from van der Neut [278]).

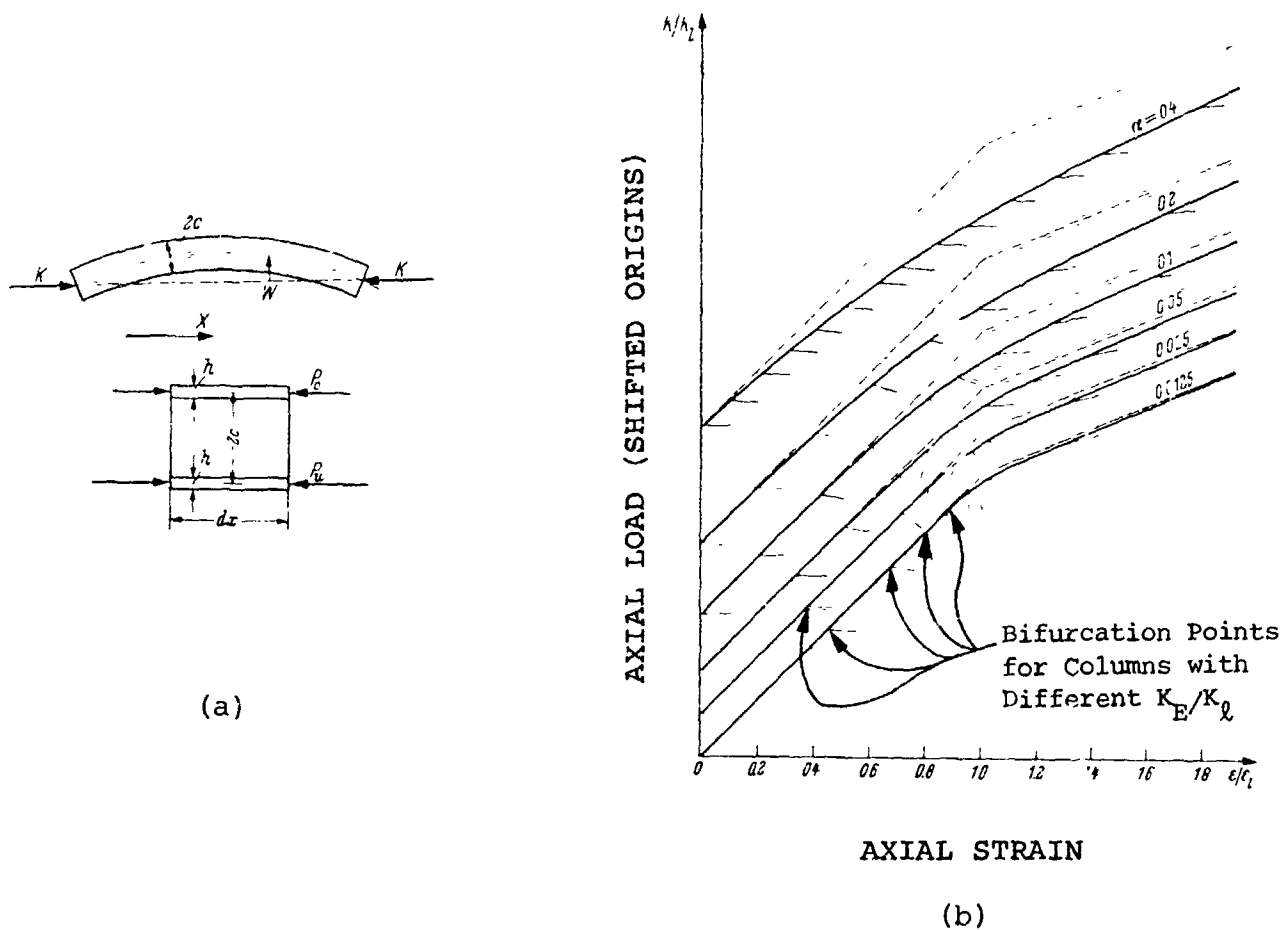


Figure 226 P- ϵ curves and tangents to the load-shortening curve at the bifurcation load K_b of columns with various K_E/K_l (from van der Neut [278]).

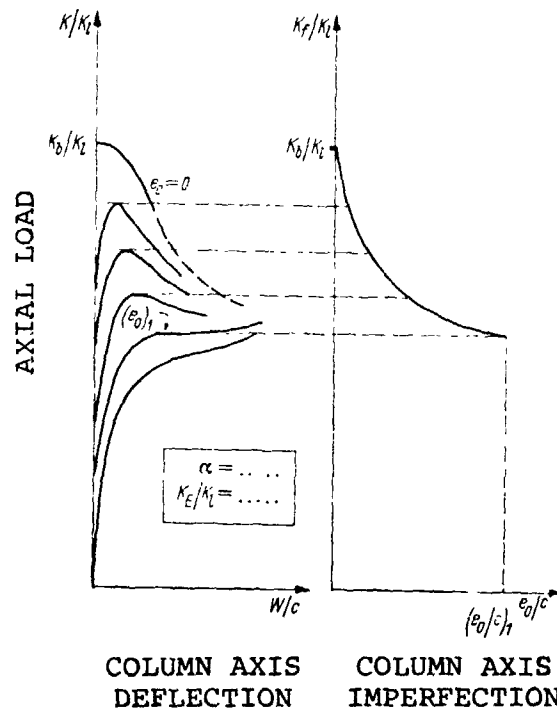


Figure 227 Strength reduction with increasing initial column axis eccentricity, e_o/c (from van der Neut [278]).

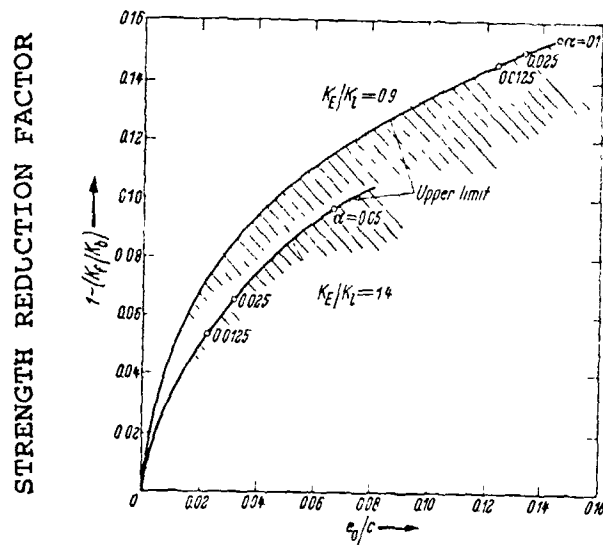


Figure 228 Reduction of column strength because of eccentricity, e_o/c (from van der Neut [278]).

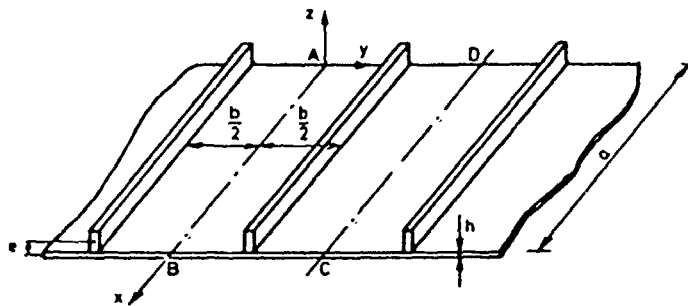


Figure 229 Part of plane, integrally stiffened panel (from Tvegaard [283]).

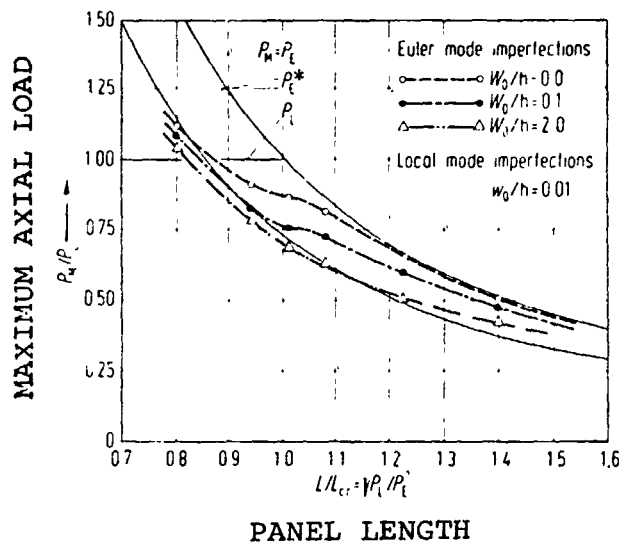


Figure 230 Maximum load P_M versus length for eccentrically stiffened panels. The curves with data points are from tests on epoxy plastic panels (from Thompson et al. [287]).

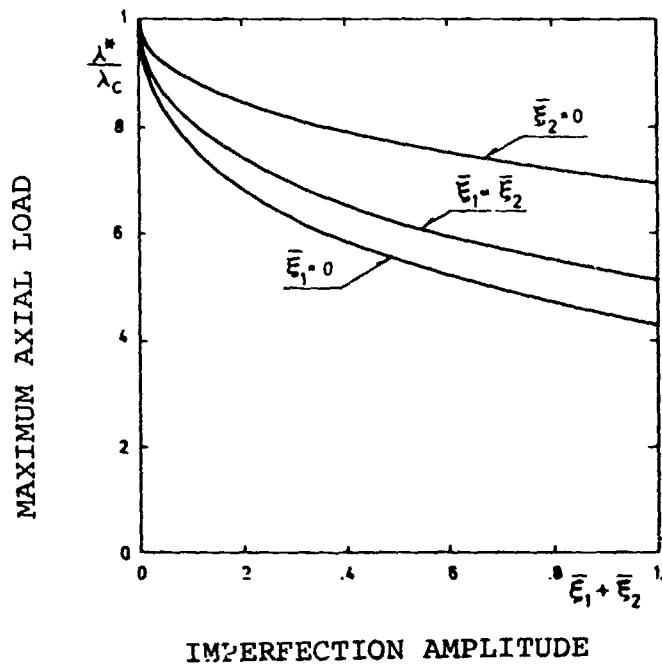


Figure 231 Carrying capacity of imperfect panel (from Tvergaard [283]).

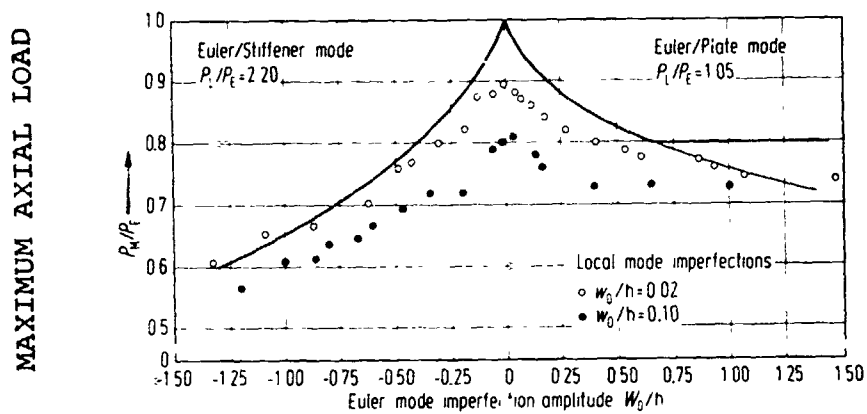


Figure 232 Experimental imperfection-sensitivity plot for a panel with thin stiffeners (from Thompson et al. [287]).

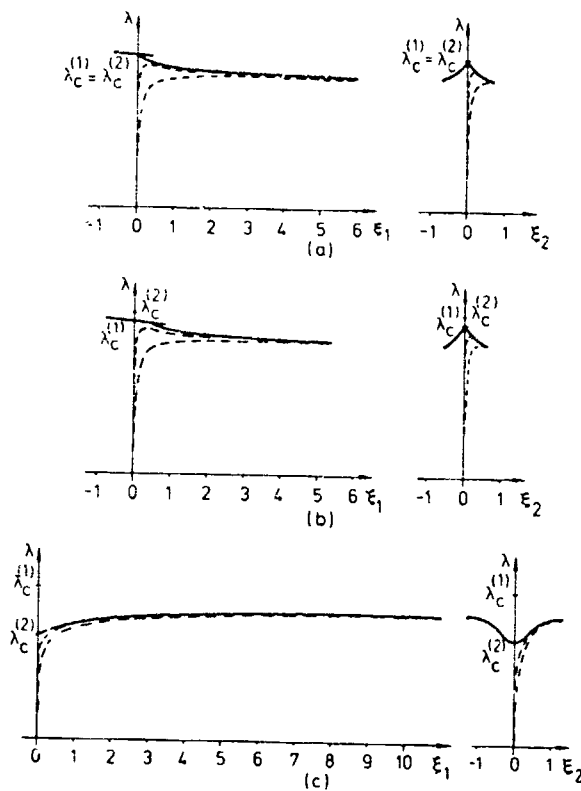


Figure 233 Dependence on load of modal deflections of eccentrically stiffened panel. Solid curves correspond to perfect panels. Dashed curves correspond to imperfect panels. Superscripts and subscripts (1) refer to the Euler wide column mode and (2) refer to the local skin buckling mode (from Tvergaard [284]).

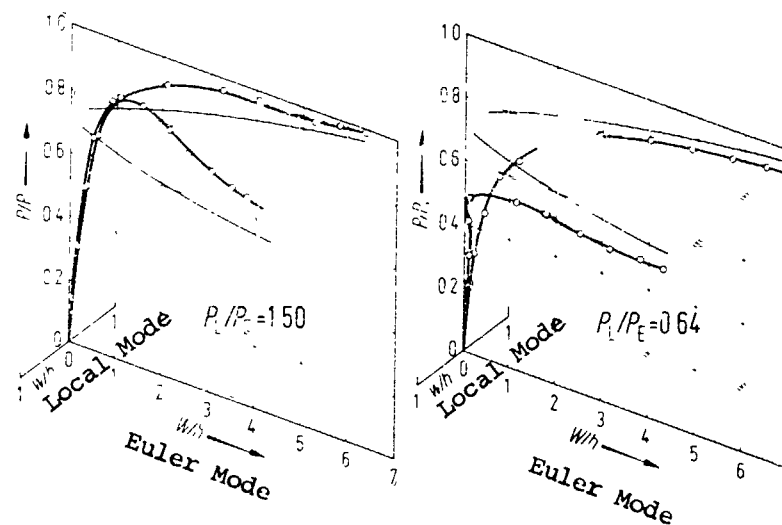


Figure 234 Experimental load-deflection curves: load versus local and Euler mode amplitudes (from Thompson et al. [287]).

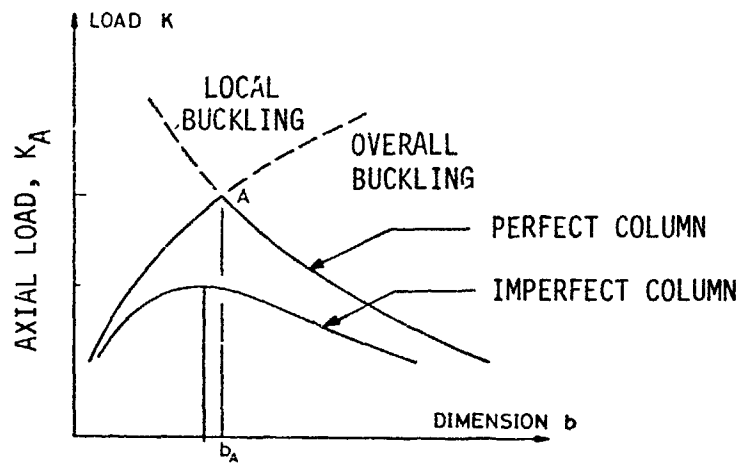
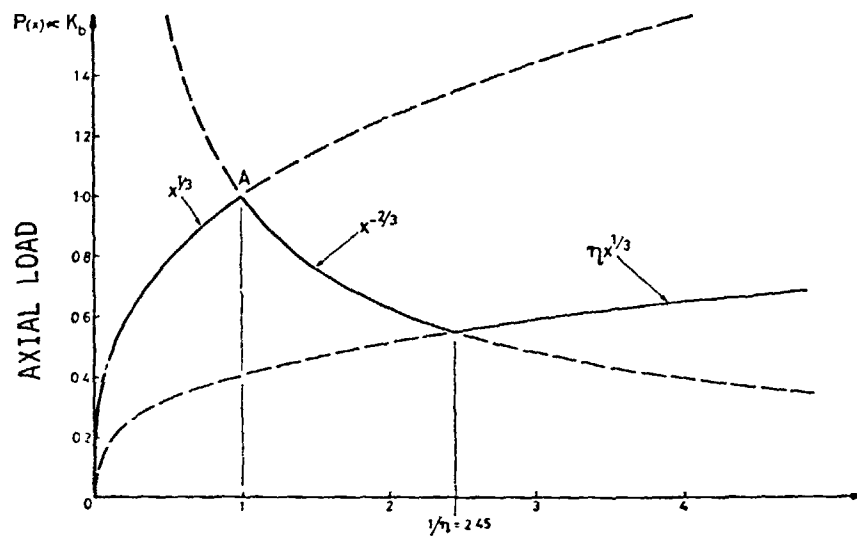
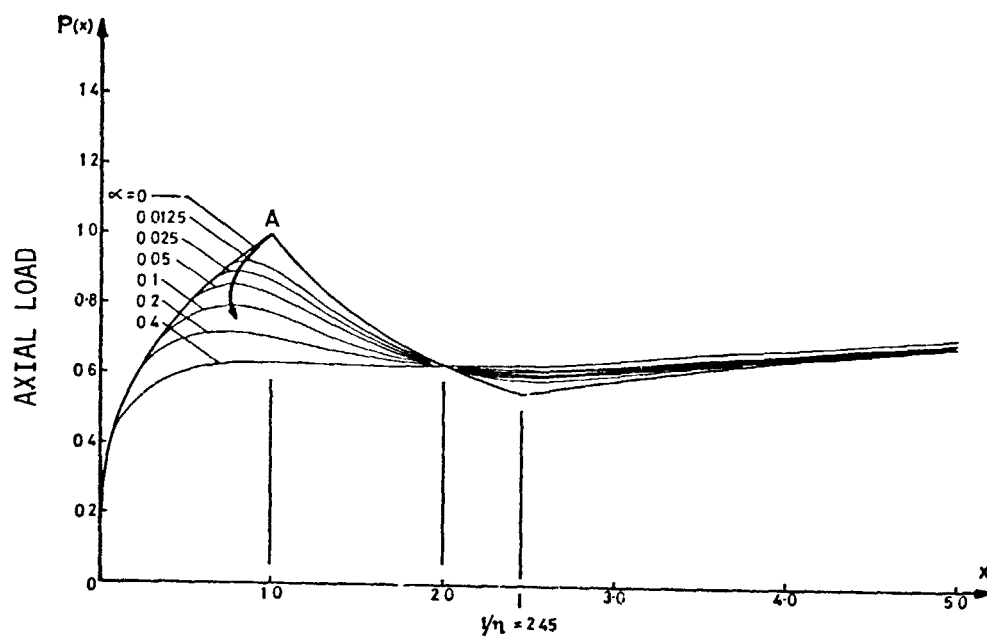


Figure 235 The degeneration of an optimum design because of imperfections (from Thompson and Lewis [279]).



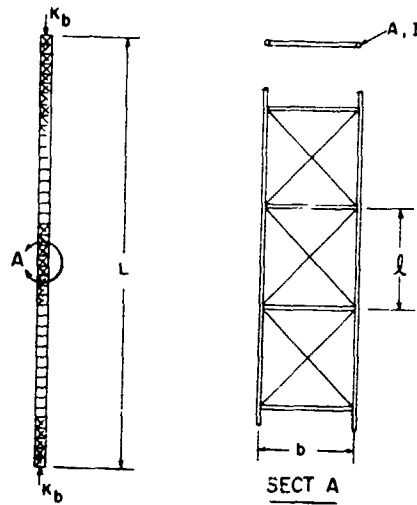
RATIO OF EULER TO LOCAL FLANGE BUCKLING LOADS, $x = K_E/K_L$

Figure 236 The optimum design for a perfect two-flange column (from Thompson and Lewis [279]).

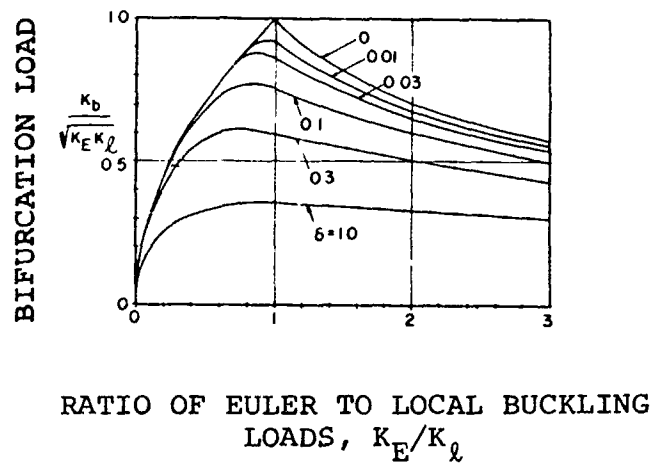


RATIO OF EULER TO LOCAL FLANGE BUCKLING LOADS, $x = K_E/K_\lambda$

Figure 237 The erosion of the optimum by initial flange imperfections (from Thompson and Lewis [279]).



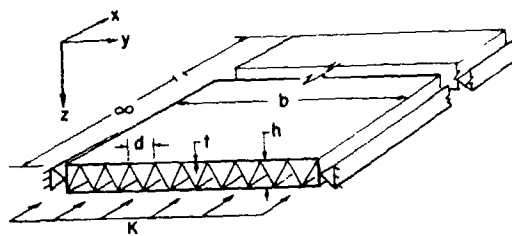
(a)



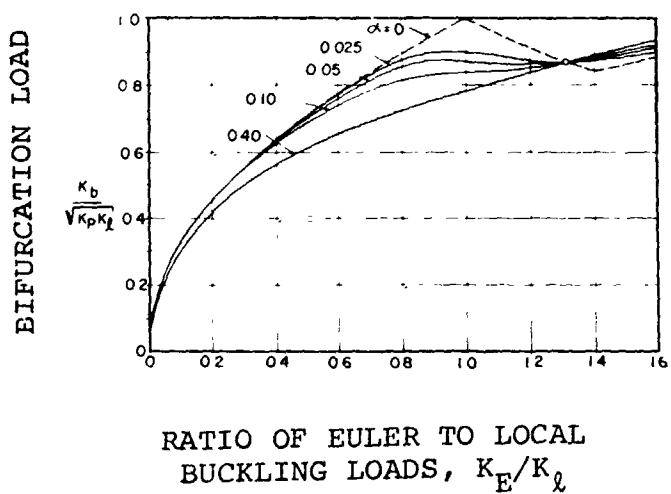
(b)

Figure 238 (a) Lattice-column structure
(b) Effect of local initial imperfections on optimum design of lattice column

(from Crawford and Hedgepeth [280])



(a)



(b)

Figure 239 (a) Truss-core sandwich panel
(b) Effect of local initial imperfections on design of truss-core sandwich panels

(from Crawford and Hedgepeth [280])

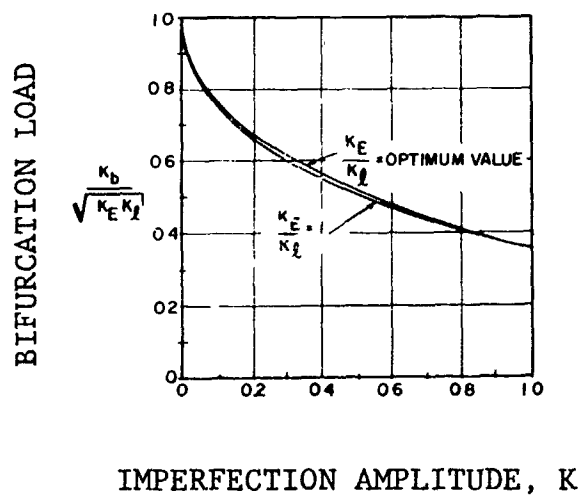


Figure 240 Strength vs. initial imperfection amplitudes for optimally and conventionally designed lattice columns (from Crawford and Hedgepeth [280]).

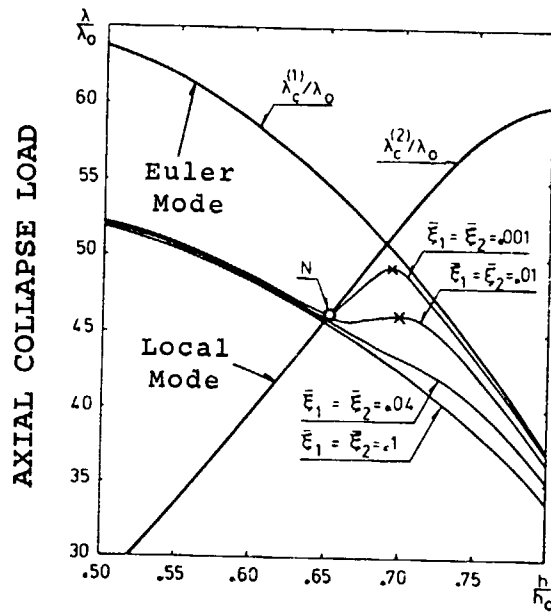


Figure 241 Maximum carrying capacity λ^*/λ_0 for a panel with $a/b = 4$, $e/b = 0.05$ and $h_0/b = 0.0128$, with imperfections $\bar{\xi}_1 = \bar{\xi}_2$. ($h_0 = h + A_s/b$, that is thickness of monocoque panel of same weight as stiffened panel of thickness h . λ_0 = wide column load of monocoque panel. $\bar{\xi}_1$ = Euler mode imperfection, W_0/h_0 ; $\bar{\xi}_2$ = local mode imperfection, w_0/h_0).

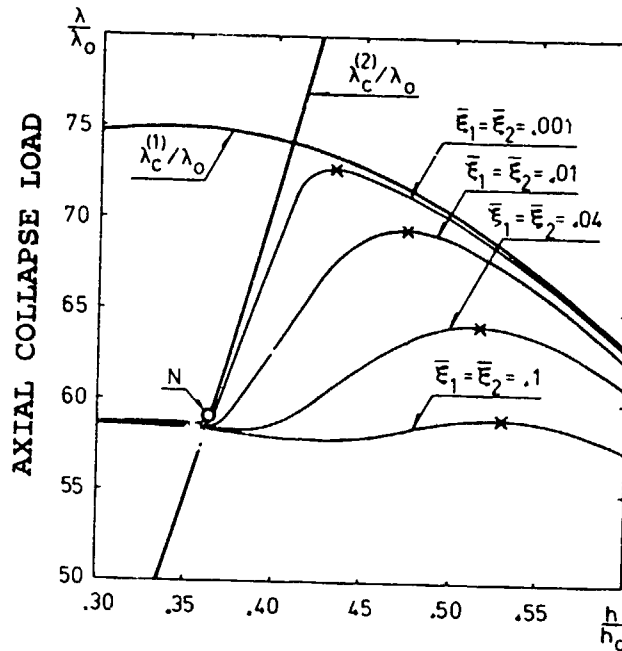


Figure 242 Maximum carrying capacity λ^*/λ_0 for a panel with $a/b = 8$, $e/b = 0.1$ and $h_0/b = 0.0256$, with imperfections $\bar{\xi}_1 = \bar{\xi}_2$.

(both from Tvergaard [284]).

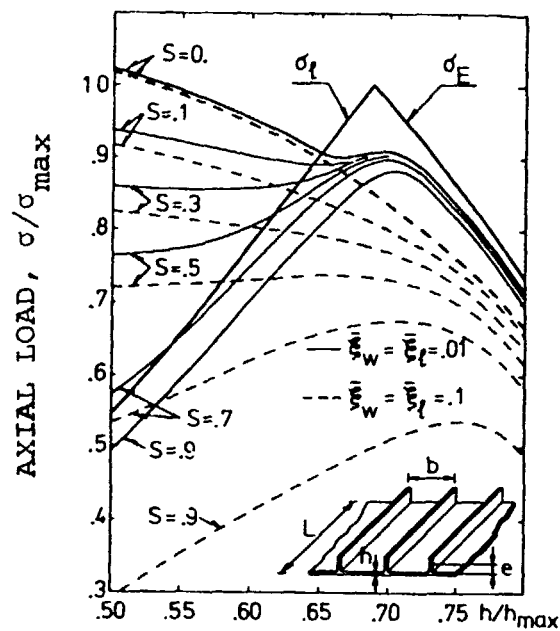
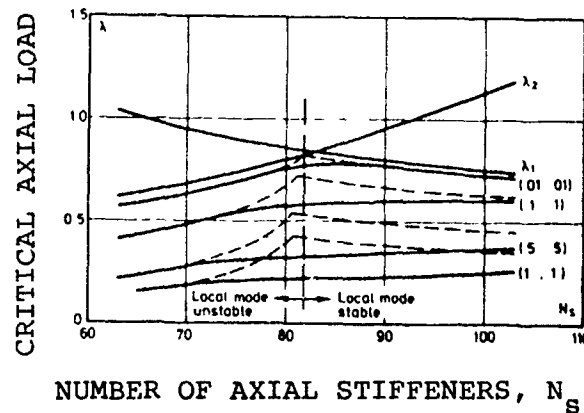
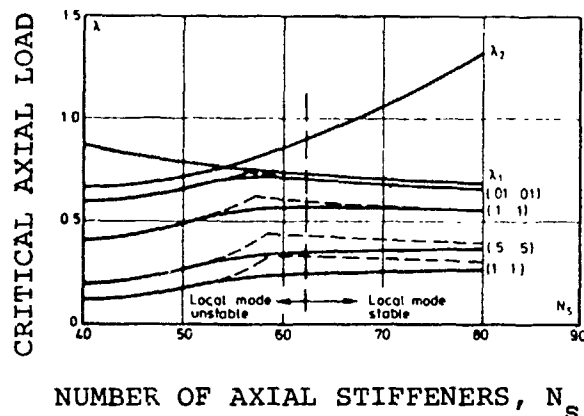


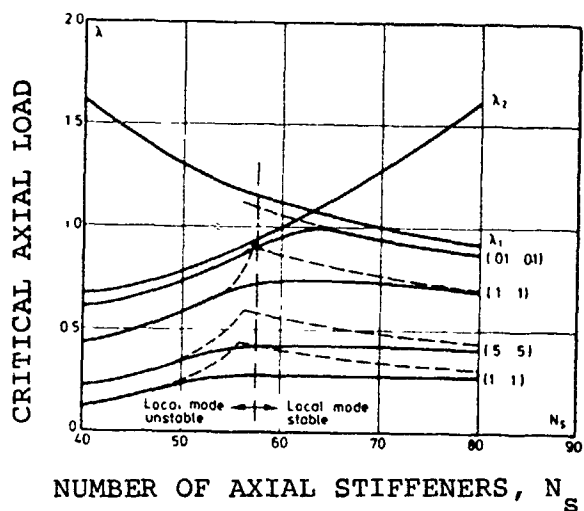
Figure 243 Maximum support load (corresponding to zero axial stiffness, $S = 0$) and compressive stiffness S for imperfect stiffened panel with $a/b = 4$, $e/b = 0.05$, $h_0/b = 0.0128$ (from Tvergaard [275]).



(a) $\alpha_s = 0.7$, $t_s/t = 4.09$, $R/L = 1.0$, $R/t = 850$ (Batdorf parameter $Z = 811$)

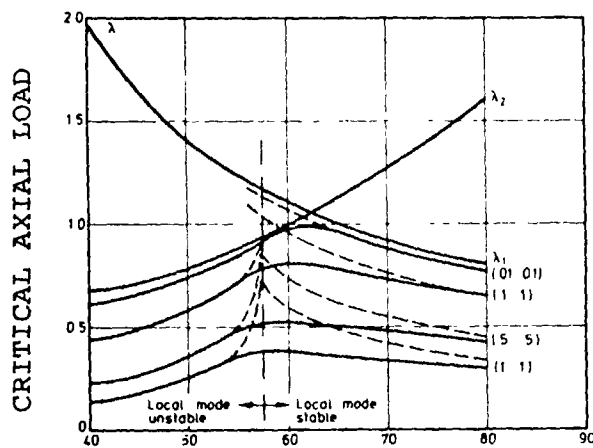


(b) $\alpha_s = 0.05$, $t_s/t = 5.15$, $R/L = 1.0$, $R/t = 525$ (Batdorf parameter $Z = 501$)



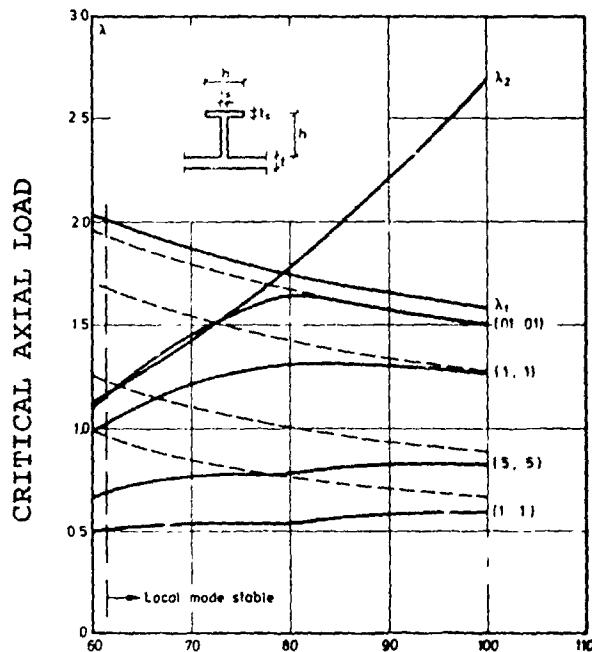
(c) $\alpha_s = 0.5$, $t_s/t = 4.12$, $R/L = 2.0$, $R/t = 420$ (Batdorf parameter $Z = 100$)

Fig. 244(a-c) Buckling of perfect and imperfect axially compressed stringer-stiffened cylinders. Dashed lines correspond to neglect or modal interaction. Stringers on the outside. $(\lambda_1, \lambda_2) = (\text{general}, \text{local})$ bifurcation of perfect shell; $(0.01, 0.01)$, etc. = $(\text{general}, \text{local})$ buckling modal imperfection amplitudes (from Byskov and Hutchinson [290]).



NUMBER OF AXIAL STIFFENERS, N_s

- (d) $\alpha_s = 0.5$, $t_s/t = 4.12$, $R/L = 5.3$, $R/t = 420$
(Batdorf parameter $Z = 37$). Inside stiffeners.



NUMBER OF AXIAL STIFFENERS, N_s

- (e) $\alpha_s = 0.2$, $h/t_s = 16$, $R/L = 2.0$, $R/t = 480$ (Batdorf parameter $Z = 114$). Outside stiffeners.

Figure 244(d,e) Buckling of perfect and imperfect axially-compressed stringer-stiffened cylinders. Dashed lines correspond to neglect of modal interaction. $(\lambda_1, \lambda_2) =$ (general, local) bifurcation of perfect shell; (0.01, 0.01), etc. = (general, local) buckling modal imperfection amplitudes (from Byskov and Hutchinson [290]).

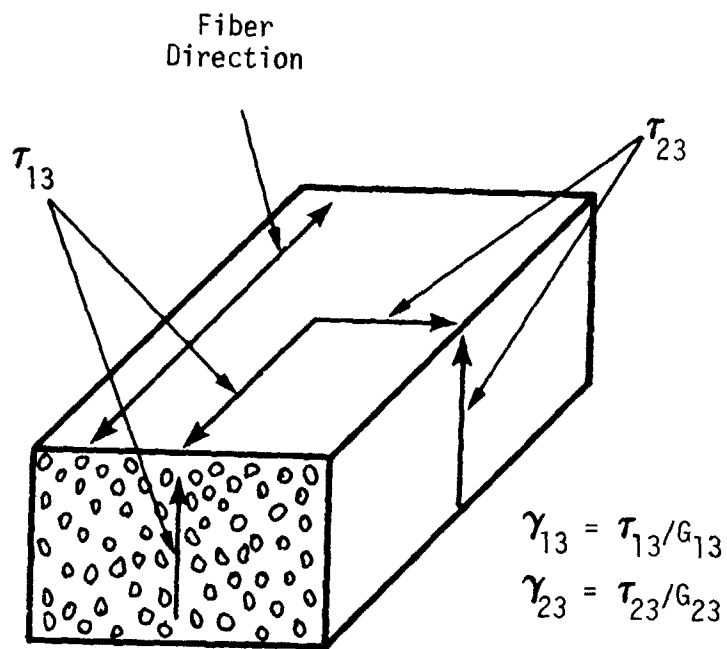


Figure 245 Directions of transverse shear stresses.

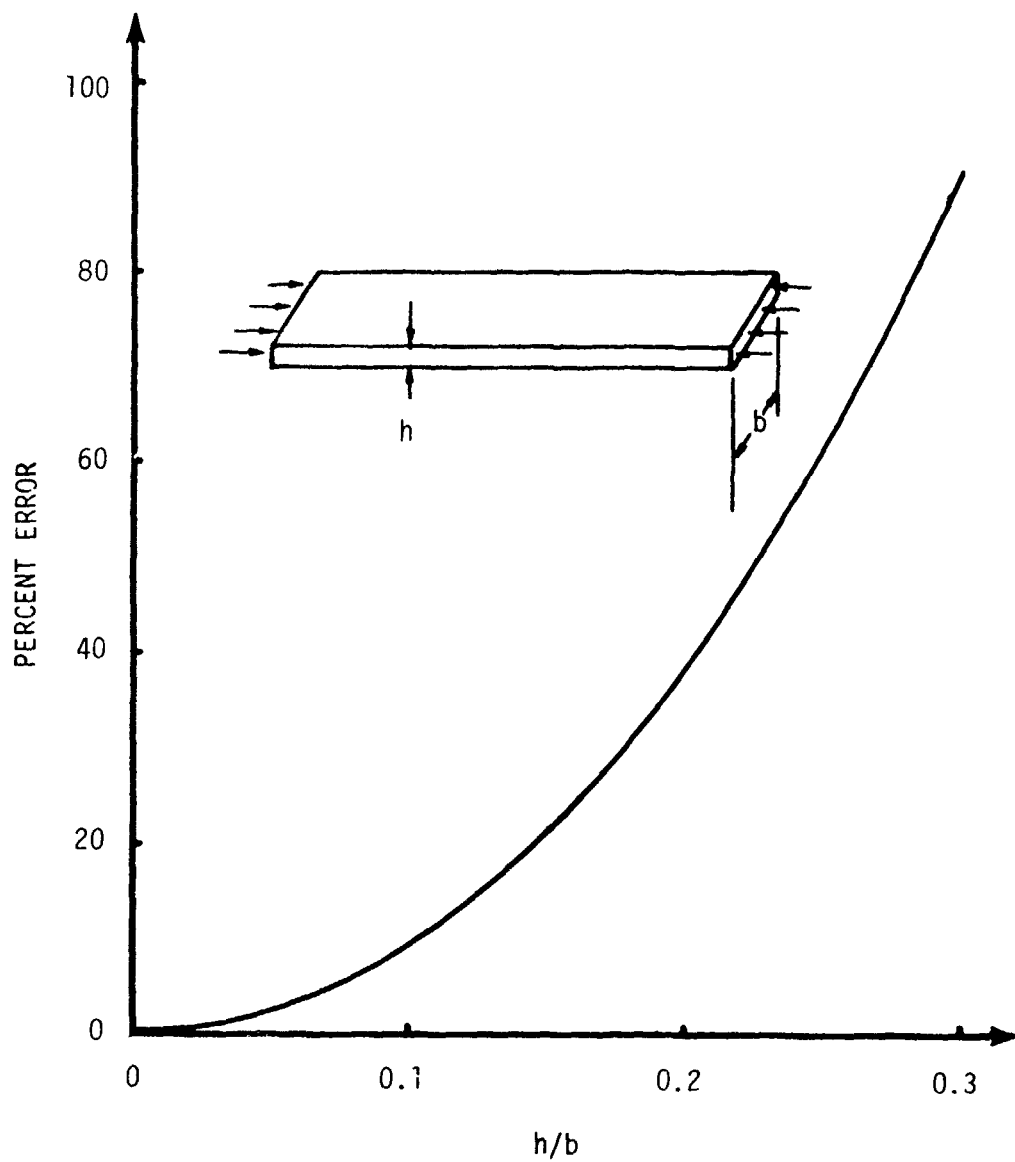


Figure 246 Error due to omission of transverse shear effects in long isotropic plates (all edges simply supported) (from Srinivas and Rao [294]).

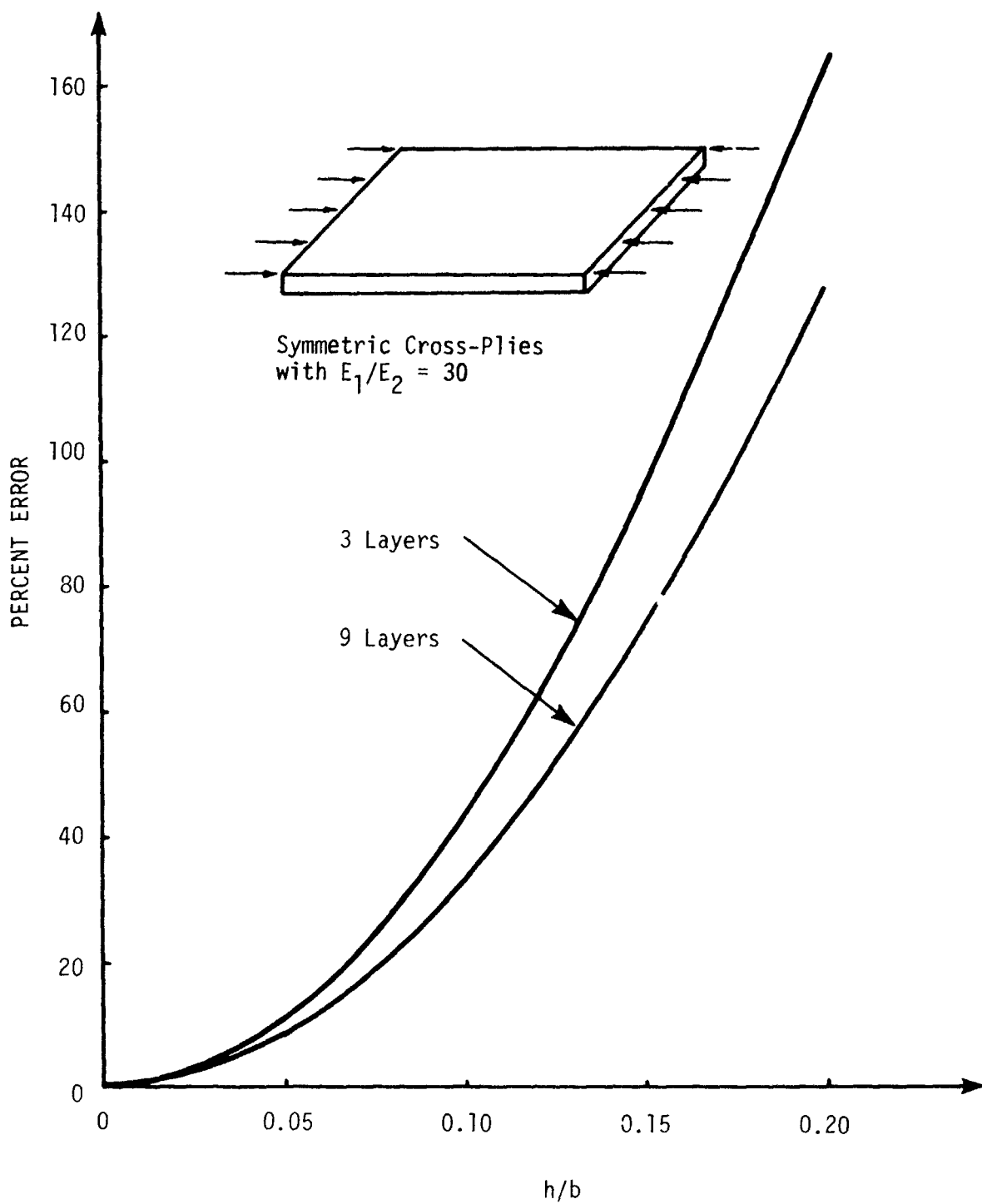
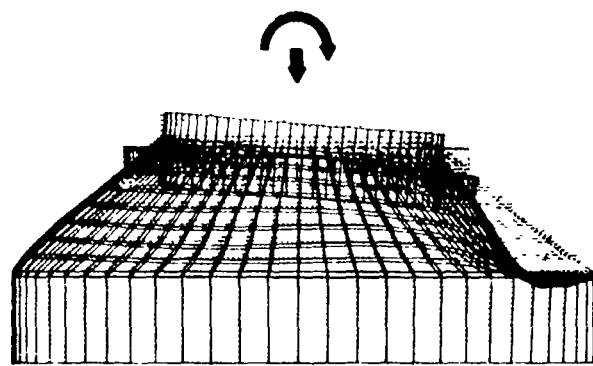
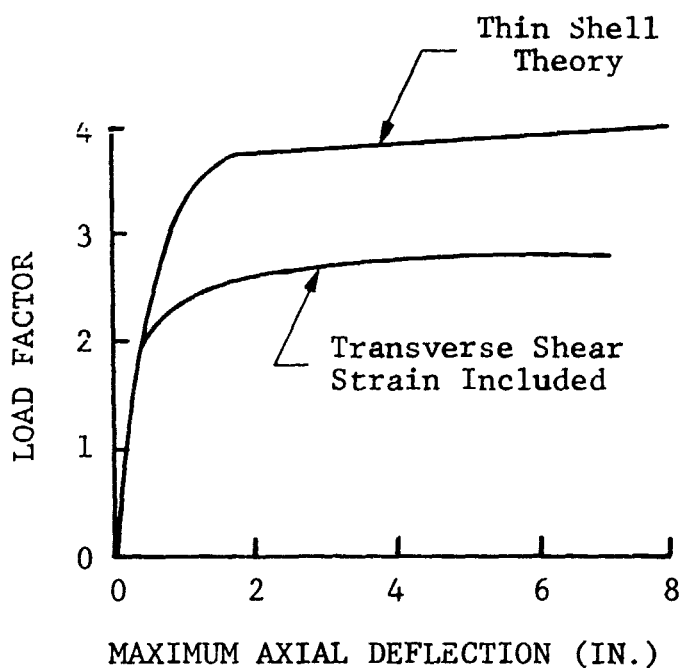


Figure 247 Error due to omission of transverse shear effects in square laminated plates (all edges simply supported) (from Noor [295]).



(a)



(b)

Figure 248 Collapse of a stiffened conical shell with sandwich wall construction: (a) deformation at collapse; (b) load-deflection curves obtained with and without transverse shear deformation effects in the core of the sandwich wall of the conical shell (from Sharifi [295]).

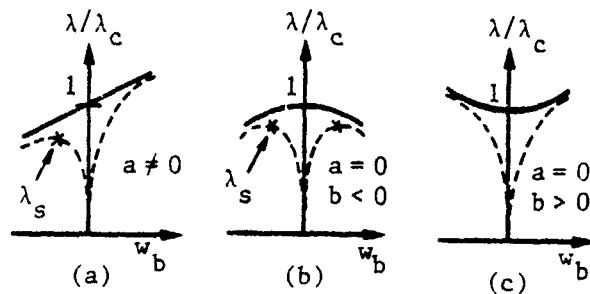


Figure 249 Initial post-buckling behavior in cases where the bifurcation mode is unique. Dashed curves show effect of small initial imperfections (from Tvergaard [7]).

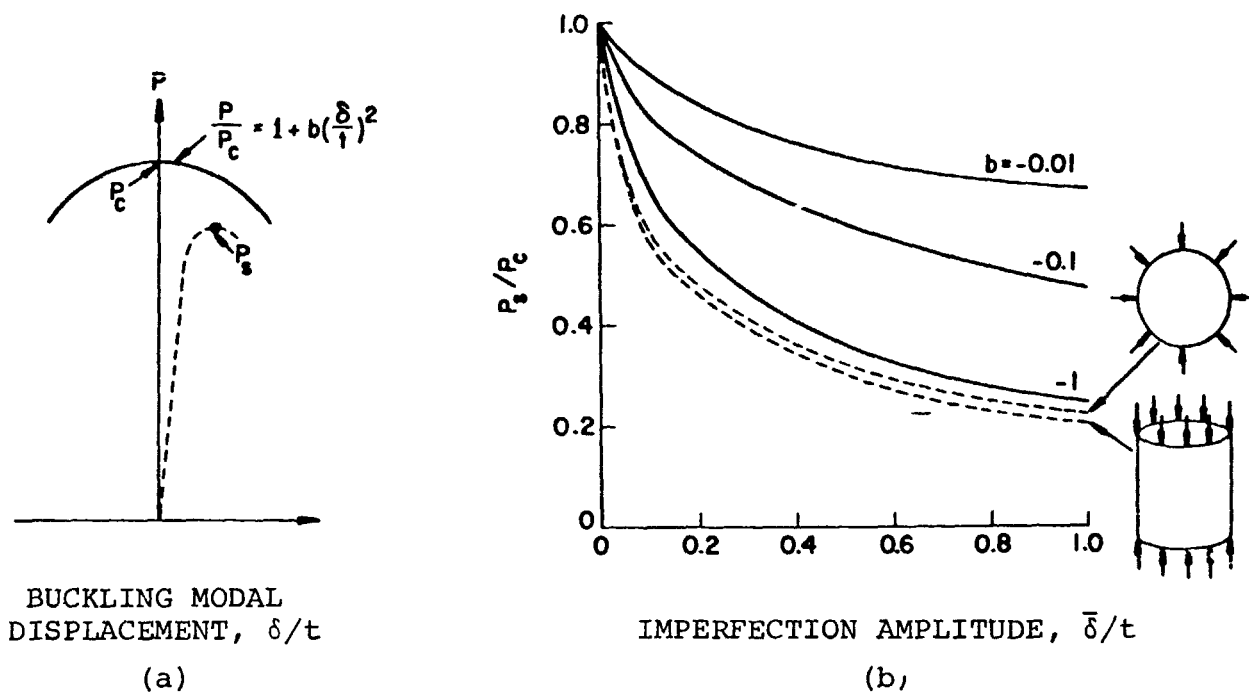


Figure 250 Imperfection sensitivity as a function of b . Although the dashed curves in (b) for the spherical and cylindrical shells are not calculated from $P/P_c = 1 + b(\delta/t)^2$, they are included in order to demonstrate the extreme imperfection sensitivity of these shells when loaded as indicated.

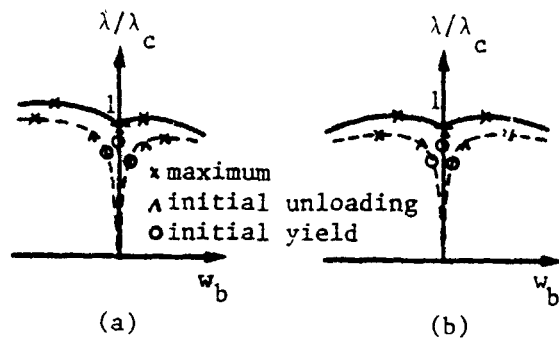


Figure 251 Initial post-buckling behavior in the plastic range in cases where the bifurcation mode is unique. Dashed curves show effect of small initial imperfections (from Tvergaard [7]).

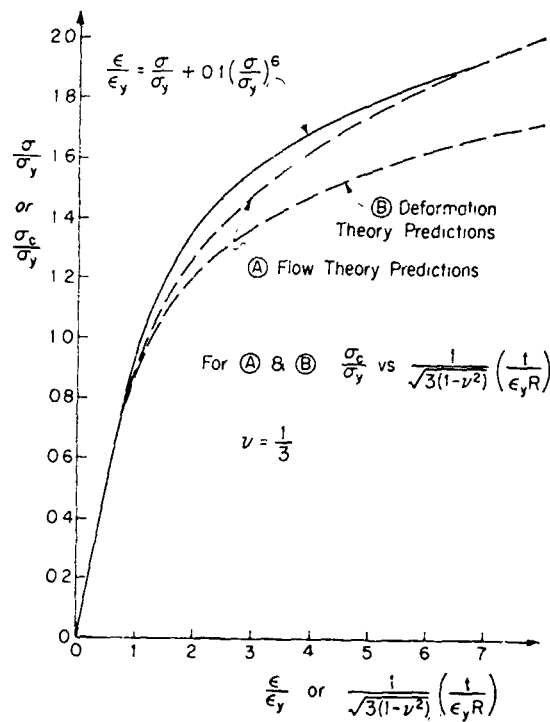


Figure 252 Tensile stress-strain curve and bifurcation stresses for a perfect spherical shell under external pressure (from Hutchinson [313]).

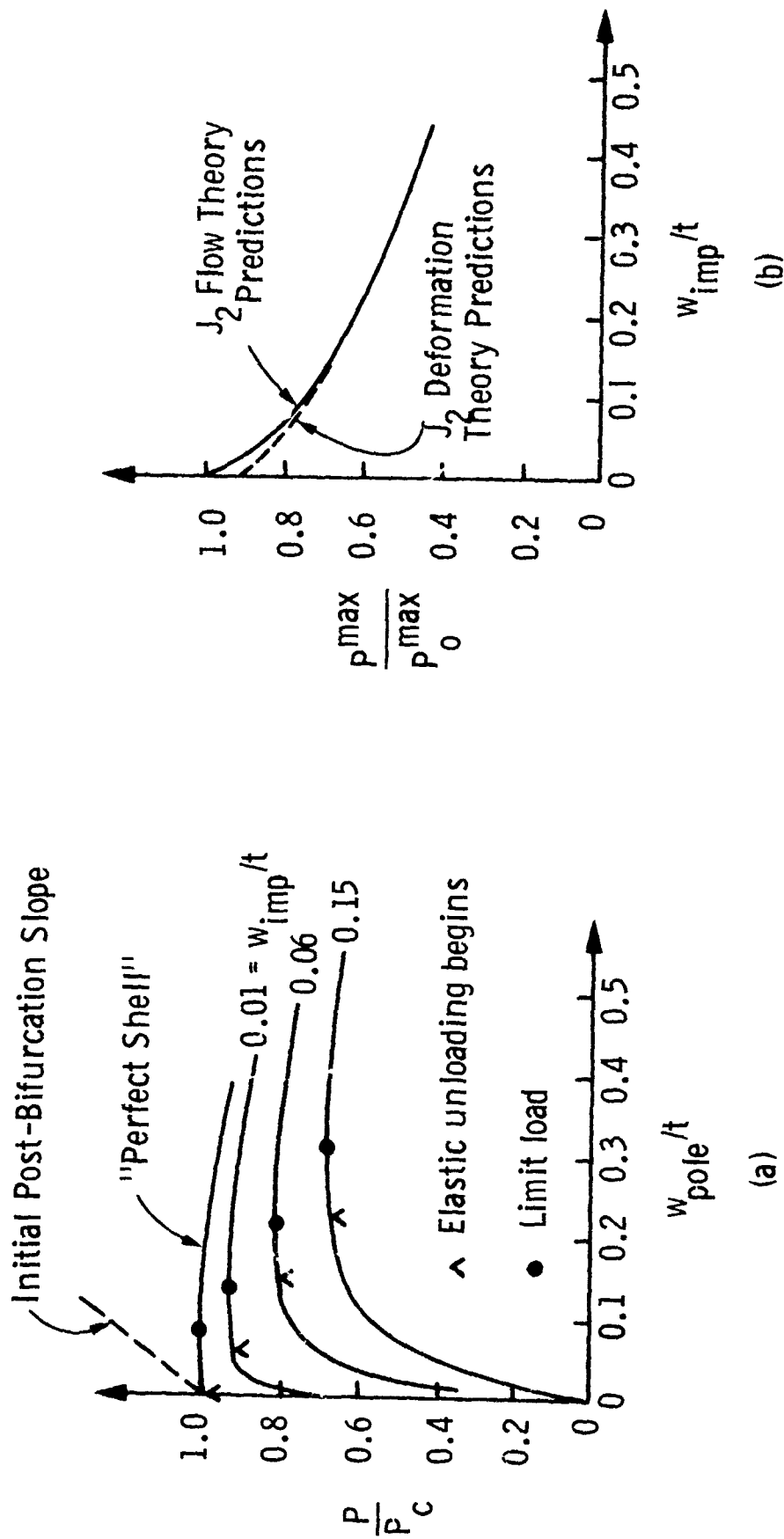


Figure 253 (a) Plastic post-bifurcation behavior and imperfection sensitivity of a spherical shell under external pressure.
 (b) Imperfection sensitivity of spherical shell showing difference between flow and deformation theories only for small imperfection amplitudes.
 (from Hutchinson [313])

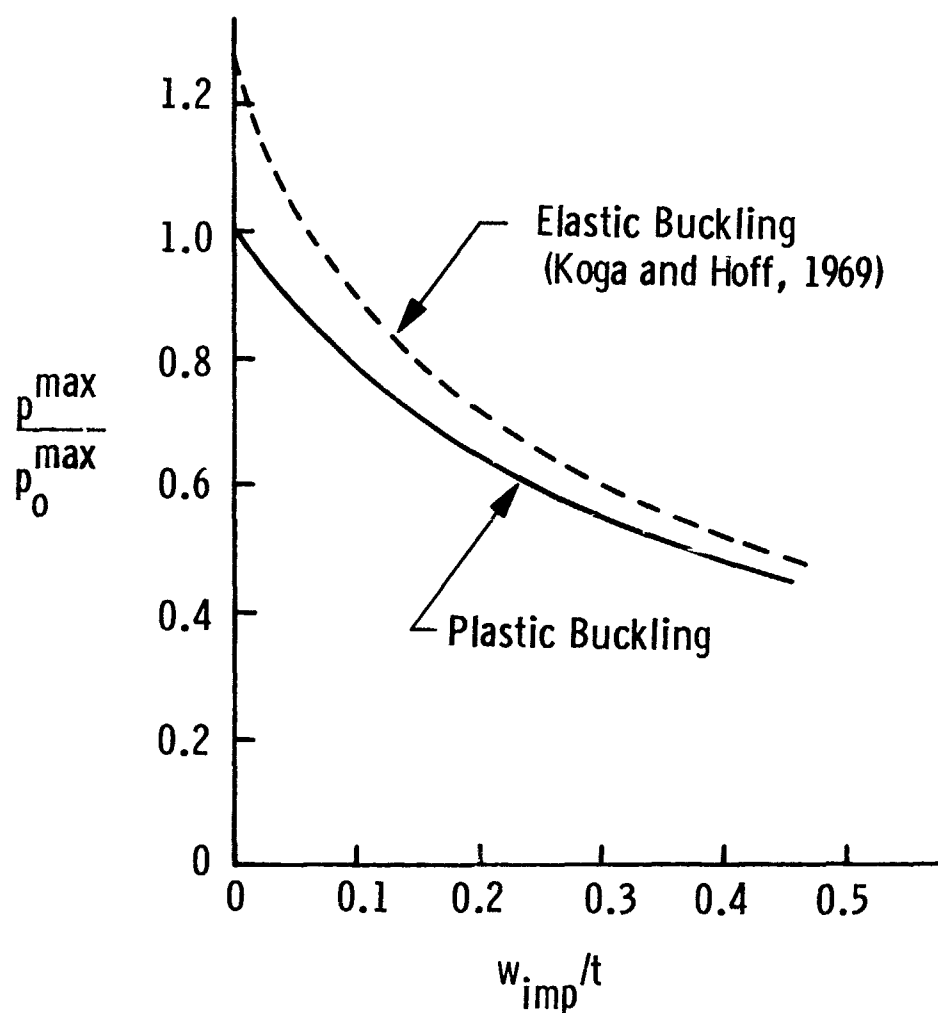


Figure 254 Buckling pressures for spherical shells with flat spot imperfections. For both curves, p_0^{\max} is the maximum support pressure of the perfect shell as predicted by J_2 flow theory (from Hutchinson [313]).

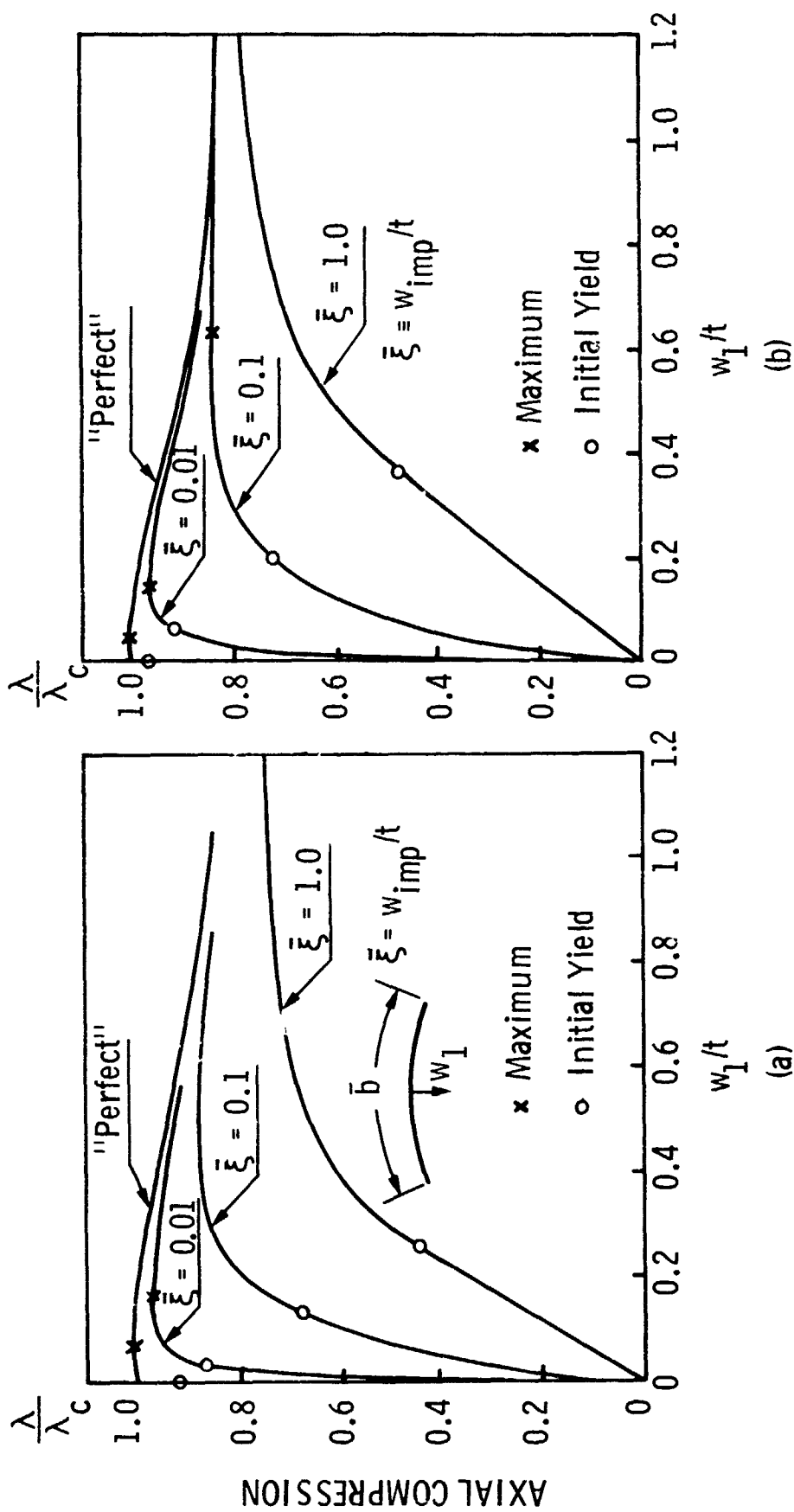


Figure 255 Load vs. modal deflection for cylindrical panel that bifurcates in the plastic range: $t/b = 0.025$; $n = 10$; $\nu = 0.3$.

(a) $\bar{\theta} = 0.5$, $\sigma_y/E = 0.002$; (b) $\bar{\theta} = 0.75$, $\sigma_y/E = 0.0028$ ($\bar{\theta}$ given in Figure 256)

(from Tvergaard [317])

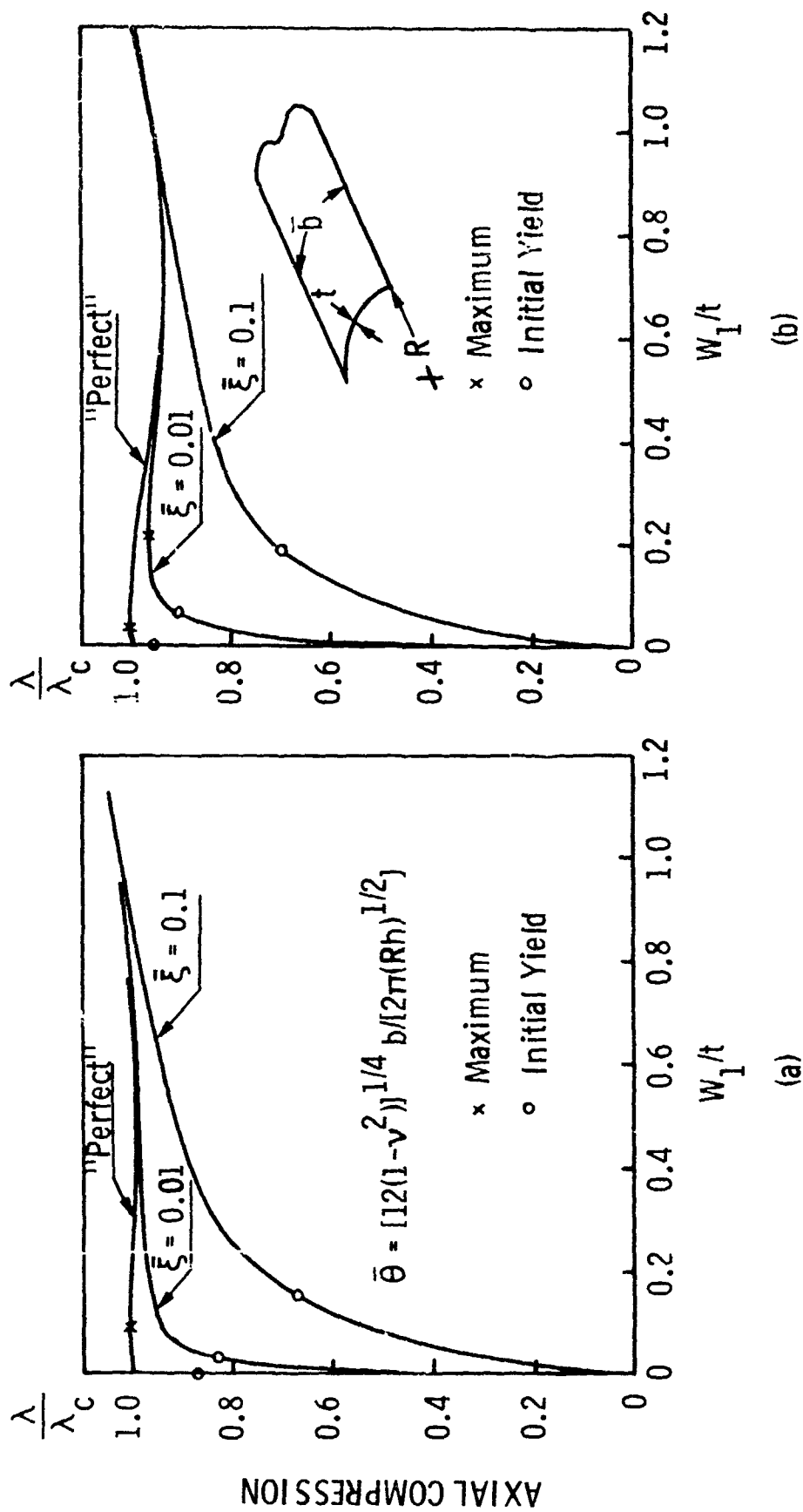


Figure 256 Load vs. modal deflection for cylindrical panel that bifurcates in the plastic range: $t/b = 0.025$; $n = 3$; $\nu = 0.3$.

(a) $\bar{\theta} = 0.5$, $\sigma_y/E = 0.002$; (b) $\bar{\theta} = 0.75$, $\sigma_y/E = 0.0028$

(from Tvergaard [317])

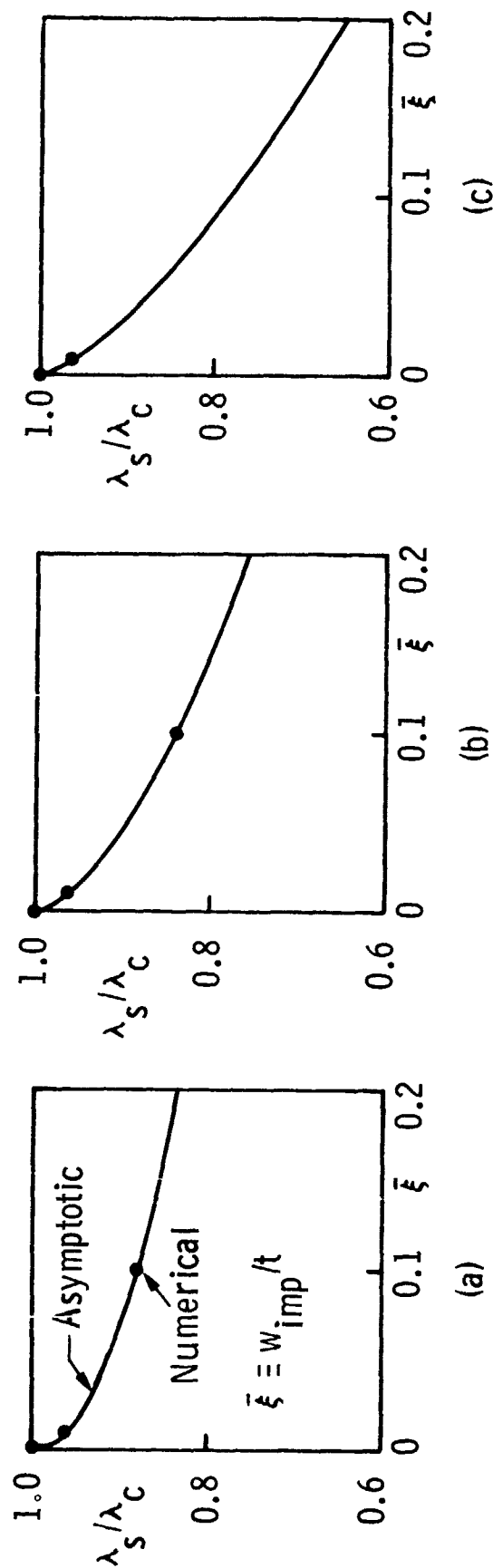


Figure 257 Comparison of numerical results with asymptotic hypoelastic predictions for the imperfection sensitivity of elastic-plastic cylindrical panels.

(a) $\bar{\theta} = 0.5$, $\sigma_y/E = 0.002$, $n = 10$

(b) $\bar{\theta} = 0.75$, $\sigma_y/E = 0.0028$, $n = 10$

(c) $\bar{\theta} = 0.75$, $\sigma_y/E = 0.0028$, $n = 3$

(from Tvergaard [317])

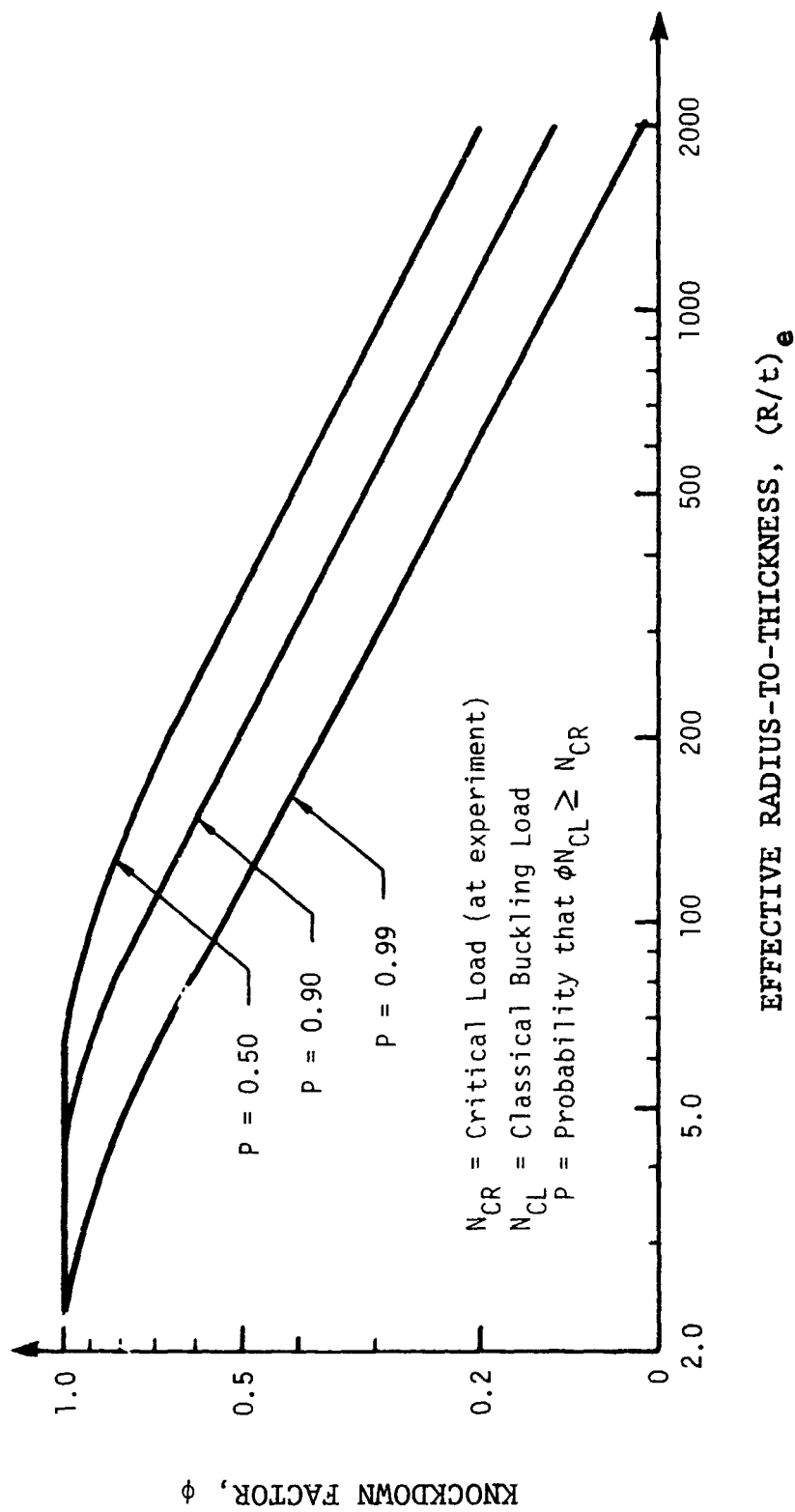


Figure 258 Empirical knockdown factor ϕ for cylinders subjected to axial compression.

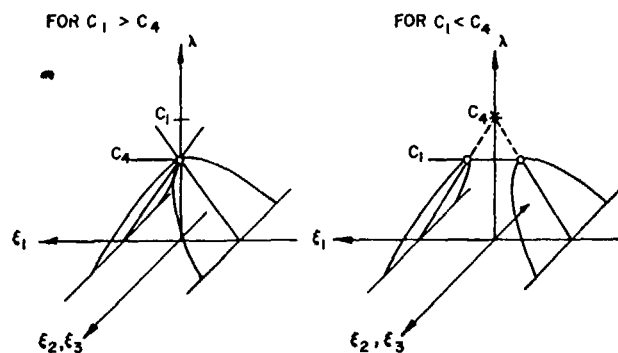


Figure 259 Postbuckling equilibrium paths for perfect monocoque cylindrical shells under axial compression. ξ_1 is the axisymmetric and ξ_2, ξ_3 are the nonsymmetric components of deformation (from Arbocz and Babcock [341]).

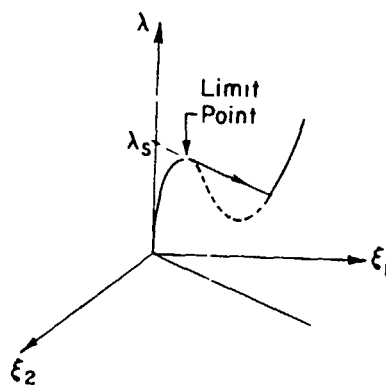


Figure 260 Equilibrium path for an imperfect shell (from Arbocz and Sechler [342]).

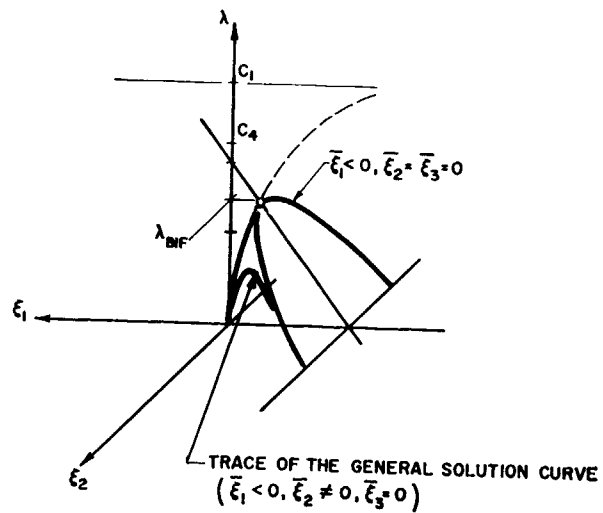


Figure 261 Postbuckling equilibrium paths for imperfect monocoque cylindrical shells under axial compression (from Arbocz and Babcock [341]).

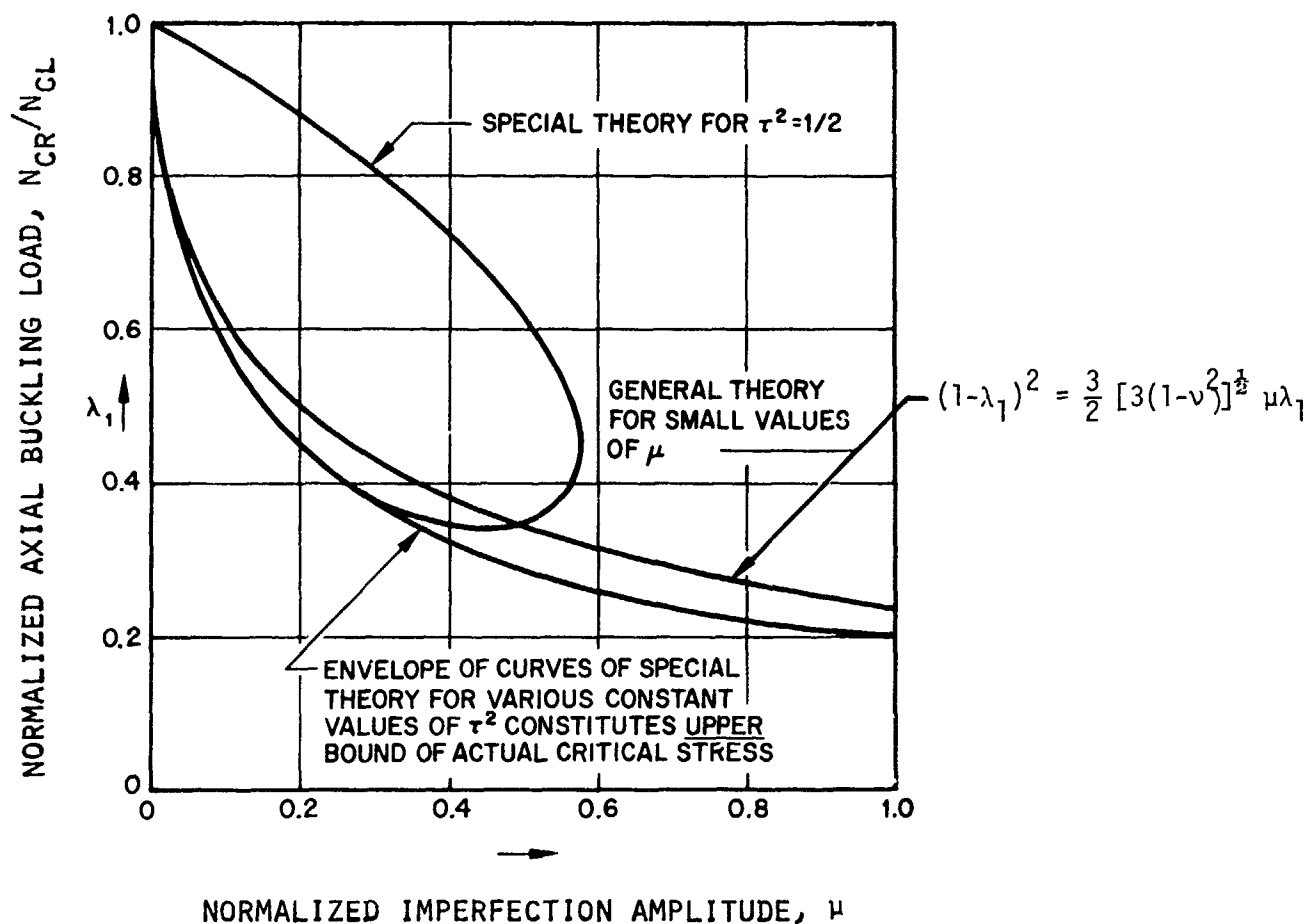


Figure 262 Critical stress for buckling in an axisymmetric periodic mode for a shell with imperfections in the shape of the axisymmetric buckling mode of a perfect cylindrical shell.

μ is amplitude of imperfections as a fraction of shell thickness.

λ_1 is critical stress as a function of classical buckling stress

τ^2 is a circumferential wave parameter, $\tau^2 = n^2(t/R) \times (1/[3(1-\nu^2)]^{1/2})$

(from Koiter [343])

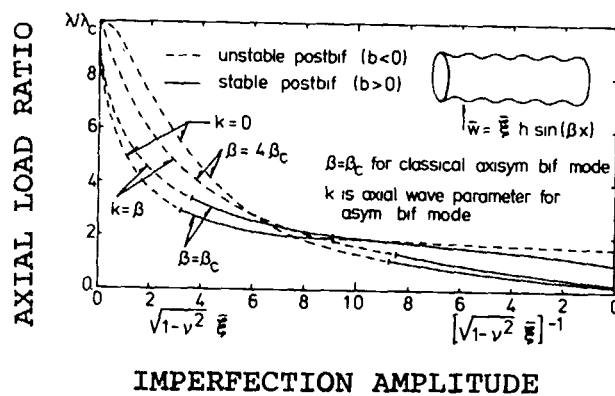


Figure 263 Bifurcation loads based on nonlinear prebuckling analysis for axially compressed cylinder with sinusoidal axisymmetric imperfections. Results for $\beta = 0.4 \beta_c$ are from Ref. [353]; results for $\beta = \beta_c$ are from Ref. [352]).

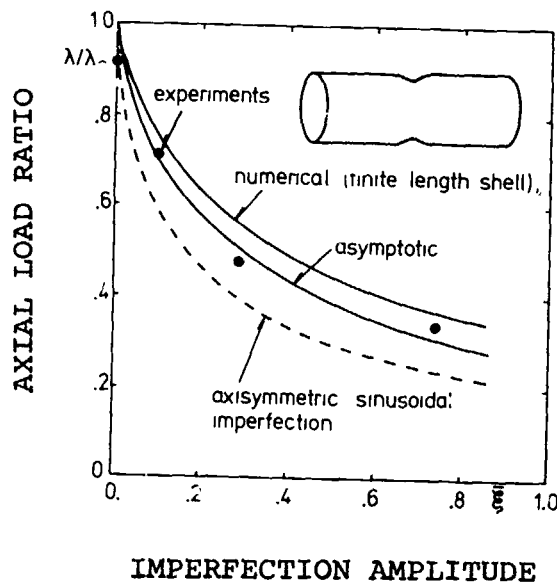
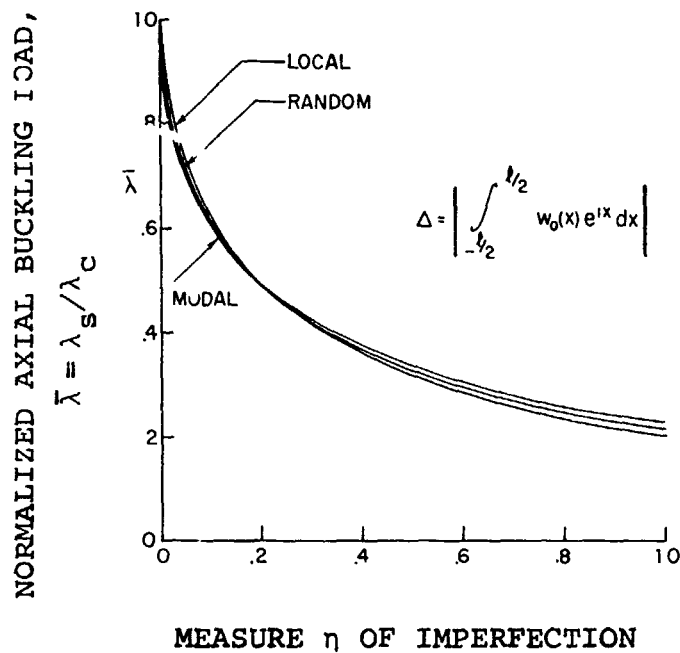


Figure 264 Comparison of buckling loads for axially compressed cylinder with axisymmetric dimple imperfection. Experimental and numerical results are from Ref. [355]; asymptotic results are from Ref. [124]; dashed line corresponds to Koiter's special theory [343]).

(both from Tvergaard [7])



$$\eta = \begin{cases} \frac{2\Delta}{l} \sqrt{1-\nu^2} & \text{MODAL} \\ \frac{\Delta}{\sqrt{2}l} \sqrt{1-\nu^2} & \text{RANDOM} \\ \frac{\Delta}{2} \sqrt{1-\nu^2} & \text{LOCAL} \end{cases}$$

Figure 265 Dependence of buckling load on imperfection magnitude. Note that $l \equiv q_0 L/R$, where q_0 is given by $q_0 = [12(1-\nu^2)]^{1/4} (R/t)^{1/2}$ (from Amazigo and Budiansky [347]).

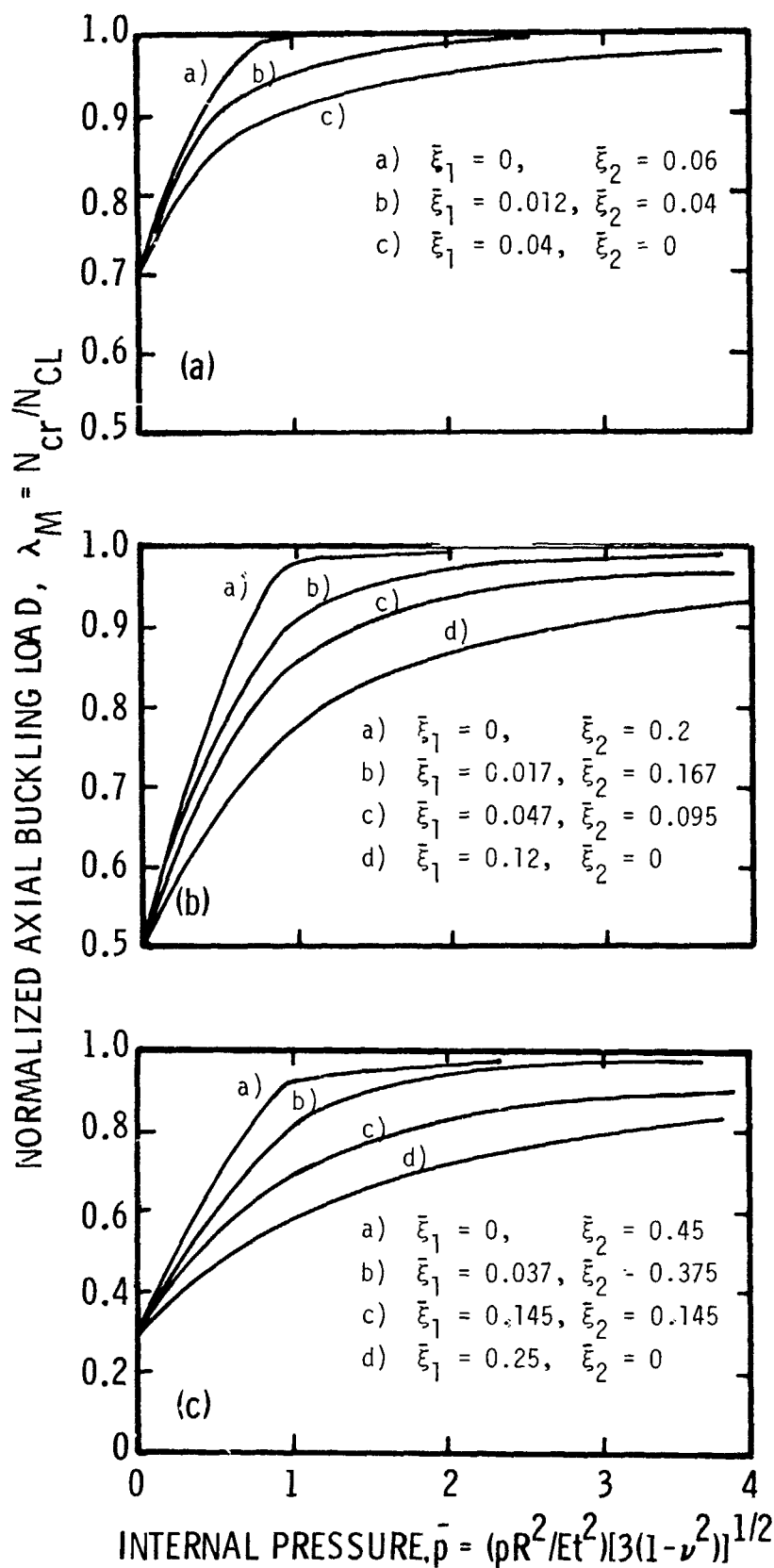


Figure 266 Effects of axisymmetric ($\bar{\xi}_1$) and non-axisymmetric ($\bar{\xi}_2$) imperfections for axially compressed monocoque cylindrical shells with internal pressure (from Hutchinson [340]).

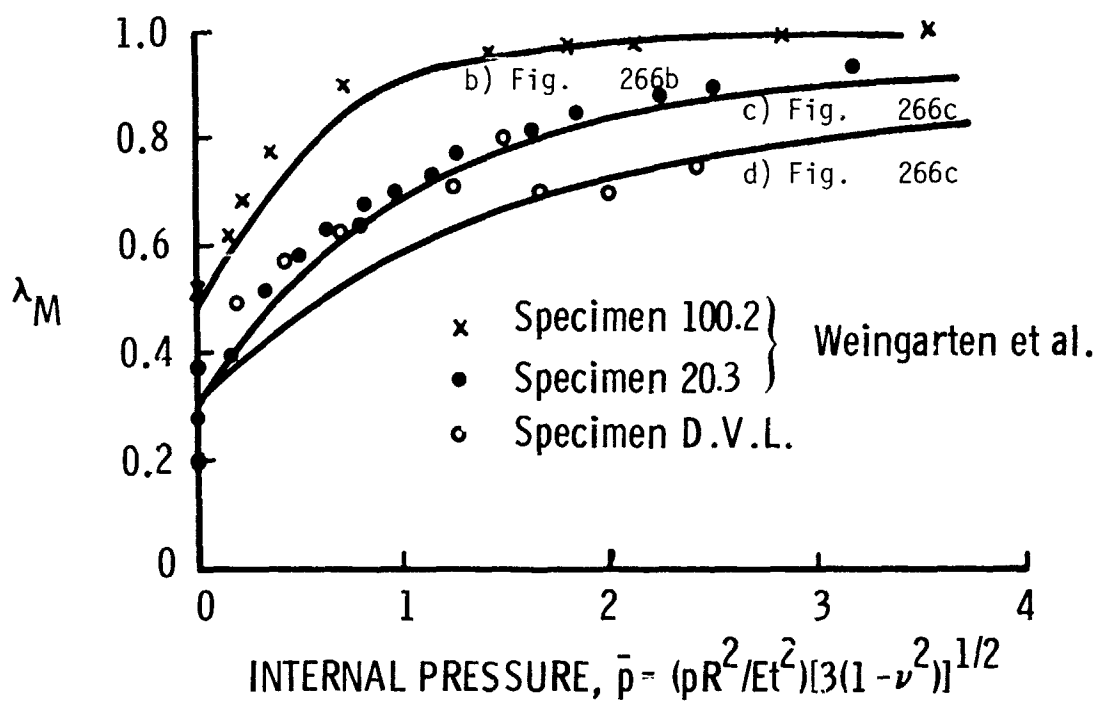
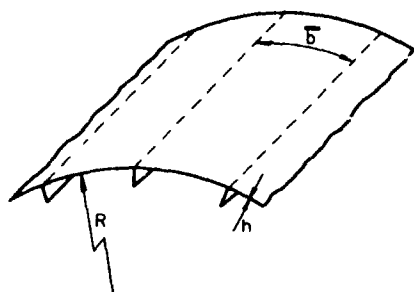
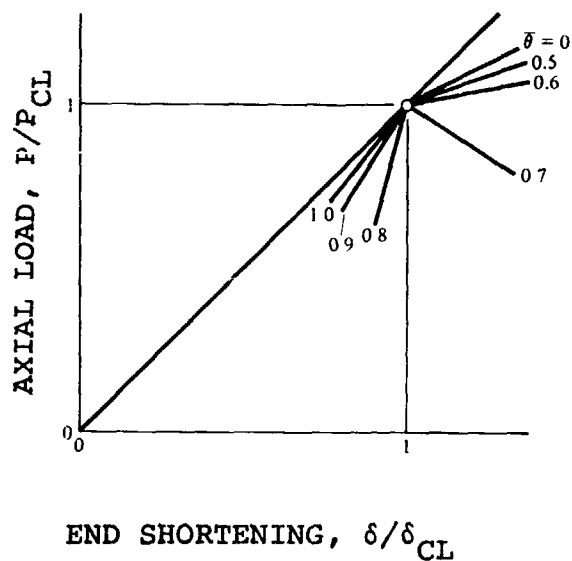


Figure 267 Axially compressed monocoque cylindrical shells with internal pressure: comparison of theoretical results from Figures 266b and c with experimental data of Weingarten et al. [364] and Thielemann [635] (from Hutchinson [340]).

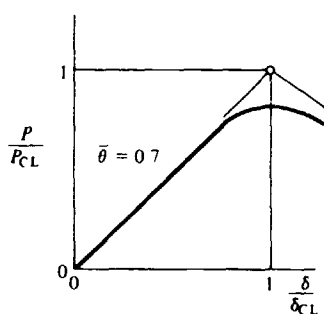


$$\bar{\theta} = [12(1-\nu^2)]^{1/4} \bar{b} / [2\pi (Rh)^{1/2}]$$

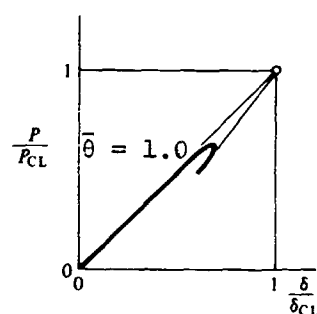
(a)



(b)



(c)



(d)

Figure 268 Post-buckling behavior of axially compressed cylindrical panels of width \bar{b} : (a) panel nomenclature. Panel is considered to be long and simply supported along straight edges where stringers exist. (b) Equilibrium paths for initially perfect panels. (c,d) Equilibrium paths for panels with imperfection amplitude equal to 10% of the shell wall thickness (from Brush and Almroth [4]).

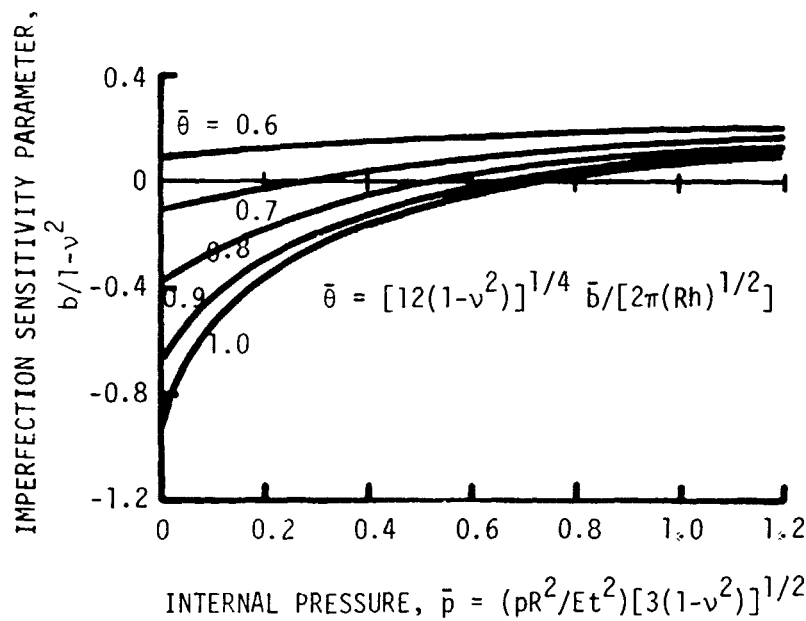
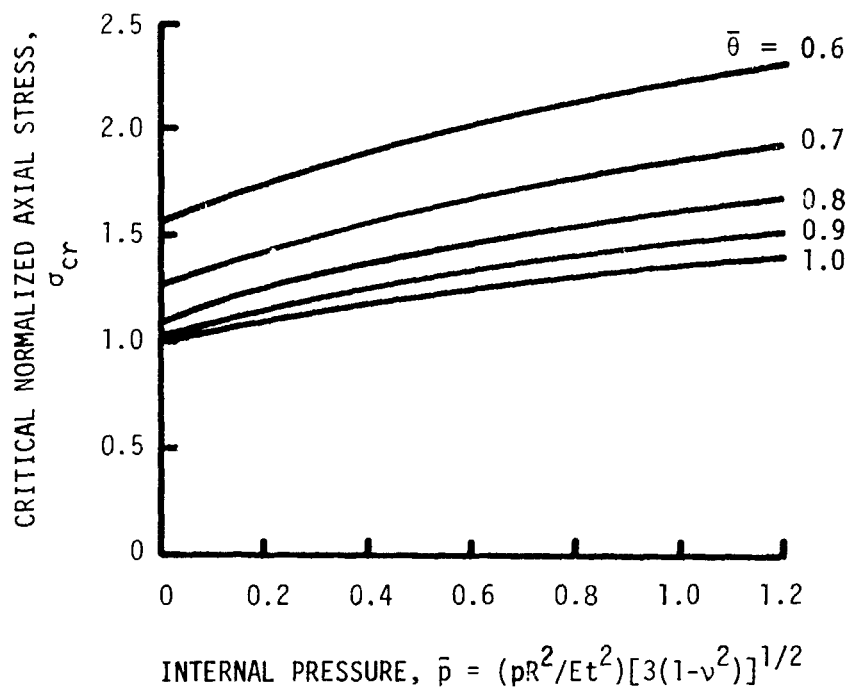


Figure 269 Axially compressed monocoque cylindrical panel: critical stress σ_{cr} and initial imperfection sensitivity b vs internal pressure p for various values of $\bar{\theta}$ at $\gamma = 0$. (Note the stringer torsional rigidity parameter

$$\gamma \equiv q_0 GJ/(DR) \text{ with } q_0 = [12(1-\nu^2)]^{1/4} (R/t)^{1/2} \\ \text{and } D = Et^3/[12(1-\nu^2)]$$

(from Stephens [367]).

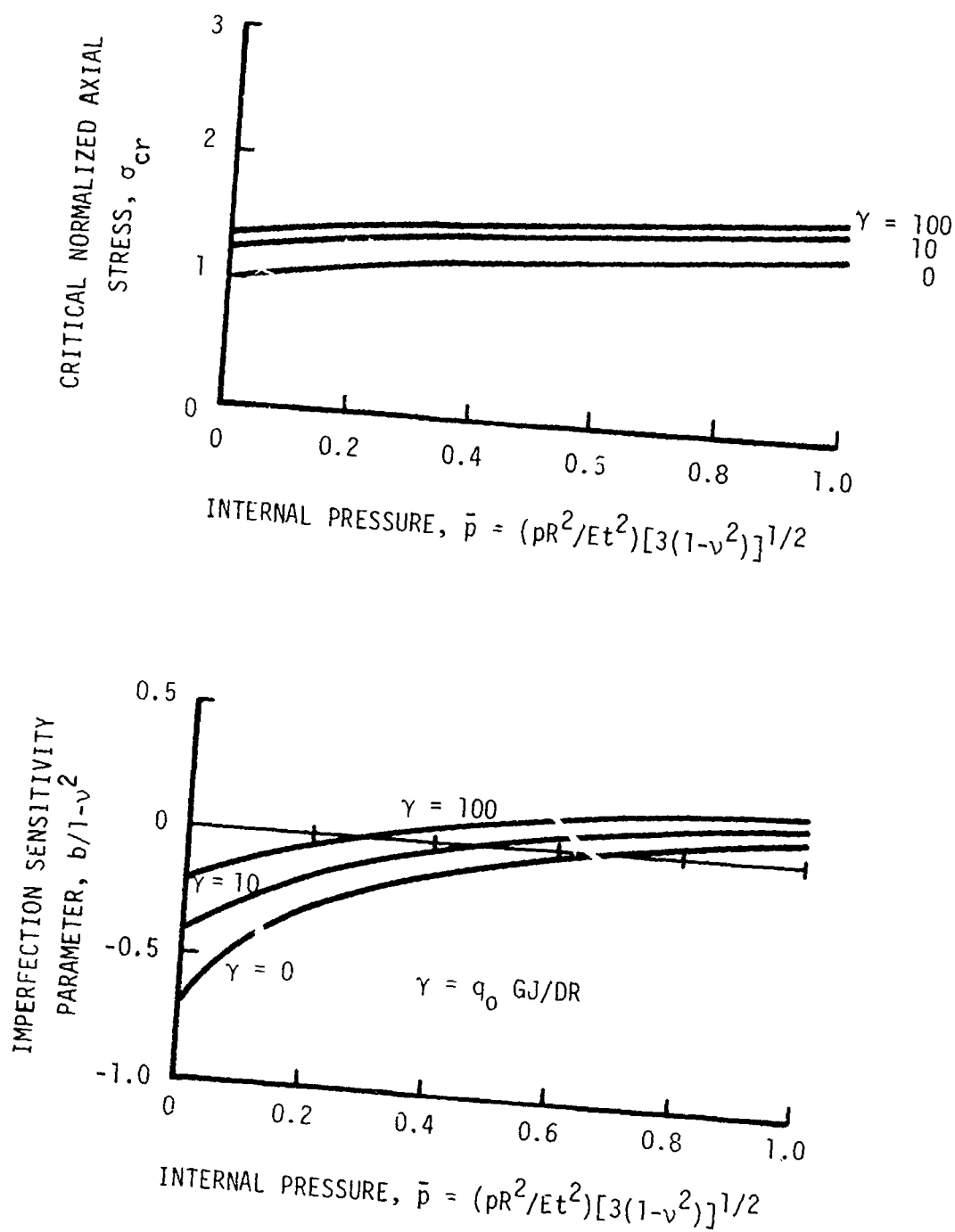
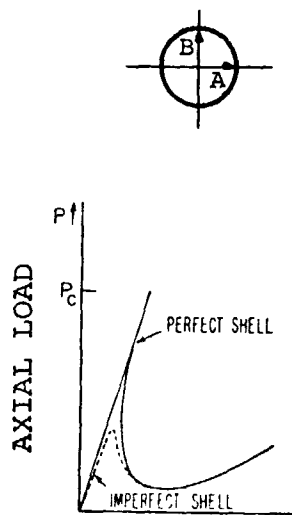


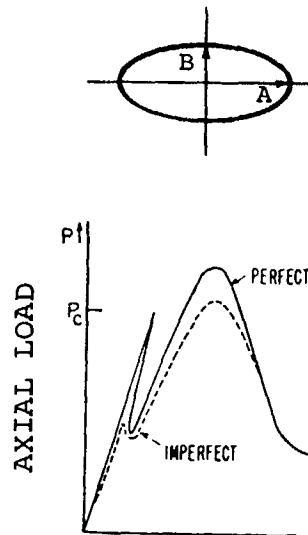
Figure 270 Axially compressed monocoque cylindrical panel: typical curves for σ_{cr} and b at $\bar{\theta} = 0.9$ as a function of internal pressure and for various values of torsional rigidity γ (from Stephens [367])



END SHORTENING

$$B/A = 1$$

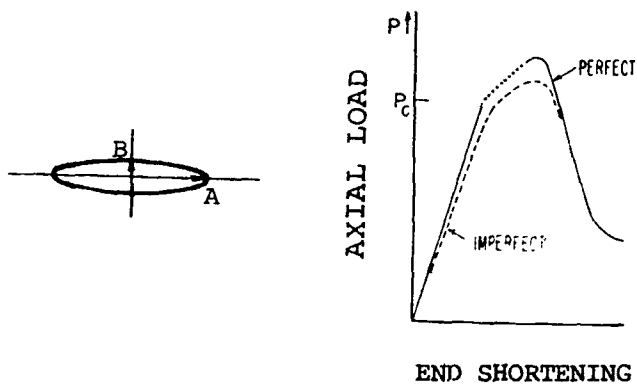
a) Circular cylinder



END SHORTENING

$$B/A < 1$$

b) Eccentric oval cylinder
(imperfection-sensitive)



END SHORTENING

$$B/A \ll 1$$

c) Eccentric oval cylinder (imperfection-insensitive)

Figure 271 Schematic load-deflection curves for axially compressed oval cylindrical shells (adapted from Hutchinson [249]).

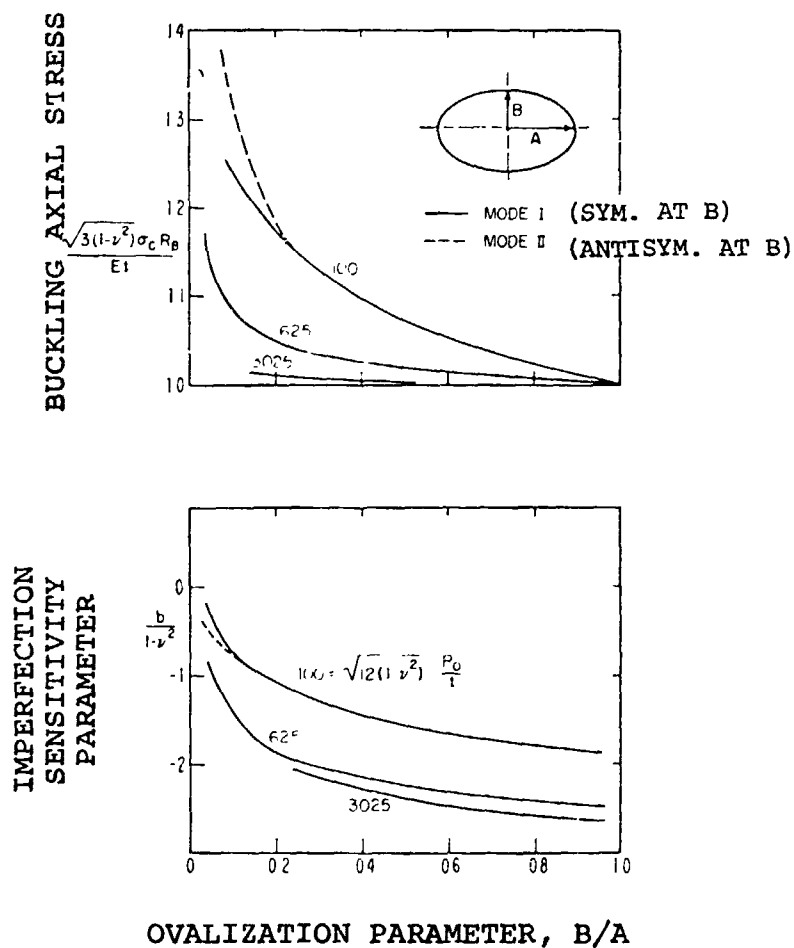


Figure 272 Classical buckling and imperfection sensitivity parameter b of elliptical cylindrical shells under axial compression. R_0 is the radius of the equivalent circular cylinder (same perimeter) (from Hutchinson [249]).

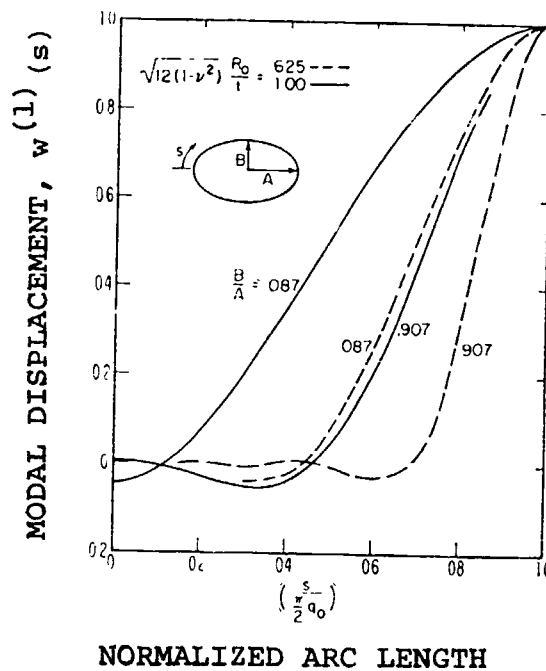


Figure 273 Circumferential variation of buckling mode amplitude (Mode 1) for axially compressed oval cylinder

$$[q_0 \equiv [12(1-\nu^2)]^{1/4} (R_0/t)^{1/2}]$$

(from Hutchinson [249])

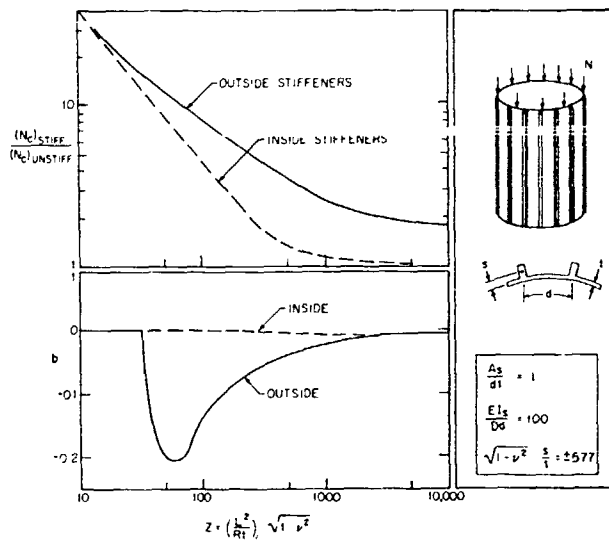


Figure 274 Classical buckling and imperfection sensitivity of simply supported stiffened cylinders under axial compression (from Budiansky and Hutchinson [305]).

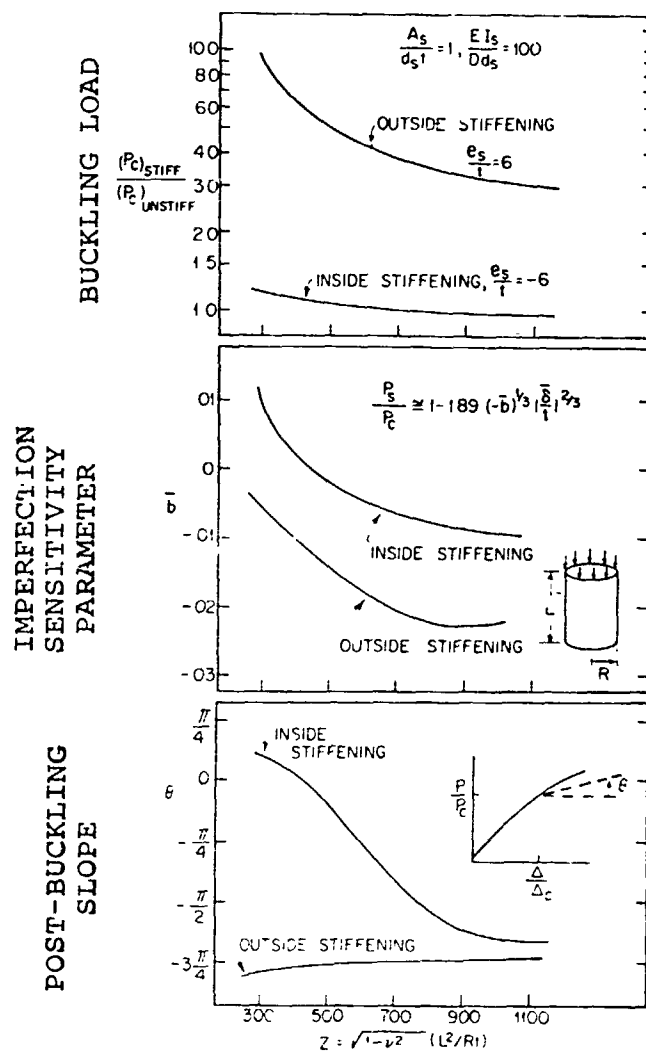


Figure 275 The effect of stringer eccentricity on the buckling and postbuckling behavior of axially stiffened cylindrical shells which are simply supported at the skin middle-surface and loaded in axial compression (from Hutchinson and Frauenthal [346]).

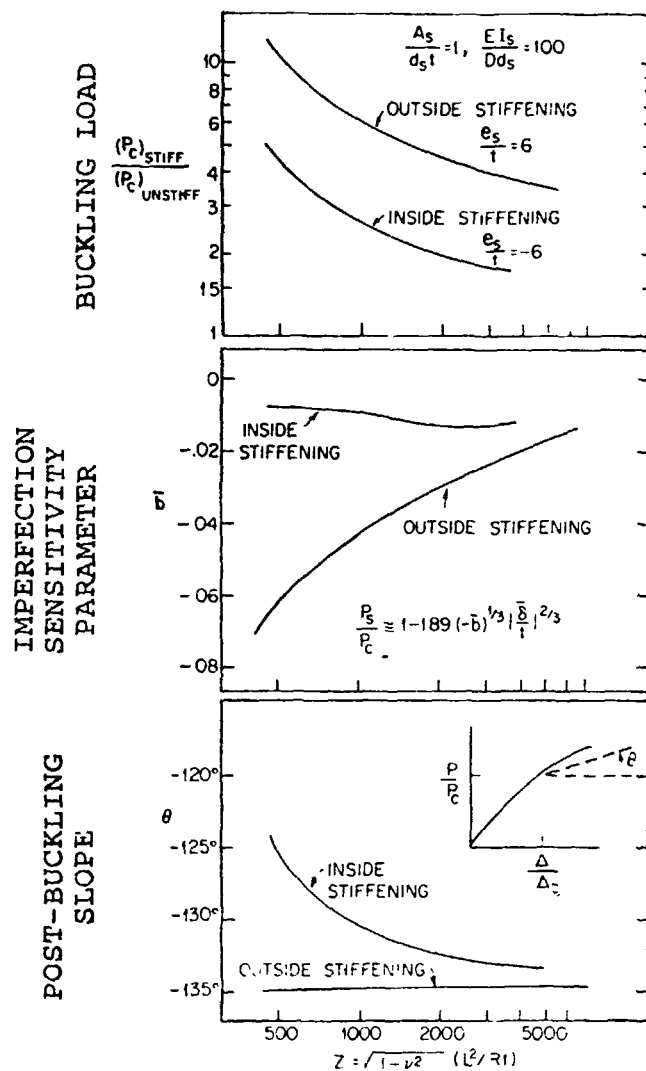


Figure 276 The effect of stringer eccentricity on the buckling and postbuckling behavior of clamped, axially stiffened cylindrical shells which are loaded in axial compression (from Hutchinson and Frauenthal [346]).

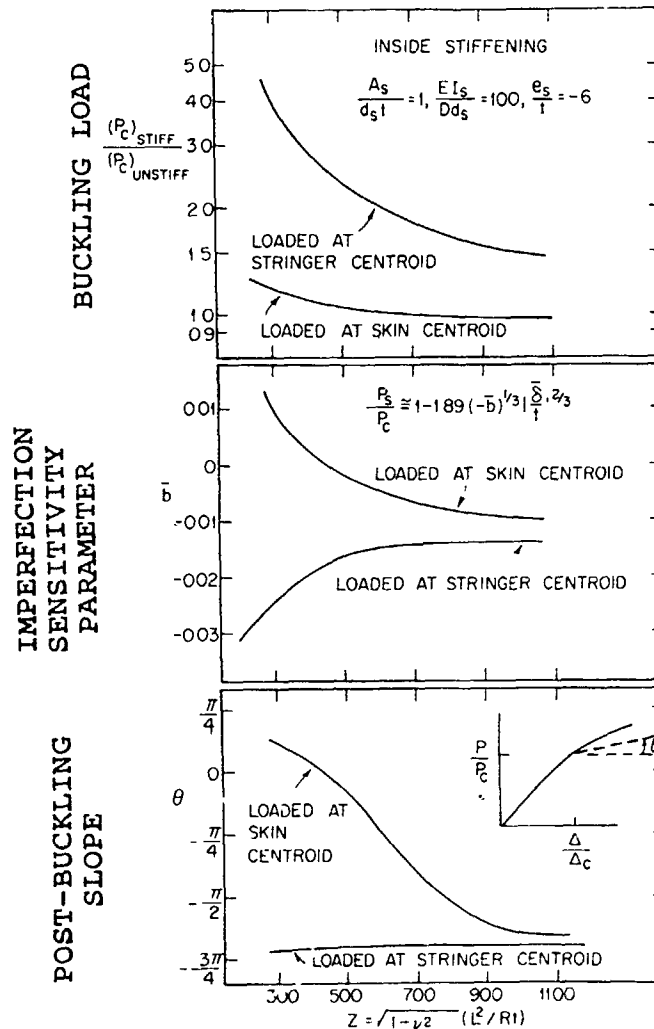


Figure 277 The effect of load eccentricity on the buckling and post-buckling behavior of axially stiffened cylindrical shells which are simply supported at either the centroid of the skin or the centroid of the stringers and subject to axial compression (from Hutchinson and Frauenthal [346]).

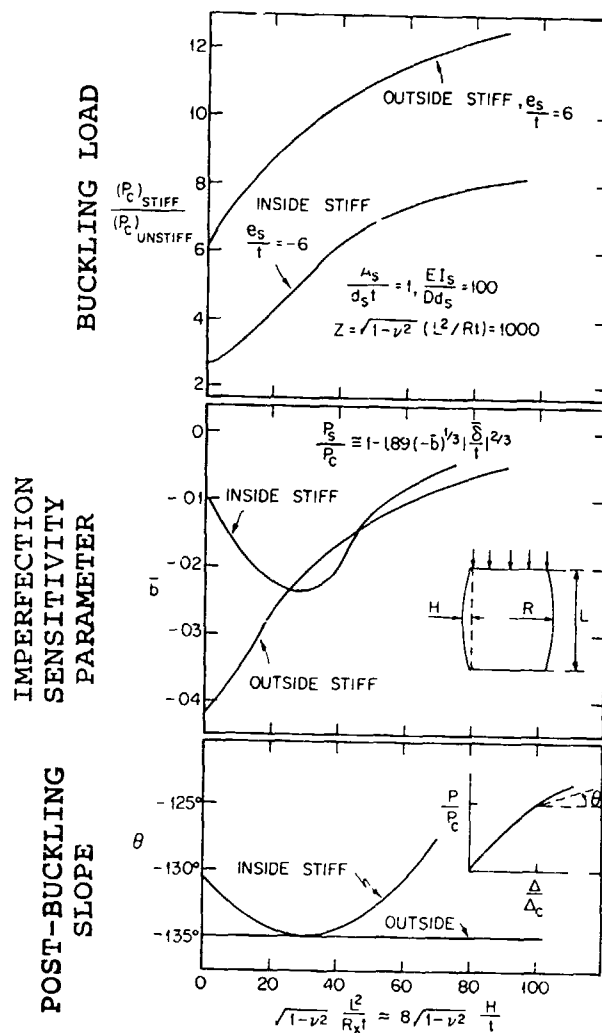


Figure 278 The effect of barrelng on the buckling and post-buckling behavior of clamped, axially stiffened cylindrical shells subject to axial compression (from Hutchinson and Frauenthal [346]).

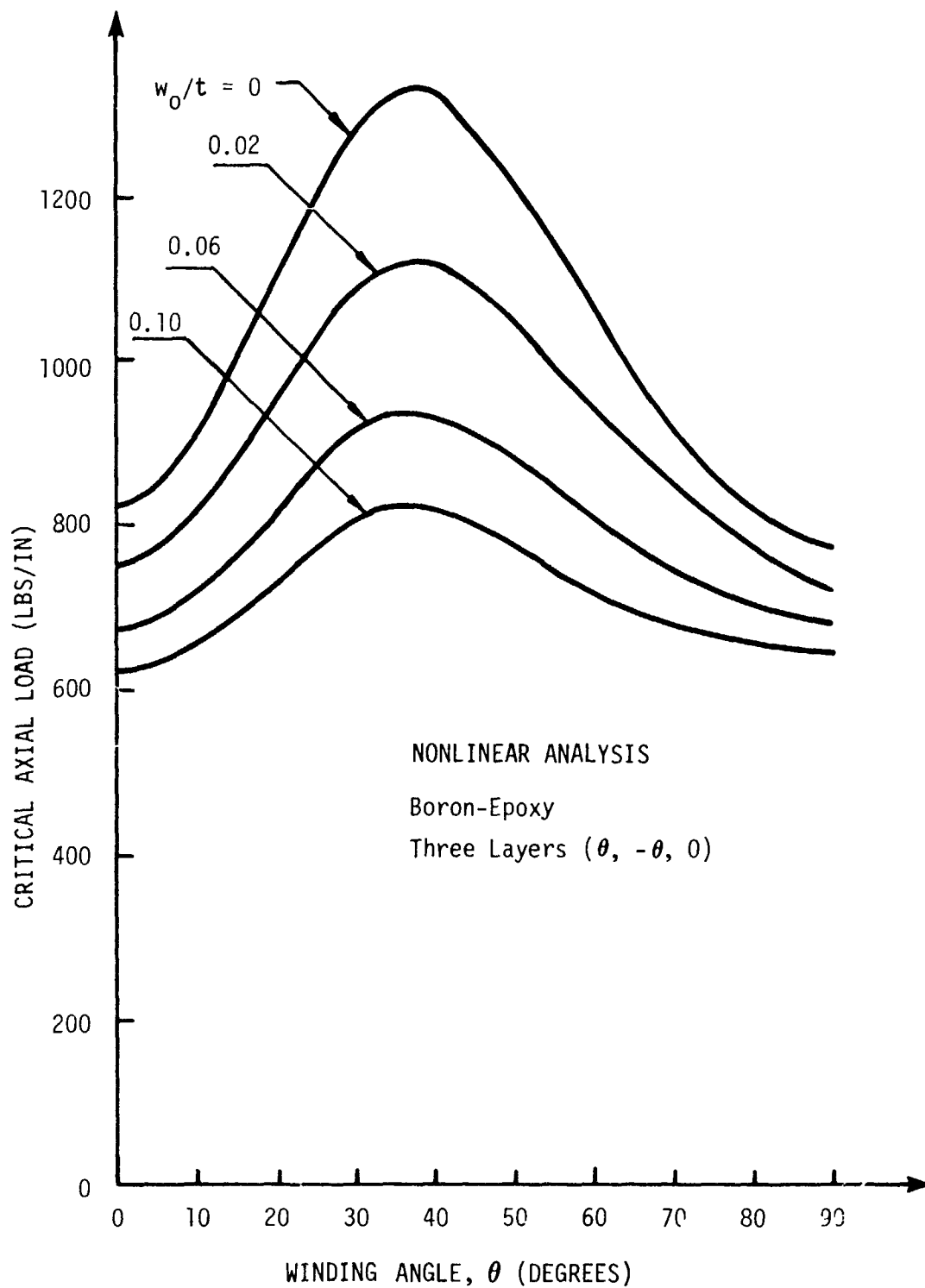


Figure 279 Effect of initial imperfection amplitude (w_0) on the buckling load of composite cylinder (results obtained by Khot [374]).

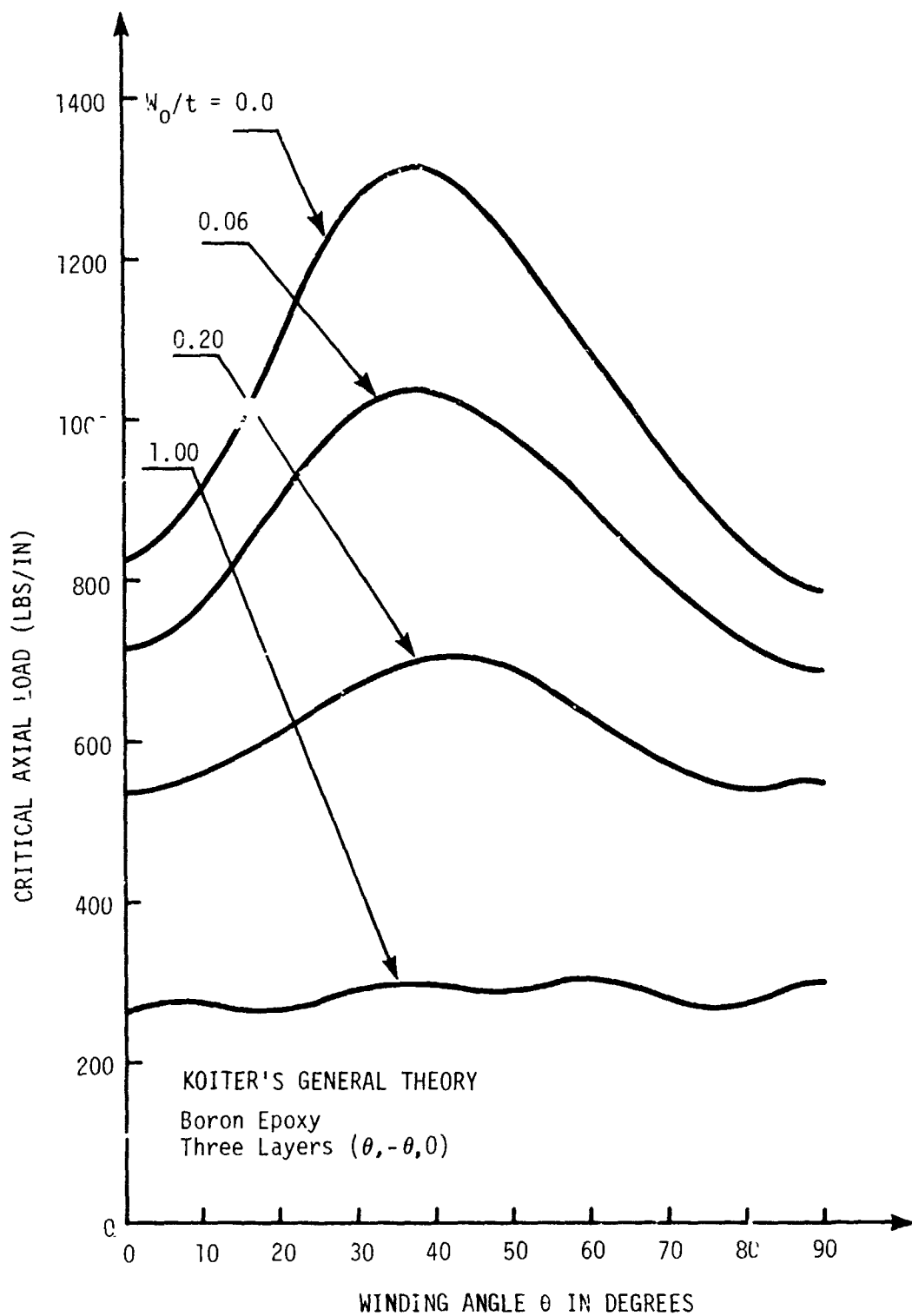
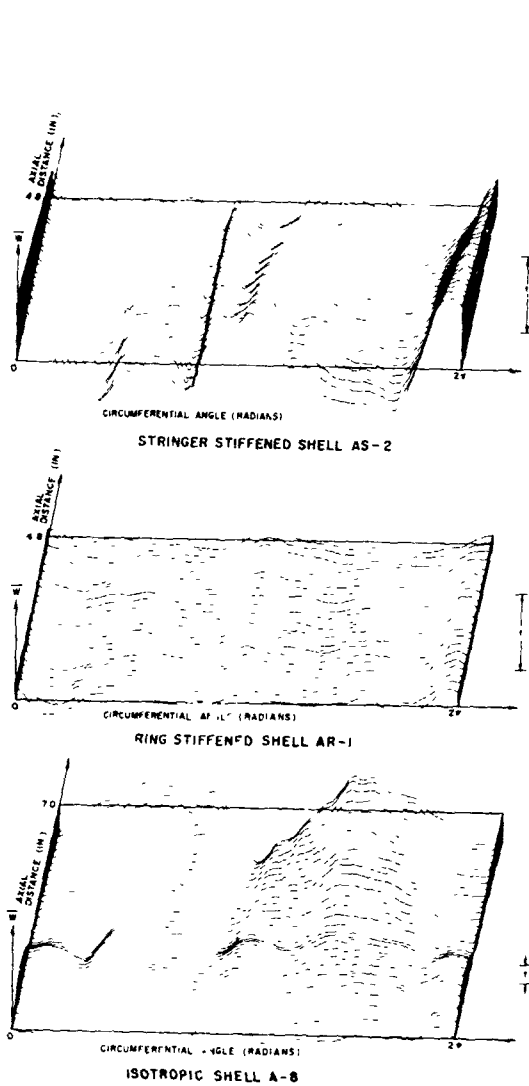
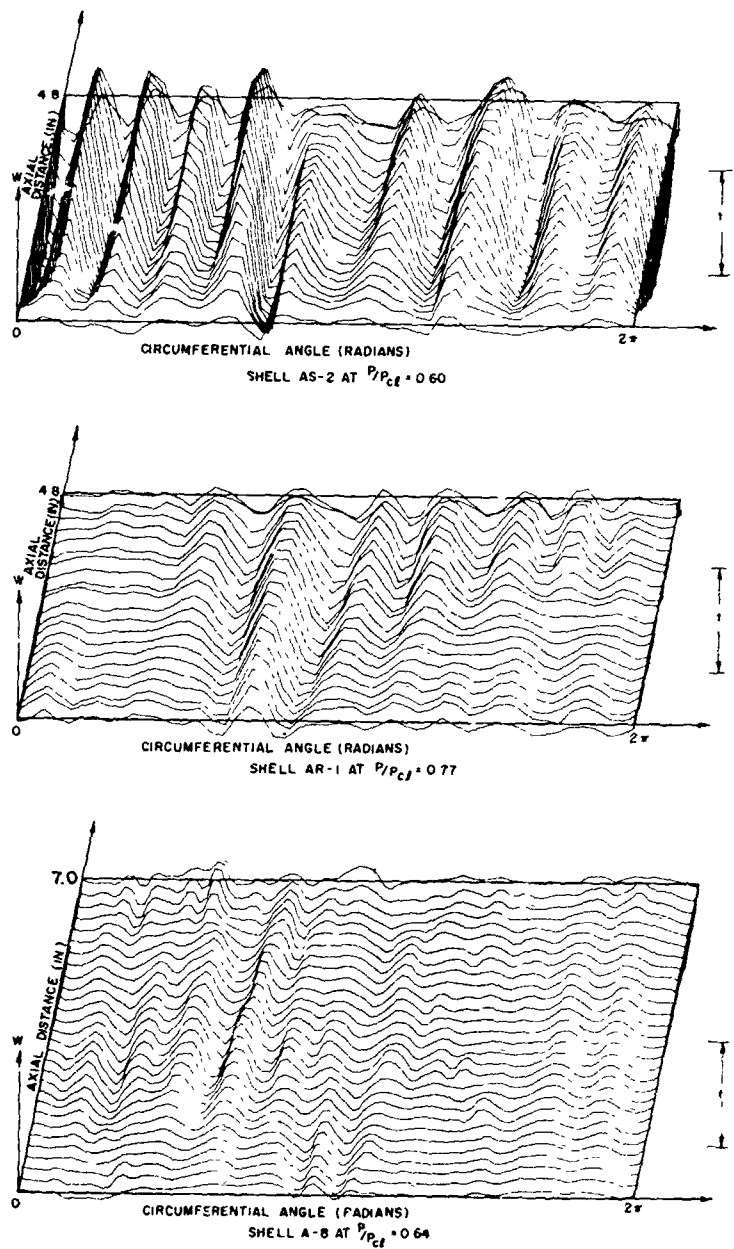


Figure 280 Effect of initial imperfection amplitude w_0 on the buckling load of composite cylinder. (Predictions are from Koiter's general theory, obtained by Khot and Venkayya [375]).



INITIAL IMPERFECTION MEASUREMENTS

(a)



PREBUCKLING DEFORMATION GROWTH

(b)

Figure 281 Initial imperfections (a) and normal displacement increment (b) at axial loads near collapse of stiffened and monocoque cylindrical shells (from Arbocz [339]).

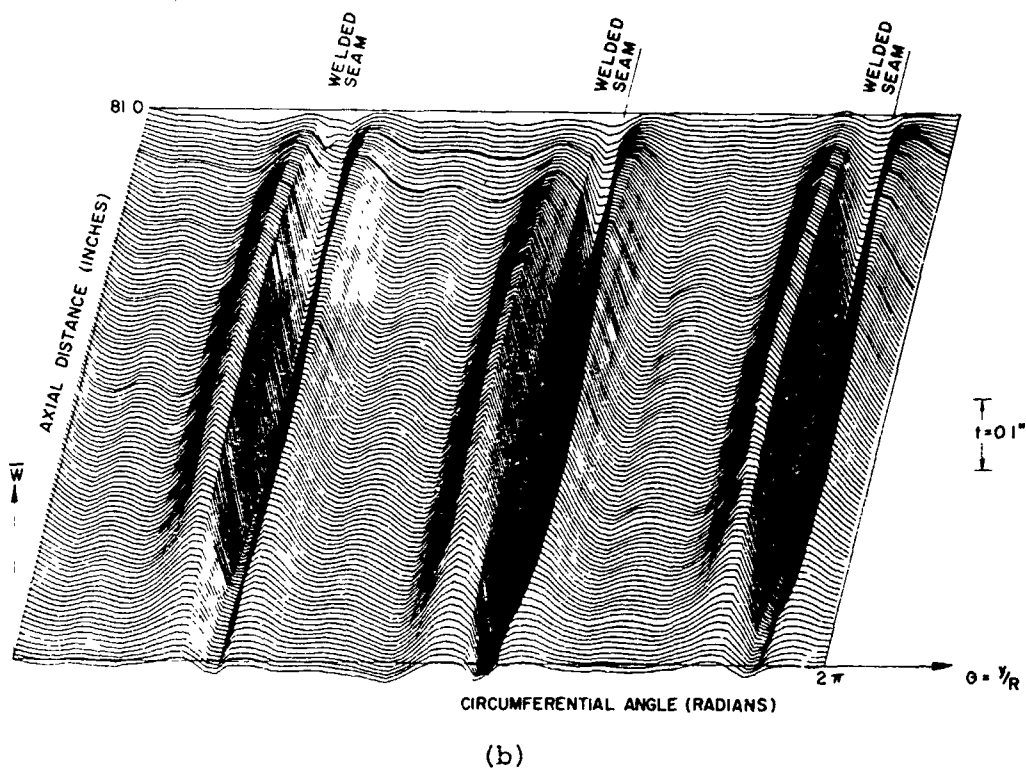
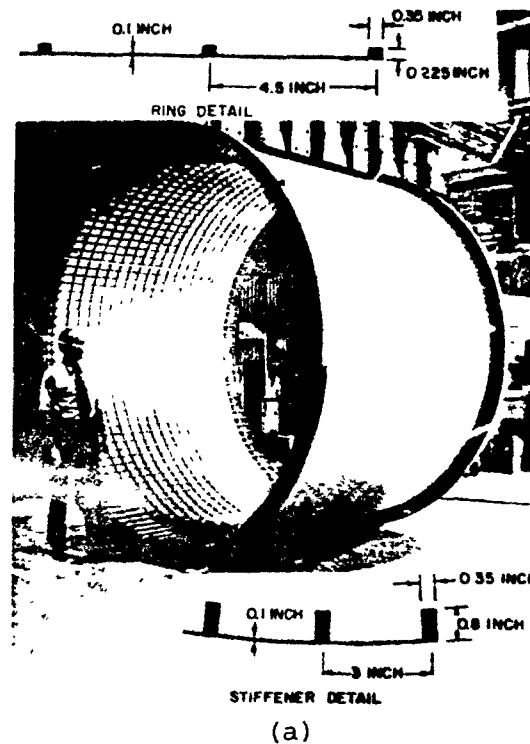


Figure 282 (a) Internally stiffened aluminum cylinder, (b) measured initial shape of the 10-ft-diameter integrally stiffened shell (from Aroncz and Williams [380]).

CRITICAL AXIAL LOAD

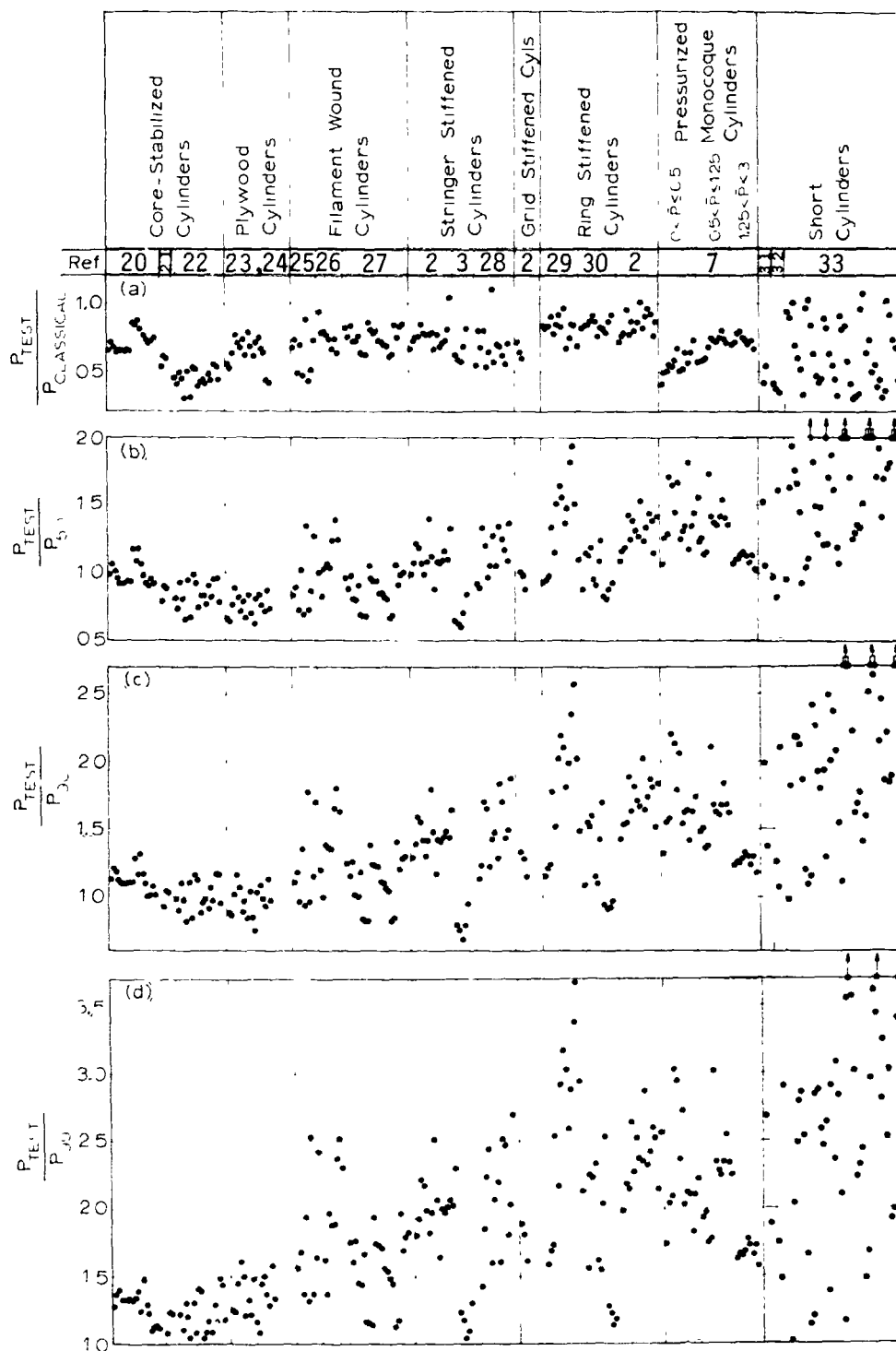


Figure 283 Axially compressed cylindrical shells: correlations between test results and (a) classical theory and the maximum of the wide column load [Eq. (141)] or the prediction from the extended version of Koiter's special theory [Eq. (144)] for (b) 50% probability predictions, (c) 90% probability predictions, and (d) 99% probability predictions (from Almroth, Burns, and Pittner [34]).

CRITICAL AXIAL STRESS
 $\sigma_{cr} \cdot [\sigma_{cr} \cdot \sigma_{cr} / (E t / R)]$

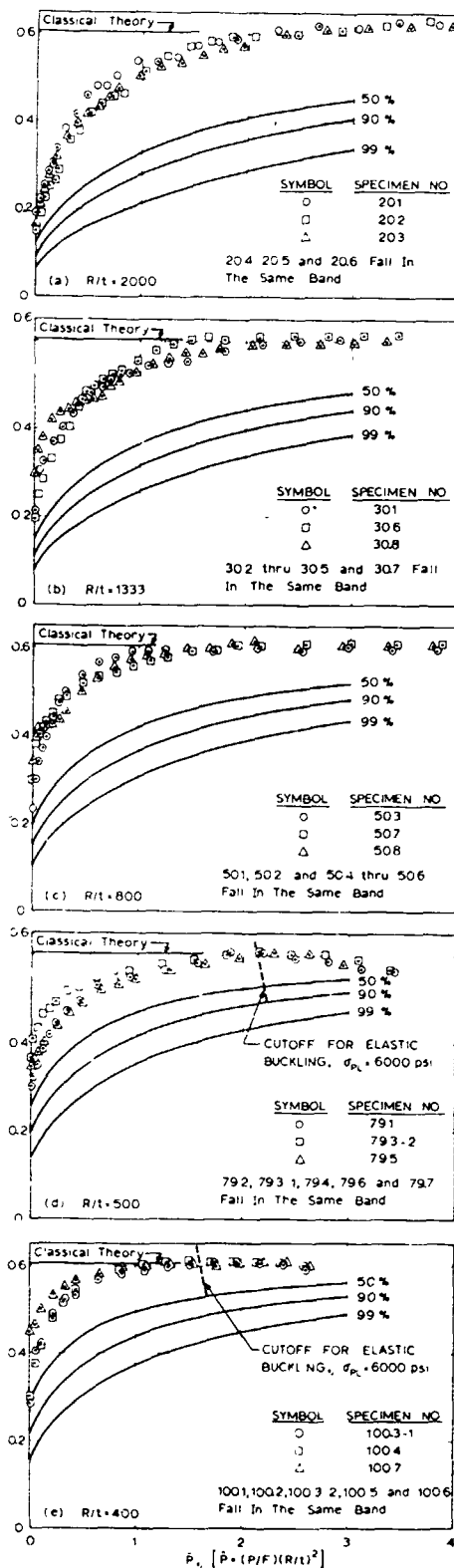


Figure 284 Axially compressed cylindrical shells: comparison between the pressurized cylinder data of [364] and predictions with use of the extended version of Koiter's special theory for three probability levels: (a) $R/t = 2000$; (b) $R/t = 1333$; (c) $R/t = 800$; (d) $R/t = 500$; (e) $R/t = 400$ (from Almqvist, Burns and Pittner [34]).

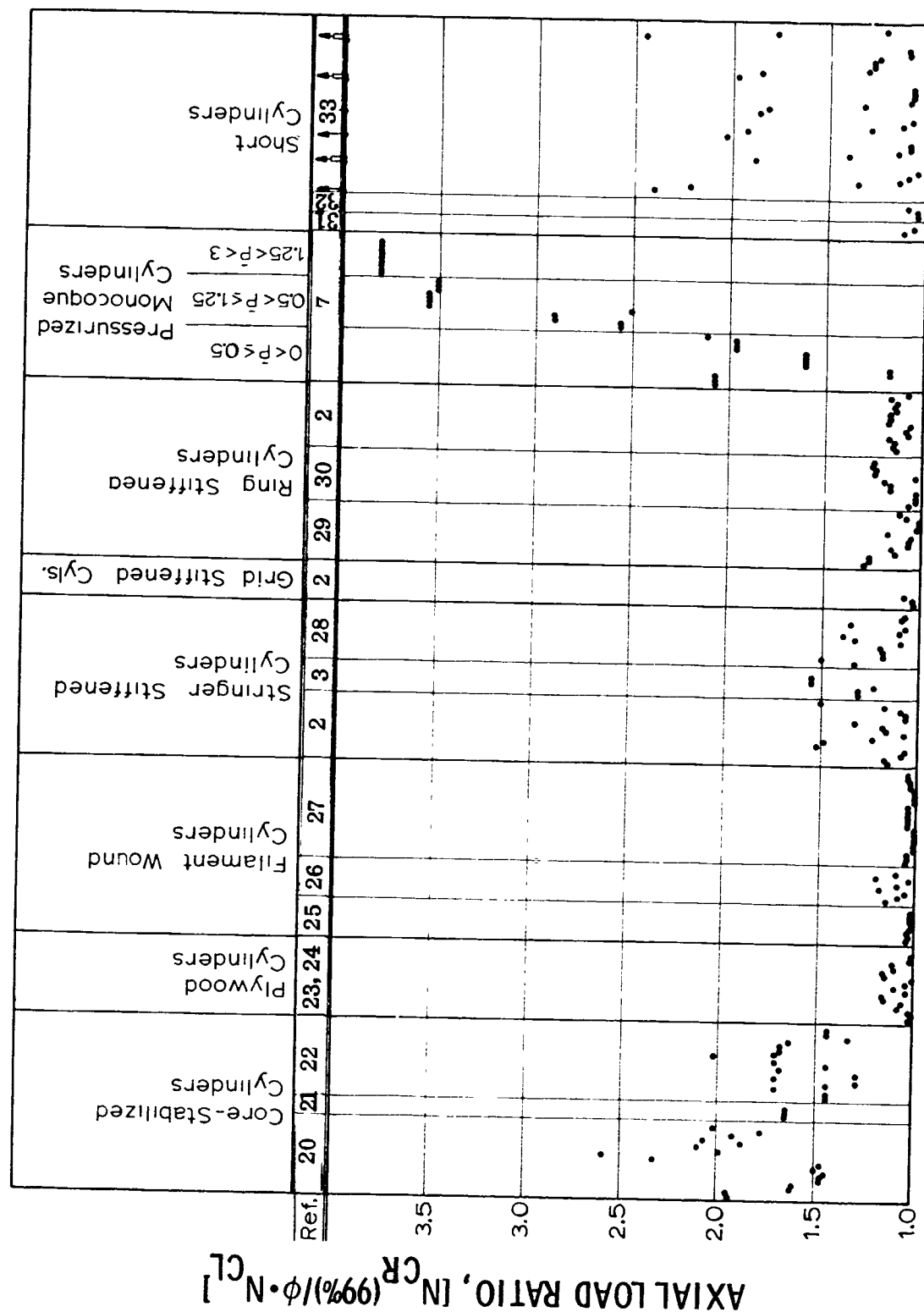


Figure 285 Axially compressed cylindrical shells: Comparison of 99% probability predictions, NCR(99%), obtained with the design method of Almroth, Burns, and Pittner [34], with predictions based on classical theory NCL times ϕ for a monocoque shell with the same effective R/t ratio (from Almroth, Burns, and Pittner [34]).

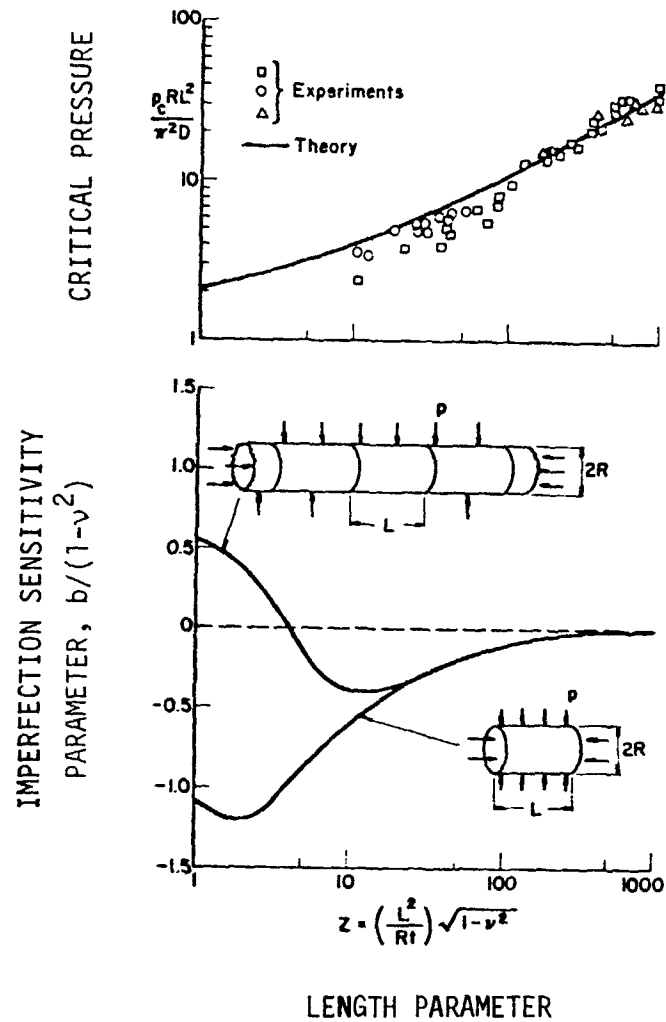


Figure 286 Comparison between test and classical theory and initial postbuckling predictions for externally pressurized cylinders (from Hutchinson and Koiter [6]).

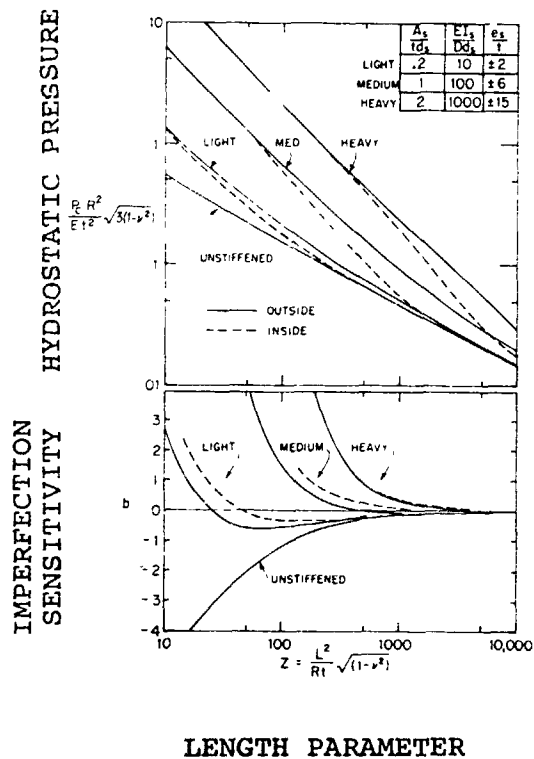


Figure 287 Classical buckling and imperfection-sensitivity of simply supported, axially stiffened cylinders under hydrostatic pressure.

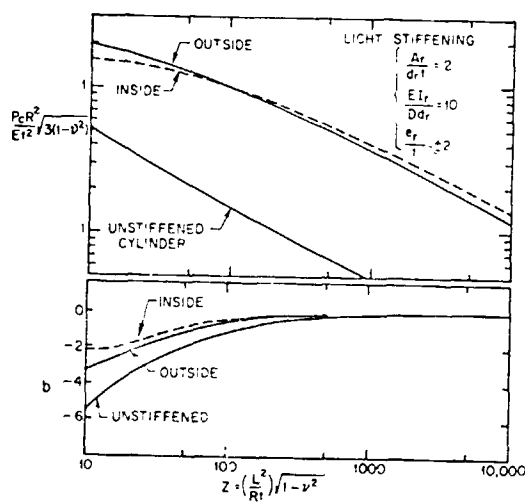


Figure 288 Classical buckling and imperfection-sensitivity of simply supported, ring stiffened cylinders under hydrostatic pressure.

(both from Hutchinson and Amazigo [345])

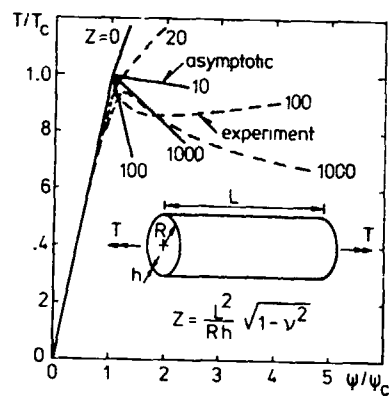


Figure 289 Torque T versus twisting angle ψ for clamped circular cylinder. Asymptotic results from Ref. [385]; experimental results from Ref. [386] (from Tvergaard [7]).

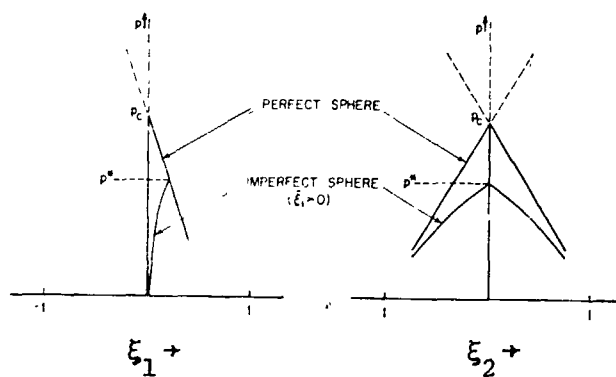


Figure 290 Pressure-modal deflection behavior, $\xi_1 = \xi_2 =$ amplitude of mode that varies in both x and y coordinates.

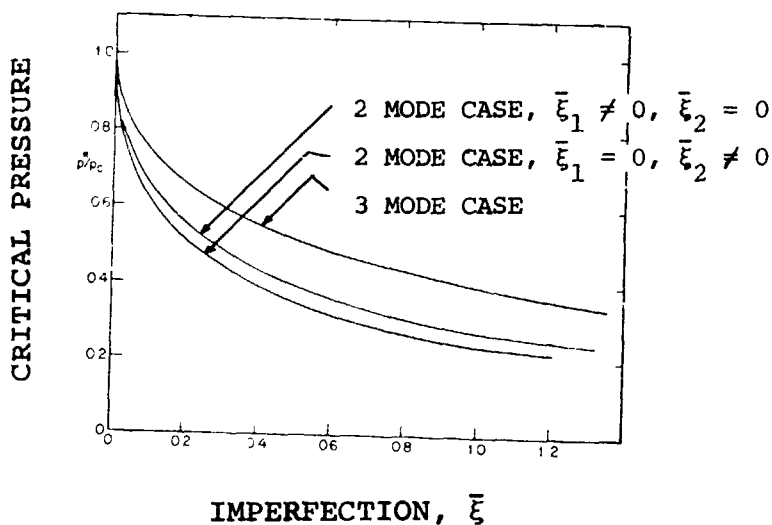


Figure 291 Buckling pressure of imperfect spherical shells ($\nu = 1/3$). $\bar{\xi}_1$ and $\bar{\xi}_2$ are amplitudes of imperfections in the prismatic (x) and (x,y) modes, respectively.

(both from Hutchinson [393]).

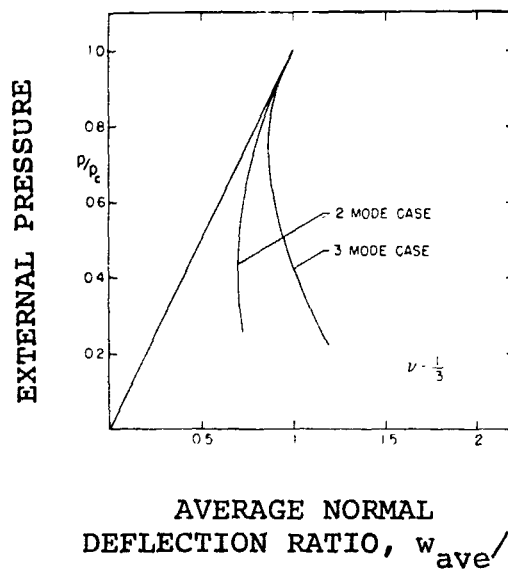


Figure 292 Generalized load-deflection curves for shallow section of perfect sphere. w_c^0 is the uniform normal deflection at the bifurcation pressure of the perfect shell.

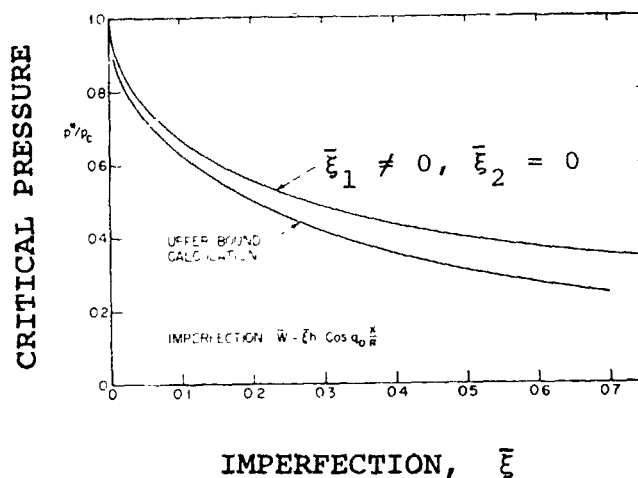


Figure 293 Buckling of externally pressurized spherical shells: comparison between general theory and an independent upper-bound calculation ($\nu = 1/3$) analogous to Koiter's special theory for axially compressed shells.

(both from Hutchinson [393])

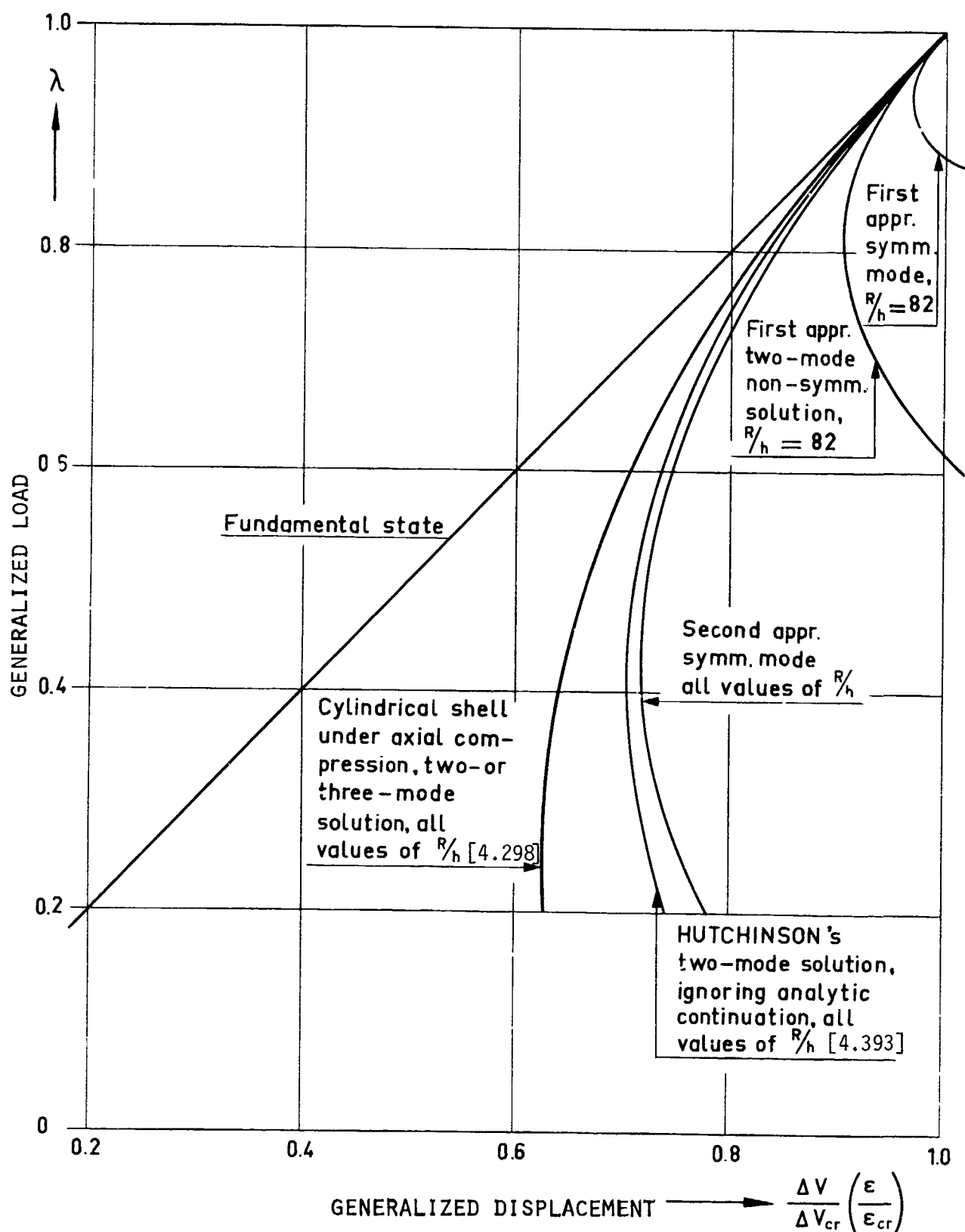


Figure 294 Equilibrium paths for spherical shells under external pressure compared with that for the cylinder under axial compression (from Koiter [390]).

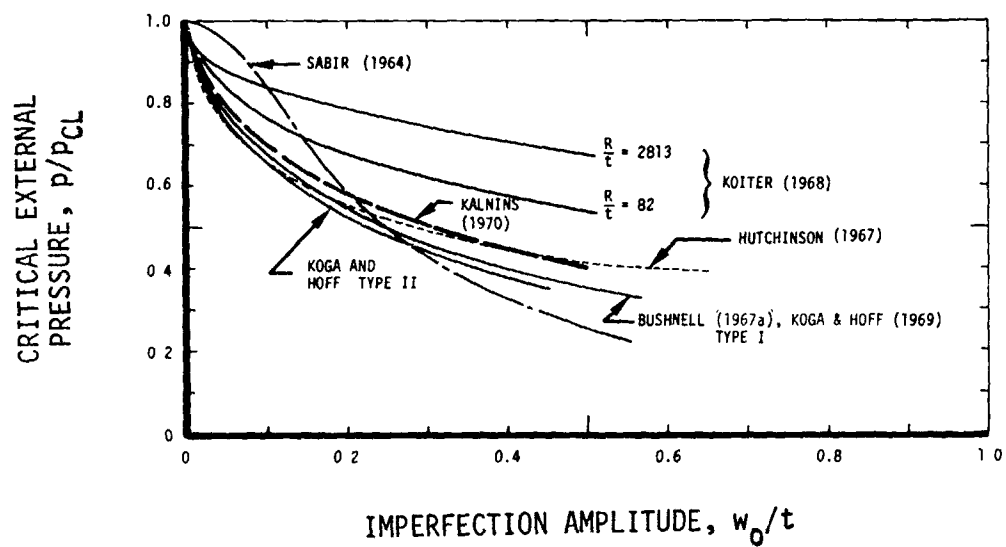


Figure 295 Analytical predictions for imperfection sensitivity of complete spherical shells (from Kaplan [37]).

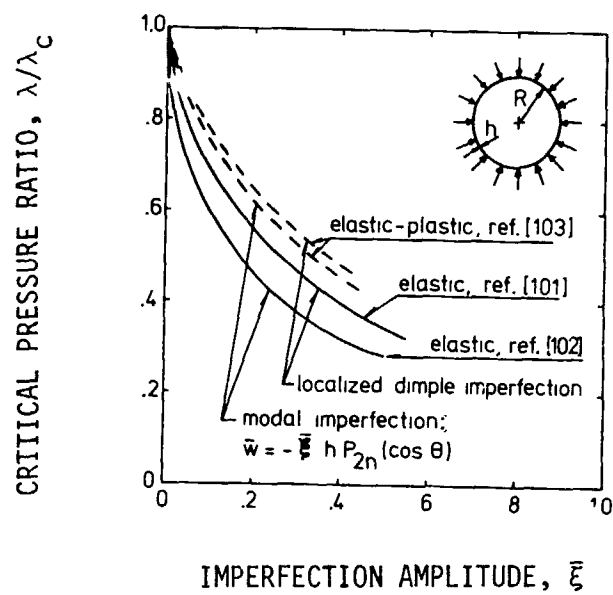


Figure 296 Imperfection sensitivity of complete spherical shells under external pressure (from Tvergaard [7]).

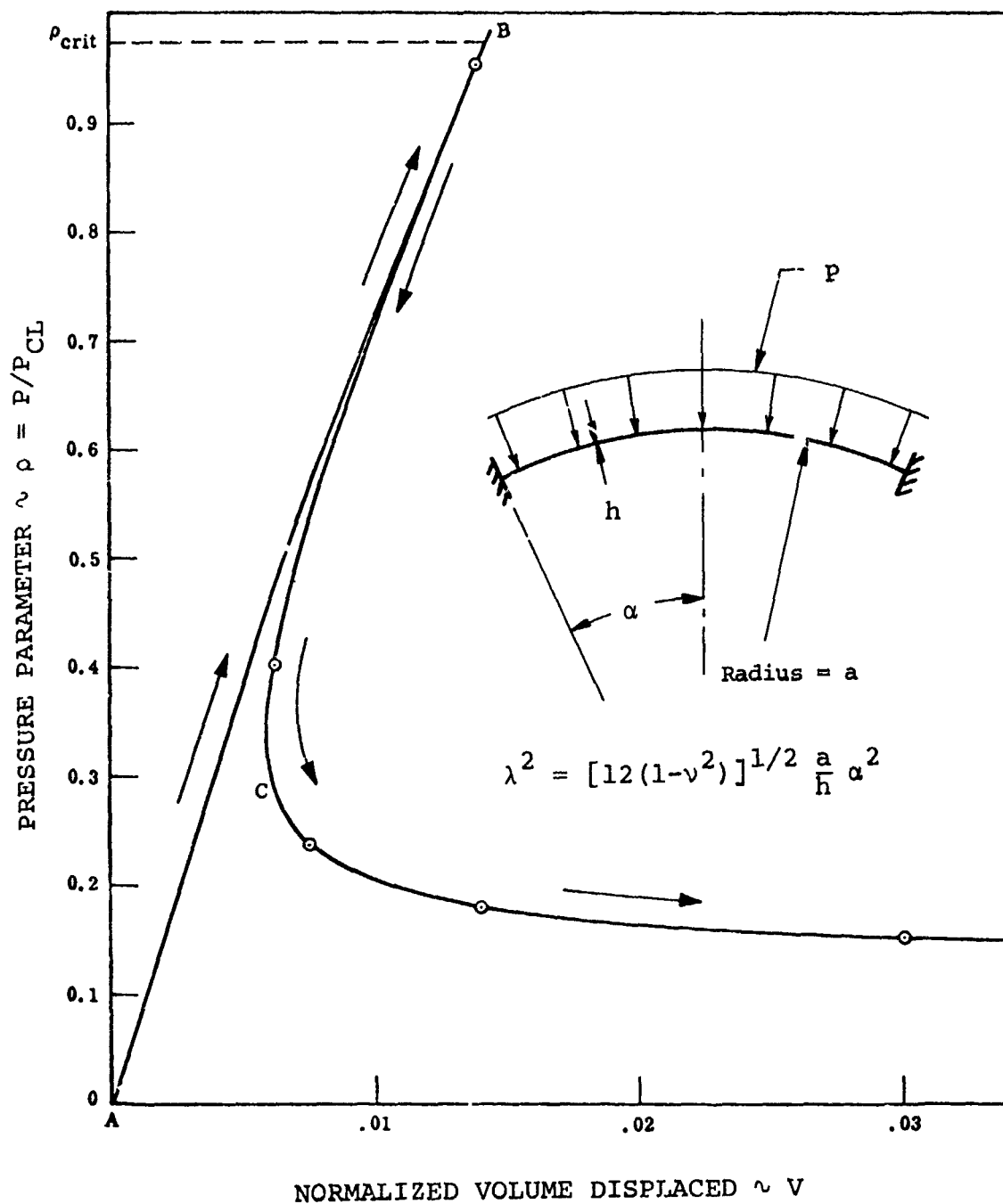


Figure 297 Load-generalized deflection curve for externally pressurized spherical clamped cap with geometric depth parameter $\lambda^2 = 20G$ (from Bushnell [401]).

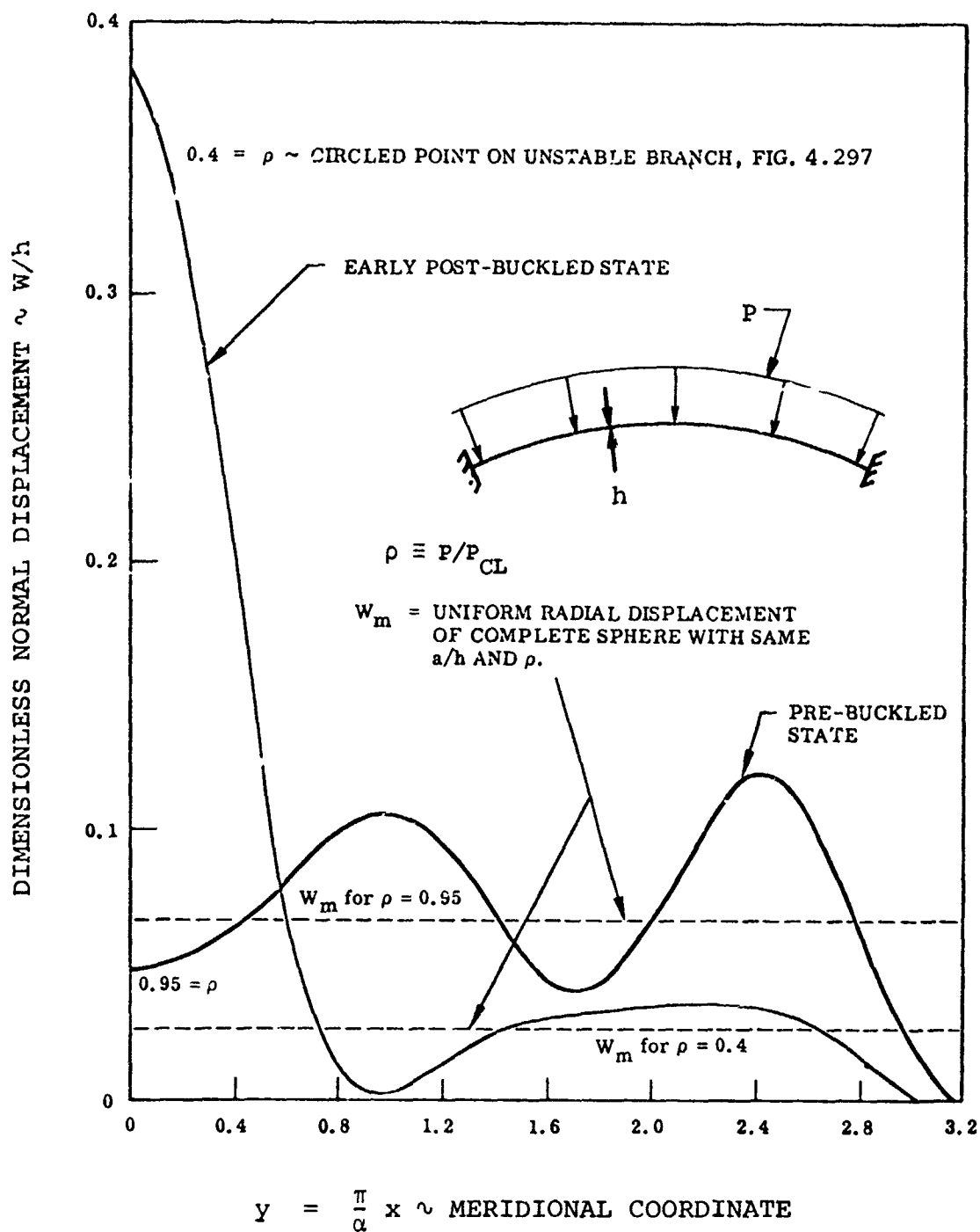


Figure 298 Dimensionless normal displacement for $\lambda^2 = 200$; prebuckled and early post-buckled states (from Bushnell [401]).

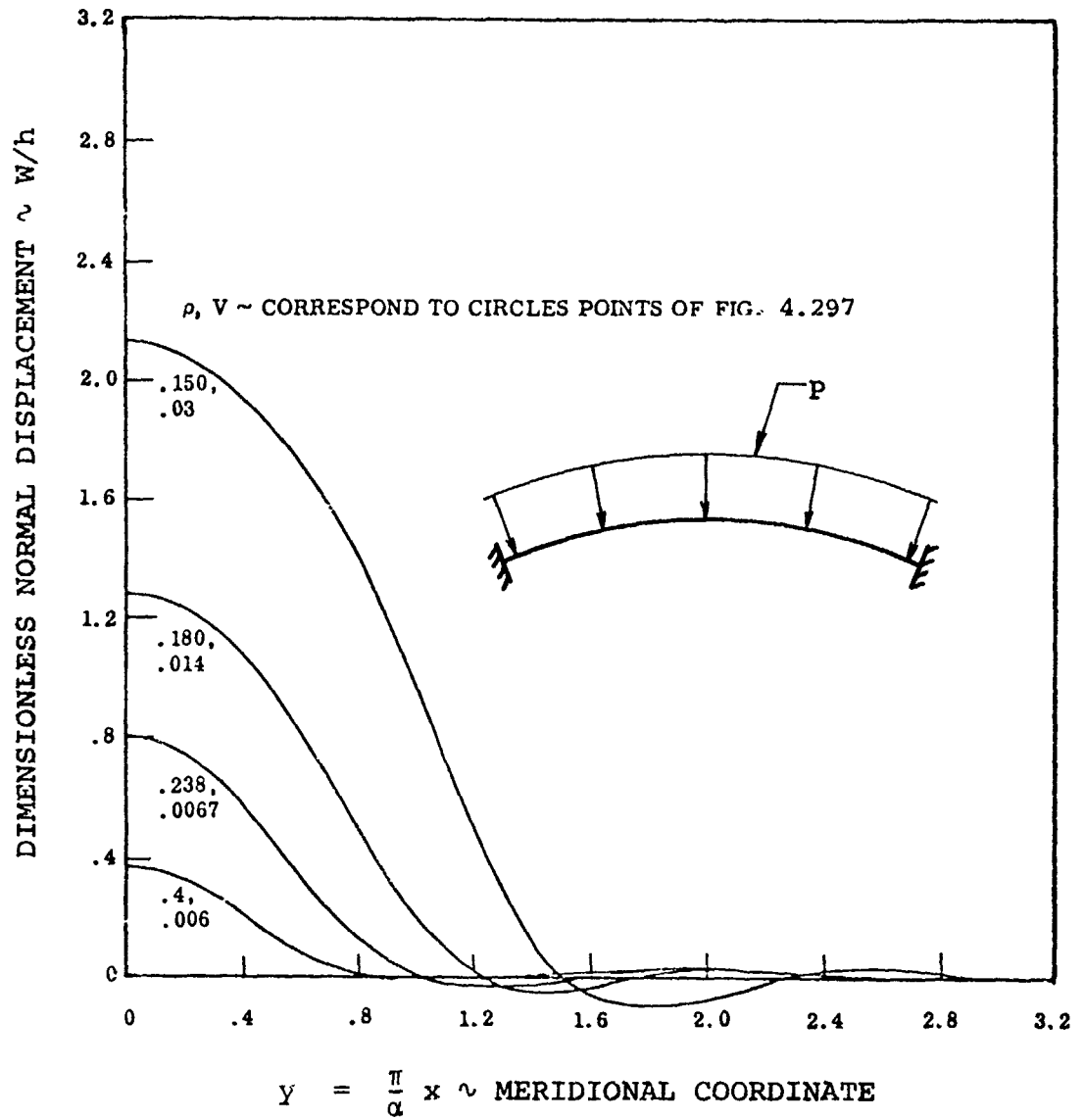


Figure 299 Dimensionless radial displacement for $\lambda^2 = 200$, showing formation of dimple after buckling (from Bushnell [401]).

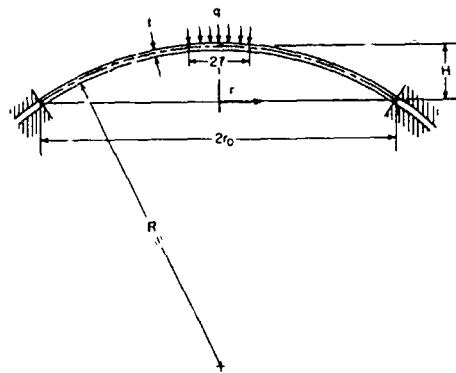


Figure 300 Geometry of a clamped spherical cap with axisymmetric loading over part of surface.

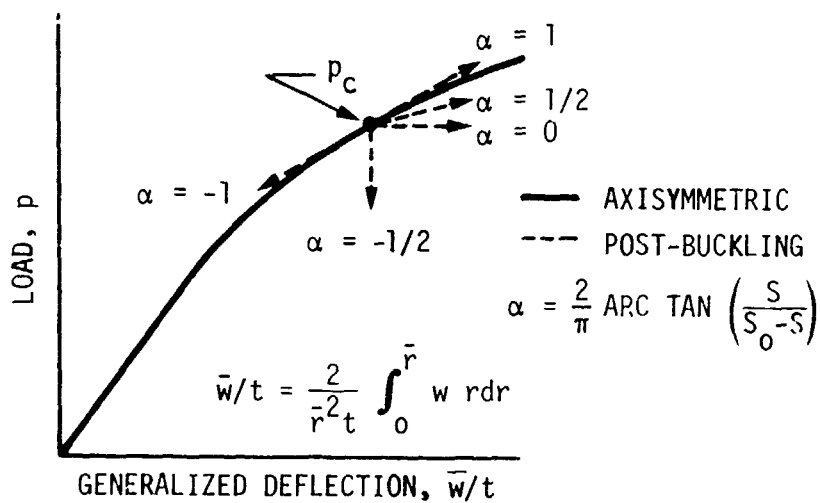


Figure 301 Interpretation of postbuckling slope parameter α , defined in terms of instantaneous axisymmetric stiffness S_0 and postbuckling stiffness S .

(both from Fitch and Budiansky [391])

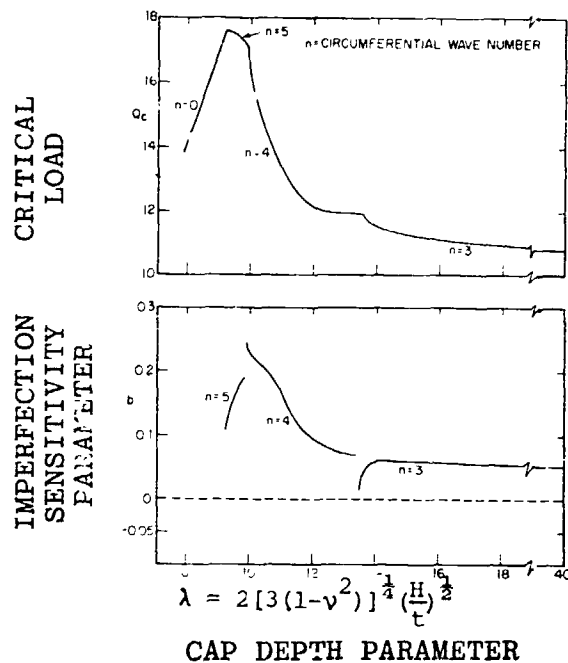


Figure 302 Buckling and postbuckling of clamped spherical cap under concentrated load P . [$Q_c \equiv (6/\pi)(1-\nu^2)PR/Et^3$] (from Fitch and Budiansky [391]).

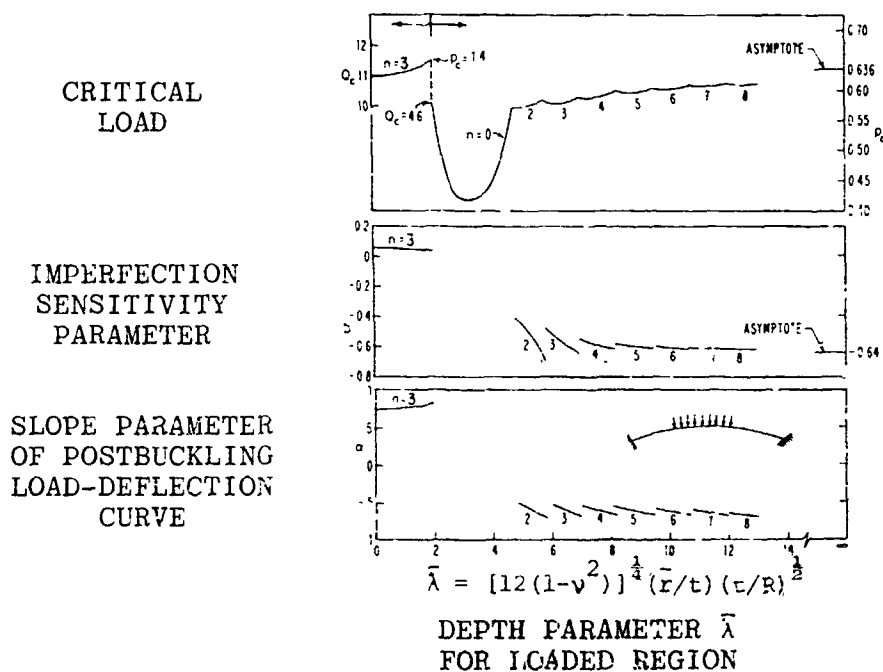


Figure 303 Buckling and postbuckling behavior of a spherical cap under distributed load in the limit as $\lambda \rightarrow \infty$. P is the pressure normalized by the classical buckling pressure p_{CL} of a complete spherical shell with the same R/t (from Fitch and Budiansky [391]).

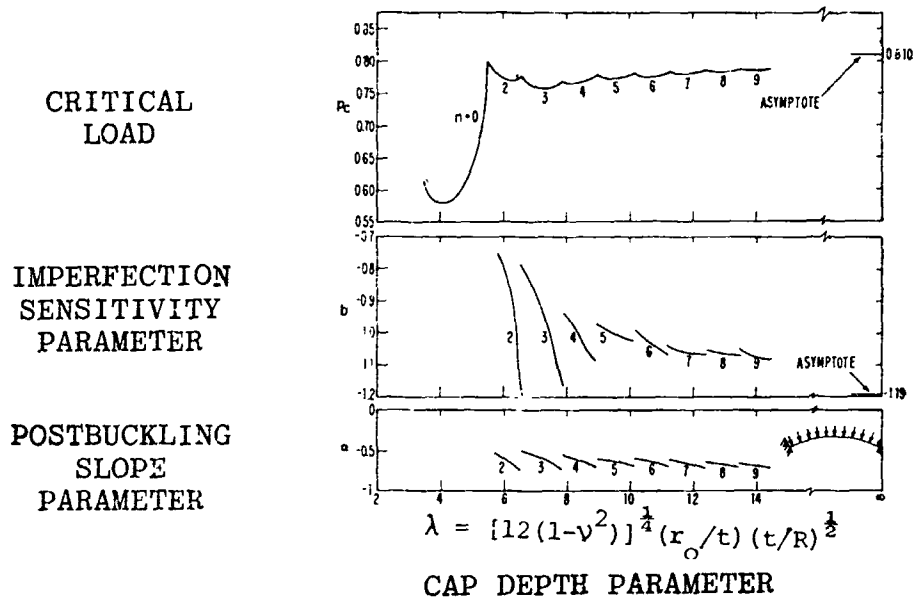


Figure 304 Buckling and postbuckling behavior of a clamped spherical cap under uniform pressure (from Fitch and Budiansky [391]).

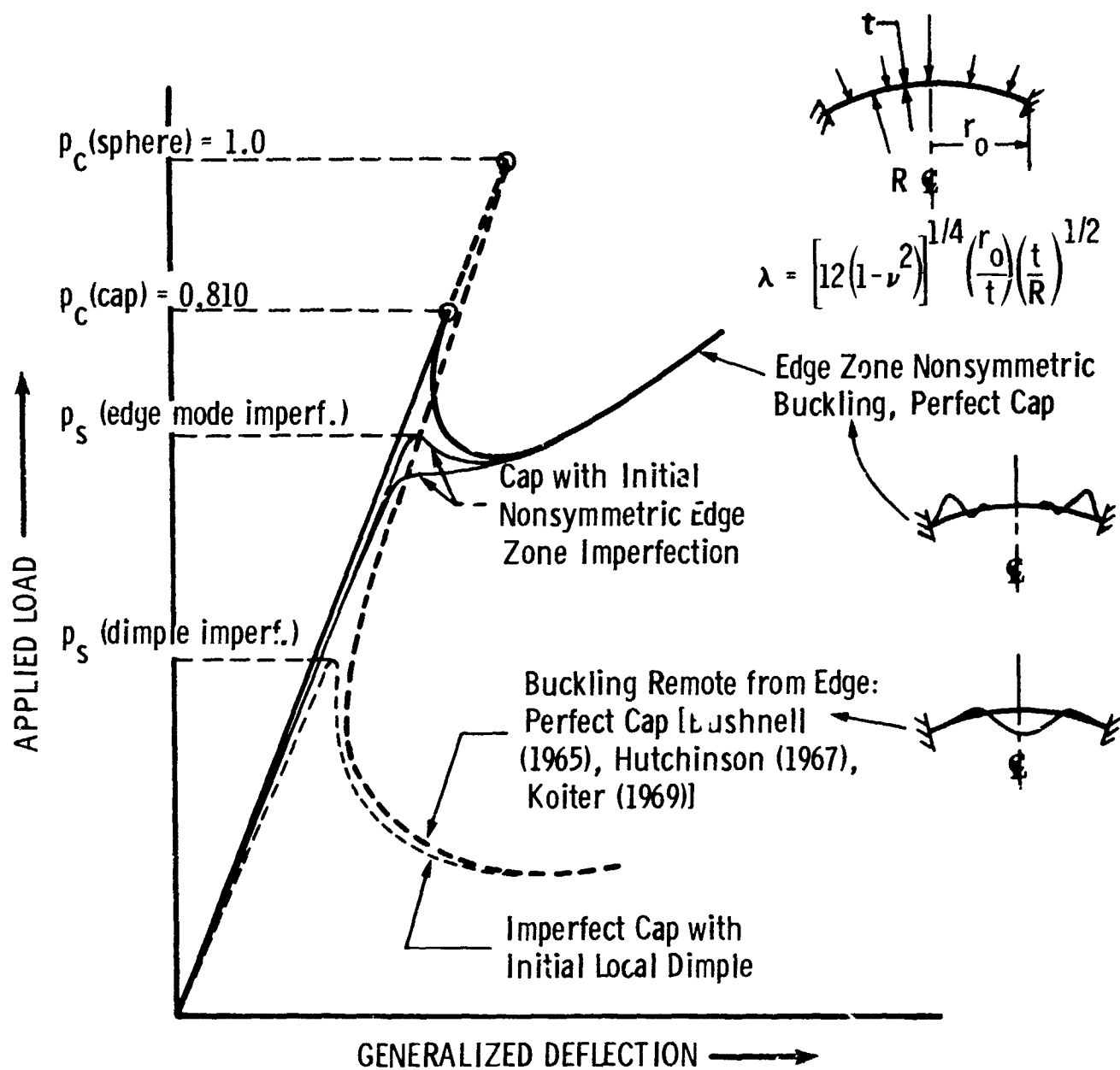


Figure 305 Post-buckling behavior of a clamped spherical cap with large depth parameter λ .

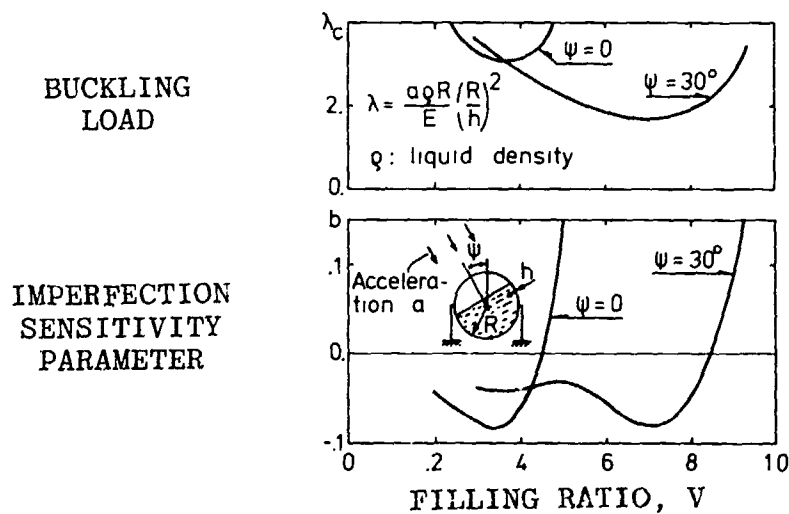


Figure 306 Critical load λ_c and postbuckling coefficient b versus liquid filling ratio V for spherical cargo tanks [112] (from Tvergaard [7]).

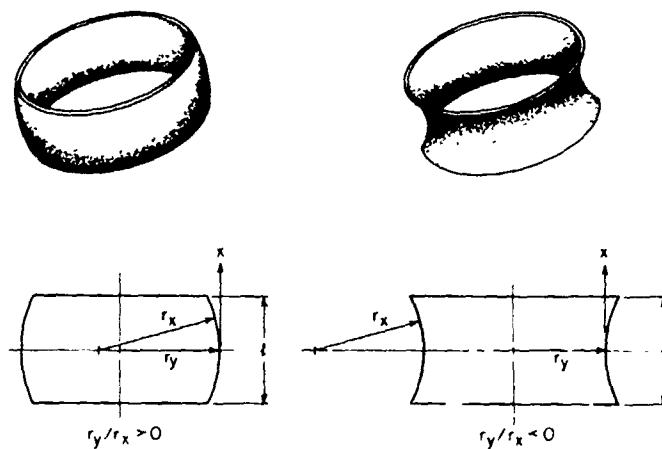


Figure 307 Configuration of toroidal segments (from Hutchinson [404]).

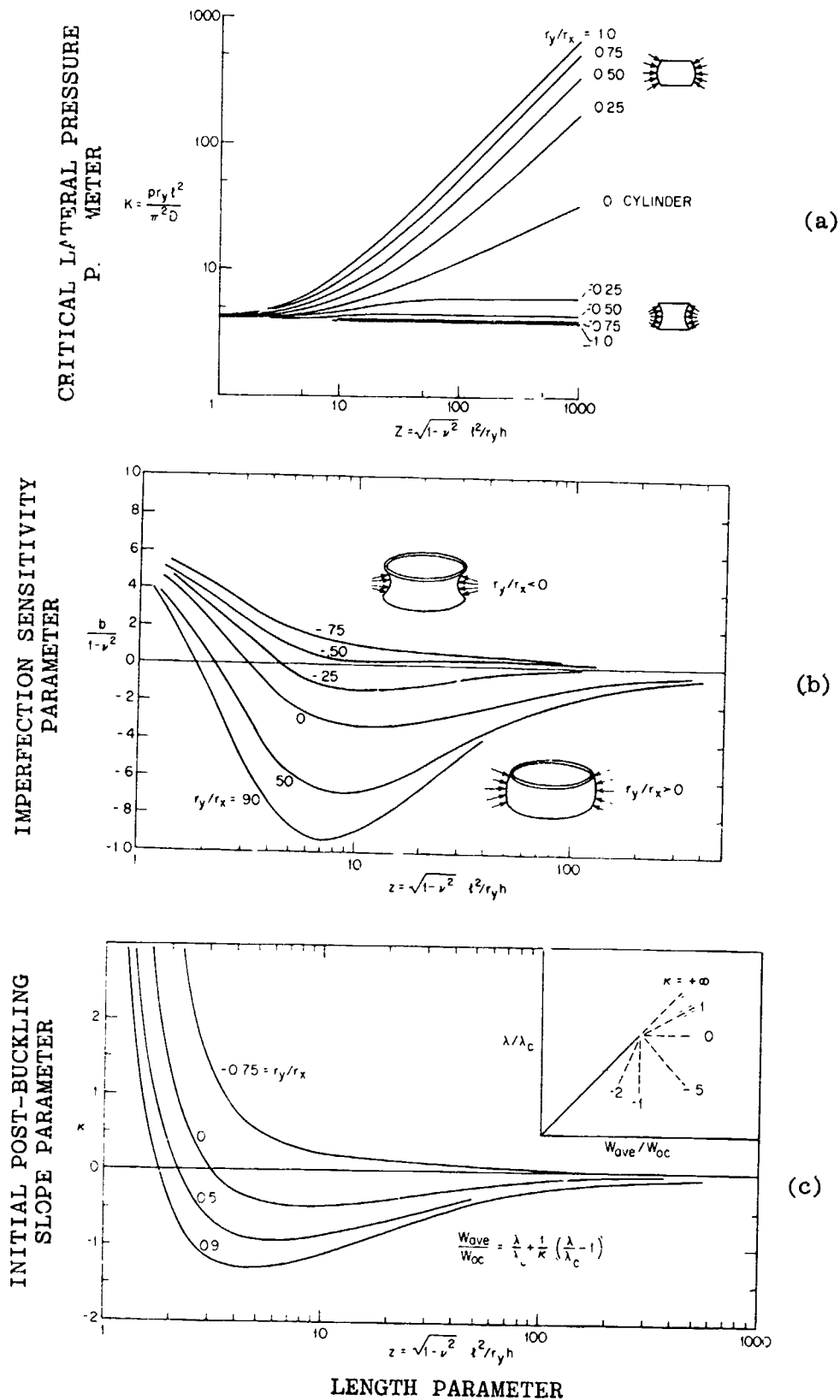
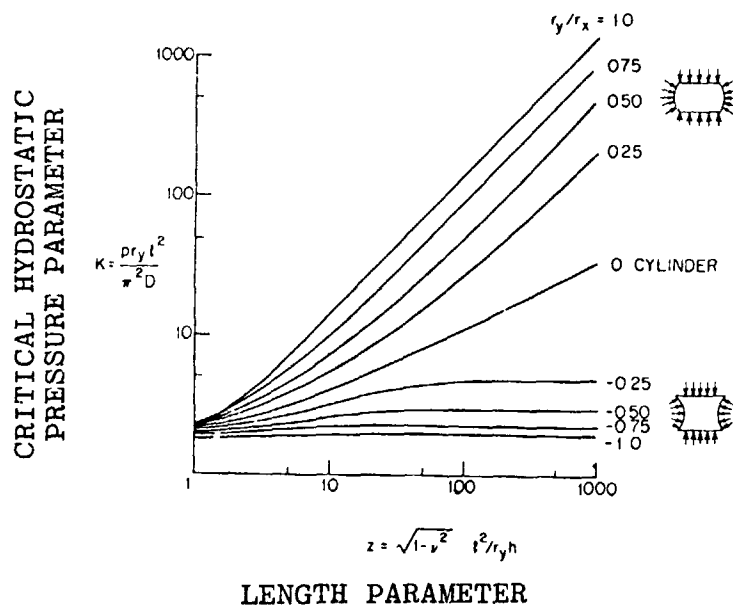
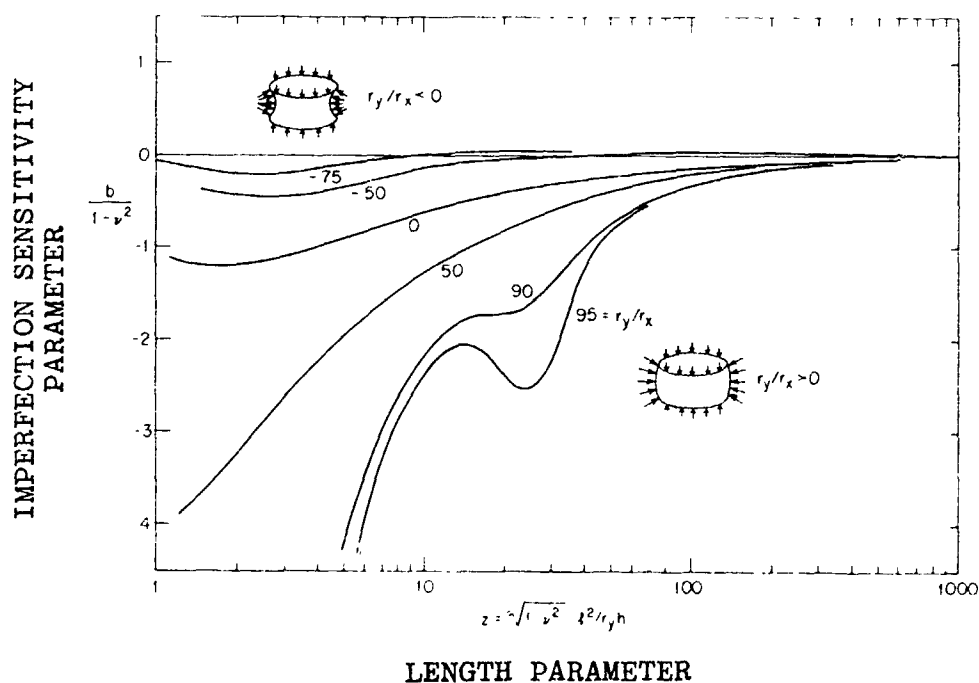


Figure 308 Bifurcation and asymptotic post-bifurcation behavior of toroidal segments under external lateral pressure: (a) classical buckling of toroidal segments under lateral pressure; (b) initial postbuckling coefficient for lateral pressure case; (c) initial postbuckling pressure-lateral deflection relation (from Hutchinson [404]).



(a) Classical buckling of toroidal segments under external hydrostatic pressure.



(b) Initial post-buckling coefficient for external pressure case.

Figure 309 Bifurcation and asymptotic post-bifurcation behavior of toroidal segments under external hydrostatic pressure (from Hutchinson [404]).

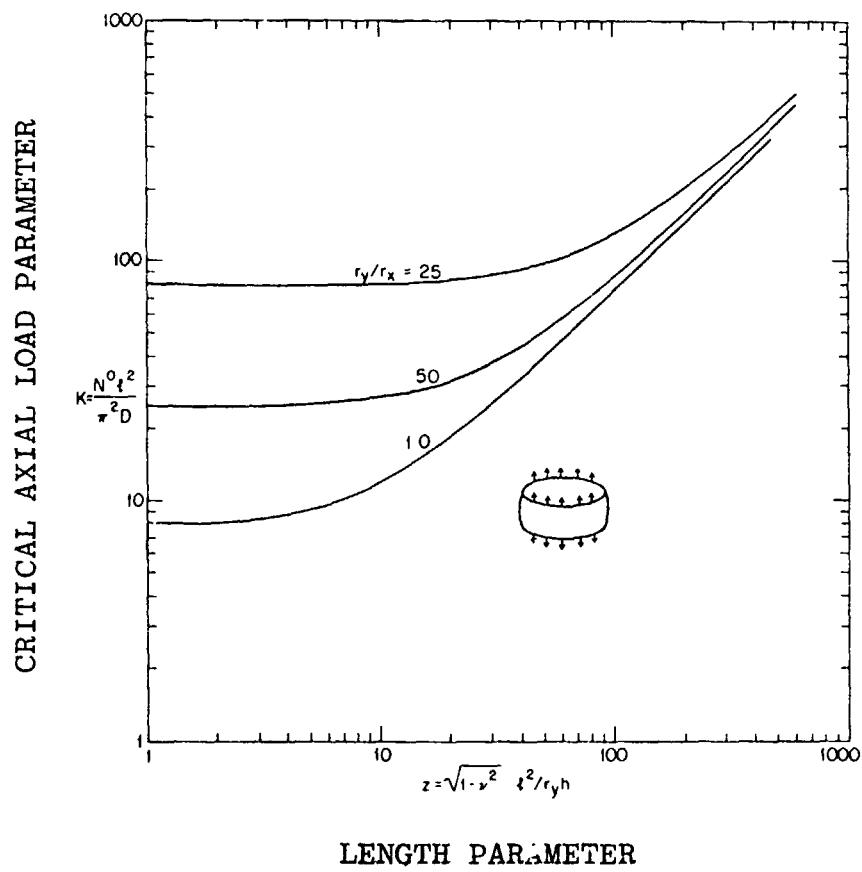
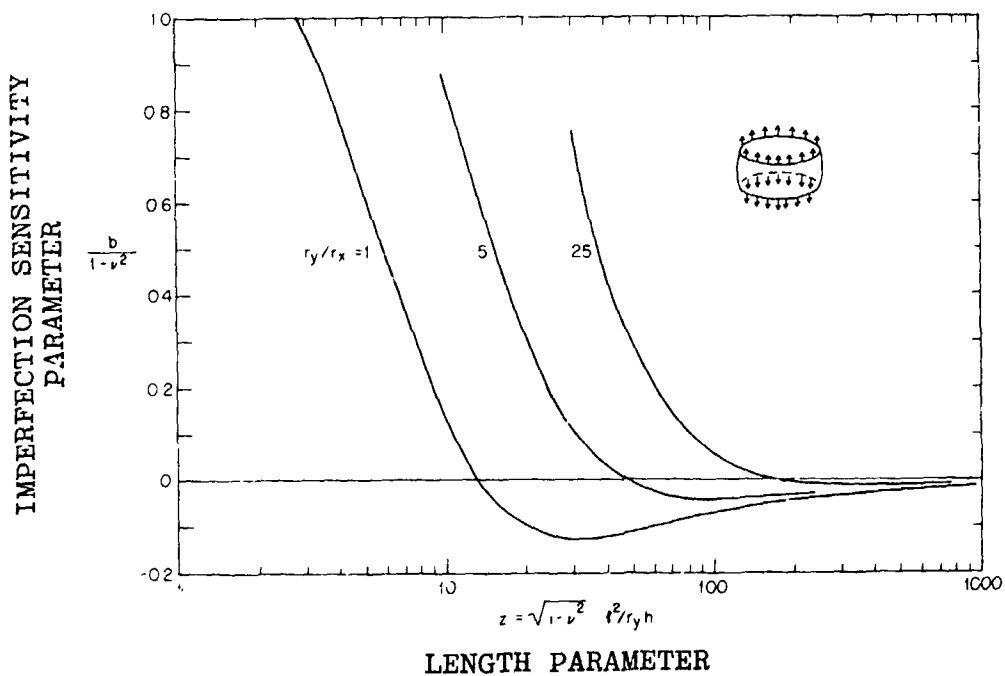
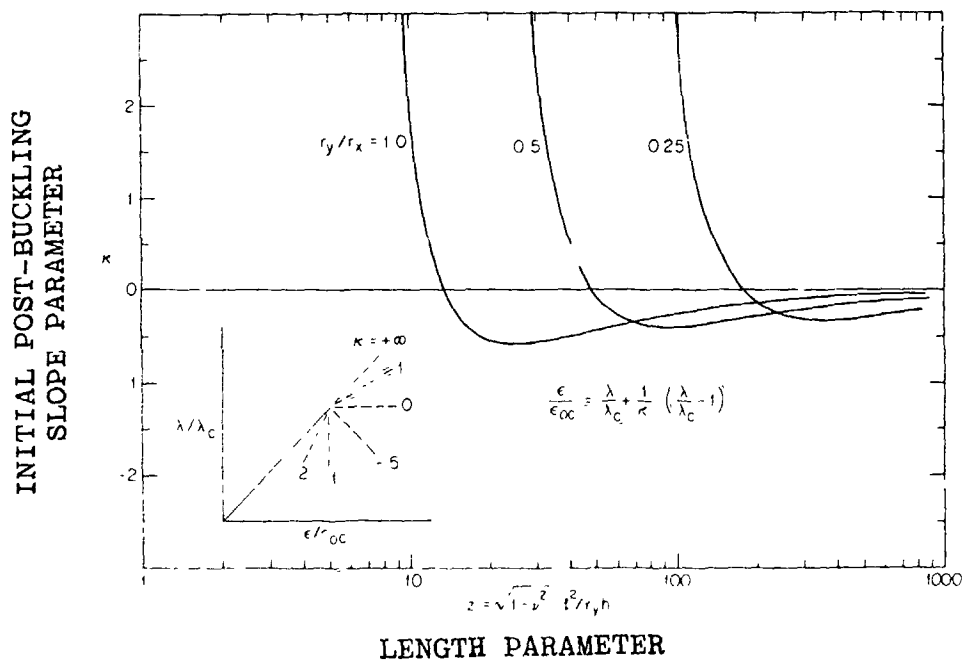


Figure 310(a) Classical buckling of bowed-out toroidal segments under axial tension (from Hutchinson [404]).

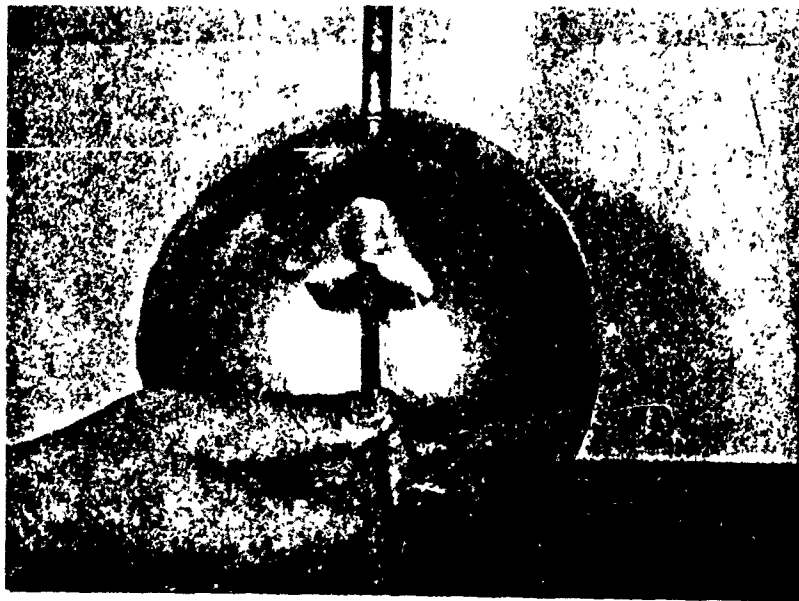


(b) Initial postbuckling coefficient for buckling under axial tension.

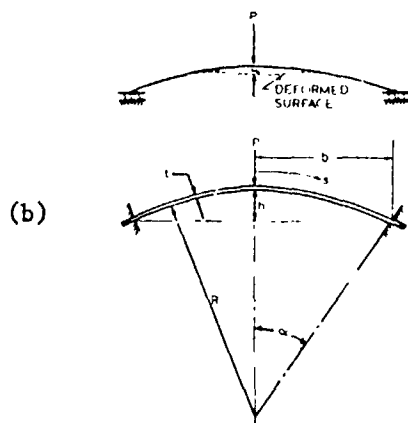


(c) Load-elongation relation in initial post-buckling of toroidal segments subject to axial tension [$\nu = 1/3$].

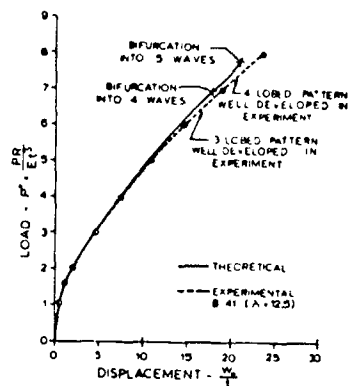
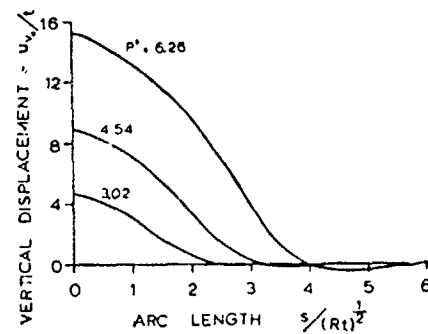
Figure 310(b,c) Asymptotic post-bifurcation behavior of bowed-out toroidal segments under axial tension (from Hutchinson [404]).



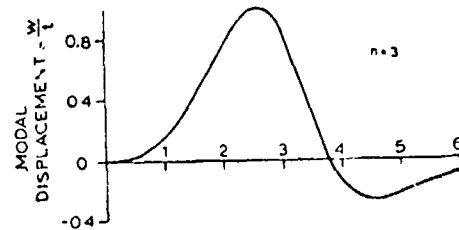
(a) Buckling of a thin-walled spherical shell by a concentrated load normal to its surface (from Horton et al. [38]).



(b)

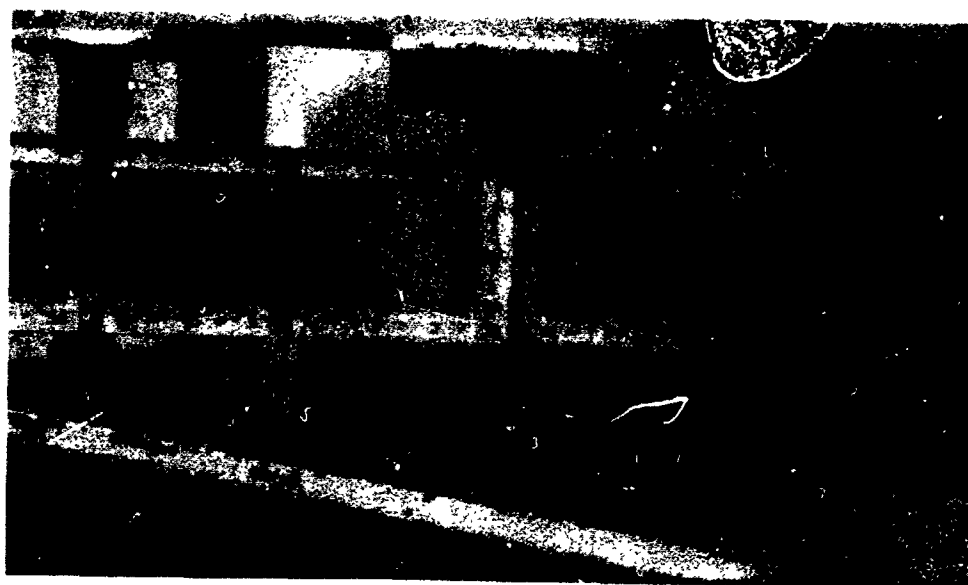


(c)



(d) Normalized prebuckling vertical (axial) displacements and buckling mode as functions of normalized arc length.

Figure 311 (a,b) Spherical shell with point load; (c) nonlinear load-deflection curve with bifurcation points; (d) prebuckling axisymmetric dimple and nonsymmetric bifurcation made with $n=3$ circumferential waves (b-d from Bushnell [111]).



(a)--Beam Before Web Buckling.



(b)--Beam After Web Buckling.

Figure 312 Development of diagonal tension field in a thin-web beam in bending (from Horton et al. [38]).

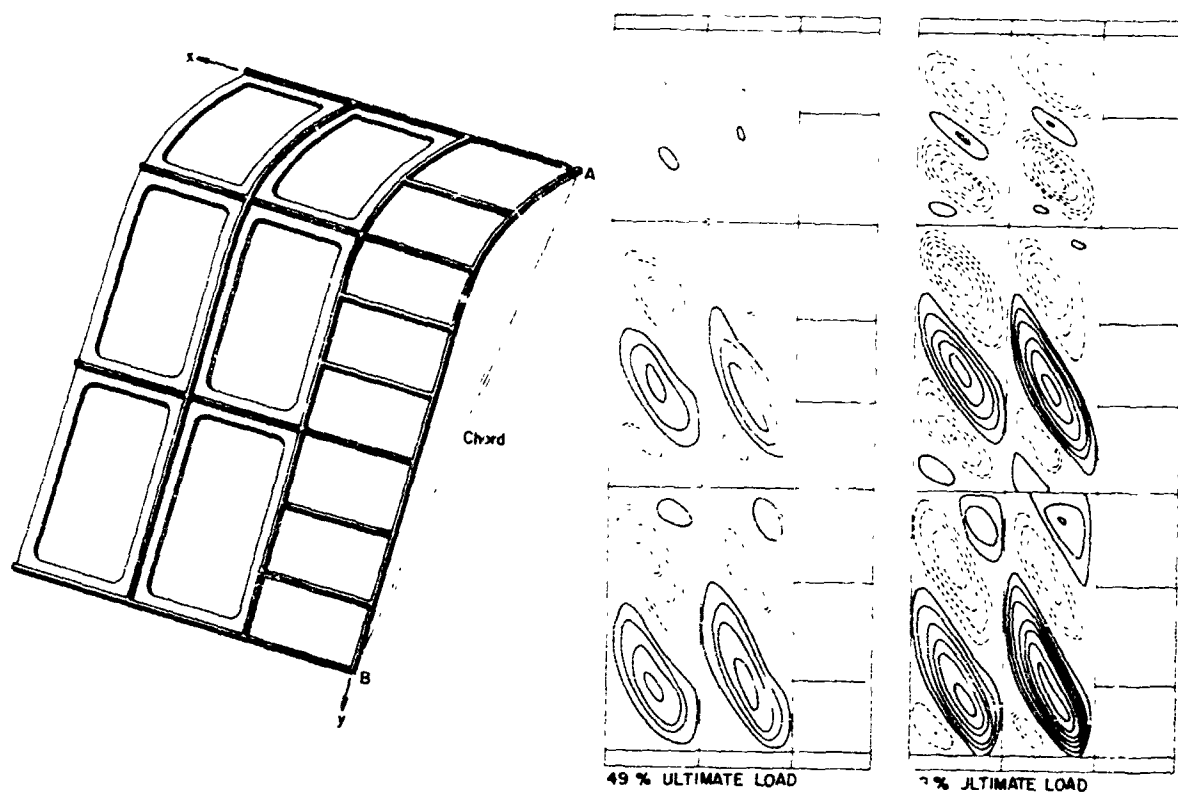


Figure 313 Complex stiffened shear panel and postbuckling behavior predicted with the STAGS computer program. Displacements are imposed at Points A and B which generate primarily in-plane shearing of the six sub-panels for which contour plots of normal displacement are displayed (from Skogh and Stern [409]).

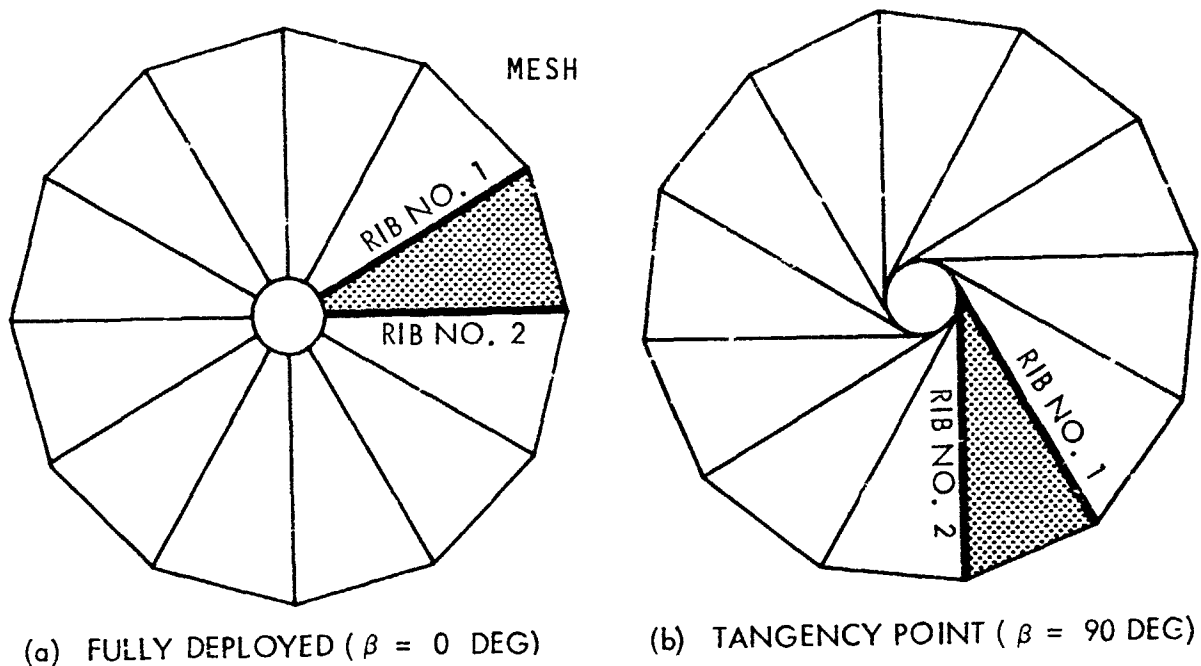


Figure 314 Plan view of a parabolic antenna with a pre-tensioned mesh to be unfurled in space. During the last phase of deployment from the tangency point (b) to the fully deployed state (a) the slack in the mesh is taken up in a way which causes loads to be applied to the ribs in a complicated sequence which depends on various patterns of wrinkles that develop in the mesh (from Bushnell [410]).

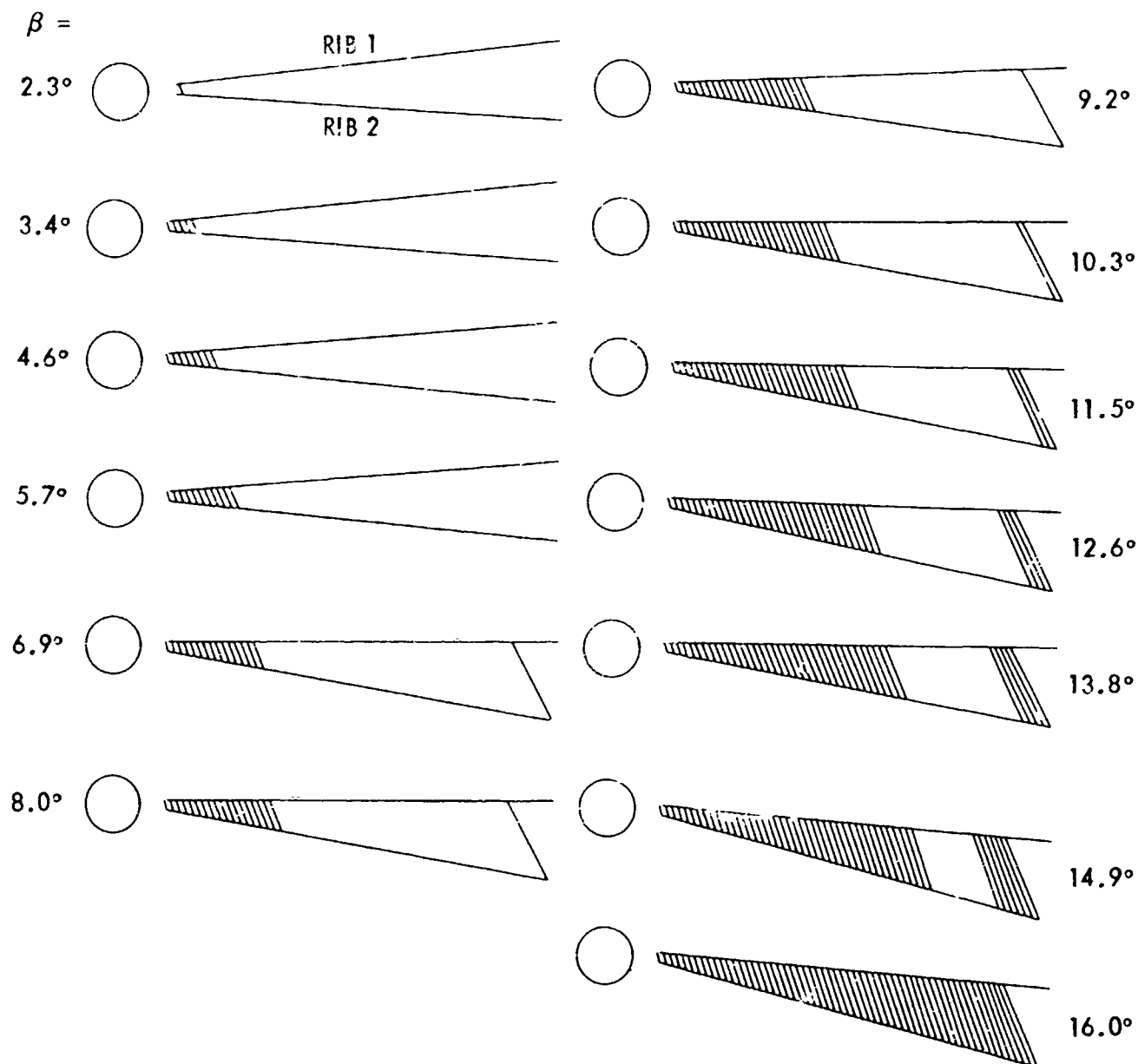


Figure 315 For the solution of this "postbuckling" problem the deployment sequence is analyzed as if the antenna is being furled instead of unfurled. This figure exhibits the predicted development as the rib root bending angle β is increased from 0 to 16° (from Bushnell [410]).



(a) Prestress



(b) $\beta \approx 30^\circ$



(c) $\beta \approx 45^\circ$



(d) $\beta \approx 85^\circ$

Figure 316 Development of wrinkles in a crude experimental model that simulates the furling of an antenna with rigid ribs. The dark lines drawn from Rib 1 to Rib 2 remain fairly straight in the smooth regions, as required in the analysis (from Bushnell [410]).

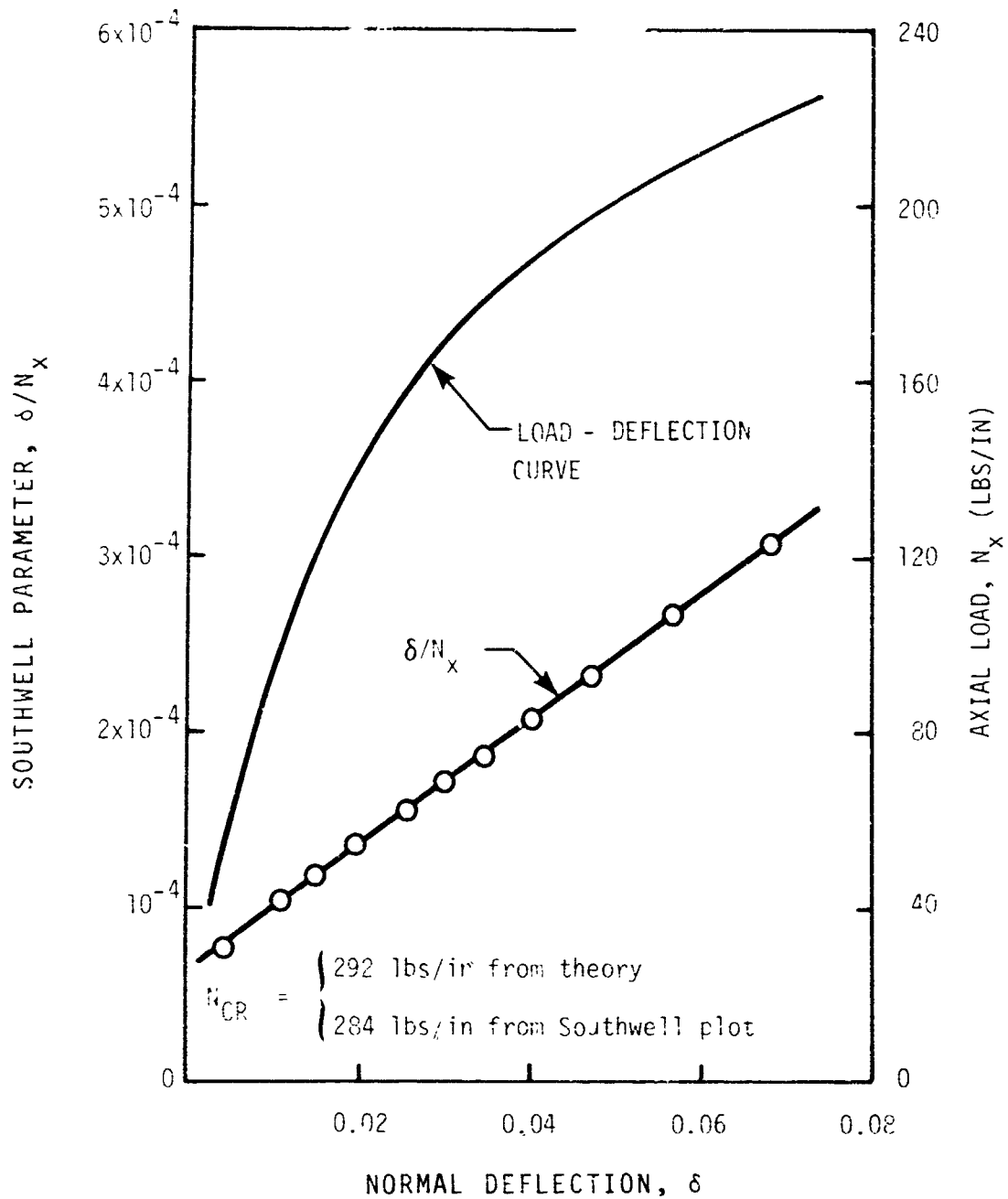


Figure 317 Load-deflection diagram and Southwell plot for axially compressed, simply-supported composite plate with an unbalanced laminate ($0^\circ, 90^\circ, 0^\circ, 90^\circ$) (from Ref. [420], Test 203b).

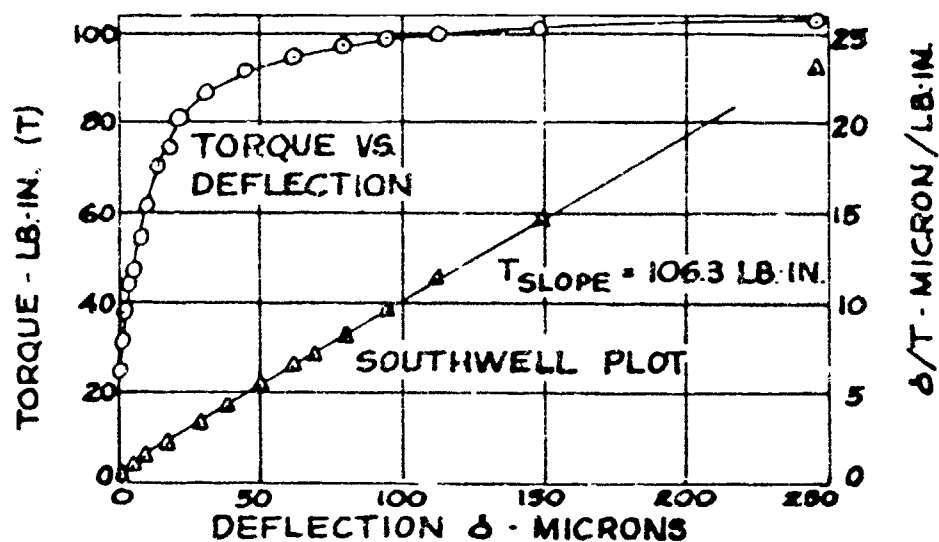


Figure 318 Torsion versus inward wall motion and corresponding Southwell plot for orthotropic cylinder (from Banks [425]).

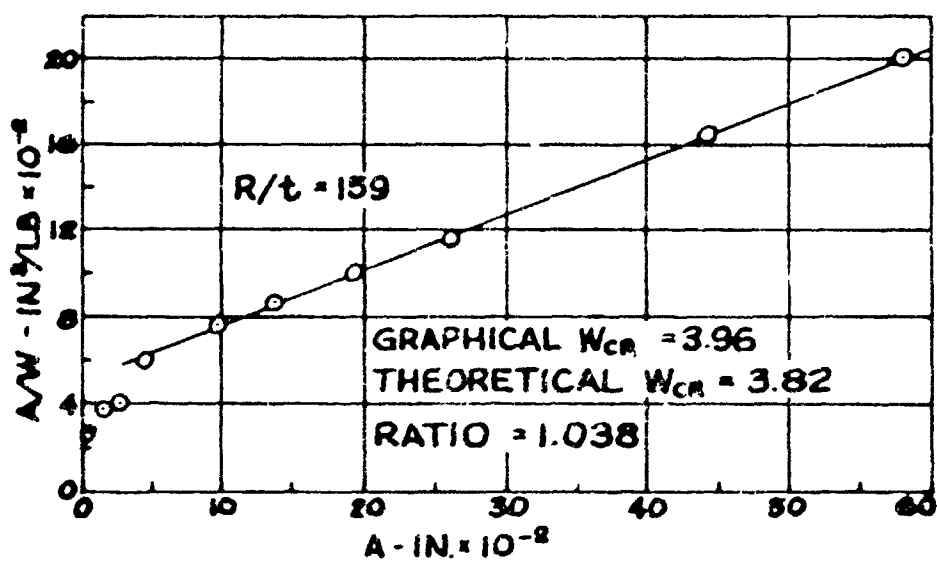


Figure 319 Circular cylindrical shell under external pressure
(data from Figure 16, Ref. 422).

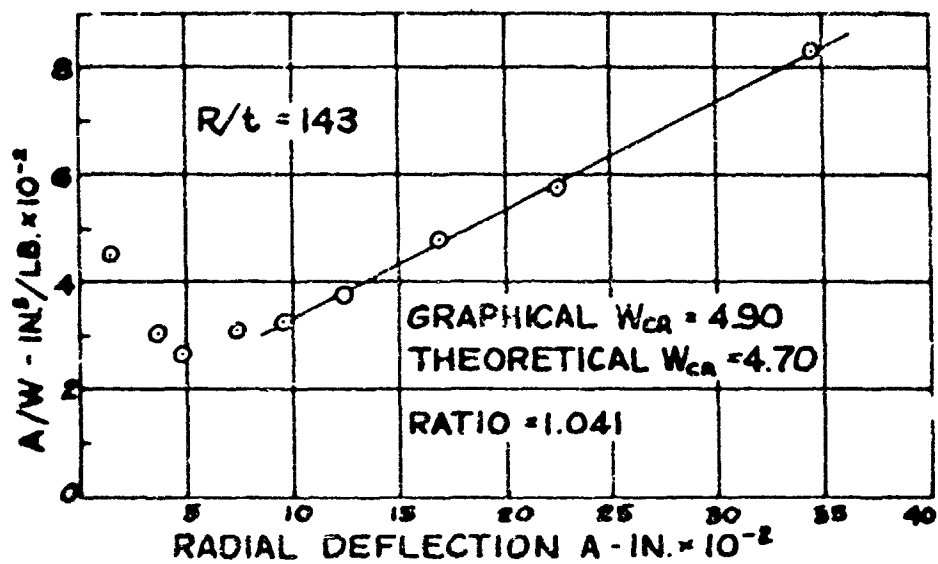


Figure 320 Circular cylindrical shell under external pressure
(data from Figure 18, Ref. 422).

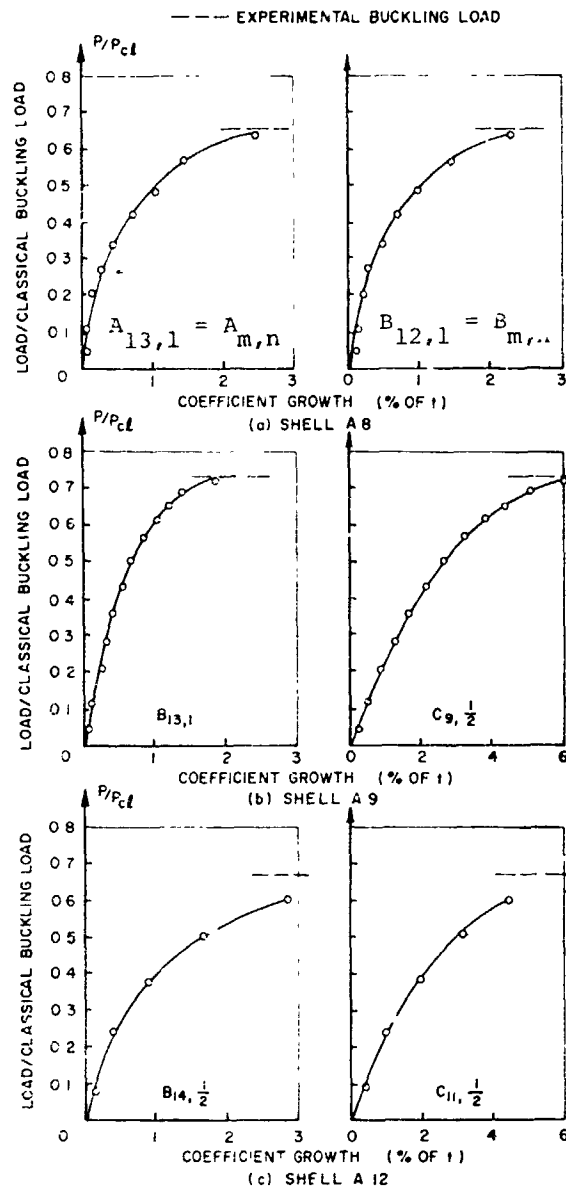
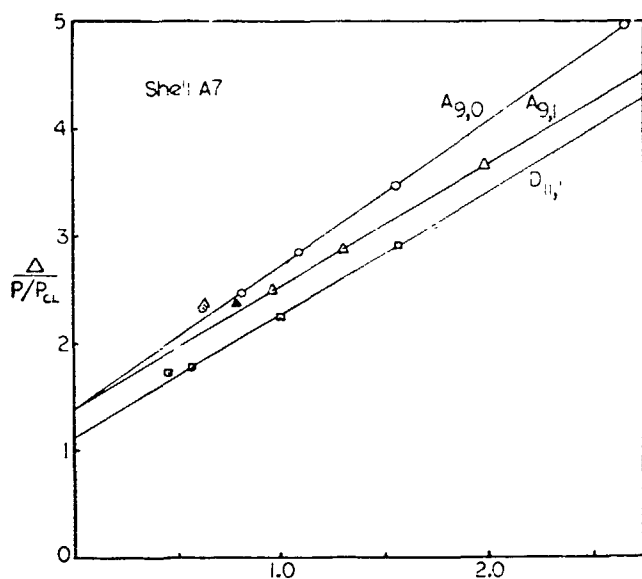


Figure 321 Imperfect monocoque cylindrical shells under axial compression: growth of selected Fourier coefficients of the dimensionless radial displacement, w , which is given by

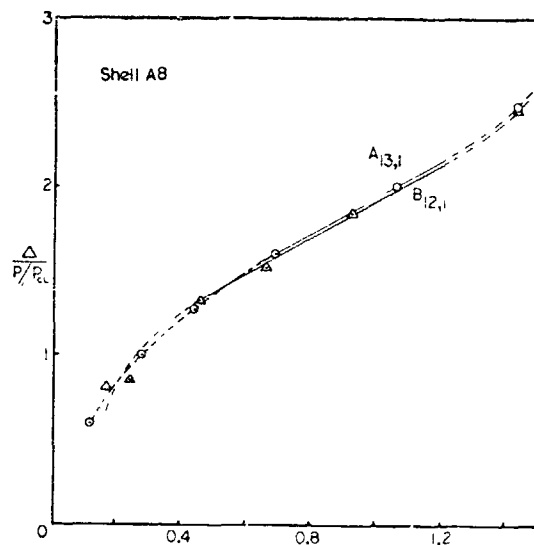
$$\begin{aligned}
 w(x, y) = & \sum_{m=0}^{\infty} \sum_{n=0}^{\infty} A_{mn} \cos m \frac{y}{R} \cos \frac{2n\pi x}{L} \\
 & + \sum_{m=1}^{\infty} \sum_{n=0}^{\infty} B_{mn} \sin m \frac{y}{R} \cos \frac{2n\pi x}{L} \\
 & + \sum_{m=0}^{\infty} \sum_{n=1}^{\infty} C_{mn} \cos m \frac{y}{h} \sin \frac{2n\pi x}{L} \\
 & + \sum_{m=1}^{\infty} \sum_{n=1}^{\infty} D_{mn} \sin m \frac{y}{R} \sin \frac{2n\pi x}{L}
 \end{aligned}$$

(from Árbocz and Babcock [341]).



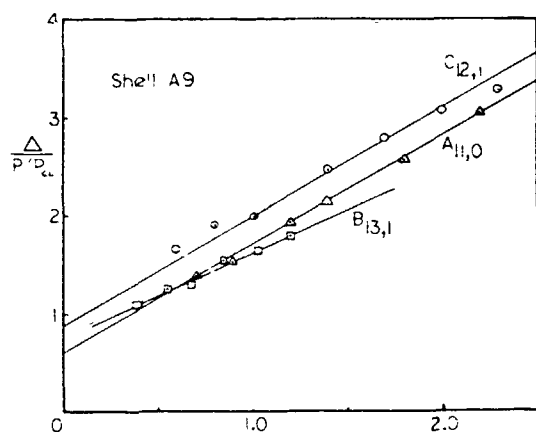
FOURIER COEFFICIENT (% of thickness)

(a) Southwell plots for data of Shell A7.



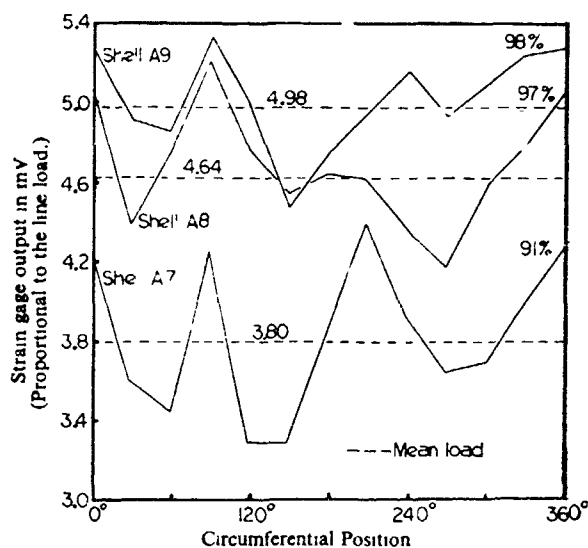
FOURIER COEFFICIENT (% of t)

(b) Southwell plots for data of Shell A8.



FOURIER COEFFICIENT (% of t)

(c) Southwell plots for data of Shell A9.



(d) Line load distributions for cylinders just prior to buckling.

Figure 322 Imperfect monocoque cylindrical shells under axial compression: (a-c) Southwell plots of growth of normal displacement harmonics for three specimens of Arbocz and Babcock [341]; (d) variation of axial line load around the circumference (from Horton and Craig [414]).

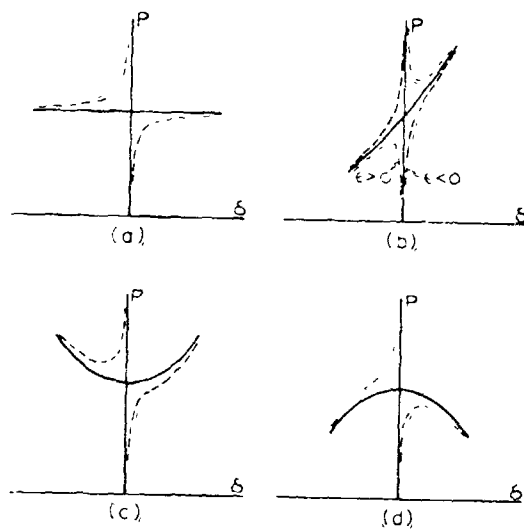


Figure 323 Types of postbuckling behavior (from Roorda [417]).

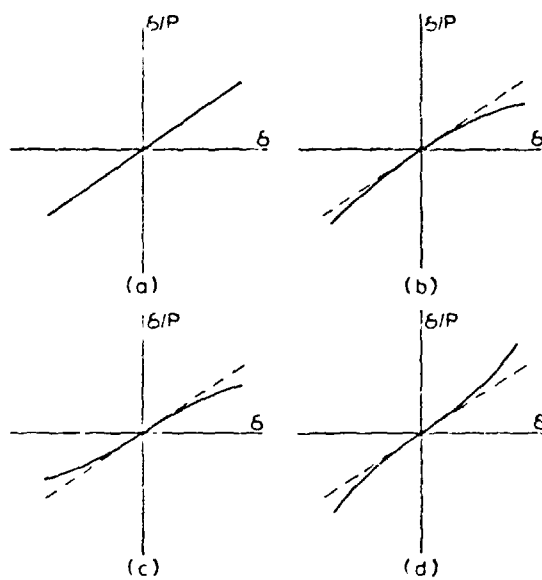


Figure 324 Southwell plots corresponding to the four types of postbuckling behavior shown in Figure 323 (from Roorda [417]).

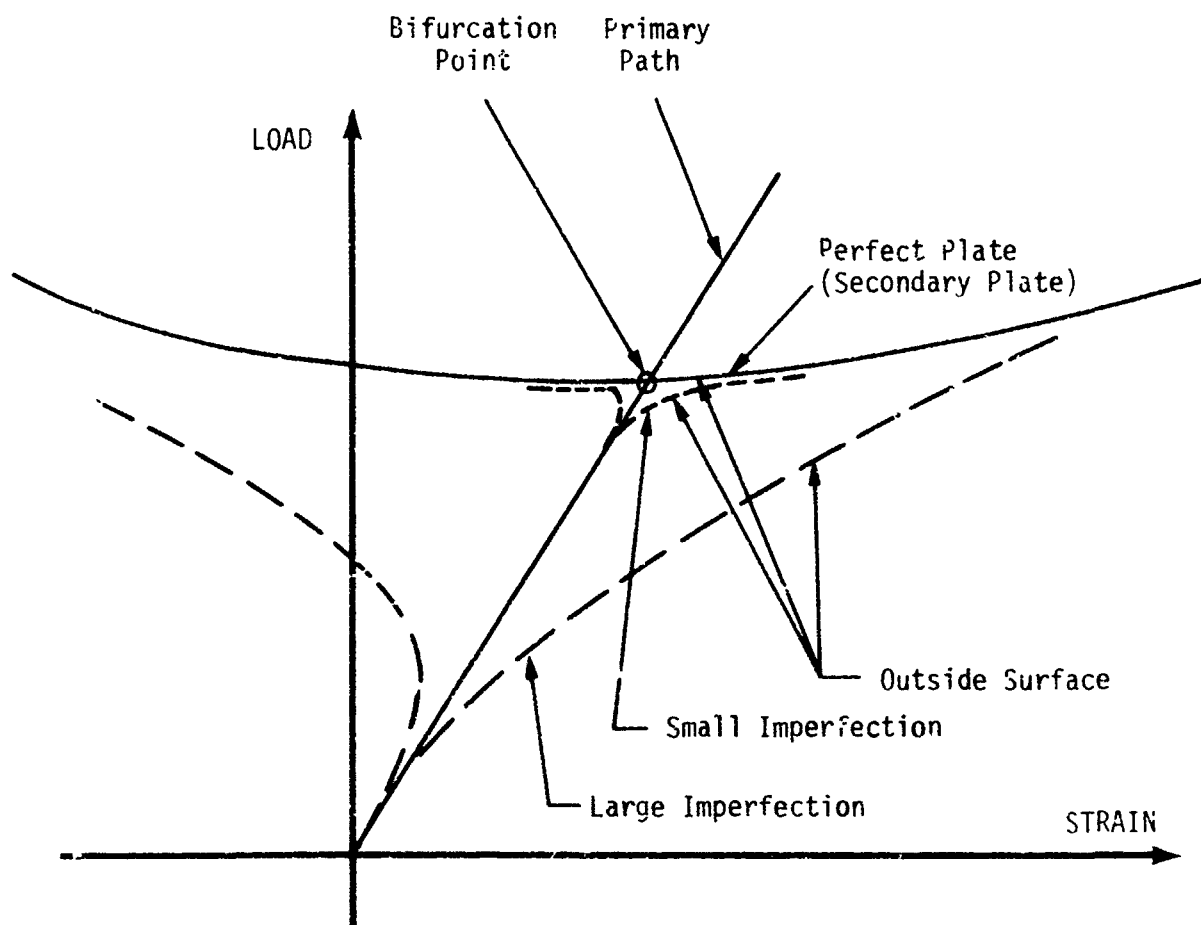


Figure 325 Load-strain behavior of axially compressed plate with small and large imperfections.

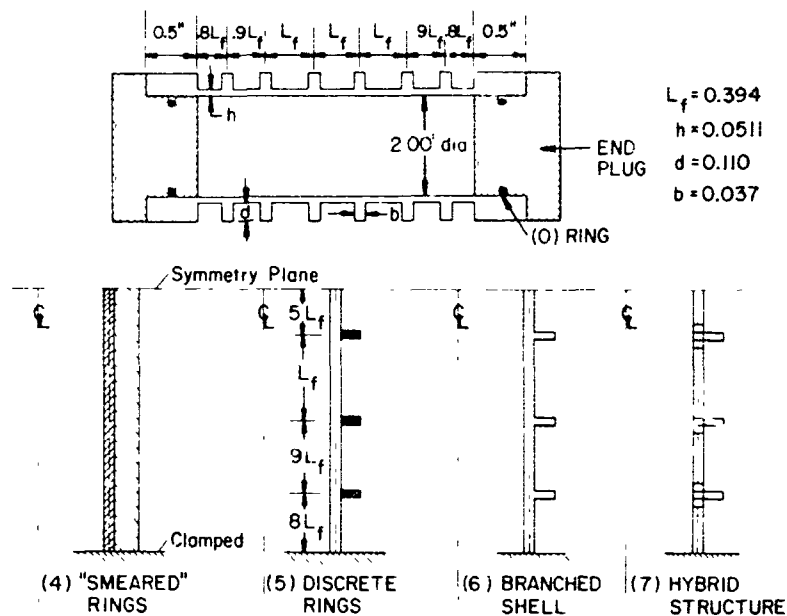


Figure 326 Aluminum ring-stiffened cylinder tested under external pressure by Boichot and Reynolds at the Naval Ship Research and Development Center, Maryland and four possible analytical models for treatment with BOSOR6.

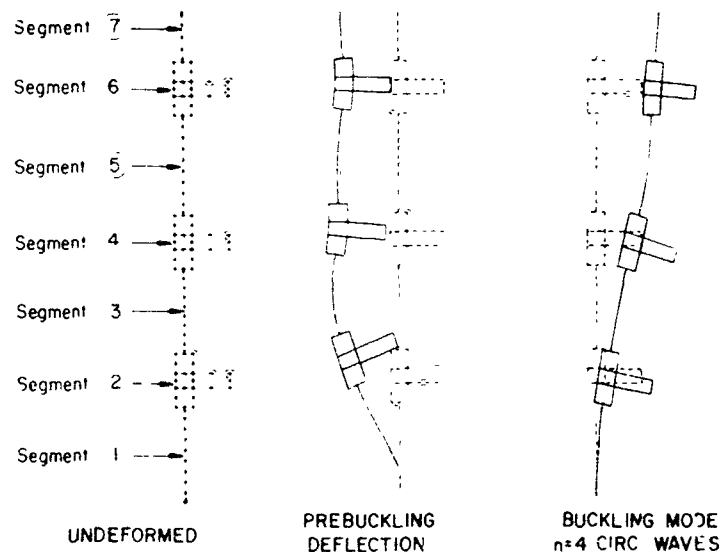


Figure 327 Ring-stiffened cylindrical shell specimen 20-52 modeled as hybrid body of revolution; prebuckling deflected shape and general nonsymmetric instability mode.

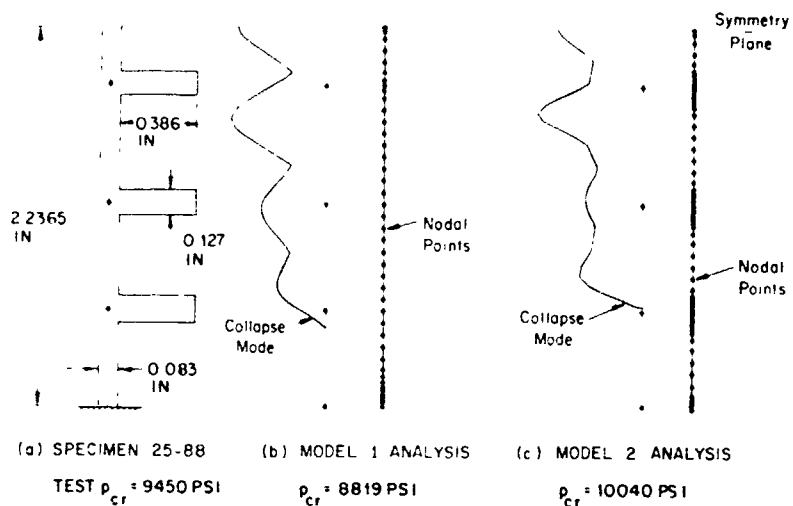


Figure 328 Predicted axisymmetric collapse modes of ring-stiffened cylindrical shell specimen 25-88 analyzed as a shell with discrete rings: (a) specimen geometry; (b) neglecting ring thickness effect; (c) including ring thickness effect.

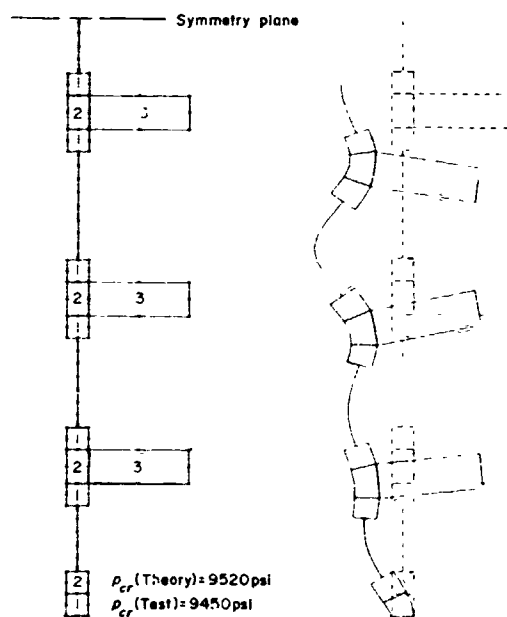
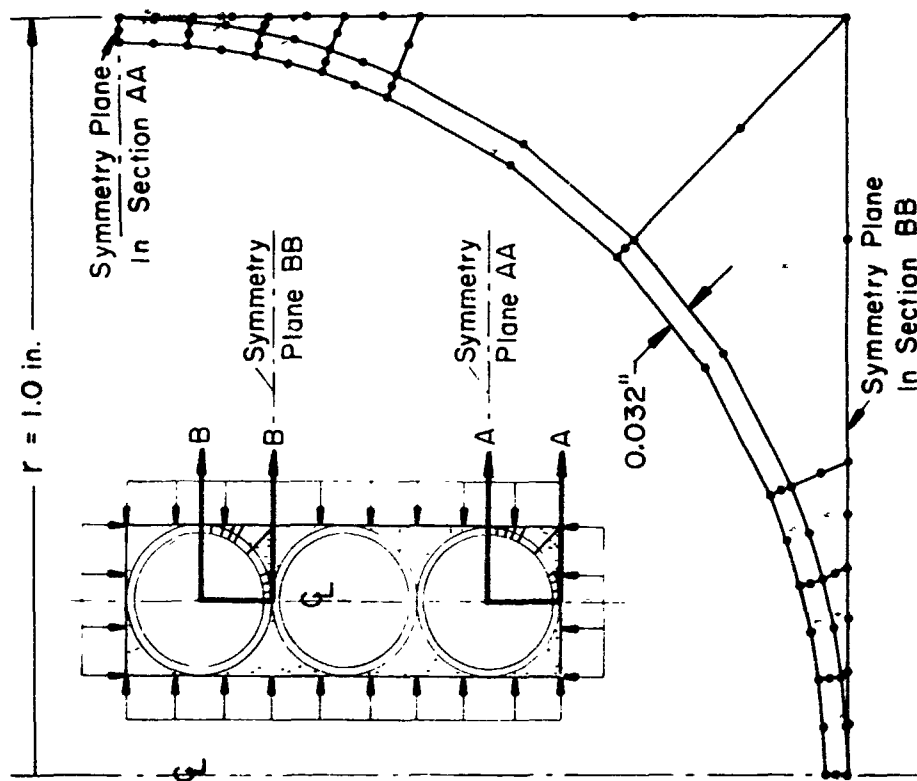
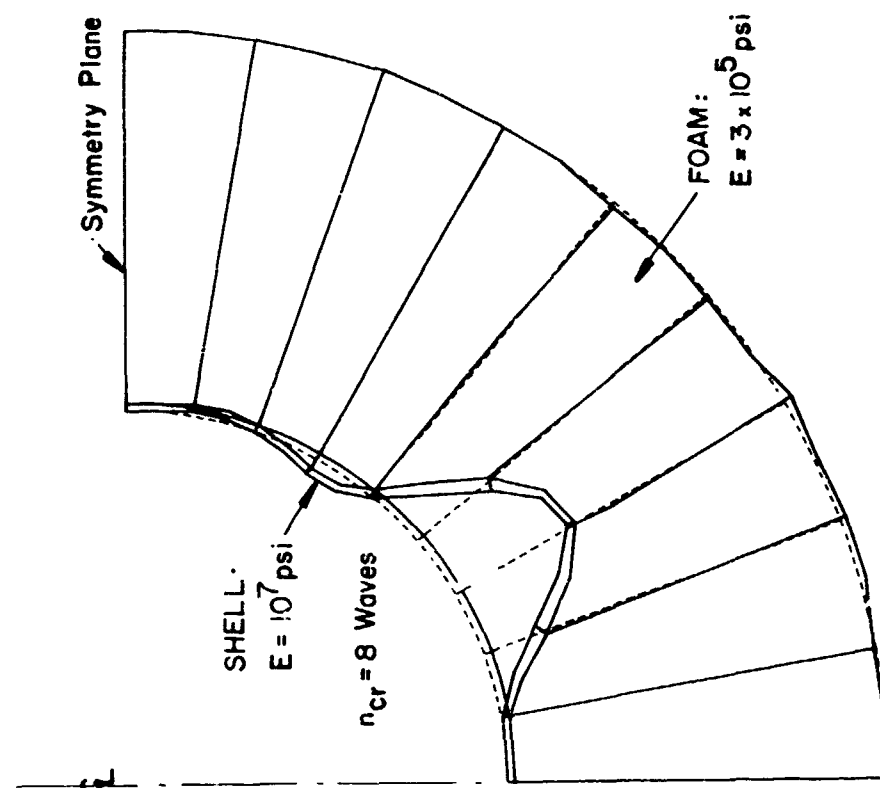


Figure 329 Specimen 25-88 modeled as a hybrid structure and axisymmetric collapse mode predicted by BOSOR6.

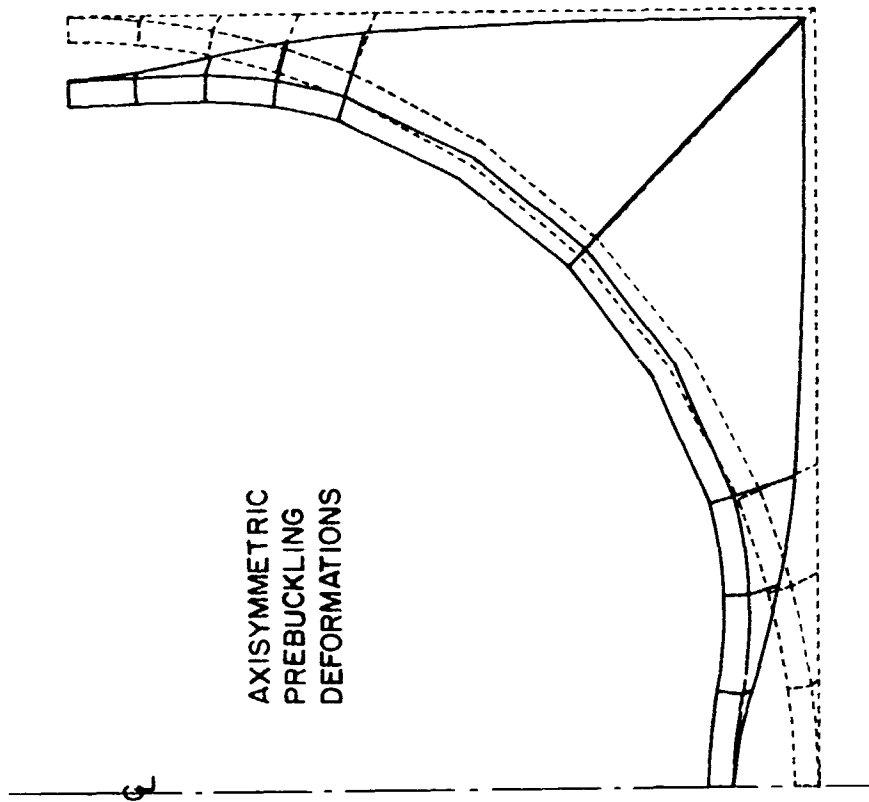


(b) Finite element model of spheres embedded in foam under external pressure.

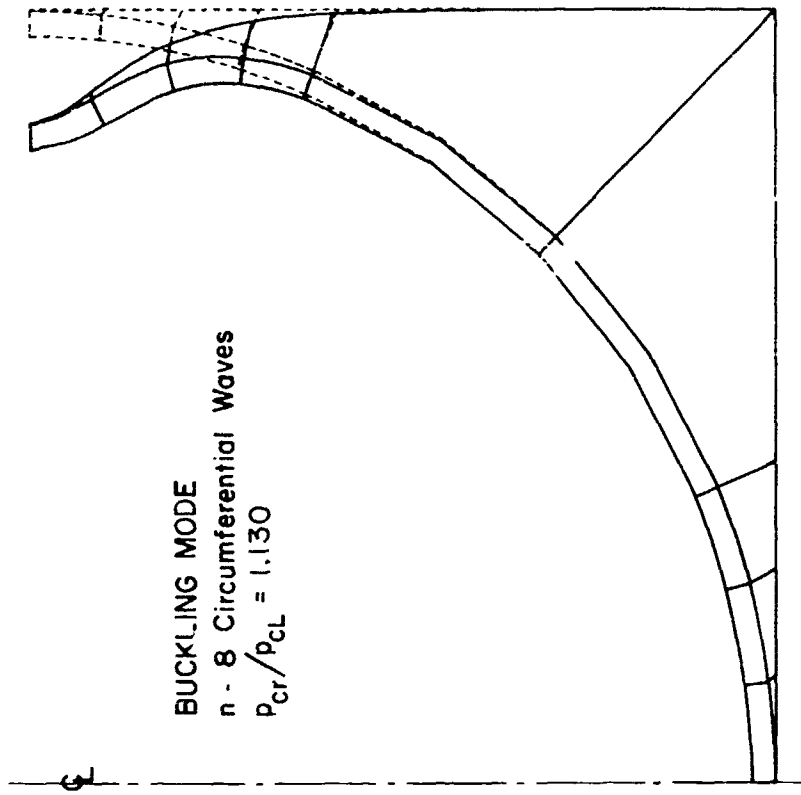


(a) Buckling of spherical shell embedded in foam subjected to uniform external pressure.

Figure 330 Buckling of foam-supported spherical shells.



(c) Prebuckling deformations of portion of structure denoted "Section AA" in (a).



(d) Buckling mode for portion of structure denoted "Section AA" in (a).

Figure 330 (continued)

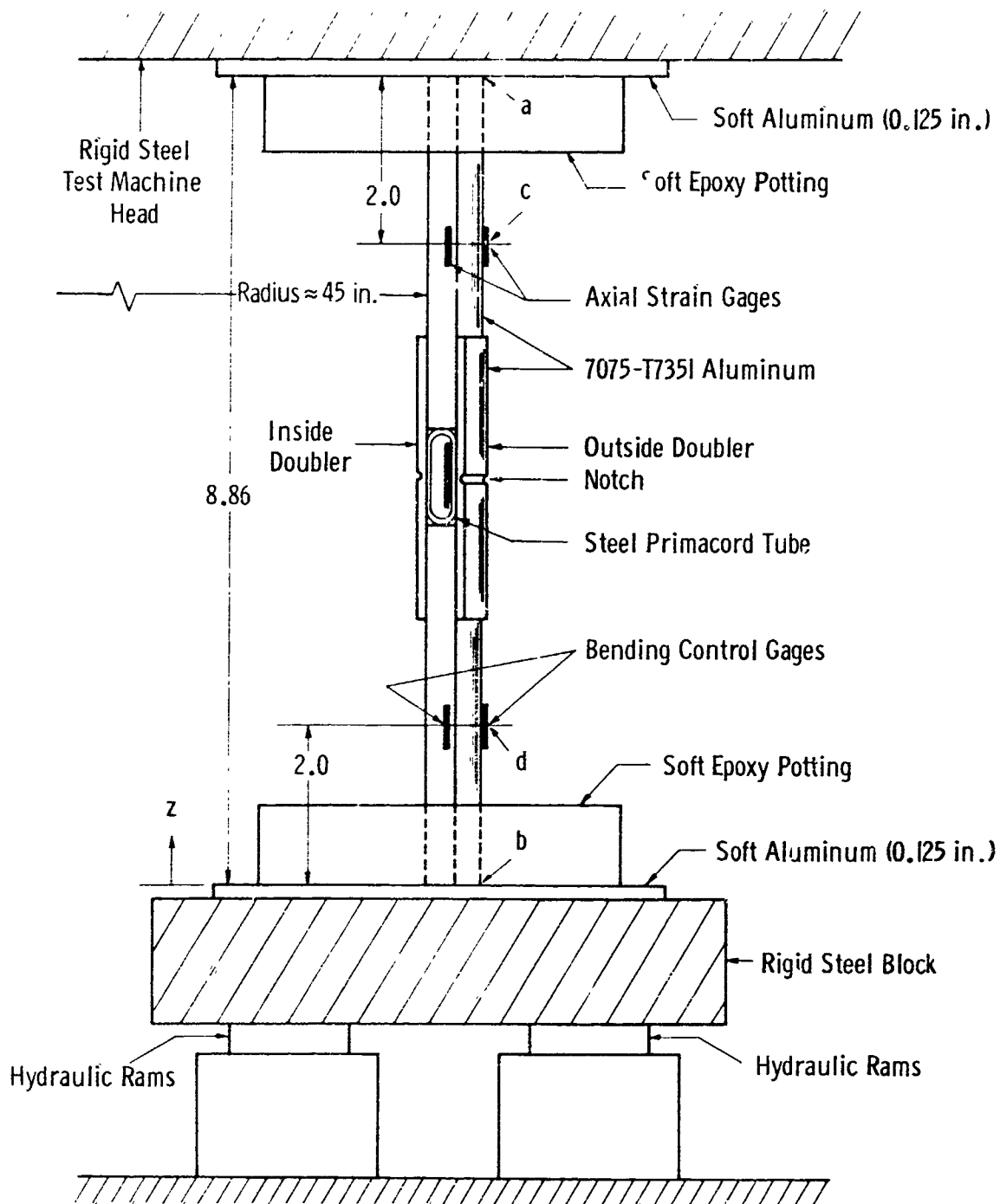


Figure 331 General configuration of cylindrical panel with frangible joint tested under uniform end shortening (from Bushnell et al. [428]).

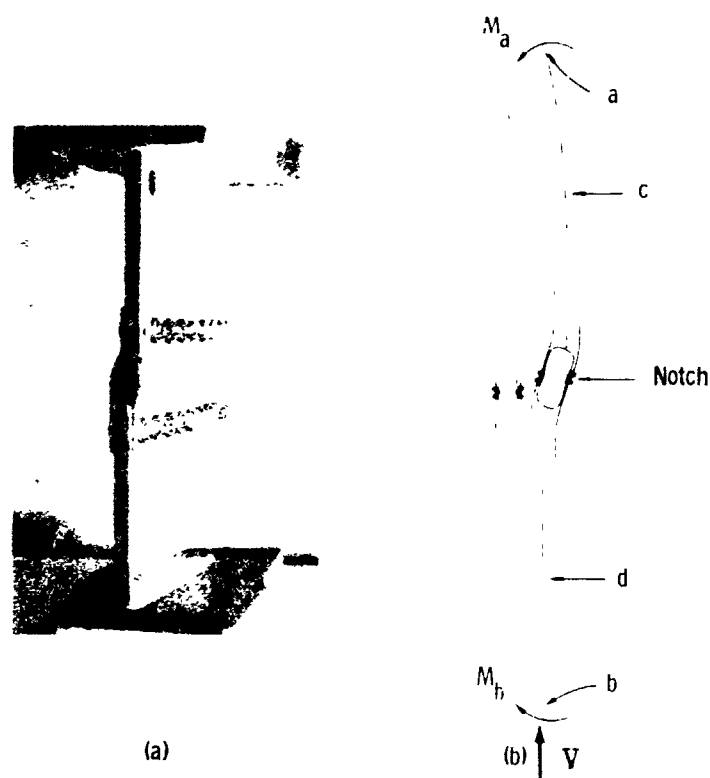
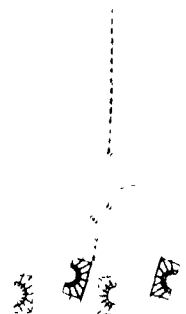


Figure 332 (a) A specimen after failure, and
 (b) the BOSOR 6 model showing the undeformed and
 deformed configurations
 (from Bushnell et al. [428]).



(a)



(b)

Figure 333 (a) Expanded view of the failed specimen, and
(b) BOSOR6 model.

(from Bushnell et al. [428]).

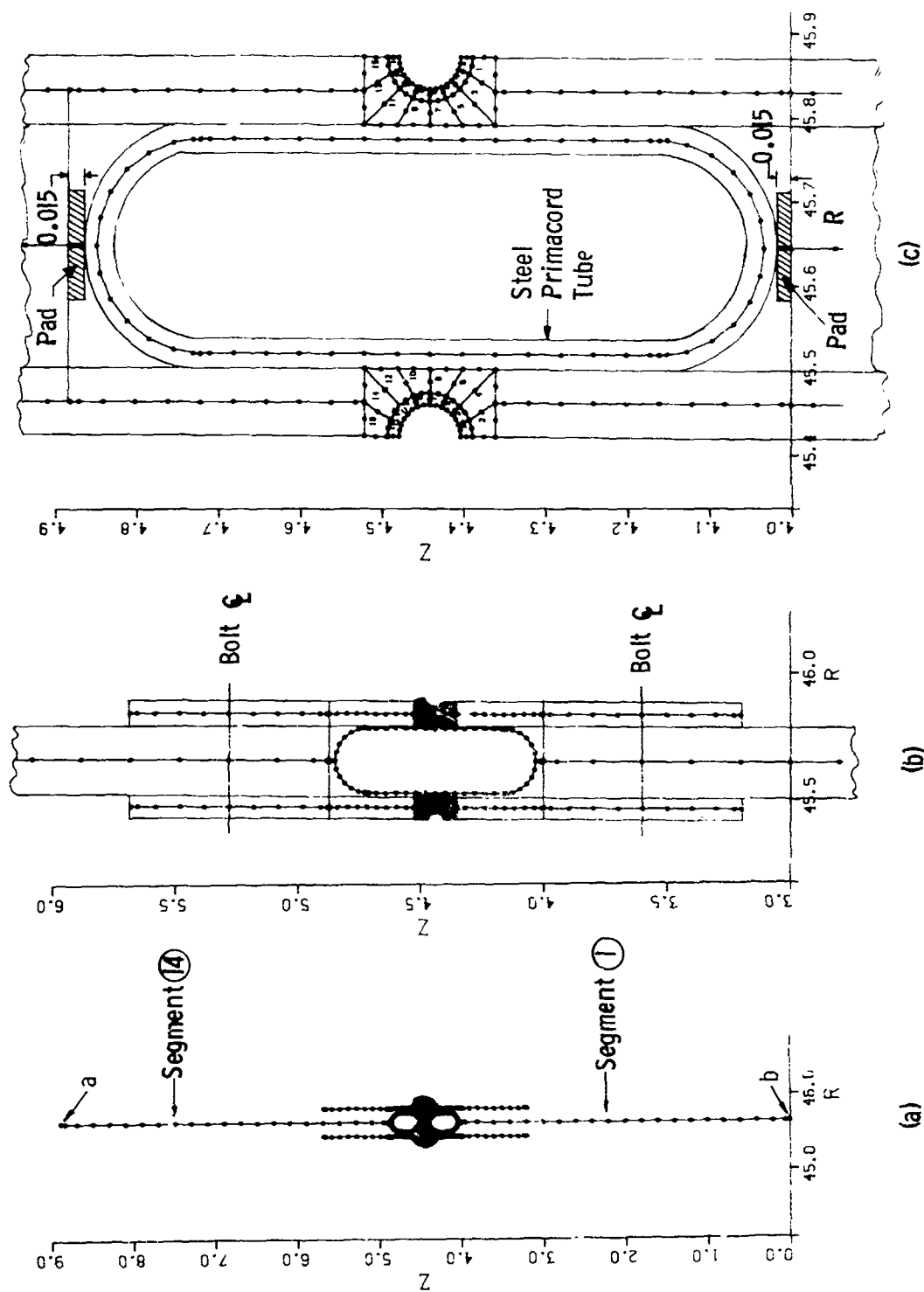


Figure 334 Discretized BOSOR6 model of specimen with primacord tube showing reference surfaces of shell segments, nodal points, and notch regions modeled with solid eight-node isoparametric finite elements of revolution (from Bushnell et al. [428]).

- = Physical contact point
- = Nodal points involved in contact constraint conditions

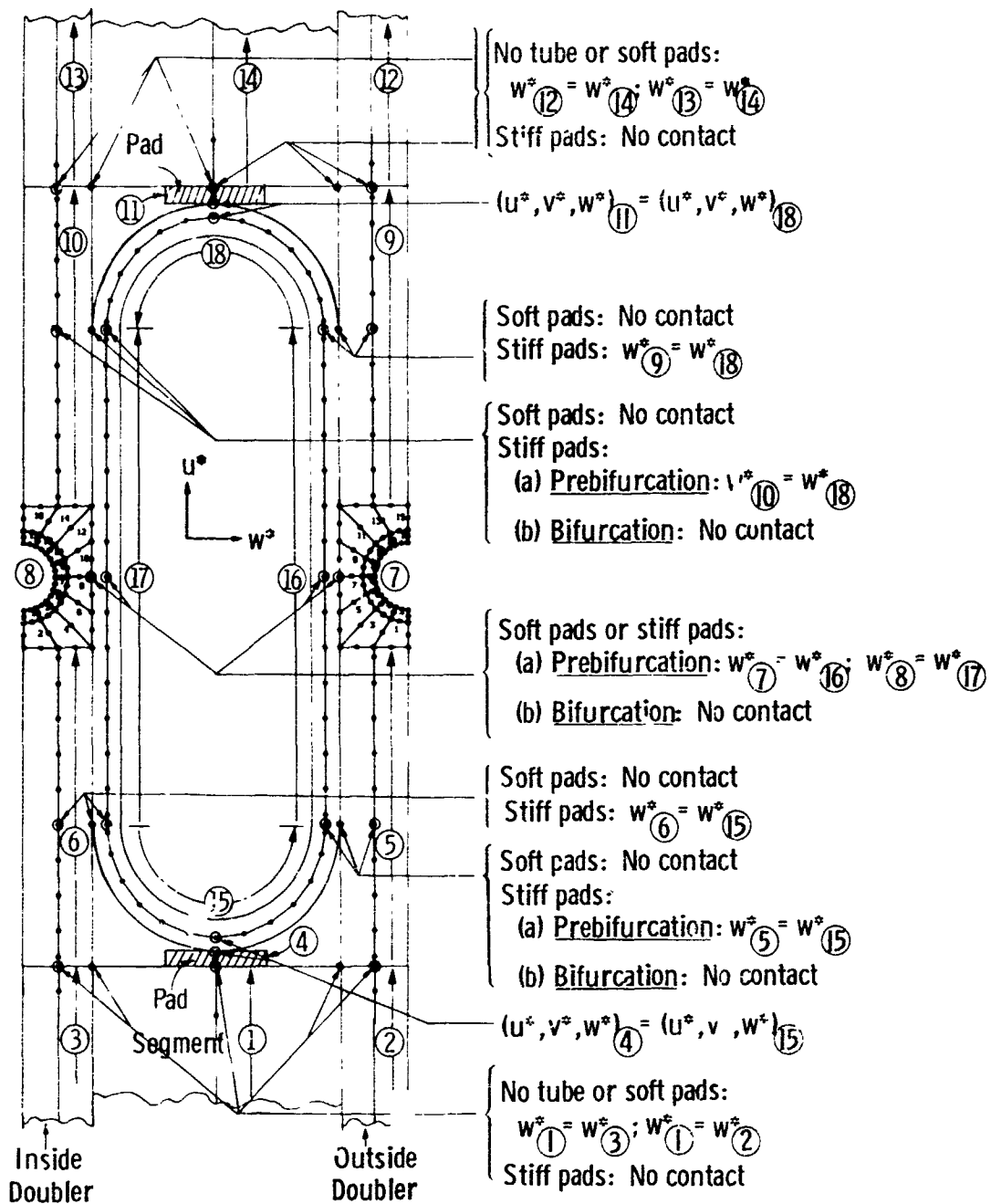


Figure 335 Detail of region near notches with prebuckling and bifurcation contact conditions. Encircled numbers indicate segments (from Bushnell et al. [428]).

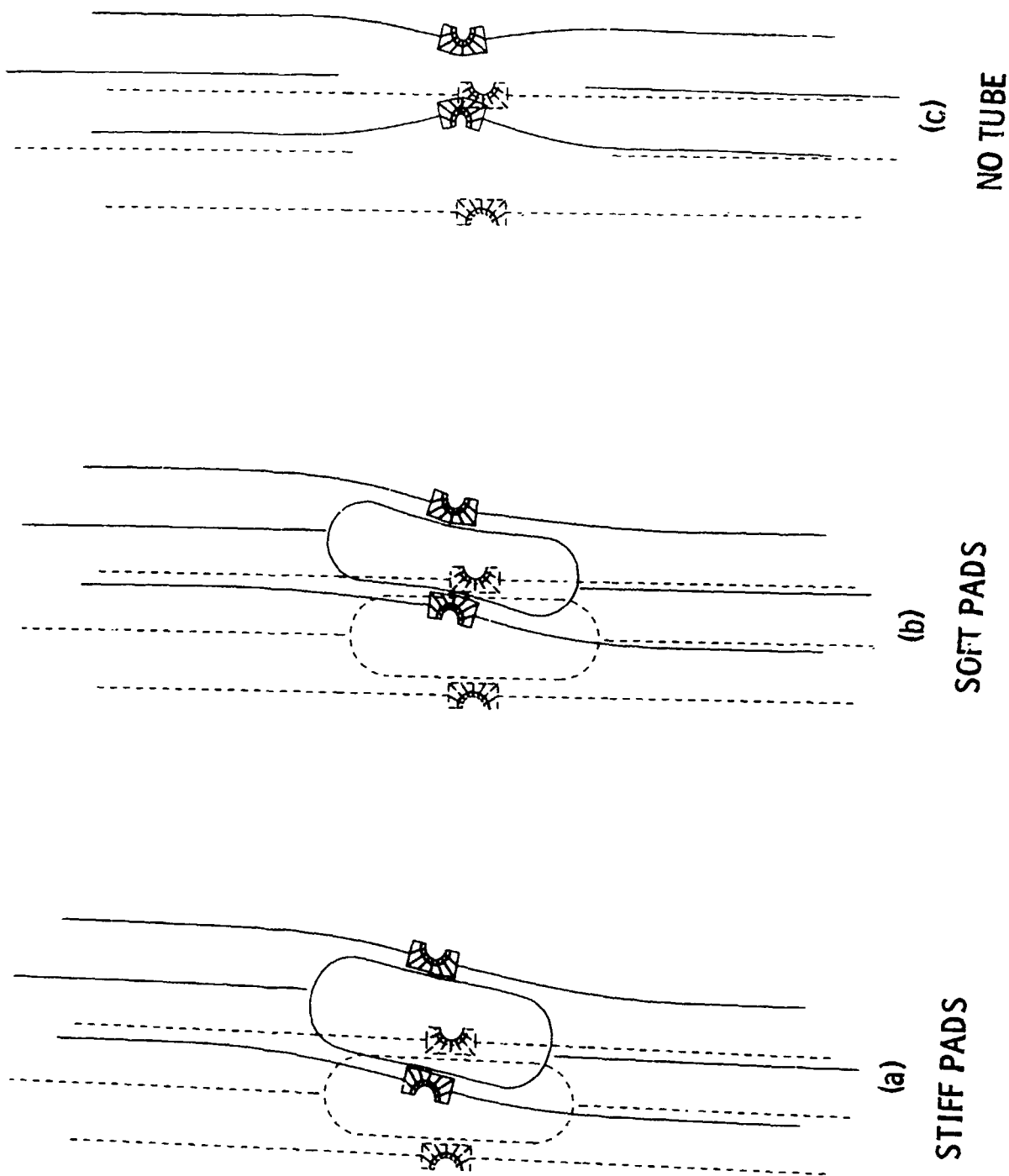


Figure 336 Deformations of an axially compressed frangible joint with: (a) snugly fitting tube, (b) loosely fitting tube, and (c) no tube (from Bushnell et al. [428]).

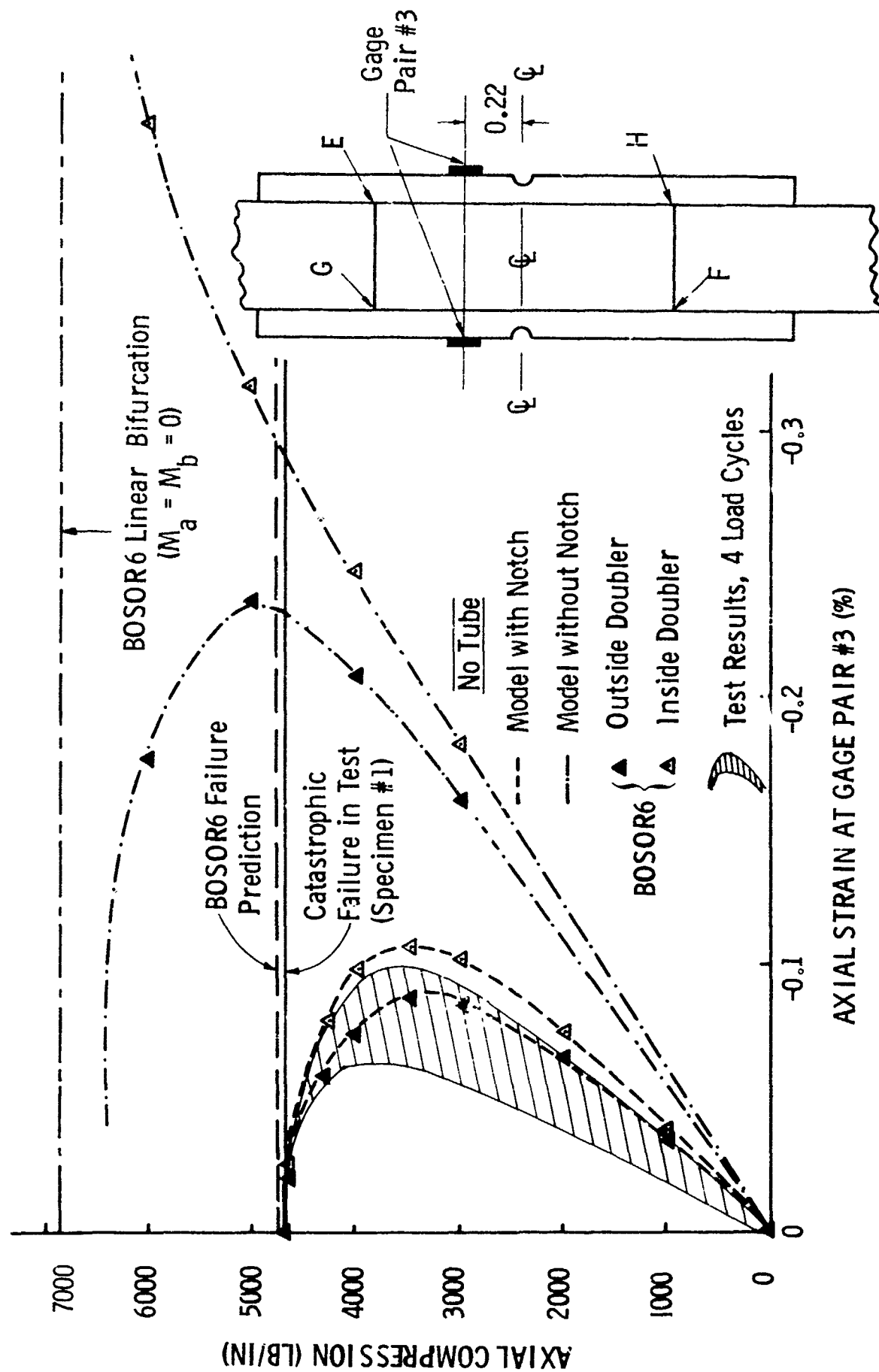


Figure 337 Axial strain including and neglecting the notches for the specimen without the primacord tube (from Bushnell et al. [428]).

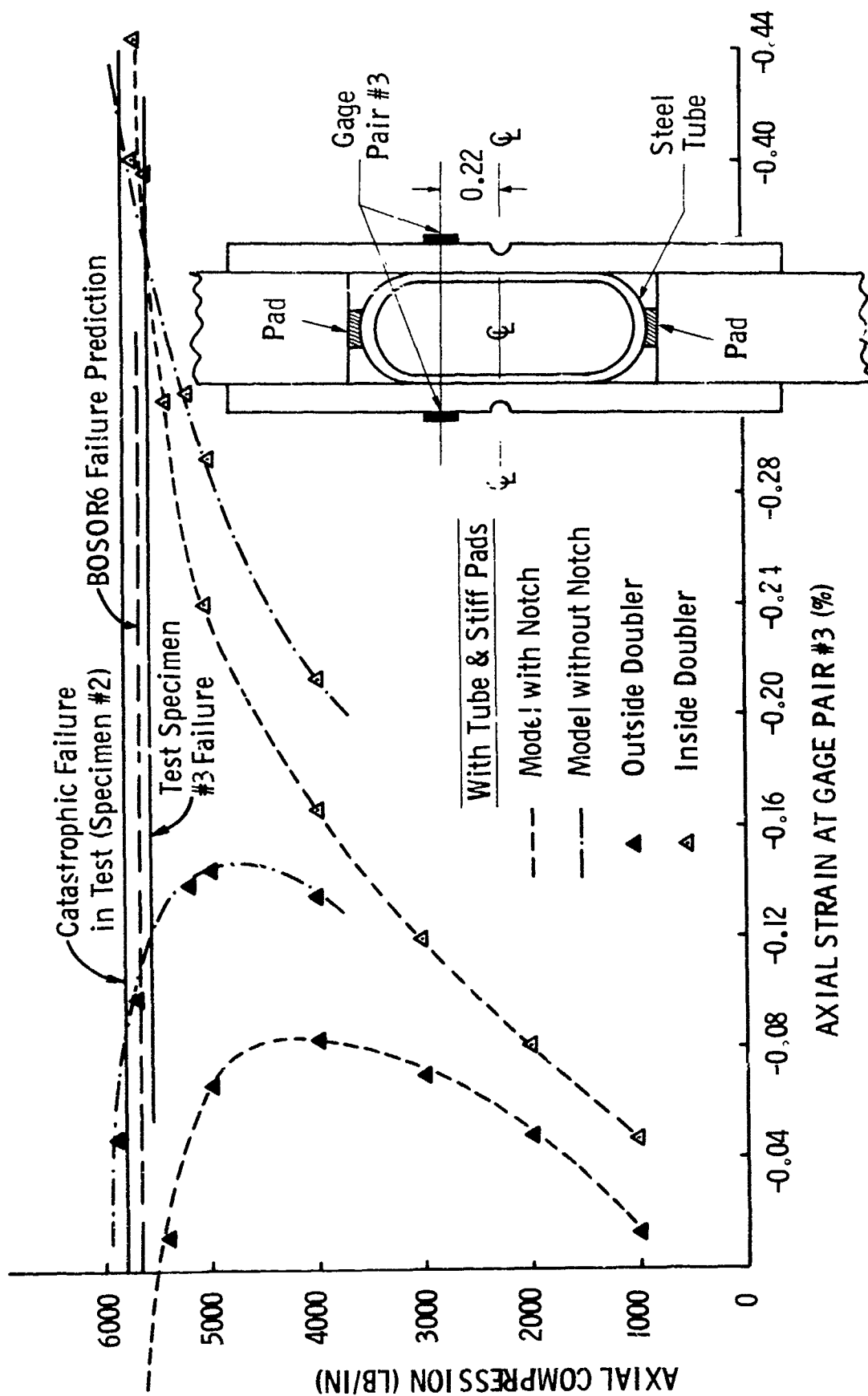


Figure 338 Axial strain including and neglecting the notches for the specimens with the primacord tube (from Bushnell et al [428]).

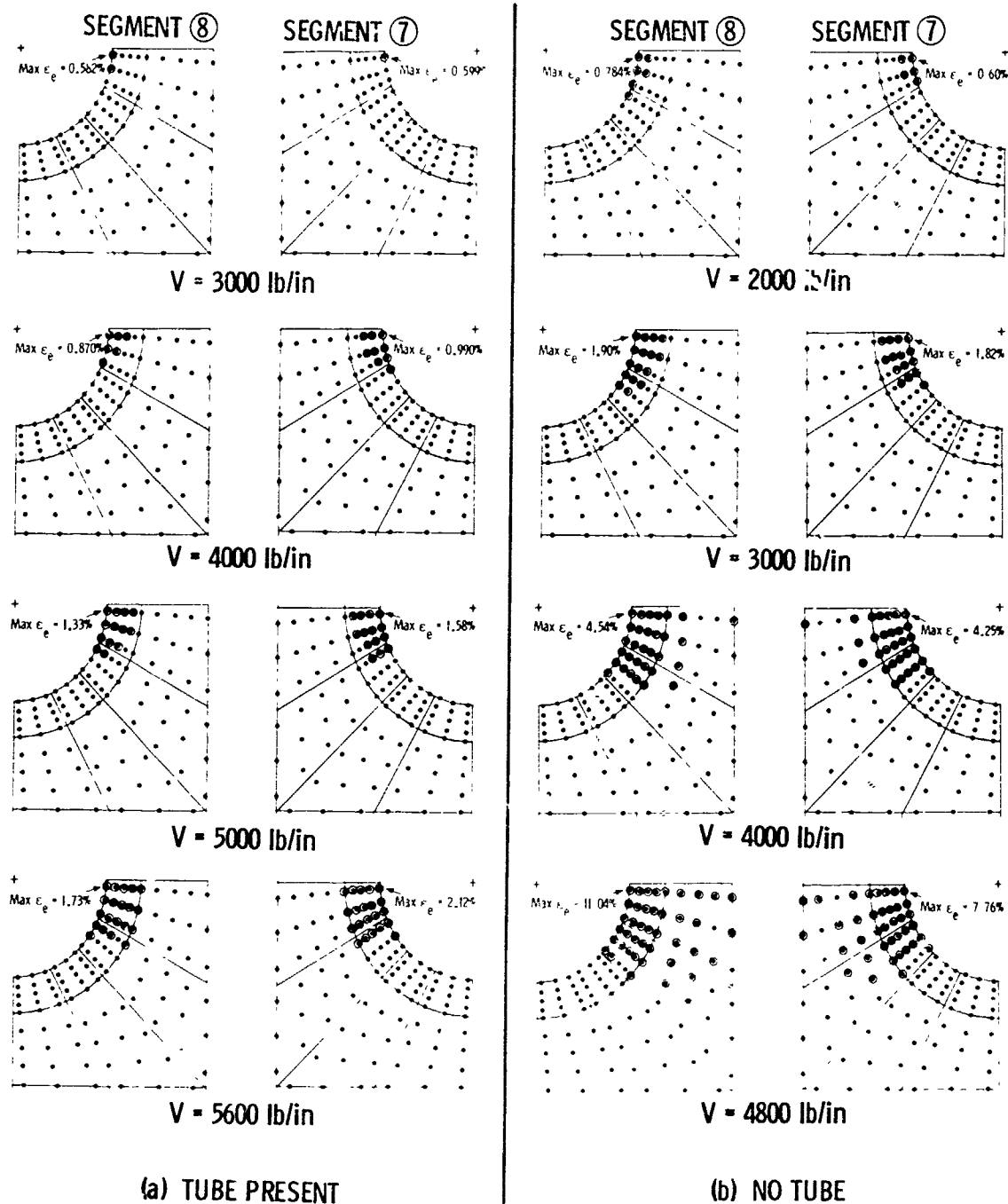


Figure 339 Development of plastic regions at the roots of the notches predicted from the BOSOR6 "half" models (stiff pads assumed) (from Bushnell et al. [428]).

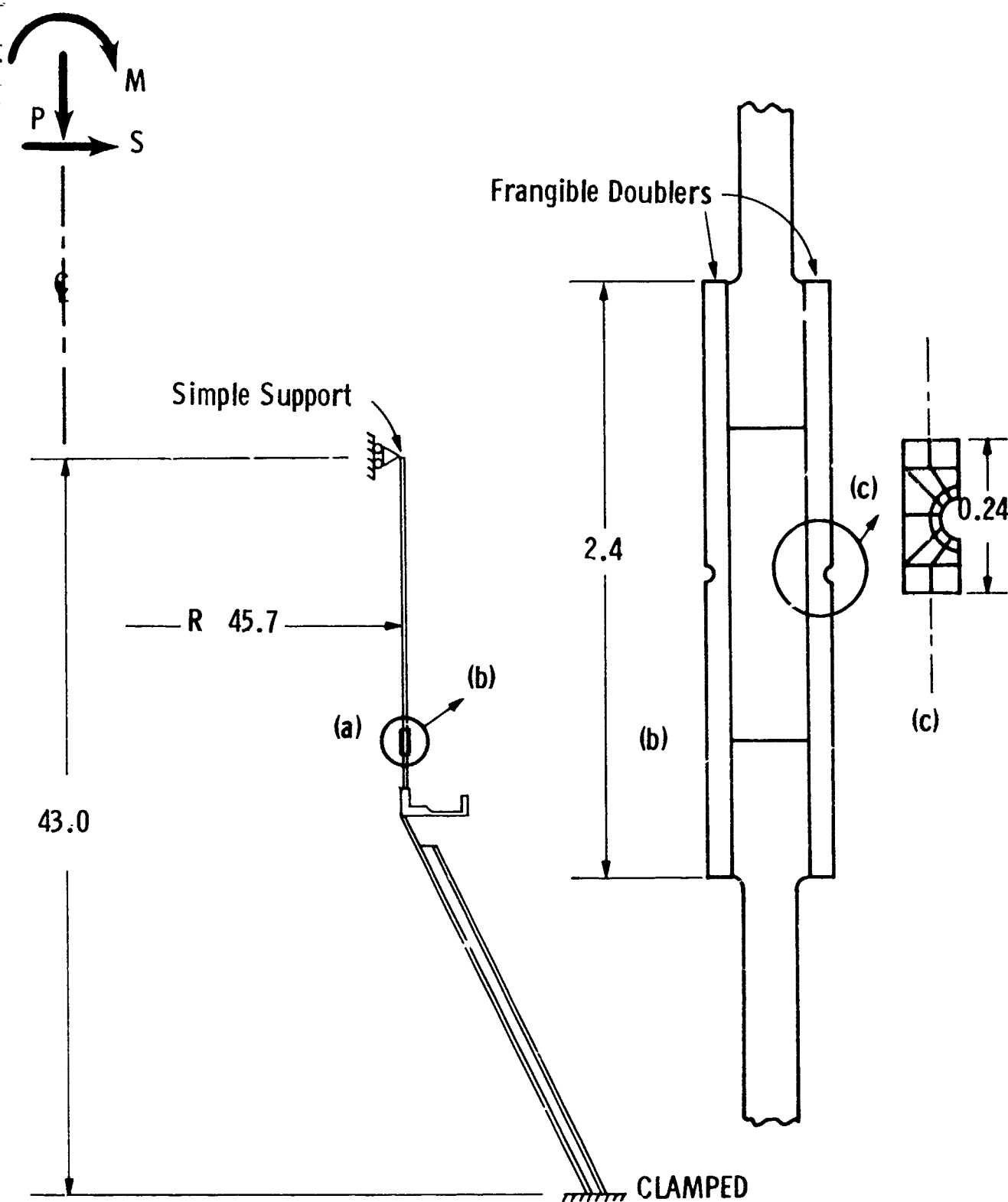
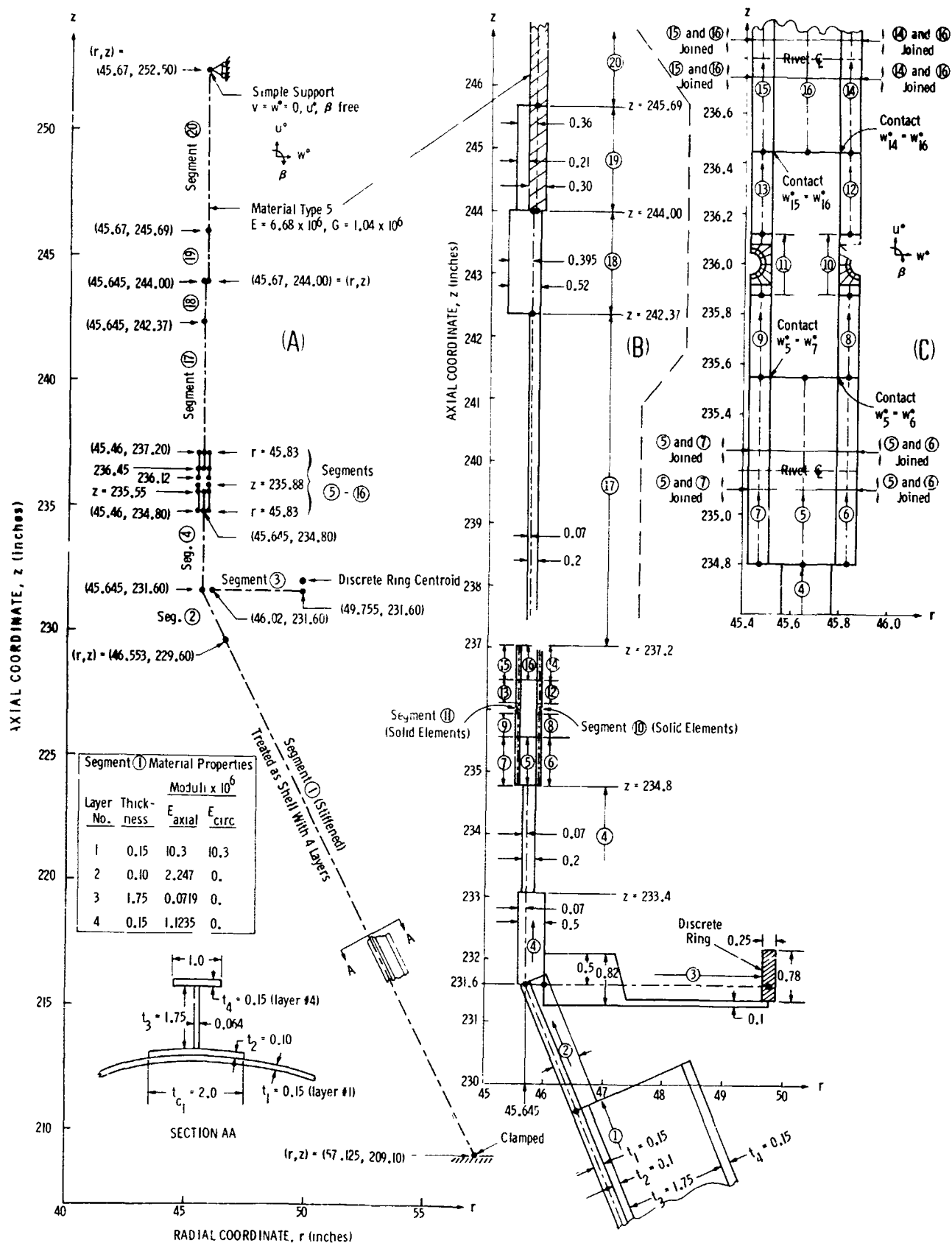


Figure 340 Rocket interstage configuration with frangible joint (dimensions in inches).



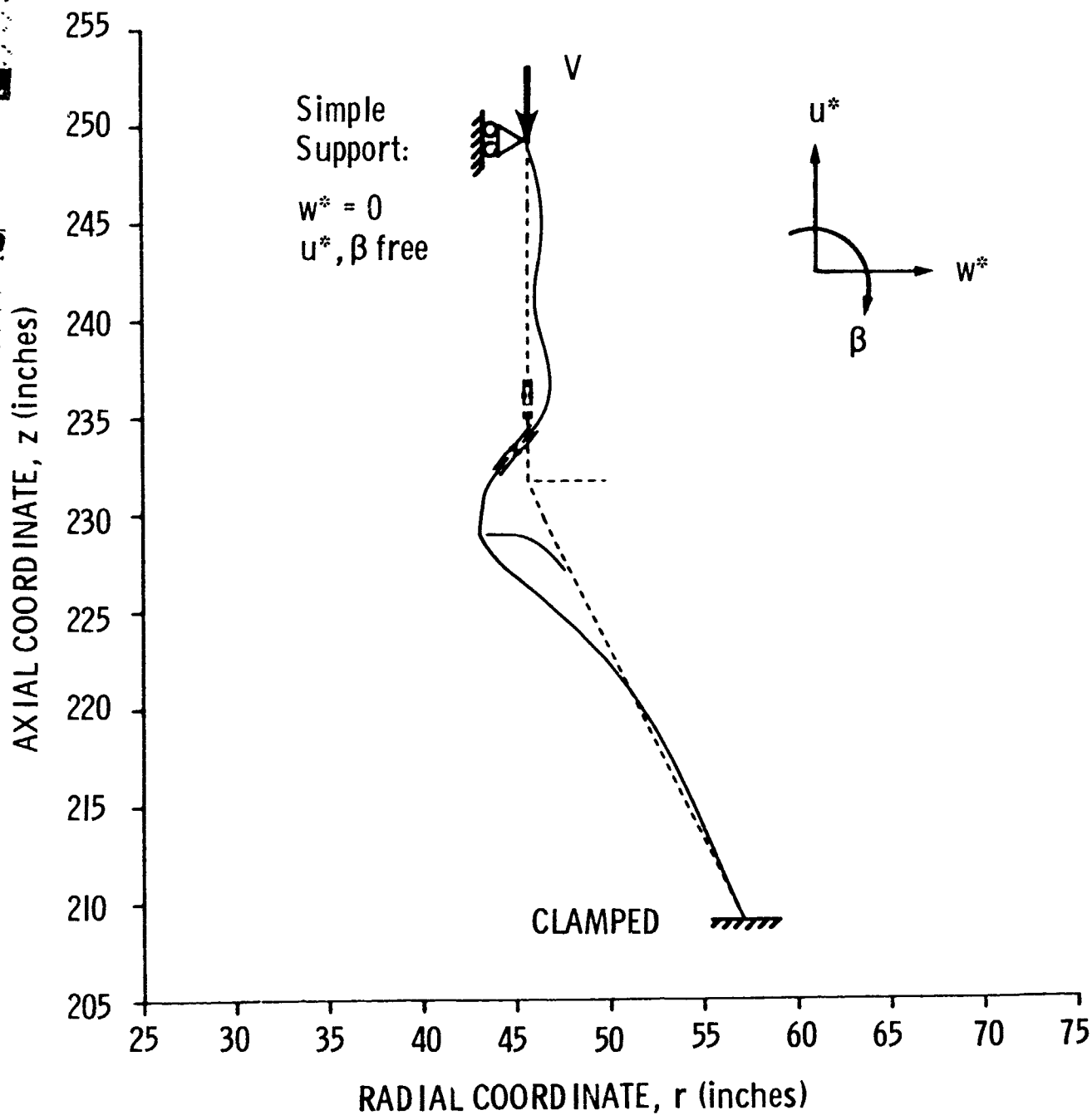


Figure 342 Deformation of rocket interstage under uniform axial compression. The frangible joint lies within the bending region of the cylinder-cone junction.

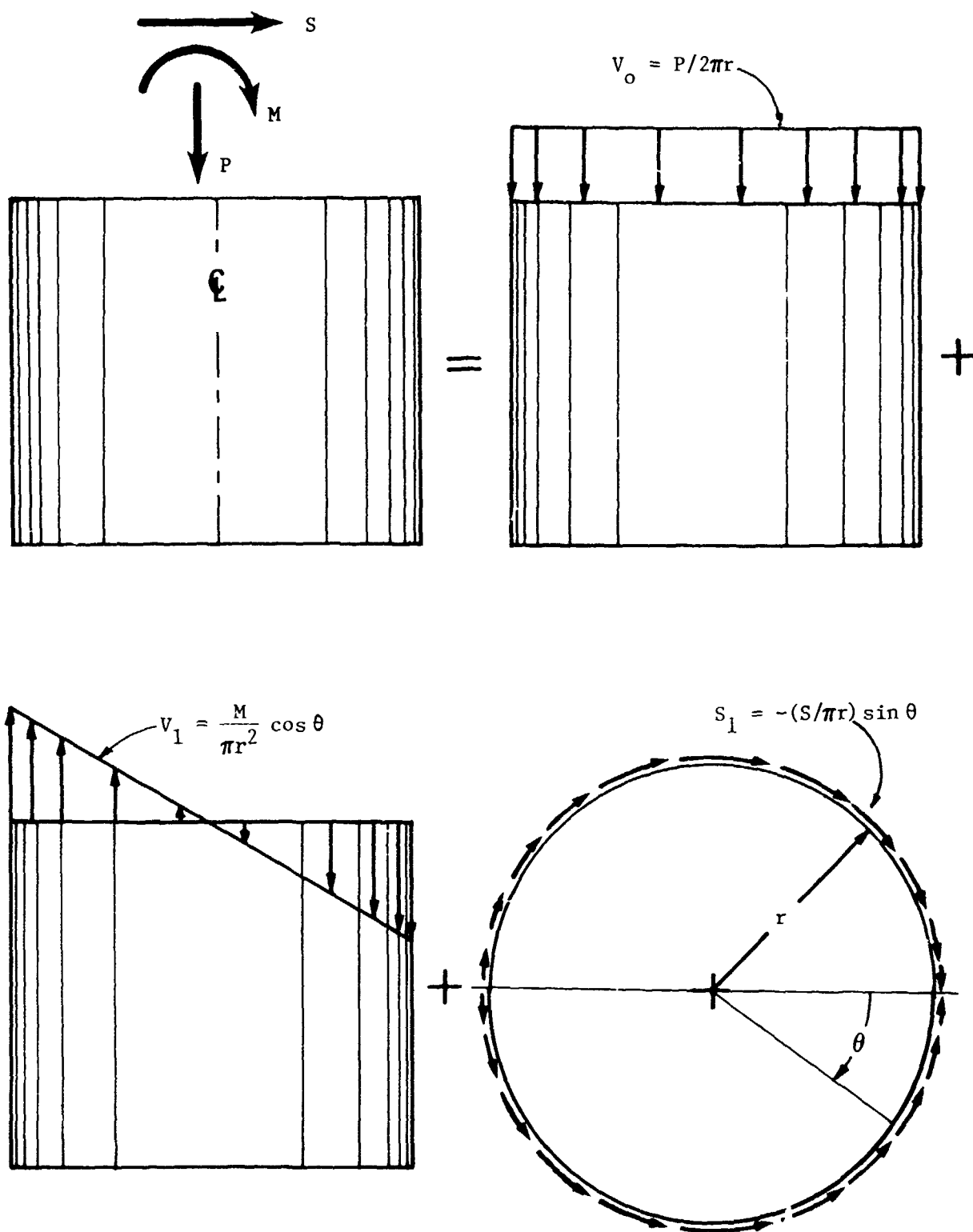
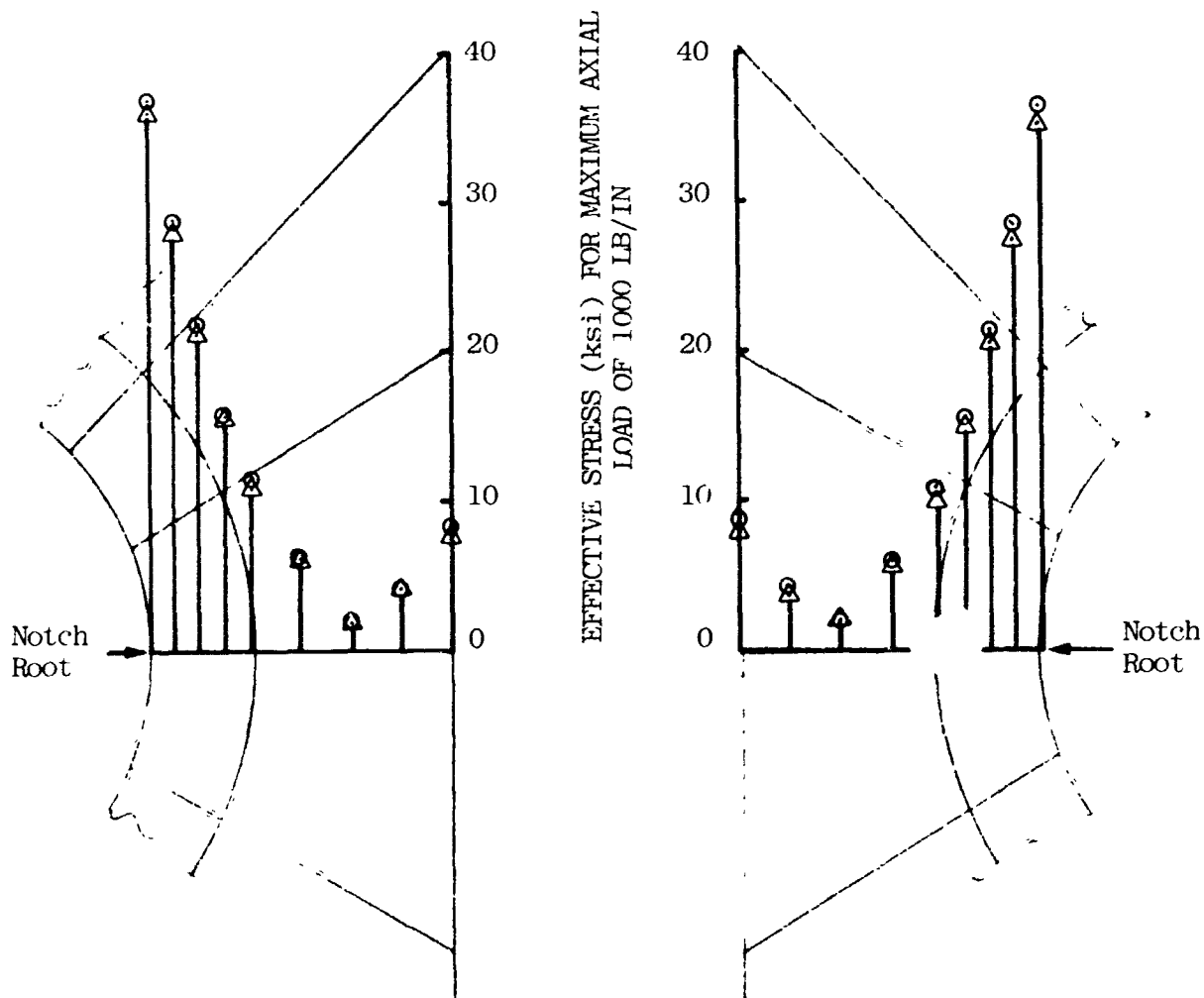


Figure 343 How the total load components S , M , and P on a shell can be transformed into applied loads/length.



SEGMENT (11)
(Inboard Doubler)

SEGMENT (10)
(Outboard Doubler)

○ Nonlinear Axisymmetric Case
△ Linear Non-axisymmetric Case

Figure 344 Comparison of results from linear non-axisymmetric and nonlinear axisymmetric analyses at a load level such that the maximum axial compression is $V_o = 1000$ lbs/in.

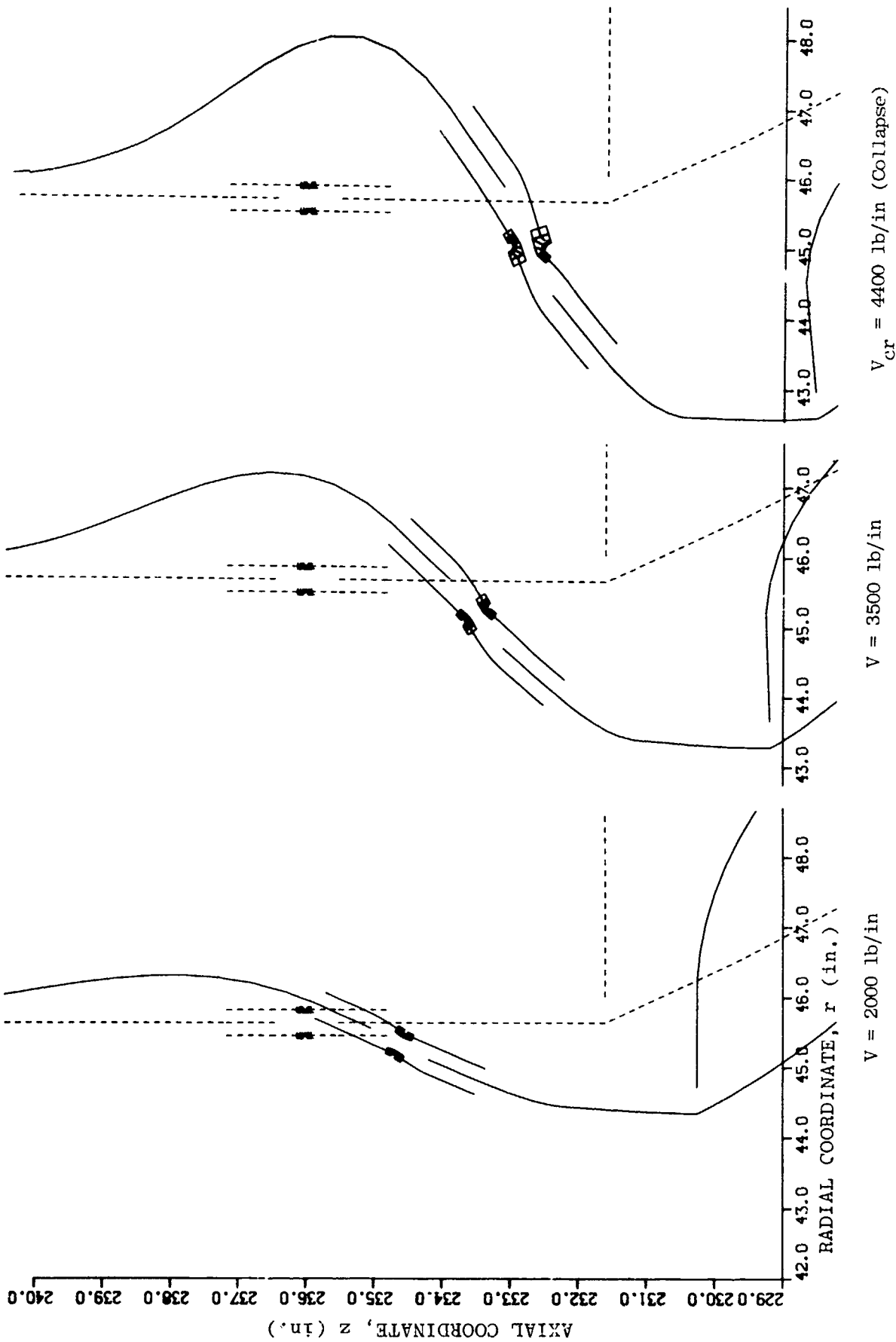


Figure 345 Deformation of rocket interstage under increasing axial compression.

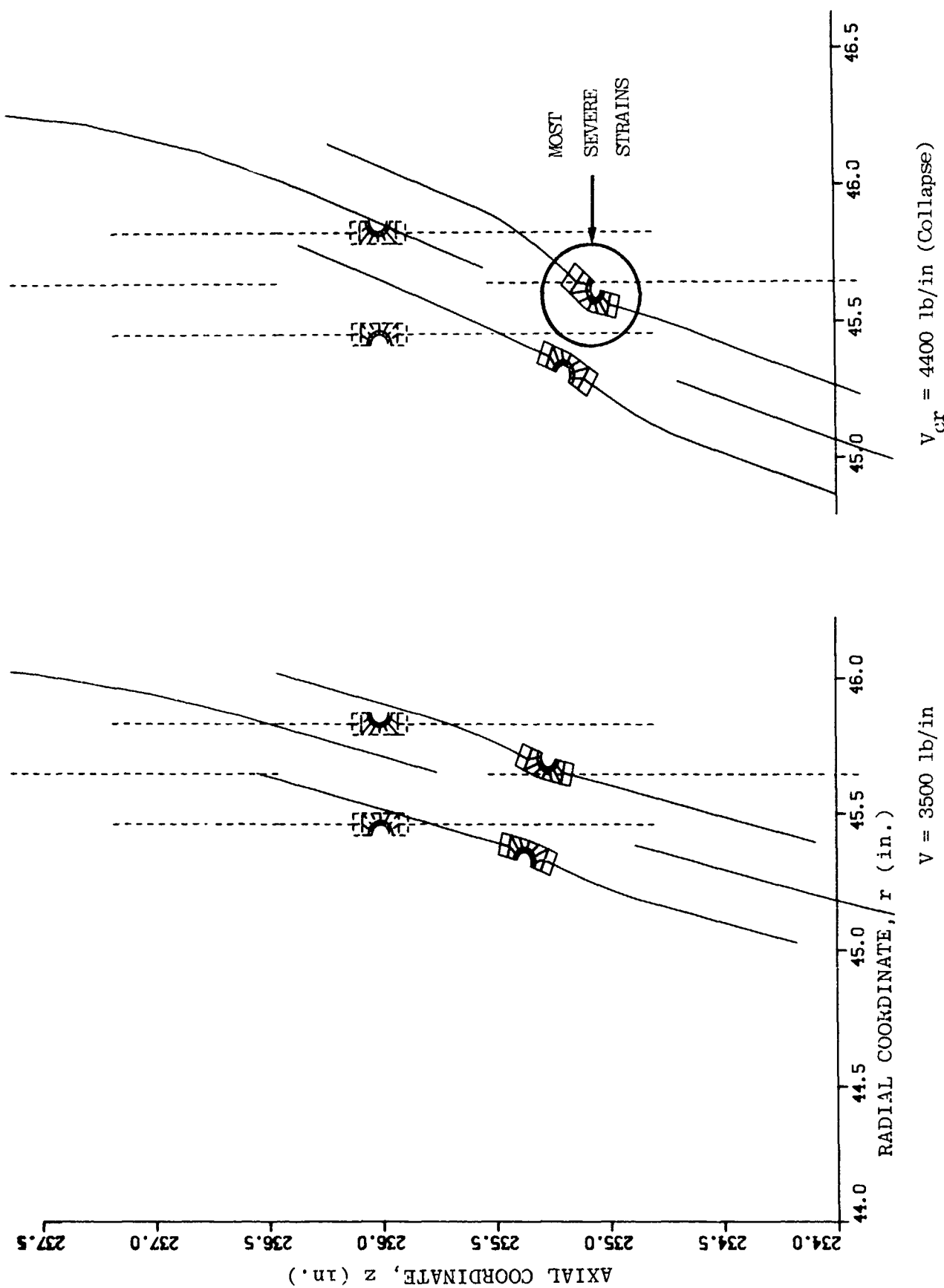


Figure 346 Enlarged view of frangible joint region.

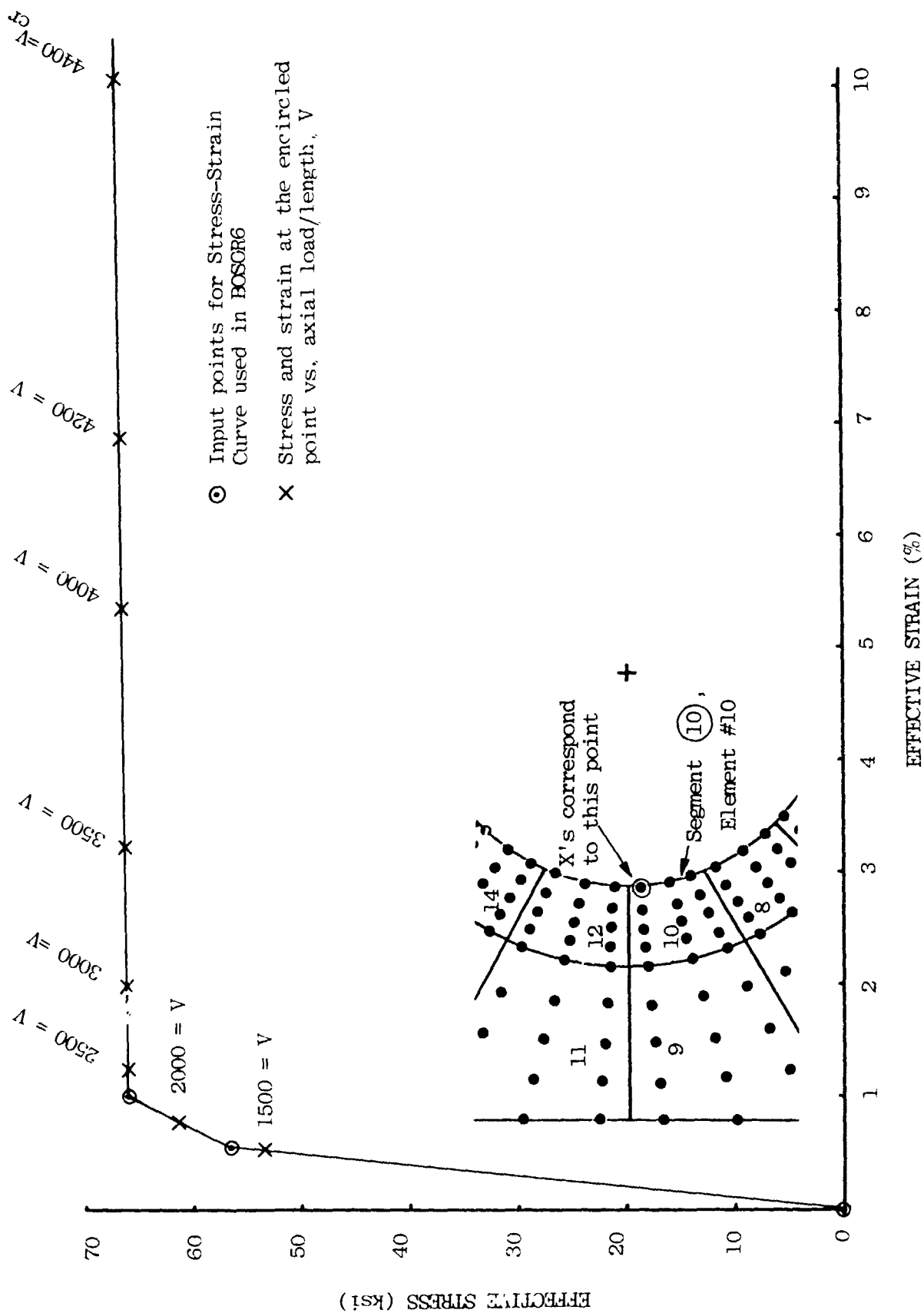
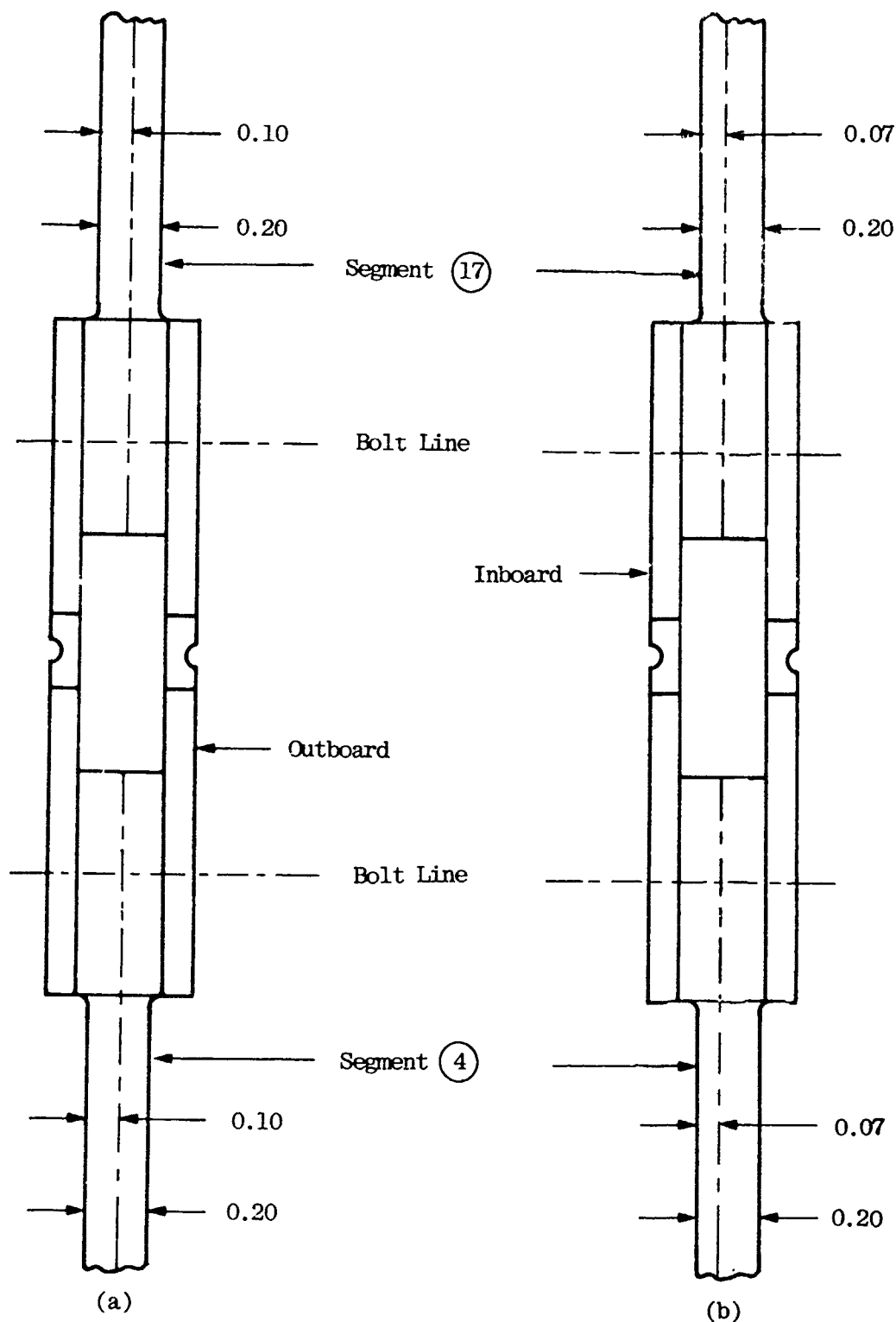


Figure 347 Stress-strain curve for the aluminum used in the frangible doublers and the effective stresses and strains vs. axial load V up to collapse of the rocket interstage shown in Figures 345 and 346.



AN ORIGINAL DESIGN

THE FINAL DESIGN

Figure 348 Frangible joint detail, showing (a) an original design and (b) the final design to which the model shown in Figure 341 corresponds. This minor change raises the compressive load-carrying capability of the rocket interstage by 10%.

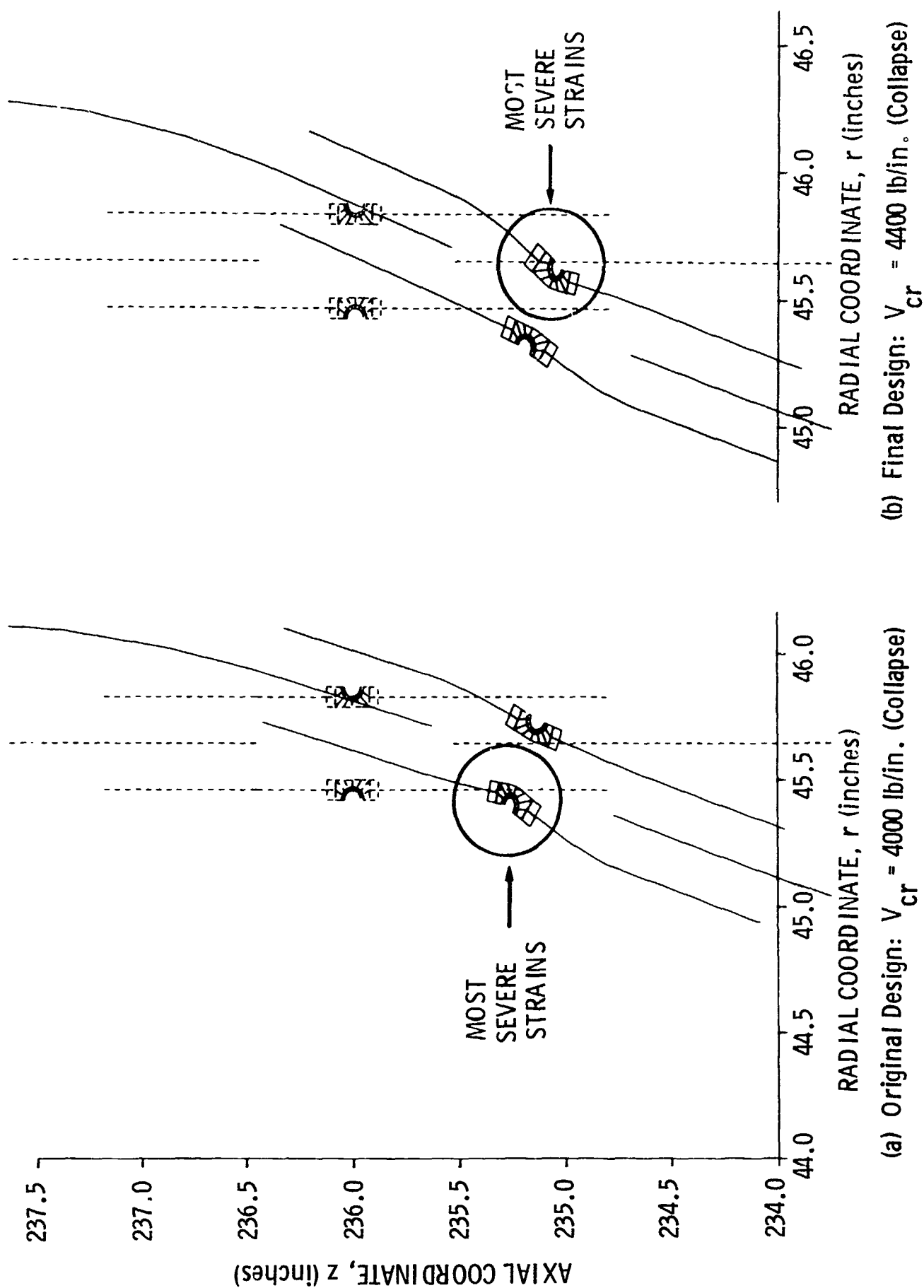


Figure 349 Comparison of deformation of the original and the final design at the collapse load of each.

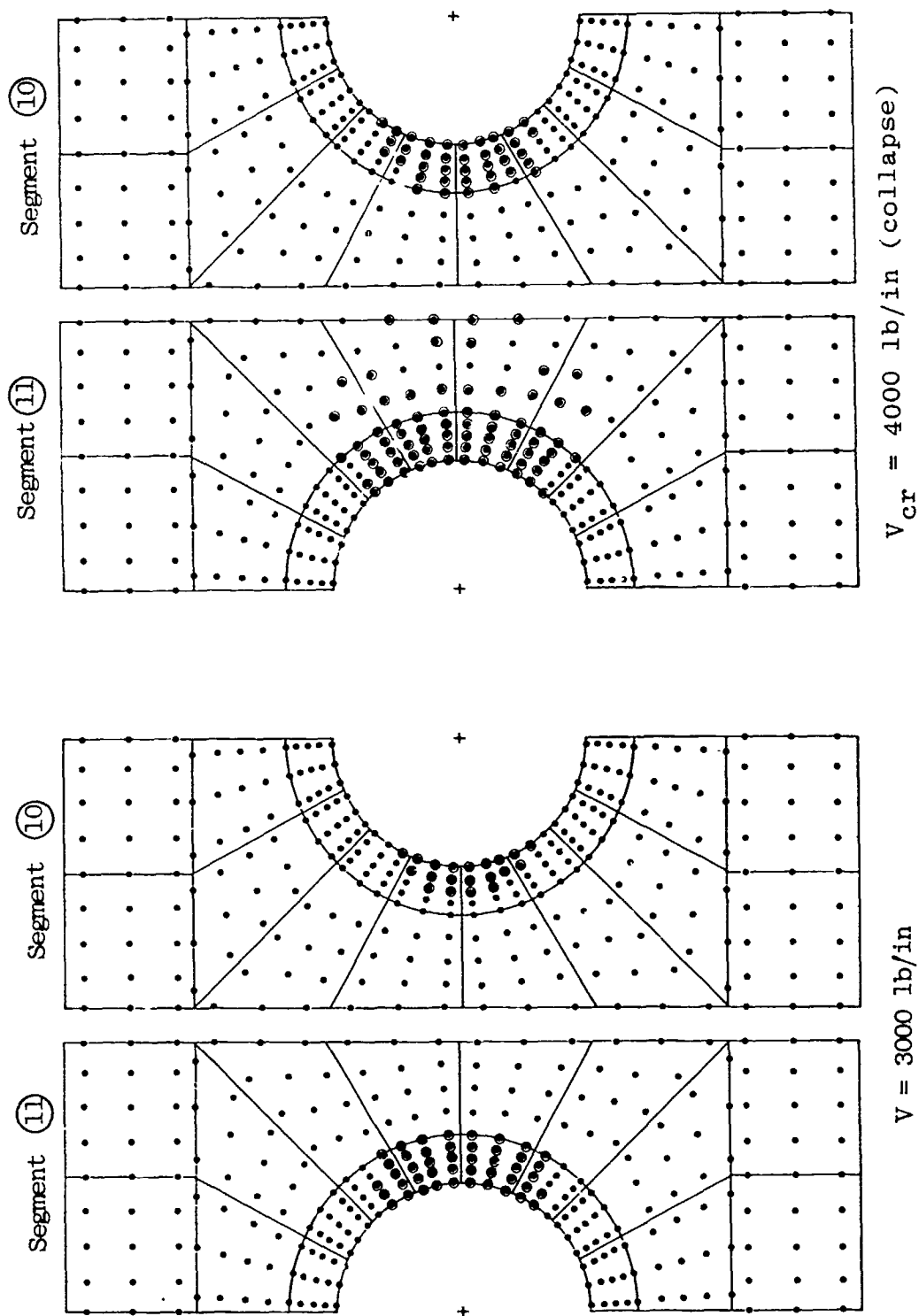


Figure 350(a) Growth of plastified regions near notch roots in the original design.

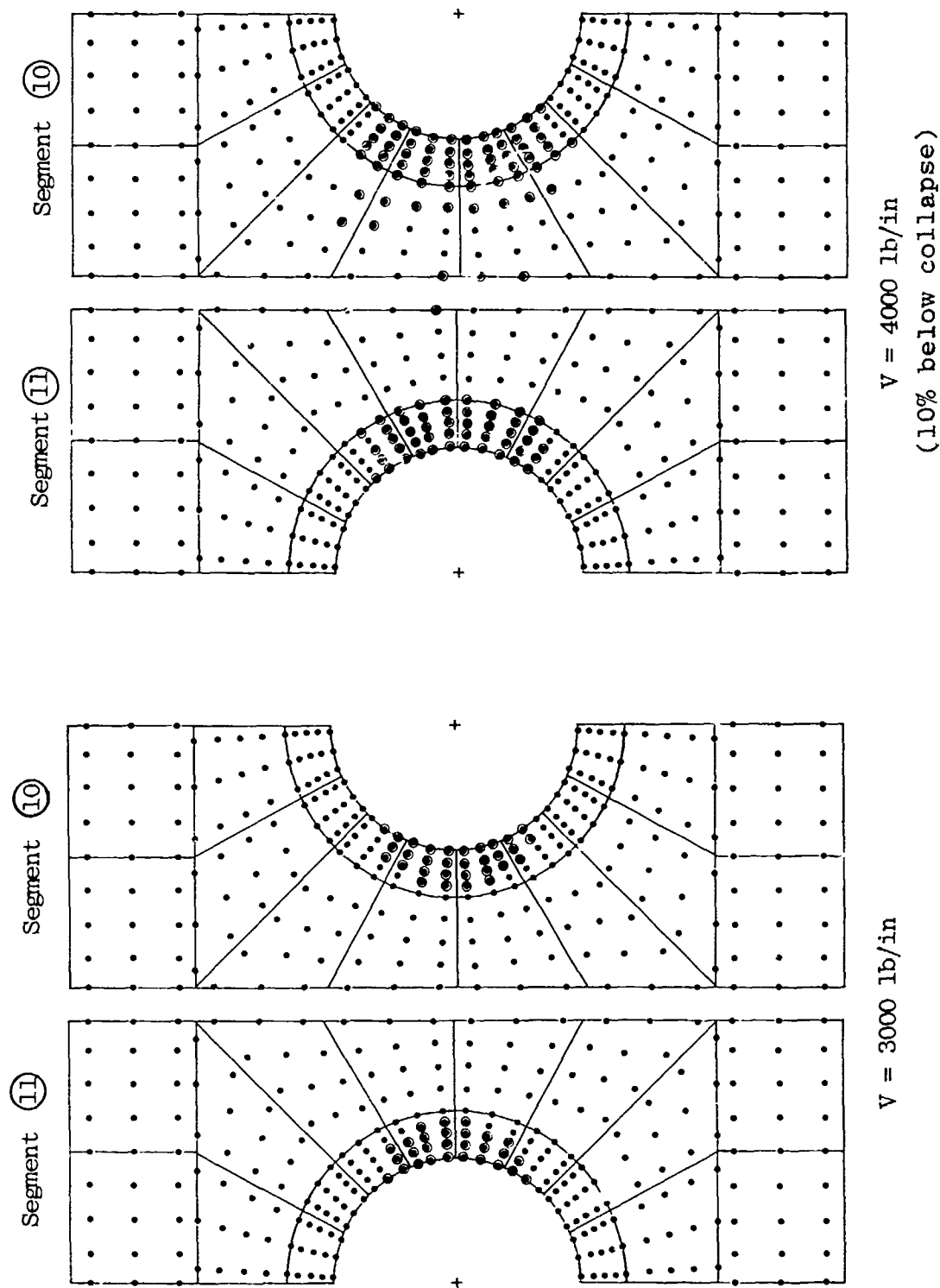


Figure 350(b) Growth of plastified regions near notch roots in the final design.

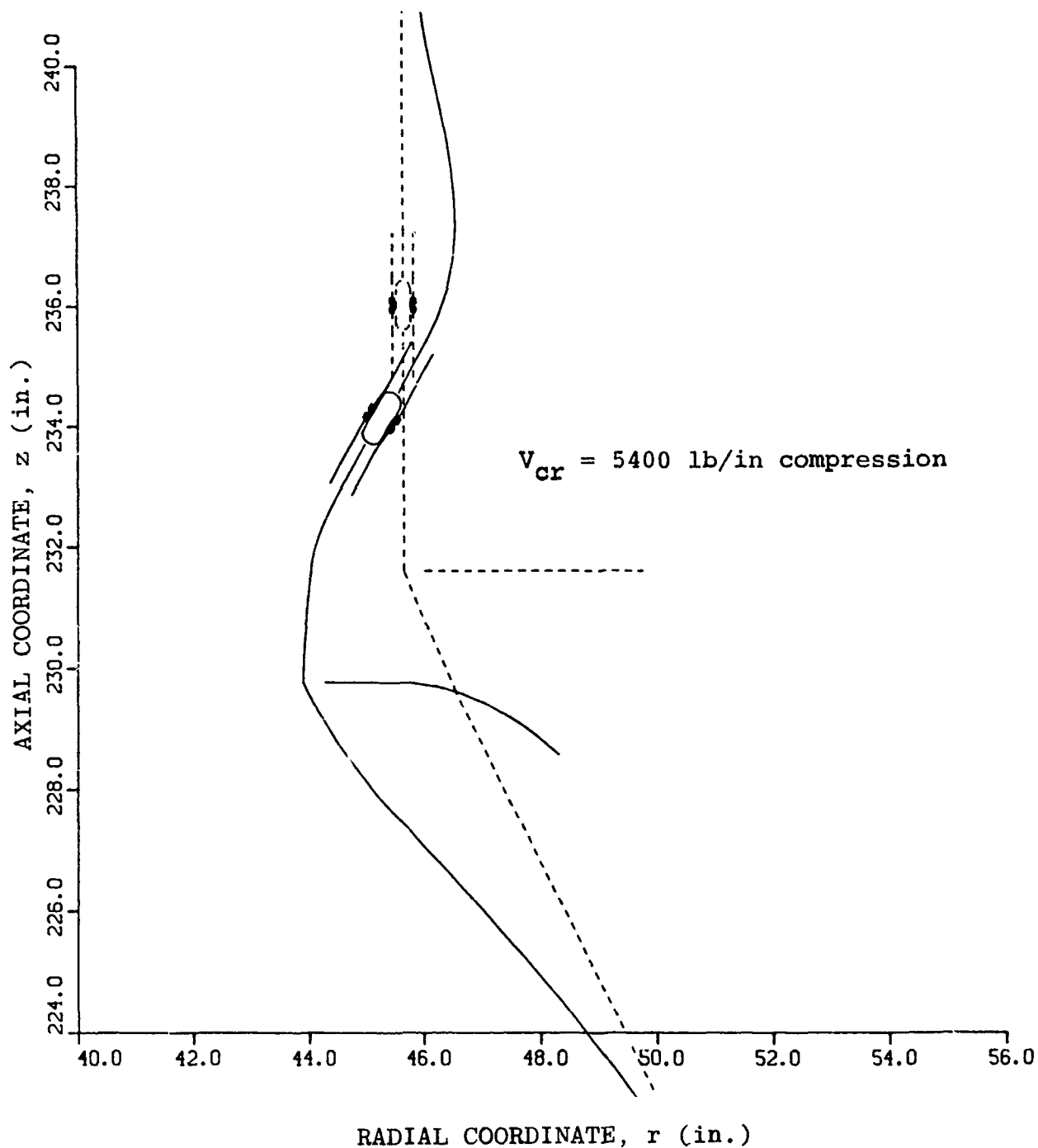


Figure 351 Axisymmetric deformation at collapse load $V_{cr} = 5400 \text{ lbs/in.}$ axial compression of the rocket interstage with the steel primacord tube included in the BOSOR6 model.